Paleoevolution of Pore Fluids in Glaciated Geologic Settings

by

Stefano Delfino Normani

A thesis
presented to the University of Waterloo
in fulfillment of the
thesis requirement for the degree of

Doctor of Philosophy
in
Civil Engineering

Waterloo, Ontario, Canada, 2009

I hereby declare that I am the sole author of this thesis. This is a true copy of the thesis, including any required final revisions, as accepted by my examiners.

I understand that my thesis may be made electronically available to the public.

Abstract

Nuclear power generation is being regarded as a solution to ever increasing demand for electricity, and concerns over global warming and climate change due to the use of fossil fuels. Although nuclear power generation is considered to be reliable, economical, clean, and safe, the wastes produced from the nuclear fuel cycle are not, and can remain hazardous for hundreds of thousands of years. An international consensus has developed over the past several decades that deep geologic disposal of low, intermediate, and high level radioactive wastes is the best option to protect the biosphere.

In this thesis, both regional scale and sub-regional scale models are created to simulate groundwater flow and transport for a representative Canadian Shield setting, honouring site-specific topography and surface water features. Sub-surface characteristics and properties are derived from numerous geoscience studies. In addition, a regional scale model is developed, centred on the Bruce Nuclear Power Development (BNPD) site near Tiverton, Ontario, and located within the Michigan Basin. Ontario Power Generation (OPG) has proposed a Deep Geologic Repository (DGR) for low & intermediate level waste (L&ILW) at the BNPD site.

Paleoclimate simulations using various combinations of parameters are performed for both the Canadian Shield Sub-Regional model, and the Michigan Basin Regional model. Fracture zone permeability is a very important parameter when modelling crystalline rock settings. Migration of a unit tracer representing glacial recharge water can occur to depth in fractures of high permeability. Representative rock compressibility values are necessary as compressibilities are used to calculate storage coefficients, and the one-dimensional loading efficiency; these affect the subsurface propagation of elevated pore pressures due to glacial loading at surface. Coupled density-dependent flow and transport in paleoclimate simulations affects deep flow systems and provides a measure of flow stability, as well as increasing the mean life expectancy at depth. Finally, hydromechanical coupling is a very important mechanism for reducing vertical hydraulic gradients during a glaciation event when a hydraulic boundary condition equal to the pressure at the base of an ice-sheet is applied at ground surface. Pore water velocities are reduced, thereby retarding migration of surface waters into the subsurface environment.

Acknowledgements

I would like to take this opportunity to thank those who have helped me in so many ways during the past six years. It's certainly been a long journey with many ups and downs; I'm quite happy to be at that journey's end!

I would like to thank my supervisor Dr. Jon Sykes for his technical guidance and long discussions related to nuclear fuel waste — an important and timely topic — throughout the duration of this research. I am especially grateful to Jon for enabling me to take a leave of absence from my duties as a Research Engineer at the University of Waterloo in order to devote my time to completing this research. I am also grateful to Jon for the ThinkPad T61p laptop computer upon which much of this thesis has been prepared.

I would like to thank my committee members: Dr. Ed Sudicky, Dr. Neil Thomson, Dr. Bill Annable, and my external examiner, Dr. Kerry MacQuarrie, for their time and suggestions relating to this research.

I would like to thank Mark Jensen, André Vorauer and Ben Belfadhel of the Nuclear Waste Management Organization (NWMO) for their insights, their financial support, and for the opportunity to explore and to be a part of developing the next generation of numerical tools and techniques for site characterization.

I would like to thank Dr. Young-Jin Park and Rob McLaren for their sense of humour, expertise, patience, and guidance in all matters relating to FRAC3DVS, and FRAC3DVS-OPG. I also thank Yong Yin for his assistance with FRAC3DVS-OPG. Portions of this work were made possible by the facilities of the Shared Hierarchical Academic Research Computing Network (SHARCNET) `www.sharcnet.ca`.

Finally, I would like to thank my family and friends for their patience, love, belief, support, and tireless encouragement — I couldn't have done it without you!

Table of Contents

List of Tables

List of Illustrations

List of Symbols

Greek

Latin

List of Abbreviations

3DGF	3D geologic framework
AECB	Atomic Energy Control Board
AECL	Atomic Energy of Canada Limited
APM	Adaptive Phased Management
ARIUS	Association for Regional and International Underground Storage
ASCII	American Standard Code for Information Interchange
BIT	backward-in-time
BLAS	Basic Linear Algebra Subprograms
BMT	benchmark test
BMT3	Bench Mark Test 3
BNPD	Bruce Nuclear Power Development
CANDU	CANadian Deuterium Uranium
CDF	cumulative density function
CNA	Canadian Nuclear Association
CNSC	Canadian Nuclear Safety Commission
DECOVALEX	DEvelopment of COupled THM models and their VALidation against EXperiments
DEM	digital elevation model
DGR	Deep Geologic Repository
DTHMC	DECOVALEX-THMC
EC	European Commission
EIS	Environmental Impact Statement
EPM	equivalent porous medium
EU	European Union
FNM	fracture network model
FRAC3DVS	FRACtured 3D Variably Saturated
FRAC3DVS-OPG	FRACtured 3D Variably Saturated – OPG
FZ	fracture zone

GIS	geographic information system
GMWL	global meteoric water line
GSM	Glacial Systems Model
HFC	hydrofluorocarbon
HGS	HydroGeoSphere
HRL	Hard Rock Laboratory
IAEA	International Atomic Energy Agency
L&ILW	low & intermediate level waste
LCC	Lambert conformal conic
LGM	last glacial maximum
MA	mean age
MBR	Michigan Basin Regional
MFR	moderately fractured rock
MIN3P	multicomponent reactive transport model
MLE	mean life expectancy
MOTIF	Model Of Transport In Fractured/porous media
NAPL	National Air Photo Library
NEA	Nuclear Energy Agency
NFWA	Nuclear Fuel Waste Act
NOAA	National Oceanic and Atmospheric Administration
NRCAN	Natural Resources Canada
NTS	National Topographic System
NWMO	Nuclear Waste Management Organization
OGS	Ontario Geological Survey
OGSR	Oil, Gas and Salt Resources Library
OPG	Ontario Power Generation
PDF	probability density function
PFC	perfluorocarbon
RAC	recharge area concept
RAM	random access memory
RHEL	Red Hat Enterprise Linux
RSA	regional study area
SAPIERR	Strategic Action Plan for Implementation of European Regional Repositories
SCS	Second Case Study
SFR	sparsely fractured rock
SHARCNET	Shared Hierarchical Academic Research Computing Network
SKB	Svensk Kärnbränslehantering AB
SMOW	standard mean ocean water
SRTM	Shuttle Radar Topography Mission

SUTRA	Saturated-Unsaturated Finite-Element Transport Model
SWIFT-II	Sandia Waste-Isolation Flow and Transport
SWIFT-III	Sandia Waste-Isolation Flow and Transport
TC	test cases
TDS	total dissolved solids
THM	thermohydromechanical
TIN	triangulated irregular network
UN	United Nations
UofT	University of Toronto
URL	Underground Research Laboratory
USD	uranium series disequilibria
USGS	United States Geological Survey
VBA	Visual Basic for Applications
WNA	World Nuclear Association
WRA	Whiteshell Research Area
WWMF	Western Waste Management Facility

Chapter 1

Introduction

Every society on Earth requires energy to function, to grow, and to maintain their standard of living; the more developed nations are the greatest consumers of energy on a per-capita basis. Energy in the form of electricity is important, and can be generated from many sources including hydro-electric, wind, solar, uranium, and fossil fuels such as coal, oil, or natural gas. The burning of fossil fuels or the fission reactions of uranium produce heat, vaporizing water into steam; the steam passes through large turbines connected to generators, thereby generating electricity.

Increasing concern about global warming and climate change lead to the Kyoto Protocol during the late 1990's which aimed to reduce global emissions of six man-made greenhouse gases — carbon dioxide (CO_2), methane (CH_4), nitrous oxide (N_2O), hydrofluorocarbons (HFCs), perfluorocarbons (PFCs) and sulphur hexafluoride (SF_6) — within participating nations to 6% below their collective 1990 emissions levels (*UN*, 1998). Fossil fuels such as oil, natural gas, and coal are primarily to blame for emissions of carbon dioxide, and are used for 66.6% of current global electricity generation (*CNA*, 2008). Although nuclear power does not contribute to greenhouse gas emissions, smog, or acid rain, the used nuclear fuel from powering nuclear reactors is very toxic and remains so for more than 100 000 years (100 ka) (*NWMO*, 2003a).

1.1 Nuclear Power Generation

In 2007, 60.1% of the electricity generated in Canada came from hydroelectric sources, 14.6% was produced by CANadian Deuterium Uranium (CANDU) nuclear reactors,

and 24.7% was produced from fossil fuels (*CNA*, 2008). Nuclear power generation in Ontario accounted for 51% of Ontario's generating capacity and 91.6% of Canada's nuclear generating capacity in 2007 (*CNA*, 2008). According to the *CNA* (2008), 22 CANDU nuclear reactors are located in Canada, of which 20 are located in Ontario, 1 in Québec and 1 in New Brunswick. The Government of Ontario recently announced their 20 year energy plan, whereby new nuclear reactors will replace aging units to maintain existing nuclear generating capacity at 14 000 MWe, while eliminating coal-fired generation by 2014 (*Government of Ontario*, 2008). Bruce Power, which currently operates reactors at the Bruce Nuclear Power Development (BNPD) in the municipality of Kincardine, Ontario, is currently studying the feasibility of building nuclear reactors in northern Alberta to provide power, steam, and hydrogen generation for the oil refining process and the production of synthetic crude oil. Hydrogen can be produced by steam reforming of natural gas, or by high temperature electrolysis of water, to produce oxygen and heavy water (*WNA*, 2008b). According to *WNA* (2008a), 3 reactors are planned and 4 reactors are proposed for Canada.

For CANDU reactors, nuclear fuel in the form of uranium dioxide (UO_2) ceramic pellets are placed inside a zirconium alloy tube of approximately 0.5 m in length. Up to 37 of these tubes are welded together to form a fuel bundle. Each fuel bundle produces about 1 000 000 kW·h of electricity, with an in-service life of 12 to 18 months. Nuclear fission produces heat and new unstable atoms which radioactively decay. In Canada, wastes from nuclear activities are classified into three categories, depending on their level of radioactivity: low, intermediate, and high.

1.2 Low & Intermediate Level Radioactive Waste

According to the (*CNA*, 2009), low-level waste contains small amounts of radioactivity, and in the case of hospital nuclear medicine, these wastes typically have short half-lives. Low-level wastes also include various items (tools, cleaning materials, and clothing) from nuclear medicine, research laboratories, and nuclear power plants that have become slightly contaminated with radioactivity. Intermediate-level waste typically includes used nuclear reactor parts, and ion-exchange resins and filters from the cooling system of a nuclear power plant, where reactor water systems are purified; these wastes contain a higher level of radioactivity than low-level wastes. Whereas low-level wastes do not require special protection and shielding for workers, intermediate-level wastes do.

Low and intermediate-level wastes are stored in shielded containers on-site at nuclear power plants in Québec and New Brunswick. In Ontario, all low and intermediate-level wastes from nuclear power plants in the province are transported to the Western Waste Management Facility (WWMF) at the BNPD site in the Municipality of Kincardine, Ontario, where they are stored in shielded containers (*CNSC*, 2009a).

1.3 High Level Radioactive Waste

Used fuel bundles are classified as high level radioactive waste due to their high levels of radioactivity, and contain approximately 350 types of atoms, of which 200 are radioactive and can remain so for many hundreds of thousands of years (*NWMO*, 2003a). Approximately 85 000 used fuel bundles are produced in Canada each year, and by the end of

2001, Canada had accumulated approximately 1.6 million fuel bundles, of which 89% were produced in Ontario. It is estimated that a total of 3.6 million fuel bundles will be produced by the year 2033 (*NWMO*, 2003a).

Once removed from a reactor, the used fuel bundles are placed in water-filled pools to be cooled and to provide a shield from radiation for a period of 7 to 10 years. The bundles are then removed and placed in dry storage (*NWMO*, 2003b). Dry storage is considered a short-term solution, while a longer-term disposal solution is developed. Although current storage methods are considered safe, they require continual institutional controls such as security measures, monitoring, and maintenance. The Atomic Energy Control Board (AECB)[1] prefers a disposal method in which "there is no intention of retrieval and which, ideally, [uses] techniques and designs that do not rely for their success on long-term institutional control beyond a reasonable period of time." The *AECB* (1987) also requires that the "burden on future generations be minimized by: (a) selecting disposal options for radioactive wastes, which to the extent reasonably achievable, do not rely on long-term institutional controls as a necessary safety feature; (b) implementing these disposal options at an appropriate time, technical, social and economic factors being taken into account; and (c) ensuring that there are no predicted future risks to human health and the environment that would not be currently accepted."

The resulting conclusion is that *deep geologic disposal* is the preferred alternative for long-term disposal of nuclear fuel waste in Canada. A Deep Geologic Repository (DGR) for the long-term storage of low and intermediate-level radioactive waste has been proposed by Ontario Power Generation on lands adjacent to the WWMF at the BNPD site in the Municipality of Kincardine, Ontario (*OPG*, 2008).

An international consensus has also developed stating that deep geologic disposal of low, intermediate, and high-level radioactive wastes is the best option to protect the biosphere over hundreds of thousands of years. According to the World Nuclear Association, 439 operable nuclear reactors are located in 30 countries plus Taiwan, 36 reactors are under construction, 97 reactors are being planned, and 221 reactors are proposed (*WNA*, 2008a). The countries of Canada, Finland, France, Germany, India, Japan, South Korea, Russia, Sweden, Switzerland, the United Kingdom, and the United States are either planning nuclear fuel waste repositories, or have performed detailed site characterization studies consisting of borehole exploration or the construction of underground research laboratories or both (*NWMO*, 2005).

1.4 Nuclear Waste Management

In 2002 the Government of Canada passed Bill C-27, the Nuclear Fuel Waste Act (NFWA); electricity generating companies which produce nuclear fuel waste were required to establish a waste management organization to provide recommendations to the Government of Canada on the long-term management of used nuclear fuel. The Nuclear Waste Management Organization (NWMO) was formed in 2002 by Ontario Power Generation, Hydro-Québec and New Brunswick Power Corporation in accordance with the NFWA. For the next three years, the NWMO studied various approaches for the disposal of

[1] The AECB was replaced by the Canadian Nuclear Safety Commission (CNSC) with the passage, by the Parliament of Canada, of the *Nuclear Safety and Control Act* in 1997 to better reflect current regulatory priorities and mandates. The act came into force on 31 May 2000 (*CNSC*, 2009b).

used nuclear fuel, and presented its recommendation in *Choosing a Way Forward, The Future Management of Canada's Used Nuclear Fuel – Final Study* (*NWMO*, 2005). The Adaptive Phased Management (APM) recommendation of the NWMO includes "centralized containment and isolation of used nuclear fuel deep underground in suitable rock formations," and is consistent with the earlier AECB preferred alternative. A further requirement of the NFWA is that nuclear fuel waste owners are required to establish segregated trust funds to finance the long-term management of the used fuel, beginning in 2002.

1.5 Deep Geologic Disposal Concept

Prior to the implementation of the NFWA, the concept for disposal of used nuclear fuel in Canada involved sealing the waste in corrosion-resistant containers. The containers were to be emplaced and sealed within a deep geologic repository located in plutonic rock of the Canadian Shield at a depth of 500 m to 1000 m. According to *AECL* (1994), container failure would eventually occur, leading to the release of radionuclides, which are then transported to the biosphere through groundwater pathways. The *NWMO* (2005) has since expanded the deep geologic disposal concept to include suitable sedimentary basins as well as crystalline rock. As a result, groundwater flow system behaviour and flow rates within fractured crystalline rock settings or sedimentary rock settings are important considerations for repository siting and site characterization, as well as the assessment of long-term repository safety and performance.

The technical feasibility of the used nuclear fuel disposal concept for Canada, and its impact on the environment and human health, were presented in an Environmental Impact Statement (EIS) (*AECL*, 1994; *Davison et al.*, 1994). The Second Case Study (SCS) expanded upon the EIS by investigating the long-term effects of a hypothetical repository in a permeable host-rock geologic setting (*Stanchell et al.*, 1996). Repositories are ideally located in hydraulically favourable settings within the large-scale groundwater flow system of a proposed site. In such a setting, the engineering of the repository would be adapted to the on-site lithological, hydrogeological, geochemical, geothermal, geomechanical, and geomicrobiological conditions of the host rock formation (*Stanchell et al.*, 1996).

Long-term climate change is another factor which can influence the safety and performance of a repository, particularly the occurrence of peri-glacial and glacial conditions that would change thermal, mechanical, and hydraulic boundary conditions imposed on a geosphere over a period of 10 ka to 100 ka (*Peltier*, 2002). Such climate change will also influence the behaviour and evolution of saline pore fluids. The density of such fluids at depth is a contributing factor to long residence times in deep geologic settings, which act to limit or mitigate radionuclide transport from a nuclear fuel waste repository. Evidence of such long residence times was found through hydrogeochemical analysis of pore fluids (below 500 m depth) from the Lac du Bonnet batholith at the Atomic Energy of Canada Limited (AECL) Whiteshell Research Area (WRA) in southeastern Manitoba. These pore fluids show evidence of pre-glacial warm-climate waters with residence times greater than 1.0 Ma (*Gascoyne*, 2004).

1.6 Research Objectives

This objectives of this research are to investigate the following:

- Paleoclimate episodes and the resulting boundary conditions will affect the movement and timing of surface waters to depth, as indicated by using a unit tracer applied as a Cauchy boundary condition to the top of the modelling domain.
- Rock compressibilities and their application in the calculation of storage coefficients and the one-dimensional loading efficiency in hydromechanical coupling. High rock compressibilities lead to high storage coefficients which will retain some elevated pressures caused by glacial loading. High compressibilities lead to high loading efficiencies, reduced vertical gradients, and reduced vertical movement of a unit tracer.
- Fracture permeability distribution with depth affects the mobility of pore fluids. High permeability at depth allows surface waters to migrate to the bottom of the modelling domain, reducing total dissolved solids (TDS) concentrations and enhanced movement to depth of a unit tracer.
- Coupled density-dependent flow and transport will reduce the mobility of freshwater at surface to migrate to depth, since pore waters at depth have a density 20% greater than freshwater. The movement of a unit tracer subject to density-dependent flow and transport will be less than for a freshwater flow system.

The numerical models FRAC3DVS, and FRAC3DVS-OPG are an essential component of this research. These models contain the necessary physics to simulate dual-continuum, coupled density-dependent groundwater flow systems and will be used the test the hypotheses presented above. Any required processes or physics that are not in these models and are necessary to complete this research will be added to these models and will be described in this thesis.

1.7 Research Scope

Prior modelling efforts in a Canadian Shield setting were limited to areas of approximately 700 km^2 over a 10 ka period. This research extends the regional modelling domain over a much larger area of 5734 km^2 with a finer grid resolution. All computer simulations using finite element or finite difference schemes are limited by the capability of the hardware and software to perform the required calculations in a timely manner. Computing power typically doubles every 18 months and since approximately 15 years have passed since the earlier *AECL* (1994) studies, computing power has increased nearly three orders of magnitude in that time. Transient simulations of greater length are now feasible with 100 ka or even 1 Ma simulations being commonly investigated. Paleoclimate itself is no longer simulated in steady-state snapshots, but rather numerical simulations on a continental scale, such as the work of *Peltier* (2002, 2003, 2004) which can now be incorporated as boundary conditions into long-term geosphere groundwater flow and transport simulations. The ability to characterize fracture zone networks, based on the work of *Srivastava* (2002), can now be incorporated into these simulations. Numerous field programs including the AECL Underground Research Laboratory (URL) in Canada and the various geoscience research programs in Sweden and Finland provide matrix and fracture zone properties that can be included in geosphere modelling efforts.

The scope of this research is to investigate the behaviour and evolution of pore fluids in deep geologic settings by imposing paleoclimate boundary conditions from *Peltier* (2002, 2003, 2004) at both the sub-regional scale for a representative Canadian Shield site, and at a regional scale for a sedimentary site in the Michigan Basin, related to Ontario Power Generation (OPG)'s proposed Deep Geologic Repository for low and intermediate-level radioactive waste (*Peltier*, 2008; *OPG*, 2008). The sub-regional scale will incorporate a fracture zone characterization provided by *Srivastava* (2002), along with fracture zone properties inferred from the Canadian and Finnish geoscience programs. The role of mechanical coupling is also investigated in crystalline and sedimentary rock settings since glaciation imparts a significant transient mechanical load onto the geosphere.

Numerical simulations are an integral part of this research as they provide a physically based link, through time and space, between in-situ measurements of pore fluid hydrogeochemistry; hydrologic, topographic, or geologic features; and the underlying bulk physical and chemical interaction mechanisms. Spatial and temporal relationships are explored in the context of numerical simulations, and may provide supporting evidence for how and why deep pore fluids have ages greater than 1.0 Ma. This work encompasses a wider range of model parameters, and physical processes, than were implemented in either of the earlier EIS or SCS geosphere modelling studies (*Davison et al.*, 1994; *Stanchell et al.*, 1996).

1.8 Chapter Overview

Chapter 2 provides a brief review of geosphere characteristics pertaining to the Canadian Shield and Michigan Basin, along with pore fluid bulk characteristics. A review of Canadian and international geosphere modelling studies is presented. Several geosphere numerical models applied in the Canadian geosphere modelling studies are described, along with the governing equations for fluid flow, solute transport, hydromechanical coupling, and groundwater mean age and mean life expectancy. The effects of climate change and glaciation, along with the significance of glacial meltwater are presented. Finally, the recharge area concept is introduced, and the importance of using environmental heads in variably dense groundwater flow systems is discussed.

Chapter 3 introduces the reader to the development of a regional scale (5734 km^2) flow and transport model in a representative Canadian Shield setting. The development of this regional scale model in both SWIFT-III and FRAC3DVS are discussed, along with a detailed description of the multi-simulation comparison, between these numerical models, that was undertaken to demonstrate the suitability of using FRAC3DVS to simulate coupled density-dependent flow and transport processes in deep geologic settings.

From the regional scale model in Chapter 3, a sub-region was extracted to create a sub-regional scale model of 84 km^2. Software was developed to embed a fracture network model (FNM) developed by *Srivastava* (2002) into a FRAC3DVS hexahedral mesh. As part of a Phase–II model development, a slightly larger second sub-regional model was created (104 km^2), along with a new means to calculate fracture zone permeability as a function of depth. Fracture zone porosity and width are also treated as non-uniform parameters. Paleoclimate simulations are then presented, including spatial discretization, paleoclimate boundary conditions, and model properties. A total of seven paleoclimate simulations were performed to investigate the role of alternate glaciation scenarios from

the University of Toronto Glacial Systems Model, the role of high TDS pore fluids at depth, the effect of uniform fracture zone permeability, the role of the hydromechanical one-dimensional loading efficiency, and finally, a scenario that ignores density coupling, uses uniform fracture zone permeabilities, and ignores hydromechanical coupling. Environmental heads, TDS distributions, pore water velocity magnitudes, the movement of a tracer representing glacial meltwater, and groundwater mean life expectancy are used to characterize the impact of parameter changes on the various sub-regional paleoclimate scenarios.

The development of a sedimentary rock regional scale model encompassing 18775 km^2 within the Michigan Basin is discussed in Chapter 5. The development includes a description of the geology and the three-dimensional geologic framework model (*Frizzell et al.*, 2008). The conceptual model is then presented, along with the spatial discretization, paleoclimate boundary conditions, and model properties. Finally, four paleoclimate simulations were performed to investigate the role of the hydromechanical one-dimensional loading efficiency, and the use of literature compressibility values upon TDS distributions, the movement of a tracer representing glacial meltwater, and groundwater mean life expectancy.

Numerous figures representing freshwater heads, environmental heads, pore water velocities, the ratio of vertical pore water velocity to pore water velocity magnitude, brine concentrations, glacial meltwater tracer concentrations, and mean life expectancy at various times during the paleoclimate simulations are provided in Appendix A to Appendix G for the Canadian Shield Sub-Regional paleoclimate simulations discussed in Chapter 4. Appendix H to Appendix K contain figures for the Michigan Basin Regional paleoclimate simulations discussed in Chapter 5.

Finally, the conclusions and research contributions resulting from this thesis are presented in Chapter 6.

Chapter 2

Background

The following sections provide background information on the geosphere, paleoclimate and the effects of glaciation, and the governing mathematical equations describing the physics of groundwater flow, solute transport in porous media, and hydromechanical coupling. Various numerical models commonly employed in geosphere modelling are described.

2.1 Characterizing the Geosphere

The geosphere is characterized by the rock surrounding a deep geologic repository, any sediments that overly the rock, and any groundwater within the sediment or rock pores. The deep geologic repository system requires that the geosphere protects the waste form, container, and engineered repository seals from human intrusion and natural disruptions; maintains conditions in the repository which are favourable for long-term waste isolation; and limits the rate at which contaminants from the waste could move from the repository to the biosphere through groundwater pathways (*Davison et al.*, 1994).

The *AECB* (1987) states that a nuclear waste disposal facility "should be located in a region that is geologically stable and likely to remain stable." A geologically stable region would enhance the protective function of the geosphere as well as the long-term predictability of conditions in the repository.

2.1.1 Hydrogeochemistry

In paleohydrology studies, the isotopic composition of groundwater can be used to determine its origin, and the temperature conditions that must have existed at that time. Precipitation at higher latitudes is associated with a depletion of the heavier isotopes, and can be correlated with lower temperatures. Deuterium (^{2}H) and oxygen-18 (^{18}O) compositions of water are commonly measured with respect to the standard mean ocean water (SMOW) standard (*Domenico and Schwartz*, 1990). Since both ^{2}H and ^{18}O are heavier isotopes of hydrogen and oxygen, respectively, the evaporation and condensation processes of the hydrologic cycle will affect the isotopic ratios of ^{2}H/^{1}H and ^{18}O/^{16}O. The depletion or enrichment of a particular isotope is stated as a deviation from a standard as follows:

$$\delta = \frac{R_{\text{sample}} - R_{\text{standard}}}{R_{\text{standard}}} \times 1000 \tag{2.1}$$

where δ is reported in permil (‰), and R is the isotope ratio for either the sample or standard. A δ^{18}O value of −20‰ means that the sample is depleted in ^{18}O relative to the standard by −20‰ or −2% (*Domenico and Schwartz*, 1990).

2.1.2 The Canadian Shield

Plutonic rock, which forms much of the Canadian Shield, is known to be seismically stable, has great areal extent thereby affording many siting options, and occurs in regions of low topographic relief where the driving force for groundwater movement is likely to be low (*Davison et al.*, 1994). The Canadian Shield is subdivided into major units called provinces or orogens based on structure, history of deformation, and estimated age of formation. The largest exposure of Archean rock on Earth, at more than 2.5 Ga in age, occurs within the Superior Province of the Canadian Shield, and consists of east-west trending belts of metavolcanic, metasedimentary, and plutonic rock. It comprises most of Ontario and was formed between 3.1 Ga and 2.7 Ga ago. The last major deformation occurred around 2.5 Ga ago, however, the rock was repeatedly faulted and locally intruded during the Proterozoic period of 2.5 Ga to 570 Ma ago (*Davison et al.*, 1994). The extent of the Canadian Shield across North America is shown in Figure 2.1; the Canadian Shield is characterized by rocks of Proterozoic and Archean age.

The rock is characterized by *Davison et al.* (1994) into three domains, based on the spacing and frequency of open fractures:

Fracture zone (FZ) A region of intensely fractured rock;

Moderately fractured rock (MFR) A region of rock containing a small number of relatively widely spaced discrete open fractures; and

Sparsely fractured rock (SFR) A region of rock containing microcracks and very sparsely distributed open fractures that, as a rule, are not interconnected.

The interconnectivity of fractures, especially the more permeable fracture zones, are the major structural features that govern groundwater flow in plutonic rock settings. Characterizing such features is an important step in repository siting. An equivalent porous medium (EPM) approach for the three rock domains is used when developing the geosphere conceptual model. The EPM approach uses a porous medium that provides equivalent hydraulic characteristics including bulk permeability, and porosity as the

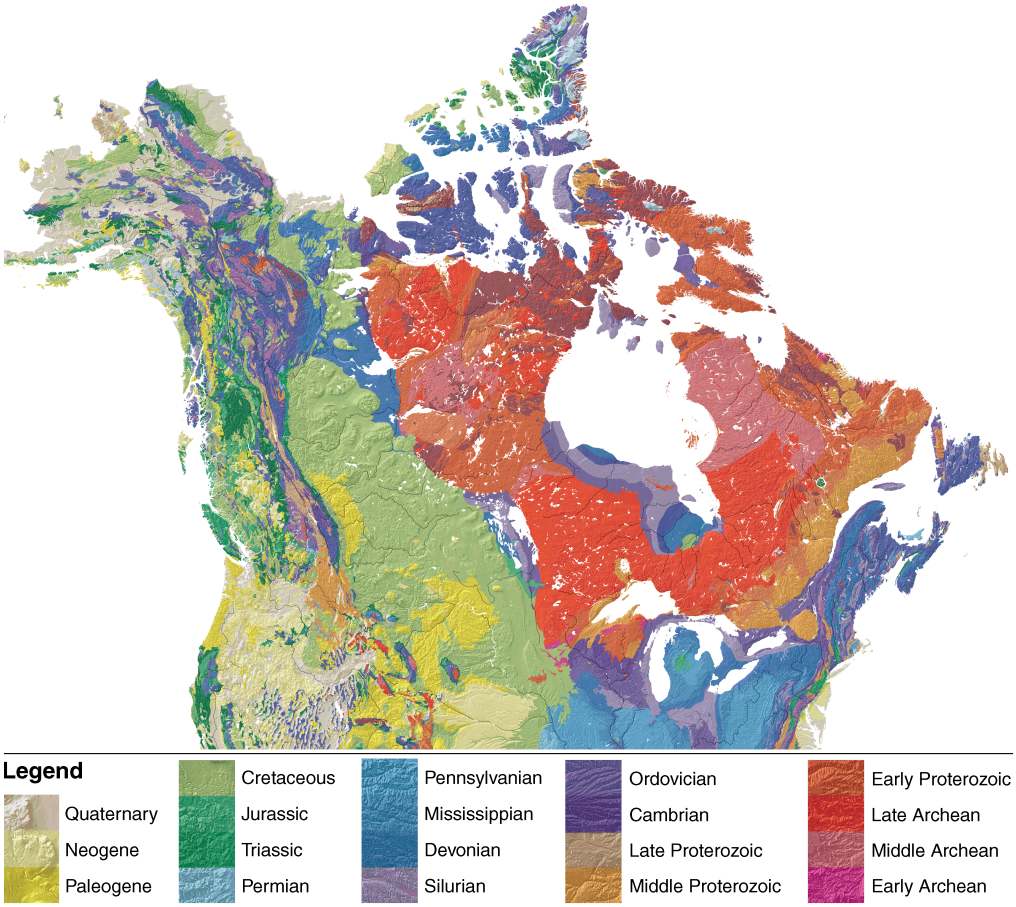

Figure 2.1 Spatial extent of the Canadian Shield in North America, ranging in age from Proterozoic to Archean. Geologic map is coloured by geologic age (Quaternary to Archean). Adapted from geologic map courtesy of the U.S. Geological Survey (*Barton et al.*, 2003).

source fractured rock mass. This is achieved by using anisotropic permeability values, where necessary, as well as correctly orienting the permeability tensor principal axes.

The salinity of groundwater generally increases with increasing depth in plutonic rock on the Canadian Shield. The highly saline pore fluids can have TDS concentrations up to 300 g/L (*Bottomley et al.*, 2002; *Frape and Fritz*, 1987). Two main theories have been postulated to explain the presence of the high TDS groundwaters in the deeper rock: (1) salinity may have originated from groundwater recharge during episodes of marine intrusion, or (2) the salinity may be a result of rock-water interactions (*Bottomley et al.*, 2002, 2003; *Frape and Fritz*, 1987). The first theory implies that sufficiently permeable fractures or pathways exist in the host rock to allow the migration of saline surface waters to depth, while the second theory implies a relatively impermeable rock mass that provides sufficient time for rock-water interactions to take place at depth (*Bottomley et al.*, 2003; *Frape and Fritz*, 1987). As an example of the former, the Con Mine studies near Yellowknife, of *Bottomley et al.* (2002, 2003) provide ^{129}I evidence of a marine origin for deep brines. *Bottomley et al.* (2003) further proposes that the Sudbury/Elliot Lake brines are also of a marine origin, although perhaps by a different mechanism than the Con Mine brines; the Sudbury/Elliot Lake brines could have been formed either by the

evaporation or freezing of sea water. Subsequent infiltration of evaporatively concentrated marine brines may have occurred during the episodes of seawater intrusion.

Clark et al. (2000) uses ^{2}H and ^{18}O to investigate the origin of groundwaters at the Con Mine in Yellowknife, Canada. Three (3) groundwaters are identified: a modern meteoric groundwater at $\delta^{18}O = -18.9 \pm 0.1‰$, a brine at $\delta^{18}O \approx -10‰$, and a water at $\delta^{18}O \approx -28‰$; this last isotopically depleted groundwater, relative to modern meteoric water, is likely meltwater from the retreating Laurentide Ice-sheet, and is indicative of precipitation at cold temperatures. This glacial meltwater was presumed to exist because groundwater data does not plot on a simple two-component mixing line between the high salinity brine ($Cl^- = 230\,g/L$) and meteoric water ($Cl^- < 10\,mg/L$). All groundwater of intermediate salinity plotted left of the binary mixing line, indicating the existence of glacial meltwater at depth; including depths of 1370 m (4500 level) or greater, being mindful that shallower waters could have migrated to these depths due to mine related activities. *Clark et al.* (2000) also uses the groundwater model SWIFT-II (precursor to SWIFT-III which is discussed in §2.3.2) to impose high hydraulic gradients to illustrate a mechanism by which the glacial meltwaters could have entered the site, however, this analysis does not include hydromechanical coupling which can increase insitu pore pressures, thereby decreasing imposed gradients. *Talbot* (1999), *Clark et al.* (2000), and *Person et al.* (2007) state that glacial meltwater can migrate to great depths, which can also lead to pore pressures in excess of lithostatic pressure, resulting in surface blow-outs, and the hydraulic lifting of large blocks of rock at depths of 500–1000 m.

Hydrogeochemical analysis of pore fluids from the Lac du Bonnet batholith at the WRA in southeastern Manitoba indicates three flow regimes: a fast near surface (< 200 m depth) groundwater flow regime with residence times of tens to hundreds of years; an intermediate zone (200 m to 500 m depth) showing evidence of glacial meltwater having residence times of 1 ka to 100 ka; and a deeper groundwater flow regime (> 500 m depth) showing evidence of pre-glacial warm-climate waters with residence times greater than 1 Ma (*Gascoyne*, 2004).

Anomalously high environmental heads (see §2.7) have been observed in some SFR test intervals at the WRA. These high heads provide supporting evidence for a very low SFR permeability, indicating that pore fluids are largely stagnant over periods of more than 1 Ma (*Sykes et al.*, 2003a).

2.1.3 The Michigan Basin

The Michigan Basin, shown in Figure 2.2, is a nearly circular deep intracratonic basin approximately 400 km in diameter and 5 km deep (*Howell and van der Pluijm*, 1999; *Chernicoff et al.*, 2002). Subsidence within the Michigan Basin resulted in approximately 5 km of sedimentation over a period of more than 200 Ma during the Paleozoic. According to *Howell and van der Pluijm* (1999), a definitive origin for the subsidence has not yet been found, although various mechanisms have been proposed. The northern edge of the basin rim represents the interface between the depositionally continuous Paleozoic sediments and the underlying Precambrian rocks (*Stonehouse*, 1969). The eastern limit of the Michigan Basin is defined by the Algonquin Arch, which separates the Michigan Basin from the Appalachian Basin to the southeast. The Algonquin Arch is a feature in the crystalline basement rock of the Precambrian and ranges in elevation from approximately 200–300 m where it outcrops, towards the northeast, to −1000 m at the Chatham Sag;

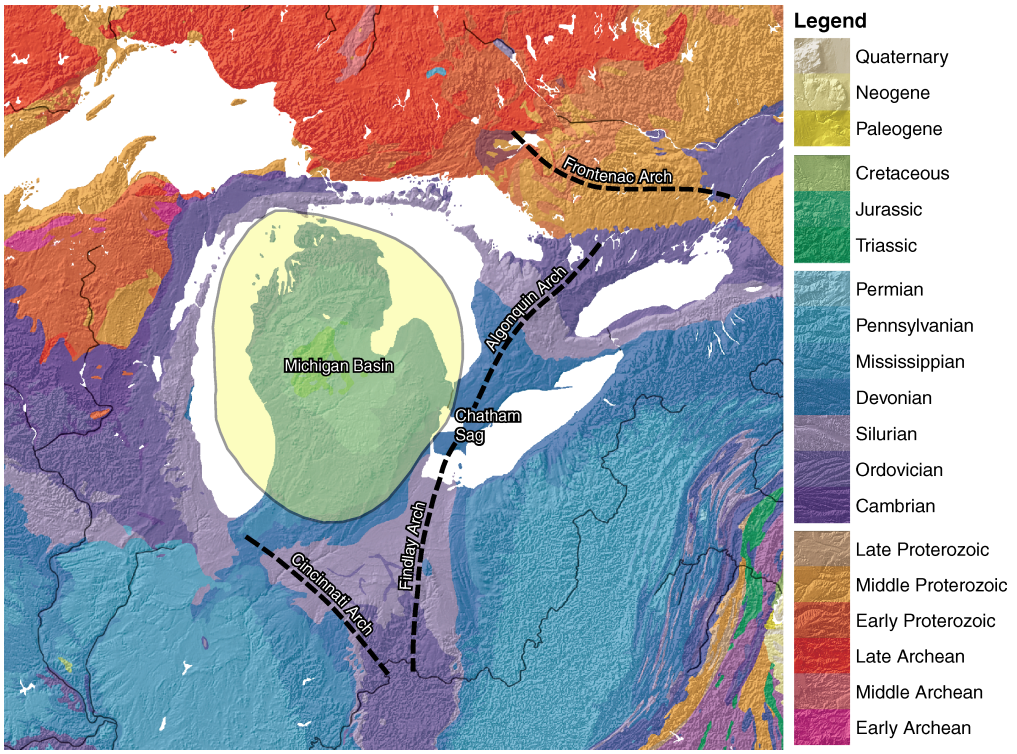

Figure 2.2 Spatial extent of the Michigan Basin and locations of the Frontenac Arch, Algonquin Arch, Chatham Sag, Findlay Arch, and Cincinnati Arch. Geologic map is coloured by geologic age (Quaternary to Archean). Adapted from geologic map courtesy of the United States Geological Survey (*Barton et al.*, 2003).

the Findlay Arch represents the southwest continuation of the Algonquin Arch, also separating the Michigan Basin from the Appalachian Basin (*Carter et al.*, 1996; *Mazurek*, 2004).

The Algonquin Arch essentially divides southwestern Ontario into two megablocks: the Bruce Megablock to the northwest, and the Niagara Megablock to the southeast (*Sanford et al.*, 1985). The Niagara Megablock is characterized by intersection fracture lineaments that act as oil and gas traps (*Carter et al.*, 1996); the Bruce Megablock has a less dense fracture pattern, as conceptualized by *Sanford et al.* (1985). Due to the economic value of oil and natural gas, extensive exploration has taken place in southwestern Ontario, and throughout Michigan to locate reserves. Although exploratory boreholes have been drilled in the Bruce Megablock, few wells have intersected oil or gas plays. An extensive database of boreholes and wells is retained by the Oil, Gas and Salt Resources Library (OGSR); a resource centre for the study of the subsurface geology; and oil, gas, salt and underground hydrocarbon storage resources of Ontario. A map showing borehole locations of the OGSR database is shown in Figure 2.3; the number of boreholes in the Niagara Megablock greatly exceeds those in the Bruce Megablock.

According to *Sanford et al.* (1985) and *Carter et al.* (1996), vertical offsets at faults are required to explain reserves of trapped oil and gas. These offsets prevent lateral flow and interrupt the continuity of the various formations that comprise the Michigan Basin. Such discontinuities are important in limiting the connectivity of high permeability units that can connect near surface groundwater flow systems to much deeper groundwater

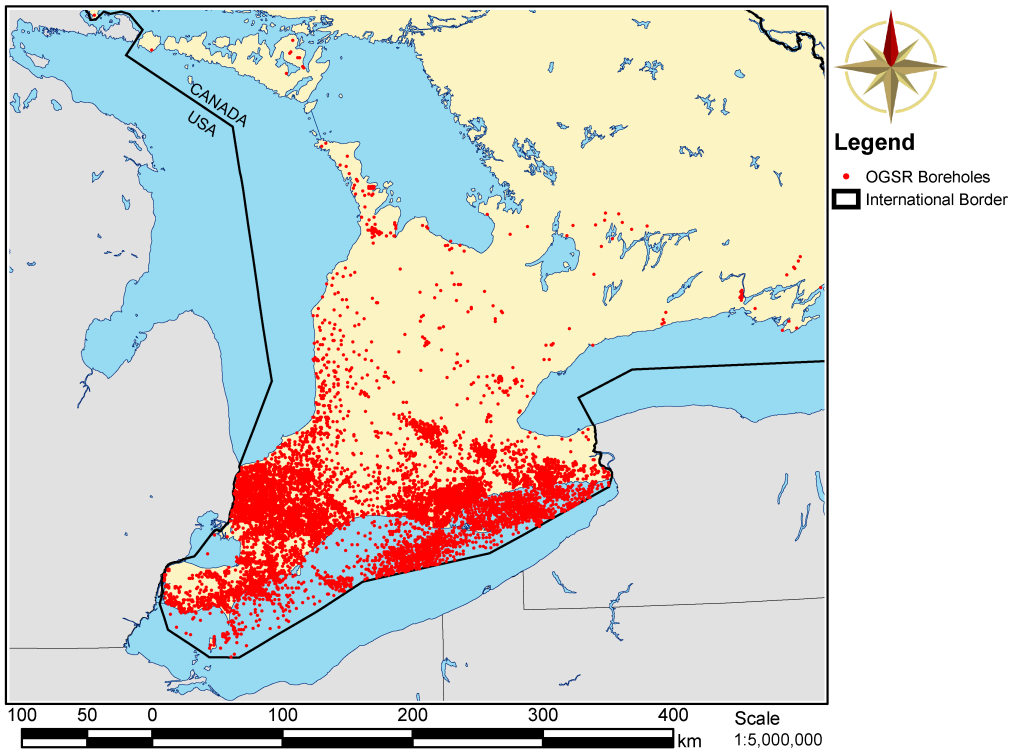

Figure 2.3 Locations of Oil, Gas and Salt Resources Library (OGSR) boreholes in southwestern Ontario.

flow systems. One such highly permeable unit is the Cambrian, found immediately above the Precambrian basement rock.

Summaries of hydrogeochemical studies that have been conducted in the Michigan Basin are provided in *Mazurek* (2004) and *Hobbs et al.* (2008); a significant contribution of this latter study is the assembly of a regional database of chemical and isotopic water compositions including published and previously unpublished field data from over 25 years of research at the University of Waterloo. The database contains 202 water samples collected in Ontario and Michigan at depths ranging from 40 m to 3500 m, although most samples were collected to study fluids in deep sedimentary settings (*Hobbs et al.*, 2008). The Michigan Basin is characterized, in *Hobbs et al.* (2008), into two geochemical systems:

- Shallow – depths < 200 m below ground surface comprised of fresh to brackish waters classified as either Na–Cl, Na–Mg–Ca–Cl, or Ca–SO_4, based on their concentration of major ions. These shallow waters have stable $\delta^{18}O$ and $\delta^{2}H$ isotopic compositions, indicating the mixing of more saline waters with glacial meltwater or recharge from precipitation; and
- Intermediate to Deep – high TDS brines (200–400 g/L) > 200 m depth classified as Na–Ca–Cl, or Ca–Na–Cl. These waters are enriched relative to the global meteoric water line (GMWL) with $-6‰ < \delta^{18}O < +3‰$ and $-55‰ < \delta^{2}H < +20‰$.

Isotopic signatures of glacial meltwaters have been found in central Ontario municipal wells screened at depths of 129 m in shallow bedrock, and at depths of 125 m in overburden, both comprising the Alliston aquifer system (*Aravena et al.*, 1995). *McIntosh and Walter*

(2006) state that paleowaters, originating in the Late Pleistocene and recharging from the Laurentide Ice-sheet into the subsurface along the northern margin of the Michigan Basin, have migrated to depths of nearly 900 ft (274 m) into Silurian-Devonian carbonate aquifers, significantly depressing the freshwater-saline interface.

2.2 Geosphere Modelling Studies

It is commonly accepted that each country that produces nuclear fuel waste is ethically and legally responsible for the safe disposal of such waste. In 1997, the "Joint Convention on the Safety of Spent Fuel Management and on the Safety of Radioactive Waste Management" became the first international legal instrument to directly deal with the safe disposal of nuclear fuel waste (*IAEA*, 1997). Due to the number of countries in Europe that produce nuclear waste, the Association for Regional and International Underground Storage (ARIUS) was founded to promote concepts for shared disposal facilities to maximize benefits and reduce costs. These facilities can be regional, serving neighbouring countries, or international. Countries also have the option of pursuing their own disposal facilities, although it is recognized that regional and international repositories can improve global safety and security, and enhance environmental benefits (*ARIUS*, 2002). The SAPIERR-I (Strategic Action Plan for Implementation of European Regional Repositories) and SAPIERR-II projects, funded by the European Commission (EC), were designed to clarify basic questions, to identify new research and technical developments, and to assess the feasibility of European regional waste repositories (*ARIUS*, 2006, 2008); otherwise, the 16 countries in the European Union (EU) that produce or have produced nuclear fuel waste would require the construction of 16 deep geologic repositories.

Numerous geosphere studies as part of the characterization of deep geologic repositories have been performed by various countries as discussed in §1.3. The following sections will describe several geosphere modelling studies that have been performed in Canada and abroad since the early 1990's.

2.2.1 Canadian Modelling Studies

AECL completed two geosphere modelling studies to explore the technical feasibility of the used nuclear fuel disposal concept, and its impact on human health and the environment. The EIS presented a case study of the long-term performance of a hypothetical implementation of a reference disposal system (*Davison et al.*, 1994), while the SCS evaluated the long-term effects of a hypothetical repository in a permeable host rock geologic setting, primarily to investigate the performance of the engineered barrier systems (*Stanchell et al.*, 1996).

The AECL URL is located within the WRA, near Lac du Bonnet, Manitoba. Both the URL and WRA have been the focus of extensive field investigations and research, gathering the geoscientific data needed to support the deep geologic disposal concept in intrusive igneous rock. The WRA includes a large portion of the Lac du Bonnet Batholith: a large granitic rock mass several kilometres deep with an exposed surface measuring over 60 km long and 20 km across at its widest point. The Batholith was intruded over 2.5 Ga ago and is comprised of several plutonic intrusions, of which the main intrusion is a grey granite that contains pink porphyritic granite at its upper surface.

2.2.1.1 Environmental Impact Statement (EIS)

The EIS describes a case study of the long-term performance of the implementation of a hypothetical reference disposal system (*Davison et al.*, 1994). The geological characteristics of the reference geosphere were developed from the extensive laboratory and field data, and engineering investigations at the WRA. The hypothetical repository was located at a depth of 500 m in sparsely fractured rock at the URL site.

Both two-dimensional and three-dimensional steady-state modelling was performed to validate the finite element groundwater model MOTIF. Three-dimensional models were developed at both a regional scale and a local scale. The spatial extent for the regional scale model encompassed an area bounded by the Winnipeg River of approximately 25.6 km by 33.2 km. The domain extended to a depth of 4000 m and included the EPM representing both MFR and SFR. Two-dimensional elements were used to represent a thin layer of surficial soils, three fracture zones identified at the URL site as FZ1, FZ2 and FZ3, and an identified fracture zone at the location of the Whiteshell Laboratories site. No-flow boundary conditions were used for the sides and bottom of the regional flow domain, while specified head values equal to surface topography were used for the top of the modelling domain. The horizontal permeability for the rock was assumed to be uniform and varied from 10^{-21} m^2 at a depth of 4000 m to 10^{-15} m^2 at the ground surface. The permeability for the FZs were assumed to be uniform at 10^{-13} m^2 (*Davison et al.*, 1994).

The spatial domain for the three-dimensional steady-state local scale modelling encompassed a region measuring 10 km by 9 km centred on the URL and extending to a depth of 1500 m. The top boundary condition of the model set specified heads equal to surface topography, while the side and bottom boundary conditions were obtained from the regional scale analysis. Similar to the regional scale model, an EPM approach was used for the three rock domains of FZ, MFR and SFR, with properties assigned specific to each rock mass. The permeability of the SFR surrounding the repository was 10^{-19} m^2 with an effective transport porosity of 0.003. Particle tracking was performed with the TRACK3D code.

The 10 ka analyses in the EIS ignored several factors, including the impact of the total dissolved solids concentration on pore water density, and transient effects caused by glaciation. Recent geosphere modelling which includes these factors is described in *Sykes et al.* (2003a).

2.2.1.2 Second Case Study (SCS)

The SCS investigated the robustness of the long-term safety case for a repository hosted in a rock formation that was more permeable than the one specified for the EIS case study. The design of the engineered barriers and repository would therefore play a more important role in the overall robustness of the repository system. The groundwater flow model MOTIF was used for the SCS (*Stanchell et al.*, 1996). The SCS was very similar to the EIS, except for the host rock permeability. The geographic setting, modelling domain extents, geometry of the FZ, MFR and SFR domains, and the depth, location, size, and orientation relative to fracture zones of the hypothetical repository were the same in both studies.

The spatial domain was vertically discretized using three EPM layers. The upper two layers (300 m thick) were assigned anisotropic permeabilities to account for sub-vertical

fractures that are observed in the shallow WRA. The vertical to horizontal permeability ratio was 5:1. The lowest layer, with a thickness of 1200 m, was assigned an isotropic permeability of 10^{-17} m^2 with an effective transport porosity ranging between 10^{-3} and 10^{-5}. Major fracture zones were included as discrete EPM features with an assumed uniform thickness of 20 m, a longitudinal permeability of 10^{-13} m^2 and a porosity of 10^{-2}. The model boundary conditions for the SCS were identical to the EIS case study (*Stanchell et al.*, 1996).

2.2.2 International Studies

A summary of international management approaches for nuclear fuel waste is provided by *McCombie and Tveiten* (2004). Several countries have fairly advanced research and implementation programs for deep geological disposal. The Swedish Nuclear Fuel and Waste Management Company, Svensk Kärnbränslehantering AB (SKB), has undertaken numerous studies at the Äspö Hard Rock Laboratory (HRL). The HRL is used to develop testing methods in bedrock, to improve scientific understanding, to develop techniques of adapting a repository to local site conditions, and to demonstrate the technology that will be used for a final geologic repository. The HRL holds a similar research function as AECL's URL. Various SKB modelling studies investigating the impacts of glaciation include *Svensson* (1999), *Boulton et al.* (2001a), *Boulton et al.* (2001b), *Jaquet and Siegel* (2003), and *Jaquet and Siegel* (2006) among others. SKB also collaborates with other nuclear waste management programs in Finland, Japan, France, and Canada.

Posiva Oy is the Finnish company responsible for final disposal of spent nuclear fuel in a deep geological repository at Eurajoki near Olkiluoto in southwestern Finland, approximately 500 m below ground surface in a 2 Ga igneous rock. An underground characterization laboratory, ONKALO, is being built at the final repository site. Various site characterization and glaciation studies include *Ahonen and Vieno* (1994), *Vaittinen et al.* (2003), *Cedercreutz* (2004), and *Hellä et al.* (2004), among others. Similar to SKB, Posiva Oy also collaborates with waste management programs in Sweden, France, Switzerland, Canada, Czech Republic, and Japan.

Cooperation amongst Nuclear Energy Agency (NEA) members regarding research and the sharing of knowledge and technology is quite common, and helps to reduce costs. According to *McCombie and Tveiten* (2004), 27 underground research laboratories are in use worldwide by various NEA members. These laboratories have either made use of existing excavations, or have been purposely constructed to advance research in site characterization, modelling, and repository design.

2.2.3 DECOVALEX

The DEvelopment of COupled THM models and their VALidation against EXperiments (DECOVALEX) project was established in 1992 as an international effort by national regulatory agencies and nuclear waste management organizations to cooperate in the development and testing of models capable of simulating coupled thermohydromechanical (THM) processes (*Tsang et al.*, 2005). As of 2005, more than 15 research teams from France, Germany, Canada, USA, Spain, Sweden, Japan, UK, and Finland have participated. According to (*Tsang et al.*, 2005), the objectives of DECOVALEX include:

- support numerical model development for THM processes in geological systems;

- investigate and implement suitable algorithms for THM modelling;
- compare model calculations with results from field and laboratory experiments;
- design new experiments to support code and model development; and
- study the application of THM modelling to performance and safety assessment of nuclear waste repositories

The DECOVALEX III project, begun in 2000, comprised a number of benchmark tests (BMTs) based on computer simulation, and test cases (TC) based on field and laboratory experiments. The two test cases and three benchmark tests include (*Tsang et al.*, 2005):

- FEBEX – two heaters are emplaced in bentonite blocks within a drift at the Grimsel Underground Testing Facility in Switzerland. Both the surrounding rock and bentonite are monitored during a heating and cooling cycle.
- DST – a set of 9 large heaters in a test drift and 50 smaller heaters in boreholes set in unsaturated tuff, with no backfill at Yucca Mountain. Measurements include temperature, displacement, saturation, effective hydraulic conductivity, as well as water samples for isotopic and chemical studies.
- BMT1 – flow and mechanical integrity in the near field (≈ 10 m) for a generic design of a hypothetical repository.
- BMT2 – upscaling of THM processes in fractured rock for a performance assessment of a large scale repository (≈ 5 km).
- BMT3 – investigate coupled THM processes and impacts of glaciation and permafrost on a generic site over a 100 ka time period.

The Bench Mark Test 3 (BMT3) modelling exercise uses the AECL WRA site geometry, properties, and fracture network to provide for realistic simulations (*Tsang et al.*, 2005; *Chan and Stanchell*, 2005; *Chan et al.*, 2005). The modelling involved both 2D cross-section and 3D models, and as described in *Tsang et al.* (2005), this modelling exercise is "one of the first attempts to assess the effects of repository depths using site-specific [...] data." The importance of glaciation scenarios for performance assessment is highlighted, along with the need for transient analysis of coupled THM processes. The modelling used simplified geometry for both the matrix and fractures, including 17 fractures representing fracture zones (*Chan and Stanchell*, 2005; *Chan et al.*, 2005). *Vidstrand et al.* (2008) extend the BMT3 modelling work to investigate underground hydraulic jacking due to high insitu pore pressures caused by the presence of permafrost, the advance and retreat of glaciers, and infiltration of glacial meltwater. Field evidence of hydraulic jacking is provided in *Talbot* (1999).

The DECOVALEX-THMC (DTHMC) framework is part of an international cooperative research effort over a period of four years that began in 2004. DTHMC focusses on the coupled modelling of thermo-hydro-mechanical-chemical processes in fractured rocks and buffer materials. A total of fourteen funding organizations from regulatory agencies to industry representatives were involved in one or more modelling tasks within the project. The Task E component dealt with the treatment of long-term climate change in performance assessment and an overall safety case for a DGR of used nuclear fuel in a crystalline rock Shield setting (*Chan and Stanchell*, 2008).

The modelling domain and its characteristics in *Chan and Stanchell* (2008) are derived from the sub-regional modelling work of *Sykes et al.* (2004). *Chan and Stanchell* (2008)

simplify their modelling domain in various ways due to the computational constraints of solving a density-dependent flow system coupled with THM. For example, the modelling study of *Sykes et al.* (2004) used 548 discrete fracture zones, while *Chan and Stanchell* (2008) selected a subset of 19 fracture zones; the basis for selection was a combination of fracture zone flow velocities from the FRAC3DVS models of *Sykes et al.* (2004) and scientific visualization methods to query the modelling results for significant flows or fracture interconnectivity. A total of four 2D and four 3D models were developed by *Chan and Stanchell* (2008) to investigate the role of salinity, permafrost, alternate glaciations, ice-sheet topography, and permafrost permeability reductions. Due to the complexity of these factors, and the high permeability contrast between fracture zones and matrix blocks, *Chan and Stanchell* (2008) encountered "severe numerical challenges [with] 3D MOTIF THM modelling." Two-dimensional simulations were required due to "impractical computational times estimated to exceed one month per complete transient run" resulting from refinement of the MOTIF finite element mesh; permeability reductions due to permafrost were only included in a single 2D simulation. The resulting 3D mesh was comprised of 40005 nodes, and 36447 hexahedral elements (*Chan and Stanchell*, 2008).

2.3 Geosphere Numerical Models

A *numerical model* is typically described as the numerical or software implementation of physical, chemical, and biological processes which have been defined using mathematical relationships between the relevant parameters. The term *model* or *site model* is used to describe the computer data files which contain the site specific geometry, parameters, properties, characteristics, loads, and boundary conditions for use in a numerical model.

Numerical models provide the means to simulate processes over spatial and temporal scales that would be intractable by any other means. This is especially true when considering the safety and performance of a high-level nuclear waste repository, and its interactions with the surrounding geosphere. Several numerical models have been developed which can aid in identifying or characterizing the important pathways for contaminant migration from a repository to the biosphere, and the factors that influence or mitigate that movement.

Several numerical models have been used for Canadian geoscience modelling studies. The finite-element code MOTIF was used to model the geosphere in both the EIS and the SCS (*AECL*, 1994; *Davison et al.*, 1994; *Stanchell et al.*, 1996), and in the DECOVALEX project (*Chan and Stanchell*, 2005, 2008). Other models that can be used to simulate the complex geosphere flow processes include SWIFT-III and FRAC3DVS. *Sykes et al.* (2003a) used SWIFT-III for a regional scale geosphere model, while FRAC3DVS was used for a sub-regional scale model in *Sykes et al.* (2004).

2.3.1 MOTIF

The MOTIF (Model Of Transport In Fractured/porous media) model is described in *Chan et al.* (1999). MOTIF 3.2 simulates three-dimensional saturated or unsaturated Darcian fluid flow, solute transport and heat transport with a dual porosity and discrete fracture formulation. The solute transport algorithm includes forced or natural convection, mechanical dispersion, molecular diffusion, equilibrium linear adsorption and single-species

radioactive decay. The heat transport algorithm includes forced or natural convection, conduction and hydrodynamic dispersion. Fluid density is a function of pressure, temperature and concentration. Dirichlet, Neumann and Cauchy boundary conditions can be used for both solute transport and heat transport. The governing equations are solved numerically using the Galerkin finite-element method. Temporal discretization is by a weighted first-order finite difference approximation. The Picard iterative scheme is used to solve the coupled non-linear flow and transport equations. MOTIF has been used extensively for the simulation of geosphere and repository processes.

2.3.2 SWIFT-III

The SWIFT-III (Sandia Waste-Isolation Flow and Transport) model was developed and maintained by Sandia National Laboratories through sponsorship by the U.S. Nuclear Regulatory Commission (*Ward et al.*, 1984). The SWIFT-III model is a fully-coupled, transient, three-dimensional finite-difference code with steady-state options. It implements the equations for groundwater flow, solute and radionuclide transport, and heat transport. Constitutive relationships for fluid density, fluid viscosity and porosity as a function of the state variables are also implemented. SWIFT-III can be used to model saturated porous and fractured media with a dual porosity formulation. Verification and field comparison of the SWIFT-III model are provided in *Ward et al.* (1984).

2.3.3 FRAC3DVS

FRAC3DVS is a model for the solution of the three-dimensional variably-saturated groundwater flow and solute transport in discretely-fractured media (*Therrien et al.*, 2004). The model includes a dual porosity formulation while discrete fractures are idealized two-dimensional parallel plates using a cubic law formulation. Alternatively, fracture zones can be represented geometrically with two-dimensional elements which are assigned porous media properties such as hydraulic conductivity, and porosity. The numerical solution to the governing equations is based on implementations of both the finite-volume method and the Galerkin finite-element method. FRAC3DVS couples fluid flow with salinity transport through pore fluid density which is itself dependent on both pressure and total dissolved solids concentrations.

A detailed model comparison study of FRAC3DVS and SWIFT-III was performed by *Normani et al.* (2004). The comparison is based on a total of nine scenarios, increasing in complexity from a steady-state freshwater simulation to a 100 ka transient saline simulation. Various combinations of brine density, hydraulic conductivity, spatially correlated hydraulic conductivity fields, and time scales comprised the nine simulations. Performance measures based on pressure, Darcy velocity, and brine concentration were applied. Both plan and cross-sectional views were used to illustrate spatial and depth dependencies while histograms were used to summarize results within layers and to compare layers to each other. The performance measures indicate that the FRAC3DVS and SWIFT-III models compare very well to each other for the same regional scale modelling domain. FRAC3DVS possesses several advantages over SWIFT-III, including:

- FRAC3DVS can be enhanced more readily than SWIFT-III, as it is in active development;

- FRAC3DVS has better and more up-to-date matrix solvers which provide for faster execution times;
- FRAC3DVS has more state-of-the-art algorithms to reduce truncation and numerical dispersion errors in mass transport;
- FRAC3DVS can more readily accommodate irregular grids and make use of different element geometries, however, density-dependent flow requires stacked grids; and
- FRAC3DVS includes the capability of specifying discrete open fractures or fracture zones.

The use of FRAC3DVS has been deprecated in favour of the enhanced capabilities and documented quality assurance and quality control processes and test cases of FRAC3DVS-OPG.

2.3.4 FRAC3DVS-OPG

FRAC3DVS-OPG is currently being developed as a branch of HydroGeoSphere (HGS), which itself was developed from FRAC3DVS, but excluding the surface water flow and transport components (*Therrien et al.*, 2008). This approach has allowed FRAC3DVS-OPG to benefit from code developments and improvements made to HGS at the University of Waterloo, and elsewhere. Improvements and enhancements over FRAC3DVS include:

- the implementation of backward-in-time (BIT) and mean life expectancy (MLE) algorithms for computing groundwater age, especially important for diffusion dominated flow systems, characteristic of deep flow environments (refer to §2.4.5);
- the implementation of variable and uncertain fracture zone widths, fracture zone porosity, and spatially variable fracture zone permeability;
- the implementation of a simplified vertical one-dimensional hydro-mechanical coupling as described by *Neuzil* (2003)
- the implementation of temperature and thermohaline processes, and subsequent coupling of temperature, density, and viscosity terms;
- the development and implementation of an ASCII based data interchange format from FRAC3DVS-OPG to Gocad™ (*Gocad*, 2009); and
- the development of a platform independent build environment using Python and SCons to compile the FRAC3DVS-OPG source code for execution on Microsoft Windows operating systems (32-bit and 64-bit), and Linux based operating systems using various optimizing Fortran95 compilers.

2.4 Governing Equations for Geosphere Numerical Models

This section presents the governing equations for groundwater flow, one-dimensional hydromechanical coupling, solute transport, and constitutive relationships for density and concentration. Boundary and initial conditions for the governing equations are not provided herein, but are widely published in the literature, for example, *Bear* (1988). Parameter definitions follow the equations, with units defined as: L = length, T = time, and M = mass.

2.4.1 Fluid Flow

According to *Bear* (1988), the equation of mass conservation for flow in a saturated porous medium is defined as:

$$-\frac{\partial}{\partial x_i}(\rho\, q_i) \pm Q = \frac{\partial}{\partial t}(n\,\rho) \qquad i = 1, 2, 3 \tag{2.2}$$

where ρ is the fluid density [M/L^3]; q_i is the Darcy flux vector in direction i [L/T]; Q is the fluid source/sink term [M/L^{3}T]; t is the time [T]; and n is the total porosity [/]. The Darcy equation relating flux to the energy potential of the fluid is defined as (*Bear*, 1988; *Frind*, 1982):

$$q_i = -K_{ij}\left(\frac{\partial h}{\partial x_j} + \rho_r \frac{\partial z}{\partial x_j}\right), \quad h = \frac{p}{\rho_0\, g} + z \qquad i, j = 1, 2, 3 \tag{2.3}$$

where K_{ij} is the porous media hydraulic conductivity tensor [L/T]; h is the freshwater head [L]; ρ_r is the relative fluid density [/]; p is the fluid pressure [M/LT^2]; ρ_0 is the reference fluid density [M/L^3]; g is the gravitational constant [L/T^2]; and z is the fluid elevation [L]. In Equation (2.3), the relative density ρ_r is defined as:

$$\rho_r = \frac{\rho}{\rho_0} - 1 \tag{2.4}$$

The hydraulic conductivity tensor in Equation (2.3) is defined as:

$$K_{ij} = \frac{k_{ij}\,\rho\; g}{\mu} \qquad i, j = 1, 2, 3 \tag{2.5}$$

where k_{ij} is the porous media permeability tensor [L^2]; and μ is the dynamic viscosity [MT/L]. In combining Equation (2.2) and Equation (2.3), the groundwater flow equation can be simplified to (*Freeze and Cherry*, 1979):

$$\frac{\partial}{\partial x_i}\left[K_{ij}\left(\frac{\partial h}{\partial x_j} + \rho_r \frac{\partial z}{\partial x_j}\right)\right] \pm Q = S_s \frac{\partial h}{\partial t} \qquad i, j = 1, 2, 3 \tag{2.6}$$

where S_s is the storage coefficient [L^{-1}]. The storage coefficient is a measure of the compressibility of the porous media and pore fluid, and is defined as the volume of water that a unit volume of aquifer releases from storage under a unit decline of piezometric head (*Freeze and Cherry*, 1979).

2.4.2 Hydromechanical Coupling

One-dimensional vertical loading and unloading due to glaciation, erosion, or deposition, is a common simplification that can be applied in hydromechanical coupling (*van der Kamp and Gale*, 1983; *Neuzil*, 2003; *Jaeger et al.*, 2007). Assuming that the porous media, solid grains, and pore fluid are all compressible, S_s is defined as:

$$S_s = \rho\, g\left[\left(\frac{1}{K} - \frac{1}{K_s}\right)(1-\lambda) + n\left(\frac{1}{K_f} - \frac{1}{K_s}\right)\right], \quad \lambda = \frac{2\alpha(1-2\nu)}{3(1-\nu)}, \quad \alpha = 1 - \frac{K}{K_s} \tag{2.7}$$

where K is the drained bulk modulus of the porous media [M/T^{2}L]; K_s is the bulk modulus of the solids in the porous media [M/T^{2}L]; K_f is the bulk modulus of the pore fluid [M/T^{2}L]; α is the Biot coefficient [/]; and ν is the Poisson's ratio [/]. The bulk modulus K is defined as the reciprocal of compressibility, therefore $K = 1/\beta$ (*Jaeger et al.*, 2007).

The effect of mechanically loading the surface of a porous media is to transfer the load to both the porous media, and the pore fluid; the amount of stress transferred depends on the relative compressibility of the porous media to the pore fluid, as well as the porosity. Since the porous media is somewhat elastic, it will compress under load, thereby reducing the size of pores, and compressing the pore fluid as a result. The pore fluid will compress, and in so doing, will resist the compression of the porous media, which will increase the pore pressure; the effects of mechanical loading and pore pressure affect each other, and are thus coupled. The groundwater flow equation listed as Equation (2.6) can be modified to account for one-dimensional hydromechanical coupling as follows:

$$\frac{\partial}{\partial x_i}\left[K_{ij}\left(\frac{\partial h}{\partial x_j}+\rho_r\frac{\partial z}{\partial x_j}\right)\right] \pm Q = S_s\frac{\partial h}{\partial t} - \frac{S_s\,\zeta}{\rho\,g}\frac{\partial \sigma_{zz}}{\partial t} \qquad i,j = 1,2,3 \tag{2.8}$$

where ζ is the one-dimensional loading efficiency [/]; and σ_{zz} is the vertical stress [M/LT^2]. A fundamental assumption of one-dimensional hydromechanical coupling is that strains can only occur in a vertical direction, implying no lateral strains. The loading efficiency is further defined as (*van der Kamp and Gale*, 1983; *Neuzil*, 2003):

$$\zeta = \frac{B(1+\nu)}{3(1-\nu)-2\alpha B(1-2\nu)}, \quad B = \frac{\left(\frac{1}{K}-\frac{1}{K_s}\right)}{\left(\frac{1}{K}-\frac{1}{K_s}\right)+n\left(\frac{1}{K_f}-\frac{1}{K_s}\right)} \tag{2.9}$$

where B is the Skempton coefficient and physically represents the ratio of change in fluid pressure to a change in mean effective stress under undrained conditions (*Neuzil*, 2003). A further simplification is commonly made in considering the solids of the porous media to be incompressible, or rigid, such that $\beta_s \to 0$ and $K_s \to \infty$, resulting in:

$$S_s = \rho\,g(\beta' + n\,\beta_f), \quad \zeta = \frac{\beta'}{\beta' + n\,\beta_f} \tag{2.10}$$

where β' is the coefficient of vertical compressibility for the porous media [LT^2/M]; and β_f is the fluid compressibility [LT^2/M]. β' can be calculated from commonly measured rock mechanics properties such as Young's elastic modulus E and Poisson's ratio ν as follows (*Neuzil*, 2003; *Jaeger et al.*, 2007):

$$K = \frac{E}{3(1-2\nu)}, \quad K' = K\frac{3(1-\nu)}{1+\nu}, \quad \beta' = \frac{1}{K'} \tag{2.11}$$

where E is the Young's elastic modulus of the porous media [M/LT^2]; and K' is the drained confined vertical modulus of the porous media [M/LT^2].

Since FRAC3DVS-OPG does not account for the geometric deformation of the grid as a mechanical load is applied, the hydromechanical term $\frac{S_s\,\zeta}{\rho\,g}\frac{\partial \sigma_{zz}}{\partial t}$ in Equation (2.8) serves

as a fluid source/sink term to effectively increase or decrease the fluid pore pressure, and hence head h, based on the temporal rate of change of vertical stress $\frac{\partial \sigma_{zz}}{\partial t}$, the storage coefficient S_s, and the one-dimensional loading efficiency ζ. A loading efficiency near zero results from a fairly stiff porous media, so little load is transferred to the pore fluid, while a loading efficiency near one represents a porous media that is more compressible than the pore fluid, so the pore fluid will support the majority of the applied load.

2.4.3 Solute Transport

The generalized solute transport equation for a saturated porous media is (*Bear*, 1988):

$$\frac{\partial}{\partial x_i}\left(n\, D_{ij}\frac{\partial C}{\partial x_j}\right) - \frac{\partial}{\partial x_i}\left(q_i\, C\right) \pm \Omega_C = \frac{\partial}{\partial t}\left(n\, C\right) \qquad i, j = 1, 2, 3 \tag{2.12}$$

where D_{ij} is the hydrodynamic dispersion tensor [L^2/T]; C is the concentration [M/L^3]; and Ω_C is the concentration source/sink term [M/L^3T]. D_{ij} is defined by *Bear* (1988) as:

$$n\, D_{ij} = \alpha_T |q| \delta_{ij} + \left(\alpha_L - \alpha_T\right) \frac{q_i\, q_j}{|q|} + n\, \tau\, D_m\, \delta_{ij} \qquad i, j = 1, 2, 3 \tag{2.13}$$

where α_T is the transverse dispersivity [L]; α_L is the longitudinal dispersivity [L]; $|q|$ is the magnitude of Darcy flux [L/T]; δ_{ij} is the Kronecker delta unit tensor [/]; τ is the tortuosity of the porous medium [/]; and D_m is the molecular diffusion coefficient [L^2/T].

For the case of variably dense fluids, fluid density in Equation (2.8) depends on pore fluid concentration as follows:

$$\rho_r = \gamma \frac{C}{C_{max}}, \quad \gamma = \frac{\rho_{max}}{\rho_0} - 1 \tag{2.14}$$

where C_{max} is the maximum concentration [M/L^3]; ρ_{max} is the maximum density [M/L^3]; and γ is the maximum relative density [/]. These relationships are commonly used when modelling heavy brines with concentrations of 300 g/L or higher. The following section describes the relationship between concentration, density, and mass fraction for dense pore fluids.

2.4.4 Constitutive Relationships

Constitutive or functional relationships link fluid or porous media properties to the pressure, temperature or concentration of a system. *Bear* (1988) and *Adams and Bachu* (2002) present various state equations with empirically determined coefficients. The theory and implementation manuals of MOTIF (*Chan et al.*, 1999) and SWIFT-III (*HSI GeoTrans*, 2000) also define the state equations for fluid density, $\rho = f(T, P, C)$, and fluid viscosity, $\mu = f(C, T)$. Similar relationships are used in FRAC3DVS-OPG.

The physical properties of groundwaters in deep sedimentary or crystalline rock environments can vary by greater than 25% for density and by one order of magnitude for viscosity. Density and viscosity changes may retard or enhance fluid flow or contaminant transport driven by other mechanisms; flow and transport are dependent on fluid density and viscosity as well as media properties such as permeability, porosity, and dispersivity. Thus, variations in fluid density and viscosity may have significant impacts on the flow system with consequences for various relevant processes (*Adams and Bachu*, 2002).

The relationships between concentration expressed as total dissolved solids (TDS), solution density, and mass fraction in characterizing solutes in water are:

$$\rho = \frac{M}{V} \tag{2.15a}$$

$$TDS = \frac{m}{V} \tag{2.15b}$$

$$X = \frac{m}{M} \tag{2.15c}$$

where TDS is the total dissolved solids [M/L^3]; M is the mass of solution [M]; V is the volume of solution [L^3]; m is the mass of solute (*e.g.*, NaCl or $CaCl_2$) [M]; and X is the mass fraction [/]. By combining these equations, a new relationship for TDS can be determined as:

$$TDS = m \cdot \frac{1}{V} = XM \cdot \frac{\rho}{M} = X\rho \tag{2.16}$$

Adams and Bachu (2002) present a study of brine density and viscosity for the Alberta Basin, consisting primarily of Na-Cl waters. The data and analyses of their paper can be used to illustrate the relationship between brine concentration given as mass fraction and fluid density. Figure 7 in their paper presents a plot of brine density versus mass fraction from 4854 formation water analyses. A mass fraction of 0.25 matches a density of approximately 1200 kg/m^3 or 1.2 kg/L. Using Equation (2.16) results in a TDS of 300 kg/m^3, or 300 g/L. For this example, in FRAC3DVS-OPG, ρ_{max} = 1200 kg/m^3 and C_{max} = 300 g/L.

2.4.5 Groundwater Age and Life Expectancy

The concept of groundwater age A and groundwater life expectancy E are related to groundwater travel time T as follows: $T = A + E$. Age is associated with forward-in-time equations, while life expectancy is associated with backward-in-time equations of groundwater transport (*Cornaton and Perrochet*, 2006a,b). The relationship between groundwater travel time T, age A, and life expectancy E along a groundwater flow line is shown in Figure 2.4. When the advection-dispersion equation is solved, the age probability density function (PDF) for any position $g_A(x_i, t)$ within a domain can be calculated. The age PDF is calculated using the following equation (*Cornaton and Perrochet*, 2006a):

$$\frac{\partial}{\partial x_i}\left(n\, D_{ij}\frac{\partial g_A}{\partial x_j}\right) - \frac{\partial}{\partial x_i}\left(q_i\, g_A\right) + q_I\, \delta(t) - q_O = \frac{\partial}{\partial t}\left(n\, g_A\right) \qquad i, j = 1, 2, 3 \tag{2.17}$$

where g_A is the age PDF [T^{-1}]; $\delta(t)$ is the Dirac delta function for time [T^{-1}]; q_I is the fluid source term [T^{-1}]; and q_O is the fluid sink term [T^{-1}]. Similarly, the life expectancy PDF is calculated as follows (*Cornaton and Perrochet*, 2006a):

$$\frac{\partial}{\partial x_i}\left(n\, D_{ij}\frac{\partial g_E}{\partial x_j}\right) + \frac{\partial}{\partial x_i}\left(q_i\, g_E\right) - q_I\, g_E = \frac{\partial}{\partial t}\left(n\, g_E\right) \qquad i, j = 1, 2, 3 \tag{2.18}$$

where g_E is the life expectancy PDF [T^{-1}]. The backwards-in-time nature of the life expectancy equation requires fluxes to be reversed.

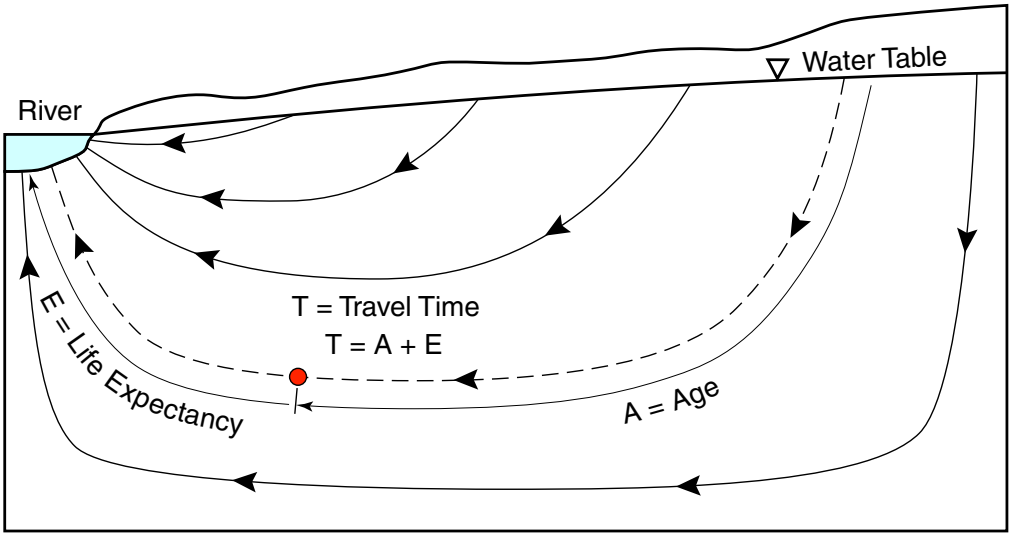

Figure 2.4 Relationship between travel time T, age A, and life expectancy E along a groundwater flow line for a representative cross-section.

For steady-state conditions the first moment of the age and life expectancy PDFs can be calculated to determine the mean of the PDFs resulting in (*Cornaton and Perrochet*, 2006a):

$$\frac{\partial}{\partial x_i}\left(n\,D_{ij}\frac{\partial\langle A\rangle}{\partial x_j}\right)-\frac{\partial}{\partial x_i}\left(q_i\,\langle A\rangle\right)-q_O\,\langle A\rangle+n=0 \qquad i,j=1,2,3 \tag{2.19}$$

$$\frac{\partial}{\partial x_i}\left(n\,D_{ij}\frac{\partial\langle E\rangle}{\partial x_j}\right)+\frac{\partial}{\partial x_i}\left(q_i\,\langle E\rangle\right)-q_I\,\langle E\rangle+n=0 \qquad i,j=1,2,3 \tag{2.20}$$

where $\langle A\rangle$ is the mean age [T]; and $\langle E\rangle$ is the mean life expectancy [T]. Using these formulations, mean ages (MAs) and MLEs will be continuously generated during groundwater flow, because porosity n acts as a source term in Equation (2.19) and Equation (2.20). According to *Goode* (1996), Equation (2.19) can also be derived using conservation of age mass. Groundwater therefore ages an average of one unit per unit time. Consequently, age and mean life expectancy are sensitive to values of porosity, as well as dispersivity values α_L and α_T used in the hydrodynamic dispersion tensor D_{ij}. Both mean age and mean life expectancy are implemented in FRAC3DVS-OPG for steady-state flow only.

2.5 Climate Change and Glaciation

Approximately nine episodes of complete glaciation have occurred during the past 900 ka over the Canadian Shield (*Peltier*, 2002). During these 900 ka, Canada has been covered by a series of continental ice-sheets. These ice-sheets could reach a maximum thickness of 4 km and extend onto the northern portions of the United States (*Peltier*, 2002). A single glaciation-deglaciation episode is comprised of multiple glacial advances and retreats, with deglaciation and isostatic depression leading to the formation of large proglacial lakes. *Peltier* (2002) states that it is "now well understood that this process of recurrent continent scale glaciation is a consequence of the small changes in the effective solar

insolation incident upon the Earth that occur as a consequence of the changing geometry of Earth's orbit around the Sun due to gravitational 'n-body effects' in the solar system."

Climate change and glaciation are of concern for the Canadian, Swedish (*Provost et al.*, 1998; *Boulton et al.*, 2001a) and Finnish deep geologic disposal concepts (*Cedercreutz*, 2004). *Peltier* (2002) and *Marshall et al.* (2000) have developed glaciological reconstructions of the Laurentide Ice-sheet over the North American continent using numerical models. According to *Peltier* (2002), these reconstructions of the Pleistocene ice-sheet history are based on three areas of study: (1) geological and paleogeological records; (2) the isostatic record of crustal deformation; and (3) the behaviour of modern day glaciers and ice-sheets. During ice-sheet advance, a repository site would evolve from periglacial to subglacial conditions with the site, depending on location, eventually overlain by up to 4 km of ice. Several hundred metres of permafrost develops below ground surface in advance of the ice-sheet. The thermal conditions at the base of the ice could be above or below the pressure melting point of the ice; a temperature above this point could result in sub-glacial flow of water or the development of streams, while colder temperatures could freeze the ice-sheet to bedrock (*Hooke*, 2005). The ice-sheet provides a thermal break between the atmosphere and the bedrock; allowing the geothermal heat flux radiating towards the ground surface to reduce the depth of permafrost (*Peltier*, 2002).

The weight of a 4 km thick ice-sheet depresses the Earth's surface up to 1 km or more, eventually rebounding once the ice-sheet retreats. The rate of rebound decreases with time, but it is, to this day, over 6 mm/year around Hudson Bay. The rate of rebound declines with distance away from Hudson Bay and approaches zero at the southern edge of the Canadian Shield (*Peltier*, 2002; *Davison et al.*, 1994). The relatively rapid melting of the ice-sheet leads to the formation of very large proglacial lakes at the southern margin of the Laurentide Ice-sheet. The magnitude of the freshwater fluxes were such that they are known to have had a strong impact on the thermohaline circulation of the oceans (*Peltier*, 2002).

Although a future glaciation scenario is of interest, a Bayesian approach is applied to examine a range of models for the most recent North American glaciation event, constrained by various long-term observations in sea level, ice core oxygen isotope ratios, maximal extent of glaciation, and continental isostatic rebound, among others. The physical model used for these simulations is the University of Toronto (UofT) Glacial Systems Model (GSM) (*Peltier*, 2008). The GSM is a physically based model, employing a *shallow ice* approximation whereby the vertical length scale is much smaller than the horizontal length scale. The model is subject to the equations of conservation of mass, momentum, and internal energy, represented as a set of non-linear coupled diffusion equations in essentially two dimensions, applied to a spherical Earth. A detailed description of the equations and model development can be found in *Deblonde and Peltier* (1991, 1993), and more recently in *Tarasov and Peltier* (1997, 1999, 2002, 2004, 2005, 2006).

The GSM is used for modelling ice-sheet evolution in a transient manner over a period of 120 ka. The model performs its calculations on a geographic grid measuring 1.0° in longitude by 0.5° in latitude. Various model outputs include normal stress on the ground surface due to an ice-sheet, permafrost depth, basal temperature relative to the pressure melting point of ice, surface lake depth, basal meltwater production, basal surface elevation subject to isostatic adjustment, surface elevation of ice-sheet, and ice-sheet thickness.

2.5.1 Glacial Meltwater

The depth of glacial meltwater penetration into the subsurface is of interest because dissolved oxygen (O_2) can be transported to great depths by infiltrating meltwater (*Guimerà et al.*, 1999). The Palmottu research site in southwestern Finland contains a uranium-thorium deposit within the 1.9–1.8 Ga old Svecofennian crust, which has been studied as part of a natural analogue research project investigating the migration of uranium in a crystalline rock setting (*Blyth et al.*, 2004). Fracture infill minerals can provide evidence of past chemical and hydrological conditions, and can provide insight into the long-term stability of a site. Uranium series disequilibria (USD) is an approach used in paleohydrogeological studies to understand uranium migration in the subsurface; specific advantages include a radio-isotope dating window of 1 Ma, matching the period of time that spent nuclear fuel must be isolated from the biosphere (*Suksi et al.*, 2001). Uranium (U) concentrations, as well as $^{234}U/^{238}U$ and $^{230}Th/^{238}U$ activity ratio distributions are used in the USD approach, and can indicate large and geologically recent uranium releases (*Rasilainen et al.*, 2003). These accumulations of U are clustered around 110 ka, 60 ka, and 40 ka, which can be correlated with previous glaciation events indicating hydrogeological activity at depth (*Suksi et al.*, 2001). Work by *Blyth et al.* (2004) has shown, using a fluid inclusion study and isotope geochemistry of fracture calcite minerals, that the movement of geologically recent waters is limited to the top 200 m, even though the area has experienced both advancing and retreating glaciation events.

Geochemical stability of the host rock is important and oxidizing conditions must be avoided in the vicinity of a repository over a significant period of time. *Spiessl et al.* (2008) state that "dissolved oxygen may promote corrosion of emplaced waste containers [...], possible instability of some of the engineered barriers [...], and in the event of repository failure, increased mobility of radionuclides and metals." *Guimerà et al.* (1999) states that glacial meltwater can contain 50–500 mg/L of dissolved oxygen at an ice depth of 1 km and a pressure of 100 atm; an independent estimate of 45 mg/L is provided by *Ahonen and Vieno* (1994). This concentration is much higher than the saturation concentration of 14.6 mg/L at 0 °C and 1 atm (*Lewis*, 2006). Migration of dissolved oxygen can be mitigated by either the presence of dissolved organic carbon, or reduced mineral phases that are present on fracture surfaces, or both. Further mitigation can occur if oxygen diffuses into a rock matrix that contains Fe(II)-bearing mineral phases such as pyrite or biotite (*Spiessl et al.*, 2008). Geochemical modelling has been performed by (*Spiessl et al.*, 2008), using the MIN3P reactive transport code, to investigate processes and key parameters that control and mitigate oxygen migration in fractured crystalline rock settings.

2.5.2 Paleoclimate Boundary Conditions

The mechanical loading upon ground surface due to the presence of an ice-sheet can be implemented as a hydraulic boundary condition in a groundwater flow model assuming the height of the ice-sheet can be replaced with an equivalent height of freshwater resulting in the same pressure or stress at its base. This approach has been applied by *Boulton et al.* (1995) and *Person et al.* (2003, 2007) for two-dimensional cross-sectional groundwater flow models. A groundwater flow model without hydromechanical coupling for glaciation processes ignores a significant factor which affects horizontal and vertical gradients during glacial advance and retreat. Mechanical loading at surface can increase insitu pore fluid

pressures, thereby reducing or completely cancelling a vertical gradient that results from a specified head boundary condition; the degree of pore pressure increase is directly tied to the value of the one-dimensional loading efficiency ζ, as described in §2.4.2. The mechanical loading is not only important for the ice-sheet, but also for proglacial lakes. Any change to water levels will also impart a change to the mechanical surface loading of the system, in addition to the change in hydraulic boundary conditions. This is formulated in the following equations:

$$\sigma_{zz} = \begin{cases} \rho_I \, g \, h_I & \text{if } h_W < \dfrac{\rho_I}{\rho_w} h_I, \\ \rho_W \, g \, h_W & \text{if } h_W \geq \dfrac{\rho_I}{\rho_w} h_I \end{cases} \tag{2.21}$$

$$\hat{h} = h_W \tag{2.22}$$

where ρ_I is the density of ice-sheet [M/L^3]; h_I is the height of ice-sheet [L]; ρ_W is the density of water [M/L^3]; h_W is the height of water [L]; and $\hat{h}$ is the specified head boundary condition [L]. The FRAC3DVS-OPG option of linearly interpolating specified heads to smoothly adjust time steps is used to mitigate abrupt changes in ice height, which could lead to unnecessarily small time steps or an unstable numerical solution.

An alternate approach for the paleoclimate boundary condition is to apply glacial meltwater as recharge to the top of the groundwater model, which will increase heads beneath the ice-sheet. If the heads increase sufficiently such that the ice-sheet will begin to float, then the system is considered unstable and a pressure limited specified head is applied as $\hat{h} = (\rho_I/\rho_W)h_I$ (*Lemieux et al.*, 2008a,b,c). The recharge is applied if permafrost does not exist below ground surface at that location. In glaciation studies and two-dimensional groundwater flow modelling of northwest Europe by *Boulton et al.* (1995) and *van Weert et al.* (1997), meltwater that cannot be discharged as groundwater by a head less than the ice pressure, is otherwise drained at the base of the ice-sheet. The drainage mechanism can include flow in a thin sheet at the ice/bed interface, flow in relatively stable channels at the ice/bed interface, or flow in canals in deformed subglacial sediments beneath the ice/bed interface (*Boulton et al.*, 1996). Further work by *Boulton et al.* (2001b) extends the modelling to three dimensions to investigate the role of tunnels forming beneath ice-sheets.

2.5.3 Permafrost

Permafrost develops in advance of the ice-sheet since the ground surface is directly exposed to climate variations, while ice-sheets thermally insulate the geosphere from climate influences (*Peltier*, 2002). Permafrost is also responsible for frost heaving of bedrock, where the displacement of blocks, panels and domes is caused by high pore water pressures, unable to escape due to a downward advancing permafrost front of lower permeability; field measurements of pore water pressures within confined zones indicate pressures of 400 kPa at depths of 2 m, considerably in excess of overburden pressures (*Dyke*, 1984). Ejected blocks of quartzite near Churchill, Manitoba can stand 3 m above surrounding terrain, with yearly vertical movements of 5 cm quite common.

In freezing pore waters, the connected flowing porosity is reduced, resulting in a much lower hydraulic conductivity. *McCauley et al.* (2002) conducted numerous ex-

periments measuring hydraulic conductivity and permeability in frozen and unfrozen soils, including organic rich silty sand, sandy silt, and silty sand fill. For a 100% ice saturated sample, the hydraulic conductivity of the frozen soil sample was approximately 5×10^{-11} m/s. For each time step in FRAC3DVS-OPG, if the depth of permafrost extends below the top of an element, calculated at the centroid of the top face, that element will be assigned the permafrost hydraulic conductivity isotropically. FRAC3DVS-OPG can vary time steps to suit groundwater flow and solute transport maximum change criteria (Δh, ΔC), as well as linearly interpolate permafrost values between successive time steps.

2.6 Recharge Area Concept

The recharge area concept (RAC) has been proposed by *Tóth and Sheng* (1996) as the foundation of a general approach for the siting of a nuclear waste repository in a Canadian Shield setting. Various two-dimensional models were created to investigate regional groundwater flow, with dimensions of 20 km in length from a topographic high to a topographic low, and 4 km in depth. A hypothetical repository is situated at a depth of 500 m.

Early hydrogeological studies of regional groundwater flow identified recharge areas, throughflow areas, and discharge areas for linear water tables (*Tóth*, 1963; *Freeze and Witherspoon*, 1967). In cases of variable topography, the groundwater flow regime can be divided into a local, intermediate and regional flow system. The group of flow lines that connect a recharge to a discharge area constitute a groundwater flow system. If the recharge and discharge areas are near to each other, then they are considered to form part of the local groundwater flow system, while recharge areas located in watershed highlands which connect to discharge areas in watershed lowlands are considered to form part of the regional flow system.

It is the regional flow system which is of interest in the RAC. According to *Tóth and Sheng* (1996), the RAC is based on two arguments:

- that a repository located in a regional recharge area ensures the maximum degree of dilution and maximum possible travel time to the biosphere; and
- that recharge environments are where the groundwater flow characteristics are sufficiently insensitive to discrepancies between actual and assumed hydrogeological conditions to allow the construction of adequately robust flow models and their validation.

The RAC has been applied by *Voss and Provost* (2001) for a site in southeastern Sweden. The *return-flow times* described by *Tóth and Sheng* (1996) are analogous to mean life expectancy in a strictly advective particle tracking sense. *Voss and Provost* (2001) implement an advective-diffusive return-flow time, similar to mean life expectancy developed in §2.4.5, by reversing flow directions and applying a source term at a rate of one per year using a modified version of SUTRA for a three-dimensional density-dependent flow model. *Voss and Provost* (2001) mostly agree with *Tóth and Sheng* (1996) in locating a repository within a regional recharge area, and add that a repository should be located in a contiguous region with a high return-flow time (mean life expectancy), should be as deep as possible to avoid local flow systems, and should be located in a region with minimal topographic variation (*i.e.*, "as smooth as possible") to avoid locating below a region with substantial surface flow systems.

The analyses presented in *Tóth and Sheng* (1996) do not account for a number of factors, including: denser pore fluids at depth, transient effects from glaciation, or the three-dimensional nature of real-world groundwater flow systems. Brines at depth tend to force freshwater flows to remain shallow and reduce, to a degree, the very deep looping paths commonly associated with regional flow systems; mixing between shallow and deeper systems at differing densities is limited (*Follin and Svensson*, 2003; *Normani et al.*, 2007). Glaciation can impart profound hydraulic and mechanical boundary conditions upon a groundwater flow system, reversing normally downward groundwater flows in the vicinity of a repository sited in a recharge area when glaciers retreat. The transient nature of glaciation can create high residual pore pressures, which depending on the site characteristics, can be a more dominant mechanism in controlling groundwater flow paths than present day topography. Finally, a two-dimensional analysis does not allow for topographic variability in the third dimension, and thus forces all flow lines to lie in-plane. The missing third dimension allows for more complicated local and intermediate flow systems to develop, and it is not intuitively apparent which recharge areas can be associated with regional flow systems. Although physically based numerical models are commonly employed for such analysis, *Follin and Svensson* (2003) developed a similar model to *Voss and Provost* (2001) and discovered significantly different particle paths, in part due to the much finer spatial discretization of their model. The presence of fracture zone networks tends to reduce the connectivity required to form regional flow systems as *Ophori* (2004) demonstrates for the Whiteshell Research Area in Canada.

Tóth and Sheng (1996) mention that a geographic information system (GIS) based approach can be developed to quickly find a group of suitable candidate sites based on the RAC. Recently, *Huang et al.* (2006) developed such an approach using various geophysical, geotechnical, geochemical, economic, transportation, and social considerations, concentrating their efforts on locating suitable repository sites in Ontario. Potential repository sites are characterized and evaluated using a suitability index based on the these considerations; a total of four sites are identified in northwestern Ontario, and one in northeastern Ontario.

2.7 Freshwater and Environmental Head

The most common groundwater studies by hydrogeologists involve freshwater systems, implying a constant density for water. The simplification of constant density allows hydrogeologists to use the concept of "head" where gradients and flow velocities can be directly calculated by knowing the difference in head Δh, and the distance between two points ΔL. A gradient i is calculated as $i = \Delta h / \Delta L$. Knowing the hydraulic conductivity between the two points and the gradient, Darcy's Law allows one to calculate the Darcy flux q and the direction of flow can be determined where $q = -Ki$. In practical terms, the piezometric head represents the free surface water elevation and is easily determined in the field.

Variable density groundwater flow systems are much less intuitive as the density affects the pore water pressure with depth, resulting in a non-linear pressure profile with depth. *Lusczynski* (1961) introduces the concepts of point-water head, freshwater head, and environmental-water head. Each approach results in a different elevation for the free surface, depending on the density of the fluid within the well. The head is calculated as

the sum of the elevation of the given location and the height of a fluid column, where the fluid pressure at the base of the column equals the pore fluid pressure at that location in the aquifer. Point-water head uses a column of fluid equal in density to the fluid density at the given location, while freshwater head uses a column of freshwater. Due to its lower density, a column of freshwater has a greater height for the same base pressure than a column of point-water. Point-water head and freshwater head are defined as:

$$h_{Pi} = z_i + \frac{p_i}{\rho_i g}, \quad h_{Fi} = z_i + \frac{p_i}{\rho_F g} \tag{2.23}$$

where h_{Pi} is the point-water head at point i [L]; z_i is the elevation of point i [L]; p_i is the fluid pressure at point i [M/LT^2]; ρ_i is the density of fluid at point i [M/L^3]; h_{Fi} is the freshwater head at point i [L]; and ρ_F is the freshwater density [M/L^3].

Environmental-water head uses a column of water that is identical in fluid density to the water that surrounds the well. One advantage of this definition is that vertical gradients can be determined when comparing the elevation of the free surface in the well casing, to the elevation of the water table immediately adjacent to the well. Unfortunately, a monitoring well in the field is unlikely to contain a fluid whose density precisely matches the fluid immediately outside the casing at any given elevation. Environmental head is more useful when applied to results from modelling studies, as most groundwater flow models that can simulate variable density flow use freshwater head as the state variable for flow. Environmental head is calculated as follows:

$$h_{Ei} = h_{Fi} - \frac{(\rho_F - \rho_A)(z_i - z_r)}{\rho_F}, \quad \rho_A = \frac{1}{z_r - z_i}\int_{z_i}^{z_r} \rho(z)\,\mathrm{d}z \tag{2.24}$$

where h_{Ei} is the environmental-water head at point i [L]; ρ_A is the average density of fluid between z_i and z_r [M/L^3]; z_r is the reference elevation of freshwater above point i [L]; and $\rho(z)$ is the fluid density as a function of z [M/L^3].

In a numerical model using density-dependent flow, such as FRAC3DVS-OPG, the environmental head is calculated from the freshwater head and brine concentration output by the model. Since the finite element nodes are vertically aligned, environmental head is calculated starting at the top of the model, iteratively progressing downwards towards the bottom, where node $j+1$ is immediately below node j as follows:

$$h_E^{j+1} = h_E^j + \left(h_F^{j+1} - h_F^j\right) - \left(\frac{C^{j+1} + C^j}{2}\right)\left(\frac{\rho_{max} - \rho_F}{\rho_F}\right)\left(z^j - z^{j+1}\right) \tag{2.25}$$

where h_E^{j+1} is the environmental-water head at node $j+1$ [L]; h_E^j is the environmental-water head at node j [L]; h_F^{j+1} is the freshwater head at node $j+1$ [L]; h_F^j is the freshwater head at node j [L]; C^{j+1} is the brine concentration at node $j+1$ [M/L^3]; C^j is the brine concentration at node j [M/L^3]; z^{j+1} is the elevation of node $j+1$ [L]; and z^j is the elevation of node j [L].

A hydrogeologist must be aware that traditional techniques for determining gradients and groundwater fluxes in constant density freshwater systems **do not** apply to variable density flow systems (*Post et al.*, 2007). Field measurements in variably dense groundwater flow systems should include electrical conductivity and pressure with depth measurements (*Post et al.*, 2007). These measurements can provide insight into how

density varies with depth due to known relationships between salinity and electrical conductivity, and between density, salinity and pressure. *Lusczynski* (1961) states that because "environmental-water heads define hydraulic gradients along a vertical, they are comparable along a vertical. This is evidently not the case for point-water or fresh-water heads. Also, because fresh-water heads define hydraulic gradients along a horizontal in groundwater of variable density, they are comparable along a horizontal. This is not the case for point-water or environmental-water heads."

Chapter 3

Canadian Shield Regional Model

A regional scale groundwater flow and transport model covering an area of 5734 km^2 was developed by *Sykes et al.* (2003a) using SWIFT-III (see §2.3.2). The modelling domain extends 102 km in an east-to-west direction and 94 km in a north-to-south direction. The objective of the regional scale study was "to undertake a comprehensive investigation of regional scale three-dimensional groundwater flow in a [representative] watershed in a crystalline rock setting" (*Sykes et al.*, 2003a). Site properties were representative of typical crystalline rock settings and were based, in part, on data gathered at geoscience research areas during the Canadian Nuclear Fuel Waste Management Program. Several criteria were developed in order to select a suitable site:

- large masses of crystalline rock must be present in the watershed;
- the Quaternary geology must also reflect the presence of crystalline rock at shallow depths;
- the topographic relief must yield regional gradients that are the same order as those measured at the WRA; and
- surface water divides must occur within the selected watershed.

This chapter describes the development of the SWIFT-III model from *Sykes et al.* (2003a) and the development of the FRAC3DVS model, documented in *Normani et al.* (2004), which was used to compare FRAC3DVS to SWIFT-III modelling results for the regional scale domain. This comparison was done to assess the applicability of using FRAC3DVS for modelling deep groundwater flow systems subject to high TDS concentrations and variably dense pore fluids.

3.1 Site Geology

The Quaternary geology for the watershed, as shown in Figure 3.1, is predominantly granite with small areas of till also occurring. The 1:1000000 bedrock geology for the watershed is shown in Figure 3.2 (*OGS*, 2000). The predominant rock type within the watershed is Unit 15: massive to foliated granodiorite to granite (see Table 3.1 for the legend). Smaller areas of Unit 15a (potassium feldspar megacrystic units) and Unit 12 (foliated to massive tonalite to granodiorite) are also present.

3.2 Digital Elevation Model and Digital Cartography

The digital elevation model (DEM) for the watershed was developed using the 1:250000 Natural Resources Canada (NRCAN) DEM. The raster data for the DEM has a $0°0'3''$ resolution, which results in a grid spacing of approximately 60 m east-to-west by 100 m north-to-south. The integer elevations range from approximately 330 m to 470 m above mean sea level within the watershed boundary. The surface water features and the DEM for the watershed are shown in Figure 3.3.

The vector features were obtained from digital 1:50000 NRCAN National Topographic System (NTS) maps and include 505 km^2 of wetlands, 460 km^2 of lakes and 2830 km of rivers. The boundary for the watershed was a surface water divide determined using ArcView GIS with the water feature map, digital contours and the DEM. The watershed contains two sub-basins which are identified as River A to the north and River B to the south. The two rivers meet near the western boundary of the watershed (*Sykes et al.*, 2003a).

3.3 SWIFT-III Based Model Development

Modelling work for the regional scale domain began in 2001 using SWIFT-III. At that time, FRAC3DVS could not simulate coupled flow and density-dependent transport. A work program was initiated to add density-dependent capabilities to FRAC3DVS. A comprehensive model comparison study between SWIFT-III and FRAC3DVS was undertaken by *Normani et al.* (2004). The comparison was based on a total of nine scenarios, increasing in complexity from a steady-state freshwater simulation to a 100 ka transient saline simulation for the 5734 km^2 regional scale domain.

3.3.1 Spatial Discretization

The spatial domain for the watershed was discretized to a depth of 1.5 km using 1534080 three-dimensional finite-difference grid blocks in 10 layers. The columns and rows were uniformly spaced on a 250 m by 250 m grid that resulted in 408 grid blocks in the east-to-west direction and 376 grid blocks in the north-to-south direction. The vertical discretization is summarized in Table 3.2. The domain's top elevation was calculated with a Visual Basic pre-processor, ArcView and the DEM at each grid block centroid. The bottom elevation of layers 1 through 5 varies to conform to surface topography and the bottom of layer 6 at an elevation of −200 m. The bottoms of layers 7 through 10 were assigned constant elevations (*Sykes et al.*, 2003a).

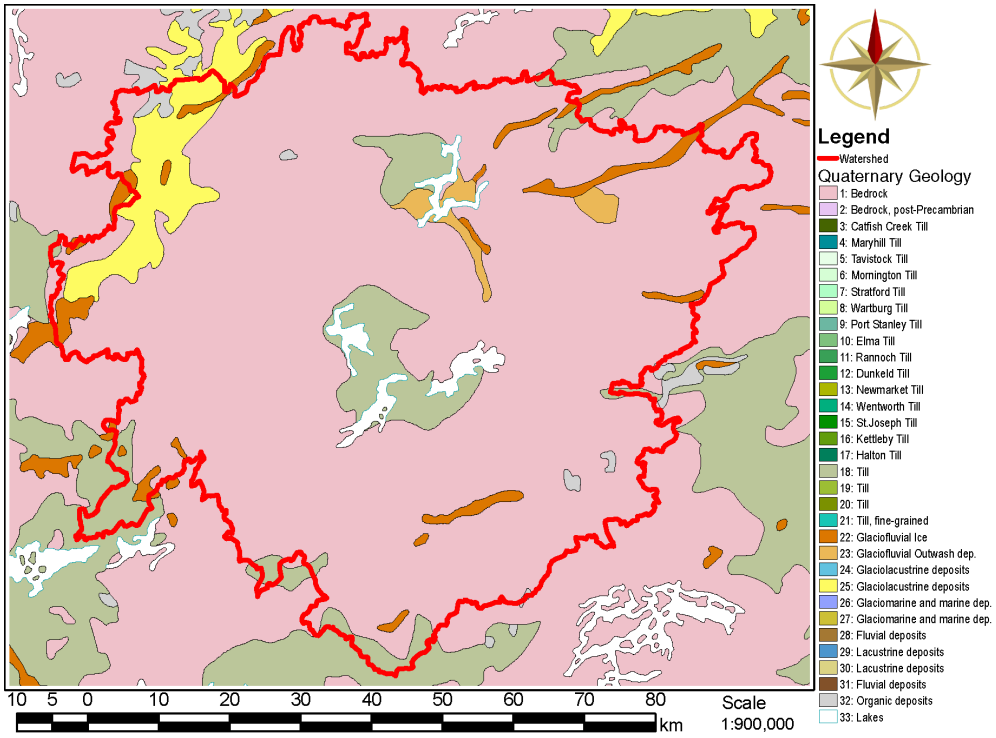

Figure 3.1 Regional scale Quaternary geology and watershed boundary for modelling domain.

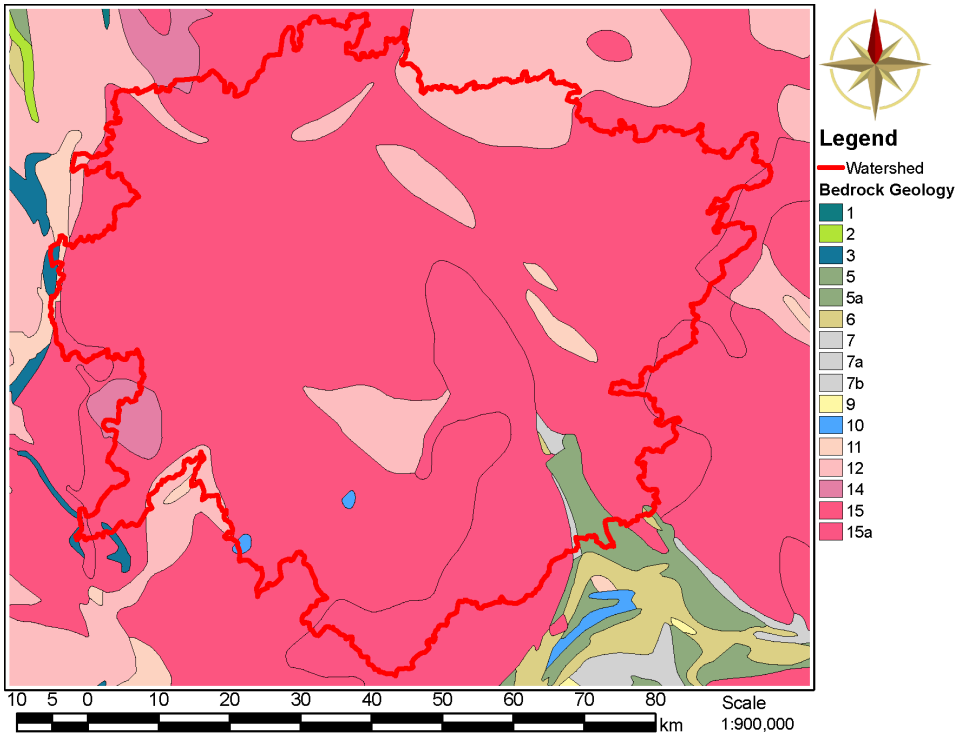

Figure 3.2 Regional scale bedrock geology and watershed boundary for modelling domain. See Table 3.1 for the legend.

Table 3.1 Ontario bedrock geology legend.

Unit	General Category	Rock Types	Era
1	Metasedimentary rocks and mafic to ultramafic metavolcanic rocks	coarse clastic metasedimentary rocks, marble, quartz arenite, iron formation, komatiite, mafic metavolcanic rocks, and minor felsic metavolcanic rocks	Mesoarchean (2.9 to 3.4 Ga)
2	Felsic to intermediate metavolcanic rocks	rhyolitic, rhyodacitic, dacitic and andesitic flows, tuffs and breccias	Mesoarchean (2.9 to 3.4 Ga)
3	Mafic metavolcanic and metasedimentary rocks	mafic metavolcanic rocks, minor iron formation	Mesoarchean (2.9 to 3.4 Ga)
5	Mafic to intermediate metavolcanic rocks	basaltic and andesitic flows, tuffs and breccias, chert, iron formation, minor metasedimentary and intrusive rocks, related migmatites	Neo- to Mesoarchean (2.5 to 3.4 Ga)
6	Felsic to intermediate metavolcanic rocks	rhyolitic, rhyodacitic, dacitic and andesitic flows, tuffs and breccias, chert, iron formation, minor metasedimentary and intrusive rocks; related migmatites	Neo- to Mesoarchean (2.5 to 3.4 Ga)
7	Metasedimentary rocks	wacke, arkose, argillite, slate, marble, chert, iron formation, minor metavolcanic rocks	Neo- to Mesoarchean (2.5 to 3.4 Ga)
9	Coarse clastic metasedimentary rocks	mainly coarse clastic metasedimentary rocks, with minor, mainly alkalic, mafic to felsic metavolcanic flows, tuffs and breccias	Neo-archean (2.5 to 2.9 Ga)
10	Mafic and ultramafic rocks	gabbro, anorthosite, ultramafic rocks	Neo- to Mesoarchean (2.5 to 3.4 Ga)
11	Gneissic tonalite suite	tonalite to granodiorite-foliated to gneissic-with minor supracrustal inclusions	Neo- to Mesoarchean (2.5 to 3.4 Ga)
12	Foliated tonalite suite	tonalite to granodiorite-foliated to massive	Neo- to Mesoarchean (2.5 to 3.4 Ga)
14	Diorite - monzonite - granodiorite suite	diorite, tonalite, monzonite, granodiorite, syenite and hypabyssal equivalents (saturated to oversaturated suite)	Neo- to Mesoarchean (2.5 to 3.4 Ga)
15	Massive granodiorite to granite	massive to foliated granodiorite to granite	Neo- to Mesoarchean (2.5 to 3.4 Ga)
15a	Massive granodiorite to granite	Potassium feldspar megacrystic units	Neo- to Mesoarchean (2.5 to 3.4 Ga)

Note: All units are in the Archean eon and Superior province.

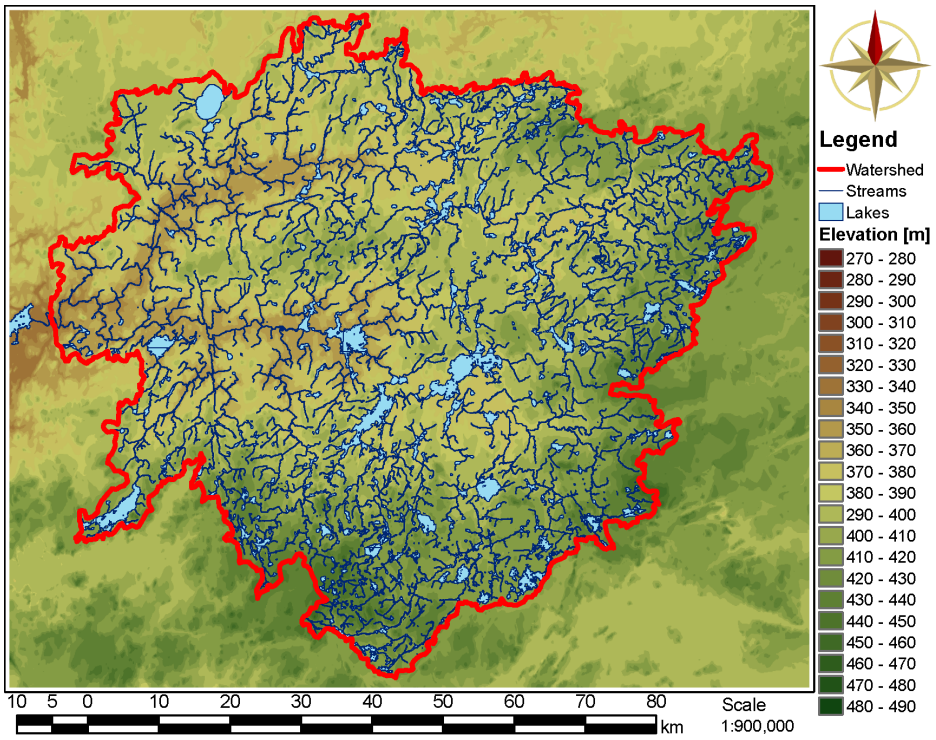

Figure 3.3 Water features and DEM for modelling domain.

Table 3.2 SWIFT-III model layers and hydraulic conductivity values.

Layer	Bottom Depth [m]	Thickness [m]	Hydraulic Conductivity [m/s]		
			Case 1 (10^{-15})	Case 2 (10^{-13})	Case 3 (10^{-11})
1	10	10	6.7×10^{-8}	6.7×10^{-8}	6.7×10^{-8}
2	30	20	6.7×10^{-9}	6.7×10^{-9}	6.7×10^{-9}
3	70	40	6.7×10^{-9}	6.7×10^{-9}	6.7×10^{-9}
4	150	80	3.0×10^{-10}	3.0×10^{-10}	3.0×10^{-10}
5	300	150	4.0×10^{-11}	4.0×10^{-11}	4.0×10^{-11}
6	500	200	2.1×10^{-12}	2.1×10^{-12}	2.2×10^{-11}
7	700	200	2.2×10^{-13}	2.2×10^{-13}	2.2×10^{-11}
8	900	200	9.1×10^{-15}	2.2×10^{-13}	2.2×10^{-11}
9	1100	200	6.7×10^{-15}	2.2×10^{-13}	2.2×10^{-11}
10	1500	400	6.7×10^{-15}	2.2×10^{-13}	2.2×10^{-11}

3.3.2 Boundary Conditions

As shown in Figure 3.4, each surface grid block (layer 1) was characterized, using ArcView, as *inactive*, *active*, *wetland*, *lake* or *river*. A Neumann boundary condition representing recharge was used for the active grid blocks while prescribed heads equal to surface topography were used for the wetland, lake and river grid blocks. Zero-flux boundary conditions were applied to the domain sides and bottom.

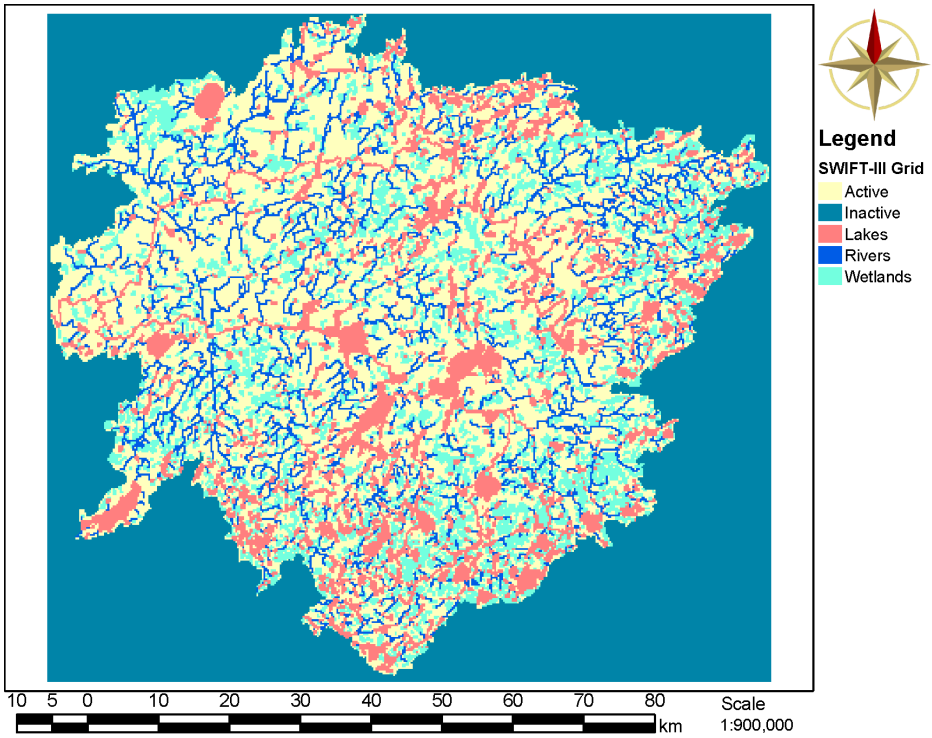

Figure 3.4 SWIFT-III finite-difference grid and surface boundary conditions.

3.3.3 Properties

A total of three different conceptualizations for horizontal hydraulic conductivity with depth were developed. The Case 1 distribution of hydraulic conductivity with depth was derived from data provided in *Stevenson et al.* (1996) while Case 2 and Case 3 hydraulic conductivity distributions were chosen to investigate groundwater flow in more permeable crystalline rock settings. The Case 2 distribution was used for the base-case simulations. The horizontal hydraulic conductivity for the three cases are presented in Table 3.2. At the WRA, MFR is typically found to a depth of 300 m with predominantly vertical fracture orientations. These discrete vertical fractures in the MFR were accounted for by increasing the vertical hydraulic conductivity by an order of magnitude, relative to the horizontal hydraulic conductivity, in model layers 1 through 5. Isotropic hydraulic conductivities were used for the rock represented by model layers 6 to 10. A constant porosity of 0.005 was used throughout the domain (*Sykes et al.*, 2003a).

The impact of high TDS concentrations on groundwater flow at depth was also investigated. Three initial concentration distributions were assumed: freshwater throughout

the domain (1.0 g/cm^3); a seawater equivalent salinity (1.03 g/cm^3) below an elevation of −200 m and freshwater above this elevation; and, a high TDS density of 1.10 g/cm^3 below an elevation of −200 m with freshwater above. An initial hydrostatic pressure distribution was calculated for the transient simulations using a pressure of 0 Pa at an elevation of 450 m and the assumed salinity distributions. The specific storage for the rock was calculated using a pore water compressibility of 4.57×10^{-10} Pa^{-1}, a rock compressibility of 2.58×10^{-7} Pa^{-1} and a rock density of 2650 kg/m^3. For the simulations which included TDS concentrations, the longitudinal and transverse dispersivities were assumed to be 125 m while the molecular diffusion coefficient was assigned a value of 2.5×10^{-12} m^2/s (*Sykes et al.*, 2003a).

3.4 FRAC3DVS Based Model Development

As listed in §2.3.3, FRAC3DVS provides several advantages compared to SWIFT-III. As such, detailed model comparison of FRAC3DVS and SWIFT-III was performed by *Normani et al.* (2004). The comparison was based on a total of nine scenarios, listed in Table 3.3, increasing in complexity from a steady-state freshwater simulation to a 100 ka transient density-dependent simulation for the regional scale domain. Various combinations of brine density, hydraulic conductivity, spatially correlated hydraulic conductivity fields, and time scales comprised the nine simulations. Performance measures based on pressure, Darcy velocity, and brine concentration were applied. Both plan and cross-sectional views were used to illustrate spatial and depth dependencies while histograms were used to summarize results within layers and to compare layers to each other.

3.4.1 Spatial Discretization

The SWIFT-III model uses a finite difference representation of the spatial domain while FRAC3DVS uses a finite element representation. Although both techniques use 3-D blocks, the calculation points, or nodes, are defined differently. An illustrative example is shown in Figure 3.5 and Figure 3.6, whereby the calculation point is at the block centroid in the finite difference method, and at the block corners in the finite element method. The finite element method can accommodate numerous element shapes such as tetrahedral, prism, triangular, quadrilateral, line, and hexahedral among others. Groups of nodes define an element's shape; for example, six nodes define a prism element while eight nodes define a block or hexahedral element. The finite element method can use elements of varying size to accommodate greater detail where it is desired and less detail further from the area of interest. Irregularly shaped domains are naturally accommodated in the finite element method due to the inherent flexibility in defining the computational grid.

The three-dimensional finite difference method is limited to three-dimensional blocks. For irregularly shaped domains, blocks which are outside the domain of interest must be set inactive, however these blocks are still defined and consume computer resources. Increasing grid resolution must be done on a row or column-wise basis, regardless of whether or not that resolution is needed along the entire column or row length. This results in a higher grid resolution where none is needed, as well as introducing blocks with large aspect ratios, which can contribute to numerical instability.

If the finite difference and finite element blocks are chosen spatially coincident, then block properties such as hydraulic conductivity, and porosity are identical in location

Table 3.3 Scenario and parameter selection matrix for regional scale modelling.

Parameters	Simulation Scenarios															
	Steady-State											Transient				
	1	2	3	4	5	6	7	8	9	10	11	12	13	14	15	16
Hydraulic Conductivity																
Case 1 (10^{-15} m/s)	□															
Case 2 (10^{-13} m/s)		■		■	□	□	■					■	■	■	■	
Case 3 (10^{-11} m/s)			■					□	■	□	□					□
Brine Density																
No brine	□	■	■	■	□	□	■	□	■	□	□			■		
1.03 g/cm^3												■			■	
1.10 g/cm^3													■			□
Correlated Hydraulic Conductivity																
λ = 2.0 km, σ = 0.2				■				□								
λ = 2.0 km, σ = 0.5					□				■							
λ = 10.0 km, σ = 0.2						□				□						
λ = 10.0 km, σ = 0.5							■				□					
Time Scale																
Steady-State	□	■	■	■	□	□	■	□	■	□	□					
10 ka												■		■		
100 ka													■		■	□

Note: □ Simulation performed in *Sykes et al.* (2003a) using SWIFT-III
■ Simulation performed in *Normani et al.* (2004) to compare SWIFT-III and FRAC3DVS

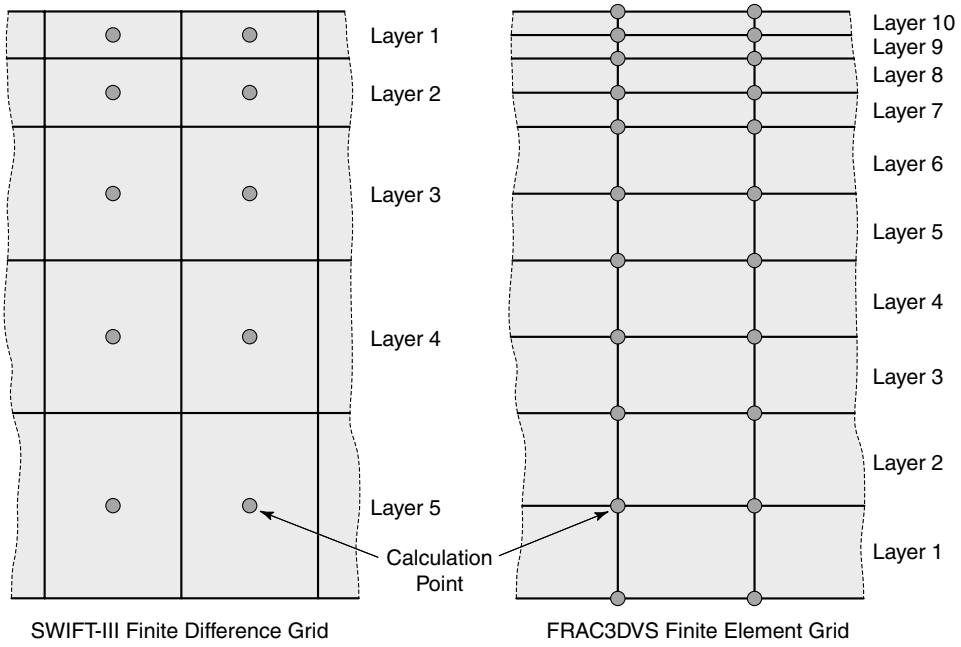

Figure 3.5 Illustrative cross-sectional view of SWIFT-III and FRAC3DVS computational grids.

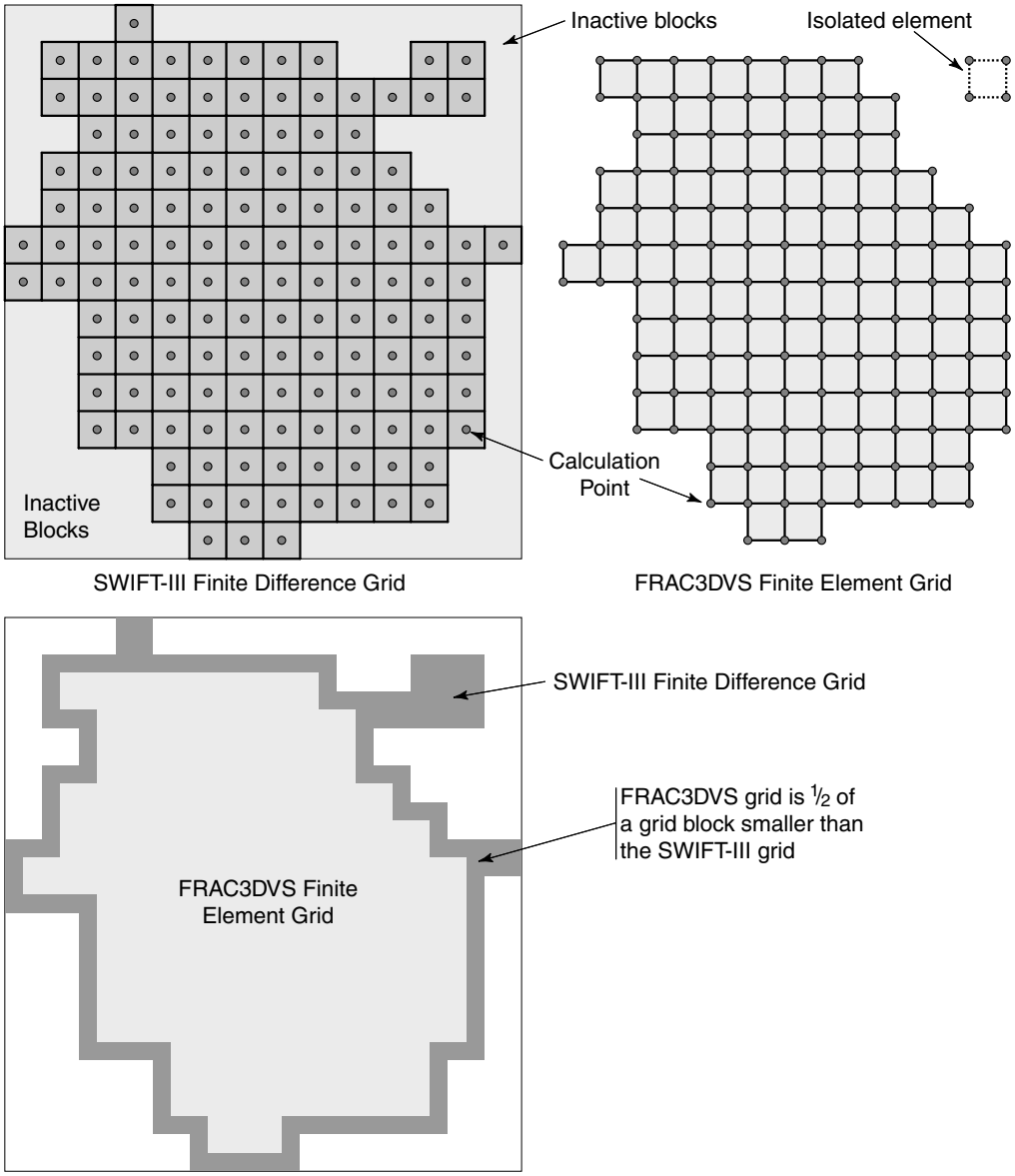

Figure 3.6 Illustrative plan view of SWIFT-III and FRAC3DVS computational grids.

and value between the two models; however, the calculation points are offset by one-half of a block which means that boundary conditions, and computed freshwater heads and concentrations need to be interpolated for a valid comparison between SWIFT-III and FRAC3DVS. This approach was attempted, but sufficient differences were discovered between freshwater heads in the two models. These differences could be directly attributed to the fact that specified head surface boundary conditions were interpolated from the four adjacent finite difference blocks, thereby smoothing the boundary conditions and hence propagating the result throughout the entire domain. A valid comparison using this approach could not be made as surface boundary conditions are the dominant driving force for freshwater head in the model.

The calculation points were therefore chosen to be coincident, with the finite element blocks being offset by one-half of a block as compared to the finite difference grid. This is clearly evident in Figure 3.6, while in Figure 3.5, the number of layers in FRAC3DVS was doubled as compared to SWIFT-III in order to ensure that the vertically variable hydraulic conductivity would coincide spatially in both models. The finite element grid is one-half of a block smaller than the finite difference grid, as shown in Figure 3.6. Several artifacts present themselves, such as the isolated element which is no longer connected to the grid, and the single finite difference blocks along the top and right that are not included in the finite element grid.

3.4.2 Initial Conditions

An initial constant freshwater head of 450 m was chosen for the four transient scenarios (see Table 3.3). This initial head results in the domain being over pressured with respect to a hydrostatic condition relative to the ground surface. In Scenarios 12, 13, and 15 where variable density simulations were performed, the equivalent freshwater head was modified from a value of 450 m to include the increased density of the brine at depth. FRAC3DVS calculates all heads as freshwater heads. Care must be taken in specifying the initial freshwater heads to account for this condition. SWIFT-III includes this capability by requesting a reference pressure head at a reference datum. The model then internally calculates the initial static freshwater head by considering the pore fluid density from the ground surface vertically downward to the base of the modelling domain. For the evaluations in this study, post-processing of the equivalent fresh water head calculated using FRAC3DVS enabled comparison to the pressures at datum that were calculated using SWIFT-III.

3.4.3 Boundary Conditions

A specified freshwater head boundary condition was applied to the top surface of both models to represent water features such as lakes, rivers, and wetlands. A recharge boundary condition with a rate of 1 mm/a was applied elsewhere. Higher recharge rates were attempted, but were found to raise the water table above ground surface. A calculated artifact of this approach is that the total areal flux due to recharge entering the domain is greater in the SWIFT-III model than the FRAC3DVS model because the FRAC3DVS model area is marginally smaller as a result of being one-half of a block smaller along the periphery of the modelling domain. The total volumetric recharge is therefore 1.61% greater in the SWIFT-III model than in the FRAC3DVS model.

3.4.4 Properties

Hydraulic conductivity varies as a function of depth from surface. Shallower rock is more fractured and weathered, and as such, has a higher hydraulic conductivity than deeper rock. Figure 3.7 graphically presents the variation in hydraulic conductivity with depth for the three different cases investigated by *Sykes et al.* (2003a), where the cases are applied as in Table 3.2.

Spatially correlated random hydraulic conductivity fields were also used to investigate the effects of variance σ and correlation length λ upon freshwater heads. As mentioned in §3.4.1, the finite element grid for FRAC3DVS is offset by one-half of a block as compared to the SWIFT-III finite difference grid block. Since hydraulic conductivity is defined on

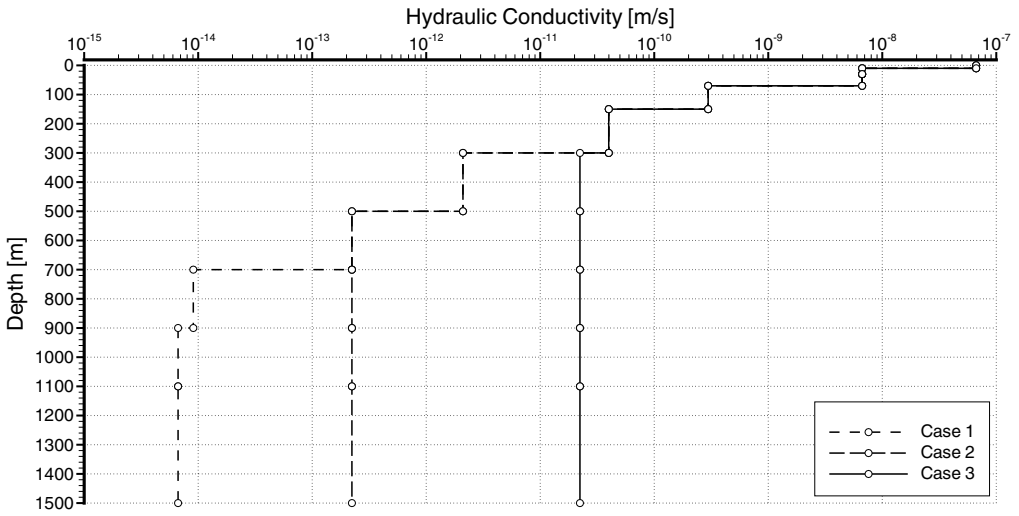

Figure 3.7 Depth variation in hydraulic conductivity for three cases in the regional scale model.

a block-wise basis, a varying hydraulic conductivity field is not spatially identically in both models. In this case, the hydraulic conductivities of the four neighbouring blocks in the same layer were averaged to obtain the new value. This procedure introduces smoothing of the hydraulic conductivity field used in FRAC3DVS; layers of constant hydraulic conductivity are not affected by this procedure. A porosity of 0.5% was chosen for the entire modelling domain.

Modelling groundwater flow in deep geologic systems requires that the compressibility of the fluid, and the matrix be included in an analysis because of the high fluid pressures that can occur at depth. SWIFT-III includes this capability and requires specification of the compressibilities of both the water and the rock. In FRAC3DVS, the specific storage is specified and can be calculated from the rock and water compressibilities, as discussed in §2.4.2.

Longitudinal and transverse dispersivities of 125 m, a tortuosity of 1.0, and a free solution diffusion coefficient of $1.15779\times10^{-2}\,m^2/a$ are used throughout the modelling domain. A rock density of $2650\,kg/m^3$ in SWIFT-III was used to obtain the FRAC3DVS bulk density of $2636.75\,kg/m^3$ by accounting for a void space of 0.5%.

3.5 Model Comparison Performance Measures

Several performance measures were chosen as the basis of comparing output from SWIFT-III and FRAC3DVS: freshwater head, Darcy velocities and concentration. Numerous detailed figures were produced to aid the description of the performance measure comparison, and were provided as nine separate appendices, one appendix for each scenario comparison (*Normani et al.*, 2004).

3.5.1 Freshwater Head

Freshwater head was plotted for SWIFT-III layers 1, 4, 7, and 10 and the equivalent FRAC3DVS layers. These layers were chosen as they represent the top (layer 1 of 5 m depth) and bottom (layer 10 of 1300 m depth) of the domain, while layer 7 represents a typical repository depth of 600 m, and layer 4 represents a depth of approximately 130 m.

Since SWIFT-III uses a finite difference scheme, the calculation point is at the centroid of each block, hence these depths are measured to the vertical mid-point of each layer.

Freshwater head differences between SWIFT-III and FRAC3DVS were plotted for all ten SWIFT-III layers. A freshwater head difference was used to demonstrate subtle spatial variations in freshwater head between the two models. Similarly, histograms of freshwater head differences for each layer illustrated trends with depth or trends from layer to layer.

3.5.2 Darcy Velocities

Darcy velocities are vectors with both magnitude and direction; these two measures form the basis of the vector comparison in *Normani et al.* (2004). If two vectors have the same magnitude and the in-plane angle between them is zero, then the vectors are identical. Subtracting magnitudes provides no indication of the relative importance of the calculated difference to the velocity magnitudes in either SWIFT-III or FRAC3DVS. For example, a magnitude difference of 10^{-6} m/a is insignificant if the velocity magnitudes are on the order of 10^{-1} m/a, but can be quite important if the velocity magnitudes are of the same order as the calculated difference. Instead of subtracting the Darcy velocity magnitudes, a ratio is calculated. Since velocities can vary over several orders of magnitude across the modelling domain, comparisons can be made across different layers.

The angular separation between the SWIFT-III and FRAC3DVS Darcy velocity vectors is a relative indication of whether the velocities are in the same direction; a small angle indicates that the velocities are nearly in the same direction while an angle of 180° indicates that the velocity vectors are in opposite directions. Figure 3.8 provides a graphical representation of the angular separation and magnitude ratio for Darcy velocity vectors.

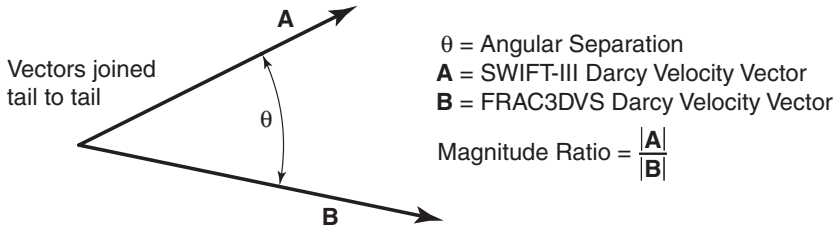

Figure 3.8 Determining angular separation and magnitude ratio for Darcy velocity vectors.

3.5.3 Fractional Brine Concentration

Fractional concentrations were used because fluid density was related to the solute concentration; fractional concentrations are in the range of 0.0 to 1.0, where a value of 1.0 represents the maximum solute density. Solute densities of 1.03 g/cm^3 and 1.10 g/cm^3 were used as listed in Table 3.3.

Concentration ratios are calculated instead of a concentration difference because concentrations can vary by orders of magnitude across the modelling domain, thus providing a better comparative tool.

3.6 Model Comparison for Scenario 2

Although the appendices in *Normani et al.* (2004) occupy 336 pages, portions of the analysis for Scenario 2 (see Table 3.3) are provided herein.

The freshwater heads calculated from SWIFT-III and FRAC3DVS appear very similar to each other for Layer 7 as shown in Figure 3.9. Subtracting the FRAC3DVS heads from the SWIFT-III heads for Layer 7 yields Figure 3.10. As these figures illustrate, the freshwater heads calculated by SWIFT-III are greater than those calculated with FRAC3DVS, but usually less than 0.5 m. A succinct graphical summary of the freshwater head differences for each layer can be found in Figure 3.11 in the form of histograms. As can be seen, the differences, although small, increase with increasing depth from surface.

This difference becomes more pronounced with depth and can be attributed to the fact that SWIFT-III accounts for the increase in pore fluid density with depth, whereas FRAC3DVS assumes an incompressible fluid. A trial set of model runs were performed using SWIFT-III that used a water compressibility ten orders of magnitude less compressible than the accepted water compressibility value of 4.57×10^{-10} Pa^{-1}. This would have the effect of rendering the water incompressible within SWIFT-III, solely for the purposes of determining if the pore fluid compressibilities were the primary cause of the differences in the freshwater heads. Scenario 2 was re-run with a water compressibility of 4.57×10^{-20} Pa^{-1}. Greatly reducing the compressibility of water in SWIFT-III resulted in freshwater head differences which were very small or nearly zero (compare Figure 3.11 to Figure 3.12).

Darcy velocities for both models in Layer 7 are shown in Figure 3.13. Darcy velocities are not as easily compared as freshwater heads, due to their 3-D vector nature. In the finite element formulation, velocities are calculated at the element centroid, while in the finite difference formulation, velocities are calculated at the block faces. An additional factor to consider is that two layers are required in FRAC3DVS for each layer in SWIFT-III to maintain the spatial consistency of material properties such as hydraulic conductivity or porosity. The end result is that eight FRAC3DVS Darcy velocity vectors are averaged to obtain a single vector that can be compared to SWIFT-III. The SWIFT-III block face Darcy velocities are shifted 1/2 block from the block edge to the block centroid for comparison purposes. For the 10 layer SWIFT-III model, there are 9 interior faces or edges, but a 10 layer array is produced. The first entry in each cartesian direction is assigned zero, resulting in the vertical component of Darcy velocities for Layer 1 being zero.

The vector comparison takes two forms: the angular separation between the two vectors; and their magnitude ratio. Figure 3.14 illustrates the angular separation of the velocity vectors for Layer 7. Histograms of angular separation for all layers are shown in Figure 3.15. Angular separations of 90° or more can be seen in Layer 1, and are coincident with lakes, resulting from the fact that the vertical component of the Darcy velocity is zero in SWIFT-III while it is non-zero in FRAC3DVS. Since horizontal gradients are non-existent beneath large water bodies, and vertical gradients are non-zero, the vertical gradient is the dominant direction for flow. The angular separation of 90° results from the fact that the FRAC3DVS Darcy velocity is predominantly vertical, while the SWIFT-III Darcy velocity is forced to be horizontal due to the zero vertical component. The histograms in Figure 3.15 show that the angular separation decreases with depth, and this can be primarily attributed to the fact that the freshwater heads and gradients

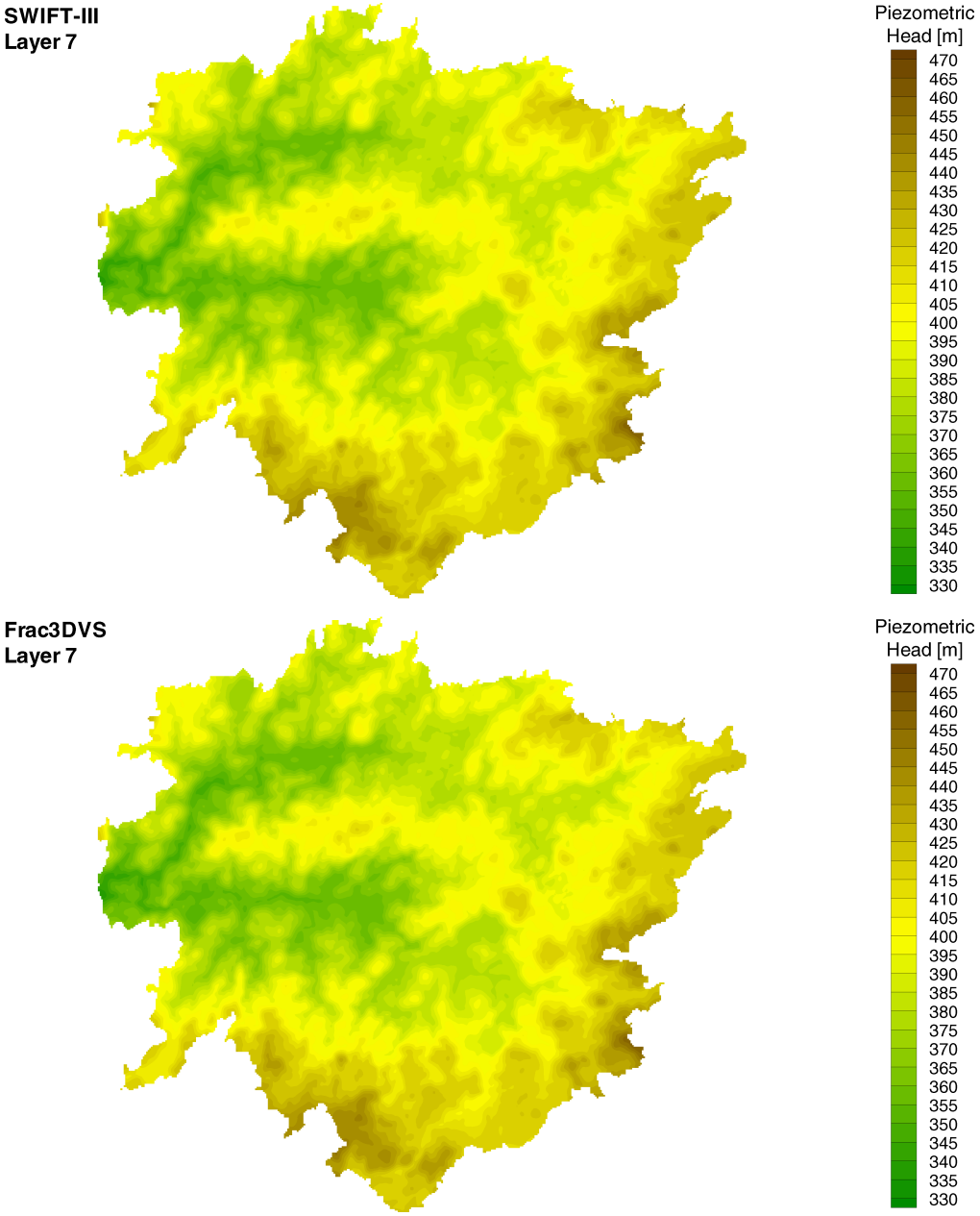

Figure 3.9 Scenario 2 freshwater heads in Layer 7 for SWIFT-III and FRAC3DVS.

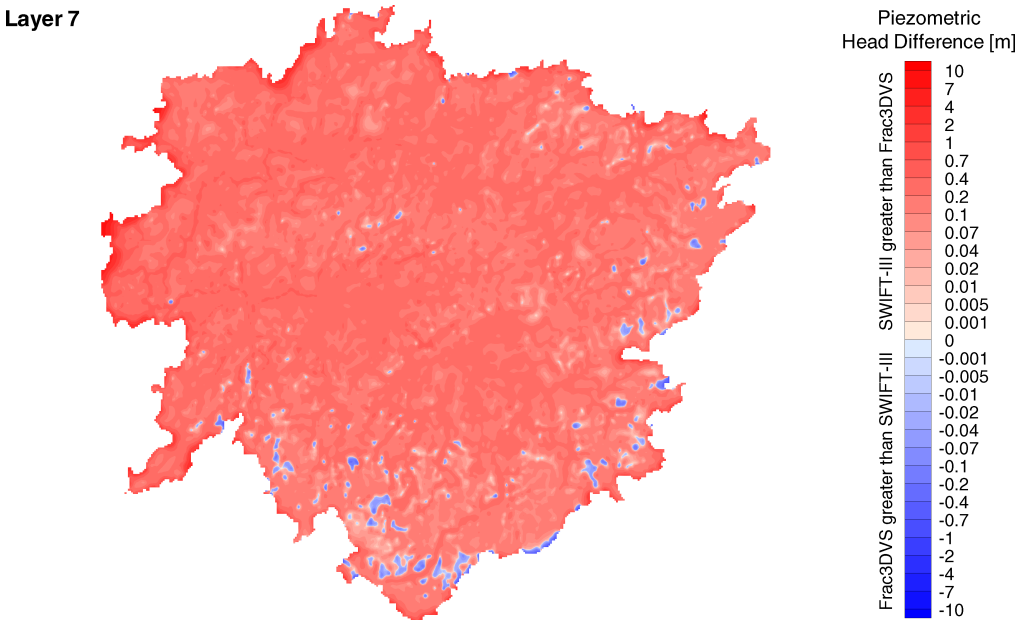

Figure 3.10 Scenario 2 freshwater head difference between SWIFT-III and FRAC3DVS for Layer 7.

vary smoothly at depth as compared to the near surface layers; hence adjacent vectors are more likely to be similar and the averaging operation introduces less variation. The greater differences seen in Layer 10 are likely due to the 400 m thickness of the layer, being represented as a single layer in SWIFT-III and two layers in FRAC3DVS.

A Darcy velocity vector is the product of the hydraulic conductivity and a gradient. The hydraulic conductivity is user-defined, while the gradient is based on the grid spacing and the computed pressure and density differences. Changes in fluid density are attributed to the presence of a solute and to fluid compressibility. SWIFT-III considers density differences due to a solute, but ignores density differences due to fluid compressibility when computing Darcy velocities. Density differences due to fluid compressibility can be small when compared with the presence of a solute and are sometimes ignored. In regions of zero or near-zero pressure gradients underneath large water bodies, hydrostatic conditions prevail, leading to essentially stagnant flow conditions. Care must be taken in comparing Darcy velocities computed in hydrostatic regions. Since a hydrostatic condition represents a near-zero pressure gradient, FRAC3DVS would compute a near-zero velocity, but SWIFT-III would not as the fluid compressibility influences the fluid density, and hence fluid pressure with depth. SWIFT-III thereby calculates a Darcy velocity due to a density difference which is not adjusted for fluid compressibility. For example, in FRAC3DVS, the variation in pressure at datum at a depth of 257 m underneath a large water body is very small (approximately 0.0002 m), while with SWIFT-III, the variation is approximately 0.0891 m. The resulting gradient is therefore greater in SWIFT-III than in FRAC3DVS. Darcy velocities are on the order of 10^{-3} m/a in SWIFT-III near the surface and decreasing to 10^{-6} m/a at a depth of 257 m, while the FRAC3DVS velocities are approximately 10^{-8} m/a throughout the same depth interval. When the fluid is made essentially incompressible, the SWIFT-III Darcy velocities over the same depth inter-

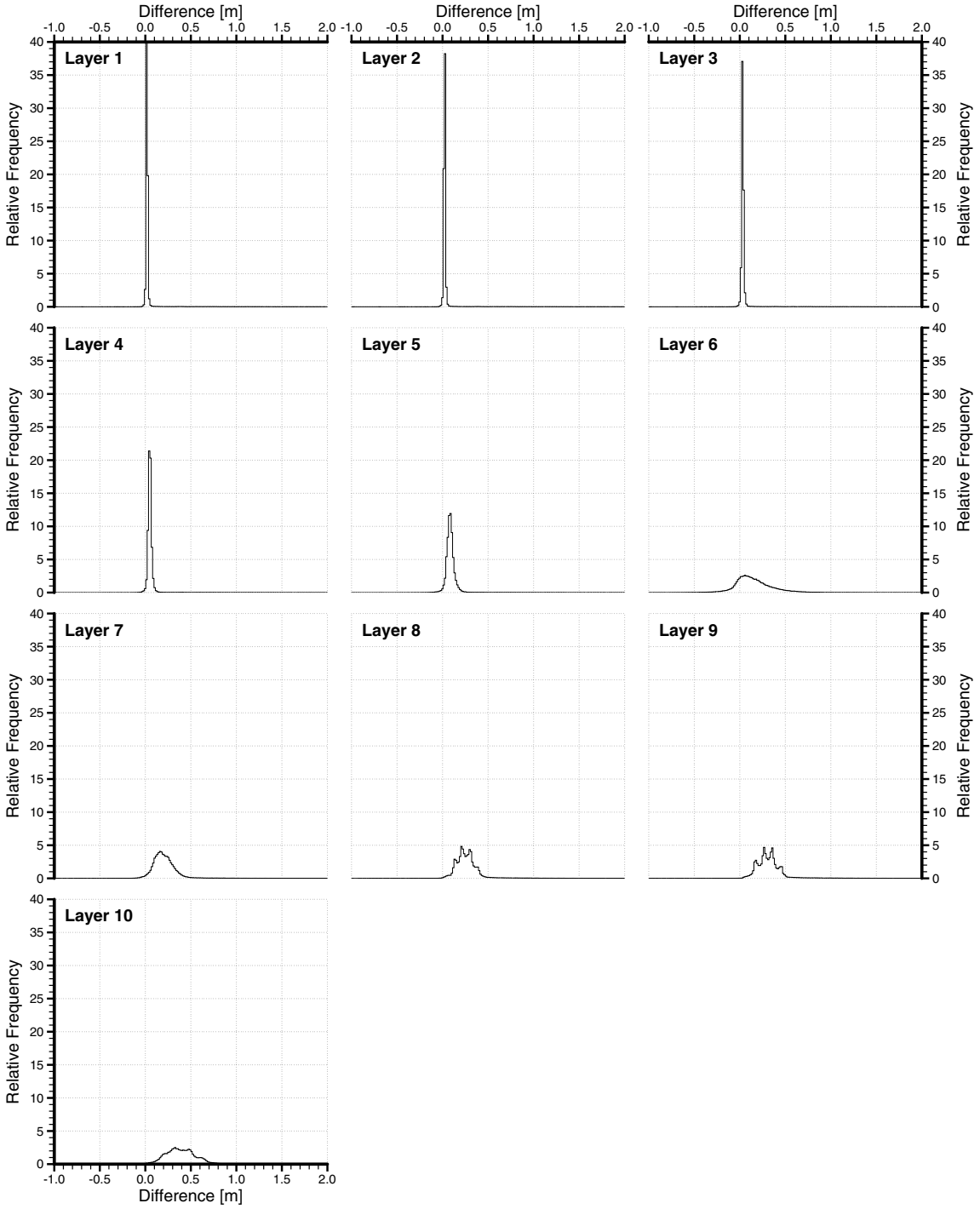

Figure 3.11 Scenario 2 freshwater head difference histograms between SWIFT-III and FRAC3DVS for Layers 1 through 10.

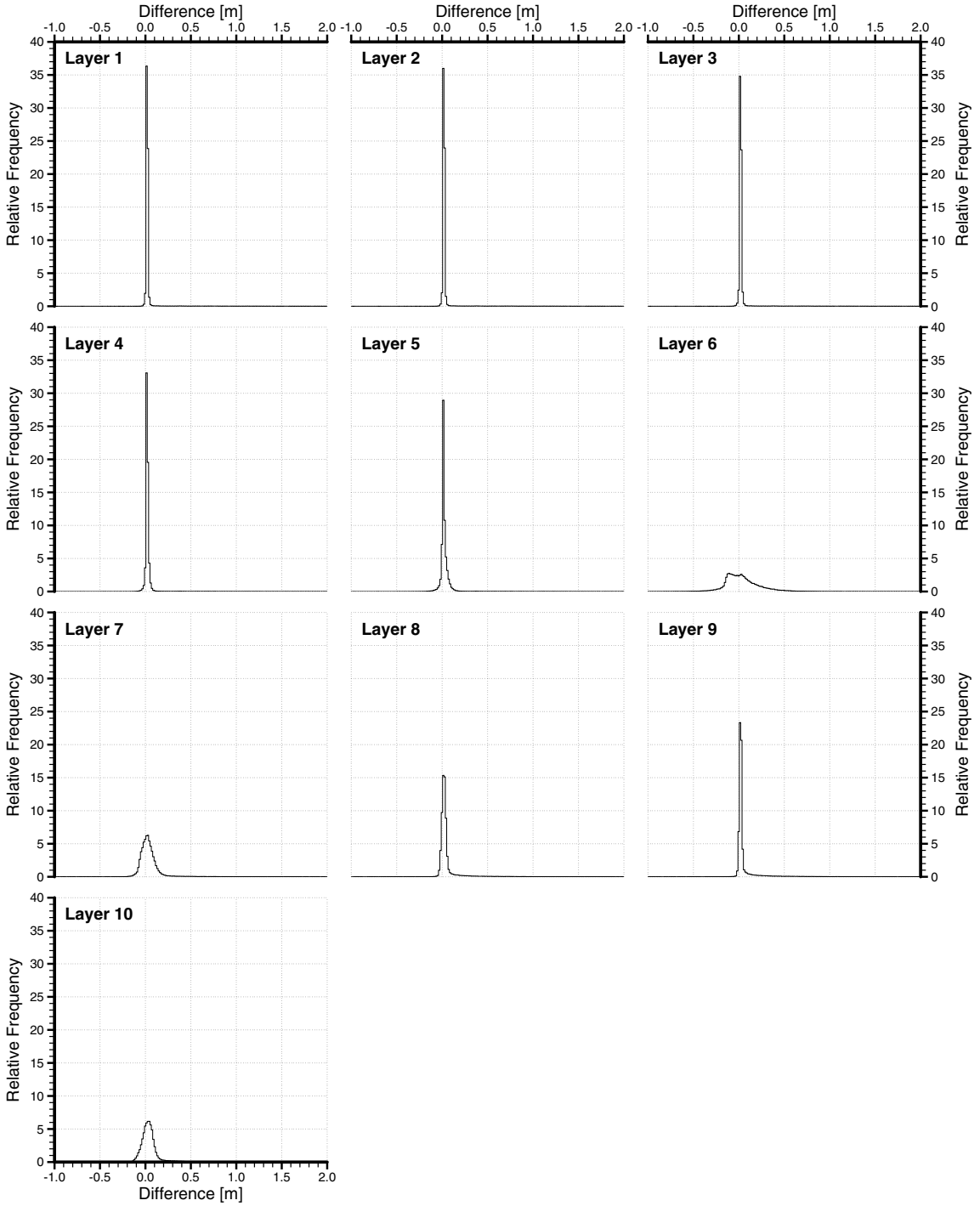

Figure 3.12 Scenario 2 freshwater head difference histograms between SWIFT-III and FRAC3DVS for Layers 1 through 10 for an incompressible water.

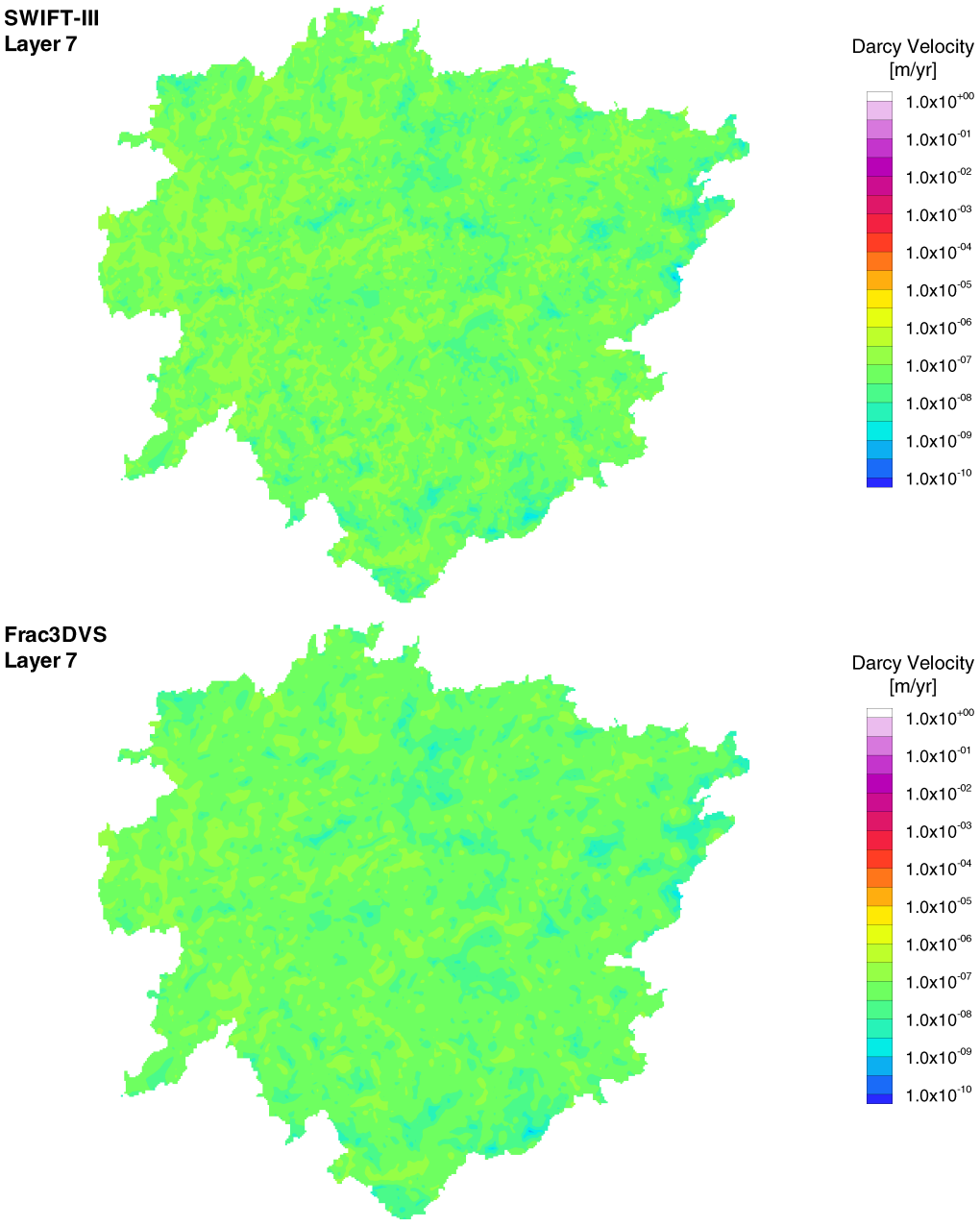

Figure 3.13 Scenario 2 Darcy velocities in Layer 7 for SWIFT-III and FRAC3DVS.

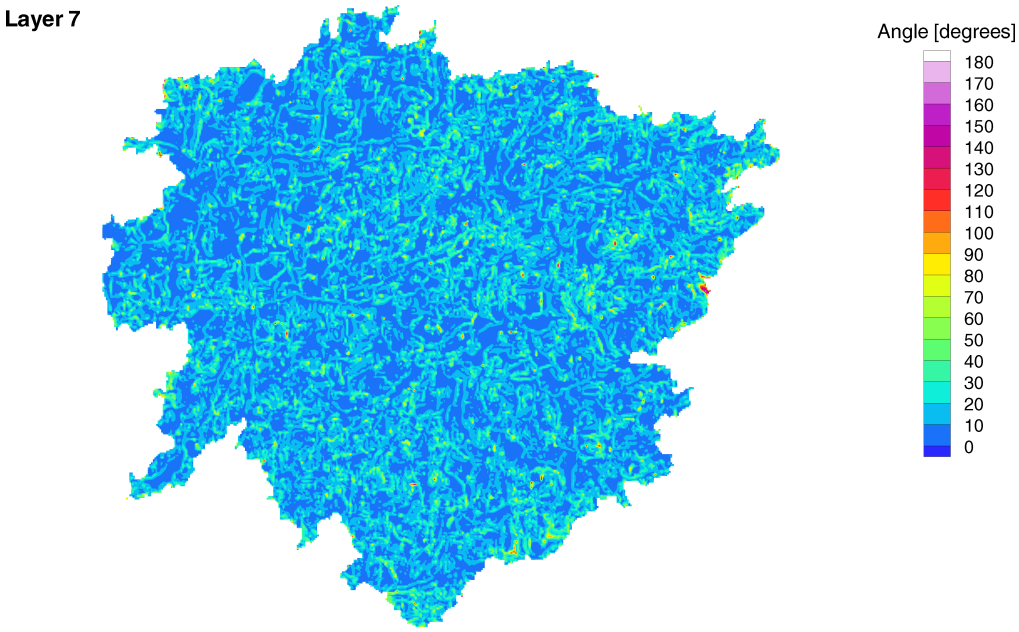

Figure 3.14 Scenario 2 angular separation in degrees between SWIFT-III Darcy velocity vector and FRAC3DVS Darcy velocity vector for model Layer 7.

val are approximately 10^{-8} m/a, similar to FRAC3DVS, and essentially comparable to diffusive processes.

The ratio of the velocity vector magnitudes from both numeric models should tend towards unity. Figure 3.16 demonstrates that the velocity vector magnitude ratios tend towards unity, except in certain areas that can be associated with prescribed surface features such as lakes and wetlands, due principally to fluid compressibility being included in SWIFT-III, as mentioned in the preceding paragraphs. When using an incompressible fluid in SWIFT-III, the magnitude ratio tends towards unity in all parts of the modelling domain, including beneath lakes and wetlands.

The histograms of Figure 3.17 illustrate that the velocity vector magnitudes are centred about unity. The deeper layers show less variation with narrower histograms than the near surface layers.

3.7 Summary

The regional scale model developed in *Sykes et al.* (2003a) using the finite difference model SWIFT-III was used as the basis for developing the same regional scale model using the finite element model FRAC3DVS. The purpose of this study was to compare analysis results from both models using the same regional scale watershed, representative of a Canadian Shield setting. The comparison was based on nine simulations (see Table 3.3), increasing in complexity from a steady-state freshwater simulation to a 100 ka transient saline simulation. Various combinations of brine density, hydraulic conductivity, spatially correlated hydraulic conductivity fields, and time scales comprised the nine simulations. Performance measures based on freshwater head, Darcy velocity, and brine concentration were applied. Both plan and cross-sectional views were used to illustrate spatial and depth dependencies while histograms were used to summarize results within layers and

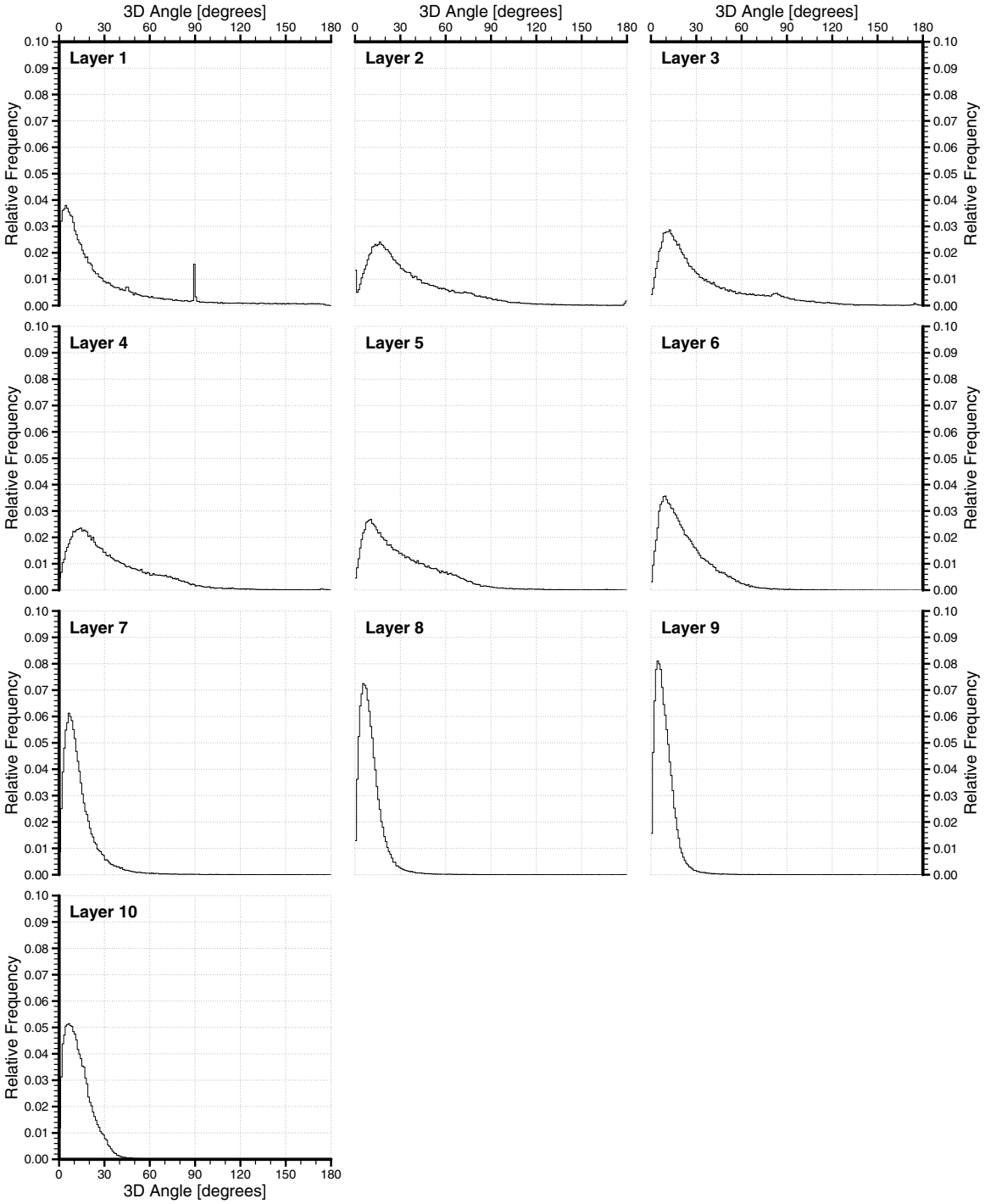

Figure 3.15 Scenario 2 histograms of angular separation in degrees between SWIFT-III Darcy velocity vector and FRAC3DVS Darcy velocity vector for model Layers 1 through 10.

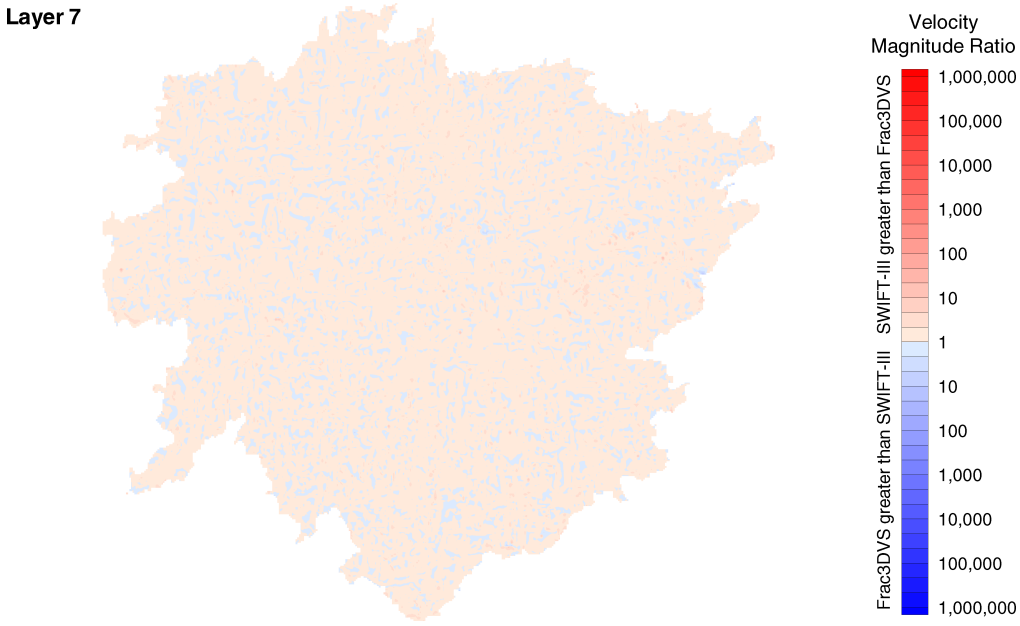

Figure 3.16 Scenario 2 ratio of Darcy velocity magnitude in SWIFT-III to the Darcy velocity magnitude in FRAC3DVS for Layer 7. The red band indicates that the SWIFT-III velocity is greater than the FRAC3DVS velocity by the factor indicated.

to compare layers to each other. Approximately 40 figures for each comparison scenario are provided in the nine appendices of *Normani et al.* (2004).

The comparison of results from FRAC3DVS and SWIFT-III presented various challenges and required several compromises due to the different grid structures and solution techniques implemented in each model. Although the freshwater heads or pressures at datum, and concentrations could be directly compared since the calculational points were made coincident, eight FRAC3DVS Darcy velocities were averaged to allow comparison to SWIFT-III Darcy velocities which were themselves shifted 1/2 grid block in the x, y, and z directions to obtain the same calculational point. The FRAC3DVS grid also contained twice the number of layers as SWIFT-III to ensure that material properties were spatially coincident in both models. The spatially correlated hydraulic conductivities in FRAC3DVS were calculated as the average of four neighbouring SWIFT-III grid blocks within a layer due to the model grids being offset by one-half of a grid block to obtain spatially coincident calculational points.

The performance measures indicate that the models compare very well to each other. In terms of freshwater head or pressure at datum, the mean difference at the base of the modelling domain was approximately 0.5 m. Since SWIFT-III includes fluid compressibility and the version of FRAC3DVS used in this study did not, an additional simulation was performed to address the effects of fluid compressibility (see *Normani et al.*, 2004, Appendix J). The fluid compressibility was changed to 4.57×10^{-20} Pa^{-1} from its native value of 4.57×10^{-10} Pa^{-1} in SWIFT-III, resulting in a mean difference of nearly zero for freshwater heads, thereby confirming that the differences between the results for the two models were due to fluid compressibility being implemented in SWIFT-III.

Darcy velocity vector magnitudes and directions from SWIFT-III and FRAC3DVS compared quite well to each other. Darcy velocity vector magnitudes were typically

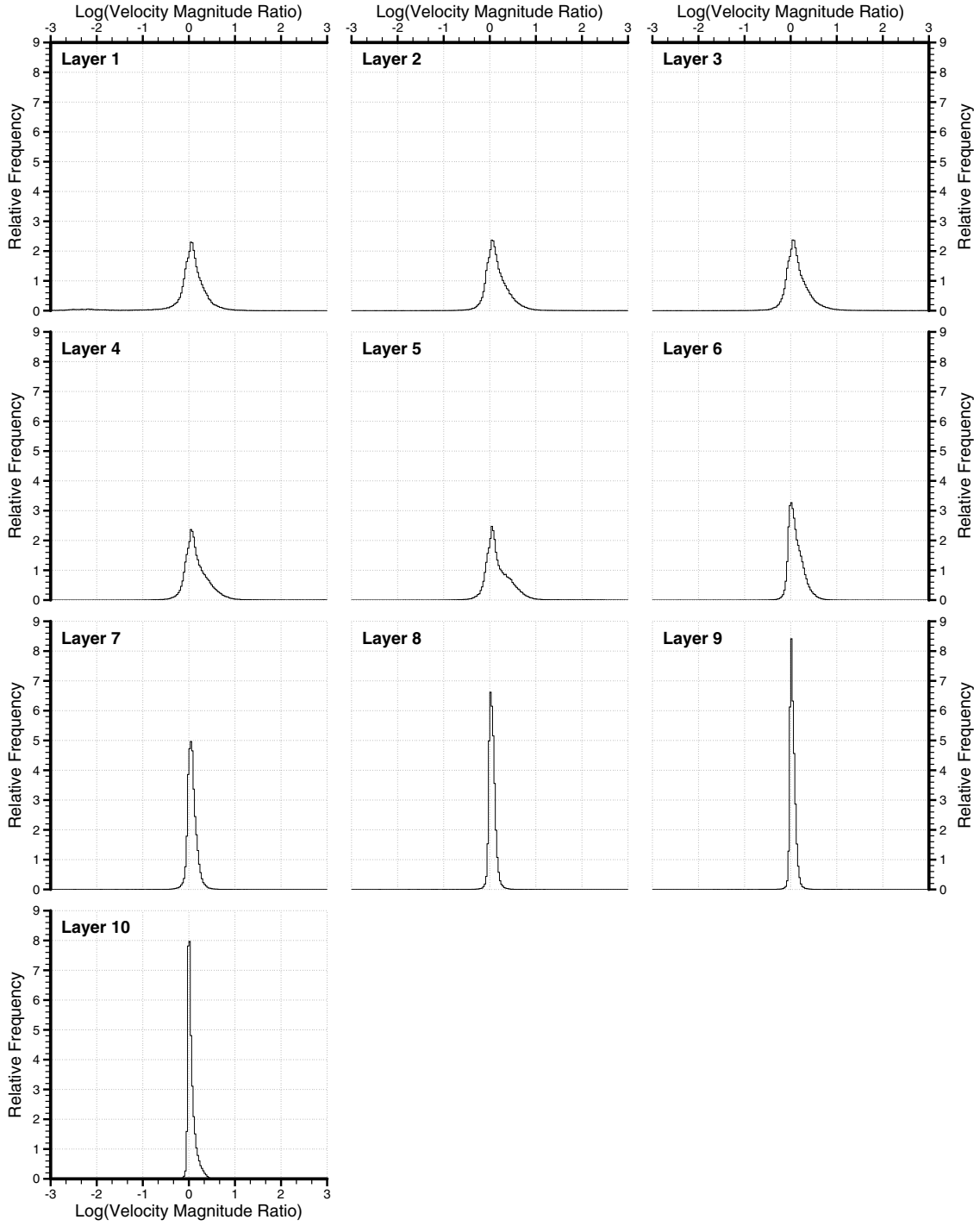

Figure 3.17 Scenario 2 histograms of angular separation in degrees between SWIFT-III Darcy velocity vector and FRAC3DVS Darcy velocity vector for model Layers 1 through 10.

nearly equal, while angular separations were typically less than 10°. These differences are attributed in part to the averaging procedures which were required to obtain spatially comparable Darcy velocity vectors. Fluid compressibility also had an effect on the calculation of gradients and hence velocities and was especially noticeable in regions of virtually no gradient (essentially hydrostatic conditions), namely beneath large water bodies such as lakes or wetlands. Although the Darcy velocities in such regions were on the order of 10^{-8} m/a, the calculated Darcy velocities from SWIFT-III were greater than FRAC3DVS. Once again, the inclusion of fluid compressibility in SWIFT-III resulted in fluid density variations, which were not compensated for in the calculation of Darcy velocities. Assuming an incompressible fluid for SWIFT-III, as shown in Appendix J of *Normani et al.* (2004), clearly shows that fluid compressibility was the mechanism by which these differences appeared between SWIFT-III and FRAC3DVS.

In terms of fractional or relative concentrations, differences were noted in the results from both models and were influenced by: differences in the velocity fields, the number of model layers, and the various numerical algorithms implemented in either model to control numerical dispersion and other numerical artifacts. These artifacts are commonly encountered in the solution of the advection-dispersion equation.

Finally, the work of *Normani et al.* (2004) demonstrates the suitability of using FRAC3DVS to model deep groundwater flow systems comprised of dense pore fluids.

Chapter 4

Canadian Shield Sub-Regional Model

Based on the success of the regional scale modelling of a representative Canadian Shield site described in Chapter 3, a modelling domain of similar extent to the EIS (see §2.2.1.1) and SCS (see §2.2.1.2) case studies was proposed. This sub-regional domain would include discrete fracture zones, incorporate a high resolution spatial discretization, and use FRAC3DVS as the numerical model, namely due to its suitability for modelling deep groundwater flow systems with coupled density-dependent transport. FRAC3DVS implements a dual continuum capability to represent fractures as two-dimensional planar elements between adjacent three-dimensional hexahedral elements representing the moderately or sparsely fractured rock matrix.

4.1 Phase–I Model Development

A representative sub-regional modelling domain was chosen from four candidate sites within the regional modelling domain investigated by *Sykes et al.* (2003a); the sites are shown in Figure 4.1. Sub-region 2 was selected due to its size, and proximity to major basin divides and hydrologic features. The northern boundary is defined by the surface water divide between the basins for two large rivers, one that drains the northern basin, and the other river drains the southern basin. The southern boundary is coincident with the large river that drains the southern basin. Locations of all rivers are shown in Figure 3.3. The eastern and western boundaries of the sub-region are defined by either tributaries or surface water divides. Sub-region 2 has an area of approximately 84 km^2, an easting extent of 10.8 km and a northing extent of 12 km. Further details concerning

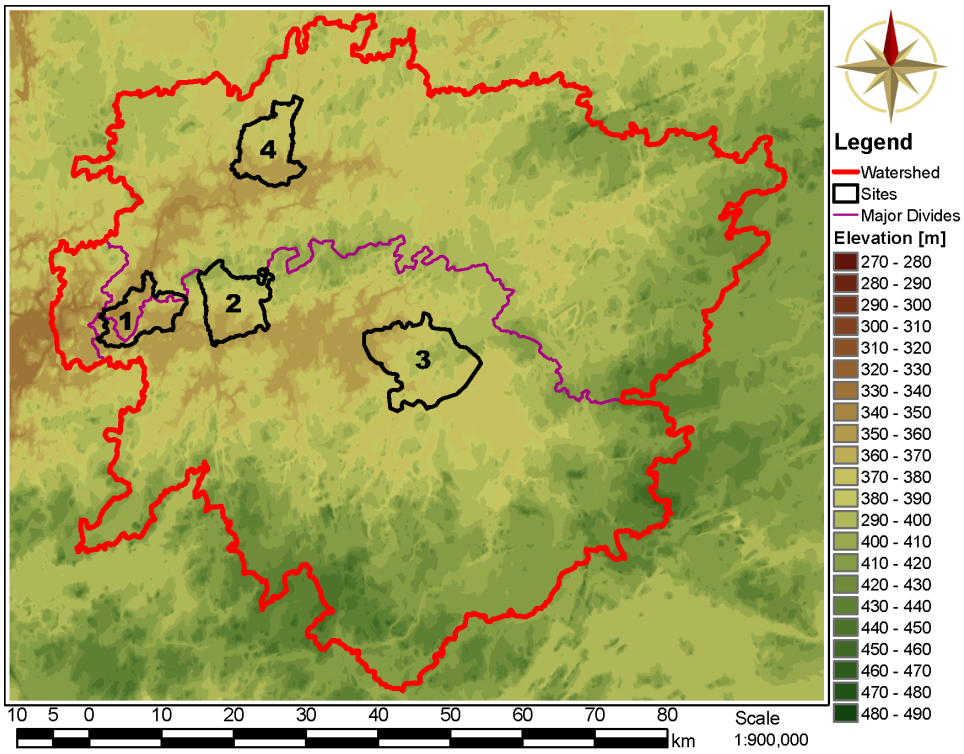

Figure 4.1 Location of four sub-regions within regional domain.

the development and simulation results of the sub-regional model are provided in *Sykes et al.* (2004).

GIS based data sources such as a DEM and digital NTS maps were obtained. Aerial photography at a scale of 1:60000 was obtained from the National Air Photo Library (NAPL). The aerial photography was digitized, orthorectified, and mosaiced using PCI OrthoEngine 8.0 and aligned to the digital NTS maps, as shown in Figure 4.2, while the water features and topography are shown in Figure 4.3. Both figures also show the modelling boundary.

4.1.1 Spatial Discretization

The three-dimensional sub-regional domain was discretized into 568442 hexahedral elements with a total of 610320 nodes. The grid is orthogonal with each EPM block having the same lateral dimensions of 50 m by 50 m. The site model was discretized vertically into 19 layers as listed in Table 4.1. The top of model layer 19 is defined by the DEM using the linear interpolation method within the Spatial Analyst package in ArcView 3.2a. Layers 1 through 14, inclusive, have a constant thickness, while Layers 15 through 19 have a variable thickness which depends on the elevation of surface topography. The thicknesses noted in Table 4.1 for Layers 15 through 19 sum to a thickness of 350 m. This base thickness is linearly scaled for each grid block column to account for the variation in the actual thickness between the elevation of the ground surface and an elevation of zero; layer thicknesses are scaled proportionately.

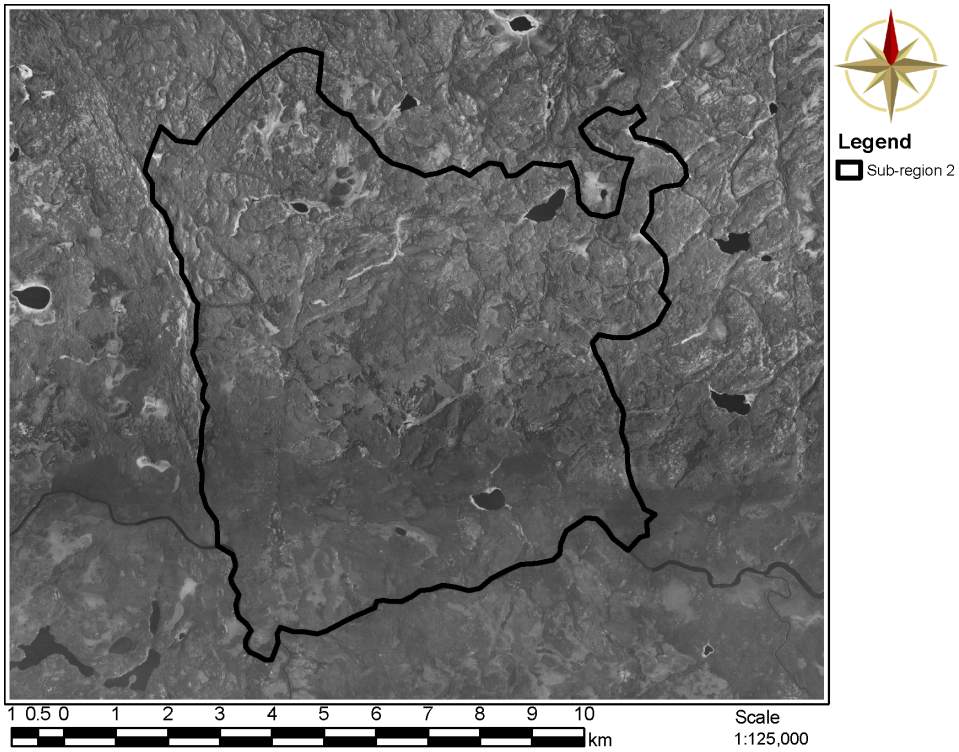

Figure 4.2 Aerial photograph and modelling boundary for Phase–I sub-region 2.

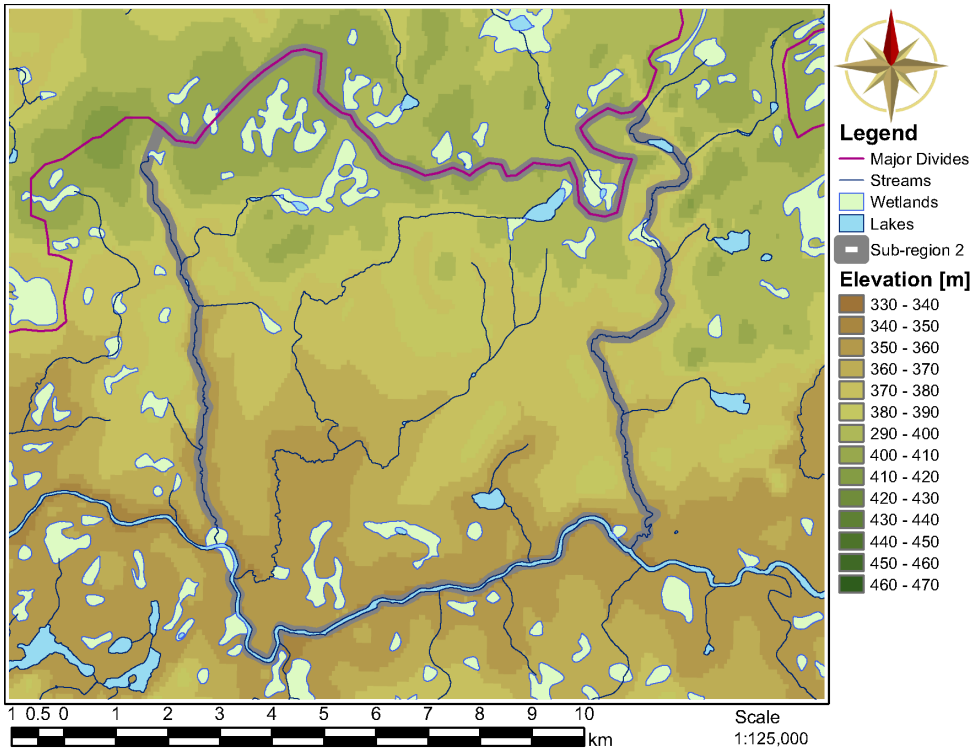

Figure 4.3 Phase–I sub-region 2 showing streams, lakes, wetlands and topography.

Table 4.1 Phase–I sub-regional model layer thicknesses and hydraulic conductivities.

Layer	Thickness [m]	Bottom Elevation [m]	Hydraulic Conductivity [m/s]		
			Case 1 (10^{-13})	Case 2 (10^{-12})	Case 3 (10^{-11})
19	10	Variable	7.0×10^{-8}	7.0×10^{-7}	7.0×10^{-7}
18	20	Variable	7.0×10^{-9}	7.0×10^{-8}	7.0×10^{-8}
17	40	Variable	7.0×10^{-9}	7.0×10^{-8}	7.0×10^{-8}
16	80	Variable	6.0×10^{-11}	8.0×10^{-10}	5.0×10^{-9}
15	100	Variable	4.0×10^{-12}	7.0×10^{-11}	1.0×10^{-9}
14	100	0	4.0×10^{-12}	7.0×10^{-11}	1.0×10^{-09}
13	100	−100	1.0×10^{-12}	3.0×10^{-11}	5.0×10^{-10}
12	100	−200	1.0×10^{-12}	3.0×10^{-11}	5.0×10^{-10}
11	75	−275	8.0×10^{-13}	7.0×10^{-12}	5.0×10^{-11}
10	50	−325	8.0×10^{-13}	7.0×10^{-12}	5.0×10^{-11}
9	50	−375	8.0×10^{-13}	7.0×10^{-12}	5.0×10^{-11}
8	50	−425	2.0×10^{-13}	1.0×10^{-12}	1.0×10^{-11}
7	50	−475	2.0×10^{-13}	1.0×10^{-12}	1.0×10^{-11}
6	50	−525	2.0×10^{-13}	1.0×10^{-12}	1.0×10^{-11}
5	75	−600	2.0×10^{-13}	1.0×10^{-12}	1.0×10^{-11}
4	100	−700	2.0×10^{-13}	1.0×10^{-12}	1.0×10^{-11}
3	150	−850	2.0×10^{-13}	1.0×10^{-12}	1.0×10^{-11}
2	200	−1050	2.0×10^{-13}	1.0×10^{-12}	1.0×10^{-11}
1	200	−1250	2.0×10^{-13}	1.0×10^{-12}	1.0×10^{-11}

4.1.2 Triangulated Fracture Network Model

A surface lineament analysis of the aerial photography was conducted by *Srivastava* (2002) to define the major fracture features for the fracture network model (FNM), and are mainly coincident with surface drainage features that exhibit linearity. Additional surface lineaments were generated to extend existing major lineaments, and to increase the fracture density in areas where overburden cover would obscure surface lineaments. A lack of image contrast in the southern third of Figure 4.2 also required the generation of additional surface lineaments. The generated surface fracture features are shown in Figure 4.4, and are based on the lineament and fracture statistics for the Lac du Bonnet region of the WRA. Fracture zone orientation, fracture zone length, and area density distribution statistics are preserved, thereby representing both sensible and geomechanically plausible fracture behaviour (*Srivastava*, 2002).

To create three-dimensional curve-planar fracture zones, the surface lineaments shown in Figure 4.4 are propagated to depth until one of the following conditions are met:

- the fracture zone's down-dip width reaches the prescribed length to width ratio;
- the fracture zone truncates against an existing fracture zone; or
- the fracture zone reaches the edge or bottom of the modelled domain.

A network of 548 discrete curve-planar fractures was generated by *Srivastava* (2002) for the sub-regional domain to represent fracture zones. The generated FNM is one realization of many possible FNMs that could be generated for the sub-regional domain.

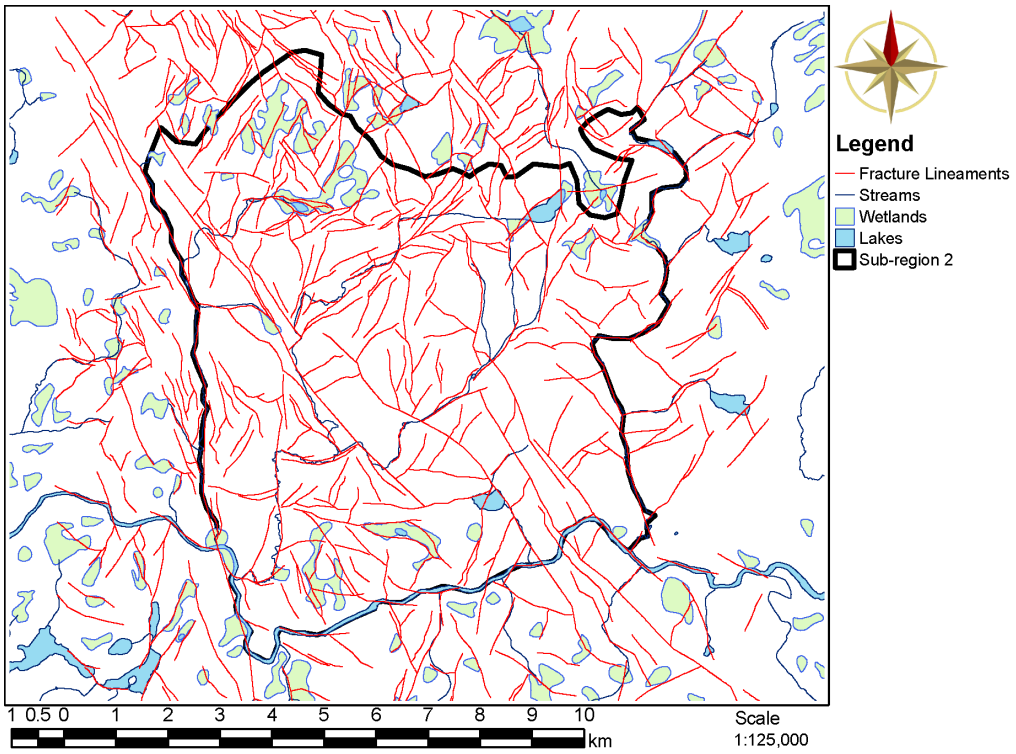

Figure 4.4 Phase–I sub-region 2 domain with water features and fractures that intersect ground surface.

Intersections of horizontal planes with the fracture zone network at depths of 500 m, 750 m and 1000 m are superimposed on the sub-regional domain orthophoto in Figure 4.5. Fracture network density decreases with increasing depth and minor fracture features are shallower than major fracture features. The resulting FNM contains a high degree of realism that honours many geological, statistical, and geomechanical constraints (*Srivastava*, 2002).

4.1.3 Orthogonal Fracture Network Model for FRAC3DVS

The geometry of individual curve-planar FNM fractures is described by a mesh of triangular facets as shown in Figure 4.6. This approach can also be used to assign spatially variable fracture properties, although this was not done in this thesis. The generation of a three-dimensional tetrahedral mesh for FRAC3DVS which can accommodate the complex geometries and orientations of the 548 discrete FNM fractures was not possible due to the lack of a suitable and robust mesh generator.

Since an orthogonal hexahedral finite element mesh was used, software was written in Visual Basic for Applications (VBA) to calculate the orthogonal grid block or element faces that best represents each curve-planar FNM fracture. The procedure used to generate the orthogonal FNM from a triangulated FNM is as follows:

- The FNM file provided by *Srivastava* (2002) is structured as one text line per triangular facet, comprised of a fracture number, and three coordinate triples (x,y,depth) representing each corner of the triangular facet.

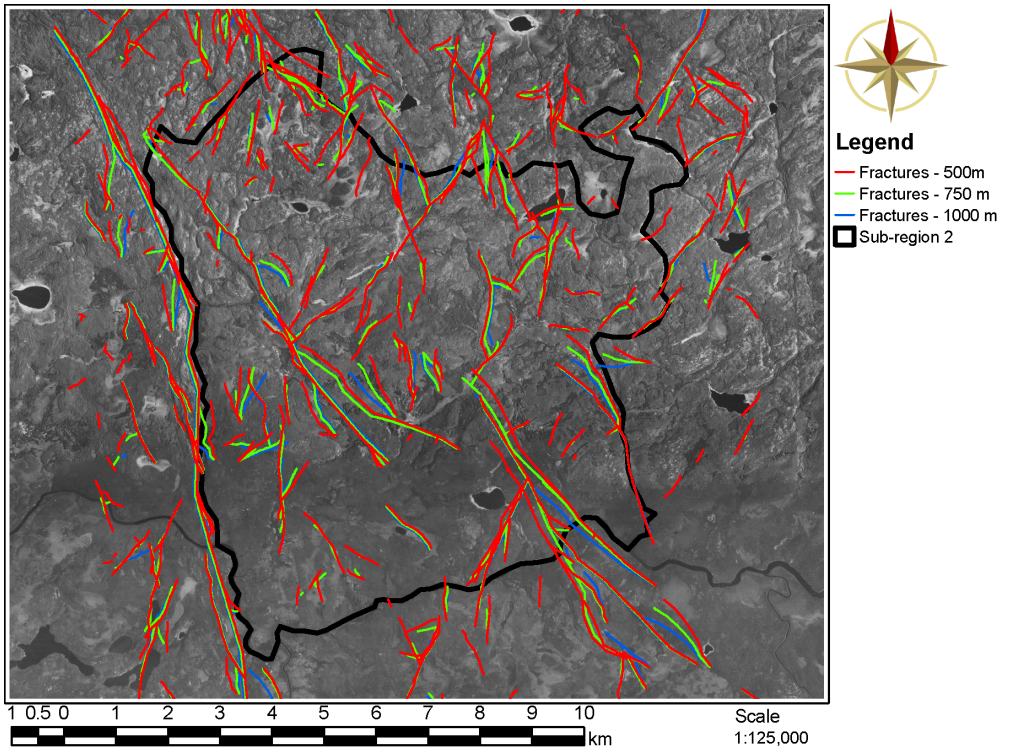

Figure 4.5 Phase–I sub-region 2 showing aerial photo and fracture intersections at depths of 500 m, 750 m, and 1000 m.

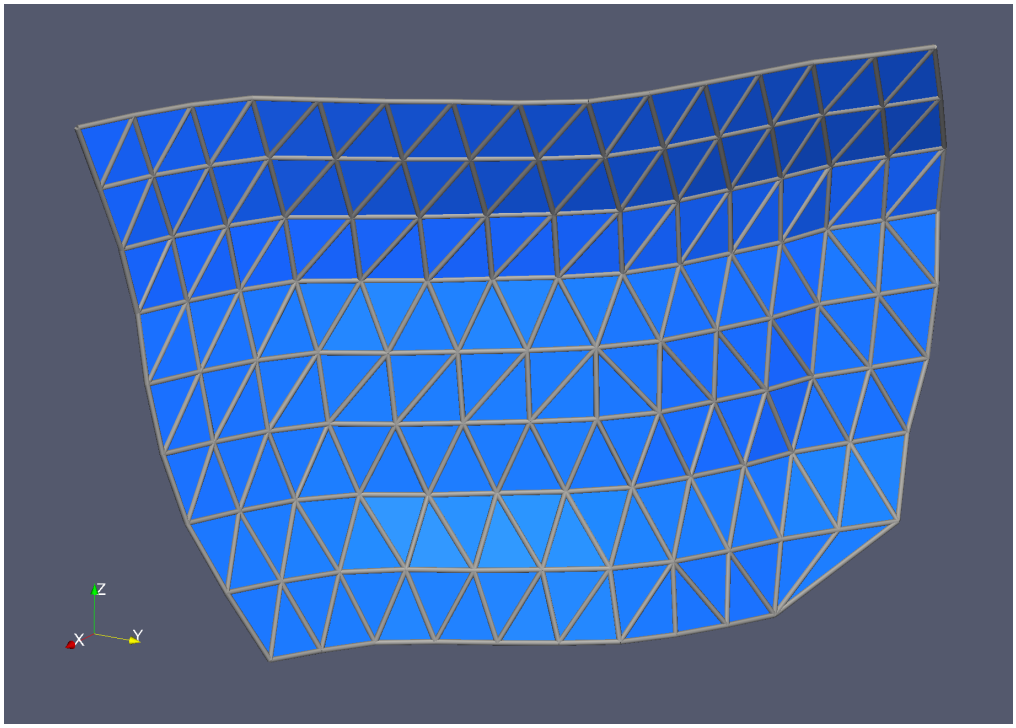

Figure 4.6 View of a single FNM fracture.

- The FNM file is processed to produce a new FNM file in which the triangular facets are represented by nodal coordinates and triangular element indices. Elevation is calculated by subtracting depth from the ground surface elevation at that location using a DEM. The ordering (clockwise or counter-clockwise) of element indices are such that they match the ordering of the first triangular element of a fracture. A fracture is comprised of numerous triangular elements.
- Process FRAC3DVS grid to determine face numbers (planar elements) associated with each hexahedral element based on an (i,j,k) ordering scheme.
- Read all triangular elements associated with a given fracture.
- Search for all FRAC3DVS hexahedral elements that intersect a given triangular element.
- Conduct this search for all triangular elements associated with a fracture number to produce a list of hexahedral elements which are intersected by the triangulated fracture, and output the list of hexahedral elements to a binary file.
- Loop over chosen hexahedral elements to select all exterior quadrilateral faces.
- Select a contiguous subset of quadrilateral faces that are either on one side of the triangulated fracture or on the other side, and output to a binary file.
- Repeat the above process for all fractures in a FNM file.
- Generate separate ASCII files of hexahedral elements intersected by the triangulated fractures, and face numbers of quadrilateral elements representing orthogonal fracture faces.

Figure 4.7 shows the FRAC3DVS orthogonal grid block faces that best represent the FNM fracture. The stepped nature of the orthogonal discretization clearly accommodates both the dip and orientation of the original curve-planar FNM fracture.

4.1.4 Boundary Conditions

Within the model domain, surface water features, such as lakes, rivers, and wetlands, were defined using Dirichlet boundary conditions. The elevation of these water features and of the top layer of the numerical model were interpolated from the DEM. A Dirichlet boundary condition of fixed piezometric head equal to surface topography was applied instead of using a recharge boundary condition. The average steady-state flux at the surface was calculated to be 1.3 mm/a. The use of a Dirichlet boundary condition was based on the fact that the water table is typically a subdued reflection of surface topography and that for watersheds in crystalline rock, the water table is typically very close to the ground surface (*Sykes et al.*, 2004). It is assumed that these boundary conditions are valid for all simulations.

Unfortunately, the DEM was quantized to integer elevation values, which resulted in the model's surface topography varying incrementally rather than continuously, which can lead to numerical modelling artifacts when using a Dirichlet surface boundary condition. As a result, the surface boundary condition is changed in the Phase–II model development, described in §4.2.

The northern model boundary was chosen based on a major topographic divide, while the eastern, southern, and western model boundaries were chosen coincident with rivers. An implied assumption from the use of rivers as model boundaries is that water does not underflow these rivers. A zero-flux boundary condition was used for the bottom and sides of the sub-regional model domain. It is also assumed that topographic or river

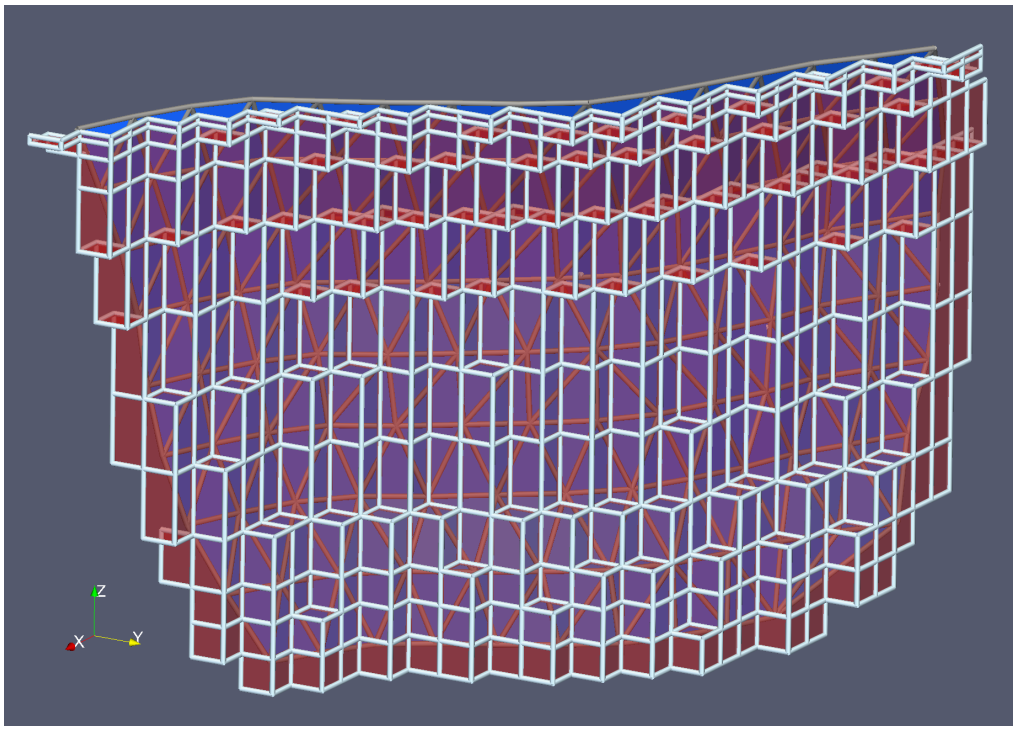

Figure 4.7 View of the single fracture and the FRAC3DVS orthogonal faces that best represent the fracture.

divides are suitable as lateral boundaries for the modelling domain. The work of *Sykes et al.* (2003a) shows that major divides are retained at depth, and are thus appropriate as lateral boundaries for a smaller domain.

4.1.5 Properties

The FRAC3DVS sub-regional model is comprised of 19 layers. A porosity of 0.002 was used for the rock matrix throughout the model. Table 4.1 lists the layer thicknesses, the bottom elevations, and the hydraulic conductivities for three modelled cases. The three cases represent different hydraulic conductivities for the deeper rock (i.e. below 700 m depth). Case 1 represents a 10^{-13} m/s hydraulic conductivity, while Case 3 represents a 10^{-11} m/s hydraulic conductivity. Case 2 represents an intermediate hydraulic conductivity of 10^{-12} m/s for the deeper rock, midway between Case 1 and Case 3, and similar to that used in the EIS study. Unlike the EIS or SCS, the hydraulic conductivities listed in Table 4.1 are isotropic for all layers and all cases. The variation in the hydraulic conductivity with depth for the three cases is plotted in Figure 4.8. The higher hydraulic conductivity values for the shallow depths represent the presence of moderately fractured rock while the lower hydraulic conductivity values at depth represent sparsely fractured rock.

Fracture zone properties are uniform with a hydraulic conductivity of 10^{-6} m/s, similar to the uniform permeability of 10^{-13} m^2 chosen for FZs in the EIS case study (see *Davison et al.*, 1994), and a FZ width of 1.0 m. Since only steady-state flow was investigated, storage coefficients were not required.

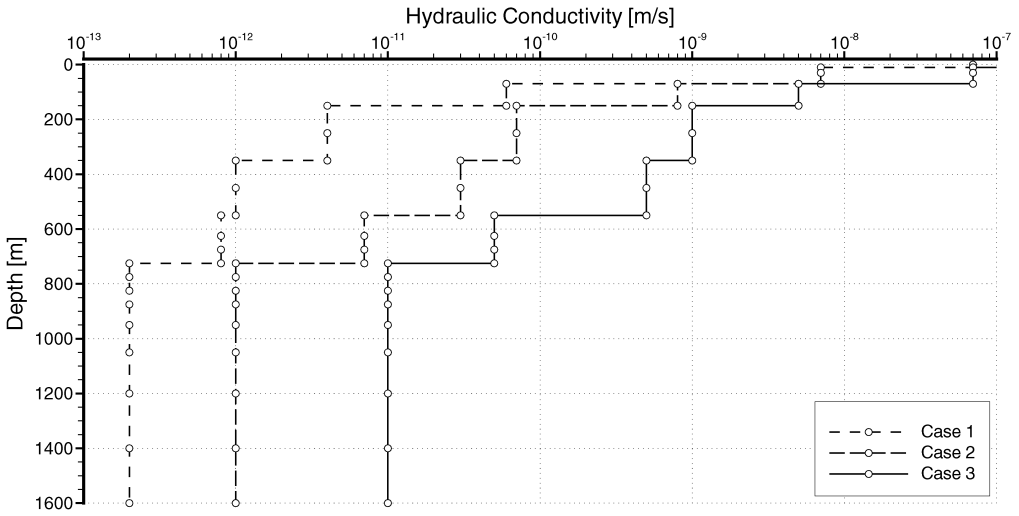

Figure 4.8 Hydraulic conductivity versus depth for Cases 1, 2, and 3 of the Phase–I sub-regional model.

4.2 Phase–II Model Development

In §4.1, the sub-regional model was developed, but several issues became apparent once the model results were interpreted. The following sections note the deficiencies and new approaches used for the Phase–II work.

4.2.1 Spatial Discretization

Due to the choice of Dirichlet boundary conditions for the top surface, and the use of a DEM which was quantized to integer elevation values, a "stair-step" effect was noticed when plotting the Darcy flux. The relatively abrupt step change in elevation from one plateau to the next lead to seepage faces forming along contour lines (see Figure 4.9). This modelling outcome is due to artifacts in the DEM, and is not related to any physical groundwater phenomenon.

A new DEM was constructed using the following GIS vector data: contour lines, rivers, wetlands, and lakes. The paper NTS maps for the area were used to define an elevation for the wetlands and lakes based on their relative position to nearby contours, as well as their hydrologic relationship to connected rivers, lakes, and wetland features within the same contour interval. River elevations were then linearly interpolated along their length, honouring any contour which crossed the rivers, as well as the elevations which were previously specified for lakes and wetlands. The revised DEM is shown in Figure 4.10, and a comparison of the Phase–I and Phase–II modelling extents is shown in Figure 4.11.

The eastern extent of the Phase–I sub-regional modelling domain was defined along a divide described by a river. A number of the generated FNM fractures also follow rivers, leading to the situation where a fracture could be partially inside the modelling domain, and partially outside the domain, thereby violating its connectedness. The sub-regional modelling domain was laterally extended to surface water divides along topographic highs for the eastern and western portions of the modelling domain. The large river to the south would remain, as would the topographic divide to the north.

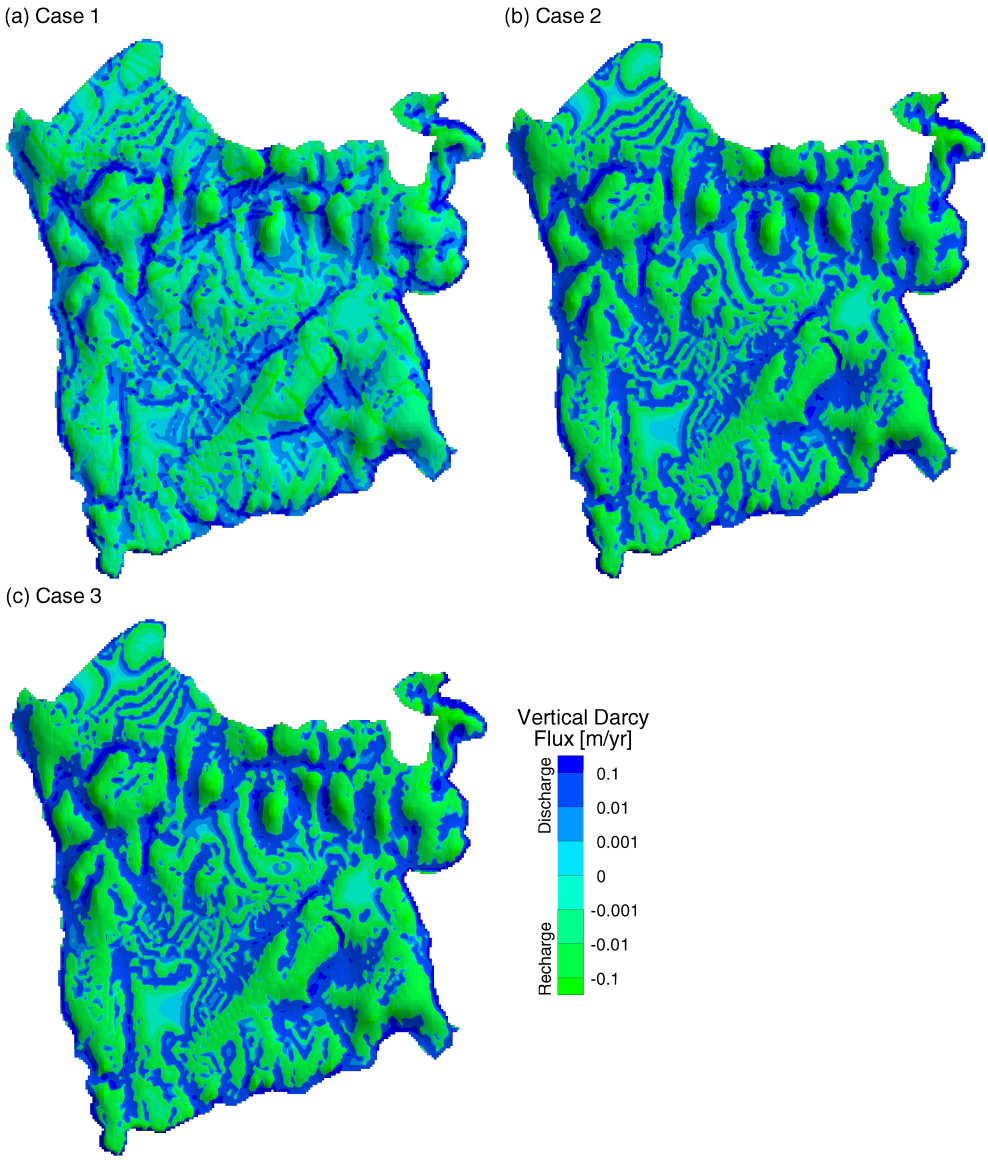

Figure 4.9 Vertical Darcy flux at ground surface for Case 1, 2, and 3 of the Phase–I sub-regional model.

ArcView GIS 3.2a was used to create a triangulated irregular network (TIN) using the contour lines, lakes, wetlands, and sloping rivers for the revised modelling boundary plus a 1 km buffer. From the TIN, a 10 m square DEM ASCII grid was created. Since some of the FNM fractures extend beyond the revised modelling boundary and 1 km buffer, a 20 m square DEM was generated using the NRCAN 1:250 000 DEM converted to Lambert conformal conic (LCC) projection. Both DEMs are used when calculating the elevation of fractures; any triangular fracture facet vertices within the modelling boundary (and buffer) use the TIN derived DEM, while all other vertices use the NRCAN derived DEM. The three-dimensional sub-regional domain was discretized into 847 080 nodes, and 789 887 brick elements, covering an area of 104 km^2.

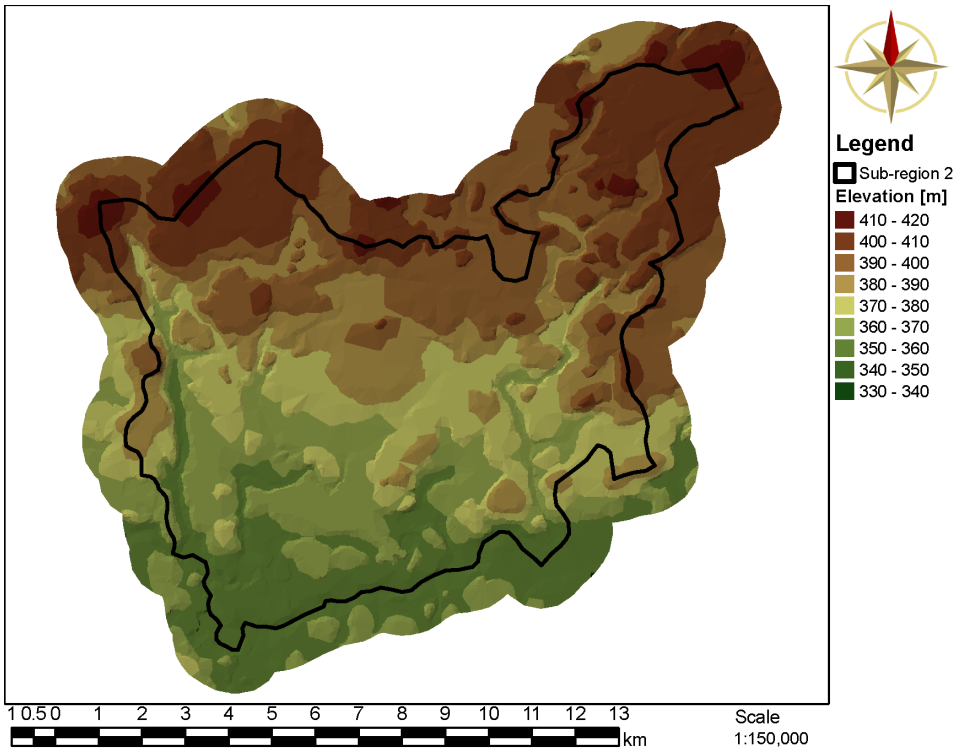

Figure 4.10 Phase–II DEM based on vector data for the expanded sub-regional modelling domain.

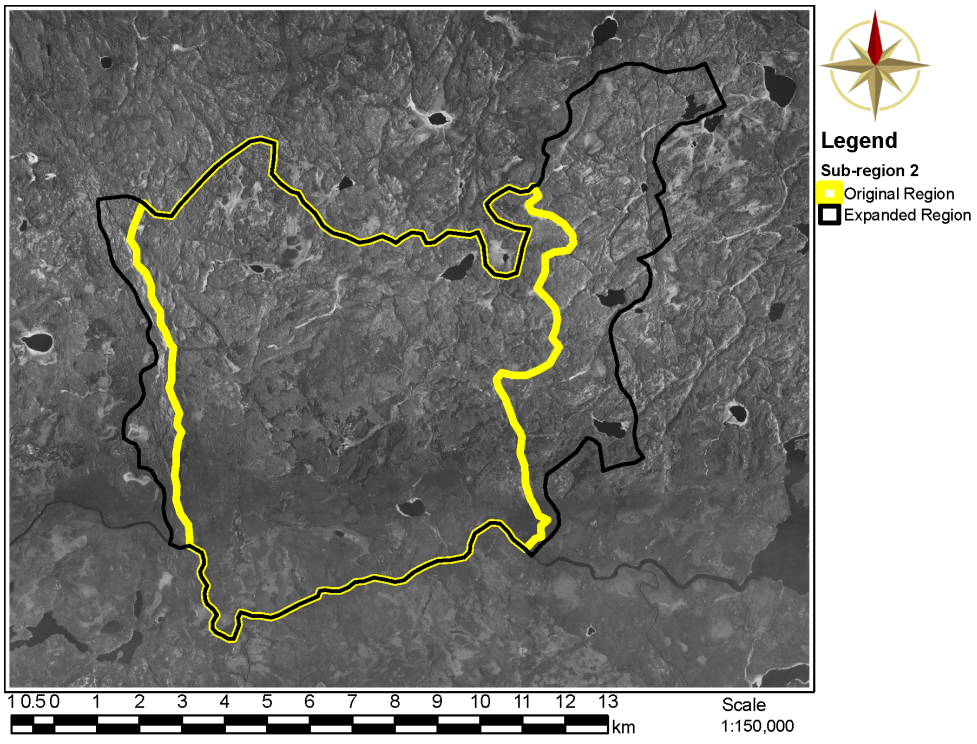

Figure 4.11 Phase–II sub-regional modelling domain (black line), Phase–I sub-regional modelling domain (yellow line) and aerial photo.

4.2.2 Fracture Network Models

As discussed in §4.1.2, *Srivastava* (2002) developed a framework for generating equally likely fracture network models. For the Phase–I work, 100 FNM realizations were generated conditioned on the same surface fracture lineament analysis. Since the surface lineaments are also generated from lineament and fracture statistics for the Lac du Bonnet region of the WRA, 100 equally likely surface lineaments were generated. The resulting 100 FNMs were considered to be unconditioned since different surface lineaments were used to generate each FNM. A total of 100 conditioned and 100 unconditioned FNMs were provided in *Srivastava* (2005). Since the modelling domain was extended westward and eastward, the FNM extents needed to be enlarged to suit the updated modelling domain (*Srivastava*, 2005). For the purposes of this chapter, only the first unconditioned FNM of 100 FNMs was used, and is shown in Figure 4.12; a total of 980 fracture zones are shown.

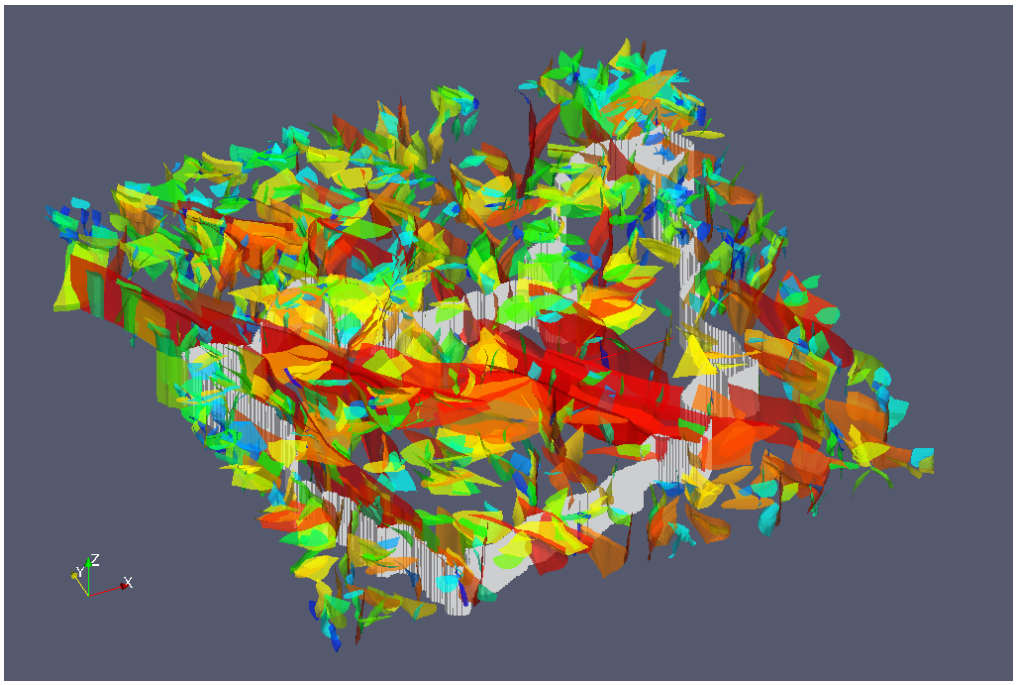

Figure 4.12 3-D perspective view of the first unconditioned FNM and the Phase–II modelling domain boundary.

4.2.3 Boundary Conditions

The Dirichlet surface boundary condition which was previously applied to the entire top surface of the model, was subsequently applied only at nodes which were within lakes or wetlands, or within 36 m of a river (approximately $\frac{50\sqrt{2}}{2}$, where a grid block is 50 m per side). This ensured that rivers would be continuous while considering the grid discretization. A recharge boundary condition is now applied to the top surface of the model at a rate of 1.0 mm/a, as was used in the regional scale model. These changes in surface boundary conditions on the Darcy flux at ground surface for Case 3 hydraulic

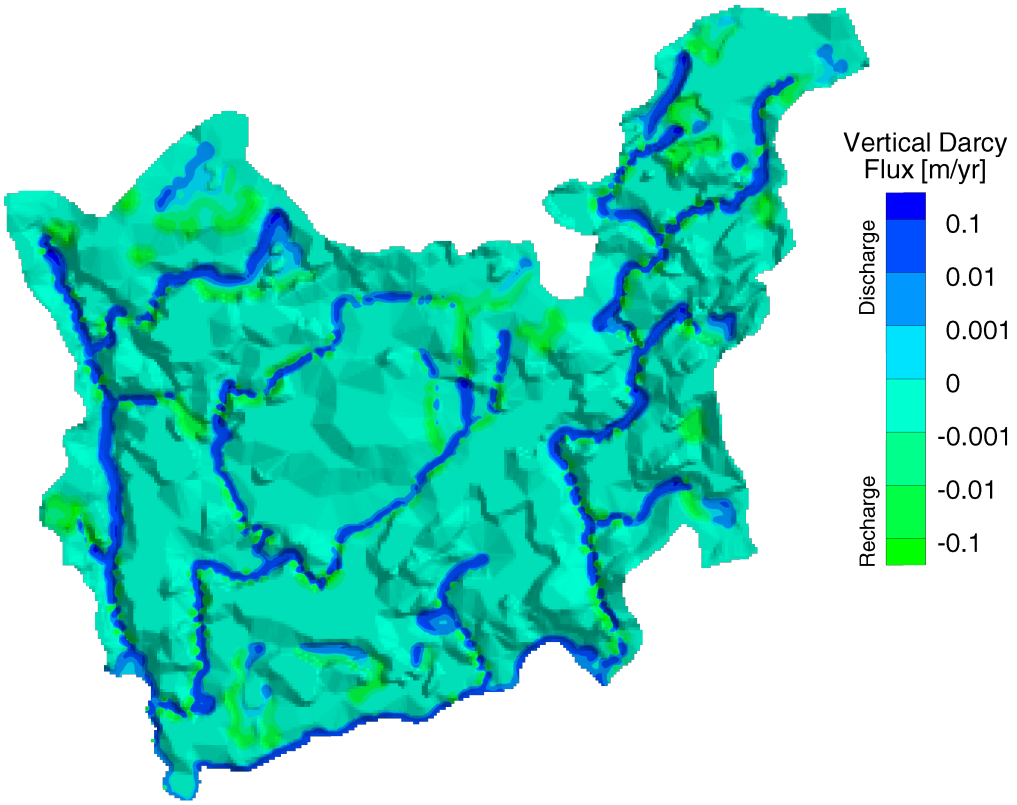

Figure 4.13 Vertical Darcy flux at ground surface for Phase–I Case 3 hydraulic conductivities using a recharge boundary condition for the Phase–II sub-regional model.

conductivities can be seen in Figure 4.13. Discharge fluxes now appear along rivers, lakes and wetlands.

4.2.4 Properties

The Phase–I sub-regional hydraulic conductivities were based on the original regional scale modelling of 10 vertical layers (see Table 3.2). Due to the need to account for variations in hydraulic conductivity due to changes in fluid density and viscosity within the Phase–II model, permeabilities are instead used. Both the horizontal and vertical permeabilities are expressed as follows:

$$k_H = 10^{-14.5-4.5(1-e^{-0.002469d})} \tag{4.1}$$

$$k_V = \begin{cases} 10k_H, & \text{for } d \le 300 \text{ m}; \\ [0.09(400-d)+1]k_H, & \text{for } 300 < d \le 400 \text{ m}; \\ k_H, & \text{for } d > 400 \text{ m}. \end{cases} \tag{4.2}$$

where k_H is the horizontal permeability [L^2]; k_V is the vertical permeability [L^2]; and d is the depth below ground surface [L]. The matrix permeabilities, defined by Equation (4.1) and Equation (4.2), and listed in Table 4.2, provide a smoother permeability transition from layer to layer, exponentially decreasing with increasing depth from ground surface. The horizontal and vertical permeabilities as a function of depth are also plotted in Figure 4.14.

Table 4.2 Phase–II sub-regional model matrix permeability by layer and depth.

Layer	Depth [m]	Average Depth [m]	Anisotropy Ratio k_V:k_H	Permeability [m^2]	
				k_H	k_V
19	0–10	5	10	1.0×10^{-13}†	1.0×10^{-12}
18	10–30	20	10	1.0×10^{-14}†	1.0×10^{-13}
17	30–70	50	10	9.5×10^{-16}	9.5×10^{-15}
16	70–150	110	10	2.7×10^{-16}	2.7×10^{-15}
15	150–250	200	10	5.6×10^{-17}	5.6×10^{-16}
14	250–350	300	10	1.4×10^{-17}	1.4×10^{-16}
13	350–450	400	1	4.7×10^{-18}	4.7×10^{-18}
12	450–550	500	1	2.0×10^{-18}	2.0×10^{-18}
11	550–625	587.5	1	1.1×10^{-18}	1.1×10^{-18}
10	625–675	650	1	8.0×10^{-19}	8.0×10^{-19}
9	675–725	700	1	6.3×10^{-19}	6.3×10^{-19}
8	725–775	750	1	5.1×10^{-19}	5.1×10^{-19}
7	775–825	800	1	4.2×10^{-19}	4.2×10^{-19}
6	825–875	850	1	3.6×10^{-19}	3.6×10^{-19}
5	875–950	912.5	1	3.0×10^{-19}	3.0×10^{-19}
4	950–1050	1000	1	2.4×10^{-19}	2.4×10^{-19}
3	1050–1200	1125	1	1.9×10^{-19}	1.9×10^{-19}
2	1200–1400	1300	1	1.5×10^{-19}	1.5×10^{-19}
1	1400–1600	1500	1	1.3×10^{-19}	1.3×10^{-19}

Note: †Permeability manually set.

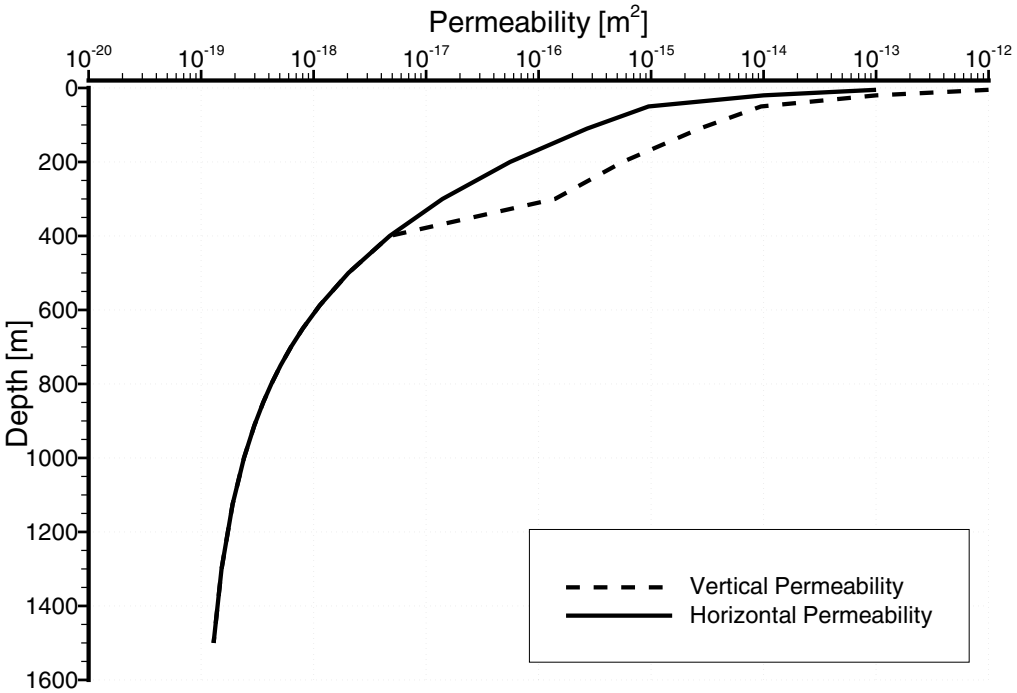

Figure 4.14 Horizontal and vertical matrix permeabilities as a function of depth for the Phase–II sub-regional model.

A matrix porosity of 0.003 was chosen based on the work of *Stevenson et al.* (1996). Matrix and fracture properties for solute transport include a longitudinal dispersivity of 50 m, a transverse horizontal dispersivity of 5 m and a transverse vertical dispersivity of 0.5 m. A matrix bulk density of 2642.05 kg/m^3 (2650 kg/m^3 × (1 – 0.003)) is also used.

Fracture permeabilities (or conductivity), which were constant in the Phase–I work, are now defined on both a stochastic and a depth dependent basis. A plot of fracture permeability versus depth for the WRA (*Stevenson et al.*, 1996) and the Finnish Olkiluoto site (*Hellä et al.*, 2004; *Vaittinen et al.*, 2003) are shown in Figure 4.15. As can be seen, it can be quite difficult to determine a depth trend from the wide permeability scatter in the data.

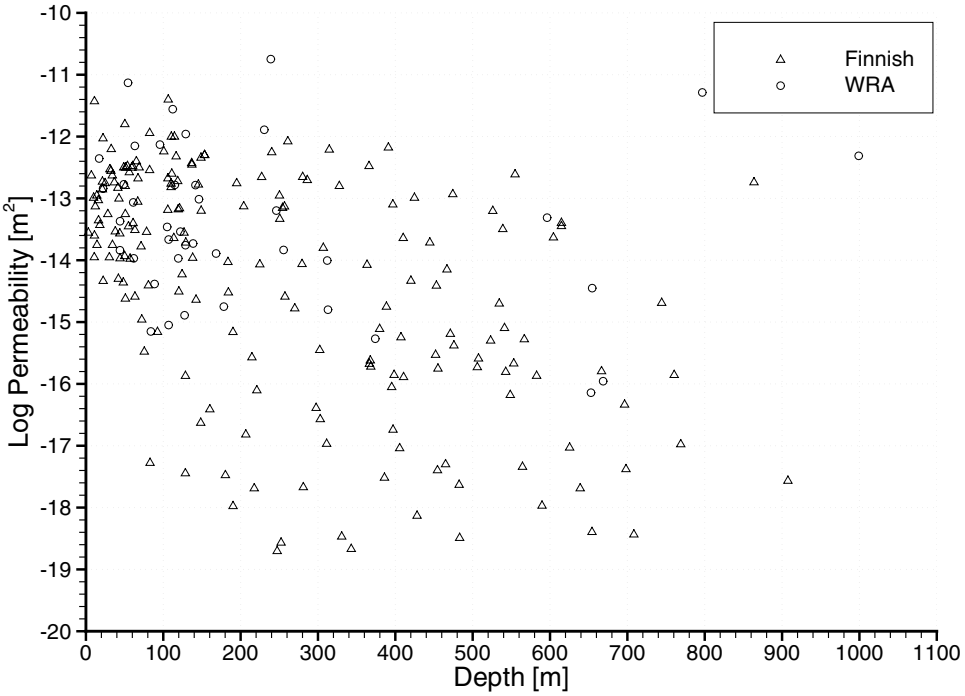

Figure 4.15 Fracture zone $\log_{10}$ permeability data for the Finnish Olkiluoto site and the WRA.

A depth trend was noticeable when rank statistics were used to calculate the 5th, 25th, 50th, 75th, and 95th percentiles. A total of eight depth ranges r of 50 m, 100 m, 150 m, 200 m, 250 m, 300 m, 350 m, and 400 m were selected. Percentiles were calculated for all permeability values within $r/2$ metres of a specified depth d. Permeability percentile plots for r = 100 m and r = 200 m are shown in Figure 4.16 and Figure 4.17 respectively.

As can be seen, the various percentile curves can be quite irregular, although they do become smoother when selecting a larger r or depth range. Figure 4.17 was used as the basis for calculating cubic splines to best fit the various percentiles. The splines were interactively fit using Microsoft Excel™ for visualization, writing the necessary spline routines in VBA and linking the VBA code to the Excel spreadsheet. The resulting splines and the percentile curves from Figure 4.17 are shown in Figure 4.18.

Once the percentile cubic spline curves were created, another cubic spline interpolation was required to determine intermediate percentile values for a given depth. An

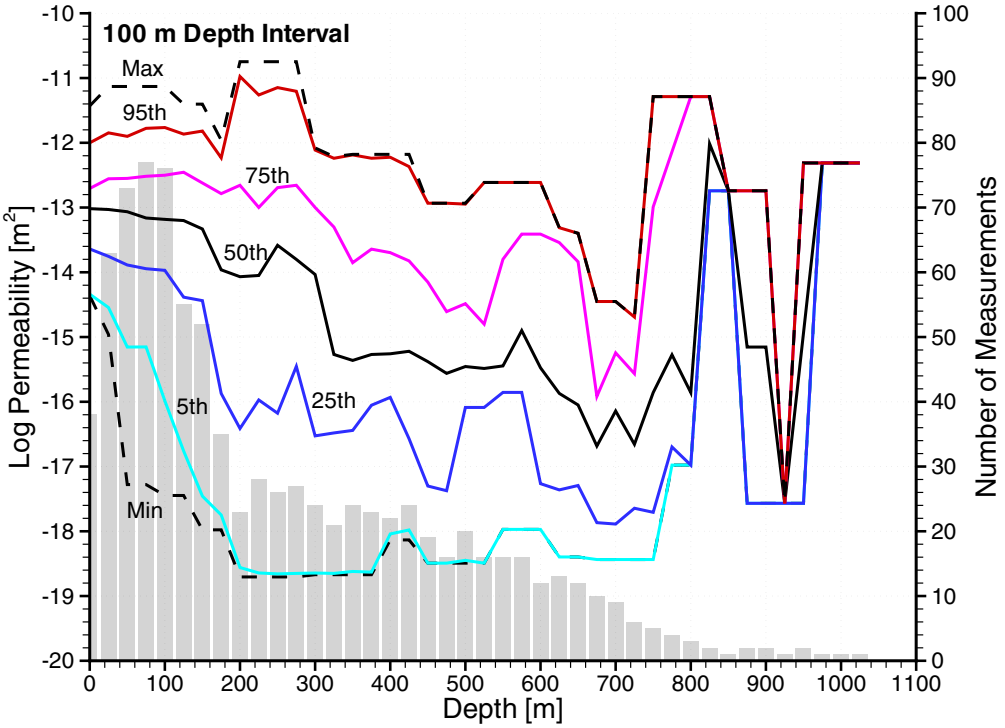

Figure 4.16 Log_{10} permeability percentiles with depth for a 100 m depth range.

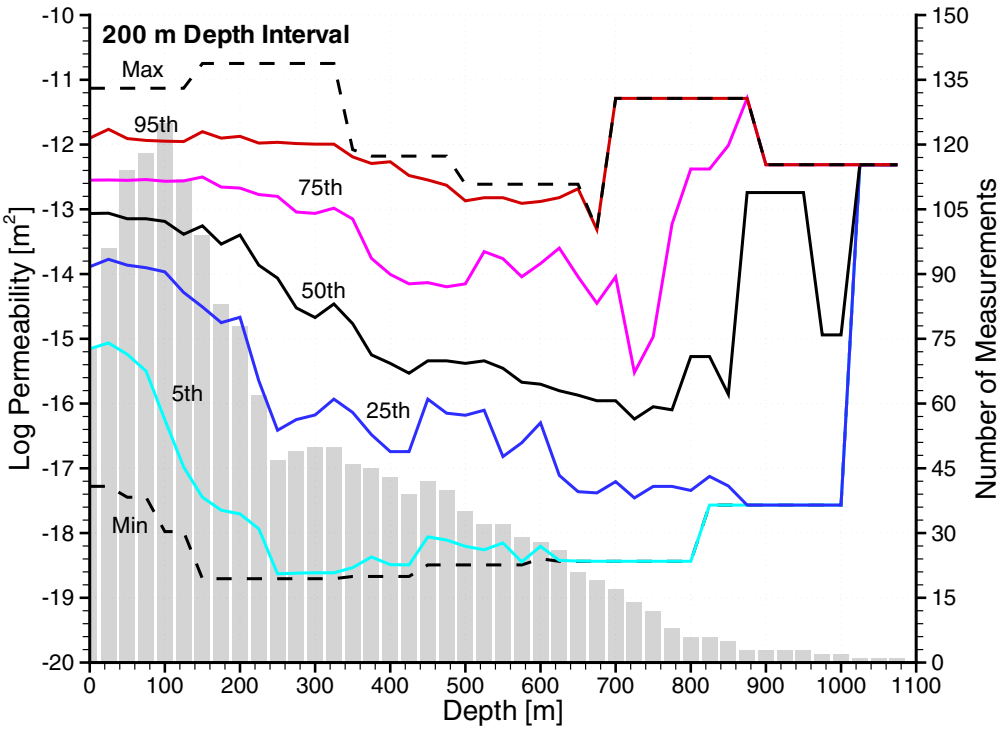

Figure 4.17 Log_{10} permeability percentiles with depth for a 200 m depth range.

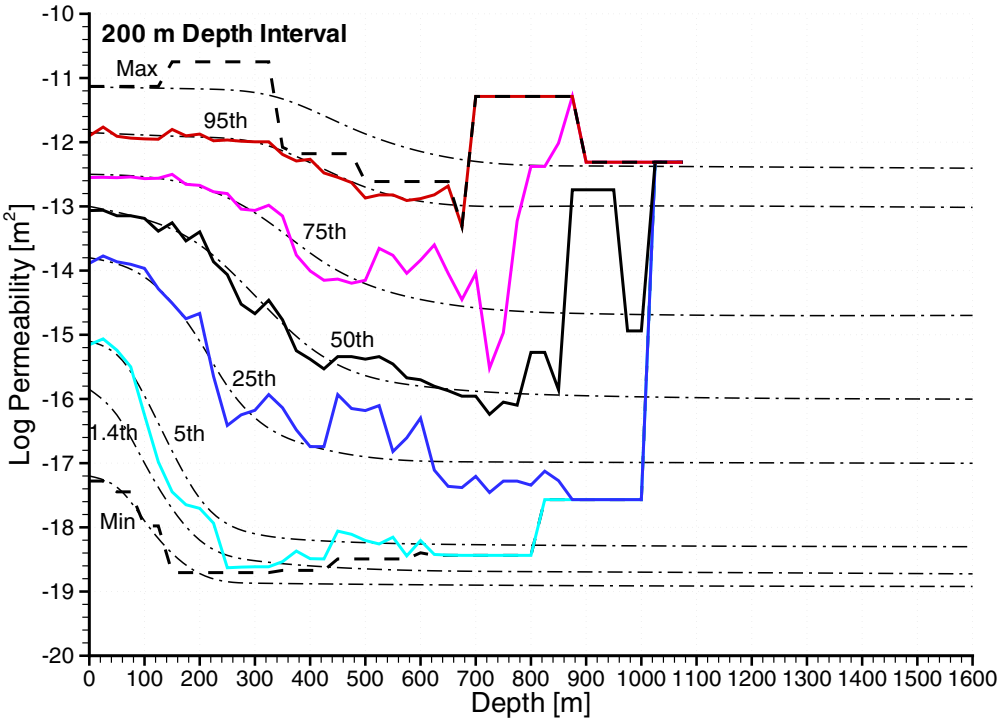

Figure 4.18 Log_{10} permeability percentile with depth for a 200 m depth range and best-fit cubic splines.

additional spline curve representing the 1.4^{th} percentile was necessary in order to ensure that the cumulative density function (CDF) was monotonically increasing, or it's slope was always greater than zero. The slope or first derivative of a CDF is the PDF. The final CDF for fracture permeability is shown in Figure 4.19, while the PDF is shown in Figure 4.20. A three-dimensional view of the PDF is shown in Figure 4.21. Although the CDF is quite smooth, the locations chosen for the cubic splines in Figure 4.18 greatly influenced the shape of the PDF. Multi-modal as well as negative values for the PDF were discovered during the creation of the CDF. As a result, the location of the cubic splines were somewhat influenced by the PDF, thereby ensuring that the PDF was unimodal throughout the entire depth range of interest. The PDF for fracture permeabilities at depths below 700 m are nearly identical, primarily due to the lack of supporting fracture permeability data. Figure 4.21 clearly shows the depth dependent nature of the fracture permeability, in that the greatest expectation (PDF peaks) varies from approximately $10^{-13}\,\text{m}^2$ to $10^{-16}\,\text{m}^2$.

A random fracture permeability variate can be calculated from the depth dependent PDF by using the inverse CDF (see Figure 4.22). Given a depth and a uniform random variate, the $\log_{10}$ permeability random variate can be calculated by bi-linearly interpolating the inverse CDF surface. The fracture permeability k_F is therefore calculated as:

$$k_F = 10^{CDF(d,U[0,100])^{-1}} \tag{4.3}$$

where k_F is the fracture permeability [L^2]; U is the uniform random variate [/]; and $CDF()^{-1}$ is the inverse CDF [/]. A correlated random fracture permeability field can then be calculated using a correlated random uniform variate field.

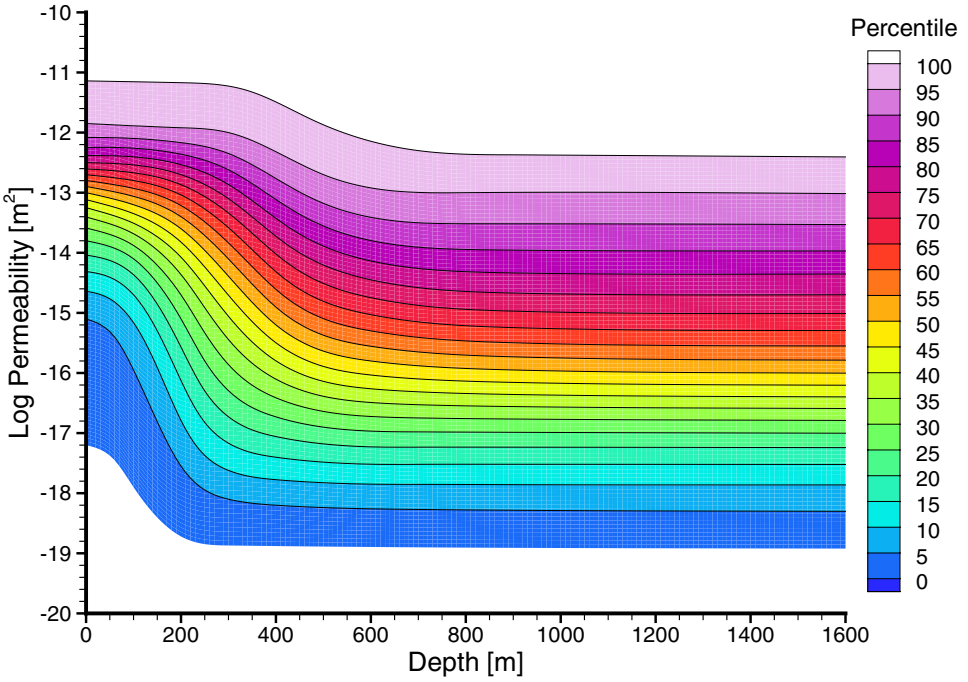

Figure 4.19 Cumulative density function for $\log_{10}$ of fracture permeability.

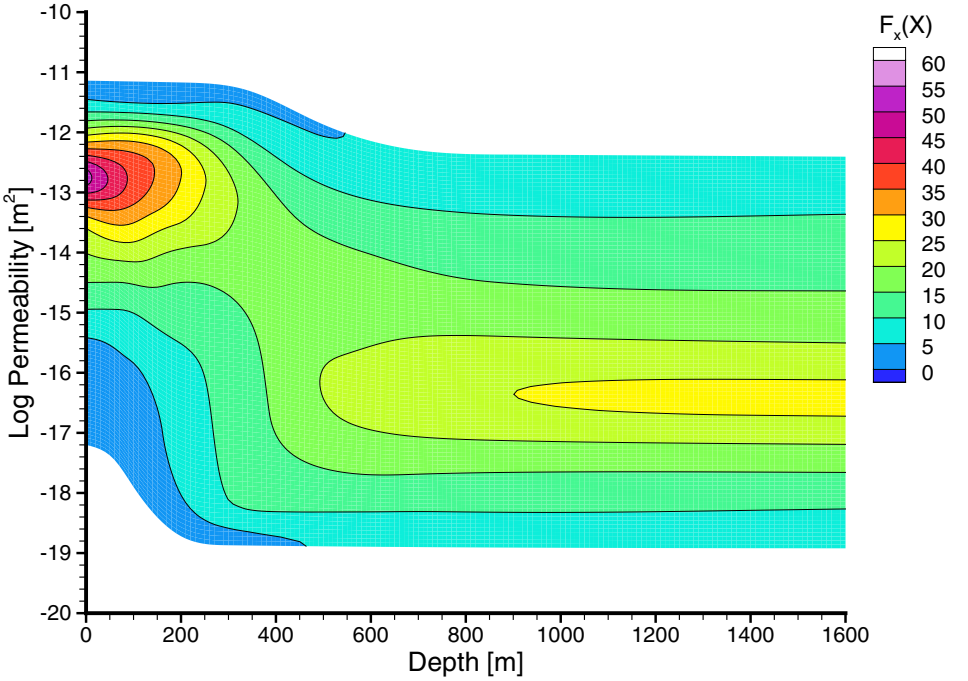

Figure 4.20 Probability density function for $\log_{10}$ of fracture permeability.

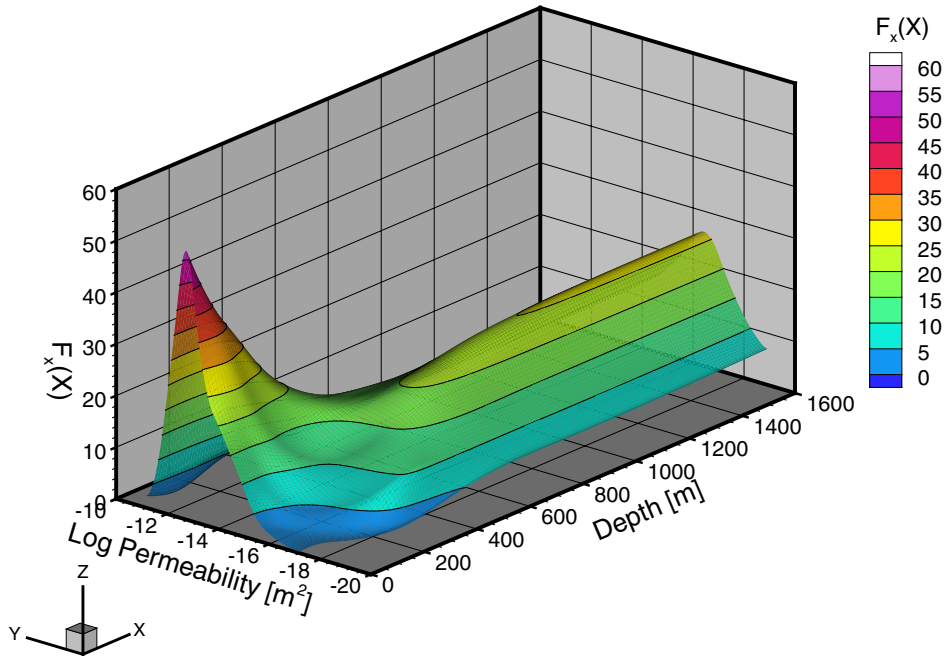

Figure 4.21 3-D view of the probability density function for $\log_{10}$ of fracture permeability.

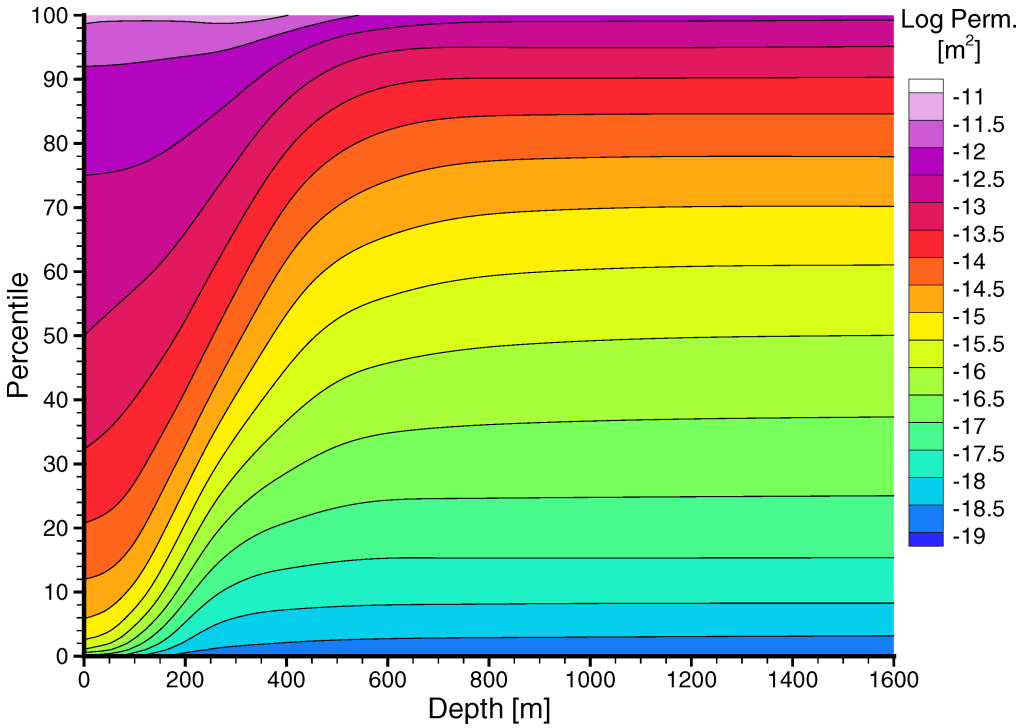

Figure 4.22 Inverse cumulative density function for $\log_{10}$ of fracture permeability.

In the Phase–I model, fracture zone width was represented with a constant width of 1.0 m. Since a probability density function for fracture zone width is also desired, the WRA data in Figure 7 from *Stevenson et al.* (1996) was plotted as a histogram and a minimum error log-normal probability distribution was developed:

$$F_X(x) = \frac{1}{x\sigma\sqrt{2\pi}}\, e^{-\frac{1}{2}\left(\frac{\ln(x/m)}{\sigma}\right)^2} \tag{4.4}$$

where $\sigma = 0.48289$ and $m = 3.26841$. The log-normal PDF and WRA fracture width histogram are shown in Figure 4.23.

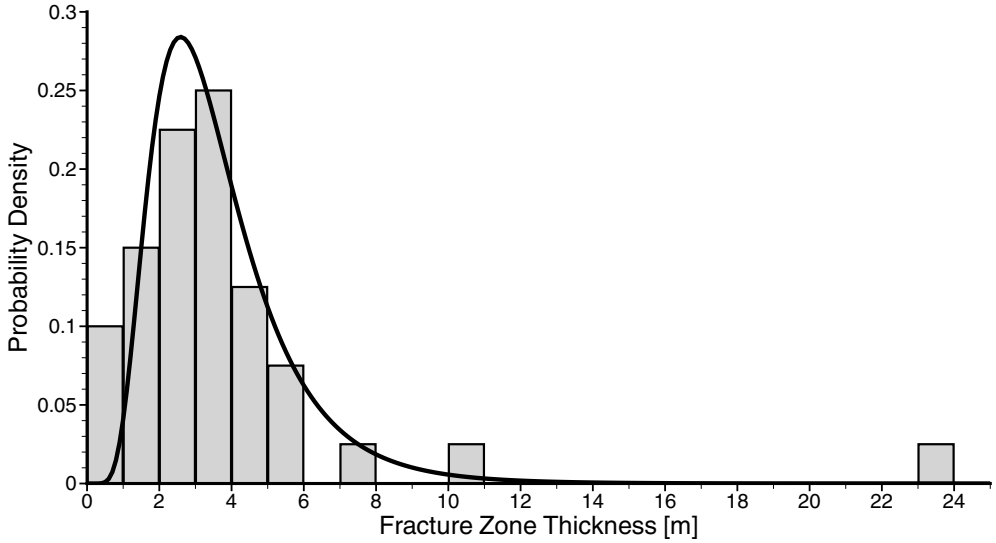

Figure 4.23 Fracture zone width histogram and log–normal PDF.

A fracture zone porosity can then be calculated from the fracture zone permeability and a given fracture frequency (*Cornaton and Park*, 2005). The bulk fracture zone permeability tensor and bulk fracture zone porosity are defined as:

$$k_{F_{ij}}^{bulk} = \sum_{i=1}^{j} k_{F,i}(\mathbf{I} - \mathbf{n}_i \otimes \mathbf{n}_i) + (1 - \phi_F)k_{M_{ij}} \tag{4.5}$$

$$\phi_F^{bulk} = \phi_F + (1 - \phi_F)\phi \tag{4.6}$$

where $k_{F,i}$ is the single fracture permeability in direction i [L^2]; n is the number of discrete fractures [/]; $\mathbf{I}$ is the identity matrix [/]; $\mathbf{n}_i$ is the unit vector normal to fracture plane i [/]; ϕ_F is the volumetric fracture fraction [/]; $k_{M_{ij}}$ is the porous matrix permeability tensor [L^2]; and ϕ is the porous matrix porosity [/]. $k_{F,i}$ and ϕ_F are then defined as:

$$k_{F,i} = \frac{\gamma_i\, a_i^3}{12} \tag{4.7}$$

$$\phi_F = \sum_{i=1}^{n} \gamma_i a_i \tag{4.8}$$

where γ_i is the fracture density in direction i [fractures/L]; and a_i is the fracture aperture in direction i [L]. For the case of three sets of orthogonal fractures with identical apertures and fracture spacing, $k_{F_{ij}}^{bulk}$ and ϕ_F^{bulk} become:

$$k_{F_{ij}}^{bulk} = \frac{\gamma\, a^3}{6} + (1 - 3\gamma a) k_{M_{ij}} \tag{4.9}$$

$$\phi_F^{bulk} = 3\gamma a + (1 - 3\gamma a)\phi \tag{4.10}$$

Hence, given a fracture permeability from Equation (4.3), a fracture aperture, a, can be calculated using Equation (4.9), and then substituted into Equation (4.10) to determine the fracture zone porosity (*Cornaton and Park*, 2005).

4.3 Paleoclimate Model Development

The paleoclimate model development builds upon the Phase–II model development of §4.2. Both steady-state and pseudo steady-state simulations need to be run prior to paleoclimate simulations. For a given modelling scenario, a steady-state simulation without TDS is run using FRAC3DVS-OPG. The resulting freshwater heads from the steady-state simulation are modified to account for the presence of high TDS, where the development of the initial TDS distribution is described in §4.3.3. The adjusted freshwater heads and initial TDS distribution form the initial conditions for a 1 Ma transient simulation, whose final state at 1 Ma represents a pseudo steady-state. The resulting pseudo steady-state freshwater heads and TDS distribution are used as the initial conditions for the paleoclimate simulations.

4.3.1 Paleoclimate Modelling Scenarios

Various paleoclimate modelling scenarios were chosen to investigate various parameterizations of a Shield like setting. The sub-regional modelling of *Sykes et al.* (2004) only considered groundwater flow systems lacking density-dependent flow. At the time of that study, FRAC3DVS could not calculate coupled density-dependent flow and transport in fracture elements. A subsequent modelling study by *Normani et al.* (2007) used the enlarged modelling domain as part of the Phase–II model development described in §4.2, and investigated the role of fluid density, fluid viscosity, fracture properties (porosity, permeability, and width), and fracture geometry using 100 FNM realizations upon groundwater flow and MLE. *Normani et al.* (2007) also investigated the migration of a tracer for two glaciation scenarios provided by *Peltier* (2003, 2006). The paleoclimate simulations in *Normani et al.* (2007) were done assuming a fracture zone width of 1.0 m, a constant fracture zone hydraulic conductivity of 10^{-6} m/s, similar to the EIS and SCS case studies (see §2.2.1.1 and §2.2.1.2, respectively), excluding coupled density-dependent flow and transport for TDS. The role of hydromechanical coupling on the flow system was not considered.

This thesis extends the earlier work of *Sykes et al.* (2004), and *Normani et al.* (2007) to include variable fracture permeability with depth, coupled density-dependent flow and transport, and hydromechanical coupling for glaciation. The various scenarios investigated in this thesis are listed in Table 4.3. An increase in permafrost will reduce the depth to which a unit tracer can migrate, and is investigated in Scenario 2. Ignoring

coupled density-dependent flow and transport in Scenario 3 will reduce MLE compared to the base case of Scenario 1, and enhance tracer migration to depth. Allowing high permeability fracture zones in Scenarios 4 and 7 to propagate to depths beyond 1 km will allow greater movement of surface freshwaters to depth. This will result in lower MLE values and deeper migration of a unit tracer. Ignoring hydromechanical coupling in Scenario 5 will enhance vertical gradients during glacial events, leading to increased vertical pore velocities and deeper migration of a unit tracer. Conversely, applying full hydromechanical coupling in Scenario 6 will lead to reduced vertical migration since insitu pressures are increased throughout the water column in such a way as to counter act the applied hydraulic boundary condition from the presence of an ice-sheet.

Table 4.3 Scenario and parameter selection matrix for sub-regional scale paleoclimate modelling.

Parameters	Simulation Scenarios						
	1	2	3	4	5	6	7
Glaciation Scenario							
NN2008		■					
NN2778	■		■	■	■	■	■
Fracture Permeability							
Uniform at 10^{-6} m/s				■			■
Median with depth	■	■	■		■	■	
Hydromechanical Coupling							
Computed ζ	■	■	■	■			
$\zeta = 0$					■		■
$\zeta = 1$						■	
Density-Dependent Coupling							
With Density	■	■		■	■	■	
Without Density			■				■

Scenarios 2 to 6 investigate the effect of changing a given parameter relative to Scenario 1. Scenario 7 uses the same combination of parameters from the earlier studies of *Sykes et al.* (2004) and *Normani et al.* (2007) for comparison to Scenario 1. Analysis of the paleoclimate simulations is discussed in §4.5, while figures for each scenario are presented in Appendix A to Appendix G inclusive.

4.3.2 Spatial Discretization

The same spatial discretization presented in the Phase–II model development section is used for the steady-state, pseudo steady-state and paleoclimate models.

4.3.3 Initial Conditions

Most of the paleoclimate simulations in this chapter require coupled density-dependent flow and transport due to the high TDS concentrations found deep in the Canadian Shield, as discussed in §2.1.2. An initial TDS distribution is required for the pseudo steady-state model. A plot of TDS versus depth for groundwaters from the Canadian Shield, based on Figure 2b in *Frape and Fritz* (1987), is shown in Figure 4.24. The dashed line represents

an upper bound for TDS as a function of depth. Equation (4.11) represents the dashed line in Figure 4.24, where TDS is in units of g/L.

$$TDS = \begin{cases} 10^{0.001981697d}, & \text{for } d \leq 1250\,\text{m}; \\ 300, & \text{for } d > 1250\,\text{m}. \end{cases} \tag{4.11}$$

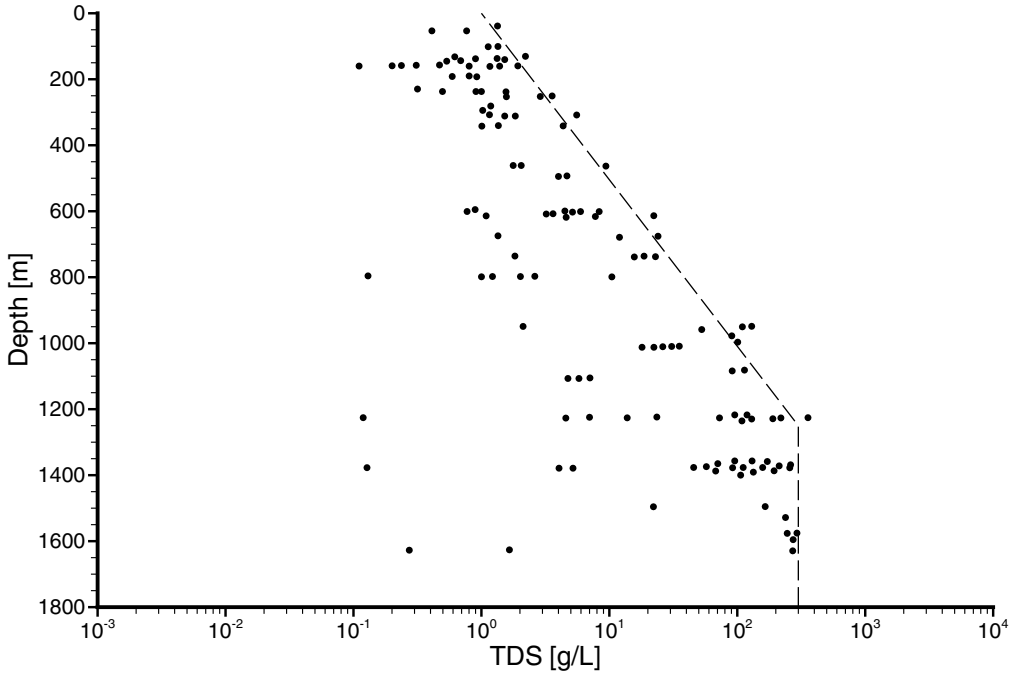

Figure 4.24 Plot of TDS versus depth for groundwaters from the Canadian Shield. The dashed line represents Equation (4.11). Adapted from Figure 2b in *Frape and Fritz* (1987).

Setting an upper bound for the TDS distribution as an initial condition allows recharge waters to reduce the TDS concentrations in fractures, and in the nearby rock matrix during the pseudo steady-state simulations, providing a more representative initial condition for the paleoclimate simulations.

An initial concentration of zero was used for the tracer representing recharge water, as the tracer can only enter the groundwater flow system from recharge or influx at specified head nodes at the surface of the modelling domain.

4.3.4 Boundary Conditions

For the steady-state and pseudo steady-state models discussed in §4.3, surface boundary conditions from the Phase–II model development were used, namely specified head for surface nodes associated with water features, and a recharge rate of 1.0 mm/a across the top of the model. A zero-flux boundary condition for flow was applied to the model's sides and bottom.

For the pseudo steady-state models which include TDS, a Cauchy boundary condition with a concentration of zero was applied to nodes associated with the top surface of the model. This allows recharge water with zero TDS concentration to enter the modelling domain, while not affecting TDS concentrations of effluxing nodes. Nodes associated

with the bottom of the modelling domain were assigned a specified concentration equal to 300 g/L to reduce computational run-times and improve numerical stability, especially near fracture zones.

For the paleoclimate simulations, a tracer associated with water entering the groundwater model from the top surface is used to investigate glacial meltwater migration in the subsurface during and subsequent to a glaciation and deglaciation episode. A Cauchy boundary condition at the model's top surface is used with a tracer concentration of unity, while a specified concentration of zero is applied to nodes along the bottom of the modelling domain. Although a specified concentration is not required at the bottom, FRAC3DVS-OPG requires a value to be specified since a given boundary condition is applied to all solute species. In paleoclimate simulations described in this thesis, a Cauchy boundary condition at the top of the modelling domain requires that a concentration value be specified both for TDS and tracer, while a specified concentration boundary condition at the bottom of the modelling domain also requires a concentration value for both TDS and tracer.

A plot of various NN2008 GSM model outputs for the grid cell containing the sub-regional modelling domain are shown in Figure 4.25. These outputs include ice thickness, meltwater production rate, lake depth, permafrost depth, and ice-sheet basal temperature relative to the pressure melting point of ice. Only the ice thickness, lake depth, and permafrost depth outputs are applied to the paleoclimate groundwater flow simulations in this chapter. Similarly, the NN2778 GSM model outputs for the grid cell containing the sub-regional modelling domain are shown in Figure 4.26. The main difference between the two glaciation scenarios, is the duration of permafrost during the 120 ka GSM simulation; the length of time NN2778 is subject to permafrost conditions is less than NN2008. The paleoclimate boundary conditions presented in Figure 4.25 and Figure 4.26 are applied to the paleoclimate simulations listed in Table 4.3.

4.3.5 Fracture Network Model

The first unconditioned FNM from *Srivastava* (2005) was chosen for all paleoclimate simulations in this chapter. Although the orthogonal FNM contains quadrilateral fracture elements which extend to the bottom of the modelling domain, all fracture elements were removed that were along either the top or bottom of the lowest layer of hexahedral elements, or within that layer. All quadrilateral fracture elements that existed on the top of the modelling domain were also removed. These fracture elements were removed to enhance numerical stability, especially when simulating density-dependent flow and transport. The resulting orthogonal FNM is shown in Figure 4.27.

4.3.6 Properties

Properties for the paleoclimate simulations listed in Table 4.3 are provided in Table 4.4 and Table 4.5. The values for Young's Modulus E and Poisson's ratio v are provided in *Chan and Stanchell* (2008). The calculation of specific storage S_s and one-dimensional loading efficiency ζ assume the Biot coefficient $\alpha = 0.73$ (*Chan and Stanchell*, 2008), and a fluid compressibility of 4.4×10^{-10} Pa^{-1}. Pore fluid viscosity is assumed to be constant, even though pore fluid viscosities will increase by several factors with higher TDS values (*Adams and Bachu*, 2002). Fracture properties for solute transport include a longitudinal dispersivity of 250 m, and a transverse dispersivity of 25 m. These dispersivities were

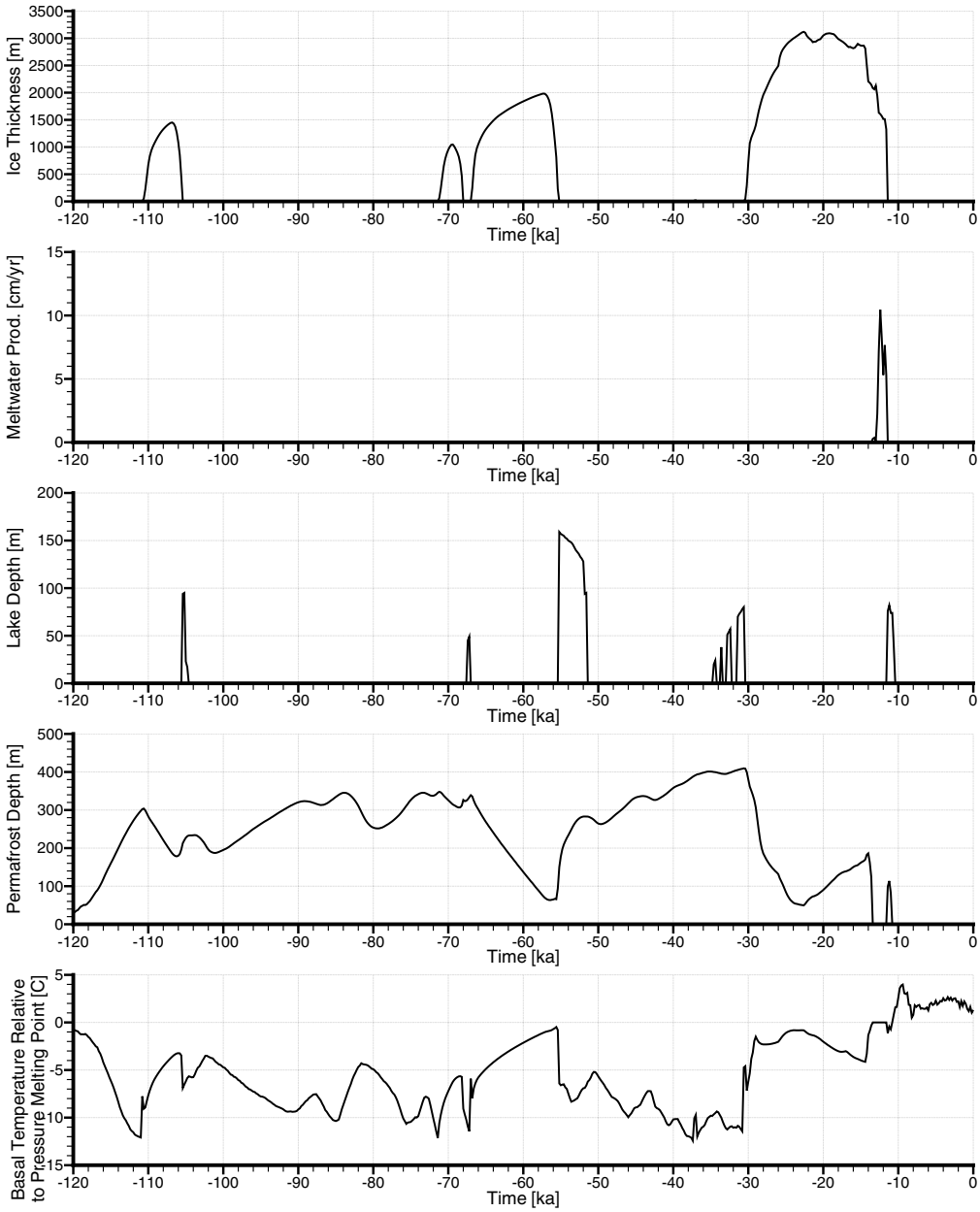

Figure 4.25 Plots of ice thickness, meltwater production rate, lake depth, permafrost depth, and ice-sheet basal temperature relative to pressure melting point versus time for the nn2008 GSM grid block containing the sub-regional modelling domain, provided by *Peltier* (2006).

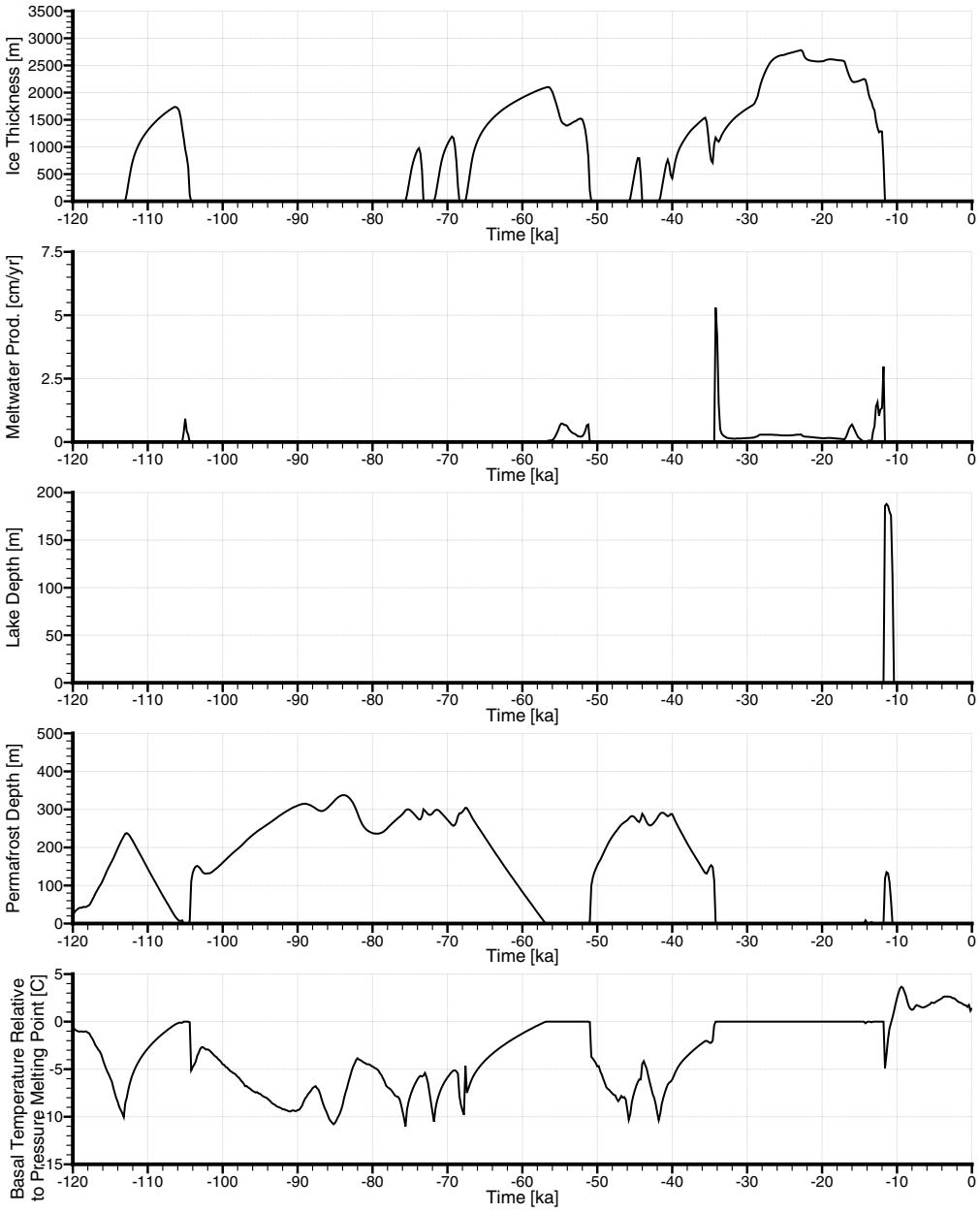

Figure 4.26 Plots of ice thickness, meltwater production rate, lake depth, permafrost depth, and ice-sheet basal temperature relative to pressure melting point versus time for the nn2778 GSM grid block containing the sub-regional modelling domain, provided by *Peltier* (2006).

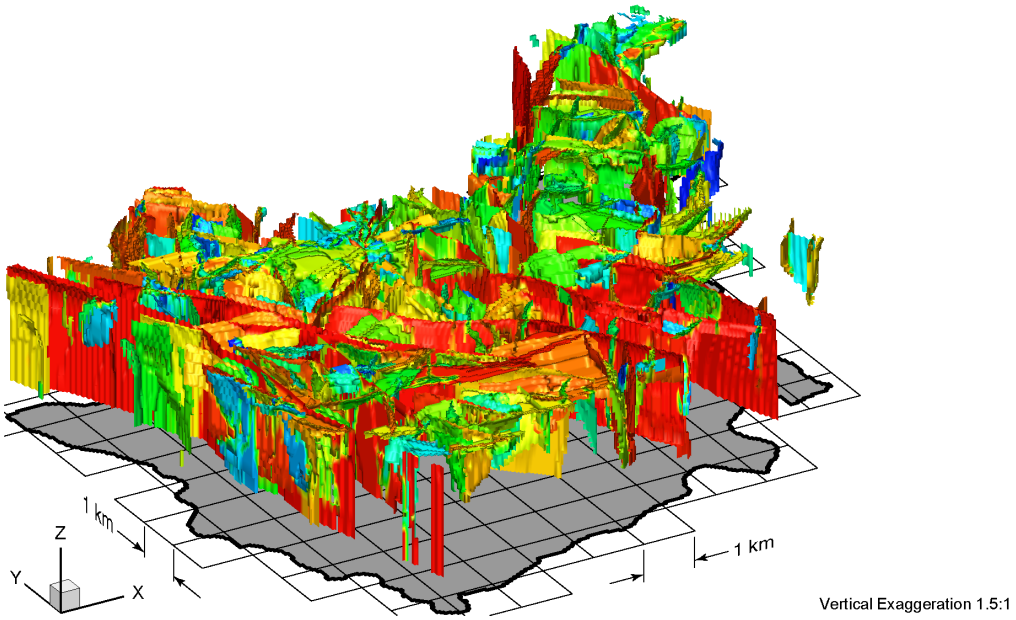

Figure 4.27 3-D perspective view of orthogonal FNM.

increased from earlier modelling efforts in order to enhance the stability of the numerical solution and to reduce the computational runtime. Dispersivities for the matrix are unchanged with a longitudinal dispersivity of 50 m, a transverse horizontal dispersivity of 5 m and a transverse vertical dispersivity of 0.5 m.

Matrix values of permeability and porosity are taken from the Phase–II model development described in §4.2. Fracture zone permeability is represented by the median permeability (50^{th} percentile) in Figure 4.19, and is shown in Figure 4.28. Fracture zone permeabilities are assumed to be temporally invariant, neglecting mechanical effects, precipitation reactions, and sedimentation under proglacial lakes. Using the fracture zone permeability and Equation (4.10), fracture zone porosity can be calculated and is shown in Figure 4.29.

The permafrost depths were used to select any FRAC3DVS-OPG grid block whose top face was within the permafrost zone for each time step. A permafrost hydraulic conductivity of 5×10^{-11} m/s was applied and assumed to be valid for fractured rock systems, even though *McCauley et al.* (2002) performed experiments with frozen soils. Permeability reduction in FRAC3DVS-OPG only applies to hexahedral elements. Since fractures are also subject to permafrost, this functionality was added to FRAC3DVS-OPG. Any fracture which is adjacent to a hexahedral element whose permeability has been reduced due to the presence of permafrost, is itself subject to the same permeability reduction. Figure 4.30 shows the maximum depth of permafrost penetration into the subsurface for the matrix and fractures.

4.4 FRAC3DVS-OPG Computational Performance

Due to the high computational demands of this work, all simulations were performed on computers equipped with 64-bit AMD Opteron™ processors, and at least 8 GB of memory, running derivatives of 64-bit Red Hat Enterprise Linux (RHEL) as the operating

Table 4.4 Sub-regional model properties for paleoclimate simulations without density-dependent coupling.

Layer	Depth Range [m]	Midpoint Depth [m]	k_H [m^2]	k_V [m^2]	k_V/k_H [/]	n [/]	TDS [g/L]	ρ [kg/m^3]	E [GPa]	ν [/]	S_s [m^{-1}]	ζ [/]
19	0–10	5.0	1.0×10^{-13}	1.0×10^{-12}	10	0.003	0.00	1000.0	20.0	0.25	3.76×10^{-7}	0.80
18	10–30	20.0	1.0×10^{-14}	1.0×10^{-13}	10	0.003	0.00	1000.0	20.0	0.25	3.76×10^{-7}	0.80
17	30–70	50.0	9.5×10^{-16}	9.5×10^{-15}	10	0.003	0.00	1000.0	20.0	0.25	3.76×10^{-7}	0.80
16	70–150	110.0	2.7×10^{-16}	2.7×10^{-15}	10	0.003	0.00	1000.0	20.0	0.25	3.76×10^{-7}	0.80
15	150–250	200.0	5.6×10^{-17}	5.6×10^{-16}	10	0.003	0.00	1000.0	30.0	0.25	2.55×10^{-7}	0.78
14	250–350	300.0	1.4×10^{-17}	1.4×10^{-16}	10	0.003	0.00	1000.0	30.0	0.25	2.55×10^{-7}	0.78
13	350–450	400.0	4.7×10^{-18}	4.7×10^{-18}	1	0.003	0.00	1000.0	60.0	0.25	1.34×10^{-7}	0.75
12	450–550	500.0	2.0×10^{-18}	2.0×10^{-18}	1	0.003	0.00	1000.0	60.0	0.25	1.34×10^{-7}	0.75
11	550–625	587.5	1.1×10^{-18}	1.1×10^{-18}	1	0.003	0.00	1000.0	60.0	0.25	1.34×10^{-7}	0.75
10	625–675	650.0	8.0×10^{-19}	8.0×10^{-19}	1	0.003	0.00	1000.0	60.0	0.25	1.34×10^{-7}	0.75
9	675–725	700.0	6.3×10^{-19}	6.3×10^{-19}	1	0.003	0.00	1000.0	60.0	0.25	1.34×10^{-7}	0.75
8	725–775	750.0	5.1×10^{-19}	5.1×10^{-19}	1	0.003	0.00	1000.0	60.0	0.25	1.34×10^{-7}	0.75
7	775–825	800.0	4.2×10^{-19}	4.2×10^{-19}	1	0.003	0.00	1000.0	60.0	0.25	1.34×10^{-7}	0.75
6	825–875	850.0	3.6×10^{-19}	3.6×10^{-19}	1	0.003	0.00	1000.0	60.0	0.25	1.34×10^{-7}	0.75
5	875–950	912.5	3.0×10^{-19}	3.0×10^{-19}	1	0.003	0.00	1000.0	60.0	0.25	1.34×10^{-7}	0.75
4	950–1050	1000.0	2.4×10^{-19}	2.4×10^{-19}	1	0.003	0.00	1000.0	60.0	0.25	1.34×10^{-7}	0.75
3	1050–1200	1125.0	1.9×10^{-19}	1.9×10^{-19}	1	0.003	0.00	1000.0	60.0	0.25	1.34×10^{-7}	0.75
2	1200–1400	1300.0	1.5×10^{-19}	1.5×10^{-19}	1	0.003	0.00	1000.0	60.0	0.25	1.34×10^{-7}	0.75
1	1400–1600	1500.0	1.3×10^{-19}	1.3×10^{-19}	1	0.003	0.00	1000.0	60.0	0.25	1.34×10^{-7}	0.75

Table 4.5 Sub-regional model properties for paleoclimate simulations with density-dependent coupling.

Layer	Depth Range [m]	Midpoint Depth [m]	k_H [m^2]	k_V [m^2]	k_V/k_H [/]	n [/]	TDS [g/L]	ρ [kg/m^3]	E [GPa]	ν [/]	S_s [m^{-1}]	ζ [/]
19	0–10	5.0	1.0×10^{-13}	1.0×10^{-12}	10	0.003	1.02	1000.7	20.0	0.25	3.76×10^{-7}	0.80
18	10–30	20.0	1.0×10^{-14}	1.0×10^{-13}	10	0.003	1.10	1000.7	20.0	0.25	3.76×10^{-7}	0.80
17	30–70	50.0	9.5×10^{-16}	9.5×10^{-15}	10	0.003	1.26	1000.8	20.0	0.25	3.76×10^{-7}	0.80
16	70–150	110.0	2.7×10^{-16}	2.7×10^{-15}	10	0.003	1.68	1001.1	20.0	0.25	3.76×10^{-7}	0.80
15	150–250	200.0	5.6×10^{-17}	5.6×10^{-16}	10	0.003	2.56	1001.7	30.0	0.25	2.55×10^{-7}	0.78
14	250–350	300.0	1.4×10^{-17}	1.4×10^{-16}	10	0.003	4.03	1002.7	30.0	0.25	2.56×10^{-7}	0.78
13	350–450	400.0	4.7×10^{-18}	4.7×10^{-18}	1	0.003	6.37	1004.2	60.0	0.25	1.34×10^{-7}	0.75
12	450–550	500.0	2.0×10^{-18}	2.0×10^{-18}	1	0.003	10.05	1006.7	60.0	0.25	1.35×10^{-7}	0.75
11	550–625	587.5	1.1×10^{-18}	1.1×10^{-18}	1	0.003	14.81	1009.9	60.0	0.25	1.35×10^{-7}	0.75
10	625–675	650.0	8.0×10^{-19}	8.0×10^{-19}	1	0.003	19.54	1013.0	60.0	0.25	1.36×10^{-7}	0.75
9	675–725	700.0	6.3×10^{-19}	6.3×10^{-19}	1	0.003	24.55	1016.4	60.0	0.25	1.36×10^{-7}	0.75
8	725–775	750.0	5.1×10^{-19}	5.1×10^{-19}	1	0.003	30.84	1020.6	60.0	0.25	1.37×10^{-7}	0.75
7	775–825	800.0	4.2×10^{-19}	4.2×10^{-19}	1	0.003	38.74	1025.8	60.0	0.25	1.37×10^{-7}	0.75
6	825–875	850.0	3.6×10^{-19}	3.6×10^{-19}	1	0.003	48.67	1032.4	60.0	0.25	1.38×10^{-7}	0.75
5	875–950	912.5	3.0×10^{-19}	3.0×10^{-19}	1	0.003	65.26	1043.5	60.0	0.25	1.40×10^{-7}	0.75
4	950–1050	1000.0	2.4×10^{-19}	2.4×10^{-19}	1	0.003	98.38	1065.6	60.0	0.25	1.43×10^{-7}	0.75
3	1050–1200	1125.0	1.9×10^{-19}	1.9×10^{-19}	1	0.003	179.62	1119.7	60.0	0.25	1.50×10^{-7}	0.75
2	1200–1400	1300.0	1.5×10^{-19}	1.5×10^{-19}	1	0.003	269.40	1179.6	60.0	0.25	1.58×10^{-7}	0.75
1	1400–1600	1500.0	1.3×10^{-19}	1.3×10^{-19}	1	0.003	300.00	1200.0	60.0	0.25	1.61×10^{-7}	0.75

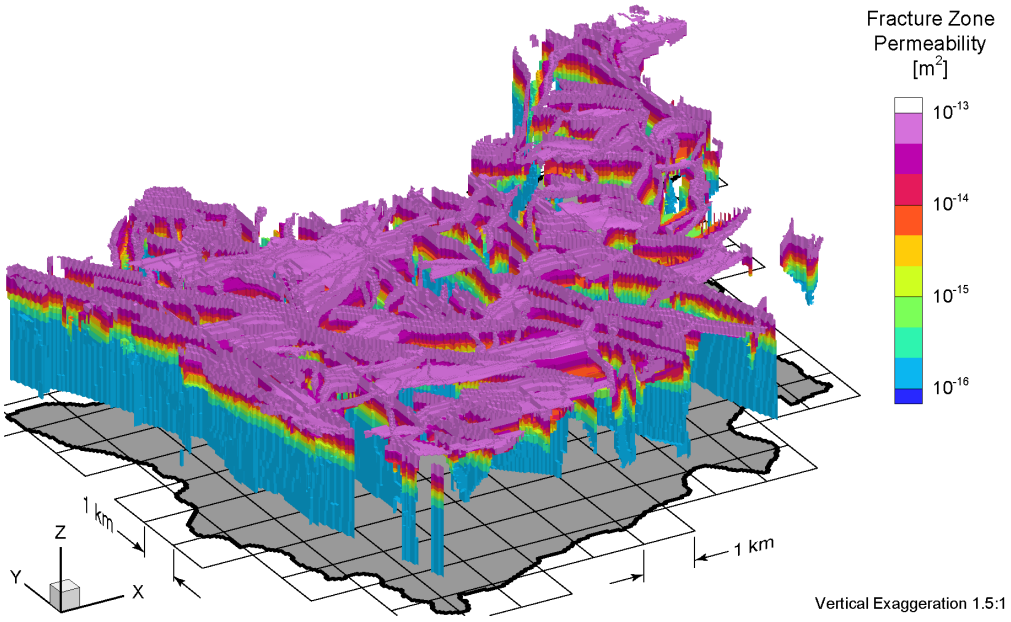

Figure 4.28 View of fracture zone permeability with depth.

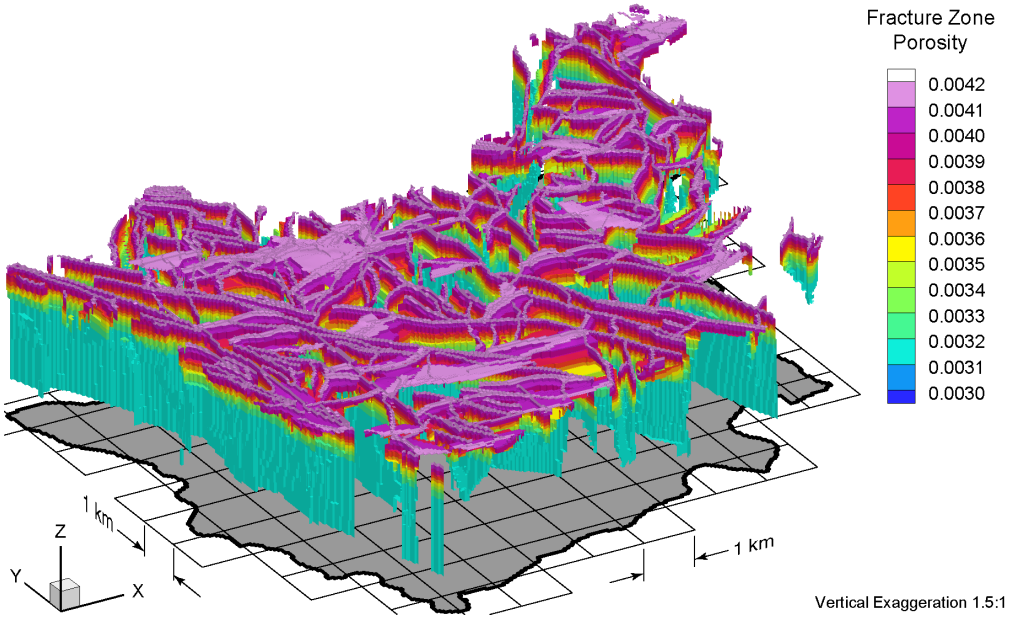

Figure 4.29 View of fracture zone porosity with depth.

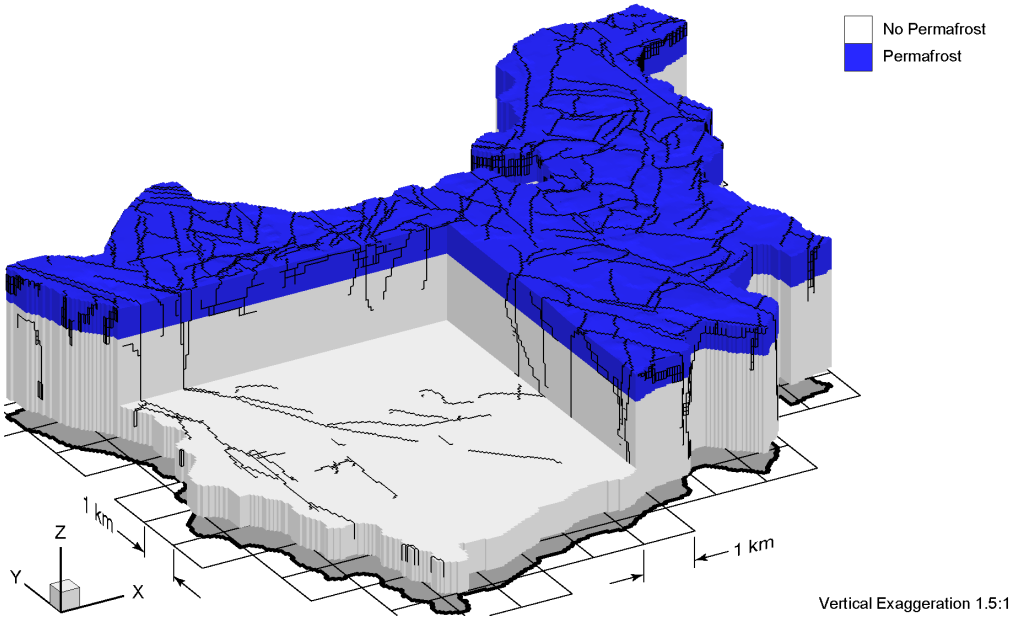

Figure 4.30 Block cut view of maximum permafrost depth for the Canadian Shield Sub-Regional Scenario 1 paleoclimate simulation.

system. FRAC3DVS-OPG was compiled for a 64-bit memory model using the Sun Fortran95 compiler, and optimized for execution on AMD Opteron™ processors. The Sun Performance Library was linked to FRAC3DVS-OPG to provide processor optimized Basic Linear Algebra Subprograms (BLAS) routines called by the WATSIT solver in FRAC3DVS-OPG.

Various factors contribute to the computational demands of geosphere paleoclimate simulations:

- Coupled density-dependent flow and transport requires iterating between flow and transport of TDS until both solutions converge.
- Simulation timescales range from 10 ka to 1 Ma.
- Model properties can vary by several orders of magnitude, namely the permeability reduction due to the presence of permafrost.
- Hydromechanical coupling whereby mechanical loads imposed on the geosphere from ice or large lakes, compress the rock matrix, thereby also compressing pore fluids, increasing their pressure, and influencing groundwater flow directions and gradients.
- Mechanical or hydraulic boundary conditions vary in time and space, due to glacial advance and retreat. These boundary conditions can also vary across large ranges, necessitating small time steps to achieve a stable numerical solution.
- A fine spatial discretization is required to capture large changes in state variables, as well as allowing smaller dispersivities to be used, which are important for transport simulations of TDS or the calculation of MLE.
- Large spatial extents are needed to allow large scale phenomenon such as glacial advance and retreat to affect distant portions of the modelling domain, without resorting to the selection of boundary conditions which may not be appropriate.

Since paleoclimate simulations can run for days or weeks, the ability to learn from failed runs is greatly slowed. FRAC3DVS-OPG includes a pre-processor called PREF3D, the model itself called F3DOPG, and a post-processor to produce Tecplot formatted files called F3DPLOT. Table 4.6 provides runtime statistics for the various paleoclimate scenarios. All simulations except Scenario 2 require approximately the same amount of random access memory (RAM). For PREF3D, Scenario 2 required nearly 10.4 GB of RAM to process the paleoclimate boundary conditions and permafrost. The NN2008 glaciation scenario had a longer duration of permafrost than the NN2778 glaciation scenario which was used for the other paleoclimate simulations, and hence required larger arrays in memory. F3DOPG also shows that Scenario 2 required more RAM to execute. In terms of runtime, Scenario 3 was the fastest since coupled density-dependent flow is not simulated, while Scenario 4 was the slowest due to the combined effects of a uniform hydraulic conductivity of 10^{-6} m/s for fracture zones, and simulating density-dependent flow requiring small time steps. The number of time steps, and reduced time steps are also shown in Table 4.6 for all paleoclimate simulations. The "bull" cluster on the Shared Hierarchical Academic Research Computing Network (SHARCNET) system was the only computer system available with sufficient RAM.

Table 4.6 PREF3D and F3DOPG execution statistics for the Canadian Shield Sub-Regional paleoclimate simulations on an AMD Opteron™ 2.4 GHz processor.

Scenario	PREF3D			F3DOPG				
	RAM [MB]	Swap† [MB]	Time [h:m:s]	RAM [MB]	Swap† [MB]	Time [h:m:s]	Total Steps	Reduced Steps
1	7517	7677	0:17:46	4666	4710	24:42:23	1130	10
2	10383	10543	0:18:44	5112	5161	24:04:54	1004	10
3	7496	7655	0:17:29	4608	4649	14:48:47	746	0
4	7517	7677	0:19:50	4657	4703	133:36:19	2627	13
5	7505	7675	0:17:57	4665	4710	25:03:22	1059	5
6	7505	7677	0:18:07	4664	4710	21:47:47	901	8
7	7496	7655	0:18:39	4605	4643	48:35:22	760	2

Note: †Swap refers to virtual memory.

4.5 Paleoclimate Simulations

A sequence of simulations were performed to obtain paleoclimate results. First, steady-state flow simulations were performed which provide the initial conditions for the pseudo steady-state density-dependent simulations. The steady-state simulations did not include brine, while the pseudo steady-state simulations were transient for a period of 1 Ma and included brine and density-dependent flow. Pseudo steady-state simulations were required to allow density-dependent flow to equilibrate; the end of the simulation was used as the initial conditions for the transient paleoclimate simulations.

All results of the 120 ka paleoclimate simulations at times of 80 ka before present, 40 ka before present, and at present for Scenarios 1–7 are shown in Appendix A to Appendix G. The parameters used in each paleoclimate scenario are listed in Table 4.3.

4.5.1 Pseudo Steady-State Simulation for Scenarios 1, 2, 5, and 6

A steady-state simulation was performed, followed by a pseudo steady-state density-dependent simulation which was used as the initial conditions for the paleoclimate simulations in Scenarios 1, 2, 5, and 6. Various results from this pseudo steady-state density-dependent simulation are provided in Figure 4.31 to Figure 4.40. Plots of freshwater heads are shown in Figure 4.31 for a block cut view and in Figure 4.32 for a fence view. Fracture zone traces are visible as black lines in both views. At depth, freshwater heads are lower within fracture zones. Since increasing freshwater heads at depth in variably dense flow systems is related to the increased freshwater head of higher density pore fluids, environmental heads are calculated and shown in Figure 4.33 for a block cut view and in Figure 4.34 for a fence view. Variations in heads can be seen between fracture zones and the adjacent matrix.

Pore velocity magnitudes are shown in Figure 4.35 and Figure 4.36. Pore velocities generally decrease with depth, indicative of the higher matrix and fracture permeabilities near ground surface. Higher pore velocities are visible in the matrix adjacent to fracture zones, and in the fracture zones themselves. The ratio of vertical pore velocities to the pore velocity magnitudes is shown in Figure 4.37 and Figure 4.38. The influence of fracture zones is also seen in the direction of flow. Most flow in the matrix appears downward, while flow leading to fracture zones is nearly horizontal.

The purpose of pseudo steady-state density-dependent simulations is to allow the flow system to equilibrate from the initial TDS distribution. Solute free recharge water tends to flush fracture zones and reduce TDS in the adjacent matrix blocks. This is evident in both Figure 4.39 and Figure 4.40. At a given elevation, TDS concentrations are higher in the matrix than in the fracture zones, as a concentration gradient exists in the matrix towards the lower TDS concentrations in the fracture zones.

4.5.2 CSSR Scenario 1 Paleoclimate Simulation

The first paleoclimate simulation uses the parameters listed in Table 4.5 and Table 4.3, and represents the base-case analysis. Scenario 1 uses the NN2778 glaciation scenario, with median fracture zone permeability with depth, a computed one-dimensional loading efficiency, and coupled density-dependent flow and transport. The subsequent scenarios represent variations on the base-case to investigate the influence of changes to the base-case parameters on the modelling results. The simulation results are presented in Appendix A; a summary of figure numbers for 2 views, 7 parameters, and 3 points in time are presented in Table A.1. Block cut and fence views are shown for various parameters at paleoclimate simulation times of 80 ka before present (−80 ka), 40 ka before present (−40 ka), and at present (0 ka).

Freshwater head plots are shown in Figures A.1 to A.6, and environmental head plots are shown in Figures A.7 to A.12. The −80 ka time occurs after the first glacial advance and retreat, and both heads are slightly elevated compared to the initial conditions of Figures 4.33 to 4.34. At −40 ka, the third glacial loading cycle is underway and the environmental head gradients are strongly downward in Figures A.9 and A.10. At present time (0 ka), in Figures A.11 and A.12, the environmental heads have reduced due to the deglaciation cycle, and are still dissipating, as compared to the initial condition.

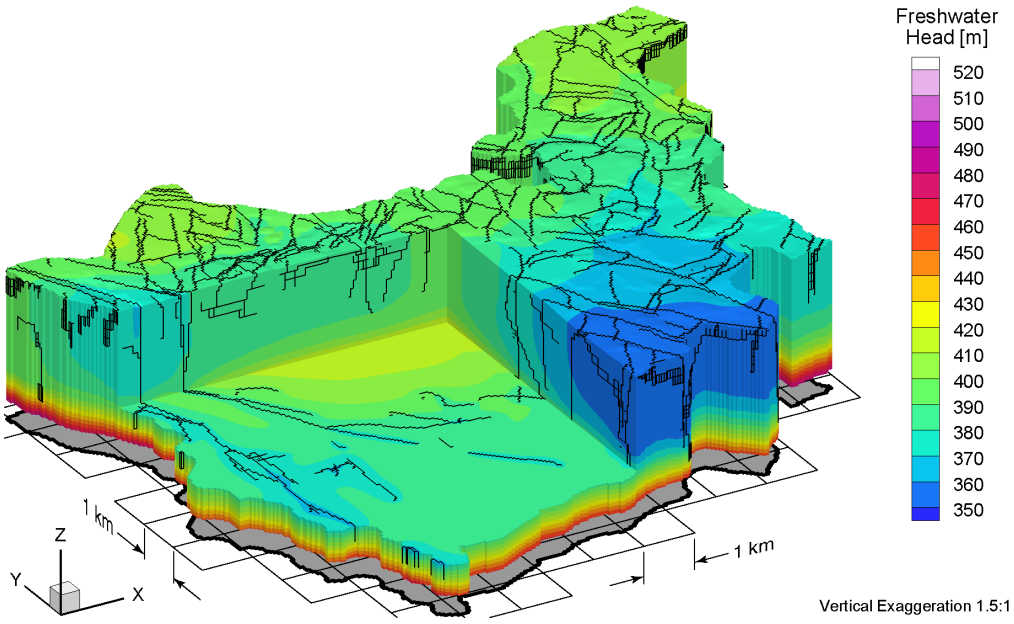

Figure 4.31 Block cut view of heads at 1 Ma for pseudo steady-state simulation, which is used as the initial condition for Scenarios 1, 2, 5, and 6.

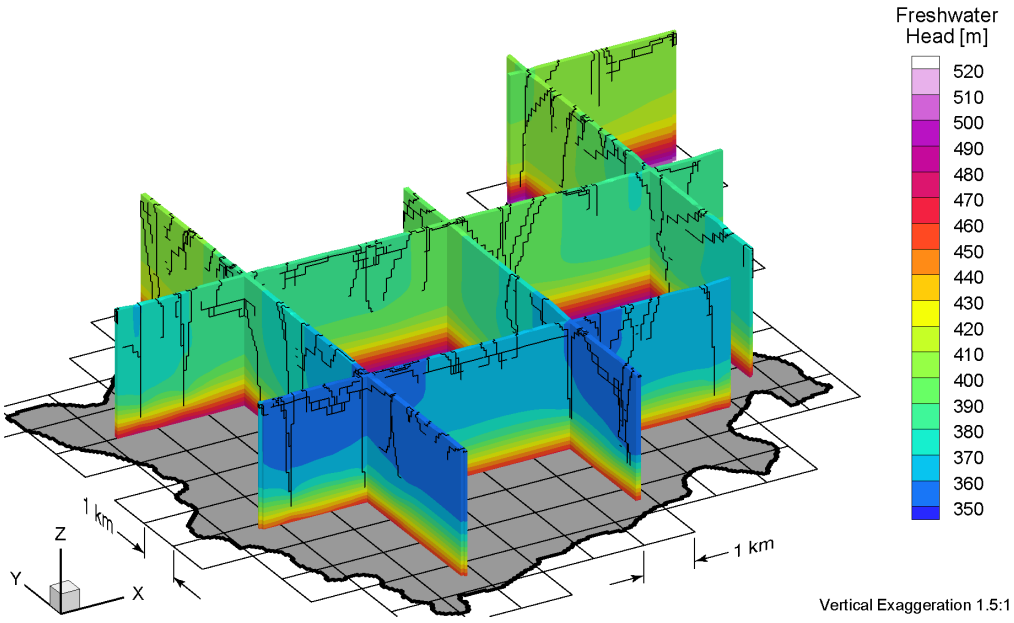

Figure 4.32 Fence view of heads at 1 Ma for pseudo steady-state simulation, which is used as the initial condition for Scenarios 1, 2, 5, and 6.

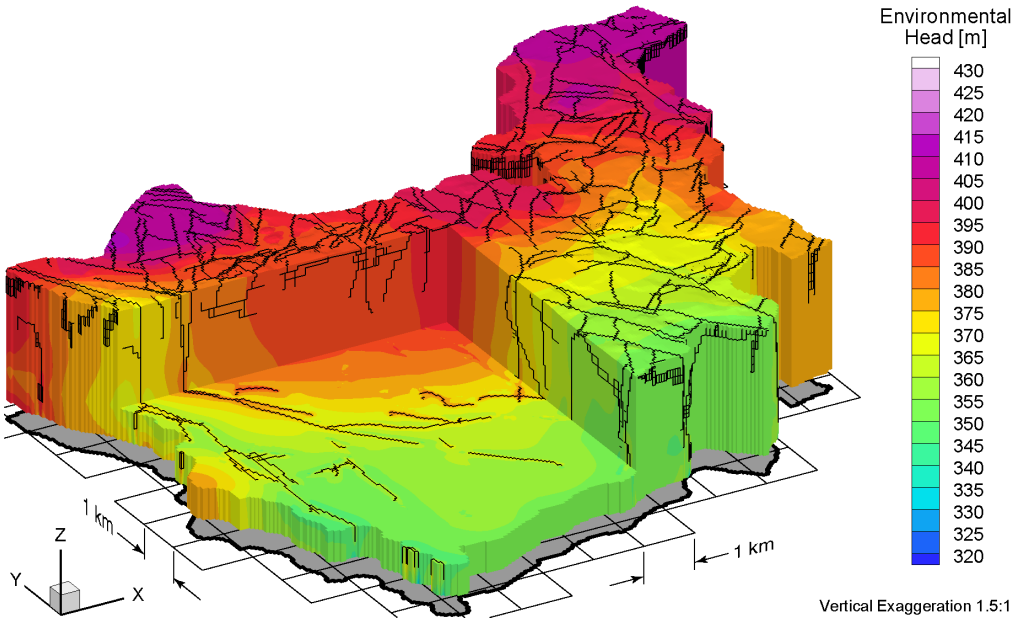

Figure 4.33 Block cut view of environmental heads at 1 Ma for pseudo steady-state simulation, which is used as the initial condition for Scenarios 1, 2, 5, and 6.

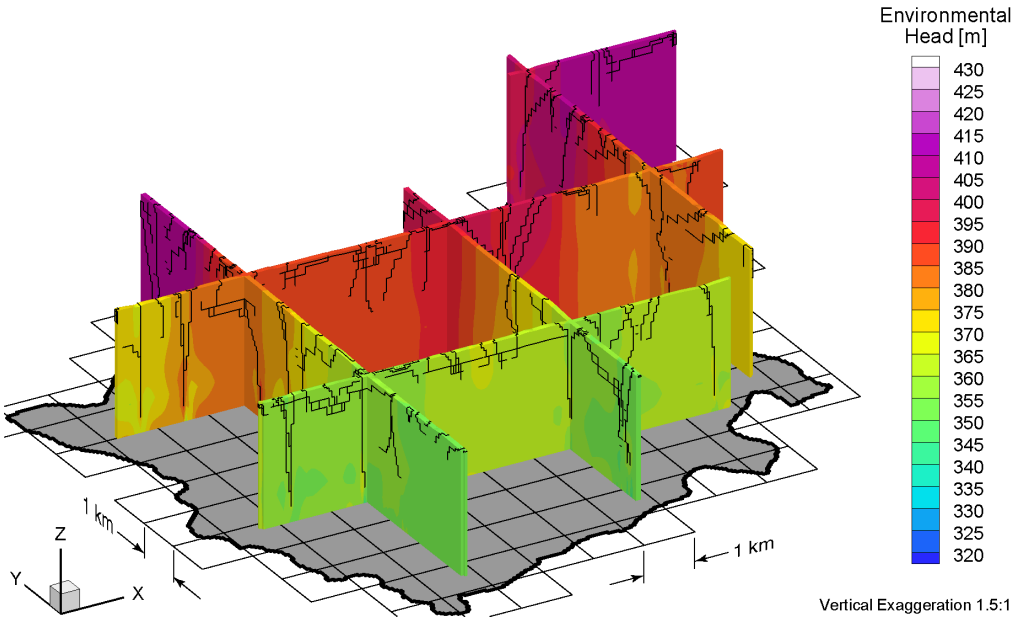

Figure 4.34 Fence view of environmental heads at 1 Ma for pseudo steady-state simulation, which is used as the initial condition for Scenarios 1, 2, 5, and 6.

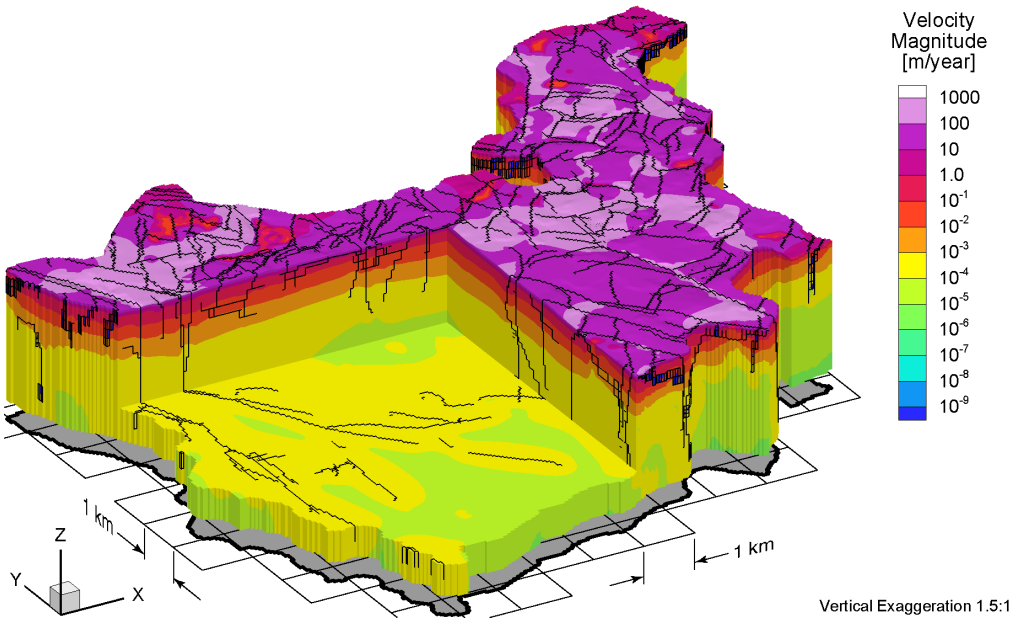

Figure 4.35 Block cut view of pore velocity magnitudes at 1 Ma for pseudo steady-state simulation, which is used as the initial condition for Scenarios 1, 2, 5, and 6.

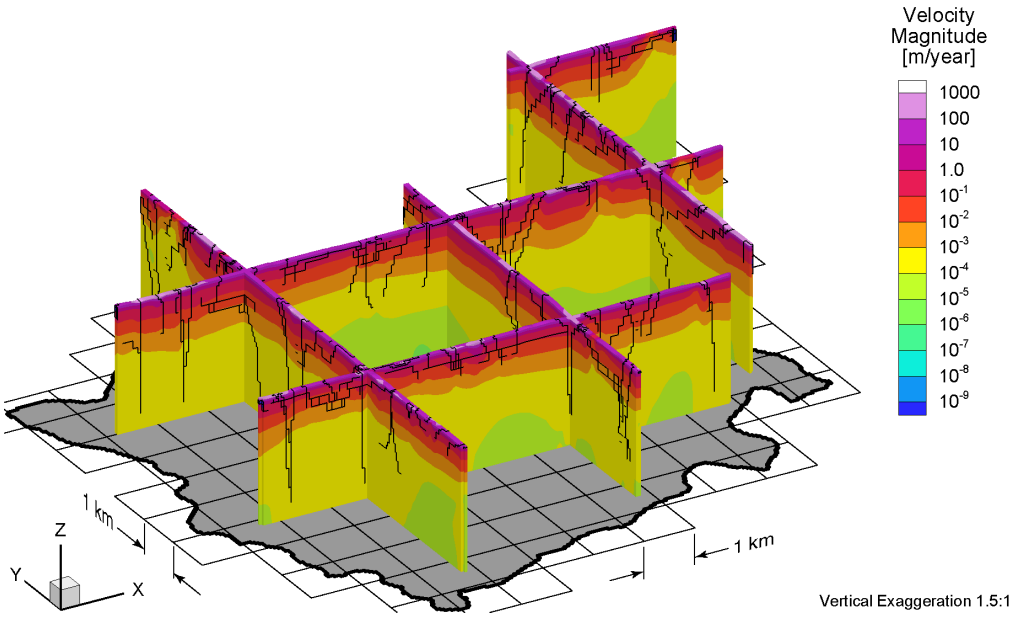

Figure 4.36 Fence view of pore velocity magnitudes at 1 Ma for pseudo steady-state simulation, which is used as the initial condition for Scenarios 1, 2, 5, and 6.

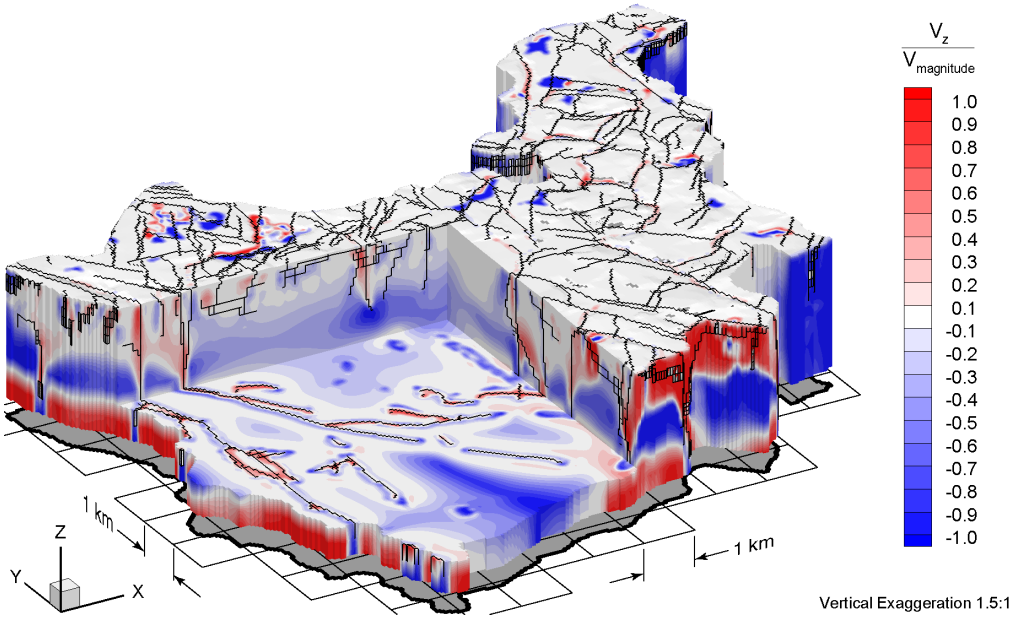

Figure 4.37 Block cut view of ratio of vertical pore velocities to pore velocity magnitudes at 1 Ma for pseudo steady-state simulation, which is used as the initial condition for Scenarios 1, 2, 5, and 6.

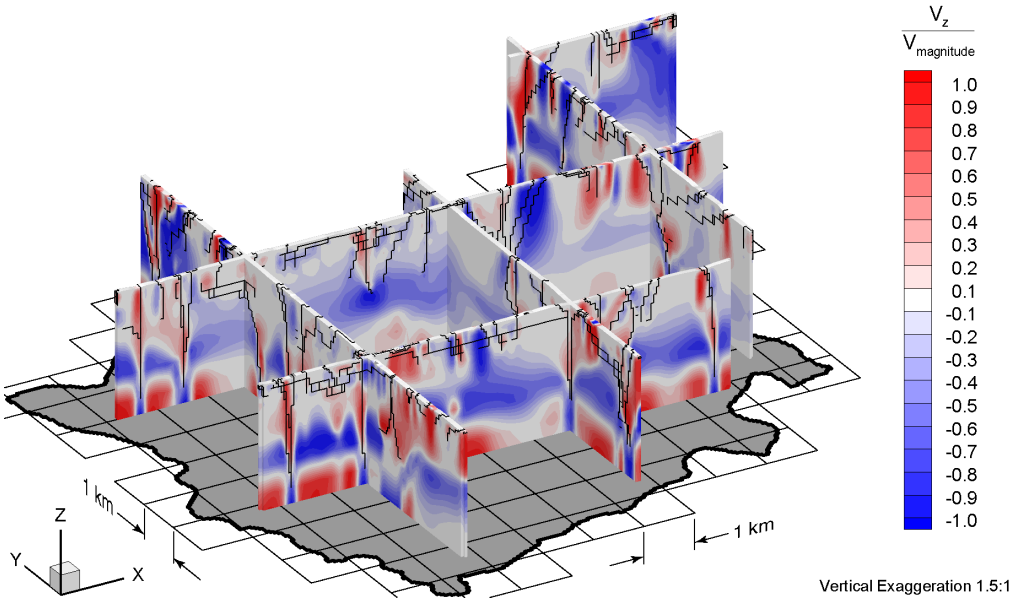

Figure 4.38 Fence view of ratio of vertical pore velocities to pore velocity magnitudes at 1 Ma for pseudo steady-state simulation, which is used as the initial condition for Scenarios 1, 2, 5, and 6.

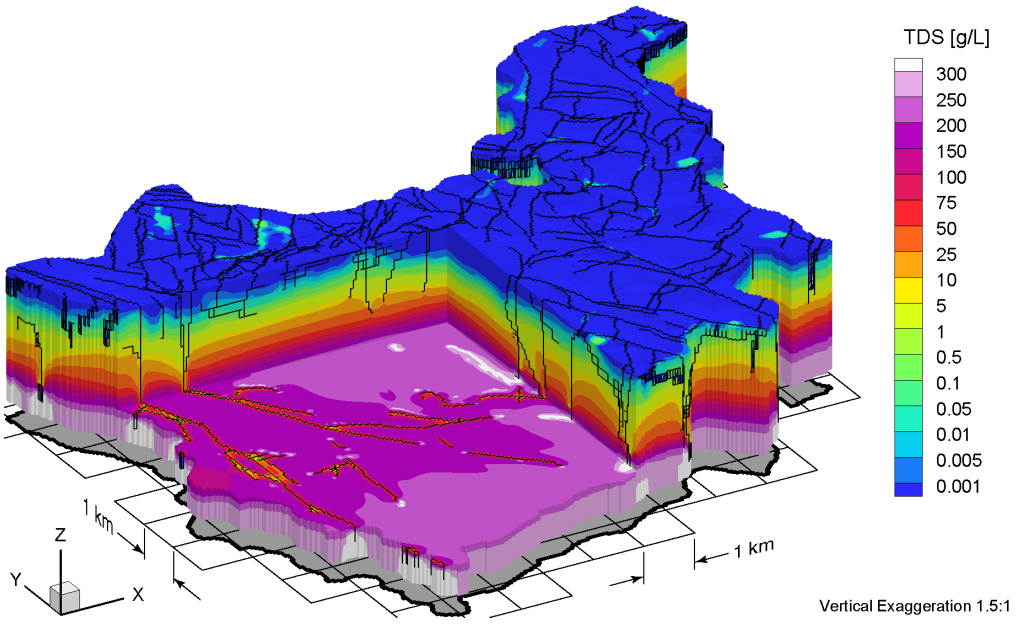

Figure 4.39 Block cut view of brine concentrations at 1 Ma for pseudo steady-state simulation, which is used as the initial condition for Scenarios 1, 2, 5, and 6.

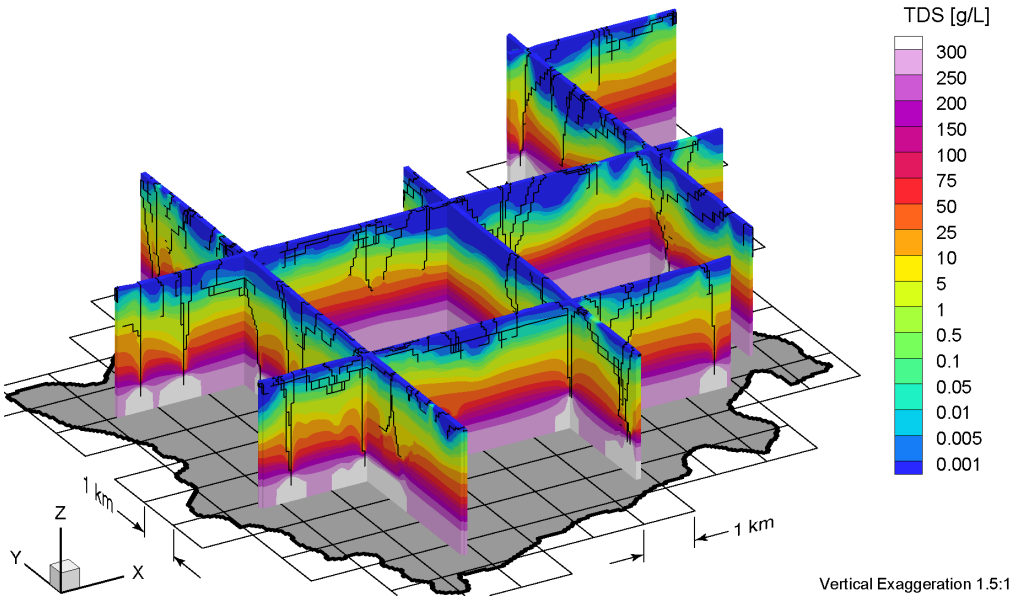

Figure 4.40 Fence view of brine concentrations at 1 Ma for pseudo steady-state simulation, which is used as the initial condition for Scenarios 1, 2, 5, and 6.

Pore water velocity magnitudes are presented in Figure A.13 to Figure A.18, and the ratio of vertical pore velocities to pore velocity magnitudes are presented in Figure A.19 to Figure A.24. In comparing the −80 ka plots of Figure A.13 to the initial condition of Figure 4.36, the effect of permafrost can be seen; velocities near the surface are 3–4 orders of magnitude less than for the initial condition. As the simulation progresses, at −40 ka, pore water velocities increase as the glacial loading increases (see Figure A.13). At present time, the flow system is similar to the initial condition with higher pore water velocities near surface. In terms of directions, flows tend to be more downward than for the initial conditions depicted in Figure 4.37 and Figure 4.38. At −40 ka, the flow direction is clearly downward in Figure A.21, while at present time, the flow directions near the bottom of the domain trend upwards, as shown in Figure A.23. This is due to slightly elevated heads at depth, initially caused by glacial loading, and dissipating towards the surface of the domain.

Brine concentrations are presented in Figure A.25 to Figure A.30. In the initial conditions, Figure 4.39 displays a greater difference in concentration between the fracture and the adjacent matrix. When the domain is subject to permafrost, the pore water velocities reduce, allowing more time for diffusion to take place, and increase the concentration in the matrix adjacent to fractures. This is evident in the temporal progression of figures from Figure 4.39, to Figure A.30.

Fracture zones are characterized in FRAC3DVS-OPG using orthogonal quadrilateral elements, either horizontal or vertical, that lie between adjacent hexahedral elements. The initial TDS distribution with depth, shown in Figure 4.24, is applied to the entire modelling domain at the beginning of pseudo steady-state density-dependent simulations. After 1 Ma, sufficient time has passed to allow TDS distributions to equilibrate in the system, and allow for solute free recharge waters to dilute the TDS concentrations contained in permeable and connected fracture zones. Figure 4.41 provides a plot of the TDS probability density function (PDF) and cumulative density function (CDF) for vertical fracture elements, as a function of depth. Vertical quadrilateral elements that are contained within the matrix are also plotted, in terms of their TDS PDF and CDF values. To calculate depth-dependence of TDS, all vertical faces, either associated with fractures, or within the matrix are used. For a given vertical face, the TDS values for the top two nodes are averaged, then the TDS values for the bottom two nodes are averaged. Depth from surface for these two midpoints are calculated in a similar manner from their elevation. TDS values at specified depths are linearly interpolated from each vertical fracture face. The interpolated TDS values are either associated with fractures or matrix, and binned at each depth to produce a PDF distribution. The CDF at that depth can then be calculated.

The CDF plots of the fractures and matrix allow the determination, in a depth-dependent way, of the median and spread of TDS values for both fractures and matrix. In Figure 4.41, the median percentile occurs at a lower TDS value in fractures, than in the matrix, deep in the system, while the opposite occurs shallow. It's interesting to note that very low TDS values can occur to a depth of approximately 500 m, but their lower bound is quickly raised, below those depths. Figure 4.41 can provide a useful TDS comparison between scenarios, and between fracture zones and the matrix.

A tracer of unit concentration is applied as a Cauchy boundary condition to all inflow surface nodes at the beginning of the paleoclimate simulation. This tracer is used to

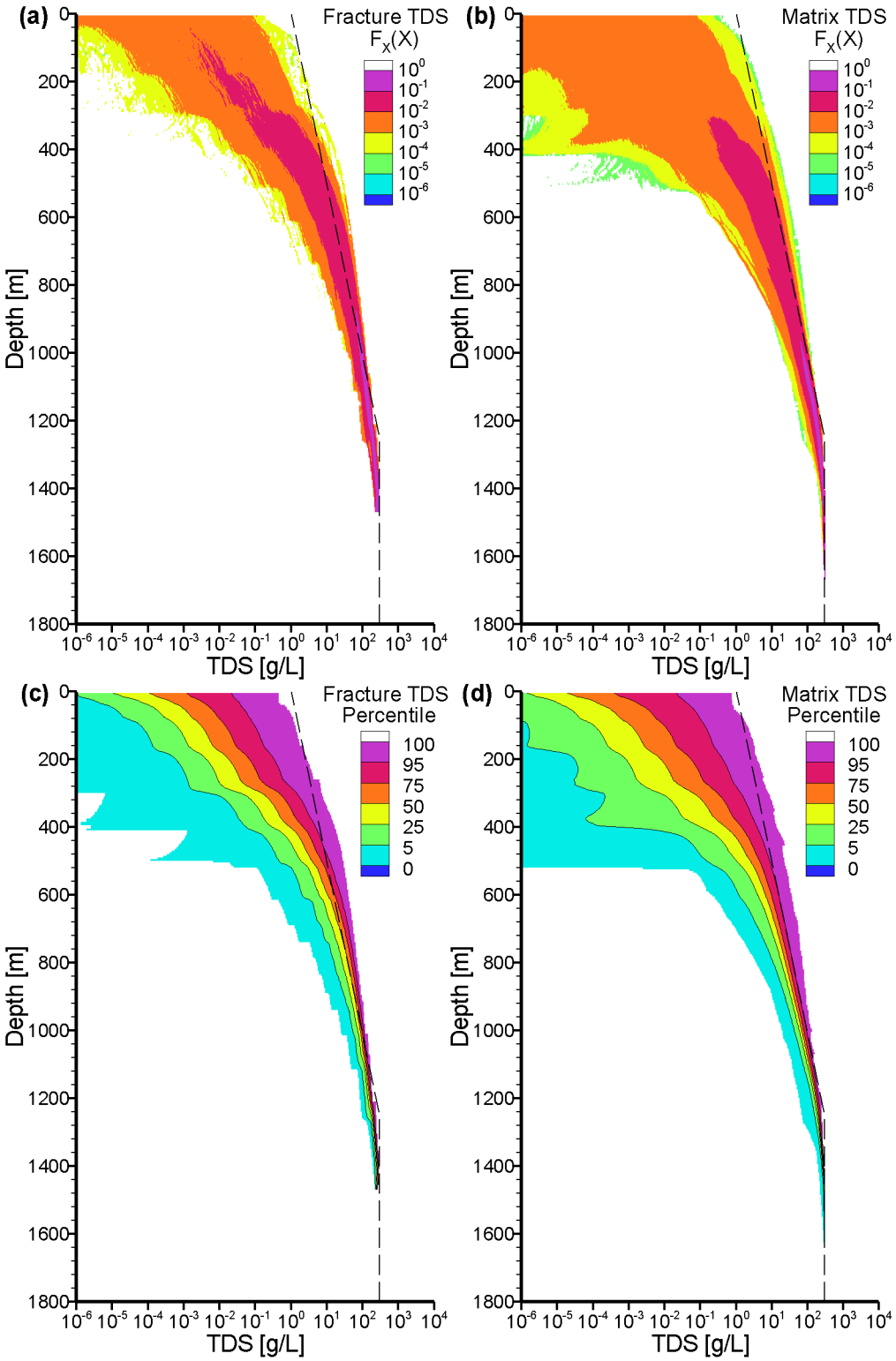

Figure 4.41 Scenario 1 probability density functions (PDF) and cumulative density functions (CDF) of brine concentration (TDS) as a function of depth for vertical faces associated with fractures and matrix blocks.

characterize the migration, from the surface, of recharge water that occurs during the paleoclimate simulation; the recharge water includes glacial meltwater, whose importance was discussed in §2.5.1. Tracer concentrations for the modelling domain are presented in Figure A.31 to Figure A.36. The evolution of the tracer is shown over the 120 ka paleoclimate simulation. At the present time, the tracer is predominantly in the matrix with some tracer appearing in fractures at mid-depth.

The infiltration or recharge into the modelling domain for all scenarios is shown in Figure 4.42. For Scenario 1 in Figure 4.42a, the infiltration rate ranges between approximately 5×10^{-5} m/a and 1×10^{-1} m/a. The higher infiltration rates coincide with a lack of permafrost as shown in Figure 4.26. A recharge boundary condition was not used for the paleoclimate simulations due to the linear interpolation of both permafrost and the surface Dirichlet boundary condition used to represent the presence of an ice-sheet. The recharge rate would have to be adjusted to account for the variable permafrost permeability between time steps. As such, the infiltration rate of 1×10^{-1} m/a is much higher than the average recharge rate of 1×10^{-3} m/a, but the infiltration rate beneath glaciers subject to permafrost is much less at 5×10^{-5} m/a. Figure 4.43 provides the total flux across the surface of the modelling domain, positive representing inward to the domain, and negative representing outward. For Scenario 1 in Figure 4.43a, net inflows occur during advance of glaciers where high heads lead to vertically downward gradients, while net outflows occur during the retreat of glaciers and resulting gradients are upwards.

Mean life expectancies are also calculated for the final velocity distribution and are shown in Figure A.37 for a block cut view and in Figure A.38 for a fence view. MLEs are calculated using present day pore water velocities and brine distributions, determined at the end of the paleoclimate simulation. At depth, most MLE values are greater than 10 Ma. In the vicinity of fractures, MLE values drop by an order of magnitude, to greater than 1 Ma. The undulation in the MLE isochrones depends on the location of recharge and discharge areas on the surface of the modelling domain.

MLE cumulative density function (CDF) for all paleoclimate scenarios are plotted in Figure 4.44 at a depth below ground surface of 625 m. This figure, and Figure 4.45 at depth of 1200 m illustrates the variation in MLE at that depth, where the median MLE is represented by the 50^{th} percentile. At 625 m depth, the median MLE is approximately 700 ka, while at 1200 m depth, the median MLE is slightly more than 10 Ma.

4.5.3 CSSR Scenario 2 Paleoclimate Simulation

The second paleoclimate simulation investigates the role of an alternate glaciation scenario, NN2008, in which the domain is subject to a longer period of permafrost than in NN2778, used for Scenario 1. All figures are presented in Appendix B, and a summary of the figures is presented in Table B.1. A significant difference from the NN2778 scenario results is noticeable in the −40 ka plots, primarily because NN2778 is undergoing a glacial loading event, while NN2008 is not. The Scenario 2 figures for freshwater heads, environmental heads, pore water velocity magnitudes, ratio of vertical pore water velocities to pore velocity magnitudes, and TDS distributions (see Table B.1) at present time look nearly identical to their respective Scenario 1 figures.

The tracer migration figures presented in Figure B.31 to Figure B.36 illustrate the impact of permafrost, when compared to Figure A.31 to Figure A.36 from Scenario 1. For the present time, the tracer migrates deeper into the domain in Scenario 1 than in

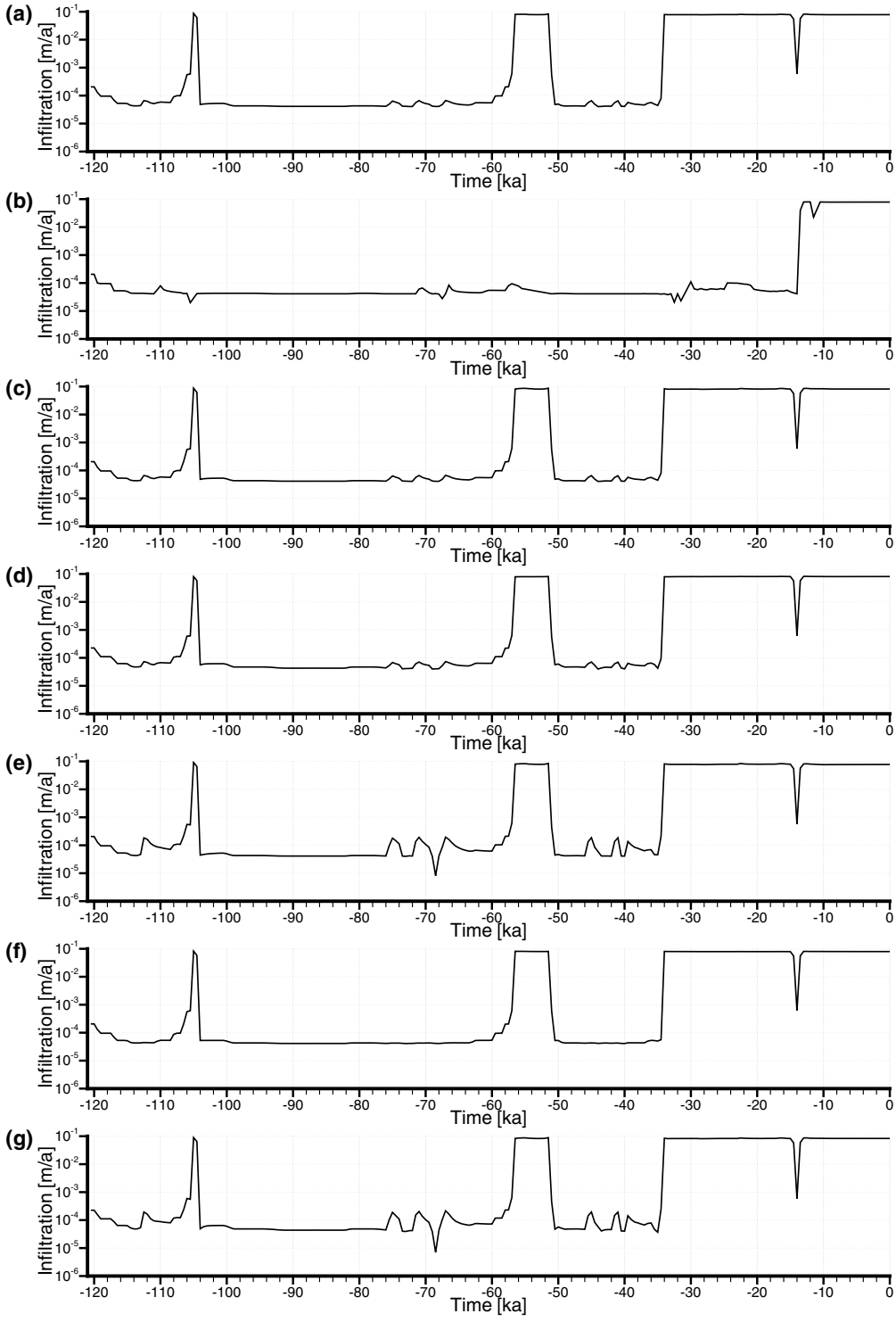

Figure 4.42 Average infiltration across entire modelling domain for (a) Scenario 1, (b) Scenario 2, (c) Scenario 3, (d) Scenario 4, (e) Scenario 5, (f) Scenario 6, and (g) Scenario 7.

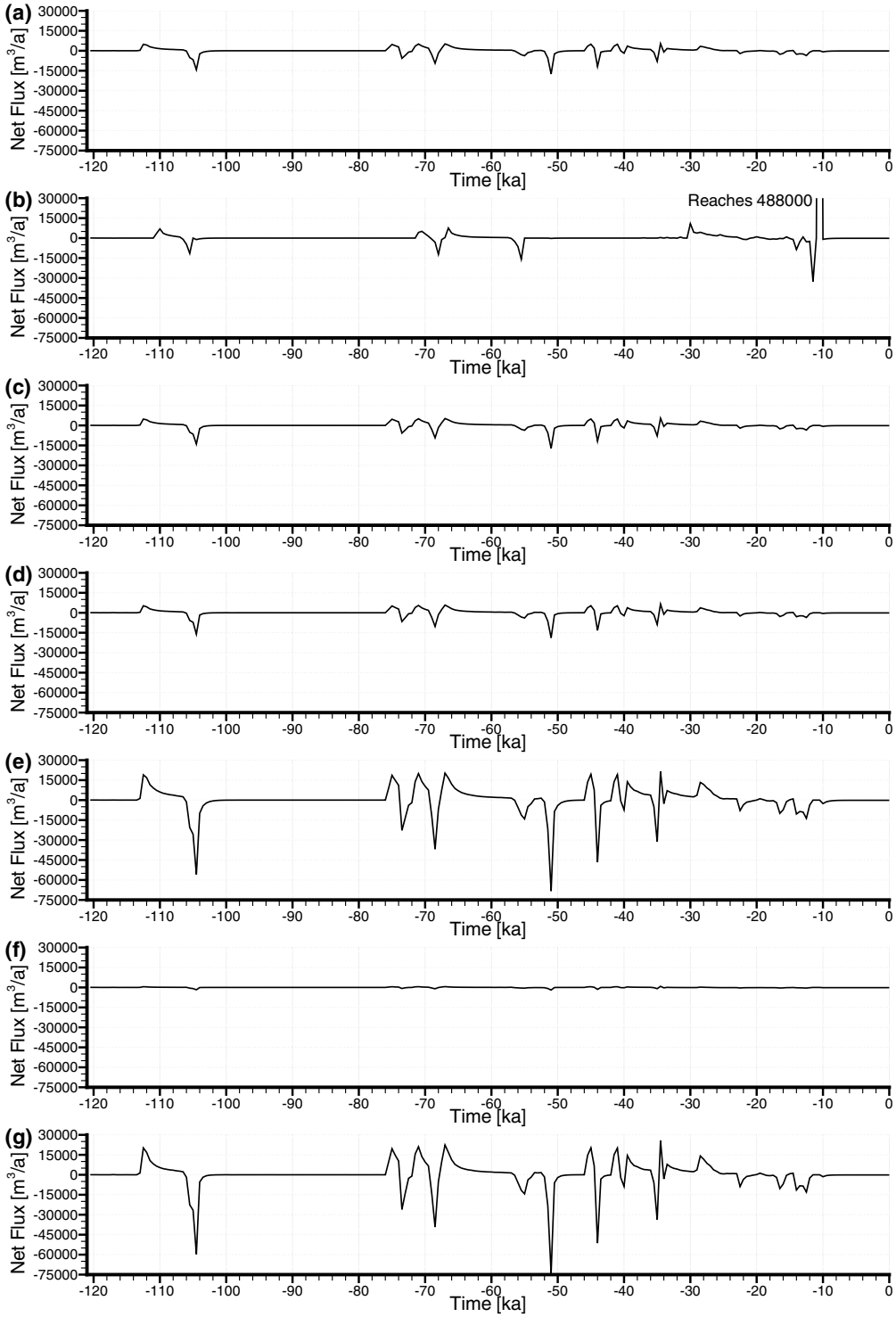

Figure 4.43 Net surface flux across entire modelling domain for (a) Scenario 1, (b) Scenario 2, (c) Scenario 3, (d) Scenario 4, (e) Scenario 5, (f) Scenario 6, and (g) Scenario 7.

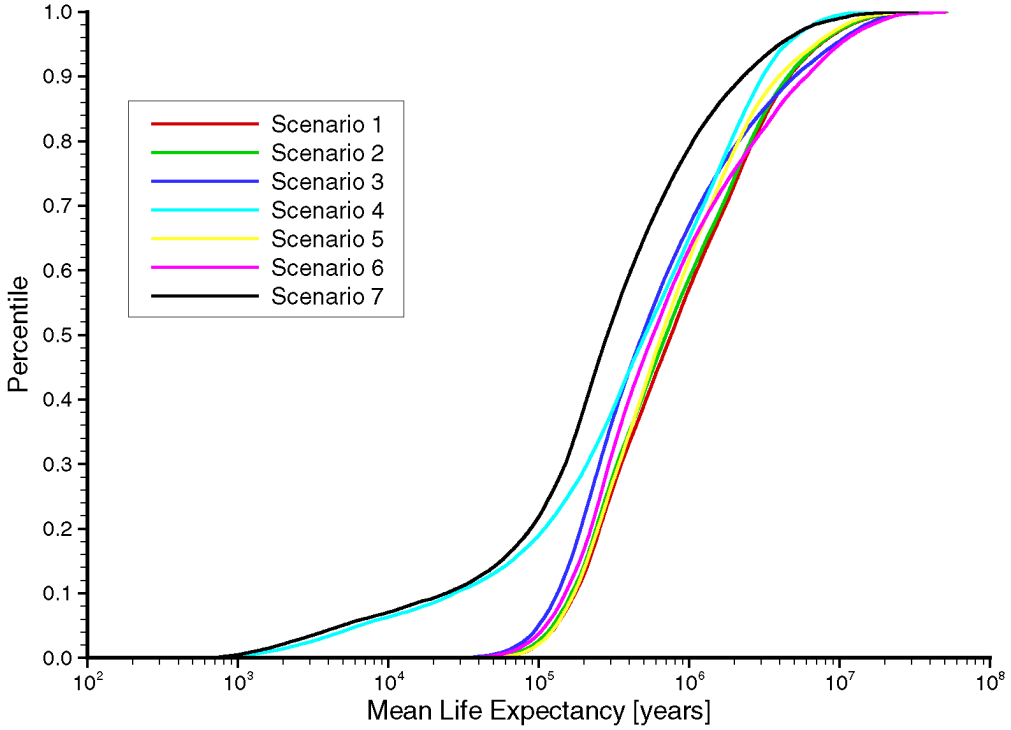

Figure 4.44 Mean life expectancy cumulative density function at 625 m depth for Canadian Shield Sub-Regional Scenarios 1 to 7.

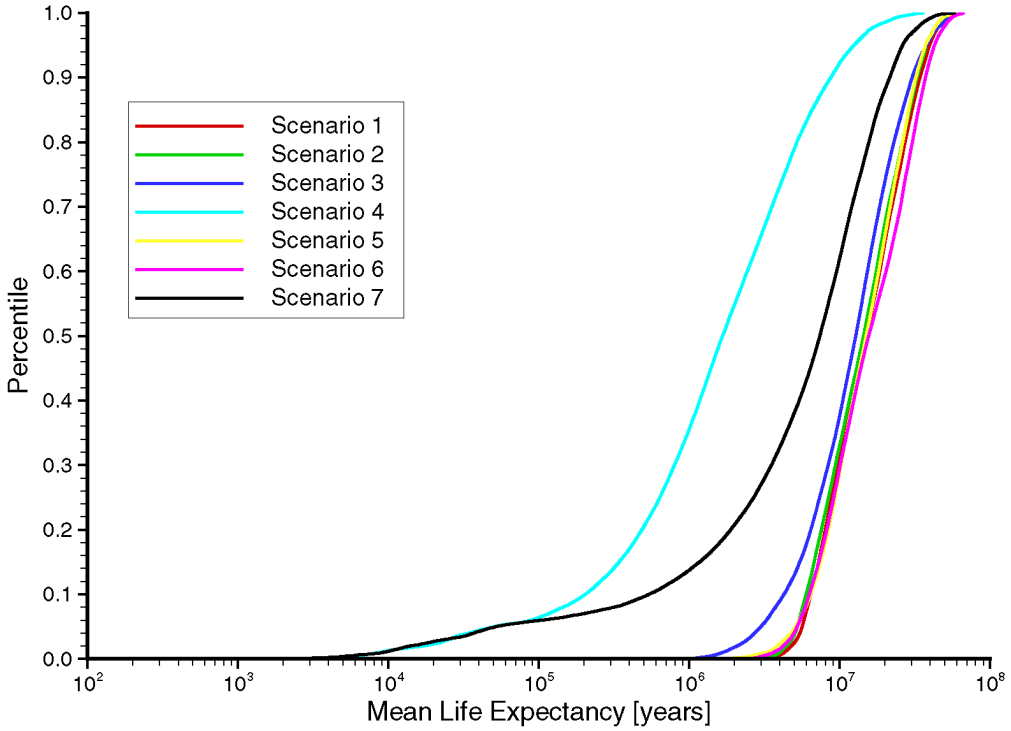

Figure 4.45 Mean life expectancy cumulative density function at 1200 m depth for Canadian Shield Sub-Regional Scenarios 1 to 7.

Scenario 2. This is attributed to the fact that less permafrost cover during the course of the paleoclimate simulation in Scenario 1 allows for a greater overall duration of recharge into the subsurface when the ground is unfrozen.

For Scenario 2 in Figure 4.42b, the infiltration rate ranges between approximately 5×10^{-5} m/a and 1×10^{-1} m/a. The higher infiltration rates coincide with a lack of permafrost as shown in Figure 4.25. Figure 4.43b provides the total flux across the surface of the modelling domain for Scenario 2. A very large efflux occurs at −12 ka coinciding with the proglacial lake that forms as shown in Figure 4.25.

In comparing MLE values, in Figure B.37 and Figure B.38 to Figure A.37 and Figure A.38, respectively, no visual difference between Scenario 2 and Scenario 1 is apparent. The MLE CDF plots in Figure 4.44 and Figure 4.45 confirm the lack of difference in MLE values for the two scenarios.

The fracture and matrix TDS PDF and CDF plots in Figure 4.46 are nearly identical to Figure 4.41, similar to the TDS figures in the appendices. The only apparent difference lies within 500 m of ground surface where the TDS values for Scenario 2 are slightly higher for a given percentile than in Scenario 1, and is attributed to the greater duration of recharge in Scenario 1.

4.5.4 CSSR Scenario 3 Paleoclimate Simulation

Scenario 3 is identical to Scenario 1, except that density-dependent flow is not simulated. All figures are presented in Appendix C, and a summary of the figures is presented in Table C.1. Due to lack of TDS in the modelling domain, freshwater and environmental head plots for the two scenarios cannot be directly compared. The pore water velocity plots in Figure C.7 to Figure C.12, can be compared to Scenario 1 plots in Figure A.13 to Figure A.18, and look very similar to each other. The ratio of vertical pore velocities to pore velocity magnitudes are presented in Figure C.13 to Figure C.18. When compared to Figure A.19 to Figure A.24, the presence of brine in Scenario 1 has the effect of changing flow directions at depth, and not allowing deep flowpaths to develop, as compared to the freshwater case in Scenario 3.

The tracer migration figures presented in Figure C.19 to Figure C.24 are nearly identical to the tracer migration figures of Scenario 1 in Figure A.31 to Figure A.36. Since the upper groundwater flow system is very dilute compared to the deep flow system, it is less affected by density. Scenario 3, which ignores brine, therefore results in a very similar tracer migration to Scenario 1.

For Scenario 3 in Figure 4.42c, the infiltration rate is very similar to Scenario 1 in Figure 4.42a and can be attributed to using the same paleoclimate boundary conditions. The same similarities occur for the net flux of Figure 4.43c as compared to Figure 4.43a.

In comparing Figure C.25 for a block cut view and Figure C.26 for a fence view, to Figure A.37 and Figure A.38, respectively, the MLE values for Scenario 3 are generally less than for Scenario 1. This outcome is also visible in the MLE CDF plots in Figure 4.44 and Figure 4.45. Based on the results from Scenario 3, the presence of dense fluids at depth leads to greater MLE values.

4.5.5 CSSR Scenario 4 Paleoclimate Simulation

Scenario 4 investigates the role of high permeability fracture zones at depth, using a uniform hydraulic conductivity of 10^{-6} m/s. All figures are presented in Appendix D,

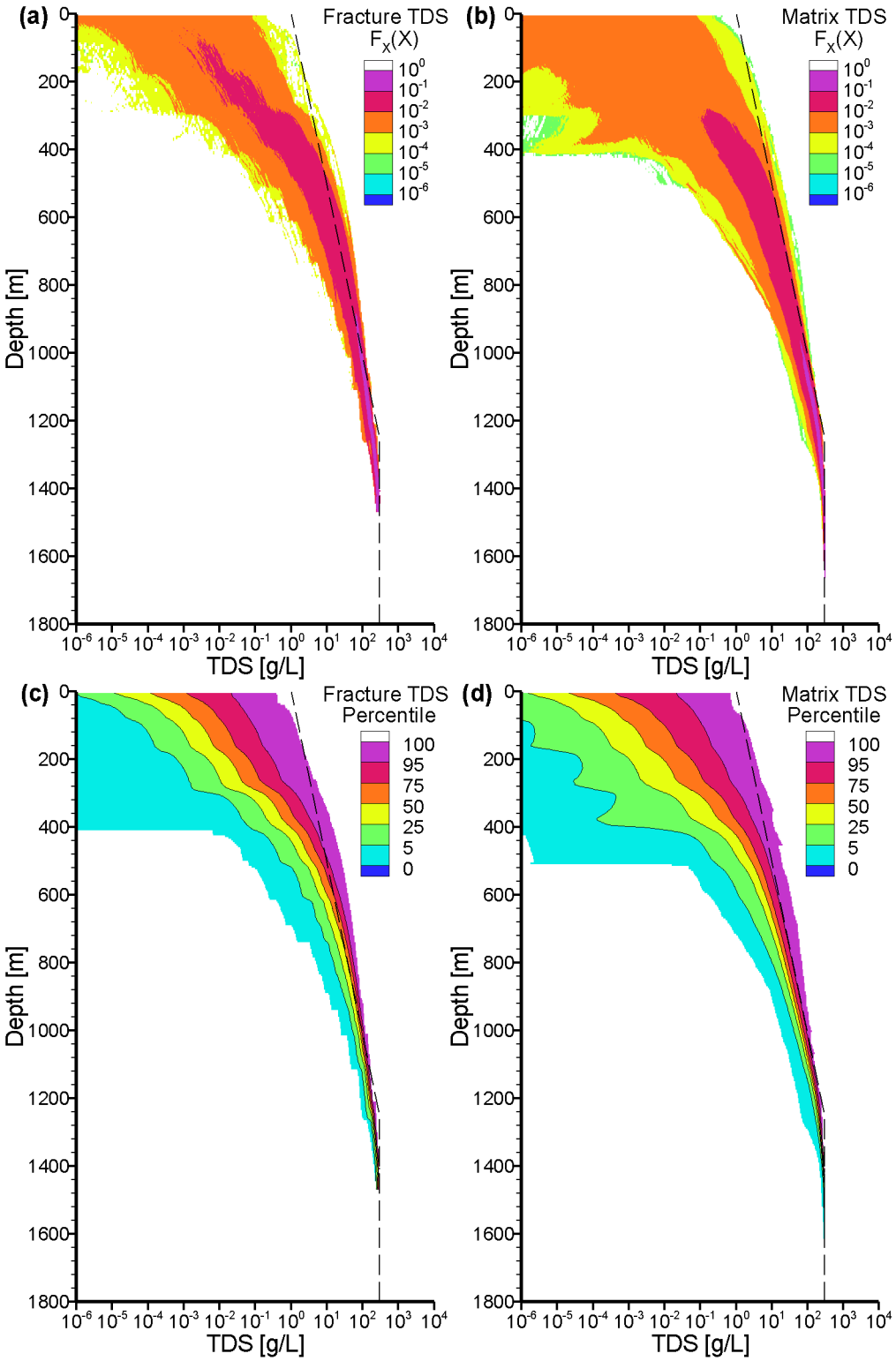

Figure 4.46 Scenario 2 probability density functions (PDF) and cumulative density functions (CDF) of brine concentration (TDS) as a function of depth for vertical faces associated with fractures and matrix blocks.

and a summary of the figures is presented in Table D.1. Since the properties of the model changed, a new steady-state model, and a new pseudo steady-state density-dependent model were created. The results from the pseudo steady-state analysis at 1 Ma are provided in Figure 4.47 to Figure 4.56.

Plots of freshwater heads are shown in Figure 4.47 for a block cut view and in Figure 4.48 for a fence view. The freshwater heads for Scenario 4 are generally lower, at depth, than for Scenario 1. A similar trend is shown in Figure 4.49 and in Figure 4.50, when compared to Figure 4.33 and Figure 4.34, respectively.

Pore velocity magnitudes shown in Figure 4.51 and Figure 4.52 are very similar to Figure 4.35 and Figure 4.36 for Scenario 1. The ratio of vertical pore velocities to the pore velocity magnitudes is shown in Figure 4.53 and Figure 4.54. When compared to Scenario 1, namely Figure 4.37 and Figure 4.38, there exists more vertically downward gradients for Scenario 4.

The distribution of TDS in Figure 4.55 and Figure 4.56 is similar to Figure 4.39 and Figure 4.40, with some notable exceptions. in Scenario 4, the higher permeability fracture zones allow greater movement of water, thereby reducing TDS concentrations at depth, within and adjacent to fracture zones. This can be seen in both the block cut view and the fence view.

Freshwater head plots are shown in Figures D.1 to D.6, and environmental head plots are shown in Figures D.7 to D.12. In comparing these plots to the Scenario 1 plots in Appendix A, the fracture zones have a greater influence on the heads, as shown in Figure D.3 during glacial advance at −40 ka, as compared to Figure A.3. This same trend can be seen in the environmental heads of the same appendices at the same simulation time.

Pore water velocity magnitudes are presented in Figure D.13 to Figure D.18, and the ratio of vertical pore velocities to pore velocity magnitudes are presented in Figure D.19 to Figure D.24. The pore water velocity plots are very similar between Scenario 4 and Scenario 1, with generally slightly higher velocities throughout the domain for Scenario 4. For the ratio of vertical pore velocities to pore velocity magnitudes, the Scenario 4 plots tend to have more downward vertical gradients than Scenario 1, throughout the paleoclimate simulation period.

Brine concentrations are presented in Figure D.25 to Figure D.30. Due to the high permeability fracture zones, TDS concentrations in and adjacent to fracture zones are lower in Scenario 4 as compared to Scenario 1. Comparing TDS PDF and CDF curves from Figure 4.57 to the Scenario 1 data in Figure 4.41 demonstrates the significant impact of high permeability fractures at depth in allowing freshwater to recharge to great depths in fracture zones. There is also a more noticeable difference between Figure 4.57c and Figure 4.57d, than compared to Figure 4.41c and Figure 4.41d, respectively.

Tracer concentrations for the modelling domain are presented in Figure D.31 to Figure D.36. The high permeability fracture zones also allow the migration of the tracer to depths of 1500 m in the groundwater flow system, notably surrounding fractures. This is not the case with Scenario 1 as shown in Figure A.31 to Figure A.36.

For Scenario 4 in Figure 4.42d, the infiltration rate is very similar to Scenario 1 in Figure 4.42a and can be attributed to using the same paleoclimate boundary conditions. The same similarities occur for the net flux of Figure 4.43d as compared to Figure 4.43a.

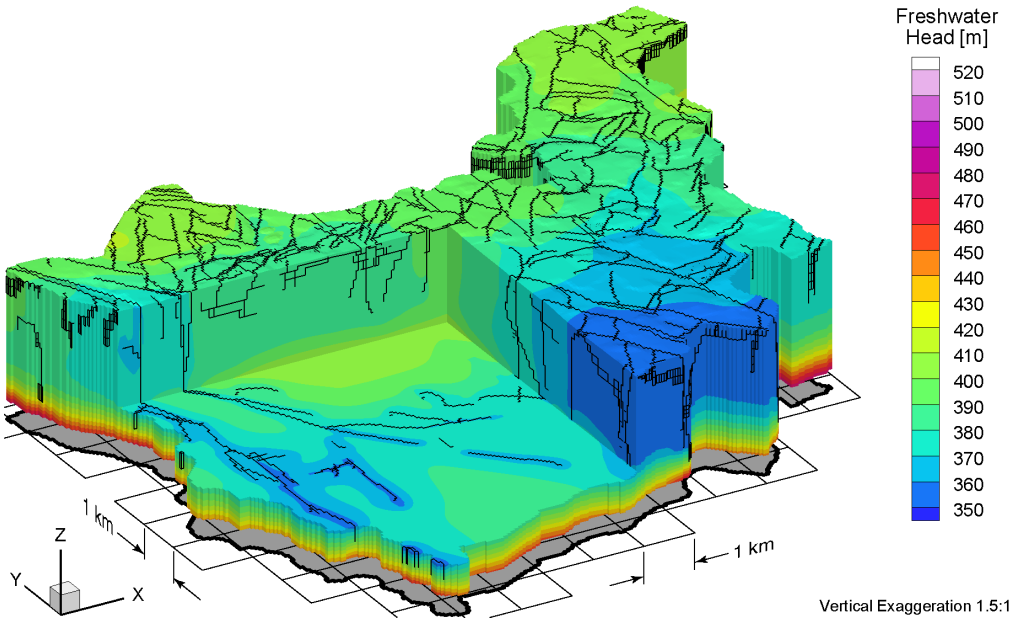

Figure 4.47 Block cut view of heads at 1Ma for pseudo steady-state simulation, which is used as the initial condition for Scenario 4.

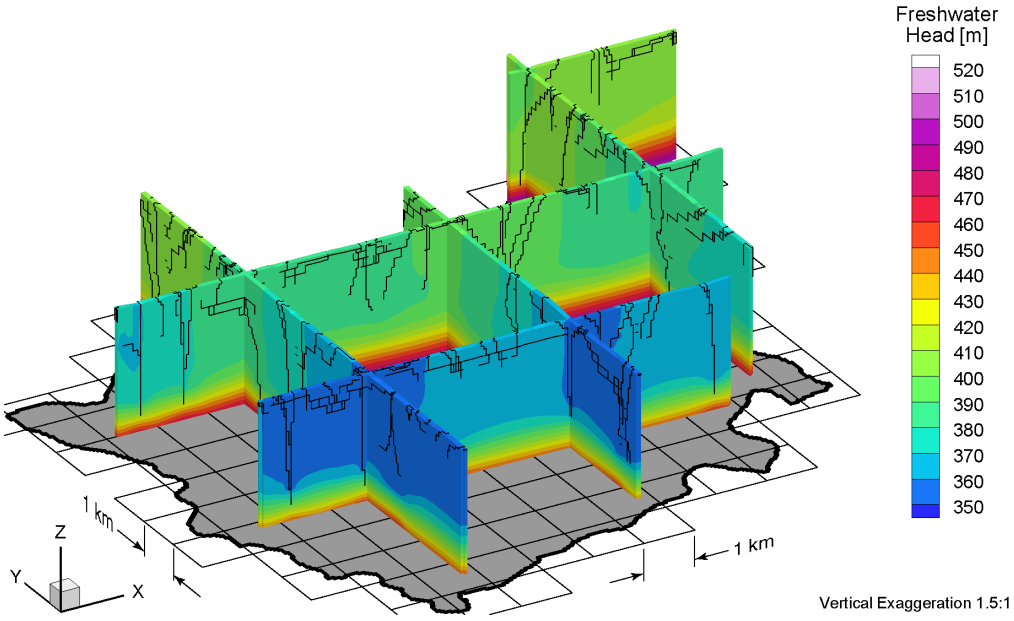

Figure 4.48 Fence view of heads at 1Ma for pseudo steady-state simulation, which is used as the initial condition for Scenario 4.

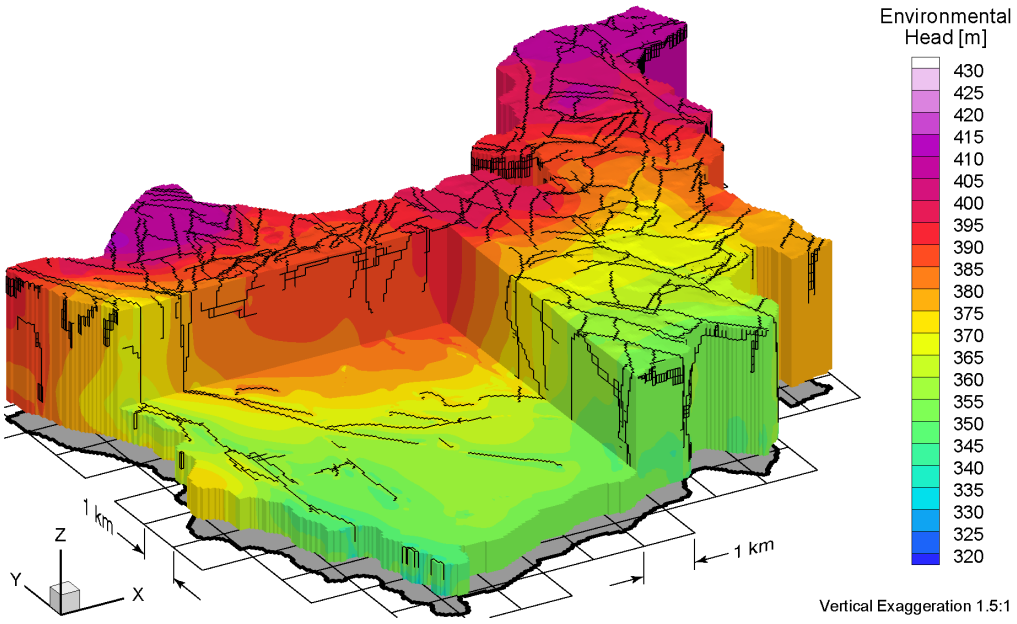

Figure 4.49 Block cut view of environmental heads at 1 Ma for pseudo steady-state simulation, which is used as the initial condition for Scenario 4.

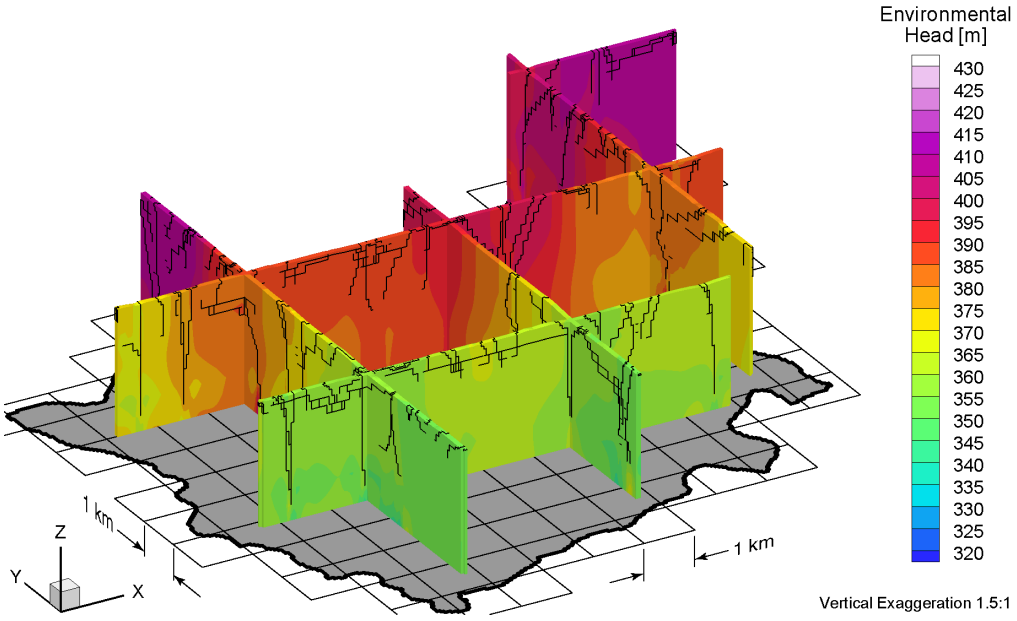

Figure 4.50 Fence view of environmental heads at 1 Ma for pseudo steady-state simulation, which is used as the initial condition for Scenario 4.

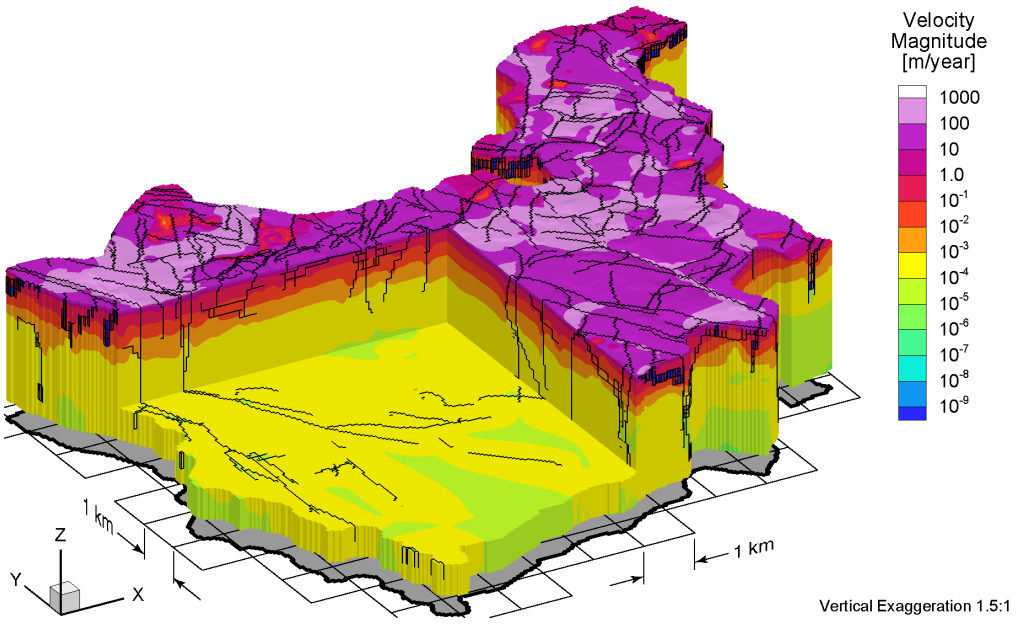

Figure 4.51 Block cut view of pore velocity magnitudes at 1 Ma for pseudo steady-state simulation, which is used as the initial condition for Scenario 4.

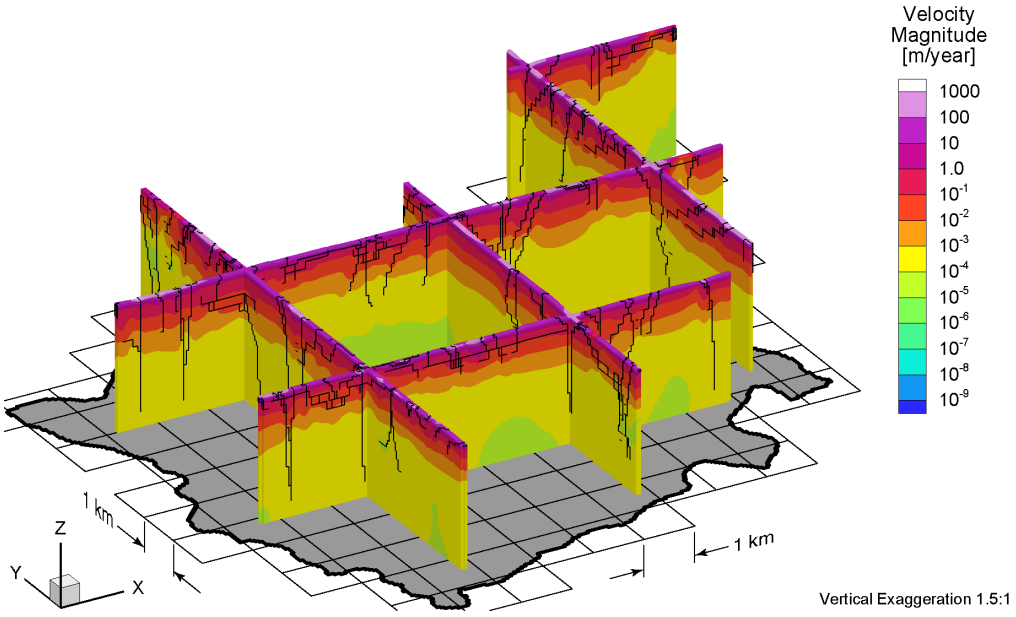

Figure 4.52 Fence view of pore velocity magnitudes at 1 Ma for pseudo steady-state simulation, which is used as the initial condition for Scenario 4.

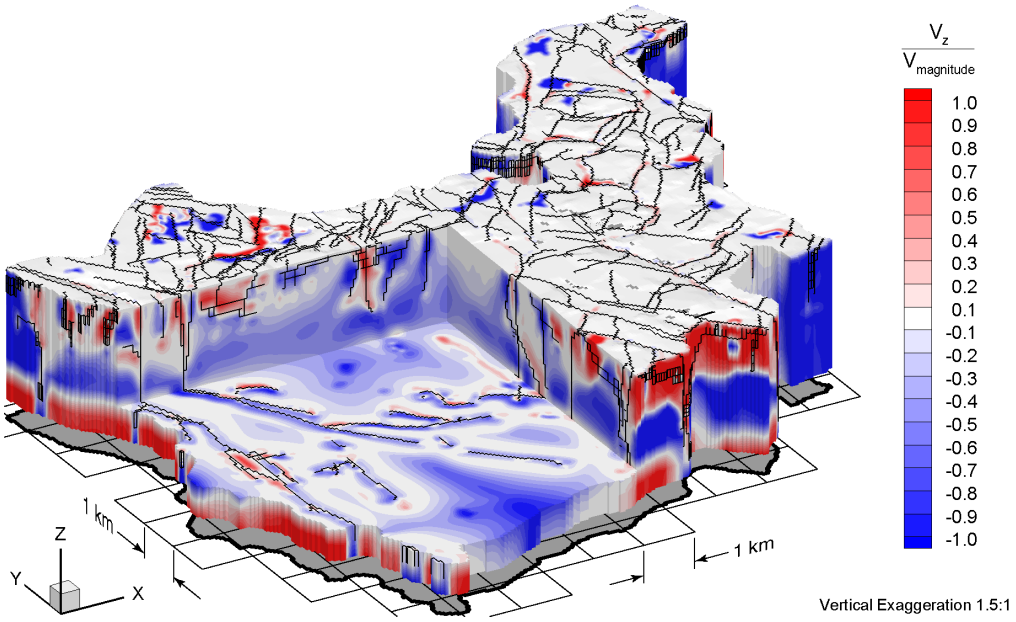

Figure 4.53 Block cut view of ratio of vertical pore velocities to pore velocity magnitudes at 1 Ma for pseudo steady-state simulation, which is used as the initial condition for Scenario 4.

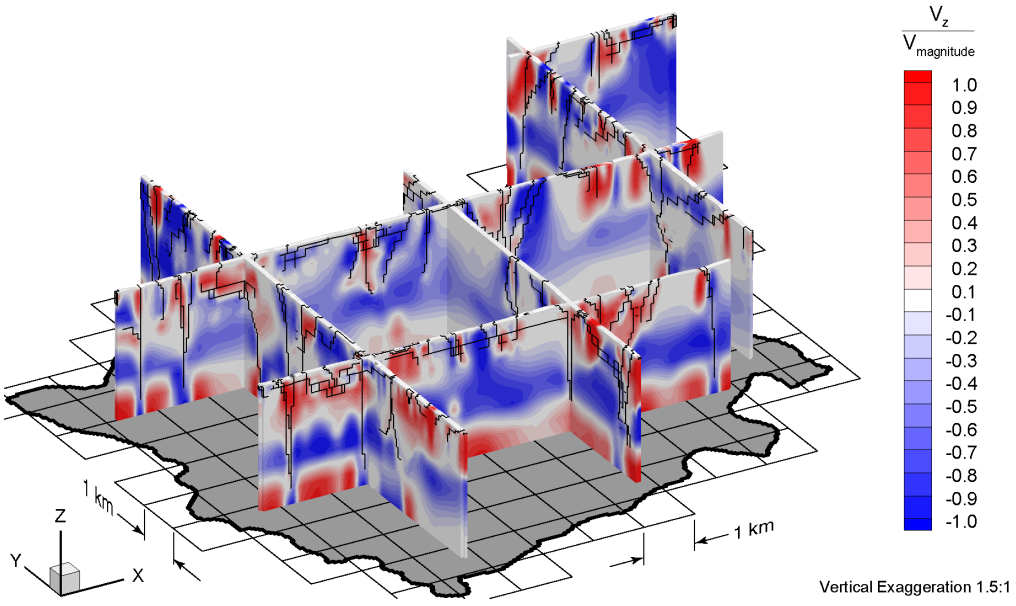

Figure 4.54 Fence view of ratio of vertical pore velocities to pore velocity magnitudes at 1 Ma for pseudo steady-state simulation, which is used as the initial condition for Scenario 4.

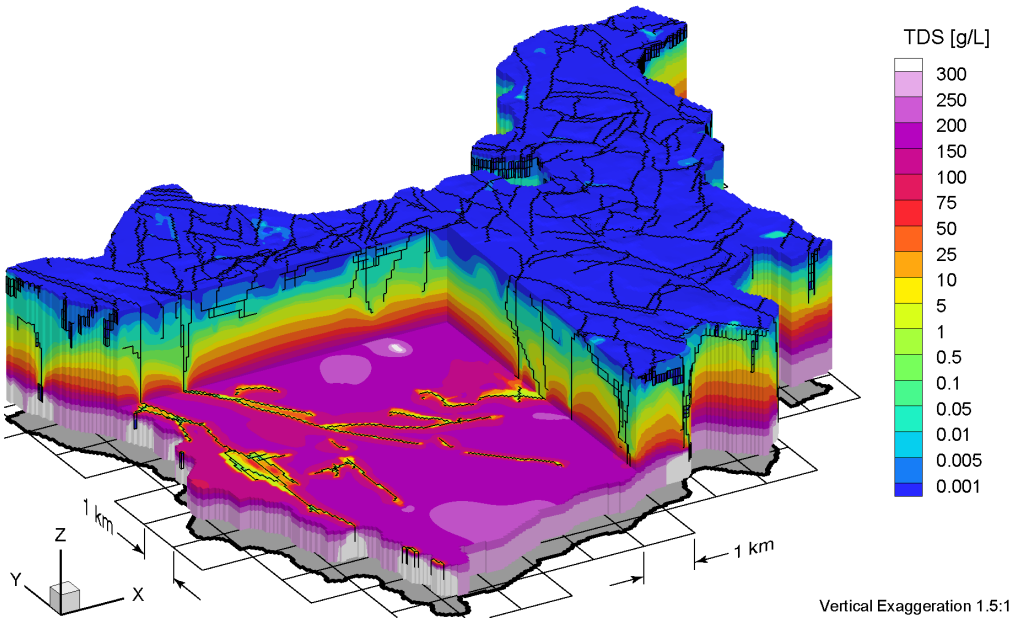

Figure 4.55 Block cut view of brine concentrations at 1 Ma for pseudo steady-state simulation, which is used as the initial condition for Scenario 4.

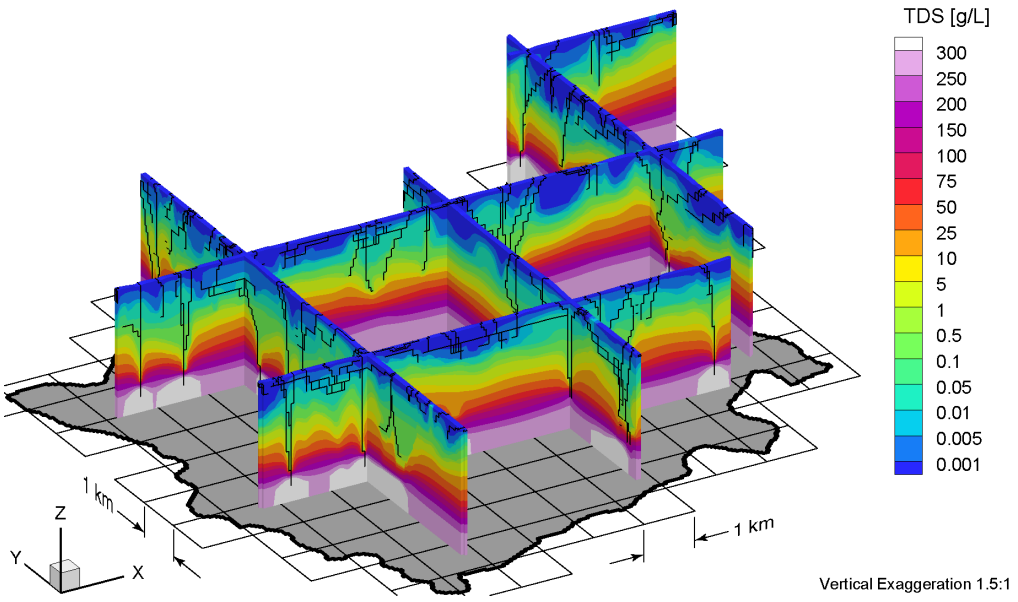

Figure 4.56 Fence view of brine concentrations at 1 Ma for pseudo steady-state simulation, which is used as the initial condition for Scenario 4.

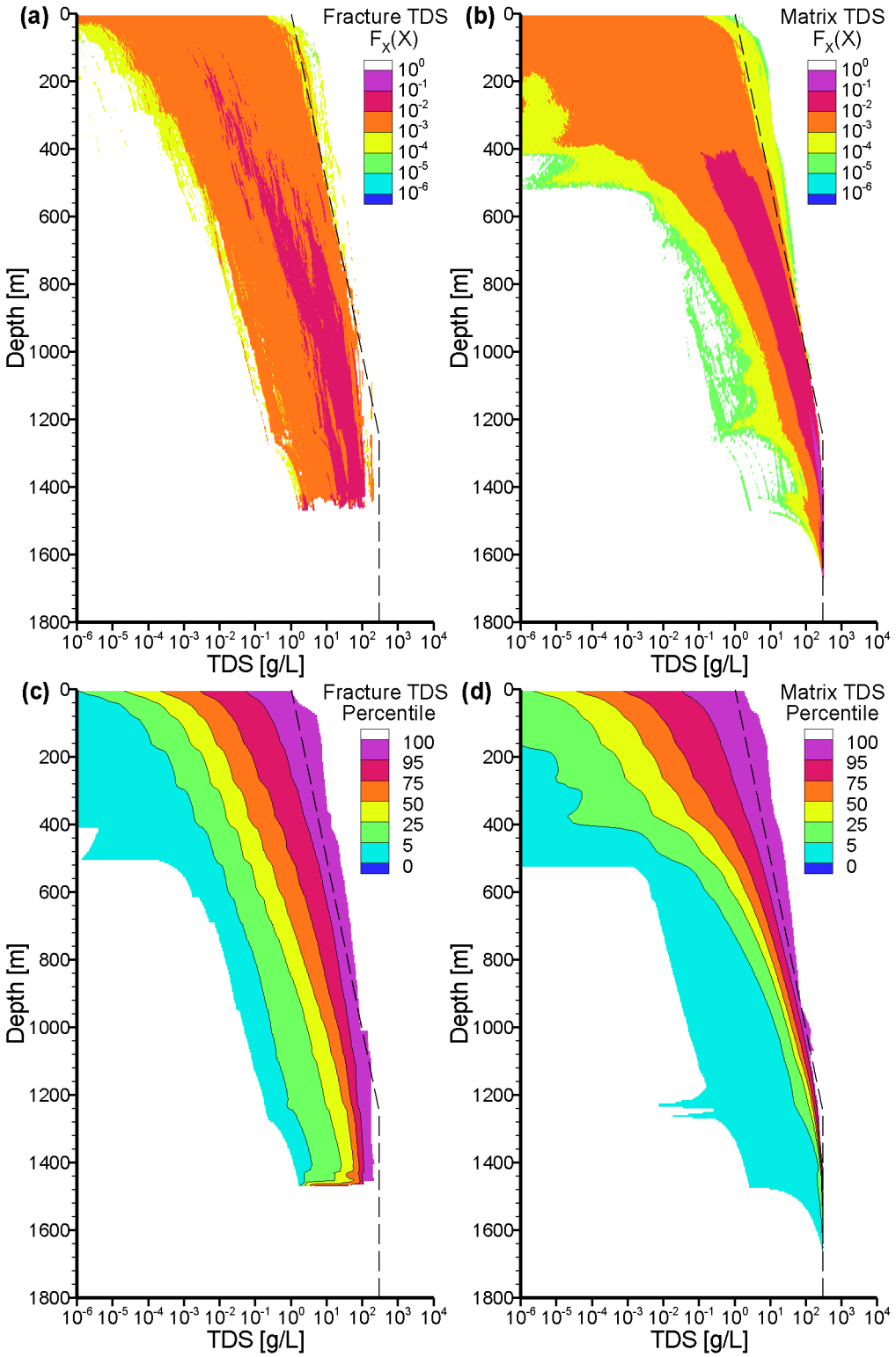

Figure 4.57 Scenario 4 probability density functions (PDF) and cumulative density functions (CDF) of brine concentration (TDS) as a function of depth for vertical faces associated with fractures and matrix blocks.

Mean life expectancies are also calculated and are shown in Figure D.37 for a block cut view and in Figure D.38 for a fence view. Due to the higher flux in fracture zones, MLE values are lower in Scenario 4 than for Scenario 1. This is also confirmed in Figure 4.44 and Figure 4.45.

4.5.6 CSSR Scenario 5 Paleoclimate Simulation

Scenario 5 investigates the role of hydromechanical coupling, by setting the one-dimensional loading efficiency, $\zeta = 0$. All figures are presented in Appendix E, and a summary of the figures is presented in Table E.1. Significant differences in freshwater and environmental heads are visible between Figures E.1 to E.12, and Figures A.1 to A.12, respectively. The main difference in Scenario 5 are the resulting large vertically downward gradients caused by glacial loading at −40 ka. At the end of the simulation, the heads look very similar between Scenario 5 and Scenario 1.

Pore water velocity magnitudes are presented in Figure E.13 to Figure E.18, and the ratio of vertical pore velocities to pore velocity magnitudes are presented in Figure E.19 to Figure E.24. For the pore water velocity magnitudes, the glacial loading event at −40 ka, shows increased velocities as compared to Scenario 1, with these being enhanced by larger gradients. At present time, the pore velocity magnitudes are similar between Scenario 5 and Scenario 1. The ratio of vertical pore velocities to pore velocity magnitudes for both scenarios are similar to each other.

Brine concentrations are presented in Figure E.25 to Figure E.30. These figures appear fairly similar to Figure A.25 to Figure A.30 from Scenario 1. Some differences are noticed when comparing Figure 4.58 to Figure 4.41, in that the range in TDS values with depth is less with Scenario 5 than with Scenario 1. This indicates that TDS concentrations in fractures are typically higher with Scenario 5 than with Scenario 1.

The tracer migration figures presented in Figure E.31 to Figure E.36 are very similar to Figure A.31 to Figure A.36 from Scenario 1. The tracer has migrated deeper into the subsurface in Scenario 5 as compared to Scenario 1, due to the increased vertical gradients resulting from ignoring hydromechanical coupling.

For Scenario 5 in Figure 4.42e, the infiltration rate is very similar to Scenario 1 in Figure 4.42a, however, the effect of the one-dimensional loading efficiency $\zeta = 0$ can be seen. Although the timing and flow direction are similar between Scenario 1 and Scenario 5, the amplitude of the fluxes in Figure 4.43e as compared to Figure 4.43a is greater in Scenario 5 due to the larger vertical gradients resulting from a lack of hydromechanical coupling.

Mean life expectancies are also calculated and are shown in Figure E.37 for a block cut view and in Figure E.38 for a fence view. In comparing these figures to Scenario 1, the MLE values are generally lower, and can be attributed to the enhanced vertical gradients due to a lack of hydromechanical coupling. This is also confirmed in Figure 4.45 and in Figure 4.44 for Scenario 5.

4.5.7 CSSR Scenario 6 Paleoclimate Simulation

Scenario 6 investigates the role of hydromechanical coupling, by setting the one-dimensional loading efficiency, $\zeta = 1$. All figures are presented in Appendix F, and a summary of the figures is presented in Table F.1. A one-dimensional loading efficiency equal to unity will not permit large vertical gradients to develop because the heads in the

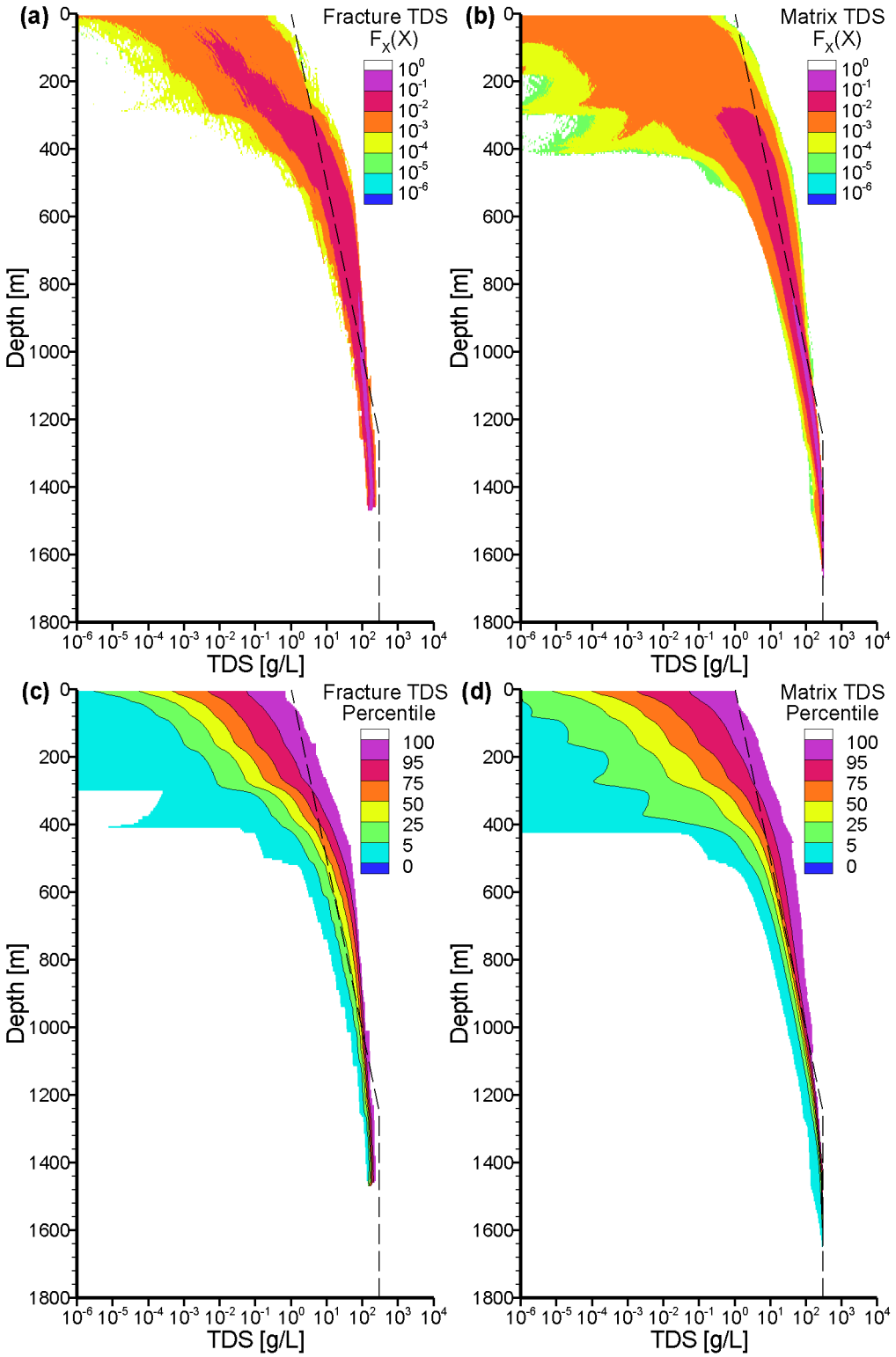

Figure 4.58 Scenario 5 probability density functions (PDF) and cumulative density functions (CDF) of brine concentration (TDS) as a function of depth for vertical faces associated with fractures and matrix blocks.

model are either nearly uniformly increased or decreased throughout a water column, depending on the surface loading condition.

Freshwater head plots are shown in Figures F.1 to F.6, and environmental head plots are shown in Figures F.7 to F.12. The −80 ka and present simulation results are very similar to those from Scenario 1, while the −40 ka results are quite different, but the vertical gradients do not appear to have changed during the Scenario 6 paleoclimate simulation.

Pore water velocity magnitudes are presented in Figure F.13 to Figure F.18, and the ratio of vertical pore velocities to pore velocity magnitudes are presented in Figure F.19 to Figure F.24. During the paleoclimate simulation, as shown at the three plotted times, the velocity magnitude and the ratio of vertical pore velocities to pore velocity magnitudes appears to be unchanged. Once again, this is indicative of little change to vertical gradients, resulting from an instantaneous propagation of surface loading to pore pressures at depth when $\zeta = 1$.

Brine concentrations are presented in Figure F.25 to Figure F.30. Very little difference is noticed compared to Figure A.25 to Figure A.30 of Scenario 1. Figure 4.59 varies from Figure 4.41, such that the former has a larger range for TDS values in both fractures and matrix.

Tracer concentrations for the modelling domain are presented in Figure F.31 to Figure F.36. Scenario 6 tracer migration into the subsurface is less than compared to Figure A.31 to Figure A.36 of Scenario 1. This difference is most noticeable in the fractures and is caused by reduced vertical gradients.

For Scenario 6 in Figure 4.42f, the infiltration rate is very similar to Scenario 1 in Figure 4.42a, however, the effect of the one-dimensional loading efficiency $\zeta = 1$ can be seen. Although the timing and flow direction are similar between Scenario 1 and Scenario 6, the amplitude of the fluxes in Figure 4.43f as compared to Figure 4.43a is much less in Scenario 6 due to the much smaller vertical gradients resulting from full hydromechanical coupling.

Mean life expectancies are shown in Figure F.37 for a block cut view and in Figure F.38 for a fence view. The MLE values for Scenario 6 are slightly lower than those for Scenario 1. This can also be shown with Figure 4.44 at 625 m depth.

4.5.8 CSSR Scenario 7 Paleoclimate Simulation

Scenario 7 combines changes that were implemented in other paleoclimate simulations. In this paleoclimate scenario, fracture zone hydraulic conductivity is set to a uniform value of 10^{-6} m/s, coupled density-dependent flow is not considered, and hydromechanical coupling is ignored by setting the one-dimensional loading efficiency $\zeta = 0$. All figures are presented in Appendix G, and a summary of the figures is presented in Table G.1.

Due to lack of TDS in the modelling domain, freshwater and environmental head plots for Scenario 1 and Scenario 7 cannot be directly compared. The propagation of elevated hydraulic heads at surface, deep into the subsurface through highly permeable fracture zones, is shown in Figure G.3 during a glacial loading event.

The pore water velocity plots in Figure G.7 to Figure G.12 can be compared to Scenario 1 plots in Figure A.13 to Figure A.18. The Scenario 7 figures show much higher pore velocity magnitudes as compared to Scenario 1 at −40 ka. The present day velocities look very similar across the two scenarios. The ratio of vertical pore velocities to pore velocity magnitudes are presented in Figure C.13 to Figure C.18. When compared to Figure A.19 to

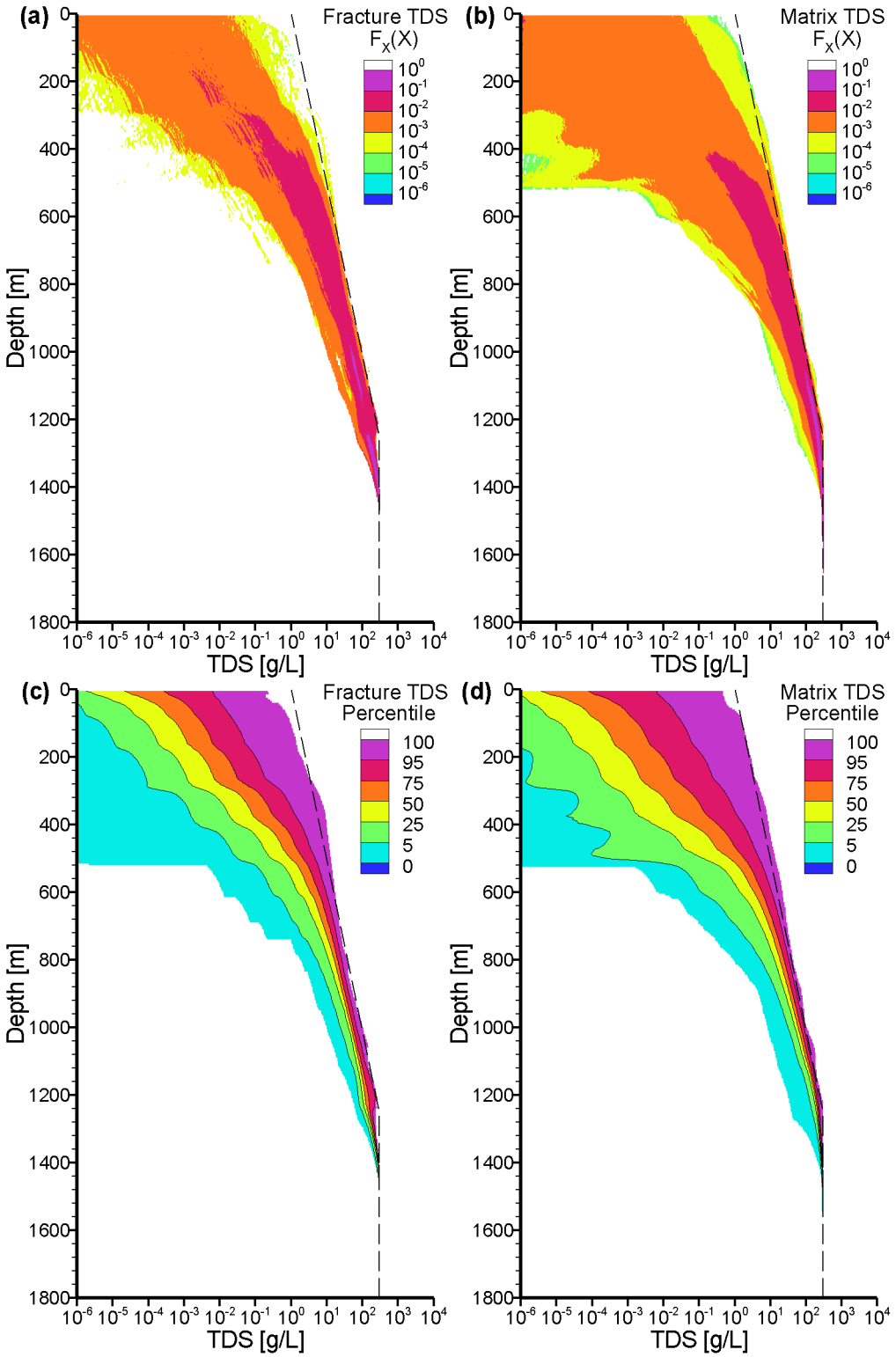

Figure 4.59 Scenario 6 probability density functions (PDF) and cumulative density functions (CDF) of brine concentration (TDS) as a function of depth for vertical faces associated with fractures and matrix blocks.

Figure A.24, the presence of brine in Scenario 1 has the effect of changing flow directions at depth, and not allowing deep flowpaths to develop, as compared to the freshwater case in Scenario 7.

Tracer concentrations for the modelling domain are presented in Figure G.19 to Figure G.24. When compared to Figure A.31 to Figure A.36 of Scenario 1, a significant difference is noted between paleoclimate simulations at −40 ka and at present. The highly permeable fracture zones allow migration of the tracer deep into the subsurface. Figure G.23 and Figure G.24 show the extent of migration.

For Scenario 7 in Figure 4.42g, the infiltration rate is very similar to Scenario 5 in Figure 4.42e since the one-dimensional loading efficiency $\zeta = 0$. A similar result occurs between these scenarios as shown in Figure 4.43g as compared to Figure 4.43e.

Mean life expectancies are shown in Figure G.25 for a block cut view and in Figure G.26 for a fence view. In the vicinity of fractures, the MLE is on the order of thousands of years, while for Scenario 1, the MLE is several orders of magnitude greater. In Figure 4.44, Scenario 7 represents the lowest MLE value, while for Figure 4.45, Scenario 7 represents the second lowest MLE value of the various paleoclimate scenarios.

4.6 Summary

This chapter introduced the development of several sub-regional models, in various phases. The Phase–I sub-regional model was selected from a portion of the larger regional scale domain developed in Chapter 3. Due to the successful comparison of FRAC3DVS and SWIFT-III, FRAC3DVS was selected as the geosphere numerical model for the work presented in this chapter. Since a crystalline rock setting was desired, software was developed to map a stochastically generated triangulated fracture network model (FNM) onto a FRAC3DVS hexahedral element mesh, using quadrilateral elements to represent fracture zones.

The Phase–II model development was initiated to address various issues that arose while developing and working with the Phase–I model. Issues included the characterization of the surface boundary conditions for the model, and the use of a uniform hydraulic conductivity for fracture zones. Numerous improvements were made, particularly in the characterization of fracture properties; namely fracture zone permeability, fracture zone porosity, and fracture zone width.

The third phase of development involved paleoclimate simulations. A total of three models were required for each paleoclimate simulation. A steady-state model was developed to simulate freshwater heads. These freshwater heads were adjusted to account for an initial TDS distribution. Both the adjusted freshwater heads and initial TDS distribution were applied as the initial conditions for the 1 Ma transient simulation; this was necessary to allow the initial TDS distribution to equilibrate with the flow system to achieve a pseudo steady-state groundwater flow system. Finally, the output from this model was used as the initial conditions for the paleoclimate simulations.

This chapter investigated seven paleoclimate scenarios, whereby certain parameters were modified, or ignored to determine their impact relative to a base-case analysis. The key parameters of interest included: alternate glaciation scenarios, selecting between uniform fracture zone permeability, or a median variation in permeability as a function of depth, various values for the one-dimensional load efficiency ζ, and including or excluding

coupled density-dependent flow and transport. Various performance measures were used in characterizing the scenario comparisons, including: freshwater and environmental water heads, pore water velocity magnitudes and directions, TDS distributions, unit tracer migration, and mean life expectancy.

From the various scenarios listed in Table 4.3, the greatest reduction in MLE values occur with Scenarios 4 and 7, which used high permeabilities for fracture zones throughout the modelling domain. TDS concentrations were also reduced within fractures and in the matrix blocks adjacent to fractures, as compared with the base case analysis of Scenario 1. The depth and extent of unit tracer migration was also greatest when high permeability fracture zones were used.

Scenario 3 investigated the effects of modelling the flow system without density-dependent flow and transport, resulting in reduced MLE values as compared with the base case. Dense pore fluids at depth increase MLE values when compared to freshwater groundwater flow systems.

The glaciation scenario used in Scenario 2 increases the proportion of time that the geosphere was subject to permafrost conditions relative to the base case analysis. The unit tracer in Scenario 2 migrated to less depth than for Scenario 1, meaning less permafrost cover results in increased migration of surface waters to depth.

From the hydromechanical coupling investigations of Scenarios 5 and 6, hydromechanical coupling has significant influences on unit tracer migration, but less of an effect on MLE values. The unit tracer migrates deeper into the subsurface when ignoring hydromechanical coupling while assuming the hydraulic boundary condition at ground surface is equal to the pressure at the base of an ice-sheet, as shown in Scenario 5. Hydromechanical coupling is a very important mechanism which affects hydraulic gradients during a glaciation event.

Groundwater flow models which do not include a suitable form of hydromechanical coupling, one-dimensional or otherwise, must be used with caution as very large vertical gradients can be generated, resulting in higher pore water velocities, and enhanced migration of surface waters into the subsurface environment.

Chapter 5

Michigan Basin Regional Model

A Deep Geologic Repository (DGR) for the long-term storage of low & intermediate level waste (L&ILW) has been proposed by Ontario Power Generation (OPG) on lands adjacent to the Western Waste Management Facility (WWMF) at the Bruce Nuclear Power Development (BNPD) site in the Municipality of Kincardine, Ontario. Figure 5.1 shows the location of the DGR site along the eastern shore of Lake Huron. The DGR would be located approximately 680 m below ground surface within the argillaceous Ordovician limestone of the Cobourg Formation (*OPG*, 2008).

5.1 Site Geology

Geologically, the DGR is located along the eastern portion of the Michigan Basin, northwest of the Algonquin Arch, and within the Bruce Megablock. The extent of the Michigan Basin and the neighbouring geologic structures are discussed in §2.1.3 and shown in Figure 2.2. Although various databases, published papers and reports can be used in developing a conceptual model for the DGR site, field investigations are also required. The Phase I field investigations are described in *INTERA Engineering Ltd.* (2006) and *INTERA Engineering Ltd.* (2008).

The primary Phase I field activities in 2007 were the wireline drilling and core logging of deep vertical boreholes: DGR-1 to the top of the Queenston shale to confirm stratigraphic sequence and general rock quality of the upper Silurian and Devonian bedrock; and an adjacent borehole, DGR-2, was rotary drilled and grout cased to the top of the Queenston shale, to allow wireline drilling and core logging of the remaining portion

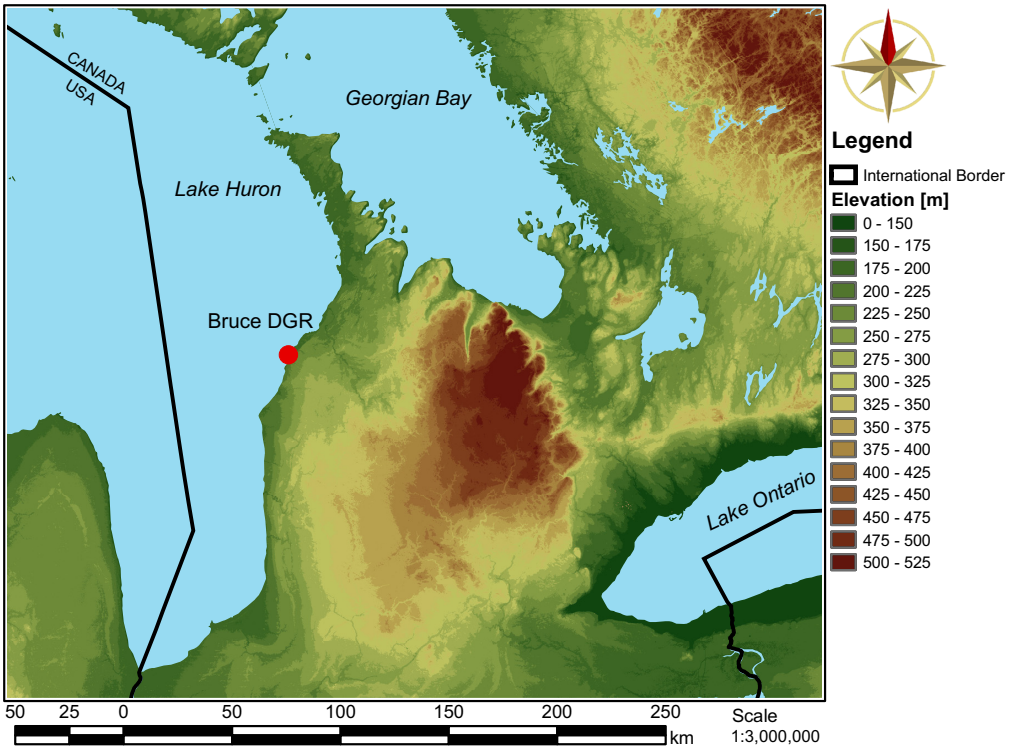

Figure 5.1 Topographic elevation map showing location of Bruce DGR site in southwestern Ontario along the eastern shore of Lake Huron.

from the Queenston shale to the Precambrian basement rock. During drilling, opportunistic groundwater samples were collected from both boreholes. A borehole diameter of 160 mm with a core diameter of 76 mm was used to obtain a nearly continuous core to a depth of 860 m. The core samples were collected for geochemical testing, porewater extraction and testing, geomechanical testing, diffusion testing and petrophysical testing. Geophysical logging, open-hole straddle packer hydraulic testing and other borehole hydraulic testing were performed as necessary. Finally, Westbay MP multi-level casings were installed in each borehole to provide pressure monitoring, groundwater sampling and hydraulic testing (*INTERA Engineering Ltd.*, 2006). Table 5.1 summarizes core log data, hydraulic test data and TDS geochemical data from DGR-1 and DGR-2.

Pressure data from the Westbay MP multi-level casings in DGR-1 and DGR-2 boreholes are used to calculate the vertical profile of equivalent freshwater head and environmental head from ground surface to depth. Pressure data from 3 March 2008 was used to estimate the environmental head (see §2.7) profile in the composite DGR-1 / DGR-2 boreholes and is plotted in Figure 5.2 (*Sykes et al.*, 2008). A ground surface elevation of 185.84 m is plotted to illustrate the pressure gradient within a formation relative to ground surface. In a hydrostatic system, all environmental head estimates would lie on a vertical line coinciding with the elevation of the water table. In this case, the water table is assumed to be very close to ground surface. In this case, estimates for the Ordovician formations are significantly under-pressured relative to the surface, while the high permeability Cambrian Formation is over-pressured. Highly saline water ejected out of DGR-2 at a high rate was field evidence of the over-pressurized Cambrian

Table 5.1 Core log data, hydraulic test data, and geochemical data for a composite DGR-1 and DGR-2 borehole. Adapted from (*Sykes et al.*, 2008).

Unit	Thickness [m]	Depth to Top [m]	K_H [m/s] †	TDS [g/L]
Drift	20.0	0		0.5
Amherstburg	55.0	20.0	1.0×10^{-5}	0.5
Bois Blanc	49.0	75.0	1.0×10^{-5}	1.6
Bass Islands	54.0	124.0	1.0×10^{-5}	1.6
G Unit	5.0	178.0		
F Unit	40.0	183.0	4.0×10^{-12} P	310
E Unit	20.0	223.0	4.0×10^{-12} P	
D Unit	1.6	243.0	1.0×10^{-10}	
C Unit	15.7	244.6	6.0×10^{-12} P	
B Unit	30.9	260.3	2.0×10^{-12} P	
B Anhydrite	1.9	291.2		
A-2 Carbonate	26.9	293.1	1.0×10^{-10} D	
A-2 Evaporite	8.0	320.0	2.0×10^{-7} S	340
A-1 Carbonate	39.0	328	2.0×10^{-12} P	300
A-1 Evaporite	3.5	367.0		
A-0 Unit	4.0	370.5	1.0×10^{-8} S	
Guelph ‡	5.5	374.5	1.0×10^{-8} S	300
Goat Island ‡	20.5	380.0		
Gasport ‡	3.75	400.5		
Lions Head ‡	4.05	404.25	2.0×10^{-11} D	
Fossil Hill	2.7	408.3	2.0×10^{-11} D	
Cabot Head	20.5	411.0	2.0×10^{-11} D	240
Manitoulin	16.15	431.5	2.0×10^{-12} P	
Queenston	70.35	447.65	1.3×10^{-11} P	
Georgian Bay	98.5	518.0	1.2×10^{-11} P	180 to 270
Blue Mountain	35.5	616.5	1.0×10^{-11} P	
Collingwood	7.5	652.0	9.6×10^{-12} P	
Cobourg	27.0	659.5	9.6×10^{-12} P	210
Sherman Fall	45.5	686.5	7.9×10^{-12} P	
Kirkfield	30.0	732.0	1.0×10^{-11} P	282
Coboconk	16.75	762.0	5.2×10^{-11} P	
Gull River	59.85	778.75	3.6×10^{-11} P	304
Shadow Lake	5.1	838.6		295
Cambrian	17.0	843.7	3.0×10^{-6} F	320
Precambrian		860.7		288

Note: † P = Pulse Test, D = Drill Stem Test, S = Slug Test, F = Flow Test

‡ The Guelph, Goat Island, Gasport, and Lions Head comprise the Niagaran Group

Formation. From Figure 5.2, it is apparent that the direction of gradients, both from above and from below, converge towards the Ordovician formations, which contain the host Cobourg Formation for the DGR. As shown in Table 5.1, the Ordovician formations ranging from the Queenston to the Shadow Lake have very low permeabilities. They also may be partially saturated (*Sykes et al.*, 2008). Recent pressure measurements from the Westbay MP multi-casings confirm the trend of decreasing pressures in the Ordovician formations.

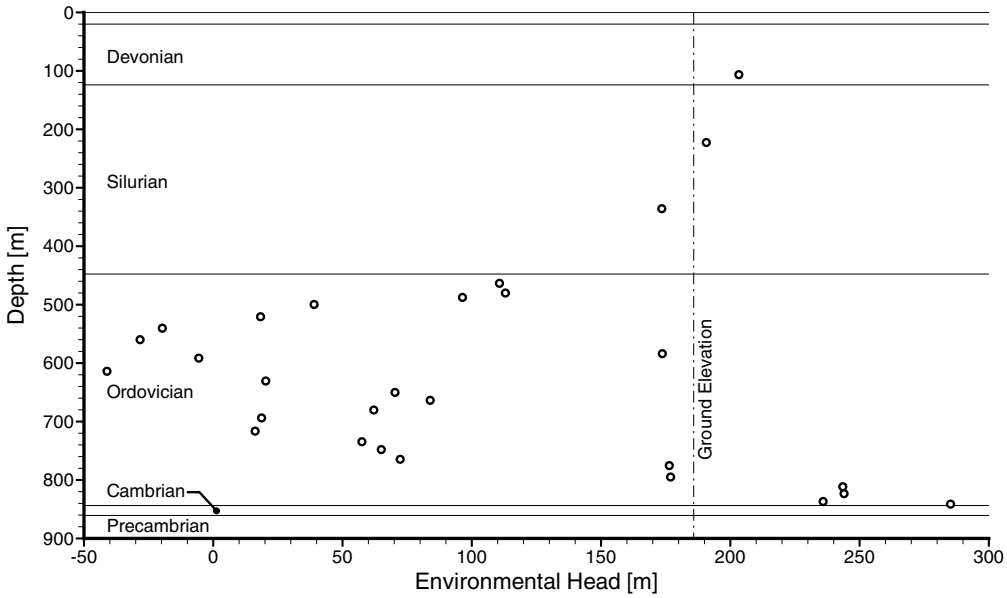

Figure 5.2 Environmental heads in a composite DGR-1 and DGR-2 borehole based on pressures measured on 3 March 2008.

5.2 Geologic Framework

A 3D geologic framework (3DGF) is developed and presented in *Frizzell et al.* (2008). The primary purpose of the framework is to present the current geological understanding of the Michigan Basin Paleozoic sedimentary formations of southern Ontario. The framework covers an area of 32000 km^2, measuring 160 km east-to-west, and 200 km north-to-south. A plan view of the regional study area (RSA) is shown in Figure 5.3 (*Frizzell et al.*, 2008). The region encompasses the conceptual model presented in §5.3.

The framework was developed using GoCAD™ software, which is an advanced 3D Earth modelling and scientific visualization system. The Precambrian basement rock represents the base of the geologic framework, extending upward to surface topography (*Frizzell et al.*, 2008). The primary data source for the 3DGF was the Oil, Gas and Salt Resources Library Petroleum Wells Subsurface Database. This database included fields such as geological formation tops, logging records, and oil/gas/water intervals for tens of thousands of petroleum wells throughout Ontario. The RSA contained 341 wells, reduced to 302 wells after a data validation process. Few wells were located in the RSA, reflecting the lack of oil and gas resources in that area. These wells were drilled to investigate salt resources near the southern portion of the RSA, and to investigate oil and gas resources

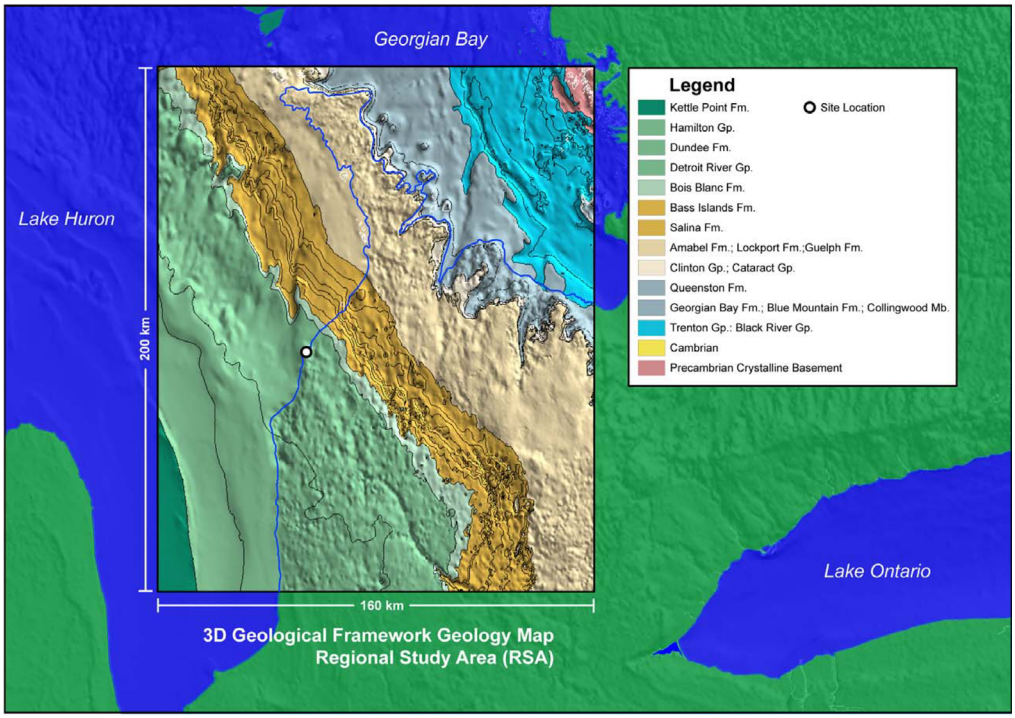

Figure 5.3 3D Geologic Framework study boundary with Paleozoic geology derived from 3D model. Adapted from *Frizzell et al.* (2008).

in the Silurian and Ordovician strata. Additional well information was obtained for 76 petroleum wells from the Michigan State Geological Survey Digital Well Database, and 57 petroleum reference wells from *Armstrong and Carter* (2006); these reference wells were used by *Armstrong and Carter* (2006) to generate a series of representative geologic cross-sections across southern Ontario. This was also used to verify and to provide consistency for the development of the 3DGF, and to ensure the geological nomenclature matched that of the Ontario Geological Survey (OGS). Other data sources included downhole geophysics, which was used to verify geologic contacts and picks, a 1:50 000 OGS Digital Bedrock Geology of Ontario, Michigan State Geological Survey mapping and Petroleum Well Database, OGS Digital Bedrock topography and overburden thickness mapping, and National Oceanic and Atmospheric Administration (NOAA) digital bathymetric mapping of Lake Huron and Georgian Bay (*Frizzell et al.*, 2008). The geologic interfaces beneath Lake Huron were extrapolated based on scarp mapping from bathymetry and land-based stratigraphic data both west and east of Lake Huron.

Data validation required both geological software modelling techniques as well as expert judgement. Well logs are usually of varying quality, and the OGSR database was no exception. A number of issues identified by *Frizzell et al.* (2008) include: various formations grouped together, missing formations, interface contacts inconsistent with current OGS nomenclature, and incorrect well locations and elevations. Various approaches including manual inspection and correction of logs, as well as semi-automated or automated means, guided by the visualization capabilities and tools of GoCAD™ were utilized. The 31 layers identified by *Frizzell et al.* (2008) represent the maximum number of units/formations/groups that could reliably be interpreted within the study area. Some

formations, such as the Ordovician Trenton and Black River Groups were added to 27 wells to more realistically reflect expert knowledge of the subsurface. The Niagaran Group is comprised of the Guelph, Goat Island, Gasport, and Lions Head Formations. The primary method was to interpolate the location of the interface based on neighbouring wells, while a secondary method of using the mean unit thickness at neighbouring wells was also applied, with preference given to the reference wells of *Armstrong and Carter* (2006). A three-dimensional view of the resulting geologic framework is shown in Figure 5.4.

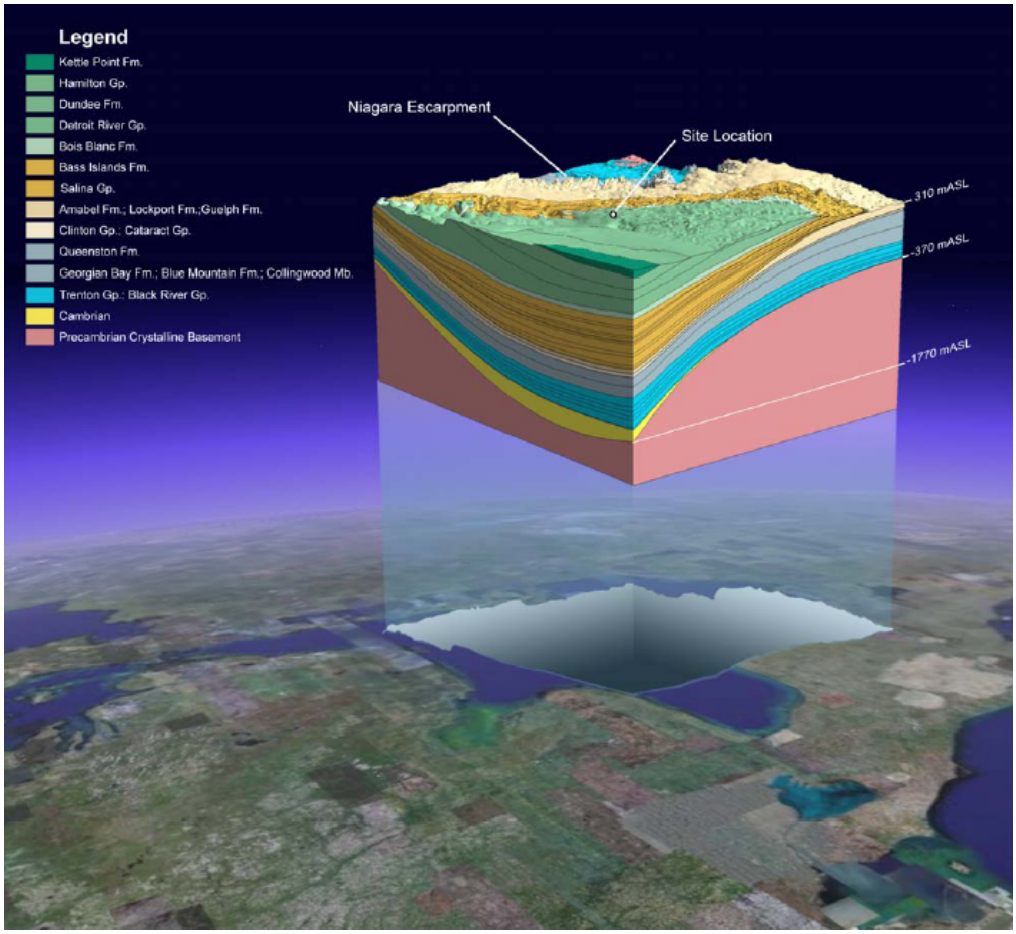

Figure 5.4 3D Geological Framework box diagram of the Regional Study Area. Adapted from *Frizzell et al.* (2008).

5.3 Conceptual Model

As discussed in *Sykes et al.* (2008), a regional scale conceptual model was developed and described in terms of three groundwater flow regimes: an upper and lower flow regime separated by an intermediate regime. The various rock layers in the Michigan Basin slope towards the centre of the Michigan Basin; since the DGR is east of the basin's centre, the rock layers will either subcrop beneath drift or outcrop as one moves eastward.

The Salina Group, comprised of the A1-Unit to the G-Unit inclusive (see *Frizzell et al.* (2008) and *Armstrong and Carter* (2006)), separates the upper regime from the

intermediate regime due to the low permeability of the evaporite deposits, and various salt units. The upper groundwater flow regime is influenced by surface topography and thus the water table represents a subdued reflection of topography. Flow is from the highlands along the Niagara escarpment, towards Georgian Bay or Lake Huron (*Sykes et al.*, 2008).

The lower groundwater flow regime is bounded above by the Manitoulin dolomites of the Lower Silurian. As indicated in Table 5.1, the lower flow regime consists of very low permeability limestones and shales. Very dense waters exist at depth due to their high TDS values; these waters are much denser than the fresh water that is expected to enter the system from the near surface and are difficult to displace. Freshwater can enter deeper layers where these layers subcrop beneath drift or outcrop towards the east. The intermediate regime, located between the upper and lower regimes, mostly consists of low permeability rocks and acts to further reduce the hydraulic connection between the upper and lower regimes. The intermediate regime includes the more permeable Niagaran Group.

Topographically, the Great Lakes are a significant source of freshwater and can impose a hydraulic gradient across significant portions of the Michigan Basin, including across the DGR site. Figure 5.5 lists the elevations of each of the five Great Lakes. The greatest elevation difference of 108.37 m exists between Lake Superior to the northwest and Lake Ontario to the southeast, relative to the DGR site. The distance between these two lakes of approximately 600 km results in a very small gradient of 1.806×10^{-4}. A larger gradient exists between Lake Huron and Lake Ontario of approximately 5.059×10^{-4}. These freshwater gradients will be reduced by the presence of deep pore waters with a TDS of approximately 300 g/L, equivalent to a specific gravity of 1.2, 20% greater than freshwater. The combination of high TDS fluids having higher viscosities, a density greater than freshwater, and the very low permeability of the host rock formations result in a very low fluid mobility due to a low hydraulic conductivity. Solute transport in the lower regime is thus expected to be dominated by diffusion, while in the upper regimes, transport is dominated by advection due to higher permeabilities, higher fluid viscosity, and freshwater densities.

The diffusion dominant deeper flow system allows the numerical analyst to limit the conceptual model, and resulting numerical model, to a portion of the Michigan Basin, rather than modelling the entire spatial extent of the Michigan Basin. According to *Sykes et al.* (2008), the criteria for determining the extent of the regional domain is that the "domain should include appropriate recharge/discharge zones for the deeper units that have high [TDS] concentrations and that the proximity of these recharge/discharge zones be the closest possible to the location of the proposed DGR."

5.4 Model Development

The modelling domain boundary was chosen by *Sykes* (2007) according to several criteria. In this thesis, the modelling domain boundary is used to define the Michigan Basin Regional (MBR) model. The southeastern portion of the boundary follows the regional surface water divides surrounding the DGR site; these divides were determined by using a DEM from the Shuttle Radar Topography Mission (SRTM) and a river network in ArcGIS. Based on the assumption that the water table is a subdued reflection of surface topography,

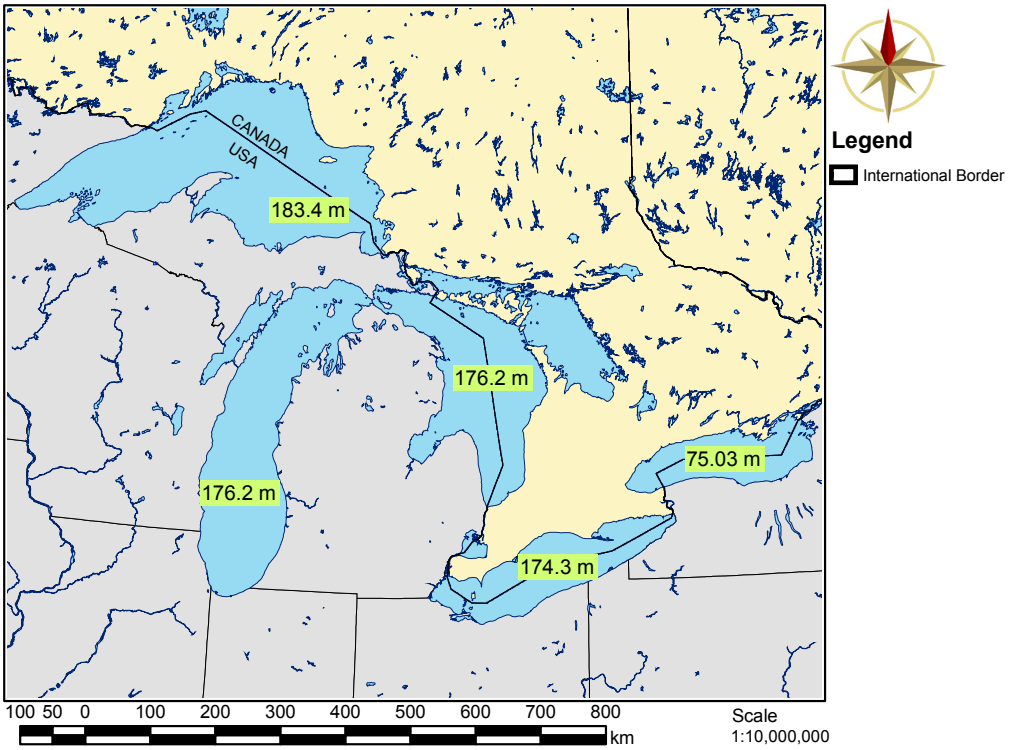

Figure 5.5 Mean water surface elevations for each of the Great Lakes.

the topographic divides are a reasonable choice for the upper flow regime, and the higher permeability Niagaran Group within the intermediate flow regime (*Sykes et al.*, 2008). Surface topography can be greatly affected by the advance and retreat of glaciers. Today's topography may not be identical to the topography that existed before the most recent glaciation, although major topographic trends and features would likely remain. Changes in topography would affect the selection of the modelling domain boundary.

The modelling domain includes the local topographic high in southern Ontario, and the domain extends to the deepest portions of both Lake Huron and Georgian Bay. The bathymetric data of both water bodies, provided by NOAA, was combined with the DEM to provide a continuous surface for the top of the Earth's solid surface. DEMs commonly define elevation as the surface elevation of a water body since bathymetric data is usually not available. The eastern boundary of the modelling domain is west of the Algonquin Arch (*Sykes et al.*, 2008). The resulting model boundary is shown in Figure 5.6, along with a DEM, and major rivers in southwestern Ontario.

5.4.1 Spatial Discretization

A two-dimensional grid was developed to fit within the conceptual modelling boundary as shown in Figure 5.7. Each quadrilateral element measures Δx = 762.794 m by Δy = 900.876 m. The grid has an east-west extent of 151.796 km, a north-south extent of 179.274 km, 27322 elements, 27728 nodes, and covers an area of 18775 km^2. The two-dimensional grid forms a horizontal template to develop the three-dimensional grid by interpolating the vertical position of each node from the 31 interfaces provided by *Frizzell et al.* (2008). Each interface was provided as a TIN.

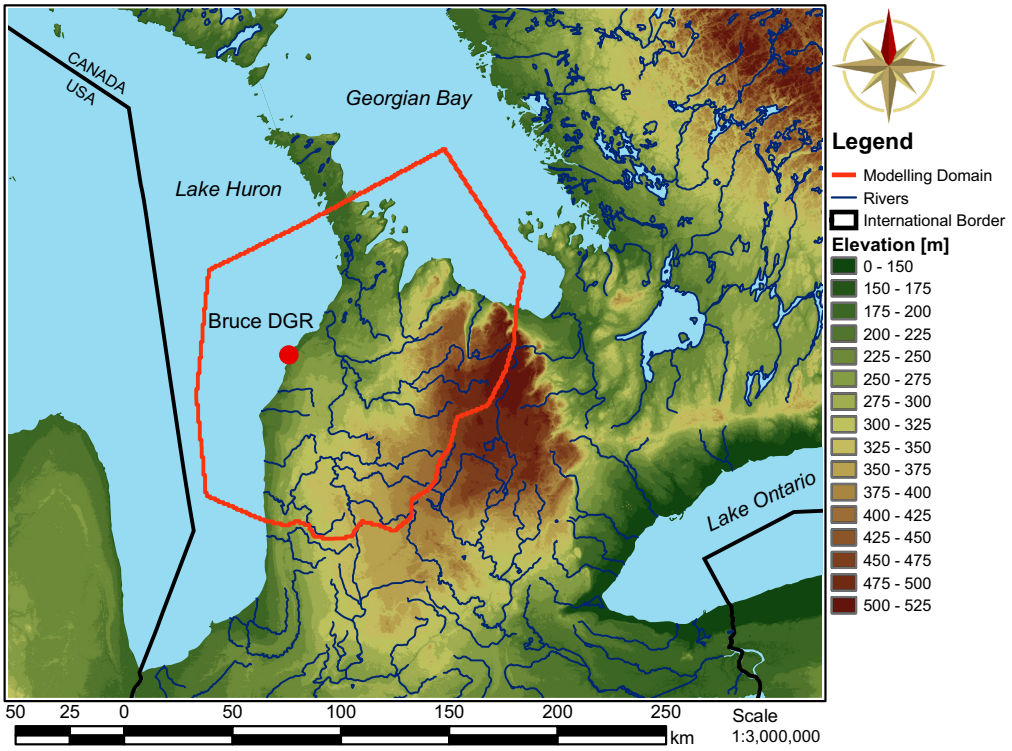

Figure 5.6 Topographic elevation map for southwestern Ontario showing major rivers in blue, and modelling domain boundary in red.

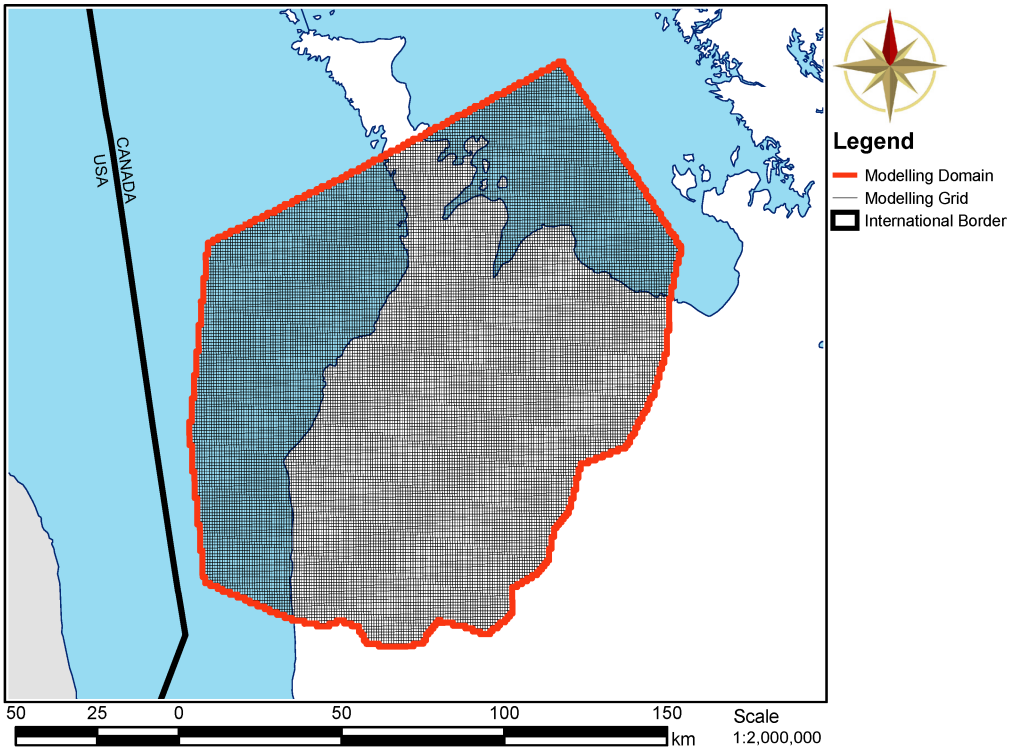

Figure 5.7 FRAC3DVS-OPG modelling grid and modelling domain extent in red.

A VBA code was written to read the two-dimensional grid and each TIN interface to determine the elevation of each node for the 31 layer model. A grid search algorithm was implemented to significantly reduce the computational time, by a factor greater than 200, of finding the triangle of each TIN that contained the grid node for which an elevation was interpolated. FRAC3DVS-OPG requires a three-dimensional grid whose nodes align vertically for density-dependent calculations; in essence, the two-dimensional grid is stacked vertically for each geologic layer, regardless if the actual geologic layers pinch out.

The process used to generate the three-dimensional grid and populate it with geologic properties is as follows:

- allocate 3D grid array to hold all elevations
- set an initial elevation for all 3D nodes of −3000 m
- loop over each interface beginning with the bottom interface, representing the top of the Precambrian
- loop over all 27728 2D nodes and use a grid based search to quickly locate the triangle that contains the grid node and interpolate its elevation
- if the thickness between the current 3D node and the 3D node immediately below it is negative, set the current 3D node to the same elevation of the node immediately below, resulting in a zero thickness. This is necessary for layers that pinch out
- check that all 3D nodes have an elevation greater than the initial elevation of −3000 m; if not, then signal an error
- the bottom of the domain is set 50 m below the top of the Precambrian, effectively setting the thickness of the Precambrian to 50 m
- loop over the 3D grid and set minimum thicknesses. If the layer thickness at a node is negative or < 0.5 m, then set thickness to zero. If the layer thickness at a node is ≥ 0.5 m and < 1 m, then set thickness to 1 m
- assign a geologic layer identifier to each node, accounting for pinched out geologic layers. If a layer has pinched out, then its thickness is zero, and it assumes the geologic layer identifier of the layer immediately below
- evenly distribute geologic layer thicknesses among 3D grid for a set of nodes which represent the same geologic layer. This is to account for layers that pinch out
- check once again for negative or zero thickness layers
- assign all nodes within 20 m of surface topography to be drift material
- up to this point, geologic layer identifiers are assigned to nodes, but they now need to be assigned to elements. Each element could have 4 different geologic layer identifiers since it is comprised of 4 nodes along its top face. The geologic layer identifier associated with the thickest node is assigned to the element
- write TecPlot and Paraview visualization files to disk along with the necessary FRAC3DVS-OPG files

A block cut view and a fence view of the assigned geologic layer zone identifiers are shown in Figure 5.8 and Figure 5.9, respectively. Each zone identifier is associated with a specific geologic layer or geologic grouping. Some of the geologic units are listed in Table 5.1. The geologic reconstruction also makes use of the outcrop limits or extent of the various geologic units, coloured by geologic period, as shown in Figure 5.10.

The Cambrian Formation, as shown in Figure 5.11, pinches out against the Precambrian flanking the Algonquin Arch (*Carter et al.*, 1996). All wells shown in the figure

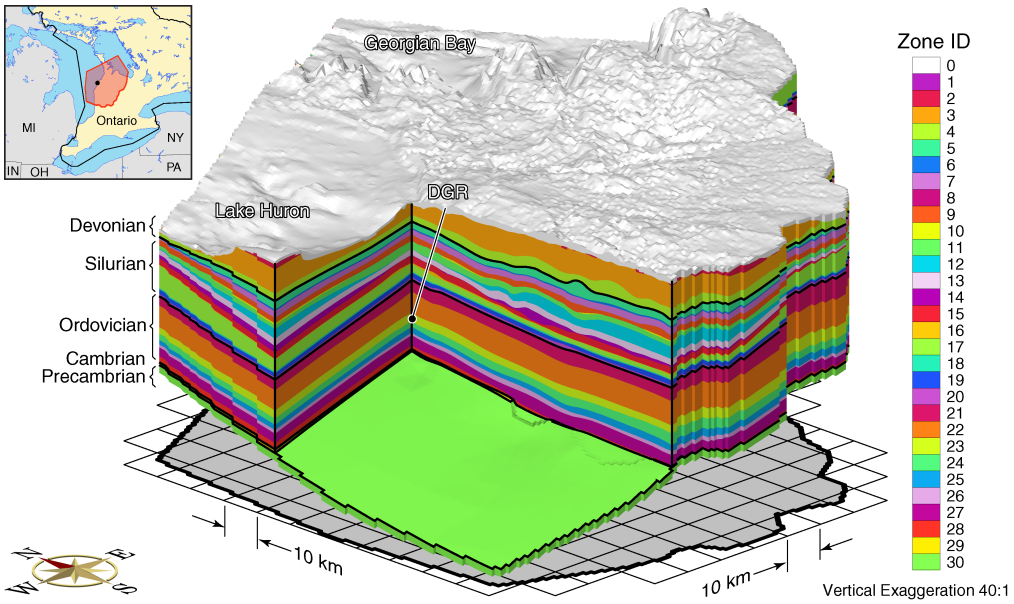

Figure 5.8 Block cut view of FRAC3DVS-OPG zone identifiers for 31 layers.

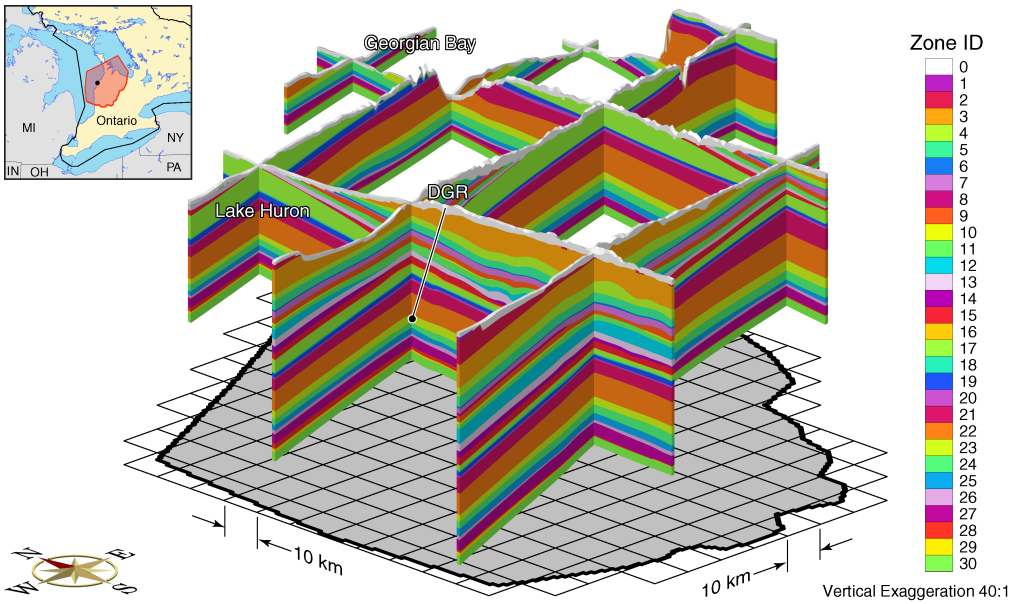

Figure 5.9 Fence view of FRAC3DVS-OPG zone identifiers for 31 layers.

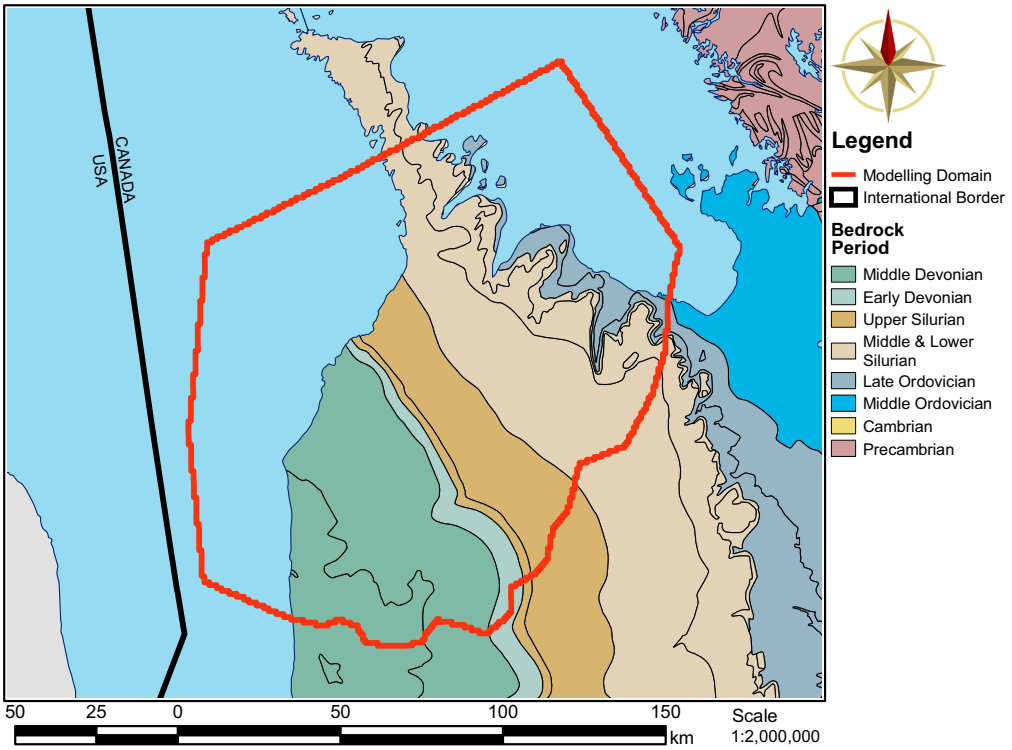

Figure 5.10 Map of bedrock subcrops, coloured by geologic period, beneath Quaternary deposits of southwestern Ontario. Modelling domain is shown in red.

intersect the Precambrian Formation, but only some of those wells also intersect the Cambrian Formation. A three-dimensional view of the Cambrian Formation as represented in the modelling grid, is shown in Figure 5.12. A view of the Middle Silurian geologic units (top of the Niagaran Group) is shown in Figure 5.13; the portion of the surface appearing rougher represents outcrops or subcrops, and has been defined using OGS Digital Bedrock topography and overburden thickness mapping. A view of all geologic units, minus the Quaternary drift deposits is shown in Figure 5.14; pinnacle reef structures are visible in Figure 5.13. Finally, a similar perspective, showing all geologic units and the Quaternary drift deposits, is shown in Figure 5.15 and as a fence view in Figure 5.16.

5.4.2 Boundary Conditions

Various boundary conditions are applied to the regional modelling domain. A Dirichlet (Type 1) hydraulic boundary condition is applied to the top nodes of the domain to set the water table 3 m below ground surface, regardless of streams or other inland water bodies such as lakes or wetlands, but not less than the elevation of Georgian Bay or Lake Huron which were set to a mean water elevation of 176 m. The scale of the model and the size of grid blocks precludes the inclusion of any hydrologic features, other than characterizing the water table as a subdued reflection of surface topography. Both the sides and bottom of the modelling domain are specified as a zero-flux boundary condition. Although this may be appropriate for the upper groundwater flow system, the intermediate and deep flow system contain the high permeability Niagaran Group and Cambrian Formation, respectively; these formations can allow influx and efflux across the model boundary

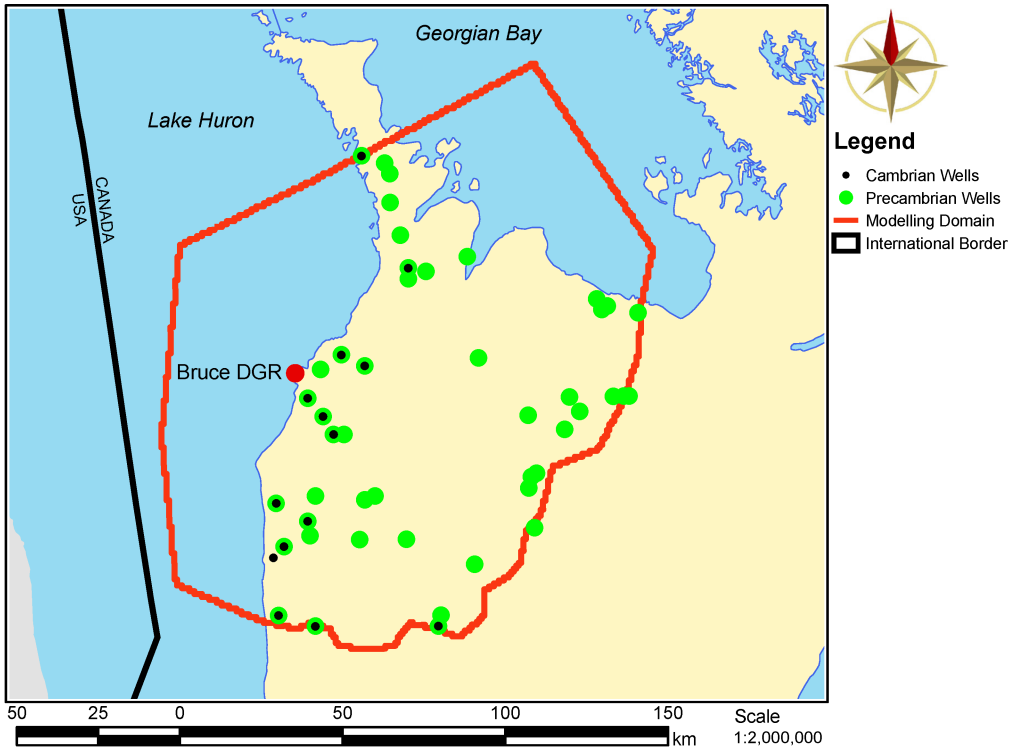

Figure 5.11 Location of wells intersecting Cambrian Formation, Precambrian Formation, or both.

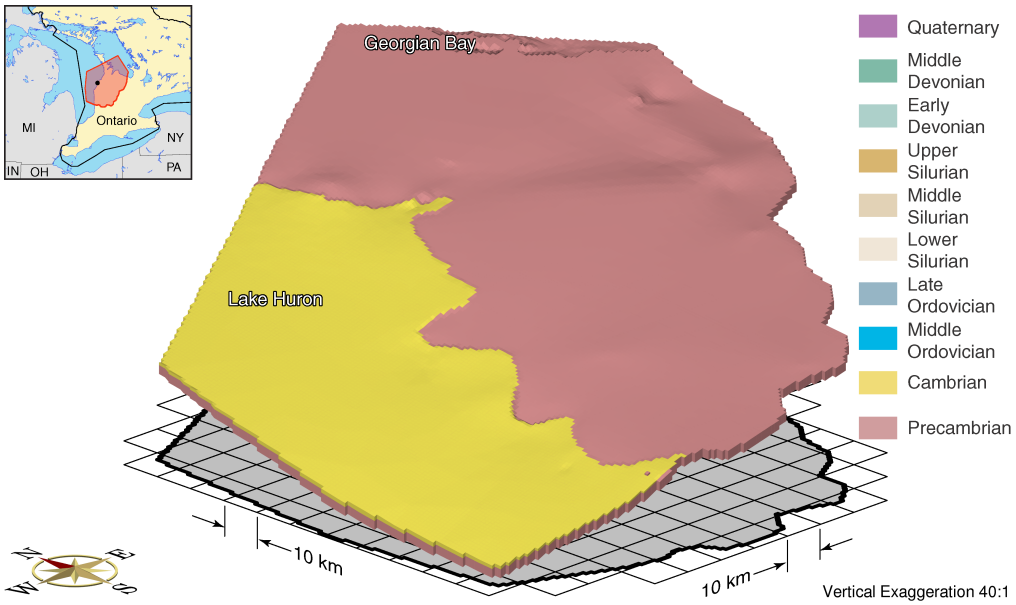

Figure 5.12 Spatial extent of the Cambrian Formation in yellow, underlain by the Precambrian basement in pink, for the regional modelling domain.

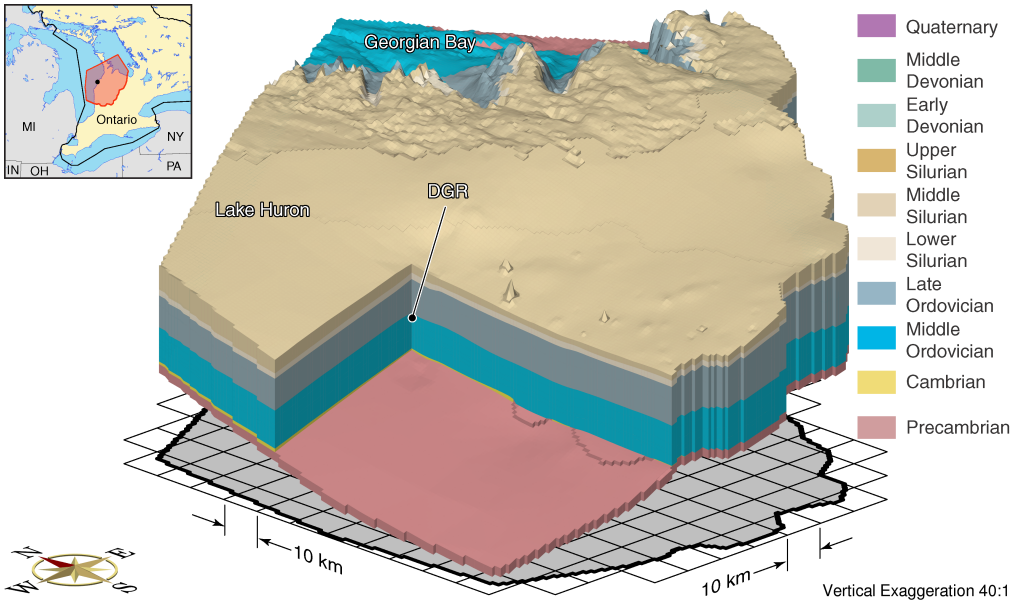

Figure 5.13 Block cut view showing spatial extent of the Middle Silurian (top of the Niagaran Group) for the regional modelling domain.

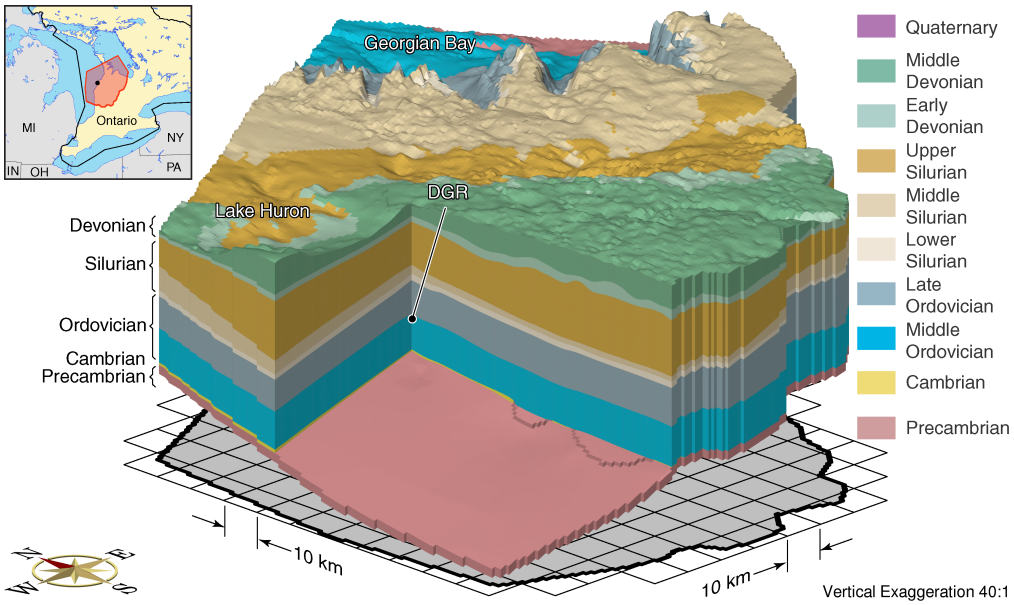

Figure 5.14 Block cut view showing spatial extent of the bedrock units with no Quaternary drift deposits for the regional modelling domain.

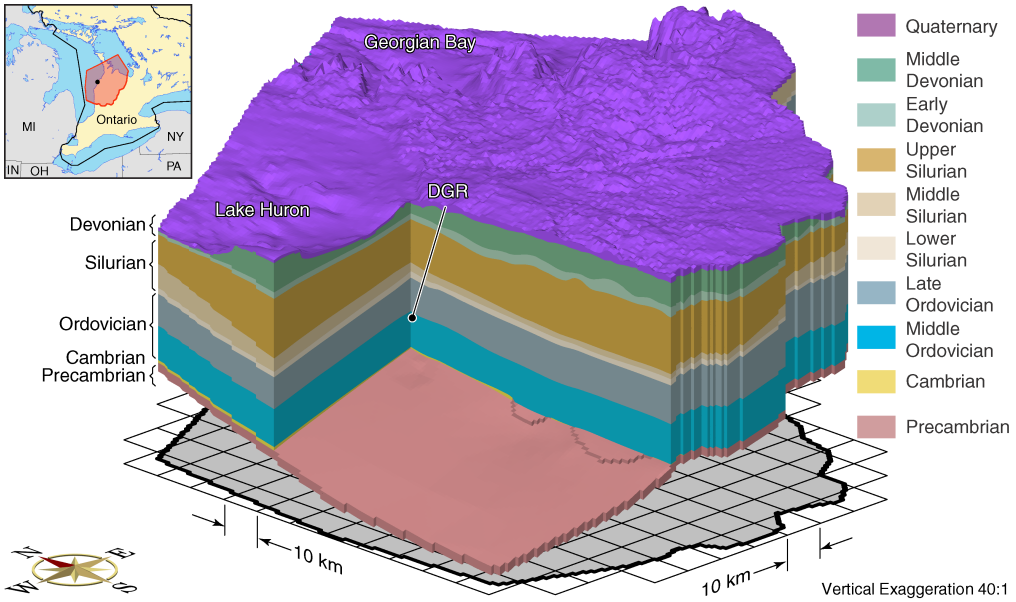

Figure 5.15 Block cut view showing spatial extent of the bedrock units with Quaternary drift deposits assigned to the top 20 m of the regional modelling domain.

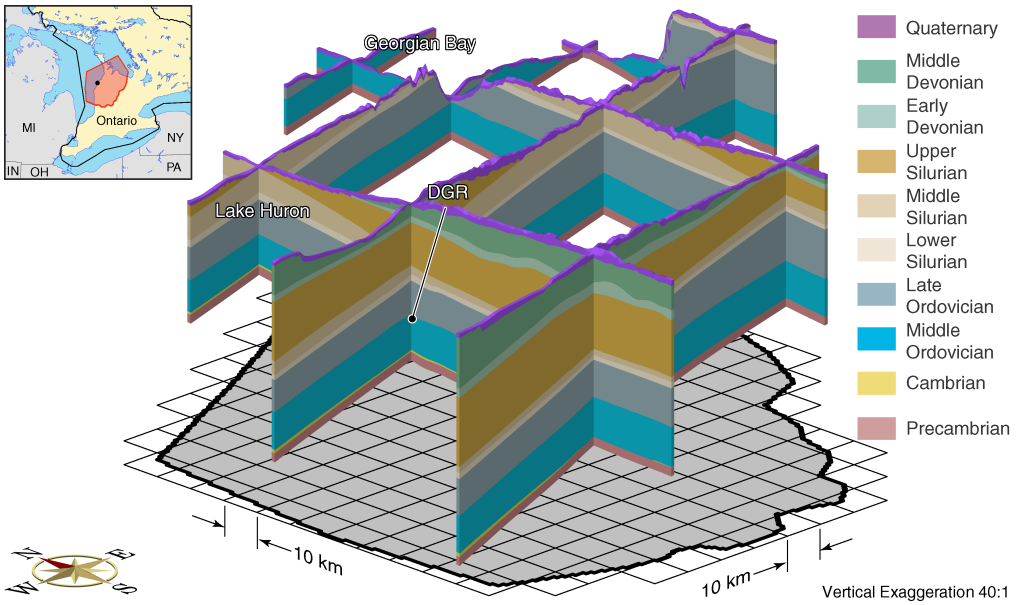

Figure 5.16 Fence view showing spatial extent of the bedrock units with Quaternary deposits assigned to the top 20 m of the regional modelling domain.

(*Sanford et al.*, 1985). *Carter et al.* (1996) hypothesize that the Cambrian Formation is not continuous due to fault blocking, and thus a no-flow boundary is considered reasonable for that unit.

The stated hydraulic boundary conditions will not enable the simulation of abnormal high environmental heads in the Cambrian Formation and the underpressurization of the Ordovician sediments. Both of these features are a result of a state that is different from that represented by the present-day boundary conditions, as shown in Figure 5.2. Further field investigations at the DGR site are planned to better understand the origin of the measured overpressures in the Cambrian Formation, and underpressures in the Ordovician sediments.

Since the modelling domain is restricted to southwestern Ontario, and the GSM developed by *Peltier* (2008) covers most of North America, vertical stress due to ice, and permafrost depth were spatially interpolated as shown in Figure 5.17. A TIN was created, whose nodes lie at the midpoint of each paleo grid block; the value of vertical stress or permafrost depth is taken at the midpoint of each paleo grid block, and linearly interpolated across each triangular facet of the TIN. Hydraulic boundary condition values for vertical stress corresponding to the FRAC3DVS-OPG grid are interpolated from the TIN for each 500 a time step in the 120 ka GSM simulation.

Peltier (2008) describes eight (8) models that "span the apparent range of model characteristics that provide acceptable fits to the totality of the observational constraints." Of these eight models, nn9921 and nn9930 are two of the best models based on aggregate misfit, and both include high resolution permafrost development. Less permafrost leads

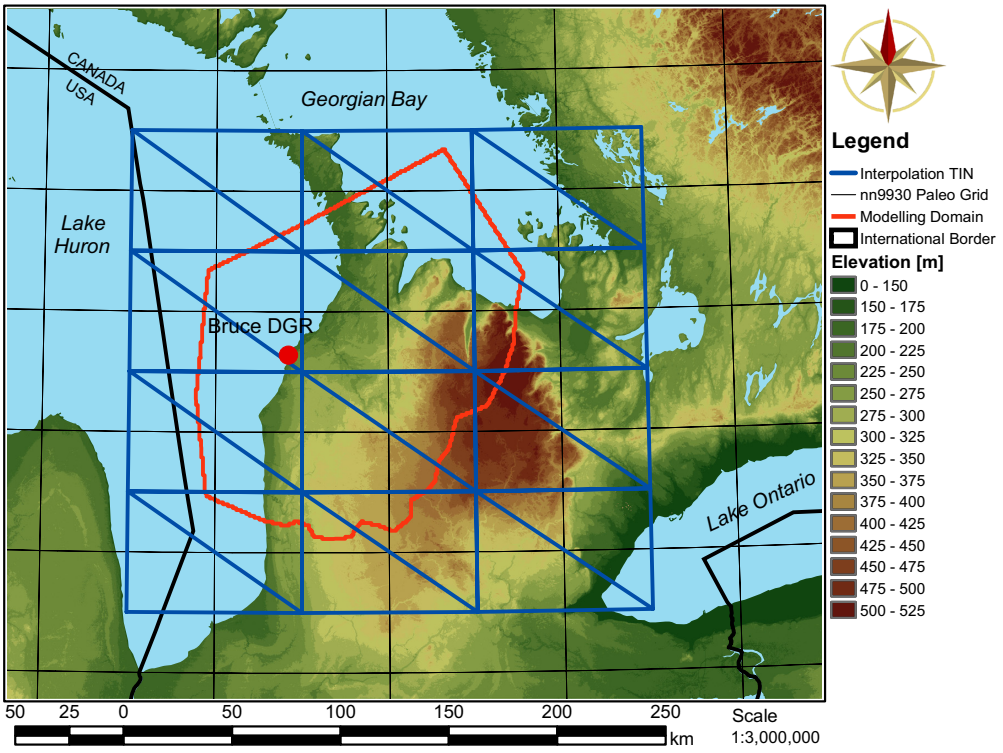

Figure 5.17 TIN used to interpolate properties for the regional-scale spatial domain from grid blocks of the *Peltier* (2008) nn9930 Glacial Systems Model.

to deeper recharge meltwater penetration into the subsurface (see *Normani et al.*, 2007); of the two models, nn9921 and nn9930, model nn9930 had less permafrost than nn9921 and was therefore selected for the paleoclimate simulations presented in this chapter.

A plot of various nn9930 GSM model outputs for the grid cell at the DGR site are shown in Figure 5.18. These outputs include ice thickness, meltwater production rate, lake depth, permafrost depth, ground elevation, and ice-sheet basal temperature relative to the pressure melting point of ice. Only the ice thickness, lake depth, and permafrost depth outputs are applied to the paleoclimate groundwater flow simulations in this chapter.

The isostatic movement of the ground surface due to ice loading is not considered; applied hydraulic boundary conditions are stated in terms of elevation, assuming the grid does not move vertically. The application of lake depth is also a relative term independent of isostatic movement, although isostatic depression is required for a proglacial lake to form. Although lake depth could be interpolated across the TIN in a similar manner to permafrost depth and vertical stress due to ice, since isostatic movement is not considered, large gradients could be created across the site which would not exist in the presence of a large proglacial body of water. Due to this, lake depth is added to the existing lake elevation and hydraulic boundary conditions are adjusted accordingly. Changes in surface topography due to glacial stripping of sediments is not considered.

5.4.3 Properties

Various properties are applied to the model and are shown in Table 5.2. Although most of the values in Table 5.2 are from Table 5.1 and *Sykes et al.* (2008), the mechanical properties E and v for the various geologic units are from *Usher et al.* (2008); not all units had mechanical properties, and in those cases, properties for similar rock types within *Usher et al.* (2008) were applied. Vertical confined compressibility β', specific storage S_s, and one-dimensional loading efficiency ζ were calculated using equations presented in §2.4.2, and a fluid compressibility of 4.4×10^{-10} Pa^{-1}. The β' values presented in Table 5.2 are lower than those presented in *Sykes et al.* (2008), which originated from literature values. The resulting storage coefficients are also less, meaning that the groundwater flow system can respond quicker to changes in boundary conditions under transient flow conditions. Constant pore fluid viscosity is assumed throughout the modelling domain, even though pore fluid viscosities will increase by several factors with higher TDS values (*Adams and Bachu*, 2002).

The TIN interpolated permafrost depths were used to select any FRAC3DVS-OPG grid block whose top face was within the permafrost zone for each time step. A permafrost hydraulic conductivity of 5×10^{-11} m/s is applied (*McCauley et al.*, 2002).

Table 5.3 summarizes various transport parameters which are used for brine movement for the variably dense pore fluids, for tracer movement to determine the depth of recharge water penetration, and for mean life expectancy calculations. Smaller dispersivity values were attempted in (*Sykes et al.*, 2008), however, severe numerical instabilities resulted due to the large grid spacing in proportion to smaller longitudinal dispersivity values. A tortuosity of 1.0 was applied in the absence of sufficient site specific data.

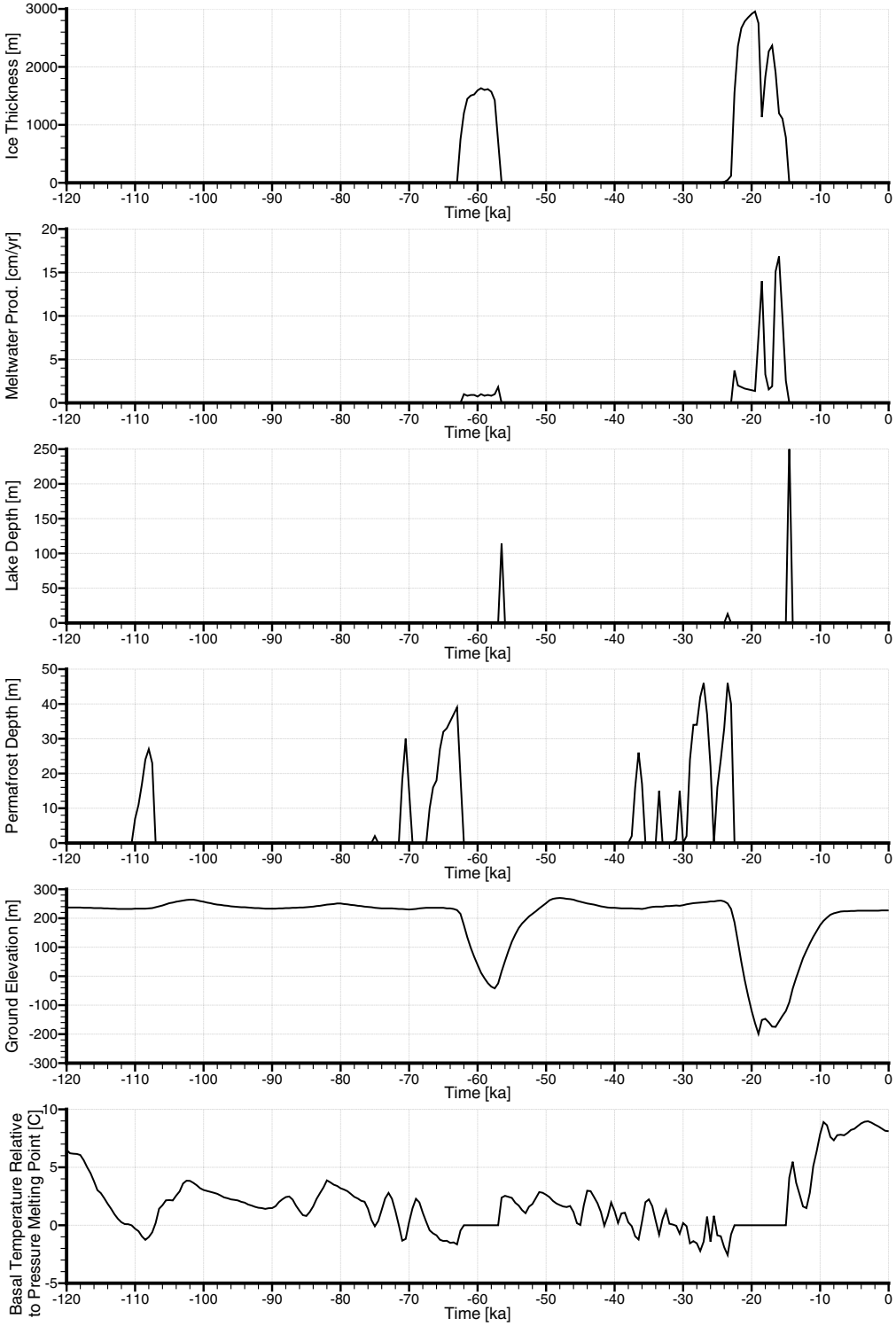

Figure 5.18 Plots of ice thickness, meltwater production rate, lake depth, permafrost depth, ground elevation, and ice-sheet basal temperature relative to pressure melting point versus time for the nn9930 GSM grid block at the DGR site, provided by *Peltier* (2008).

Table 5.2 Hydraulic and mechanical properties for MBR paleoclimate simulations.

Period	Geology	K_H [m/s]	K_V [m/s]	K_V/K_H [/]	n [/]	TDS [g/L]	ρ [kg/m^3]	E [GPa]	ν [/]	β' [Pa^{-1}]	S_s [m^{-1}]	ζ [/]
Quaternary	Drift	1.0×10^{-7}	2.0×10^{-8}	0.2	0.10	0.045	1000.03	—	—	1.00×10^{-8}	9.85×10^{-5}	1.00
Devonian	Traverse Group	1.0×10^{-7}	1.0×10^{-8}	0.1	0.10	0.045	1000.03	30.0	0.30	2.48×10^{-11}	6.74×10^{-7}	0.36
	Dundee	1.0×10^{-7}	1.0×10^{-8}	0.1	0.10	3	1002	30.0	0.30	2.48×10^{-11}	6.76×10^{-7}	0.36
	Detroit River Group	1.0×10^{-7}	1.0×10^{-8}	0.1	0.10	3	1002	30.0	0.30	2.48×10^{-11}	6.76×10^{-7}	0.36
	Bois Blanc	1.0×10^{-7}	1.0×10^{-8}	0.1	0.10	3	1002	30.0	0.30	2.48×10^{-11}	6.76×10^{-7}	0.36
Silurian	Bass Islands	1.0×10^{-7}	1.0×10^{-8}	0.1	0.10	3	1002	30.0	0.30	2.48×10^{-11}	6.76×10^{-7}	0.36
	G-Unit	1.0×10^{-7}	1.0×10^{-8}	0.1	0.08	3	1002	22.0	0.27	3.64×10^{-11}	7.03×10^{-7}	0.51
	F-Unit	4.0×10^{-12}	4.0×10^{-13}	0.1	0.03	300	1200	22.0	0.27	3.64×10^{-11}	5.83×10^{-7}	0.73
	F-Salt	1.0×10^{-13}	1.0×10^{-13}	1.0	0.08	300	1200	16.5	0.24	5.14×10^{-11}	1.02×10^{-6}	0.59
	E-Unit	4.0×10^{-12}	4.0×10^{-13}	0.1	0.08	300	1200	22.0	0.27	3.64×10^{-11}	8.42×10^{-7}	0.51
	D-Unit	1.0×10^{-10}	1.0×10^{-11}	0.1	0.03	300	1200	22.0	0.27	3.64×10^{-11}	5.83×10^{-7}	0.73
	B&C Units	4.0×10^{-12}	4.0×10^{-13}	0.1	0.08	300	1200	22.0	0.27	3.64×10^{-11}	8.42×10^{-7}	0.51
	B Anhydrite-Salt	1.0×10^{-13}	1.0×10^{-13}	1.0	0.08	300	1200	16.5	0.24	5.14×10^{-11}	1.02×10^{-6}	0.59
	A2-Carbonate	1.0×10^{-10}	1.0×10^{-11}	0.1	0.08	300	1200	30.0	0.30	2.48×10^{-11}	7.06×10^{-7}	0.41
	A2 Anhydrite-Salt	1.0×10^{-13}	1.0×10^{-13}	1.0	0.08	300	1200	16.5	0.24	5.14×10^{-11}	1.02×10^{-6}	0.59
	A1-Carbonate	2.0×10^{-12}	2.0×10^{-13}	0.1	0.08	300	1200	30.0	0.30	2.48×10^{-11}	7.06×10^{-7}	0.41
	A1-Evaporite	1.0×10^{-13}	1.0×10^{-13}	1.0	0.08	300	1200	16.5	0.24	5.14×10^{-11}	1.02×10^{-6}	0.59
	Niagaran	1.0×10^{-7}	1.0×10^{-8}	0.1	0.08	300	1200	60.0	0.35	1.04×10^{-11}	5.36×10^{-7}	0.23
	Fossil Hill	2.0×10^{-11}	2.0×10^{-12}	0.1	0.08	300	1200	33.0	0.40	1.41×10^{-11}	5.81×10^{-7}	0.29
	Cabot Head	2.0×10^{-12}	2.0×10^{-13}	0.1	0.03	300	1200	30.0	0.30	2.48×10^{-11}	4.47×10^{-7}	0.65
	Manitoulin	1.5×10^{-12}	1.5×10^{-13}	0.1	0.01	300	1200	30.0	0.30	2.48×10^{-11}	3.43×10^{-7}	0.85
Ordovician	Queenston	1.3×10^{-11}	1.3×10^{-12}	0.1	0.11	300	1200	15.0	0.40	3.11×10^{-11}	9.36×10^{-7}	0.39
	Georgian Bay/Blue Mtn.	9.1×10^{-12}	9.1×10^{-13}	0.1	0.11	300	1200	9.0	0.30	8.25×10^{-11}	1.54×10^{-6}	0.63
	Cobourg	9.6×10^{-12}	9.6×10^{-13}	0.1	0.02	300	1200	31.5	0.30	2.36×10^{-11}	3.81×10^{-7}	0.73
	Sherman Falls	9.0×10^{-12}	9.0×10^{-13}	0.1	0.02	300	1200	40.0	0.30	1.86×10^{-11}	3.22×10^{-7}	0.68
	Kirkfield	1.4×10^{-11}	1.4×10^{-12}	0.1	0.02	300	1200	50.0	0.30	1.49×10^{-11}	2.78×10^{-7}	0.63
	Coboconk	5.2×10^{-11}	5.2×10^{-12}	0.1	0.02	300	1200	50.0	0.30	1.49×10^{-11}	2.78×10^{-7}	0.63
	Gull River	3.6×10^{-11}	3.6×10^{-12}	0.1	0.02	300	1200	63.0	0.30	1.18×10^{-11}	2.42×10^{-7}	0.57
	Shadow Lake	8.0×10^{-12}	8.0×10^{-13}	0.1	0.01	300	1200	9.0	0.30	8.25×10^{-11}	1.02×10^{-6}	0.95
Cambrian	Cambrian	3.0×10^{-6}	3.0×10^{-7}	0.1	0.01	300	1200	16.1	0.18	5.72×10^{-11}	7.25×10^{-7}	0.93
Precambrian	Precambrian	8.0×10^{-12}	8.0×10^{-13}	0.1	0.01	300	1200	60.0	0.25	1.39×10^{-11}	2.15×10^{-7}	0.76

Table 5.3 Transport parameters for MBR paleoclimate simulations.

Parameter	Value
Tortuosity	1.0
Diffusion Coefficient	$0.0038\,m^2/a$
Longitudinal Dispersivity	500 m
Transverse Dispersivity/Longitudinal Dispersivity	0.1
Vertical Transverse Dispersivity/Longitudinal Dispersivity	0.01

5.5 Paleoclimate Simulations

A sequence of simulations were performed to obtain paleoclimate simulation results. First, steady-state flow simulations were performed which provide the initial conditions for the pseudo steady-state simulations. The steady-state simulations did not include brine, while the pseudo steady-state simulations were transient for a period of 1 Ma and included brine and density-dependent flow. *Sykes et al.* (2003b) showed that a 1 Ma simulation time was sufficient to provide a nearly steady-state groundwater flow system. Pseudo steady-state simulations are required to allow density-dependent flow to equilibrate; the end of the simulation was used as the initial conditions for the transient paleoclimate simulations.

The same pseudo steady-state simulation was used as the initial conditions for all paleoclimate simulations in this chapter. All results of the 120 ka paleoclimate simulations at times of 80 ka before present, 40 ka before present, and at present for Scenarios 1–4 are shown in Appendix H to Appendix K. A description of parameters used in each paleoclimate scenario is provided in Table 5.4. Ignoring hydromechanical coupling in Scenario 2 will lead to increased vertical gradients, and vertical velocities during glacial loading and unloading. A unit tracer will migrate deeper into the flow system under such circumstances. When hydromechanical coupling is fully applied in Scenario 3, vertical gradients are significantly reduced, and unit tracer migration will be significantly retarded relative to either Scenario 1 or Scenario 2. In Scenario 4, the use of higher compressibility values as compared to Scenario 2 will lead to the retention of elevated pore pressures created during glacial loading.

Table 5.4 Parameter selections for MBR paleoclimate simulations.

Paleoclimate Simulation	Description
MBR Scenario 1	Base-case parameter values from Table 5.2 and Table 5.3
MBR Scenario 2	DGR Scenario 1 parameter values with $\zeta = 0$
MBR Scenario 3	DGR Scenario 1 parameter values with $\zeta = 1$
MBR Scenario 4	Parameter values listed in Table 5.5, using literature values for one-dimensional vertical compressibility β' and $\zeta = 0$, as applied in *Sykes et al.* (2008)

5.5.1 Pseudo Steady-State Simulation

Figure 5.19 to Figure 5.28 show various groundwater flow modelling results. Freshwater heads are plotted in Figure 5.19 and Figure 5.20 as a block cut view and a fence view, respectively. In these figures, heads increase with depth, principally caused by the high

TDS pore fluids in various layers as indicated in Table 5.2. To remove the effects of density on the interpretation of heads, environmental heads are calculated and shown in Figure 5.21 and Figure 5.22. While the freshwater heads indicate a strong upward gradient, the environmental head plots indicate rather uniform heads from the top to the bottom of the model. A higher head zone is noticeable underneath Lake Huron in the fence view, coincident with the higher permeability Niagaran Group in the Middle Silurian, presenting a higher head than either above or below.

Pore velocity magnitudes for block cut and fence views are shown in Figure 5.23 and Figure 5.24, respectively. Within the Silurian formations, a high pore velocity magnitude layer is visible, representing the Niagaran Group. This unit is clearly visible in the fence view as it subcrops towards the east and is in contact with the higher permeability drift layers at the model's top surface. The drift layers are also shown to have higher pore velocities owing to their higher hydraulic conductivity as listed in Table 5.2. The following plots shown as Figure 5.25 and Figure 5.26 illustrate whether flow in a given model layer is either upward (coloured red), downward (coloured blue) or essentially horizontal (coloured white). In the southwestern portions of the modelling domain, flow from the Niagaran Group tends to be upward above the unit, and downward below the unit. The pore water flow directions beneath Lake Huron are mostly upward or downward, while the land ward portion is mostly horizontal in nature. These figures indicating flow direction must be used in conjunction with the preceding flow magnitude figures to indicate the mobility of a pore fluid. For low permeability units, flow is predominantly horizontal when no high permeability unit is adjacent, however, flow is vertical if a high permeability unit such as the Cambrian Formation is adjacent.

The final set of figures, Figure 5.27 and Figure 5.28, illustrate brine TDS concentrations. As is clearly shown, high TDS concentrations near 300 g/L predominate throughout the model beginning approximately half-way into the Silurian formations. The high permeability Niagaran Group indicates that freshwater does not enter deeply into the system over a 1 Ma pseudo steady-state simulation, primarily due to the high density that must be displaced. Higher TDS values are found at shallower depths towards the east than in the southwest, but freshwater is dominant in all near surface locations as shown in Figure 5.28.

5.5.2 MBR Scenario 1 Paleoclimate Simulation

The first paleoclimate simulation uses the parameters listed in Table 5.2 and represents the base-case analysis. The subsequent analyses represent variations on the base-case to investigate the influence of changes to the base-case parameters on the modelling results. The simulation results are presented in Appendix H; a summary of figure numbers for 2 views, 7 parameters, and 3 points in time are presented in Table H.1. Block cut and fence views are shown for various parameters, at paleoclimate simulation times of 80 ka before present (−80 ka), 40 ka before present (−40 ka), and at present (0 ka).

Freshwater head plots are shown in Figures H.1 to H.6, and environmental head plots are shown in Figures H.7 to H.12. For the first 40 ka of simulation time, Figure H.1 shows little difference from the pseudo steady-state simulation of Figure 5.19, although a brief permafrost event occurred at approximately 111 ka before present, as shown in Figure 5.18. This similarity is also observed in the environmental heads plots of Figure 5.21

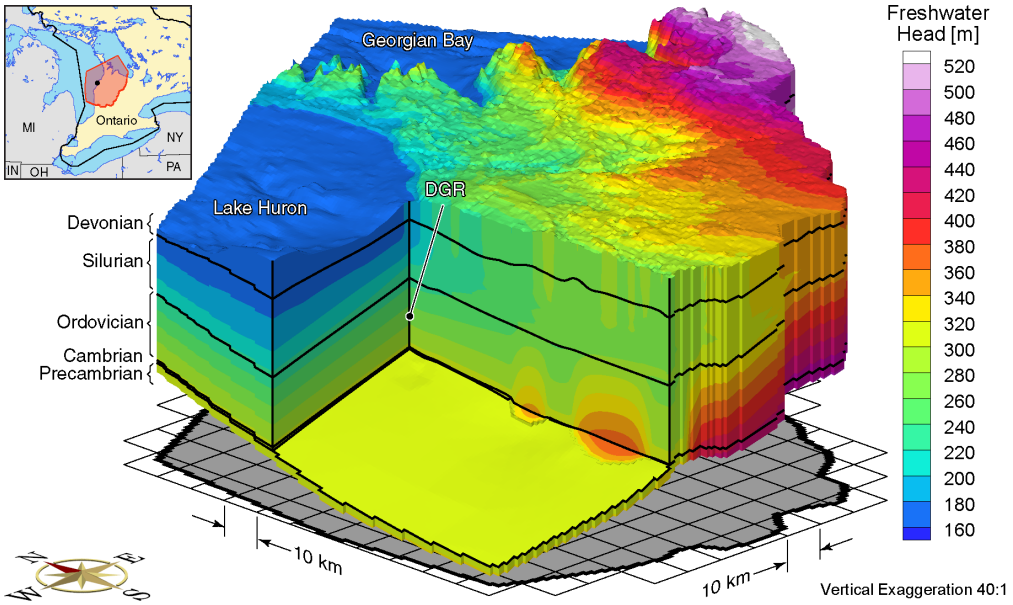

Figure 5.19 Block cut view of heads at 1 Ma for pseudo steady-state simulation.

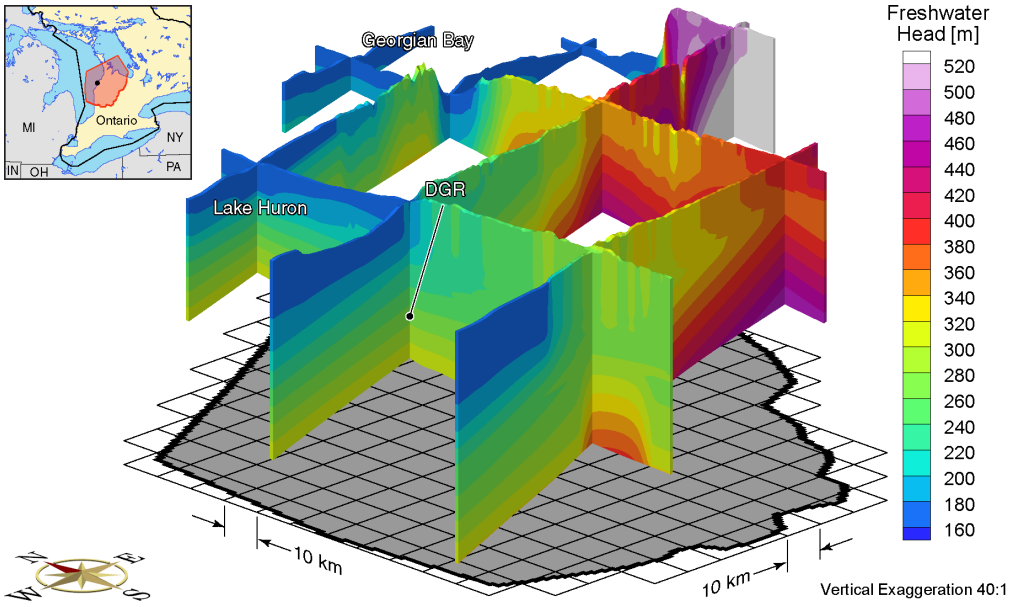

Figure 5.20 Fence view of heads at 1 Ma for pseudo steady-state simulation.

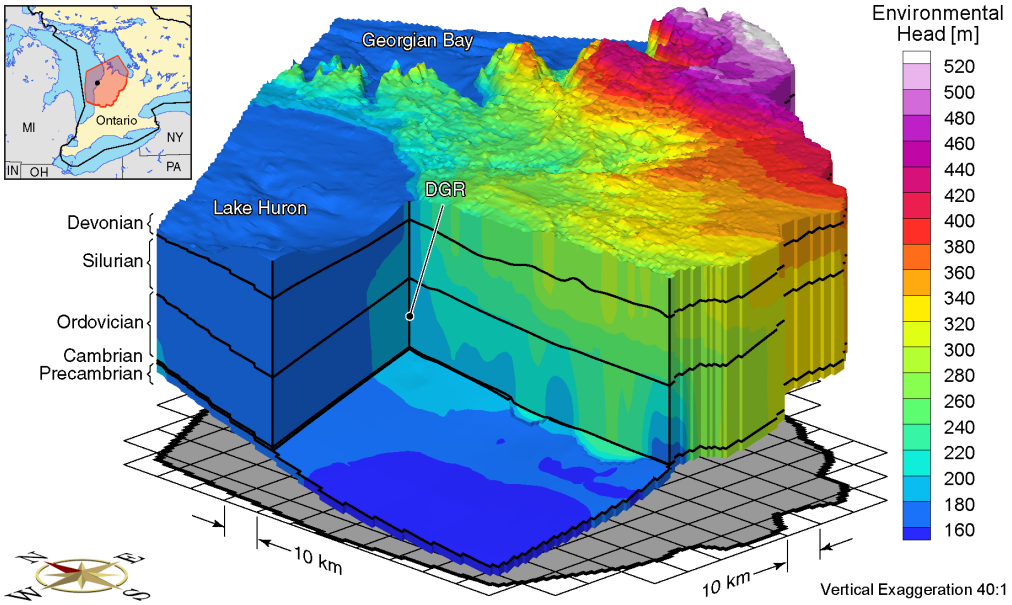

Figure 5.21 Block cut view of environmental heads at 1 Ma for pseudo steady-state simulation.

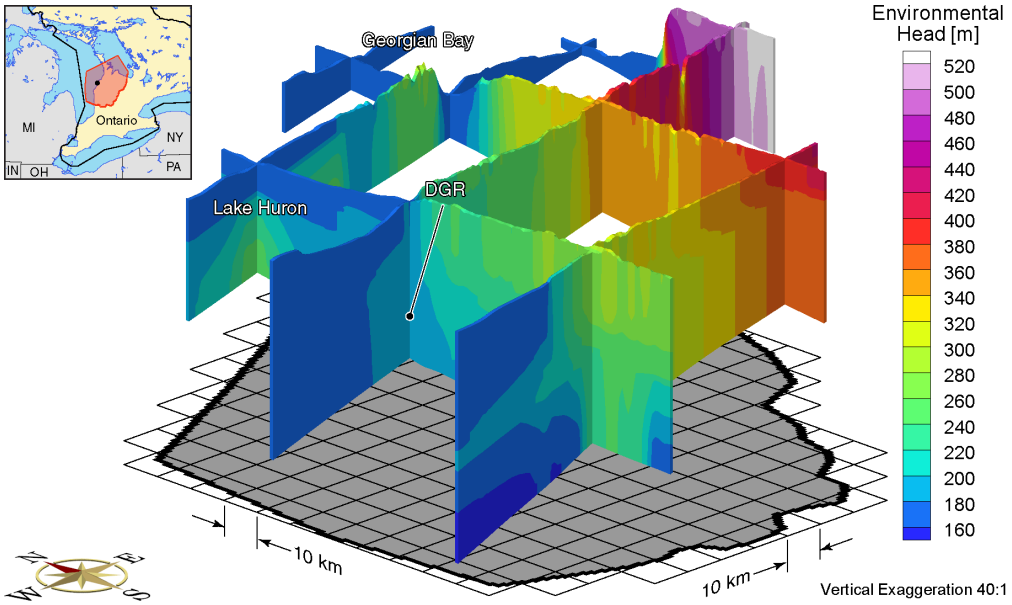

Figure 5.22 Fence view of environmental heads at 1 Ma for pseudo steady-state simulation.

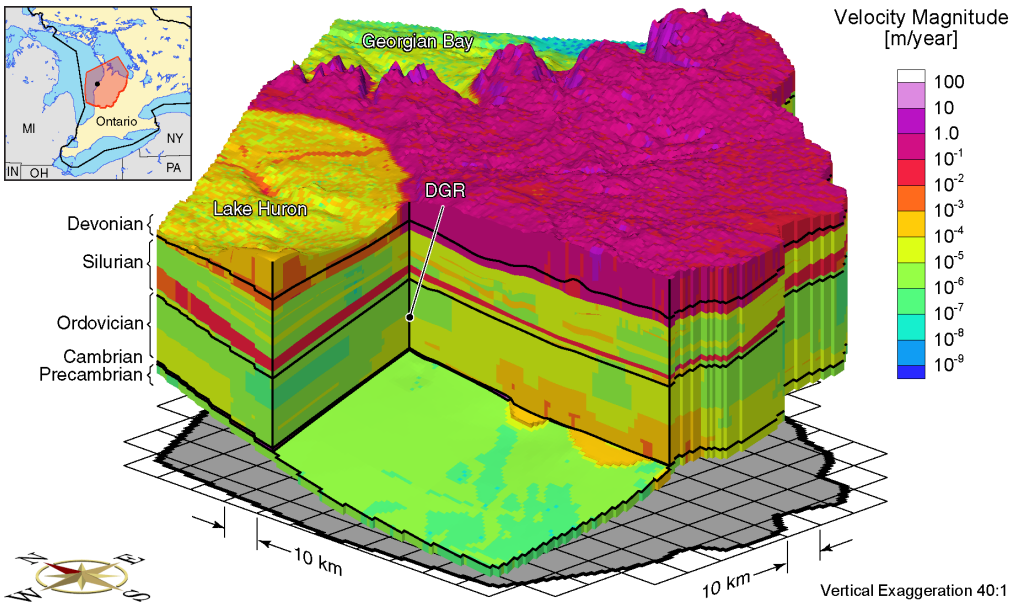

Figure 5.23 Block cut view of pore velocity magnitudes at 1 Ma for pseudo steady-state simulation.

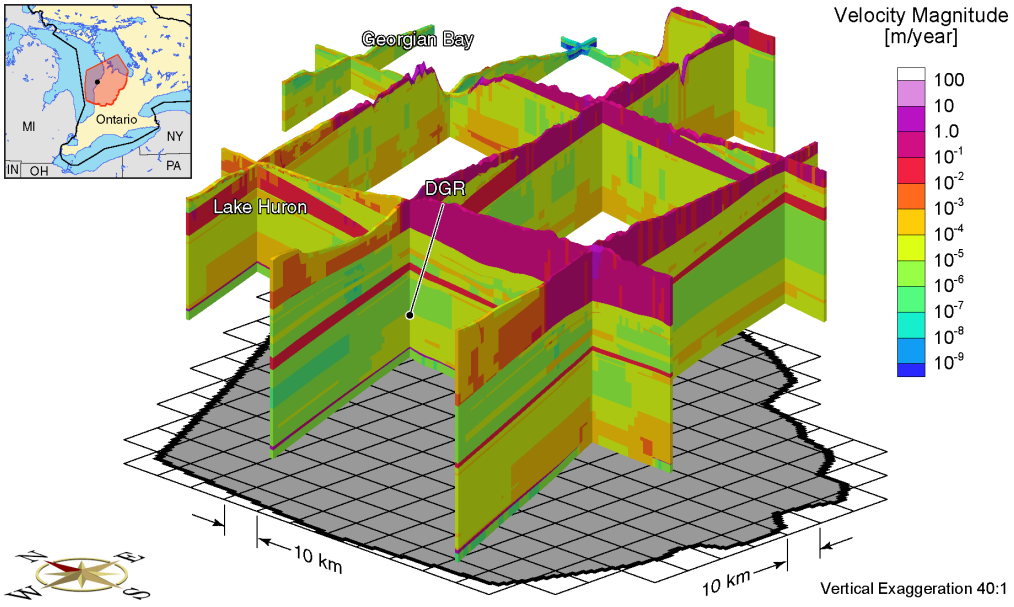

Figure 5.24 Fence view of pore velocity magnitudes at 1 Ma for pseudo steady-state simulation.

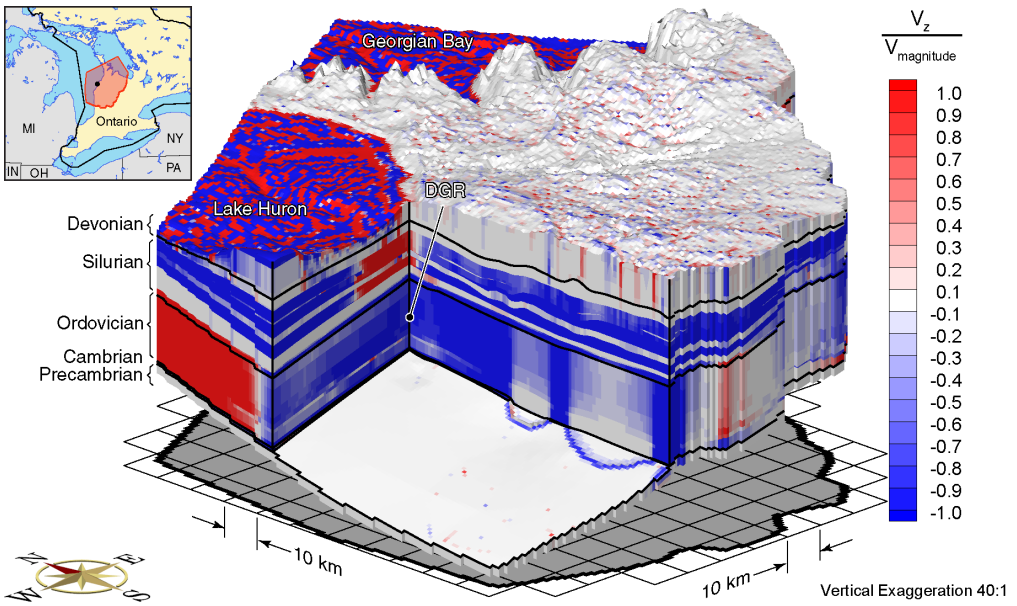

Figure 5.25 Block cut view of ratio of vertical pore velocities to pore velocity magnitudes at 1 Ma for pseudo steady-state simulation.

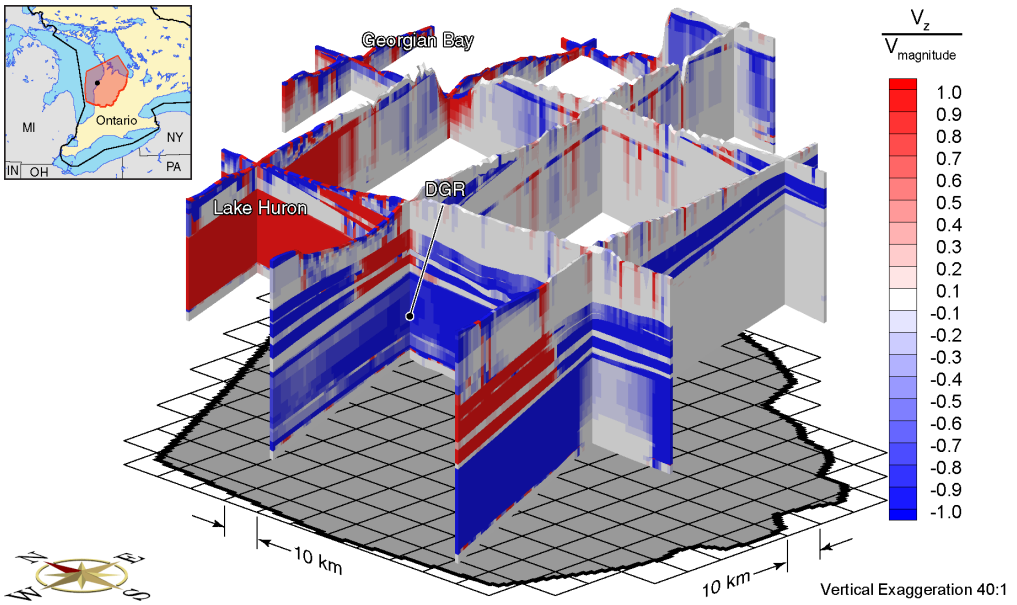

Figure 5.26 Fence view of ratio of vertical pore velocities to pore velocity magnitudes at 1 Ma for pseudo steady-state simulation.

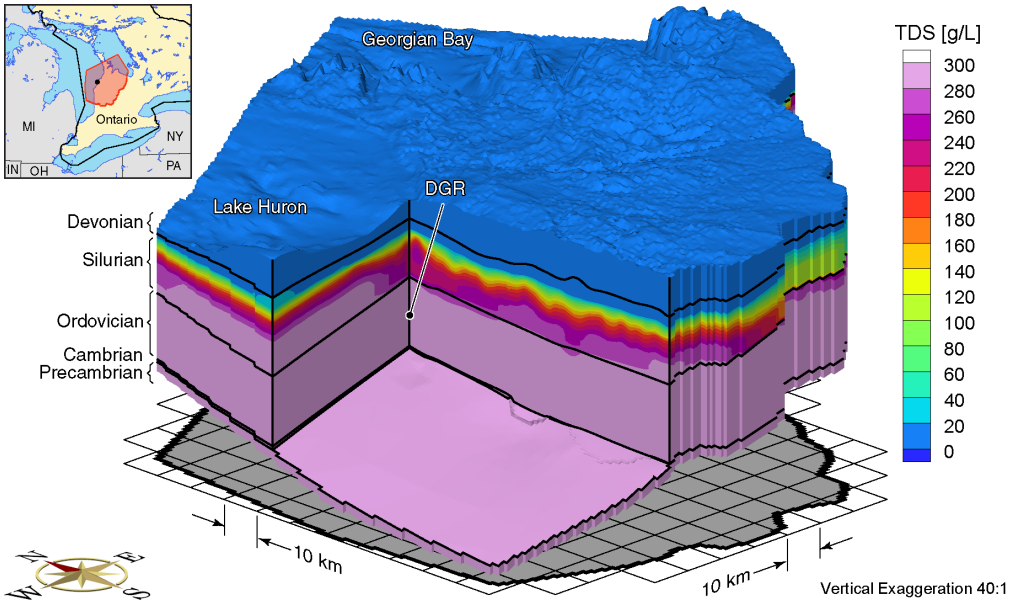

Figure 5.27 Block cut view of brine concentrations at 1 Ma for pseudo steady-state simulation.

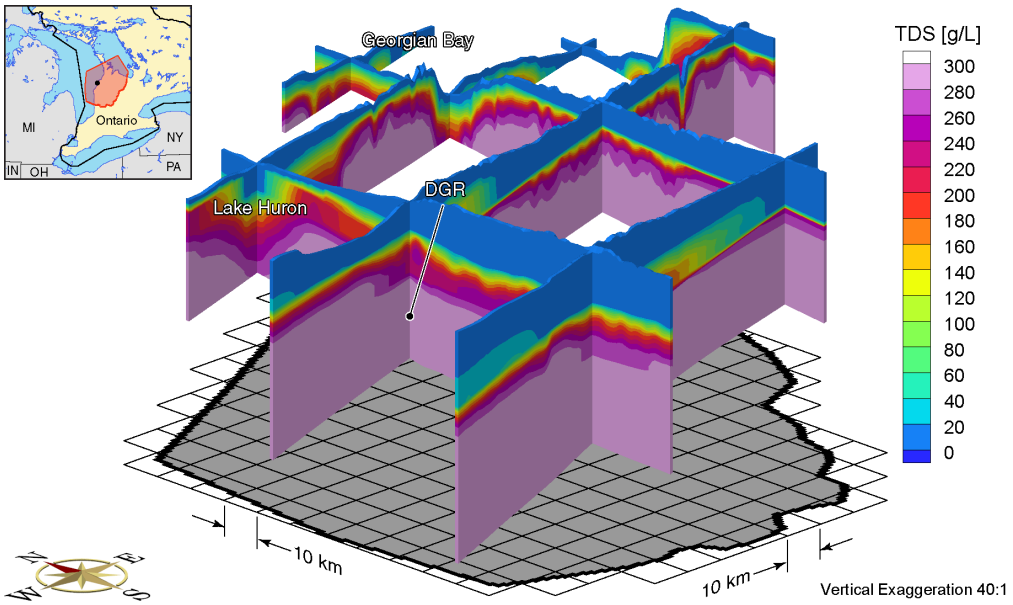

Figure 5.28 Fence view of brine concentrations at 1 Ma for pseudo steady-state simulation.

and Figure 5.22 as compared to Figure H.7 and Figure H.8, respectively. Since there were no changes in boundary conditions during the first 57 ka, a change in material properties, represented by the presence of permafrost in the near surface, is unlikely to cause broad changes in system behaviour.

The first significant change in surface boundary conditions occurs at −63 ka as shown by the ice thickness plot in Figure 5.18. The ice loading ends at −56.5 ka, and is subsequently followed by a lake depth of approximately 110 m, due in part, to the isostatic depression caused by the presence of the ice-sheet at that location (see Figure 5.18). Both the freshwater heads and environmental heads are generally higher throughout the modelling domain in comparing the −80 ka plots, represented by Figure H.7 and Figure H.8, to the −40 ka plots represented by Figure H.9 and Figure H.10, respectively. The second advance of the ice-sheet across the DGR site occurs between −24 ka and −14.5 ka, as shown in Figure 5.18. The environmental head plots for the present time (0 ka) are shown in Figure H.11 and Figure H.12; both plots illustrating the continuing trend of increasing heads throughout the domain, when compared to Figure H.9 and Figure H.10. The head plots indicate that using the parameters listed in Table 5.2, elevated heads can persist for tens of thousands of years after a deglaciation event has occurred.

Although pressure measurements have been converted to environmental heads in Figure 5.2, the current model does not consider or replicate the insitu pressure conditions at the DGR-1 and DGR-2 boreholes. For example, the Cambrian Formation is overpressured, while the Ordovician sediments are underpressured relative to ground surface; the sources of such pressure deviations are not fully understood and are presently being investigated by the NWMO. The use of FRAC3DVS-OPG in this thesis assumes that the entire modelling domain is fully saturated, while a possible cause for the underpressurization in the Ordovician units can be explained by the presence of a gas phase, indicating a partially saturated porous medium, the effective permeability in a partially saturated porous media can be significantly lower than for a fully saturated porous media.

Figure 5.29a and Figure 5.29b show the environmental heads at the DGR location along a vertical profile at 12 times, spaced 10 ka apart, beginning at −110 ka, and ending at the present time; the horizontal scale is adjusted to account for the large variation in environmental heads that occurs from applying the paleoclimate boundary conditions, with Figure 5.29b having a smaller environmental head range than Figure 5.29a. During the first 50 ka, the environmental heads are nearly identical, and overlap in Figure 5.29b. Environmental heads are higher in regions close to ground surface during the loading phase of glaciation observed at −60 ka and −20 ka in the figures, and are higher in regions near the base of the modelling domain during the unloading phase and subsequent to it. During the first 50 ka, the environmental head is highest in the Niagaran Group, with upward gradients above this group, and downward gradients below this group.

Pore water velocity magnitudes are presented in Figure H.13 to Figure H.18, and the ratio of vertical pore velocities to pore velocity magnitudes are presented in Figure H.19 to Figure H.24. Very little change is noticeable between the −80 ka plots (Figures H.13 and H.14) and the initial condition of Figures 5.23 and 5.24. A subtle change occurs between −80 ka and −40 ka whereby pore velocity magnitudes slightly increase in the Ordovician sediments, as shown in Figures H.15 and H.16. The higher velocity Niagaran Group and Cambrian Formation are clearly visible in both the block cut and fence views. Although the magnitudes do not appear to change significantly, the flow directions do

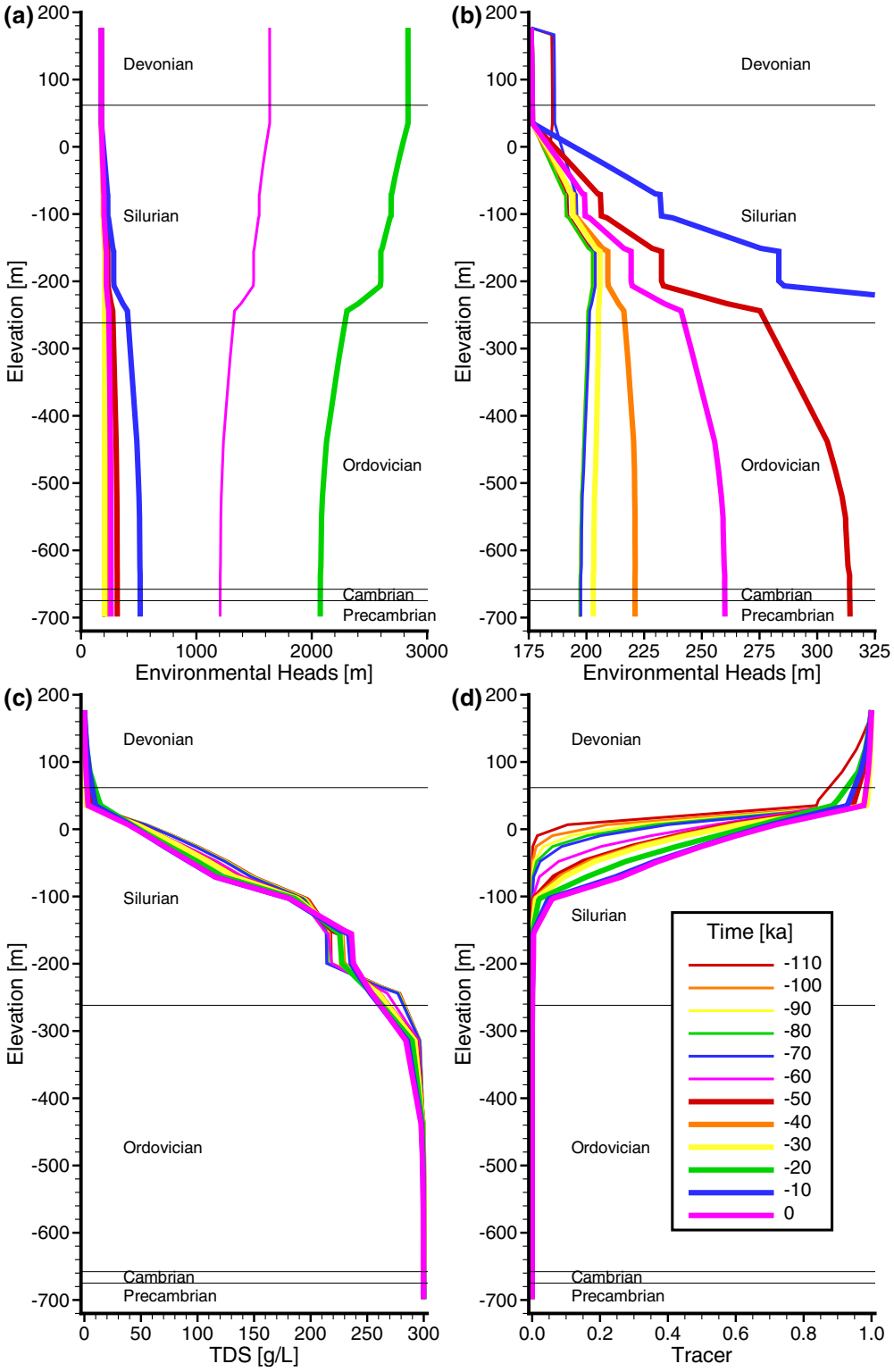

Figure 5.29 Vertical profiles every 10 ka for Scenario 1 paleoclimate simulation at DGR location: (a) and (b), environmental heads; (c), total dissolved solids; and (d), tracer concentrations.

change between −80 ka and −40 ka. Due to the first glacial advance and retreat over the DGR site, flow velocities which were horizontal or downward, are now mostly upward; this result is expected due to the dissipation of higher heads at depth imparted by the glaciation event, and is shown in Figures H.21 and H.22. This is also confirmed by looking at the environmental heads at −40 ka in Figure 5.29b, and by the vertical pore water velocity at the DGR location, for all scenarios, in the Cobourg Formation, presented in Figure 5.30. Vertically upward velocities are shown during and following a glacial retreat, while vertically downward velocities occur during a glacial advance. Figures H.17 and H.18 show, in general, an increase in pore velocities in the Ordovician sediments, and Figures H.23 and H.24 show a greater portion of the domain at the present time with vertically upward velocities, due to the last glacial maximum (LGM).

Brine concentrations are presented in Figure H.25 to Figure H.30. Over the 120 ka simulation period, the jaggedness of the brine isochlors lessens, as seen by comparing Figure 5.28 to Figure H.30. Further supporting this claim, is Figure 5.29c, where the brine concentration as a function of elevation at the DGR site shows a slight redistribution over the 120 ka paleoclimate simulation, notably increasing in the Niagaran Group and decreasing in the Lower Silurian and Upper Ordovician.

A tracer of unit concentration is applied as a Dirichlet boundary condition to all surface nodes at the beginning of the paleoclimate simulation. This tracer is used to characterize the migration, from the surface, of recharge water that occurs during the paleoclimate simulation; the recharge water includes glacial meltwater, whose importance was discussed in §2.5.1. Tracer concentrations for the modelling domain are presented in Figure H.31 to Figure H.36. A vertical profile of the tracer concentration, representing the fraction of recharge water, at the DGR location is shown in Figure 5.29d. This figure demonstrates how the tracer concentration varies with elevation as a function of time, with 10 ka intervals. The tracer appears to move downwards at a steady rate, however, the effects of glaciation are not clearly evident. Plotting the elevations of the 5% and 50% tracer concentrations at the DGR location results in Figure 5.31. The glacial advances starting at −63 ka and −24 ka clearly affect the rate at which the tracer isochlors migrate with depth, due to the downward velocities generated during glacial advance. At other times, tracer migration is more subdued, with diffusion being the dominant transport mechanism in the low permeability units of the Upper Silurian.

The infiltration or recharge into the modelling domain for all scenarios is shown in Figure 5.32. For Scenario 1 in Figure 5.32a, the infiltration rate ranges between approximately 1×10^{-4} m/a and 2×10^{-3} m/a. The higher infiltration rates coincide with a lack of permafrost as shown in Figure 5.18. Figure 5.33 provides the total flux across the surface of the modelling domain, positive representing inward to the domain, and negative representing outward. For Scenario 1 in Figure 5.33a, increases in net inflows occur during advance of glaciers where high heads lead to vertically downward gradients, while net outflows occur during the retreat of glaciers and resulting gradients are upwards.

Mean life expectancies are also calculated and are shown in Figure H.37 for a block cut view and in Figure H.38 for a fence view. MLEs are calculated using present day pore water velocities and brine distributions, determined at the end of the paleoclimate simulation. At the DGR location, specifically the bottom of the Cobourg Formation, a mean life expectancy of 3.82 Ma is calculated, while more southern and deeper portions of the domain have mean life expectancies of between 10 Ma and 100 Ma; these portions

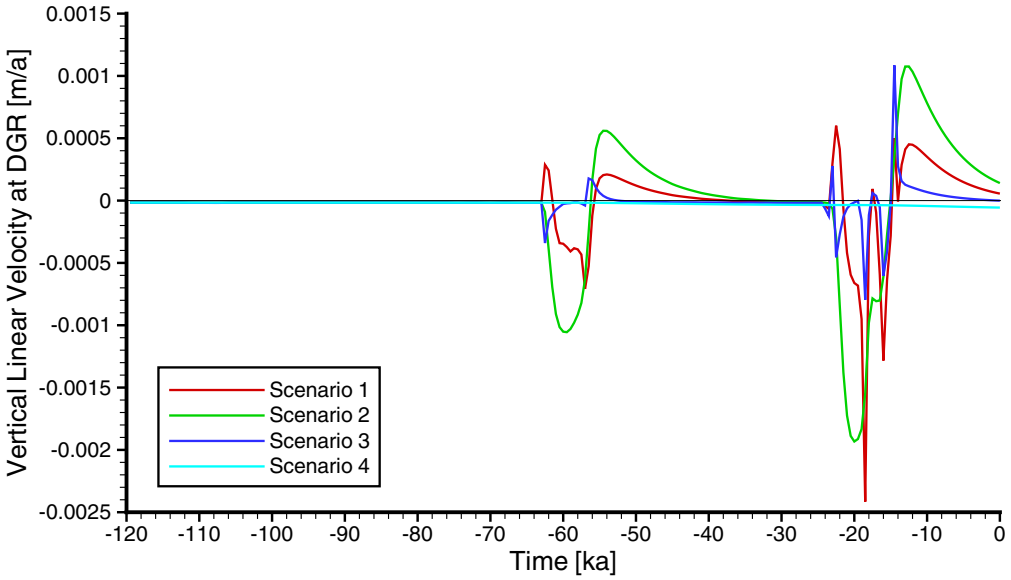

Figure 5.30 Vertical pore velocity for Scenarios 1 to 4 during 120 ka paleoclimate simulations at DGR location.

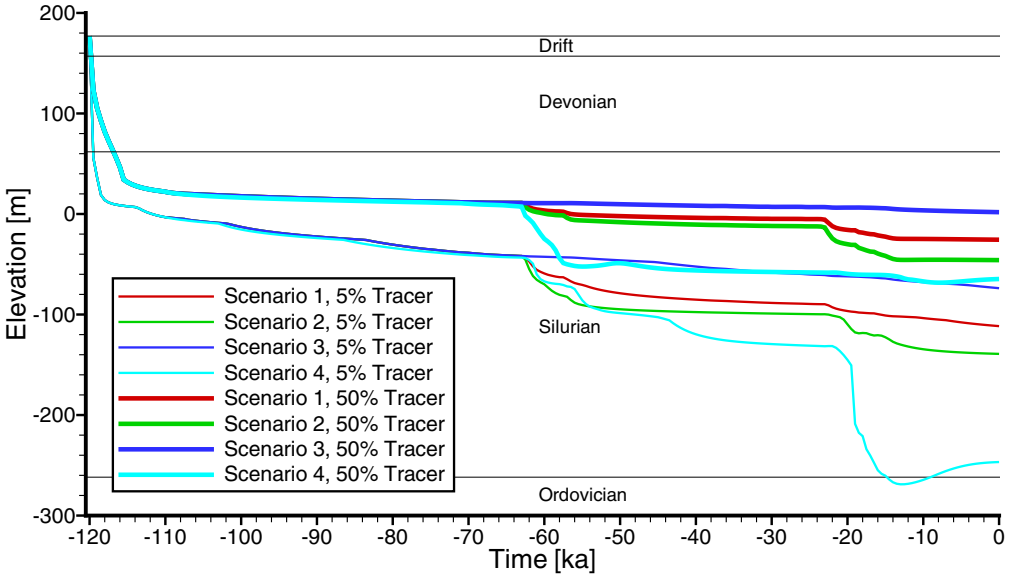

Figure 5.31 Elevation of 5% and 50% tracer concentrations for Scenarios 1 to 4 during 120 ka paleoclimate simulations at DGR location.

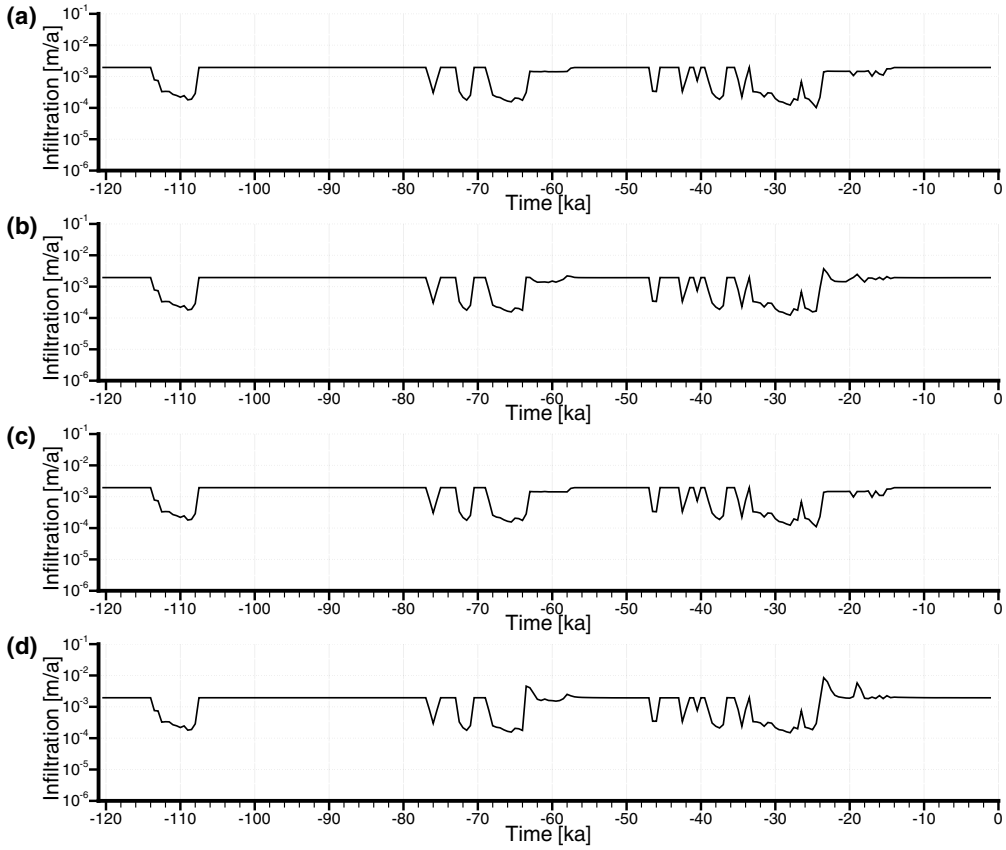

Figure 5.32 Average infiltration across entire modelling domain for (a) Scenario 1, (b) Scenario 2, (c) Scenario 3, and (d) Scenario 4.

coincide with the absence of the Cambrian Formation, since it is a high permeability layer capable of higher flow velocities, and hence shorter travel times.

5.5.3 MBR Scenario 2 Paleoclimate Simulation

The second paleoclimate simulation investigates the role of the one-dimensional loading efficiency with $\zeta = 0$. All figures are presented in Appendix I, and a summary of the figures is presented in Table I.1. Groundwater flow models rarely consider hydromechanical coupling; in this simulation, hydromechanical coupling is ignored to demonstrate the bias that can occur when using such models.

Freshwater head plots are shown in Figures I.1 to I.6, and environmental head plots are shown in Figures I.7 to I.12. Vertical profiles of environmental heads at the DGR location are shown in Figure 5.34a and Figure 5.34b. In comparing Figure 5.34 to Figure 5.29, the vertical gradients for Scenario 2 are greater than for Scenario 1. The lack of hydromechanical coupling results in larger vertical gradients since the hydromechanical term, described in §2.4.2 and behaving as a fluid source/sink term, does not allow for an increase in pore pressure throughout the domain due to glacially induced mechanical loading. For a non-zero loading efficiency, the increase in pore pressure thereby reduces the vertical fluid energy gradient. Both freshwater heads and environmental heads are higher at depth for Scenario 2 at −40 ka and at present when compared to Scenario 1.

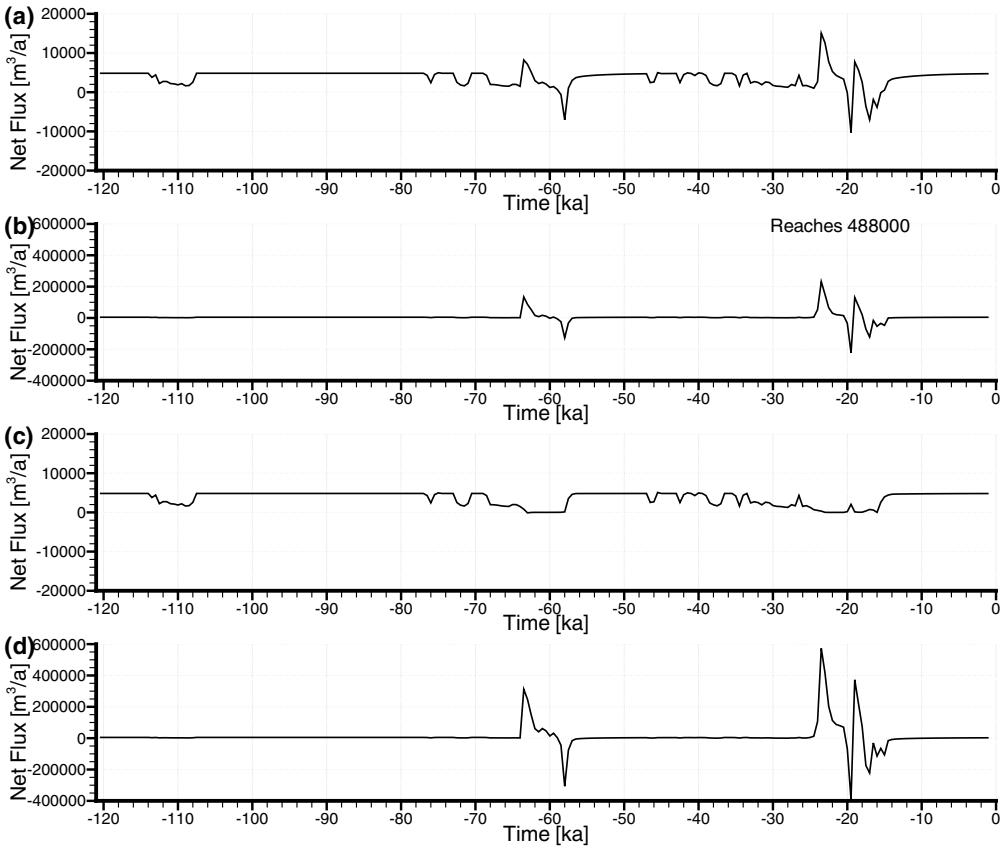

Figure 5.33 Net surface flux across entire modelling domain for (a) Scenario 1, (b) Scenario 2, (c) Scenario 3, and (d) Scenario 4.

Pore water velocity magnitudes are presented in Figure I.13 to Figure I.18, and the ratio of vertical pore velocities to pore velocity magnitudes are presented in Figure I.19 to Figure I.24. In comparing these figures to those from Scenario 1, higher velocities occur for Scenario 2 in both the Silurian and Ordovician units, primarily due to the greater gradients imposed by a lack of hydromechanical coupling. A plot of vertical pore velocities at the DGR location in the Cobourg Formation also shows greater vertical velocities for Scenario 2, both during the loading and unloading phases of glaciation. Velocity directions are quite similar between Scenario 1 and Scenario 2, when comparing Figures I.21, I.22, I.23, I.24 to Figures H.21, H.22, H.23, H.24, respectively, although in areas where flow is both horizontal and vertically upward (lighter reds), the flow directions become more upwardly vertical, signified by darker reds for Scenario 2, as compared to Scenario 1.

Brine concentrations are presented in Figure I.25 to Figure I.30, and are very similar to the Scenario 1 brine concentrations. The brine concentration for a vertical profile at the DGR location is shown in Figure 5.34c. This profile is very similar to the Scenario 1 profile of Figure 5.29c, except for the increase in brine concentration in the Niagaran Group, and the decrease in brine concentration in the Upper Ordovician.

Tracer concentrations for the modelling domain are presented in Figure I.31 to Figure I.36. A vertical profile of the tracer concentration, representing the fraction of recharge water, at the DGR location is shown in Figure 5.34d. Since vertical pore

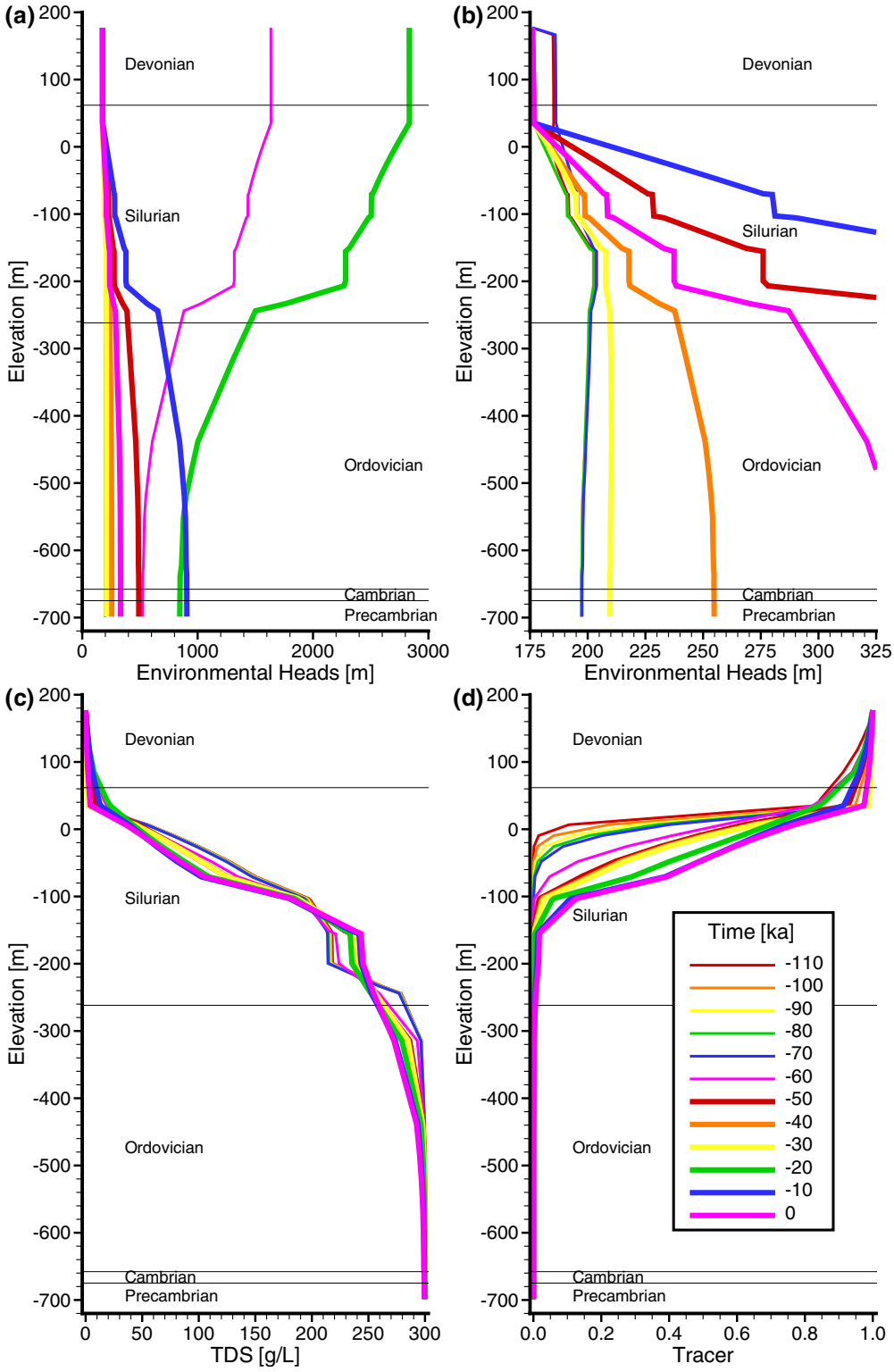

Figure 5.34 Vertical profiles every 10 ka for Scenario 2 paleoclimate simulation at DGR location: (a) and (b), environmental heads; (c), total dissolved solids; and (d), tracer concentrations.

velocities are greater without hydromechanical coupling, the tracer should migrate deeper; Figure 5.31 clearly shows this for the 5% and 50% recharge water concentrations over the 120 ka paleoclimate simulations. Throughout the simulation period, recharge water migration is deeper for Scenario 2 than for Scenario 1. A similar assessment can be made when comparing Figure I.36 to Figure H.36.

For Scenario 2 in Figure 5.32b, the infiltration rate is very similar to Scenario 1 in Figure 5.32a, however, the effect of the one-dimensional loading efficiency $\zeta = 0$ can be seen as slight variations in infiltration at −60 ka and −20 ka. Although the timing and flow direction are similar between Scenario 1 and Scenario 2, the amplitude of the fluxes in Figure 5.33b as compared to Figure 5.33a is greater in Scenario 2 due to the larger vertical gradients resulting from a lack of hydromechanical coupling.

Mean life expectancy, calculated using the velocity distribution shown in Figure B.18, is also affected by a lack of hydromechanical coupling; a shorter mean life expectancy occurs when compared to Scenario 1. This can be seen by comparing Figure I.37 to Figure H.37, and Figure I.38 to Figure H.38. The MLE at the bottom of the Cobourg Formation for DGR location is approximately 2.12 Ma, approximately 1.7 Ma less than that calculated for Scenario 1. Excluding one-dimensional hydromechanical coupling for Scenario 2 results in a smaller MLE. Longer MLE values of 10 Ma to 100 Ma are seen in the portion of the domain that is not underlain by the Cambrian Formation in Figure H.37, as compared to Figure I.37.

5.5.4 MBR Scenario 3 Paleoclimate Simulation

Scenario 3 is similar to Scenario 2 in that the role of hydromechanical coupling is also investigated, however, hydromechanical coupling is assumed to fully support the applied mechanical loads with $\zeta = 1$. A value of unity implies that the entire mechanical load is transferred to the pore water by increasing its pressure, and that the rock matrix is too compressible, relative to water, to mechanically support the applied load. All figures are presented in Appendix J, and a summary of the figures is presented in Table J.1.

Freshwater head plots are shown in Figures J.1 to J.6, and environmental head plots are shown in Figures J.7 to J.12. The present day paleoclimate environmental heads in Figures J.11 and J.12 are very similar to the initial condition represented by Figures 5.21 and 5.22. Vertical profiles of environmental heads at the DGR location are shown in Figure 5.35a and Figure 5.35b. The greatest difference between these figures and those of Scenario 1 (Figure 5.29a and Figure 5.29b), is that there is very little variation in environmental head along the vertical profile. When a glacial loading event occurs, the entire modelling domain is pressurized from top to bottom with a uniform increase in pore pressure, in balance with the mechanical loading at surface; therefore, vertical gradients are much less than in either Scenario 1 or Scenario 2.

Lower vertical gradients result in reduced pore water velocities according to Darcy's Law. Pore water velocity magnitudes are presented in Figure J.13 to Figure J.18, and the ratio of vertical pore velocities to pore velocity magnitudes are presented in Figure J.19 to Figure J.24. Generally, velocities are lower in both the Silurian and Ordovician units for this Scenario as compared to Scenario 1 (see Figures H.17 and H.18). In Figure 5.30, the vertical pore water velocities, in the Cobourg Formation at the DGR location, for Scenario 3 are generally less than those for either Scenario 1 or Scenario 2. Upward vertical velocities are less apparent in Scenario 3, shown in Figures J.23 and J.24, as compared

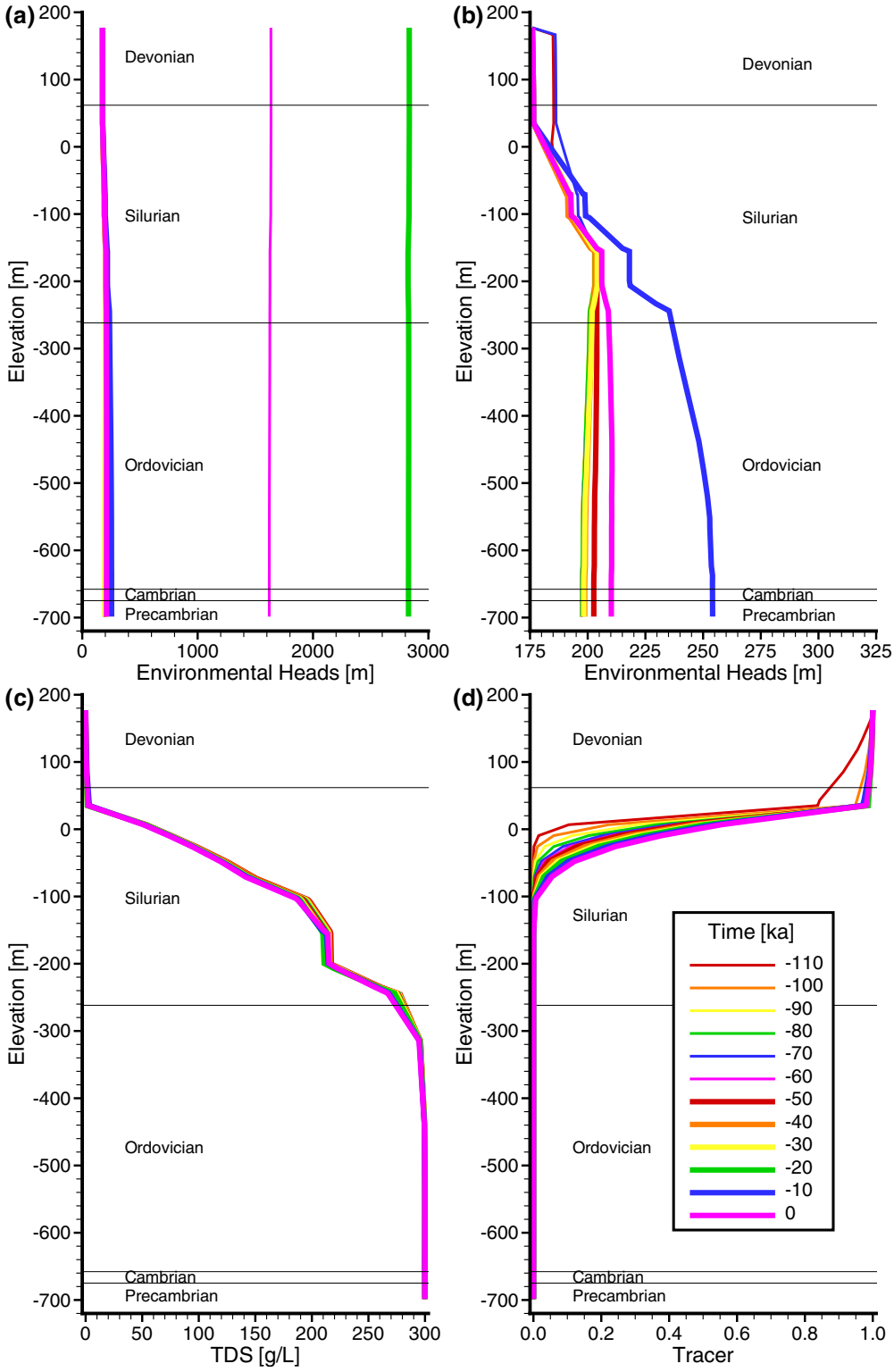

Figure 5.35 Vertical profiles every 10 ka for Scenario 3 paleoclimate simulation at DGR location: (a) and (b), environmental heads; (c), total dissolved solids; and (d), tracer concentrations.

to Figures H.23 and H.24. Vertical velocities that were upward in Scenario 1 are now downward in Scenario 3, especially in the Silurian units due to the 'flattened' gradients resulting from full hydromechanical coupling with $\zeta = 1$.

Brine concentrations are presented in Figure J.25 to Figure J.30, and are very similar to the Scenario 1 brine concentrations. The brine concentration for a vertical profile at the DGR location is shown in Figure 5.35c. This profile is similar to the Scenario 1 profile of Figure 5.29c, except there is very little variation between the various profiles spaced at 10 ka intervals. The reduction of vertical gradients, and hence velocities, means that brine movement in the Salina Group (as it is the transition zone) is dominated by diffusion, and not advection, as is clearly seen in Scenario 2.

Tracer concentrations for the modelling domain are presented in Figure J.31 to Figure J.36. The vertical depth of tracer migration is noticeably less for Scenario 3 as compared to Scenario 1 (see Figure H.35 and Figure H.36). A vertical profile of the tracer concentration, representing the fraction of recharge water, at the DGR location is shown in Figure 5.35d. The tracer migration is much less than what occurs under either Scenario 1 or Scenario 2. Further indication of this is shown in Figure 5.31, where the glaciation advances, starting at −63 ka and −24 ka, have no discernable effect on the tracer migration, as compared to Scenario 1 or Scenario 2 for either the 5% or 50% recharge water.

For Scenario 3 in Figure 5.32c, the infiltration rate is very similar to Scenario 1 in Figure 5.32a, however, the effect of the one-dimensional loading efficiency $\zeta = 1$ can be seen. Although the timing and flow direction are similar between Scenario 1 and Scenario 3, the amplitude of the fluxes in Figure 5.33c as compared to Figure 5.33a is much less in Scenario 3 due to the much smaller vertical gradients resulting from full hydromechanical coupling.

The mean life expectancy plots of Figure J.37 and Figure J.38, calculated using the velocity distribution shown in Figure C.12, result in longer times, due to the reduced pore water velocities for the scenario. The MLE at the DGR location is now approximately 8.86 Ma with 10 Ma to 100 Ma regions much more dominant within the modelling domain as compared to Figure H.37, Figure H.38, Figure I.37, or Figure I.38.

5.5.5 MBR Scenario 4 Paleoclimate Simulation

The fourth MBR paleoclimate simulation investigates the use of literature values for one-dimensional vertical compressibility β' (see *Sykes et al.*, 2008), shown in Table 5.5, as compared to calculating β' from the elastic modulus E and Poisson's ratio ν, as shown in Table 5.2. The storage coefficient S_s, and one-dimensional loading efficiency ζ are calculated based on β', however, for the purposes of this simulation, $\zeta = 0$, as was done in Scenario 2. All figures are presented in Appendix K, and a summary of the figures is presented in Table K.1.

The literature values of β' differ by a factor of between 1.2 and 404, with most factors below 10, when compared to the calculated β' in Table 5.2. The largest factors occur with units assigned one-dimensional vertical compressibilities of 1.0×10^{-8} Pa^{-1}, which were assigned by *Sykes et al.* (2008) to shale layers. Compressibilities also affect storage coefficients, which for Scenario 4 are a factor of 1.2 to 264 times larger than those used in Scenario 2. Although not used in Scenario 4, the listed one-dimensional loading efficiencies in Table 5.5 are greater for nearly all layers than those listed in Table 5.2,

Table 5.5 Hydraulic and mechanical properties for MBR Scenario 4 paleoclimate model based on literature values for β', as applied in *Sykes et al.* (2008).

Period	Geology	K_H [m/s]	K_V [m/s]	K_V/K_H [/]	n [/]	TDS [g/L]	ρ [kg/m^3]	β' [Pa^{-1}]	S_s [m^{-1}]	ζ [/]
Quaternary	Drift	1.0×10^{-7}	2.0×10^{-8}	0.2	0.10	0.045	1000.03	1.0×10^{-8}	9.85×10^{-5}	1.00
Devonian	Traverse Group	1.0×10^{-7}	1.0×10^{-8}	0.1	0.10	0.045	1000.03	1.0×10^{-8}	9.85×10^{-5}	1.00
	Dundee	1.0×10^{-7}	1.0×10^{-8}	0.1	0.10	3	1002	1.0×10^{-8}	9.87×10^{-5}	1.00
	Detroit River Group	1.0×10^{-7}	1.0×10^{-8}	0.1	0.10	3	1002	1.0×10^{-10}	1.41×10^{-6}	0.69
	Bois Blanc	1.0×10^{-7}	1.0×10^{-8}	0.1	0.10	3	1002	1.0×10^{-10}	1.41×10^{-6}	0.69
Silurian	Bass Islands	1.0×10^{-7}	1.0×10^{-8}	0.1	0.10	3	1002	1.0×10^{-10}	1.41×10^{-6}	0.69
	G-Unit	1.0×10^{-7}	1.0×10^{-8}	0.1	0.08	3	1002	1.0×10^{-10}	1.33×10^{-6}	0.74
	F-Unit	4.0×10^{-12}	4.0×10^{-13}	0.1	0.03	300	1200	1.0×10^{-8}	1.18×10^{-4}	1.00
	F-Salt	1.0×10^{-13}	1.0×10^{-13}	1.0	0.08	300	1200	1.0×10^{-10}	1.59×10^{-6}	0.74
	E-Unit	4.0×10^{-12}	4.0×10^{-13}	0.1	0.08	300	1200	1.0×10^{-10}	1.59×10^{-6}	0.74
	D-Unit	1.0×10^{-10}	1.0×10^{-11}	0.1	0.03	300	1200	1.0×10^{-10}	1.33×10^{-6}	0.88
	B&C Units	4.0×10^{-12}	4.0×10^{-13}	0.1	0.08	300	1200	1.0×10^{-8}	1.18×10^{-4}	1.00
	B Anhydrite-Salt	1.0×10^{-13}	1.0×10^{-13}	1.0	0.08	300	1200	1.0×10^{-10}	1.59×10^{-6}	0.74
	A2-Carbonate	1.0×10^{-10}	1.0×10^{-11}	0.1	0.08	300	1200	1.0×10^{-10}	1.59×10^{-6}	0.74
	A2 Anhydrite-Salt	1.0×10^{-13}	1.0×10^{-13}	1.0	0.08	300	1200	1.0×10^{-10}	1.59×10^{-6}	0.74
	A1-Carbonate	2.0×10^{-12}	2.0×10^{-13}	0.1	0.08	300	1200	1.0×10^{-10}	1.59×10^{-6}	0.74
	A1-Evaporite	1.0×10^{-13}	1.0×10^{-13}	1.0	0.08	300	1200	1.0×10^{-10}	1.59×10^{-6}	0.74
	Niagaran	1.0×10^{-7}	1.0×10^{-8}	0.1	0.08	300	1200	1.0×10^{-10}	1.59×10^{-6}	0.74
	Fossil Hill	2.0×10^{-11}	2.0×10^{-12}	0.1	0.08	300	1200	1.0×10^{-10}	1.59×10^{-6}	0.74
	Cabot Head	2.0×10^{-12}	2.0×10^{-13}	0.1	0.03	300	1200	1.0×10^{-8}	1.18×10^{-4}	1.00
	Manitoulin	1.5×10^{-12}	1.5×10^{-13}	0.1	0.01	300	1200	1.0×10^{-10}	1.23×10^{-6}	0.96
Ordovician	Queenston	1.3×10^{-11}	1.3×10^{-12}	0.1	0.11	300	1200	1.0×10^{-8}	1.18×10^{-4}	1.00
	Georgian Bay/Blue Mtn.	9.1×10^{-12}	9.1×10^{-13}	0.1	0.11	300	1200	1.0×10^{-8}	1.18×10^{-4}	1.00
	Cobourg	9.6×10^{-12}	9.6×10^{-13}	0.1	0.02	300	1200	1.0×10^{-10}	1.28×10^{-6}	0.92
	Sherman Falls	9.0×10^{-12}	9.0×10^{-13}	0.1	0.02	300	1200	1.0×10^{-10}	1.28×10^{-6}	0.92
	Kirkfield	1.4×10^{-11}	1.4×10^{-12}	0.1	0.02	300	1200	1.0×10^{-10}	1.28×10^{-6}	0.92
	Coboconk	5.2×10^{-11}	5.2×10^{-12}	0.1	0.02	300	1200	1.0×10^{-10}	1.28×10^{-6}	0.92
	Gull River	3.6×10^{-11}	3.6×10^{-12}	0.1	0.02	300	1200	1.0×10^{-10}	1.28×10^{-6}	0.92
	Shadow Lake	8.0×10^{-12}	8.0×10^{-13}	0.1	0.01	300	1200	1.0×10^{-10}	1.23×10^{-6}	0.96
Cambrian	Cambrian	3.0×10^{-6}	3.0×10^{-7}	0.1	0.01	300	1200	1.0×10^{-10}	1.23×10^{-6}	0.96
Precambrian	Precambrian	8.0×10^{-12}	8.0×10^{-13}	0.1	0.01	300	1200	1.0×10^{-10}	1.23×10^{-6}	0.96

clearly showing the effect of higher rock compressibilities. In comparing Scenario 4 to Scenario 2, the effect of a different loading efficiency is removed due to setting $\zeta = 0$ for both paleoclimate simulations, hence the effect of a change in storage coefficient on the flow system, due to an alternate choice of one-dimensional vertical rock compressibilities, is of interest in this section.

Freshwater head plots are shown in Figures K.1 to K.6, and environmental head plots are shown in Figures K.7 to K.12. A noticeable difference in freshwater heads is seen when comparing Figure K.3 to Figure I.3 at −40 ka. A zone of higher head coinciding with the lower permeability units of the Upper Silurian is clearly visible; two units in the Upper Silurian, the F-Unit and B&C-Units have very high storage coefficients, allowing high residual heads caused by glacial loading to persist over time. At present time, the environmental head plots of Figures K.5 and K.6 show high residual heads being retained within the Upper Silurian after the glacial advance which began at −24 ka. Vertical profiles of environmental heads at the DGR location are shown in Figure 5.36a and Figure 5.36b.

These environmental head profiles are markedly different from those of Figure 5.34a and Figure 5.34b. The Silurian and Ordovician units behave quite differently: in Scenario 2, the applied Dirichlet hydraulic boundary condition is able to propagate to depth as a change in environmental head throughout the vertical profile, while in Scenario 4, the change in environmental head only occurs within the Silurian units; the Ordovician units are essentially unaffected in Scenario 4. The elevated environmental heads at the end of the paleoclimate simulation in Figure 5.36 are clearly visible in the Upper Silurian. During the 120 ka simulation, significant variations in environmental head occur in the Niagaran Group and among the shallowest of the Silurian units, while the deeper units of the Upper Silurian show a lag in responding to the glacial loading during the early stages of glacial advancement, but show a higher environmental head after deglaciation has occurred.

Pore water velocity magnitudes are presented in Figure K.13 to Figure K.18, and the ratio of vertical pore velocities to pore velocity magnitudes are presented in Figure K.19 to Figure K.24. Pore water velocities are generally higher in the Silurian and Ordovician units when compared to the Scenario 2 figures. At the present time, in Figures K.17 and K.18, the higher velocity regions surround the Niagaran Group, shown in red due to high pore water velocity magnitudes resulting from its high permeability. The Precambrian portion of the domain, however, has lower pore water velocities than in Scenario 2, also demonstrating that the glacially induced changes in the surface hydraulic boundary condition do not propagate to depth to the same degree as in Scenario 2. The direction of gradients is significantly different between Scenario 2 and Scenario 4. In Scenario 2, most gradients are upward, as shown in Figure I.15 to Figure I.18, while in Scenario 4, most gradients are downward as shown in Figure K.15 to Figure K.18. The divergence in gradient directions, occurs in the high head region in the Upper Silurian, which has been able to store the high heads generated by the glacial loading due to its high storage coefficient; these high heads are dissipating both upward towards the surface, and downward towards the Niagaran Group. The plots of vertical pore water velocity in the Cobourg Formation at the DGR location are shown Figure 5.30, and clearly show that the velocity is slightly downward. It also shows that glacially induced loading does not appear to measurably change the vertical velocity at depth, unlike Scenario 2 which shows both upward and downward flows. Higher storage coefficients resulting from high rock compressibilities

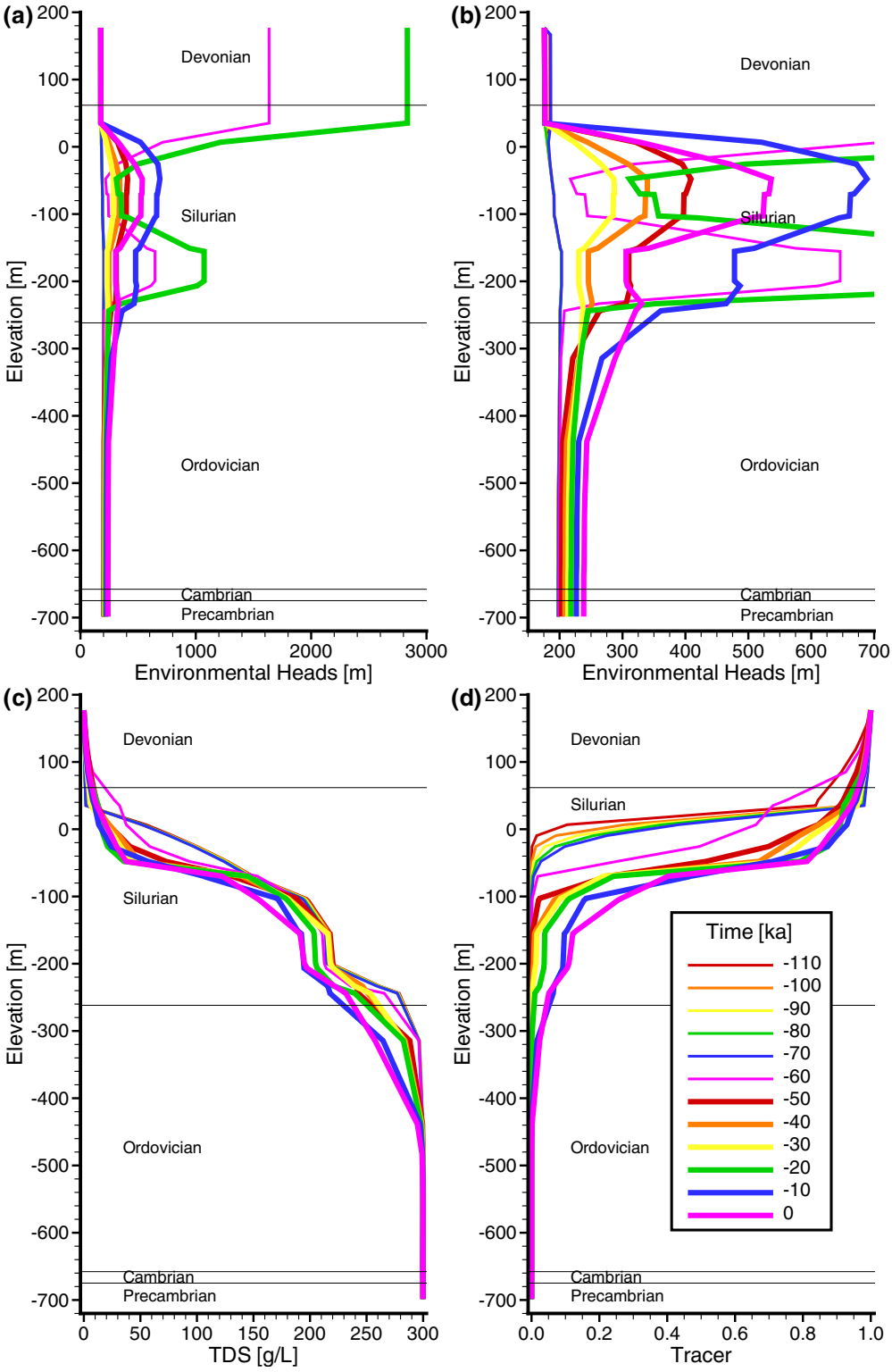

Figure 5.36 Vertical profiles every 10 ka for Scenario 4 paleoclimate simulation at DGR location: (a) and (b) environmental heads; (c) total dissolved solids; and (d) tracer concentrations.

certainly affect the deeper flow system, even though the highly compressible layers are closer to ground surface.

Brine concentrations are presented in Figure K.25 to Figure K.30, and are somewhat different from the Scenario 2 brine concentrations, in that the brine concentration gradient is smaller in Scenario 4. The brine concentration for a vertical profile at the DGR location is shown in Figure 5.36c. Comparing Scenario 2 to Scenario 4, the brine concentration is less throughout the Silurian units and the Upper Ordovician at the end of the paleoclimate simulation. This can be attributed, in part, to the longer duration of downward pore water velocities in the modelling domain.

Tracer concentrations for the modelling domain are presented in Figure K.31 to Figure K.36. The vertical depth of tracer migration is noticeably greater for Scenario 4 as compared to Scenario 2 (see Figure I.35 and Figure I.36). A vertical profile of the tracer concentration, representing the fraction of recharge water, at the DGR location is shown in Figure 5.36d; depth of tracer migration is also greater when compared to Figure 5.34d. A significant movement of the tracer occurs during the first glaciation advance, starting at −63 ka, as shown by the separation between the −70 ka line and the −50 ka line. Further indication of this is shown in Figure 5.31, where the 5% and 50% tracer concentrations strongly advance deeper during both glacial loading events beginning at −63 ka and −24 ka. The 5% tracer is able to migrate to the top of the Ordovician units at the DGR location.

For Scenario 4 in Figure 5.32d, the infiltration rate is very similar to Scenario 2 in Figure 5.32b, however, the effect of the higher storage coefficients can be seen as increased infiltration during the advancing portion of glaciation. In terms of net fluxes between Scenario 2 and Scenario 4, the amplitude of the fluxes in Figure 5.33d as compared to Figure 5.33b is much greater in Scenario 4 due to the much larger storage coefficients which allow more water into the system during glacial loading, and correspondingly, allow more water out of the system during glacial unloading.

The mean life expectancy plots of Figure J.37 and Figure J.38, calculated using the present day velocity distribution and assuming no further change in velocities, at the location of the proposed DGR. The MLE at the bottom of the Cobourg Formation for the DGR location is approximately 2.61 Ma, somewhat less than the MLE calculated for Scenario 1 of 3.82 Ma. The deeper portions of the flow domain, including the Precambrian and portions of the Ordovician units, have MLEs between 10 Ma and 100 Ma, while the Silurian has shorter MLEs in Figure K.37 when compared to Figure I.37 of Scenario 2.

5.6 Summary

This chapter has explored the sensitivity of paleoclimate simulations to the one-dimensional vertical compressibility, one-dimensional loading efficiency, and storage coefficients. Performance measures included heads, pore water velocities, mean life expectancy and the migration of glacial meltwater represented as a tracer of unit concentration for the Michigan Basin Regional model.

A total of three models were required for each paleoclimate simulation. A steady-state model was developed to simulate freshwater heads. These freshwater heads were adjusted to account for an initial TDS distribution. Both the adjusted freshwater heads and initial TDS distribution were applied as the initial conditions for the 1 Ma transient simulation;

this was necessary to allow the initial TDS distribution to equilibrate with the flow system to achieve a pseudo steady-state groundwater flow system. Finally, the output from this model was used as the initial conditions for the paleoclimate simulations.

Glaciation and deglaciation imparts a significant stress onto the geosphere. The boundary conditions applied in the paleoclimate simulations resulted from the mechanical load on the geosphere by the ice thickness and lake depth. Permeability reduction due to permafrost was also applied. Data for the depth of permafrost, along with ice thickness, and lake depth, were provided by the University of Toronto Glacial Systems Model (*Peltier*, 2008).

The one-dimensional loading efficiency can significantly change the insitu pore pressure distribution, as shown in comparing the various paleoclimate scenarios in this chapter. Vertical gradients occur due to the difference between the hydraulic boundary condition at ground surface (equal to the pressure at the base of an ice-sheet) and the insitu increase in heads generated due to hydromechanical coupling. This research has shown that large vertical gradients are created when hydromechanical coupling is neglected (one-dimensional loading efficiency $\zeta = 0$) and a hydraulic surface boundary condition equal to ice-sheet base pressure is applied. Significant migration of surface waters can occur to depth when influenced by these high downward gradients, depending on the permeability of the porous media. Setting $\zeta = 1$ results in a nearly instantaneous response in pore pressures at depth, thereby reducing vertical gradients significantly and mitigating the downward migration of surface waters, as characterized by a unit tracer. Alternate implementations of surface boundary conditions will change vertical gradients and their directions, thereby affecting tracer migration. Using conventional groundwater flow models that do not account for hydromechanical coupling, especially in paleoclimate simulations, can lead to improperly characterizing paleoclimate influences at depth.

The one-dimensional loading efficiency ζ, assuming lateral strains are zero, depends upon the compressibilities of the rock matrix and of the pore fluid. These compressibility values can be obtained from laboratory studies of field samples, or by using representative literature values. Scenario 4 demonstrates the effects of high storage coefficients, resulting from high rock compressibility values. Larger storage coefficients lead to elevated pressures, however, these pressures are not able to propagate to significant depth. In the lower storage coefficient paleoclimate simulations of Scenarios 1 to 3, elevated pressures during glacial advance or retreat were propagated to depth, but did not persist in the subsurface to the extent demonstrated in Scenario 4. It is important to use compressibility values that are representative of site conditions.

The mean life expectancies at the DGR location for the various paleoclimate scenarios are shown in Table 5.6. The choice of one-dimensional loading efficiency clearly affects this performance measure. Based on the paleoclimate simulations conducted for this thesis, a higher one-dimensional loading efficiency leads to greater MLE values, due to decreased gradients. The changes to the flow system over the course of a paleoclimate simulation also influence the MLE. *Sykes et al.* (2008) calculate MLE values for various scenarios based on the velocity distribution at the end of the 1 Ma pseudo steady-state simulations; the base-case parameters yielded an MLE value of 8.9 Ma. The DGR location MLE value for Scenario 3 is similar, likely due to less perturbation of flow gradients, when $\zeta = 1$. The lower storage coefficient for Scenario 3 also allowed the groundwater system to more quickly approach the pseudo equilibrium state after glacial retreat. Since MLE is

only implemented in FRAC3DVS-OPG for steady-state flow systems, the velocity field at the end of the paleoclimate simulations is used for the MLE calculations. The evolution of the groundwater flow system toward a steady-state condition following a paleoclimate episode is not captured in the MLE values of Table 5.6.

Table 5.6 Summary of MBR paleoclimate simulation MLE values at the bottom of the Cobourg Formation for the DGR location.

Paleoclimate Simulation	MLE [Ma]
Scenario 1	3.82
Scenario 2	2.12
Scenario 3	8.86
Scenario 4	2.61

Finally, the overpressures in the Cambrian Formation and the underpressures in the Ordovician sediments are not explained by the paleoclimate simulations undertaken in this thesis. For the simulations in this chapter, FRAC3DVS-OPG is used to model fully saturated flow and transport conditions. The likely presence of a gas phase in the Ordovician sediments would require the use of a multi-component and multi-phase numerical model. The use of FRAC3DVS-OPG at this stage is appropriate given that field and laboratory investigations, related to these abnormal pressures, are currently ongoing by the NWMO.

Chapter 6

Conclusions

Nuclear power generation is being regarded as a solution to ever increasing demand for electricity, and concerns over global warming and climate change due to the use of fossil fuels; a large portion of which are used to generate electricity throughout the world. Although nuclear power generation is considered to be reliable, economical, clean, and safe, the wastes produced from the nuclear fuel cycle are not, and can remain hazardous for hundreds of thousands of years.

An international consensus has developed over the past several decades that deep geologic disposal of low, intermediate, and high level radioactive wastes is the best option to protect the biosphere over hundreds of thousands of years. Canada has also chosen deep geologic disposal as the preferred alternative for long-term disposal of nuclear fuel waste. The Nuclear Waste Management Organization (NWMO) is mandated by the Nuclear Fuel Waste Act (NFWA) in Canada to provide recommendations to the Government of Canada on the long-term management of used nuclear fuel. The deep disposal concept of the NWMO includes suitable sedimentary basins as well as crystalline rock settings.

Various studies were completed in the mid-1990's in Canada to investigate the technical feasibility of the used nuclear fuel disposal concept for Canada and its impact on human health and the environment. These studies were limited in spatial and temporal extent, with simulations typically 10 ka in duration. This thesis investigated the role of glaciation/deglaciation cycles, hydrologic features, topography, and matrix/fracture characterization, over 100 ka timescales, on the evolution and migration of pore fluids in

deep geologic settings. The numerical models FRAC3DVS, and FRAC3DVS-OPG were an essential component of this research, and were used throughout.

A total of three models were required for each paleoclimate simulation, for both the Canadian Shield Sub-Regional and Michigan Basin Regional paleoclimate simulations. A steady-state model was developed to simulate freshwater heads. These freshwater heads were adjusted to account for an initial total dissolved solids (TDS) distribution. Both the adjusted freshwater heads and initial TDS distribution were applied as the initial conditions for the 1 Ma transient simulation; the modelling procedure was necessary to allow the initial TDS distribution to equilibrate with the flow system to achieve a pseudo steady-state density-dependent groundwater flow system. Finally, the output from this model was used as the initial conditions for the paleoclimate simulations.

Glaciation and deglaciation imposes a significant stress onto the geosphere. The boundary conditions applied in the paleoclimate simulations resulted from the mechanical load imparted on the geosphere by ice thickness, and lake depth. The effects of this hydromechanical coupling upon a deep groundwater flow system can be profound. Permeability reduction due to permafrost was also applied. Data for the depth of permafrost, along with ice thickness, and lake depth, were provided by the University of Toronto (UofT) Glacial Systems Model (GSM) (*Peltier*, 2006, 2008).

A FRAC3DVS regional scale model was developed and compared to a SWIFT-III based 5734 km^2 regional model. FRAC3DVS was ultimately selected as a replacement for SWIFT-III due to its capabilities and advanced state of development as compared to SWIFT-III. The regional model then formed the basis upon which a more detailed sub-regional model, on the scale of the original Atomic Energy of Canada Limited (AECL) Environmental Impact Statement (EIS) and Second Case Study (SCS) case studies.

The Phase-I sub-regional model was selected from a portion of the larger regional scale domain developed in Chapter 3. Since a crystalline rock setting was desired, software was developed to map a stochastically generated triangulated fracture network model (FNM) onto a FRAC3DVS hexahedral element mesh, using quadrilateral elements to represent fracture zones.

The Phase-II model development was initiated to address various issues that arose while developing and working with the Phase-I model. Issues included the characterization of the surface boundary conditions for the model, and the use of a uniform hydraulic conductivity for fracture zones. Numerous improvements were made, particularly in the characterization of fracture properties, namely, fracture zone permeability, fracture zone porosity, and fracture zone width.

The third phase of development involved paleoclimate simulations, comprised of seven scenarios, whereby certain parameters were modified, or ignored to determine their impact relative to a base-case analysis. The key parameters of interest included: alternate glaciation scenarios, selecting between uniform fracture zone permeability, or a median variation in permeability as a function of depth, various values for the one-dimensional load efficiency ζ, and including or excluding coupled density-dependent flow and transport. Various performance measures were used in characterizing the scenario comparisons, including: freshwater and environmental water heads, pore water velocity magnitudes and directions, TDS distributions, unit tracer migration, and mean life expectancy.

For the Michigan Basin Regional model, this thesis has explored the sensitivity of paleoclimate simulations to the one-dimensional vertical compressibility, and one-dimensional loading efficiency. Performance measures included heads, pore water velocities, mean life expectancy and the migration of glacial meltwater represented as a tracer of unit concentration for the Michigan Basin Regional model.

6.1 Development of Methods and Tools

Various methodologies and software were developed during the course of this research and are summarized below:

- Prior modelling efforts in a Canadian Shield setting were limited to areas of approximately 700 km^2 over a 10 ka period. The research described in this thesis has extended the modelling domain to thousands of square kilometres, over paleoclimate timescales of 120 ka.
- A detailed comparison of SWIFT-III and FRAC3DVS was performed to determine the suitability of using FRAC3DVS for coupled density-dependent flow and transport in deep geologic settings. Several performance measures were developed as the basis of comparison. The computational points for the SWIFT-III finite-difference grid and the FRAC3DVS finite-element grid needed to coincide for a valid comparison to be made.
- Models of high spatial resolution, including fracture zone networks, were developed for a representative crystalline rock setting in the Canadian Shield. A sedimentary basin model was also developed that was centred on a proposed Deep Geologic Repository (DGR) for low & intermediate level waste (L&ILW) at the Bruce Nuclear Power Development (BNPD) site in the Municipality of Kincardine, Ontario.
- A methodology was developed and software was written in Visual Basic for Applications (VBA) to calculate the orthogonal grid block or element faces that best represent curve-planar FNM fractures. The procedure used to generate the orthogonal FNM from a triangulated FNM is listed in §4.1.3.
- Using specified head boundary conditions equal to surface topography can lead to flux artifacts resulting from the digital elevation model (DEM) which defines topographic elevations.
- Since rivers can form along fractures zones, the choice of watershed boundary for the modelling domain must take this into consideration. In this thesis, the modelling extents for the sub-regional model were expanded to account for fracture zones coincident with discharge features such as rivers.
- Expressions for depth-dependent horizontal and vertical permeabilities were developed based on data from the Whiteshell Research Area (WRA) site.
- A cumulative density function (CDF) and probability density function (PDF) were developed for fracture zone permeability as a function of depth based on data from the WRA and Finnish Olkiluoto sites.
- A log-normal PDF for fracture zone width was developed based on data from the WRA site.
- A methodology was demonstrated to "boot-strap" the paleoclimate simulations by first running a steady-state simulation without TDS. Results from the steady-state model were used as initial conditions, after accounting for an initial TDS distribution,

for a 1Ma pseudo steady-state density-dependent simulation to allow the flow system to equilibrate. Freshwater heads and TDS distributions from the pseudo steady-state model are used as the initial conditions for the paleoclimate simulations.
- Develop an expression for TDS distribution as a function of depth based on the work of *Frape and Fritz* (1987).
- Development of pre and post-processors for translating the UofT GSM modelling outputs of lake depth, permafrost depth, and ice thickness for use in FRAC3DVS-OPG.

6.2 Modelling Assumptions and Limitations

Numerical modelling studies, such as those carried out in the course of this thesis, are subject to various assumptions and limitations. Due to the complex subsurface environment, coupled multi-physics processes, long time scales, and limited data for model validation, the following assumptions and limitations are listed:

- Viscosity is constant and is not adjusted to account for changes in TDS concentration. Increased TDS brine concentrations increase viscosity by several factors and reduce pore fluid mobility.
- Fracture properties do not change over time and mechanical effects due to glaciation are ignored. Permeability reduction in fractures due to permafrost is accounted for.
- Surface topography does not change over the course of a paleoclimate simulation and is unaffected by the advance and retreat of glaciers. It is known that glacial stripping and subglacial flow systems can reshape the landscape.
- Ice-sheet topography exactly mimics ground surface topography and does not change. Since both the Canadian Shield Sub-Regional and the Michigan Basin Regional domains are much smaller than the continental scale paleoclimate simulations of *Peltier* (2002, 2003, 2006, 2008), ice-sheet modelling at a smaller scale would be required to properly assess the ice-sheet topography, and hence its thickness, and resulting effects on the geosphere.
- Surface water divides can be used to represent subsurface divides, even during paleoclimate simulations. These topographic highs and lows are used to choose model domain boundaries and do not change. As mentioned earlier, glacial stripping can affect topography, and hence model boundaries.
- The advancement of a ice-sheet flexes the lithosphere, changing its surface elevation. Isostatic depression due to the weight of an ice-sheet leads to the formation of proglacial lakes upon glacial retreat. The vertical movement and inclination of the geosphere is not considered.
- Lateral strains are assumed insignificant due to the large areal expanse of ice-sheets, however, lateral strains can occur when ice-sheets are advancing and retreating. Fully three-dimensional hydromechanical coupling would be needed to investigate this situation. At this time, FRAC3DVS-OPG can only simulate one-dimensional hydromechanical coupling.
- Grid deformations due to mechanical loading are ignored. Since FRAC3DVS-OPG simulates one-dimensional hydromechanical coupling, grid deformation cannot occur. The resulting effects on fracture zones was not considered.

- Advancement of ice-sheets can create high subsurface pressures which can cause horizontal flow ahead of the ice-sheet. This horizontal flow cannot occur where lateral no-flow boundary conditions are assumed based on topographic divides.

6.3 Research Findings

Various paleoclimate modelling scenarios were developed to determine the effects of changes in parameters and boundary conditions on the subsurface infiltration of a unit tracer representing surface waters, and on mean life expectancy. Both fractured crystalline rock and sedimentary basin settings were used.

The temporal extent of permafrost in the subsurface affected the depth to which a unit tracer migrated, whereby less permafrost cover resulted in increased migration to depth. The unit tracer in Scenario 2 of Chapter 4 migrated to less depth than for Scenario 1; less permafrost cover resulted in increased migration of surface waters to depth. This result is also evident in the plots of infiltration versus time.

Coupled density-dependent flow and transport is also an important process that leads to increased mean life expectancy (MLE) values, however, unit tracer migration was not as influenced. This can be attributed to the unit tracer migrating from the top of the modelling domain downwards, towards waters of higher TDS, while higher MLE values are associated with the deeper portions of the flow system, which are subjected to high TDS waters. The results from Scenario 3 of Chapter 4 showed that dense pore fluids at depth increase MLE values when compared to freshwater groundwater flow systems.

High fracture zone permeabilities, particularly at depth, lead to the greatest changes in the flow system. From the various scenarios in listed in Table 4.3 of Chapter 4, the greatest reduction in MLE values occur with Scenarios 4 and 7, which used high permeabilities for fracture zones throughout the modelling domain. TDS concentrations were also reduced within fractures and in the matrix blocks adjacent to fractures, as compared with the base case analysis of Scenario 1. The depth and extent of unit tracer migration was also greatest when high permeability fracture zones were used. Based on the models developed in this thesis, deep highly conductive fractures can allow significant vertical flow to take place, and allow recharge waters to migrate to depths of more than 1km.

Hydromechanical coupling is a very important mechanism that affects hydraulic gradients within the geosphere when subjected to a glaciation event. The degree of hydromechanical coupling is characterized by the one-dimensional loading efficiency ζ. Vertical gradients occur due to the difference between the hydraulic boundary condition at ground surface (equal to the pressure at the base of an ice-sheet) and the insitu increase in heads generated due to hydromechanical coupling. This research has shown that large vertical gradients are created when hydromechanical coupling is neglected (one-dimensional loading efficiency $\zeta = 0$) and a hydraulic surface boundary condition equal to ice-sheet base pressure is applied. Significant migration of a unit tracer can occur to depth when influenced by these high downward gradients, depending on the permeability of the porous media and fracture zones. Setting $\zeta = 1$ results in a nearly instantaneous response in pore pressures at depth, thereby reducing vertical gradients significantly and mitigating the downward migration of surface waters, as characterized by a unit tracer.

Alternate implementations of surface boundary conditions will change vertical gradients and their directions, thereby affecting tracer migration. Groundwater flow models

which do not include a suitable form of hydromechanical coupling, one-dimensional or otherwise, must be used with caution as very large vertical gradients can be generated, resulting in higher pore water velocities, and enhanced migration of surface waters into the subsurface environment.

The one-dimensional loading efficiency ζ assumes lateral strains are zero, and depends upon both the compressibilities of the rock matrix and of the pore fluid. These compressibility values can be obtained from laboratory studies of field samples, or by using representative literature values. The use of high rock compressibility values results in high storage coefficients, which enhance the retention of elevated insitu pressures caused by glaciation. It is important to use compressibility values that are representative of site conditions.

6.4 Future Research

In general, the assumptions and limitations listed in §6.2 relate to the characterization of the flow system when subjected to paleoclimate conditions. The choice of physics, material properties, boundary conditions, and geometry are subject to available data, and the capabilities of the numerical models. These simulations exist at the extreme end of coupled multi-physics problems and require significant computational resources. Calibration is not performed due to the paucity of site specific field data. In the case of the Michigan Basin Regional model, field data is restricted to a small region in comparison to the scale of the model. Limited field and laboratory data related to the DGR project were available at the time the Michigan Basin Regional model was developed.

Due to the complexity of the geosphere system subjected to paleoclimate conditions, there remains a need for further research. Larger areal domains are required due to the expanse of continental ice-sheets, however, this cannot occur at the expense of spatial discretization. Larger models with three-dimensional hydromechanical coupling can include isostatic adjustment and the stress changes that occur within the geosphere. Higher performance numerical models are needed that can couple the various physics together in an integrated framework. At present, FRAC3DVS-OPG is single threaded; parallelization is an important consideration in this regard. Better coupling between ice-sheets and the geosphere is needed to account for sub-glacial processes and flows of water; this coupling can also improve the hydraulic boundary condition which is specified at the interface between the ice-sheet and the geosphere. The presence of water at the base of an ice-sheet can create high pressure conditions that can drive oxygen enriched waters into the subsurface, depending on the hydromechanical coupling.

Model boundaries are chosen to coincide with topographic highs and bathymetric lows. It is assumed that today's topography is applicable during the course of all simulations, even though glacial stripping can remove material, and reduce surface elevations. The locations of topographic highs and lows are used to define lateral model boundaries; it is assumed that model boundaries do not change during the course of any simulations. These assumptions need to be investigated further as to their effects on subsurface flow, unit tracer migration, and MLE values.

The Michigan Basin Regional model assumes fully saturated conditions, while recent field investigations present the possibility of a gas phase in the Ordovician sediments. In such cases, the modelling of the groundwater flow system would require the use of a multi-component and multi-phase numerical model.

Appendix A

CSSR Scenario 1 Paleoclimate Model

All figures related to the Canadian Shield Sub-Regional (CSSR) Scenario 1 paleoclimate modelling are listed in Table A.1. Block cut view and fence view figures are shown on the same page to facilitate comparison. All results of the 120 ka paleoclimate simulations are shown at times of 80 ka before present, 40 ka before present, and at present.

Table A.1 List of Canadian Shield Sub-Regional Scenario 1 paleoclimate simulation figures.

Parameters	Time Before Present					
	80 ka		40 ka		Present	
	Block Cut	Fence	Block Cut	Fence	Block Cut	Fence
Freshwater Heads	A.1	A.2	A.3	A.4	A.5	A.6
Environmental Heads	A.7	A.8	A.9	A.10	A.11	A.12
Pore Velocity Magnitudes	A.13	A.14	A.15	A.16	A.17	A.18
Ratio of Vertical Pore Velocities to Pore Velocity Magnitudes	A.19	A.20	A.21	A.22	A.23	A.24
Brine Concentrations	A.25	A.26	A.27	A.28	A.29	A.30
Tracer Concentrations	A.31	A.32	A.33	A.34	A.35	A.36
Mean Life Expectancies	—	—	—	—	A.37	A.38

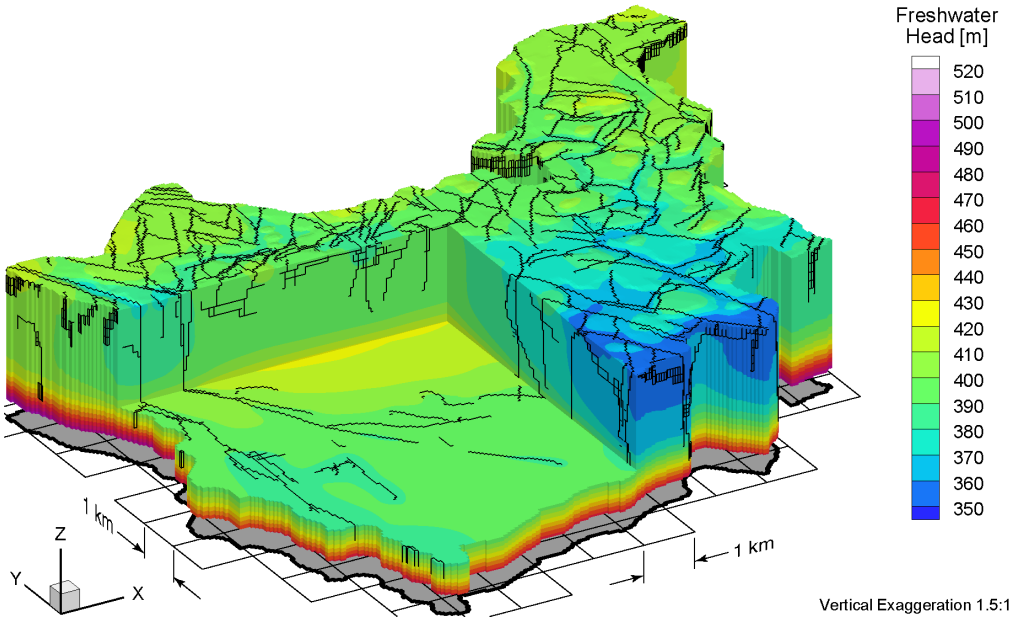

Figure A.1 Block cut view of freshwater heads at 80 ka before present for the Canadian Shield Sub-Regional Scenario 1 paleoclimate simulation.

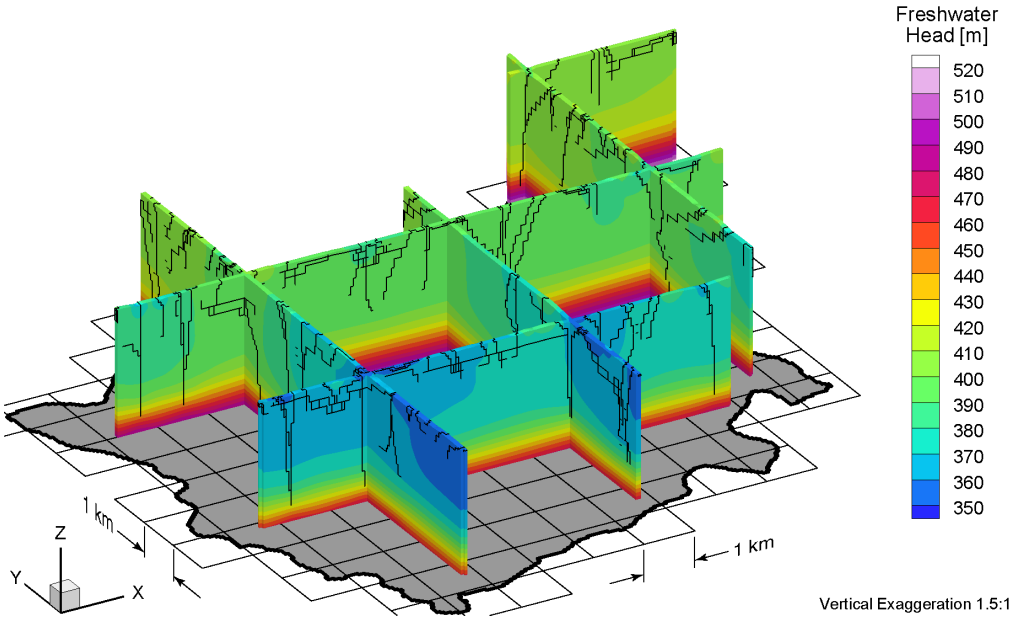

Figure A.2 Fence view of freshwater heads at 80 ka before present for the Canadian Shield Sub-Regional Scenario 1 paleoclimate simulation.

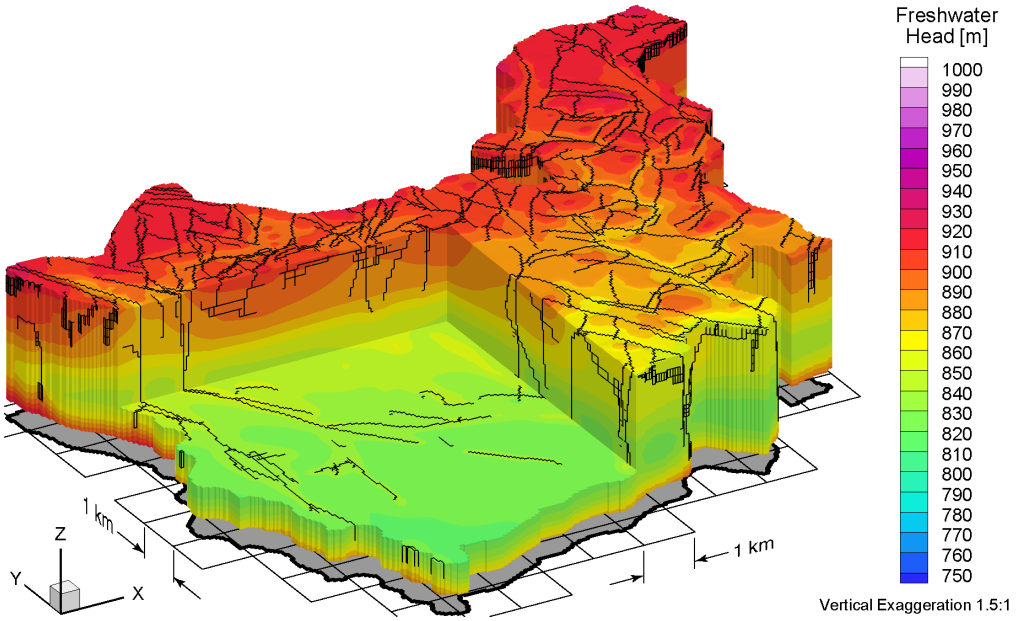

Figure A.3 Block cut view of freshwater heads at 40 ka before present for the Canadian Shield Sub-Regional Scenario 1 paleoclimate simulation.

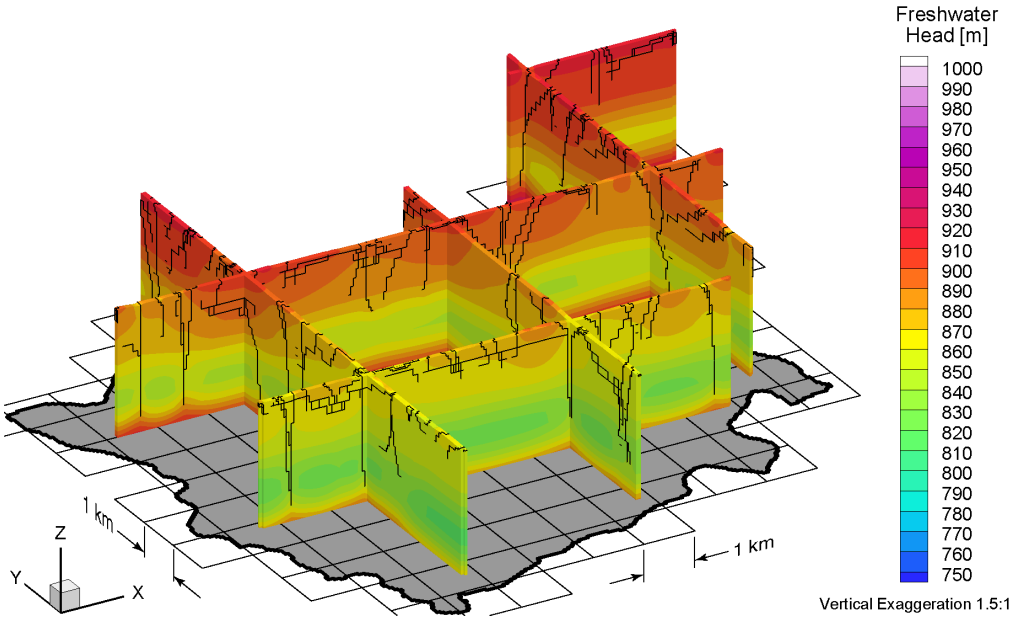

Figure A.4 Fence view of freshwater heads at 40 ka before present for the Canadian Shield Sub-Regional Scenario 1 paleoclimate simulation.

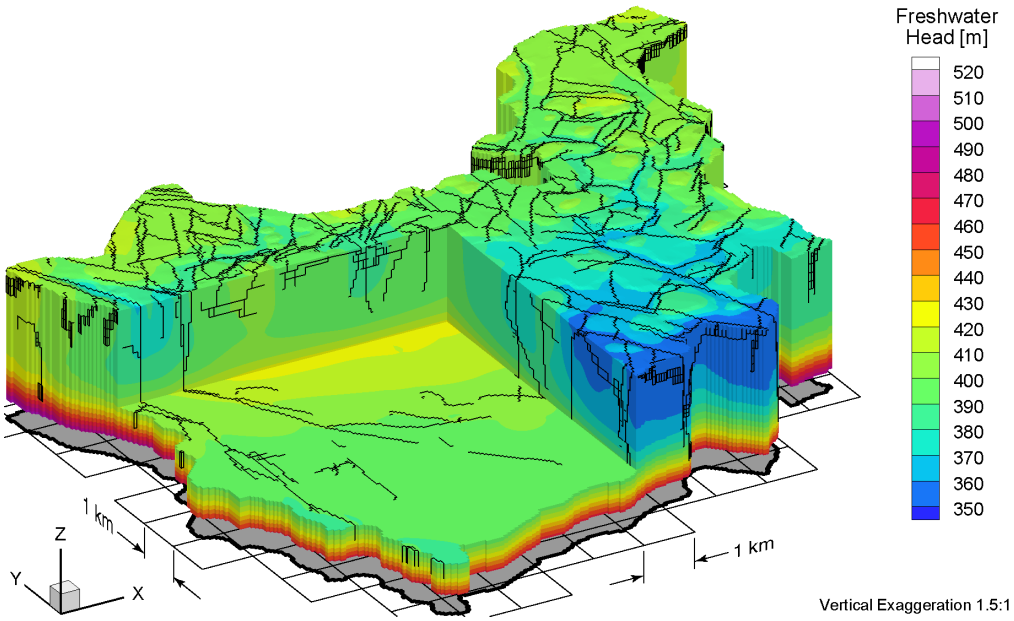

Figure A.5 Block cut view of freshwater heads at present for the Canadian Shield Sub-Regional Scenario 1 paleoclimate simulation.

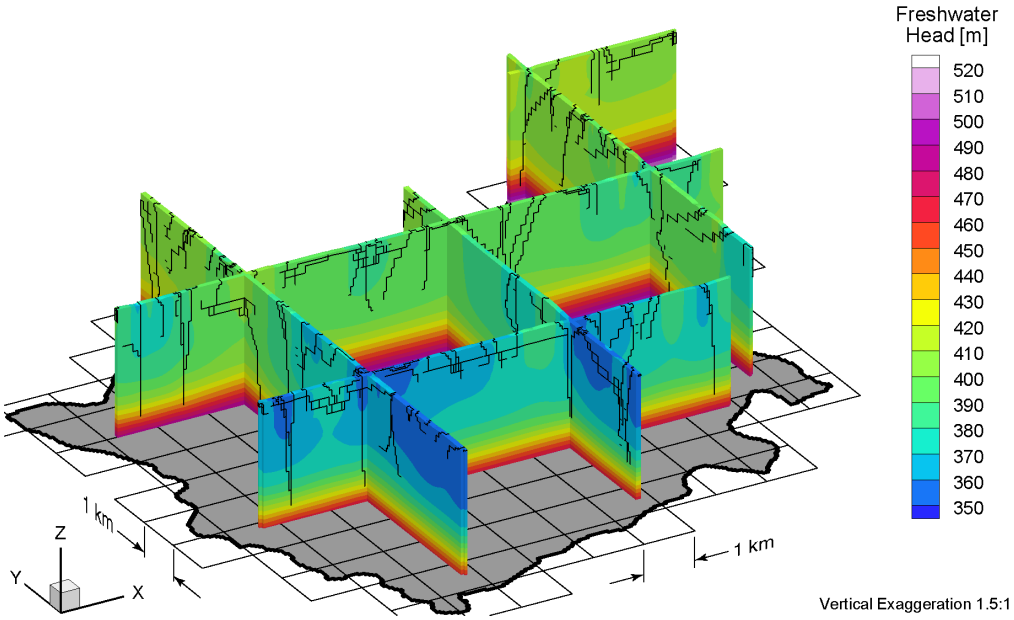

Figure A.6 Fence view of freshwater heads at present for the Canadian Shield Sub-Regional Scenario 1 paleoclimate simulation.

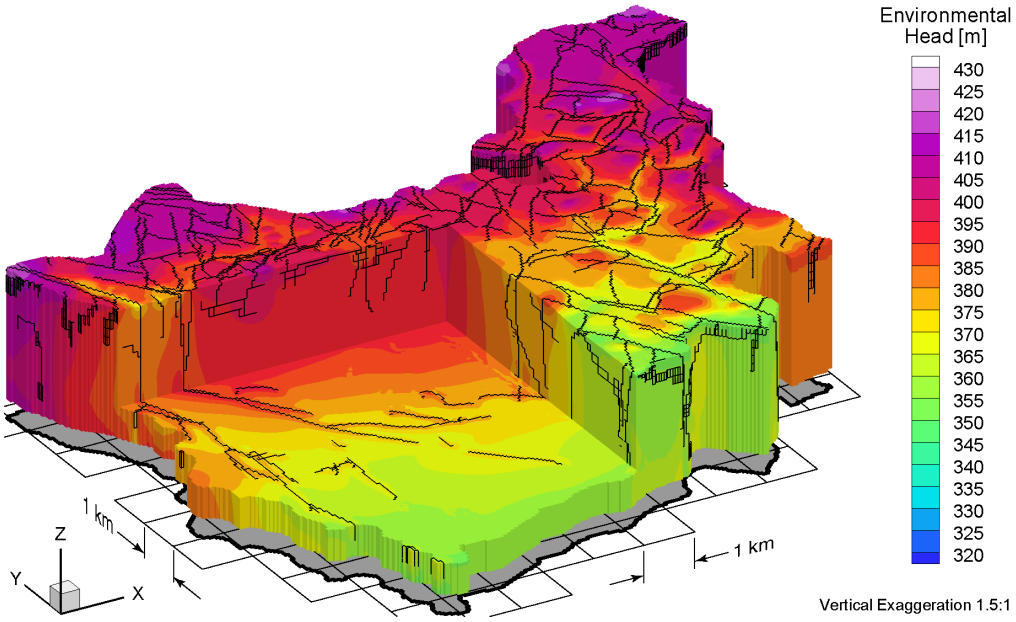

Figure A.7 Block cut view of environmental heads at 80 ka before present for the Canadian Shield Sub-Regional Scenario 1 paleoclimate simulation.

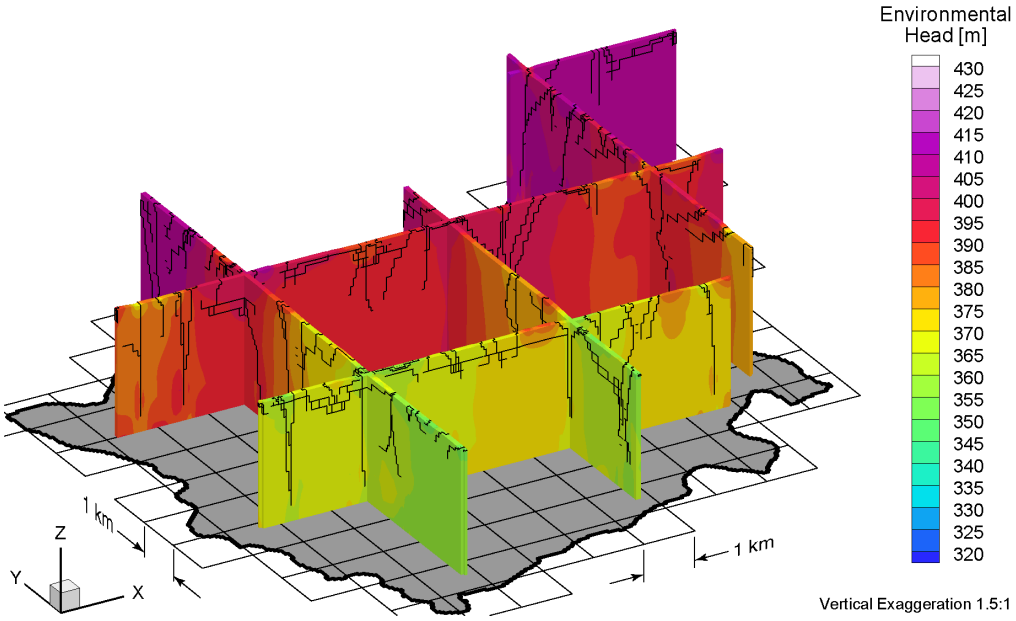

Figure A.8 Fence view of environmental heads at 80 ka before present for the Canadian Shield Sub-Regional Scenario 1 paleoclimate simulation.

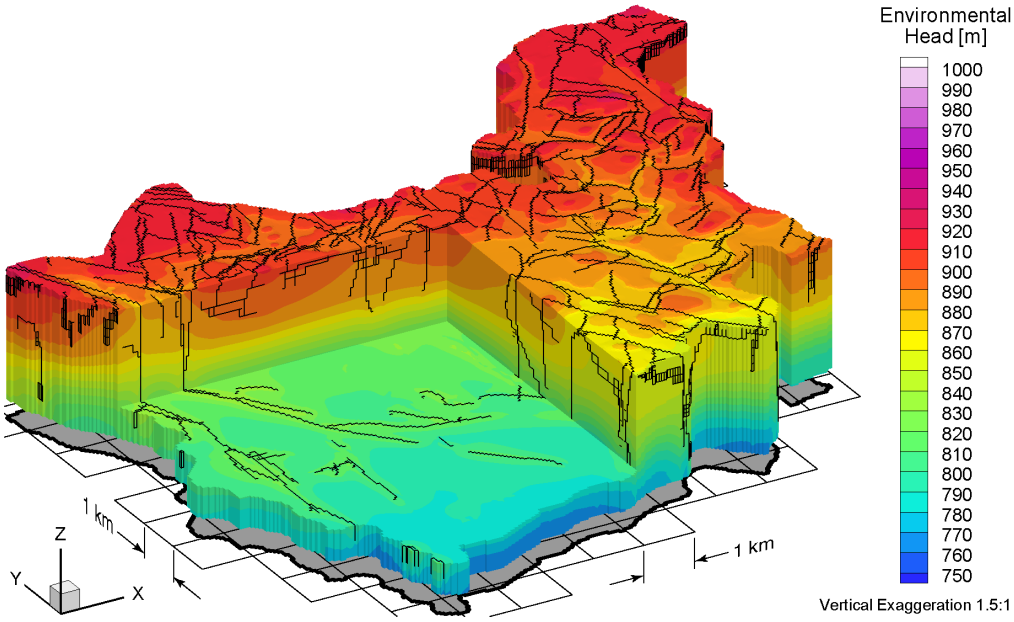

Figure A.9 Block cut view of environmental heads at 40 ka before present for the Canadian Shield Sub-Regional Scenario 1 paleoclimate simulation.

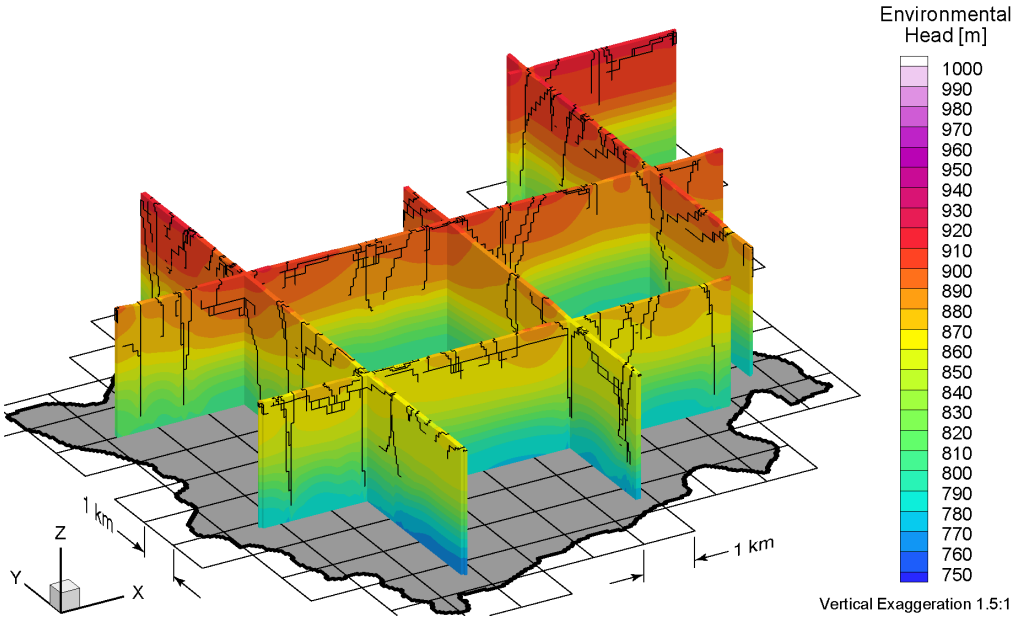

Figure A.10 Fence view of environmental heads at 40 ka before present for the Canadian Shield Sub-Regional Scenario 1 paleoclimate simulation.

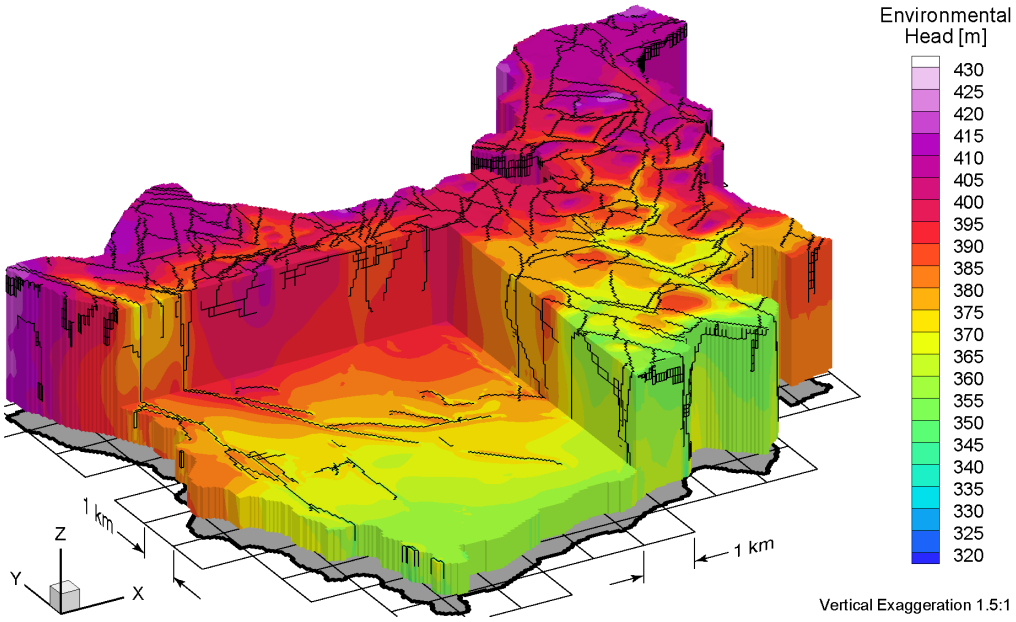

Figure A.11 Block cut view of environmental heads at present for the Canadian Shield Sub-Regional Scenario 1 paleoclimate simulation.

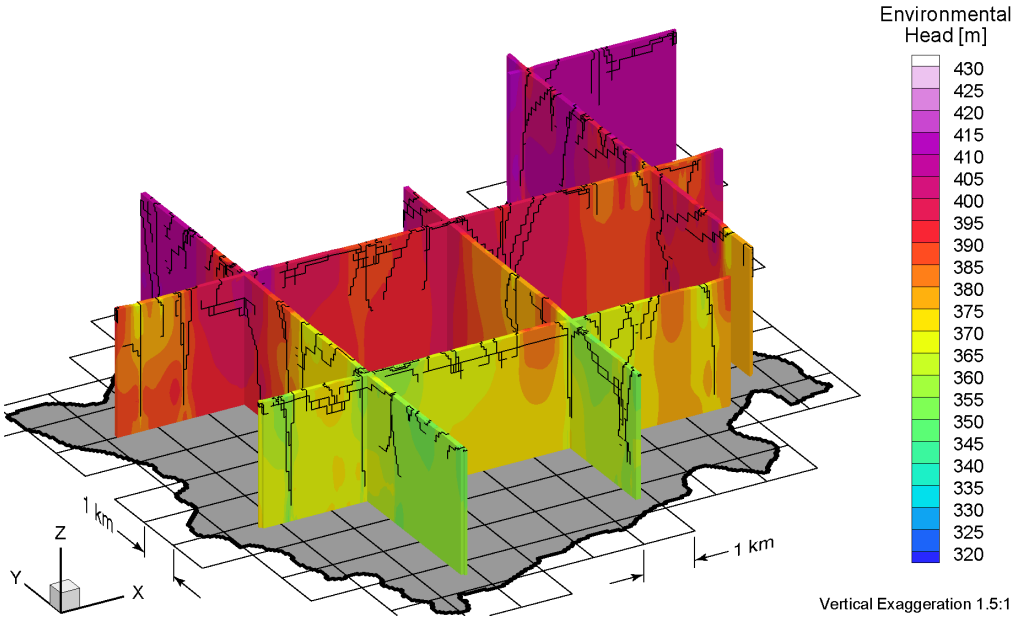

Figure A.12 Fence view of environmental heads at present for the Canadian Shield Sub-Regional Scenario 1 paleoclimate simulation.

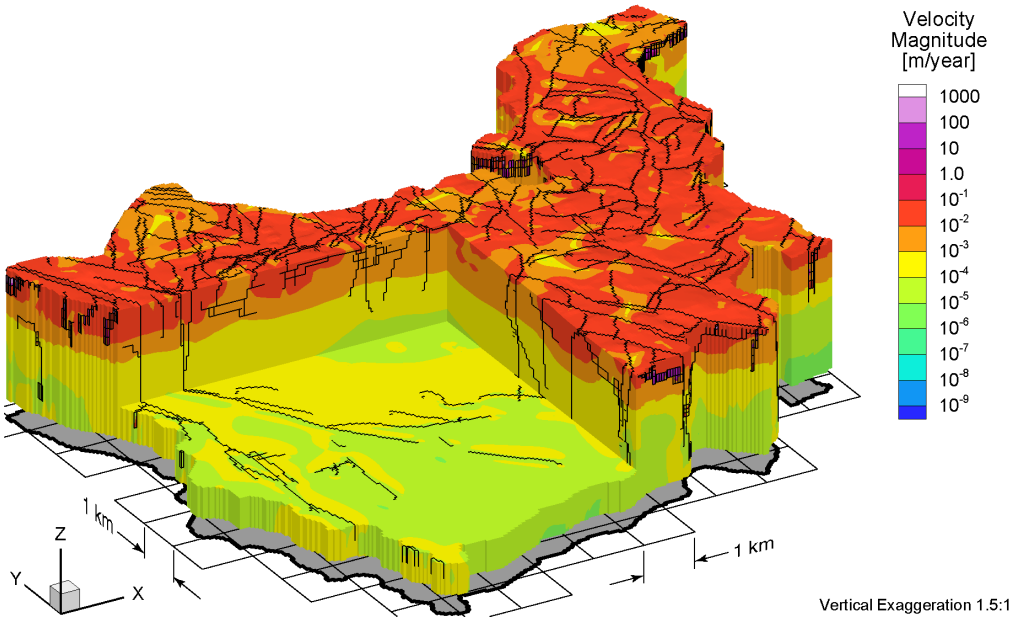

Figure A.13 Block cut view of pore velocity magnitudes at 80 ka before present for the Canadian Shield Sub-Regional Scenario 1 paleoclimate simulation.

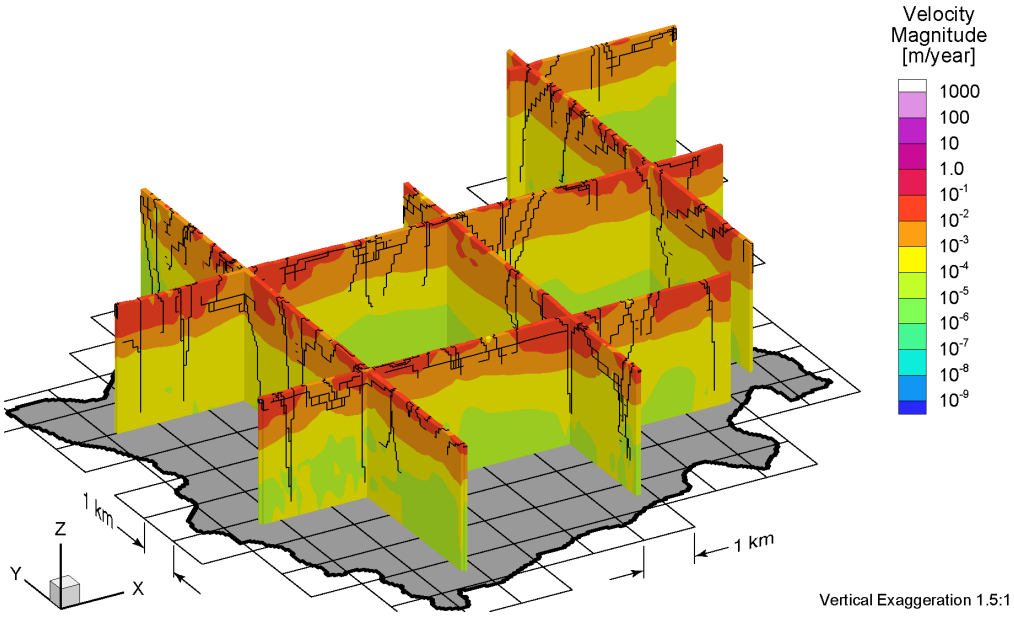

Figure A.14 Fence view of pore velocity magnitudes at 80 ka before present for the Canadian Shield Sub-Regional Scenario 1 paleoclimate simulation.

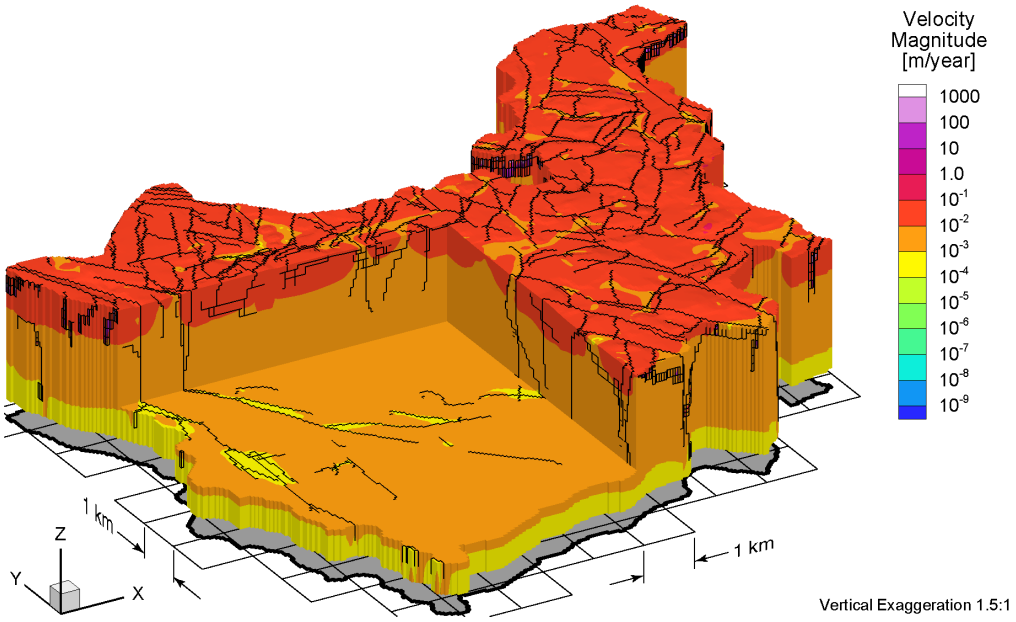

Figure A.15 Block cut view of pore velocity magnitudes at 40 ka before present for the Canadian Shield Sub-Regional Scenario 1 paleoclimate simulation.

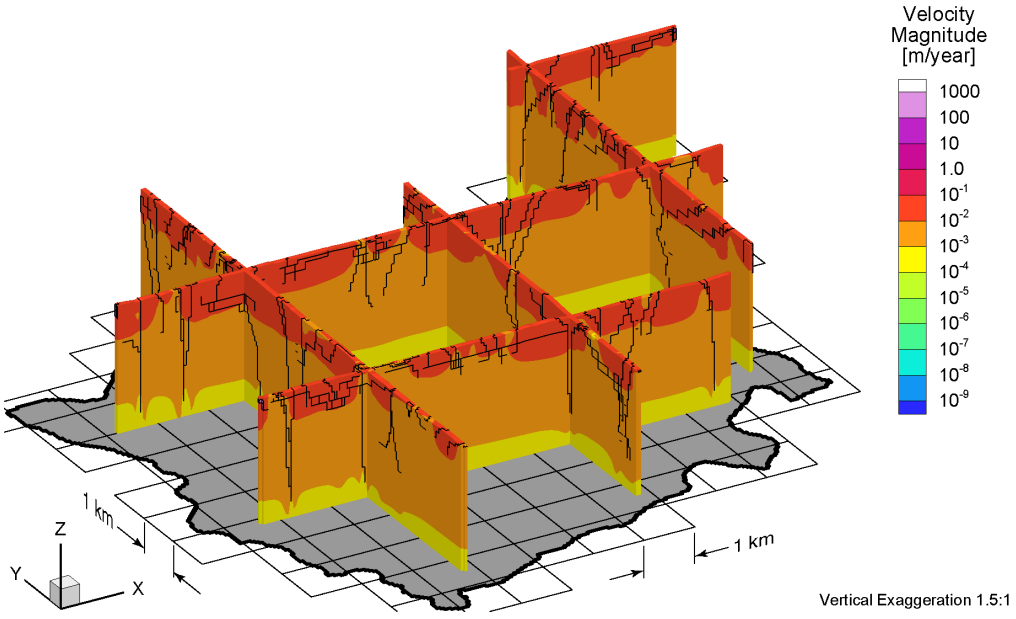

Figure A.16 Fence view of pore velocity magnitudes at 40 ka before present for the Canadian Shield Sub-Regional Scenario 1 paleoclimate simulation.

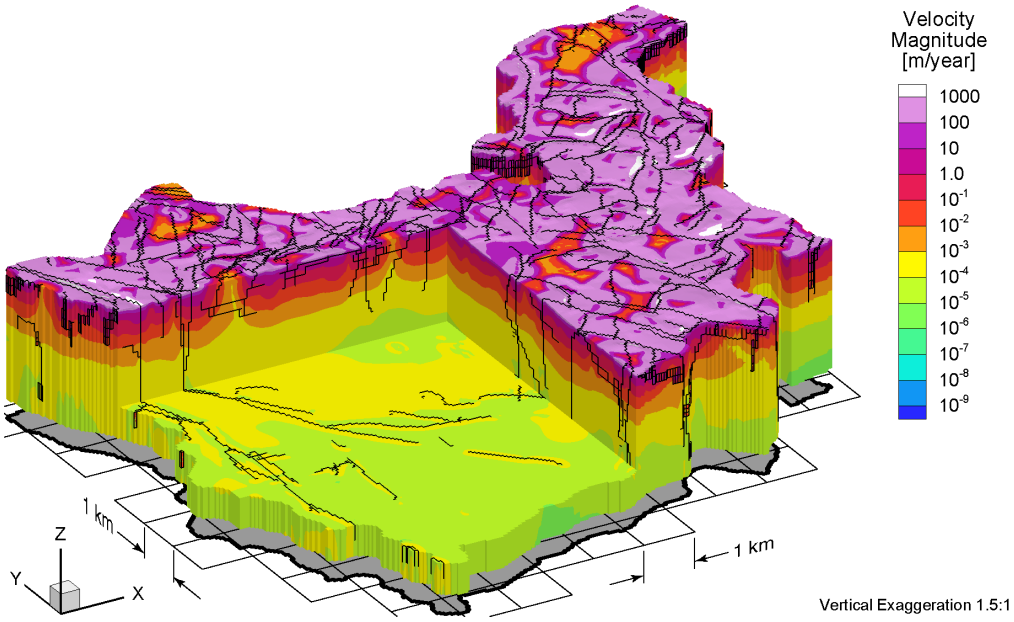

Figure A.17 Block cut view of pore velocity magnitudes at present for the Canadian Shield Sub-Regional Scenario 1 paleoclimate simulation.

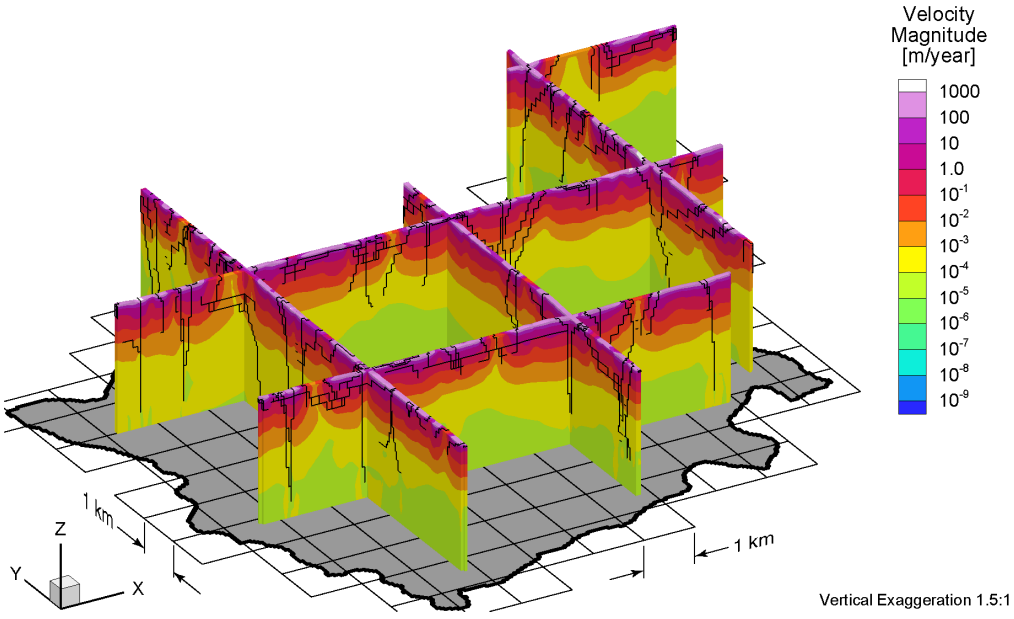

Figure A.18 Fence view of pore velocity magnitudes at present for the Canadian Shield Sub-Regional Scenario 1 paleoclimate simulation.

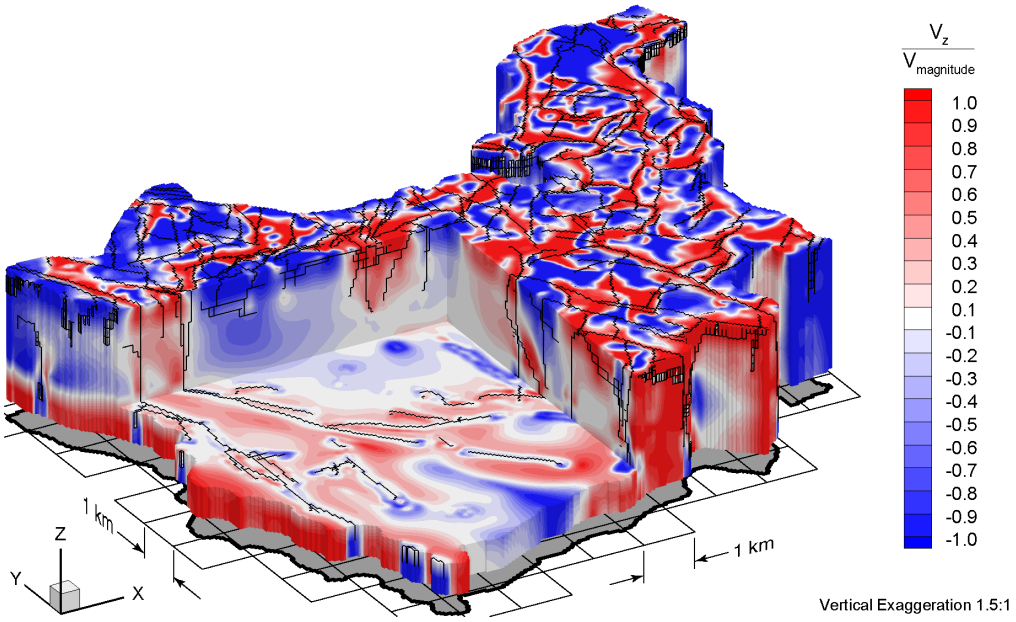

Figure A.19 Block cut view of ratio of vertical pore velocities to pore velocity magnitudes at 80 ka before present for the Canadian Shield Sub-Regional Scenario 1 paleoclimate simulation.

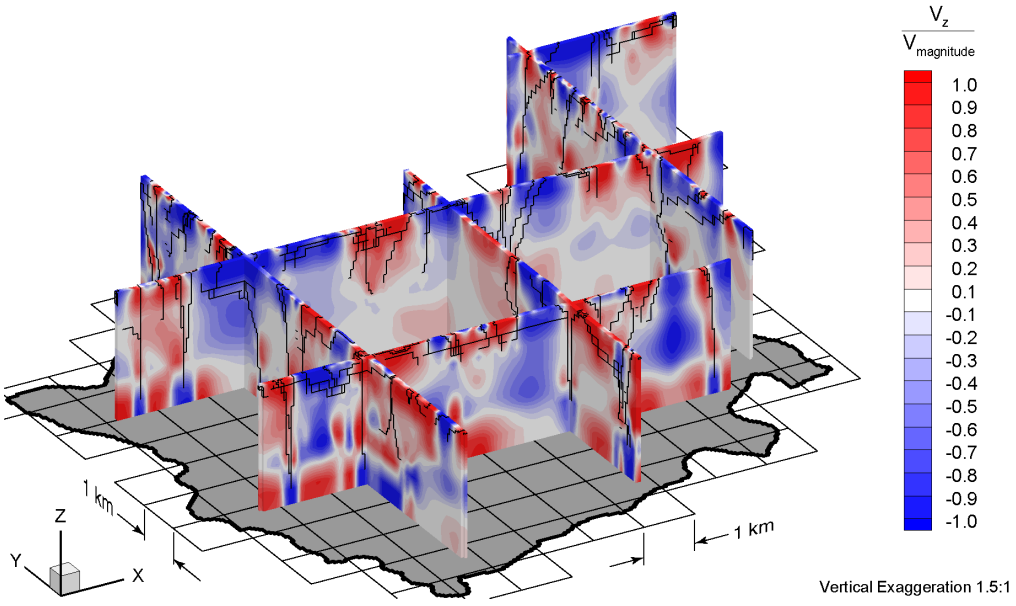

Figure A.20 Fence view of ratio of vertical pore velocities to pore velocity magnitudes at 80 ka before present for the Canadian Shield Sub-Regional Scenario 1 paleoclimate simulation.

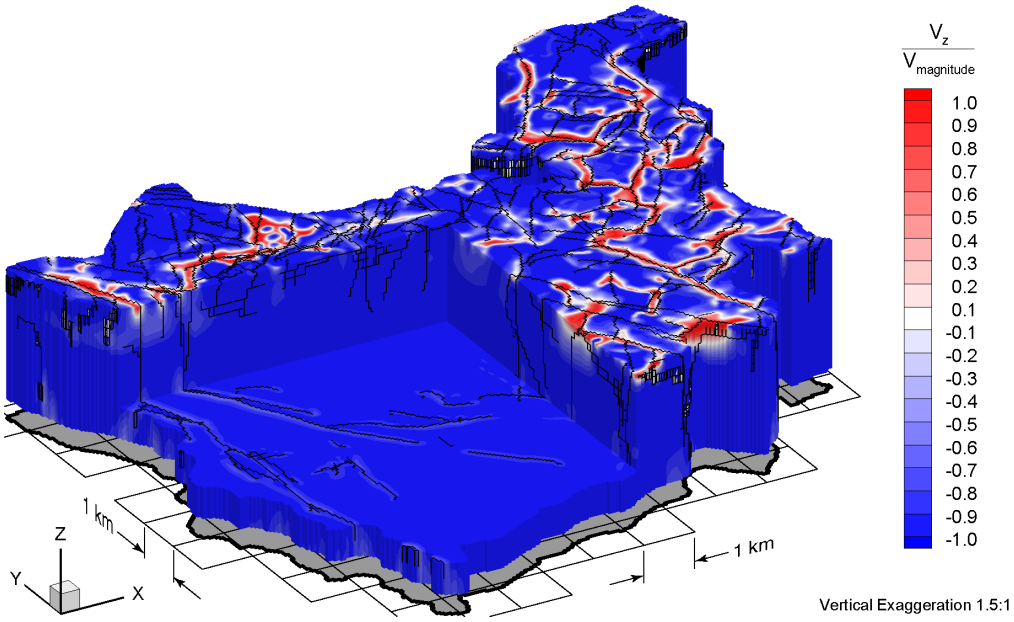

Figure A.21 Block cut view of ratio of vertical pore velocities to pore velocity magnitudes at 40 ka before present for the Canadian Shield Sub-Regional Scenario 1 paleoclimate simulation.

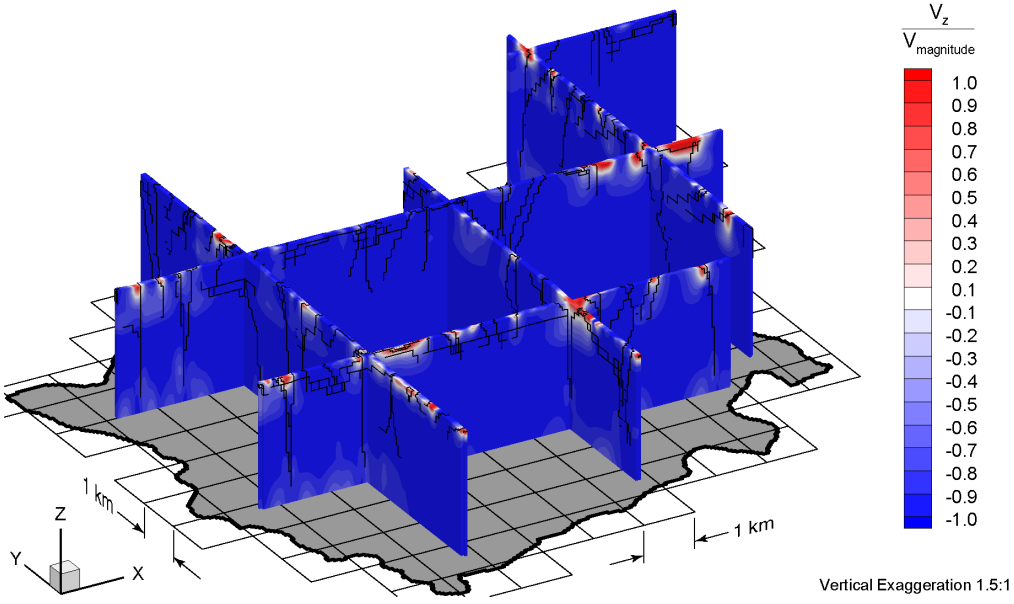

Figure A.22 Fence view of ratio of vertical pore velocities to pore velocity magnitudes at 40 ka before present for the Canadian Shield Sub-Regional Scenario 1 paleoclimate simulation.

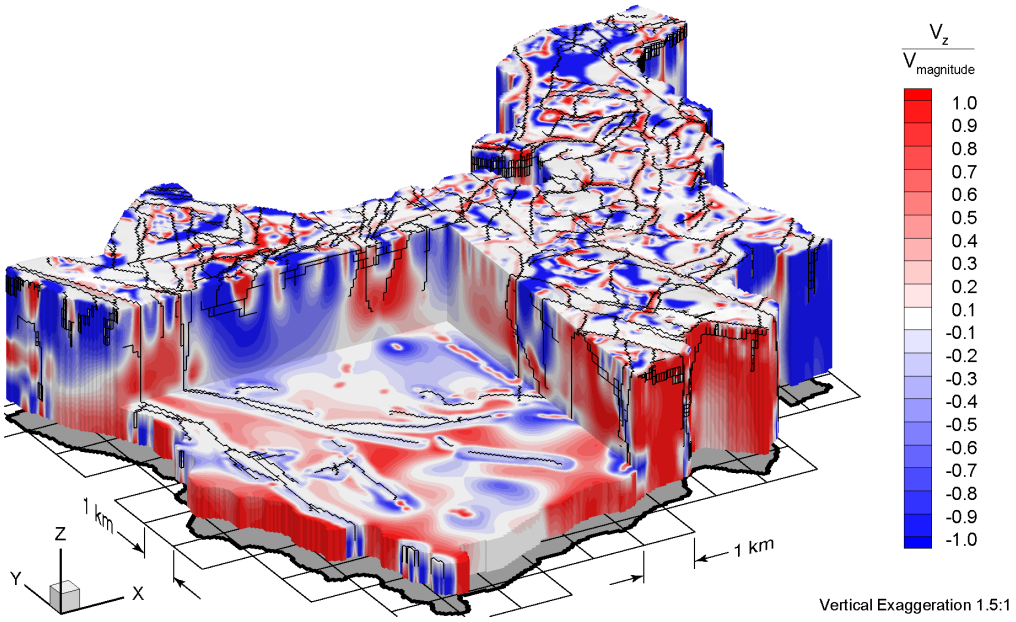

Figure A.23 Block cut view of ratio of vertical pore velocities to pore velocity magnitudes at present for the Canadian Shield Sub-Regional Scenario 1 paleoclimate simulation.

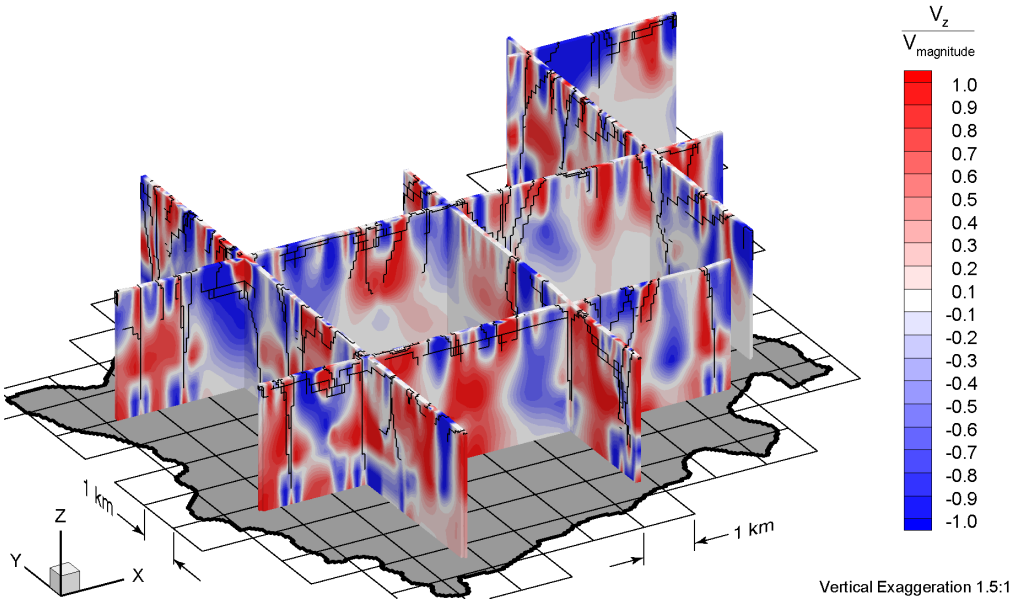

Figure A.24 Fence view of ratio of vertical pore velocities to pore velocity magnitudes at present for the Canadian Shield Sub-Regional Scenario 1 paleoclimate simulation.

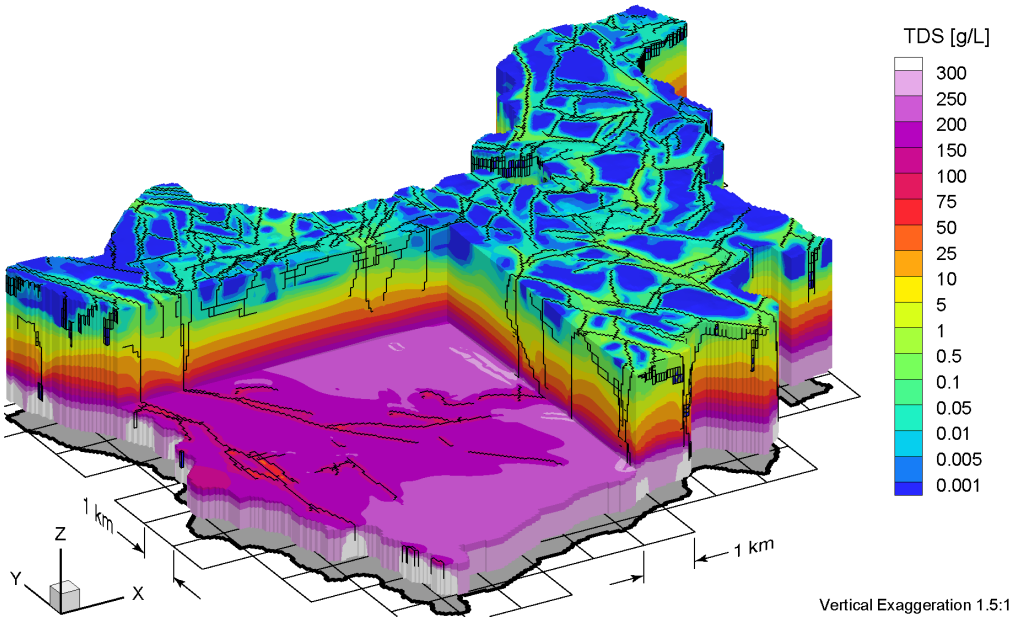

Figure A.25 Block cut view of brine concentrations at 80 ka before present for the Canadian Shield Sub-Regional Scenario 1 paleoclimate simulation.

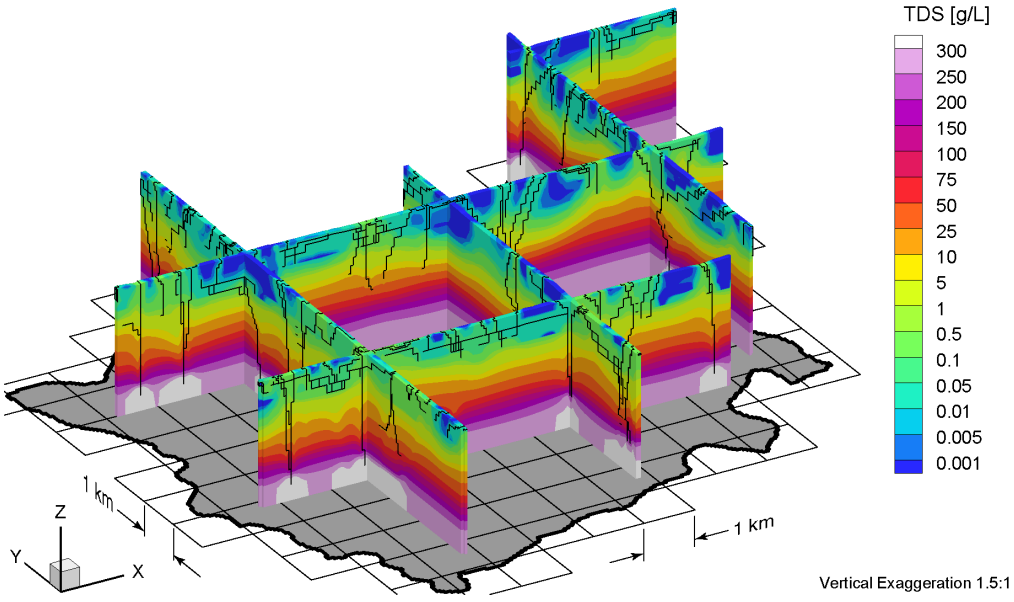

Figure A.26 Fence view of brine concentrations at 80 ka before present for the Canadian Shield Sub-Regional Scenario 1 paleoclimate simulation.

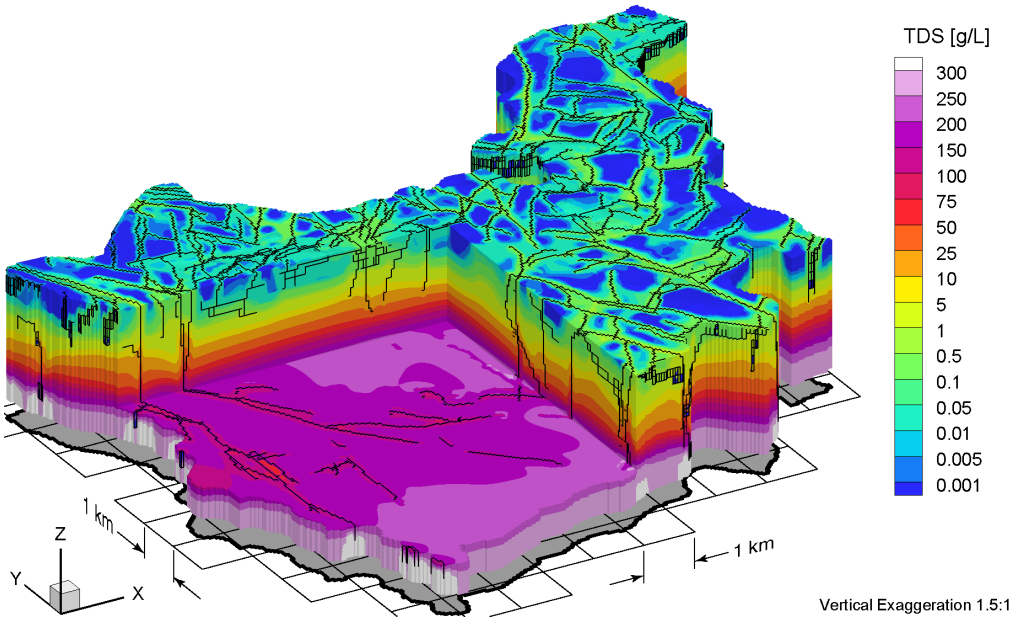

Figure A.27 Block cut view of brine concentrations at 40 ka before present for the Canadian Shield Sub-Regional Scenario 1 paleoclimate simulation.

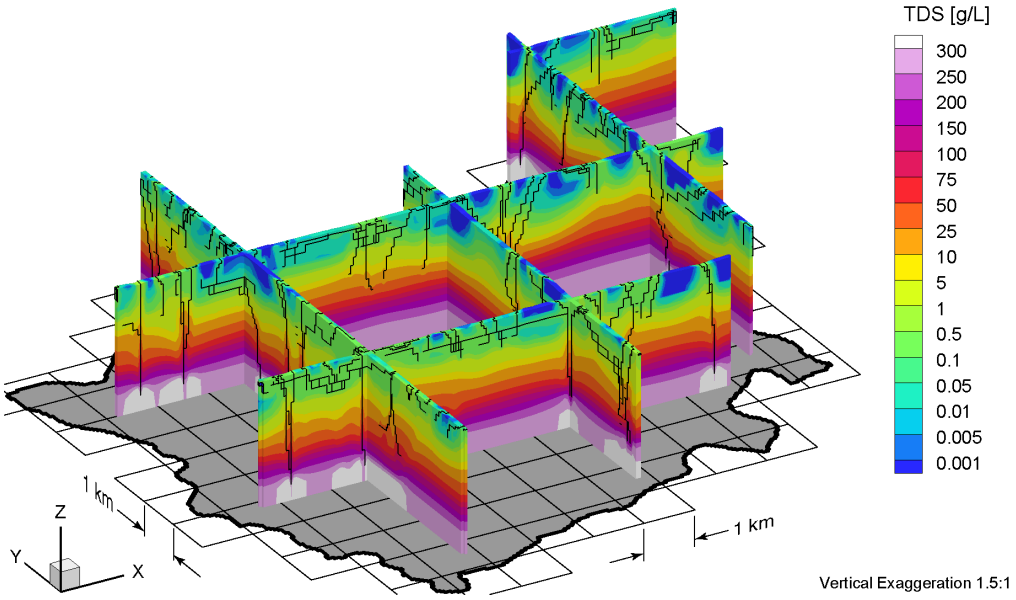

Figure A.28 Fence view of brine concentrations at 40 ka before present for the Canadian Shield Sub-Regional Scenario 1 paleoclimate simulation.

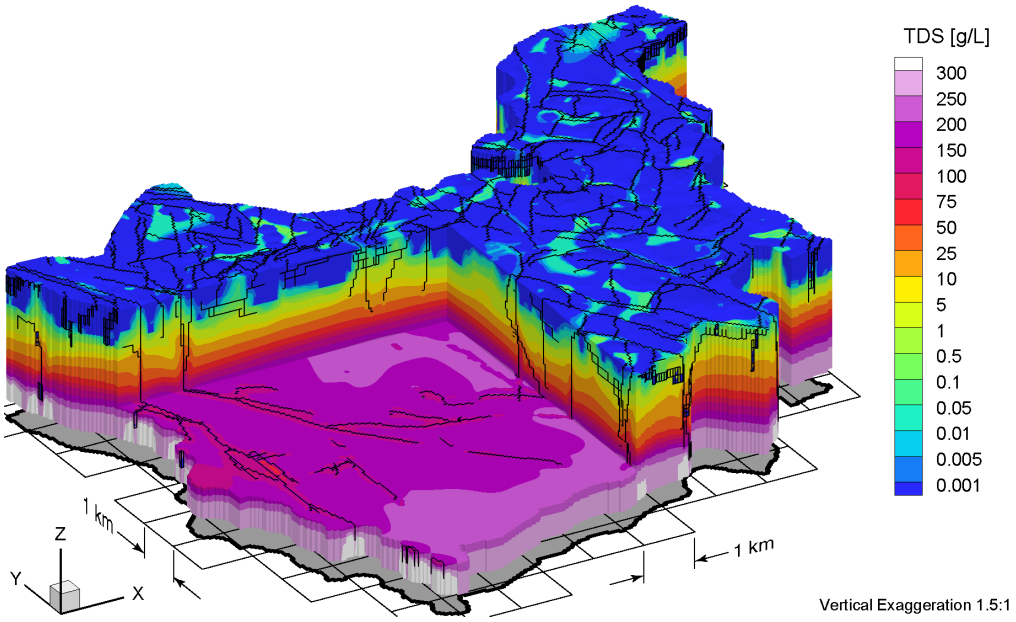

Figure A.29 Block cut view of brine concentrations at present for the Canadian Shield Sub-Regional Scenario 1 paleoclimate simulation.

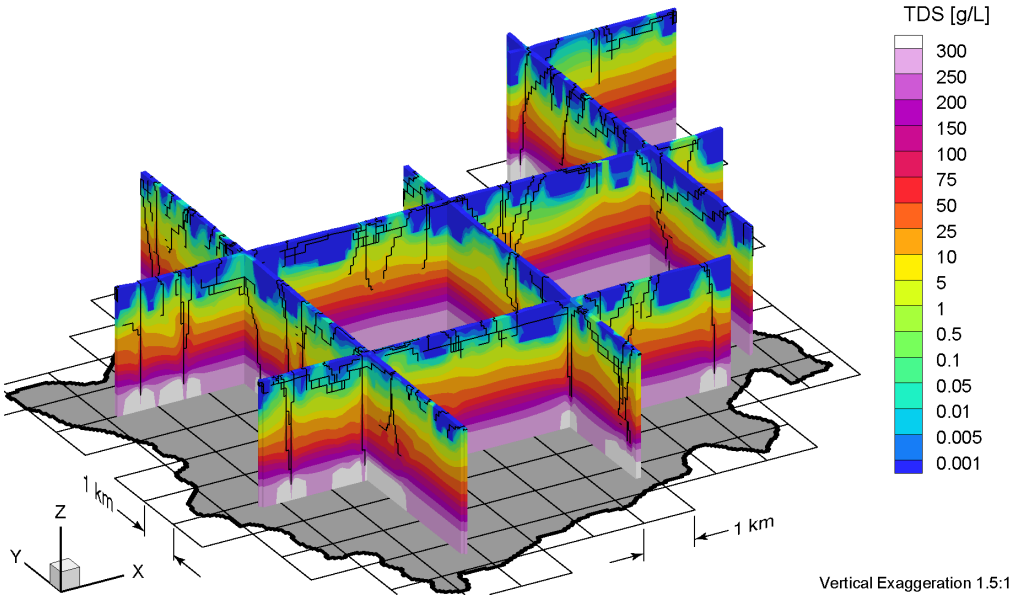

Figure A.30 Fence view of brine concentrations at present for the Canadian Shield Sub-Regional Scenario 1 paleoclimate simulation.

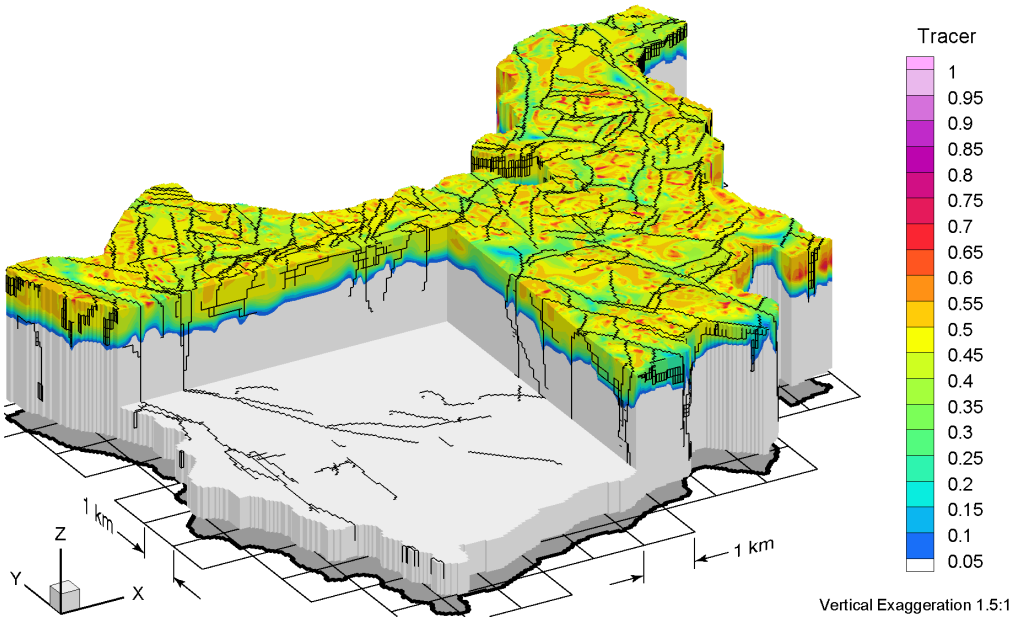

Figure A.31 Block cut view of tracer concentrations at 80 ka before present for the Canadian Shield Sub-Regional Scenario 1 paleoclimate simulation.

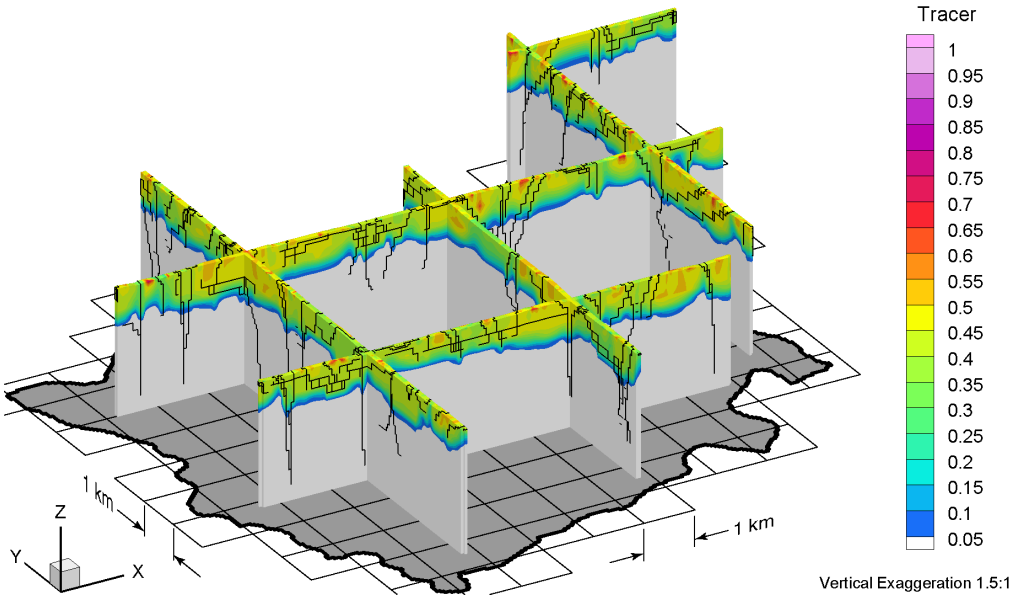

Figure A.32 Fence view of tracer concentrations at 80 ka before present for the Canadian Shield Sub-Regional Scenario 1 paleoclimate simulation.

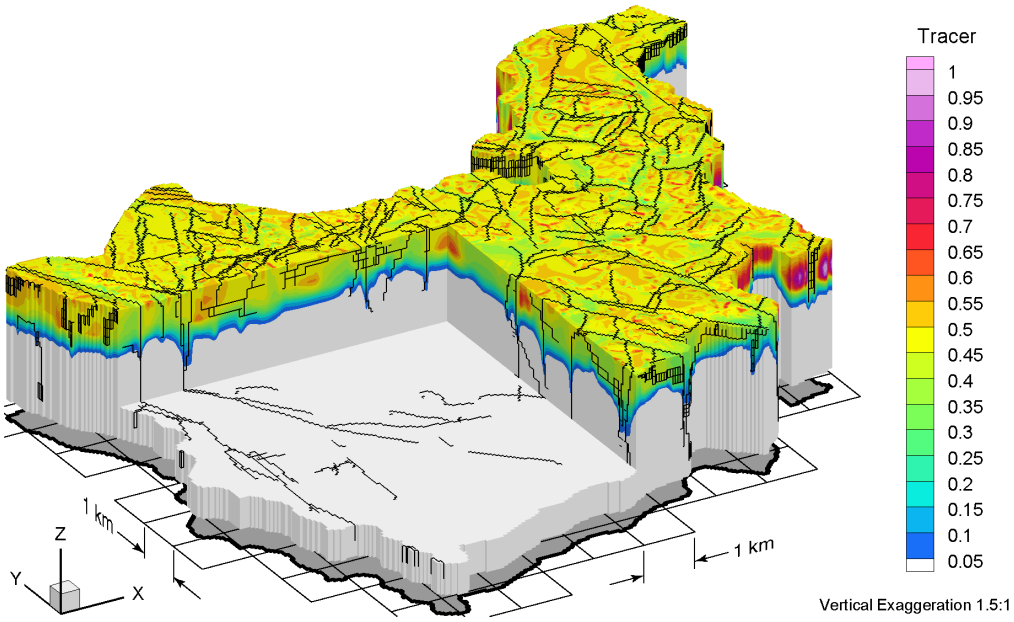

Figure A.33 Block cut view of tracer concentrations at 40 ka before present for the Canadian Shield Sub-Regional Scenario 1 paleoclimate simulation.

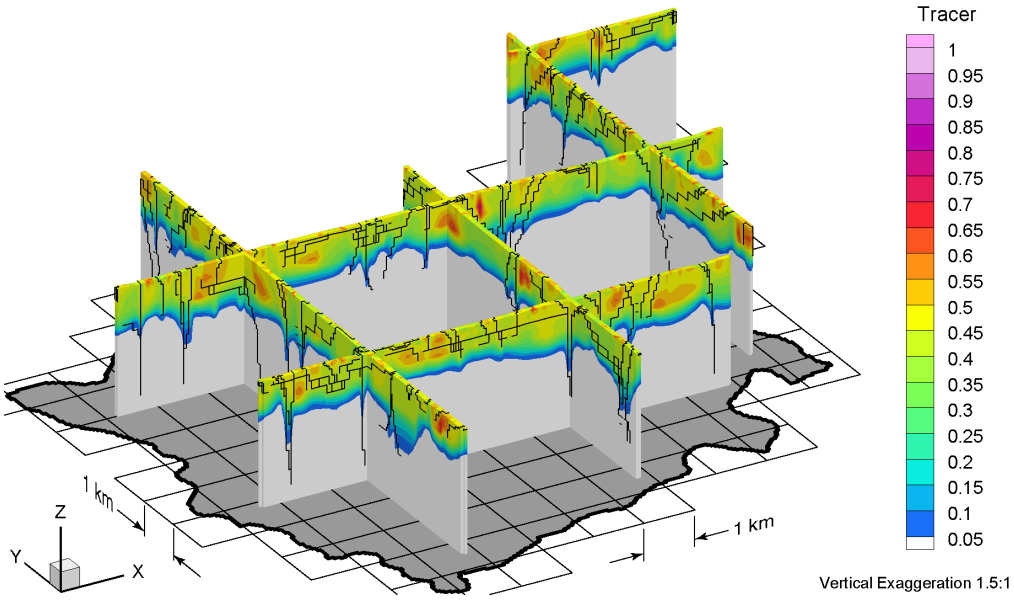

Figure A.34 Fence view of tracer concentrations at 40 ka before present for the Canadian Shield Sub-Regional Scenario 1 paleoclimate simulation.

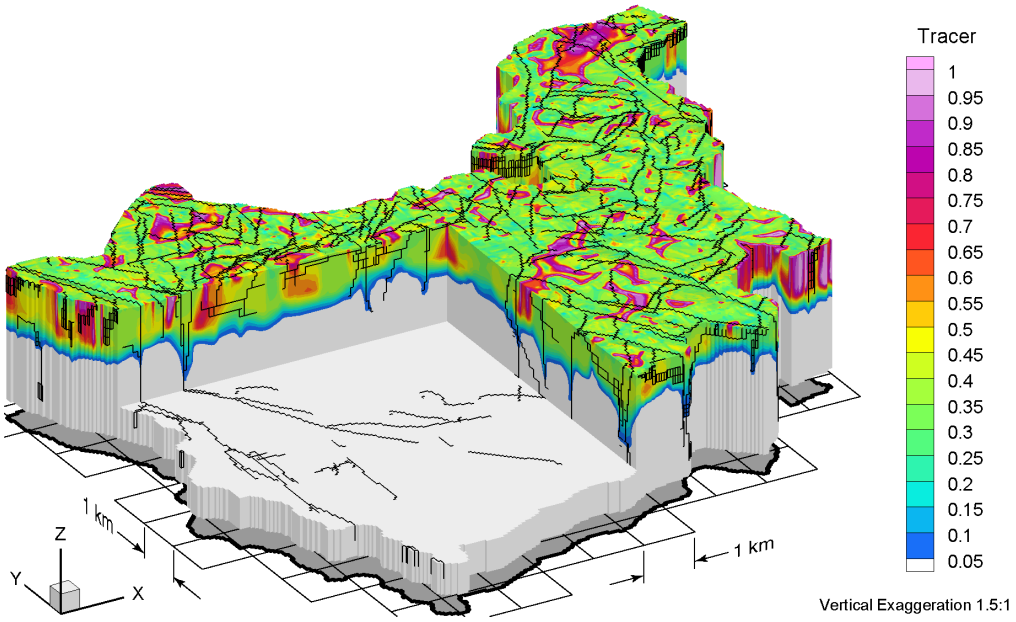

Figure A.35 Block cut view of tracer concentrations at present for the Canadian Shield Sub-Regional Scenario 1 paleoclimate simulation.

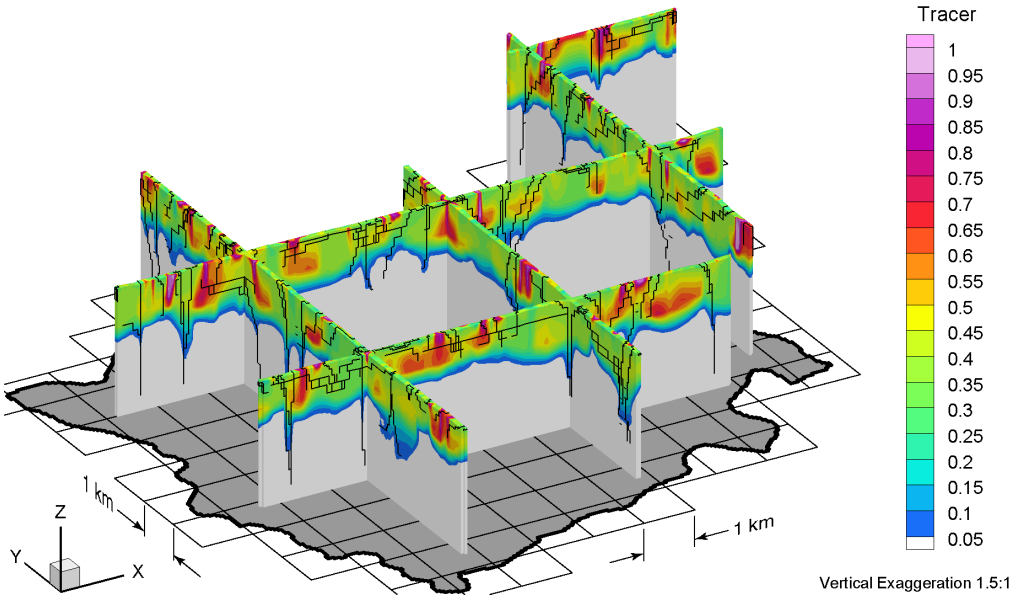

Figure A.36 Fence view of tracer concentrations at present for the Canadian Shield Sub-Regional Scenario 1 paleoclimate simulation.

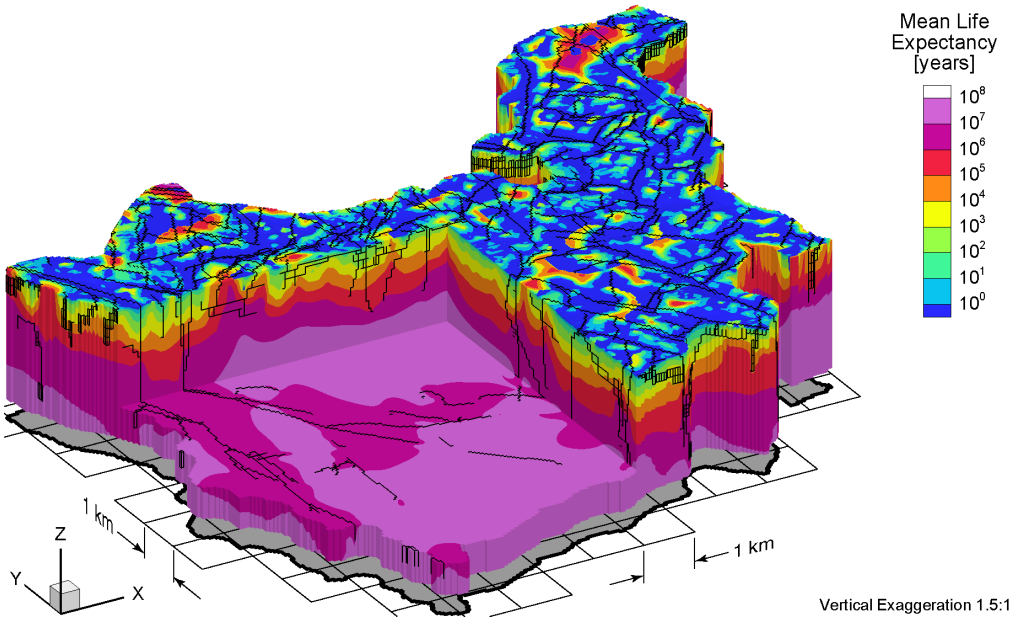

Figure A.37 Block cut view of mean life expectancies at present for the Canadian Shield Sub-Regional Scenario 1 paleoclimate simulation.

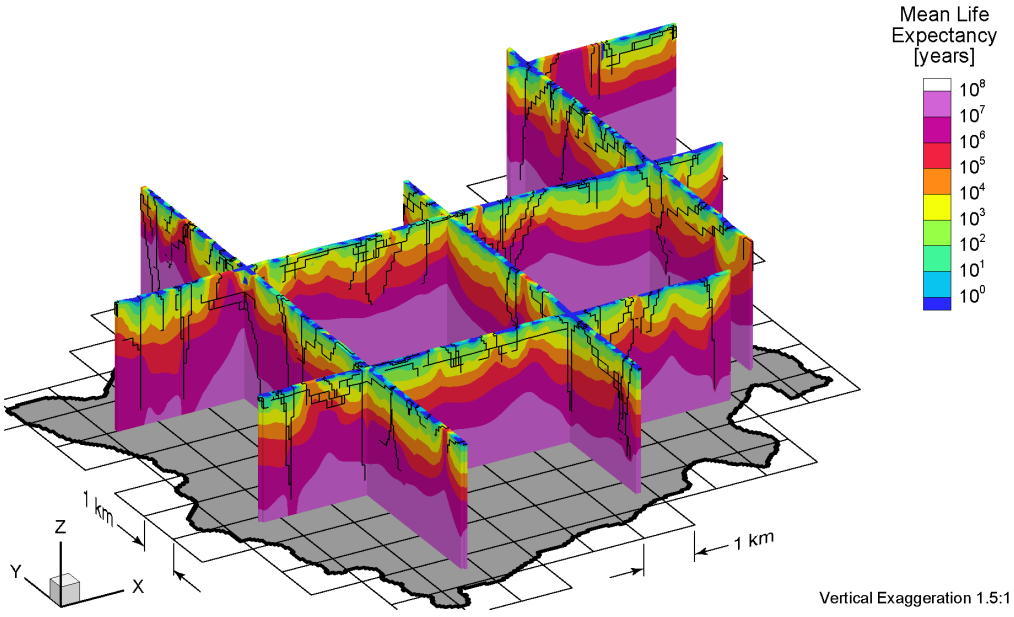

Figure A.38 Fence view of mean life expectancies at present for the Canadian Shield Sub-Regional Scenario 1 paleoclimate simulation.

Appendix B

CSSR Scenario 2 Paleoclimate Model

All figures related to Canadian Shield Sub-Regional (CSSR) Scenario 2 paleoclimate modelling are listed in Table B.1. Block cut view and fence view figures are shown on the same page to facilitate comparison. All results of the 120 ka paleoclimate simulations are shown at times of 80 ka before present, 40 ka before present, and at present.

Table B.1 List of Canadian Shield Sub-Regional Scenario 2 paleoclimate simulation figures.

Parameters	Time Before Present					
	80 ka		40 ka		Present	
	Block Cut	Fence	Block Cut	Fence	Block Cut	Fence
Freshwater Heads	B.1	B.2	B.3	B.4	B.5	B.6
Environmental Heads	B.7	B.8	B.9	B.10	B.11	B.12
Pore Velocity Magnitudes	B.13	B.14	B.15	B.16	B.17	B.18
Ratio of Vertical Pore Velocities to Pore Velocity Magnitudes	B.19	B.20	B.21	B.22	B.23	B.24
Brine Concentrations	B.25	B.26	B.27	B.28	B.29	B.30
Tracer Concentrations	B.31	B.32	B.33	B.34	B.35	B.36
Mean Life Expectancies	—	—	—	—	B.37	B.38

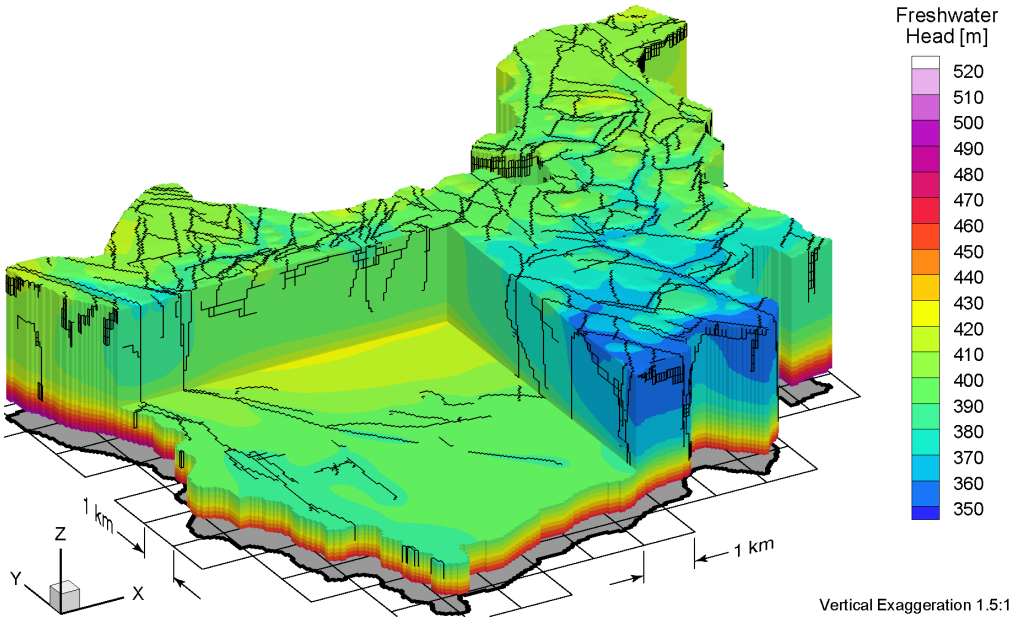

Figure B.1 Block cut view of freshwater heads at 80 ka before present for the Canadian Shield Sub-Regional Scenario 2 paleoclimate simulation.

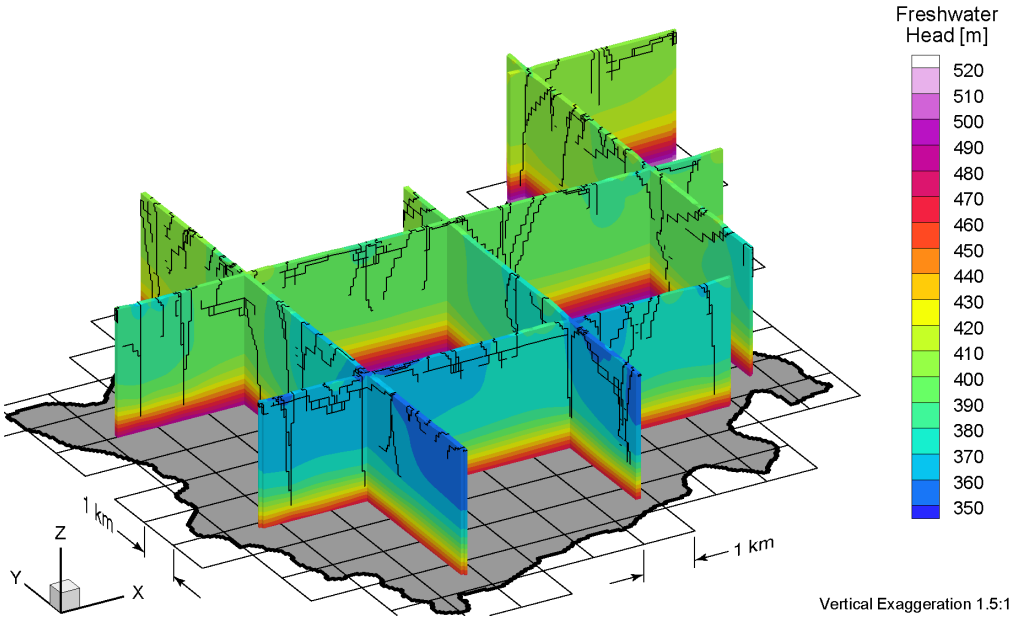

Figure B.2 Fence view of freshwater heads at 80 ka before present for the Canadian Shield Sub-Regional Scenario 2 paleoclimate simulation.

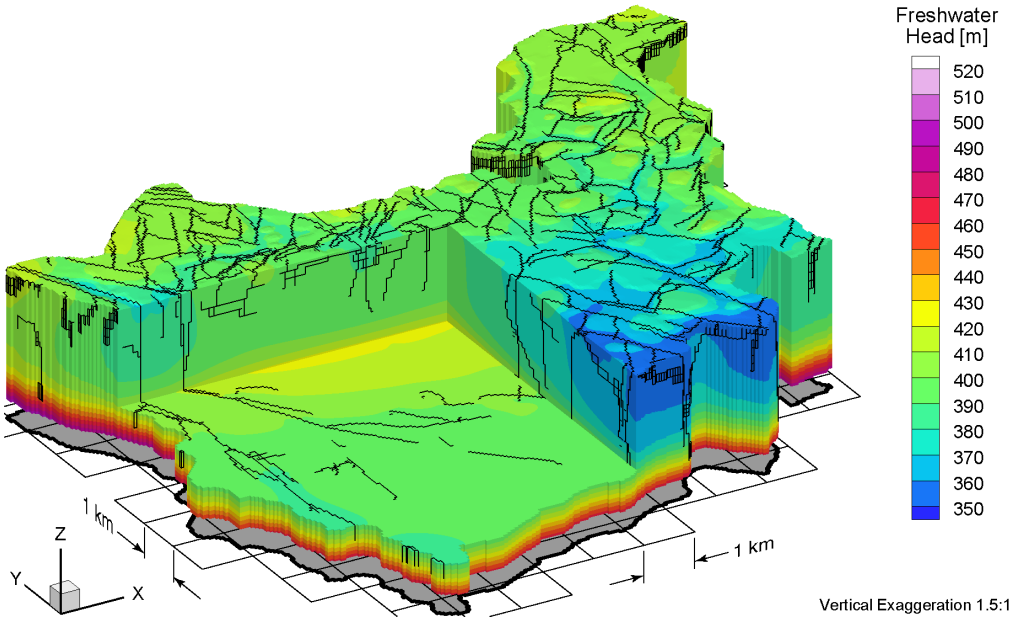

Figure B.3 Block cut view of freshwater heads at 40 ka before present for the Canadian Shield Sub-Regional Scenario 2 paleoclimate simulation.

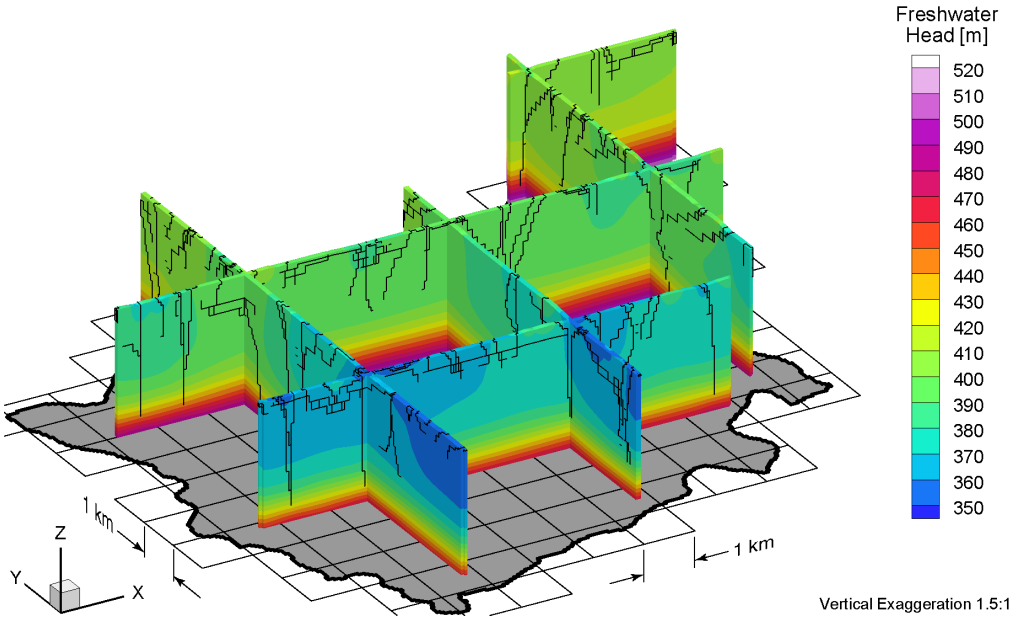

Figure B.4 Fence view of freshwater heads at 40 ka before present for the Canadian Shield Sub-Regional Scenario 2 paleoclimate simulation.

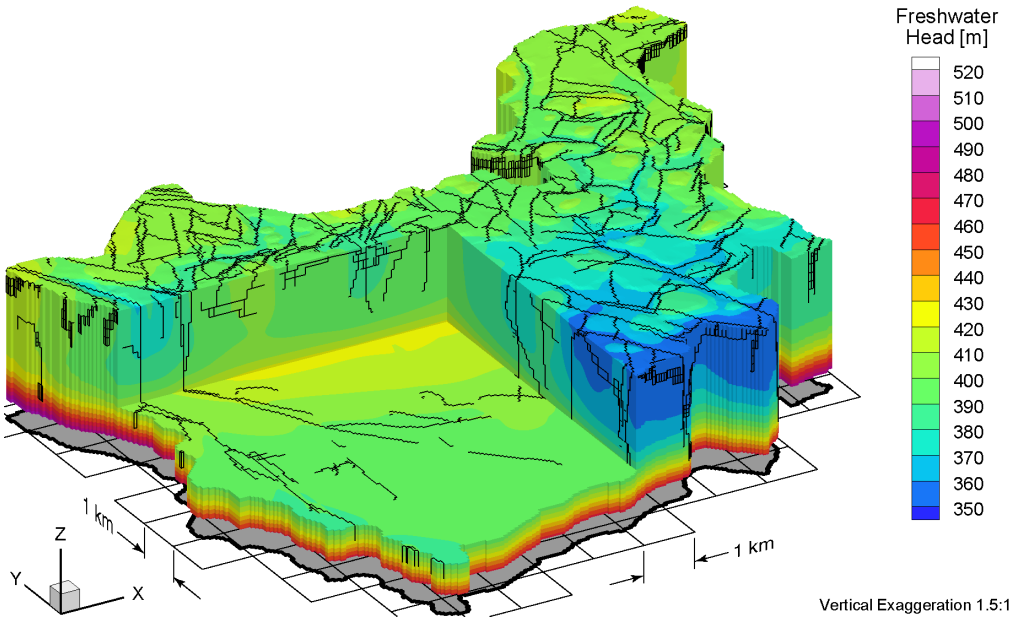

Figure B.5 Block cut view of freshwater heads at present for the Canadian Shield Sub-Regional Scenario 2 paleoclimate simulation.

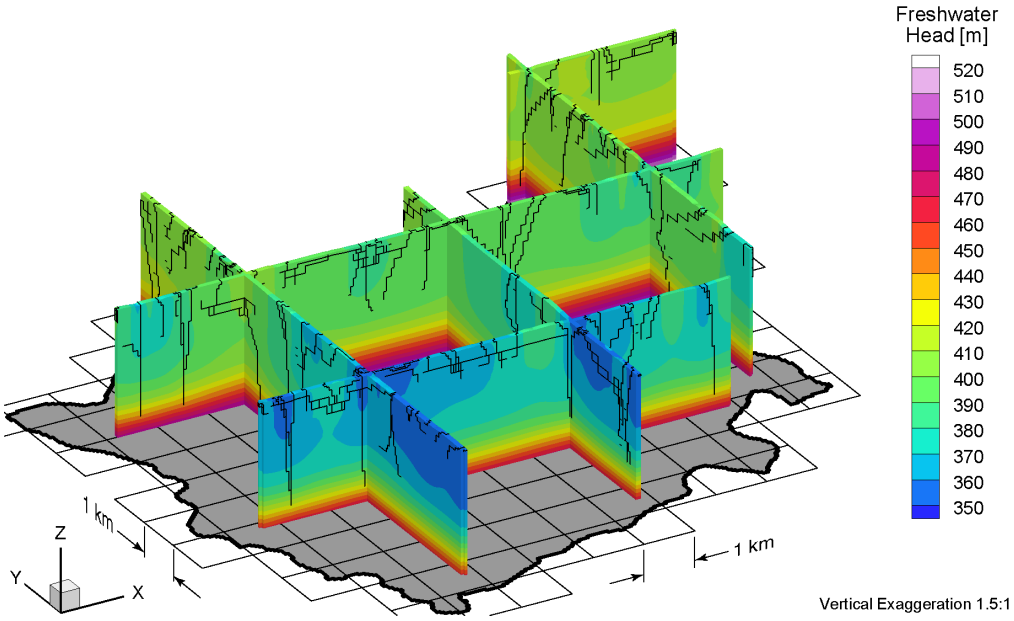

Figure B.6 Fence view of freshwater heads at present for the Canadian Shield Sub-Regional Scenario 2 paleoclimate simulation.

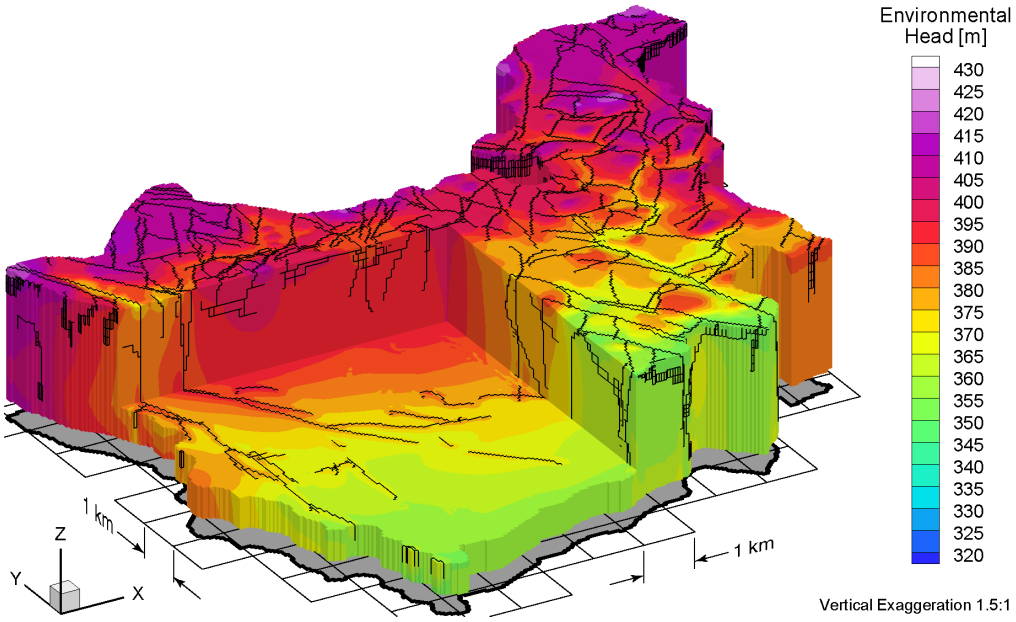

Figure B.7 Block cut view of environmental heads at 80 ka before present for the Canadian Shield Sub-Regional Scenario 2 paleoclimate simulation.

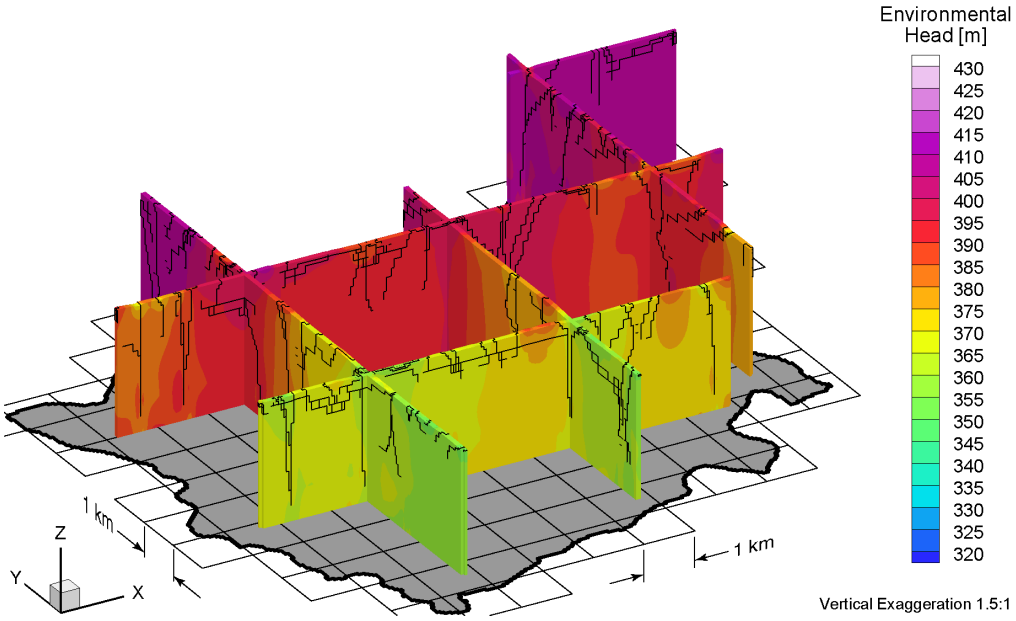

Figure B.8 Fence view of environmental heads at 80 ka before present for the Canadian Shield Sub-Regional Scenario 2 paleoclimate simulation.

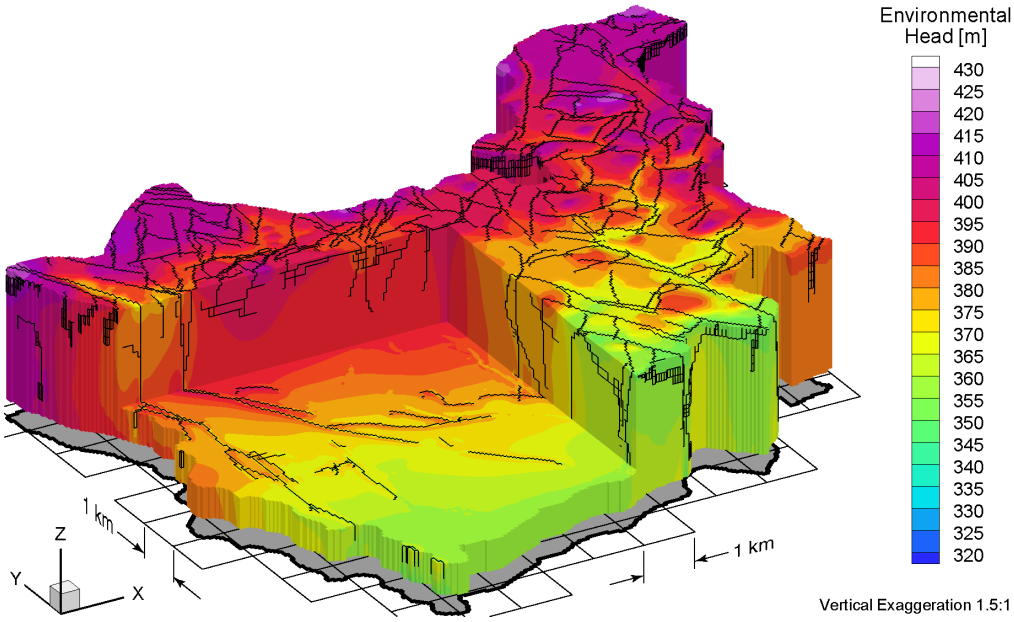

Figure B.9 Block cut view of environmental heads at 40 ka before present for the Canadian Shield Sub-Regional Scenario 2 paleoclimate simulation.

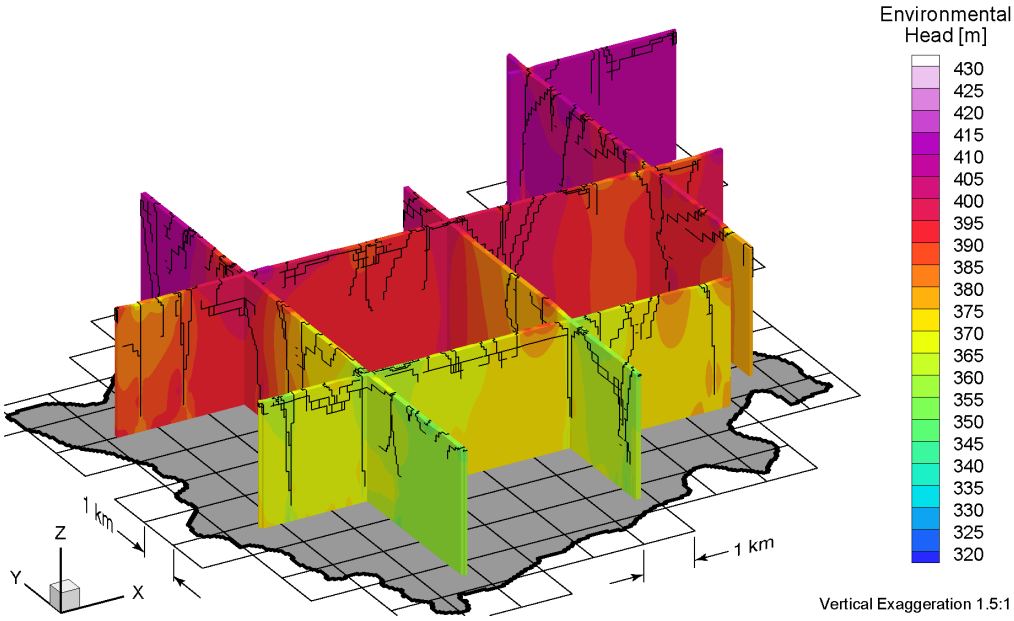

Figure B.10 Fence view of environmental heads at 40 ka before present for the Canadian Shield Sub-Regional Scenario 2 paleoclimate simulation.

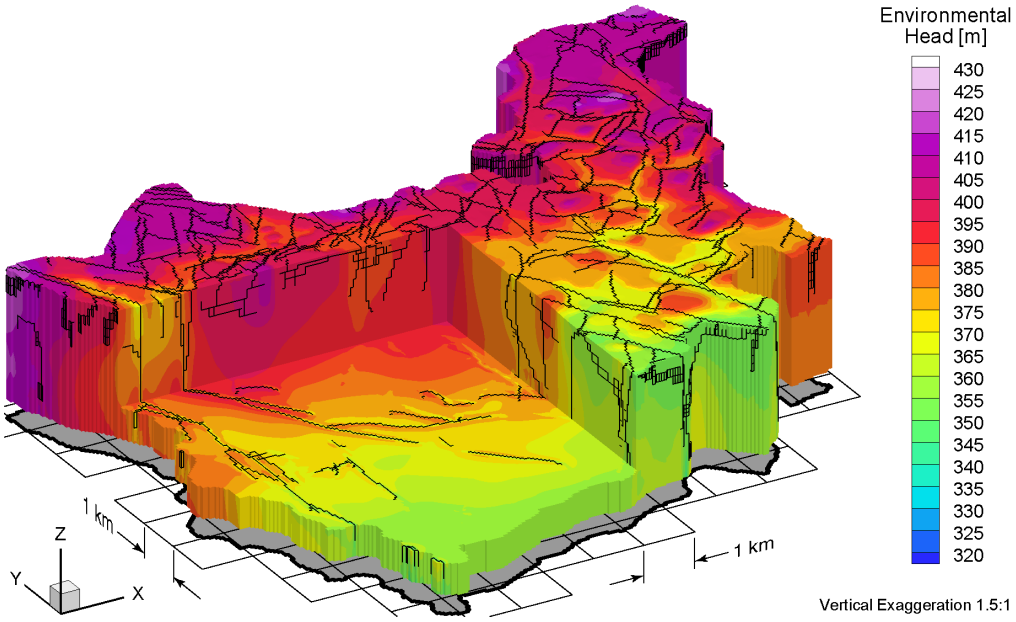

Figure B.11 Block cut view of environmental heads at present for the Canadian Shield Sub-Regional Scenario 2 paleoclimate simulation.

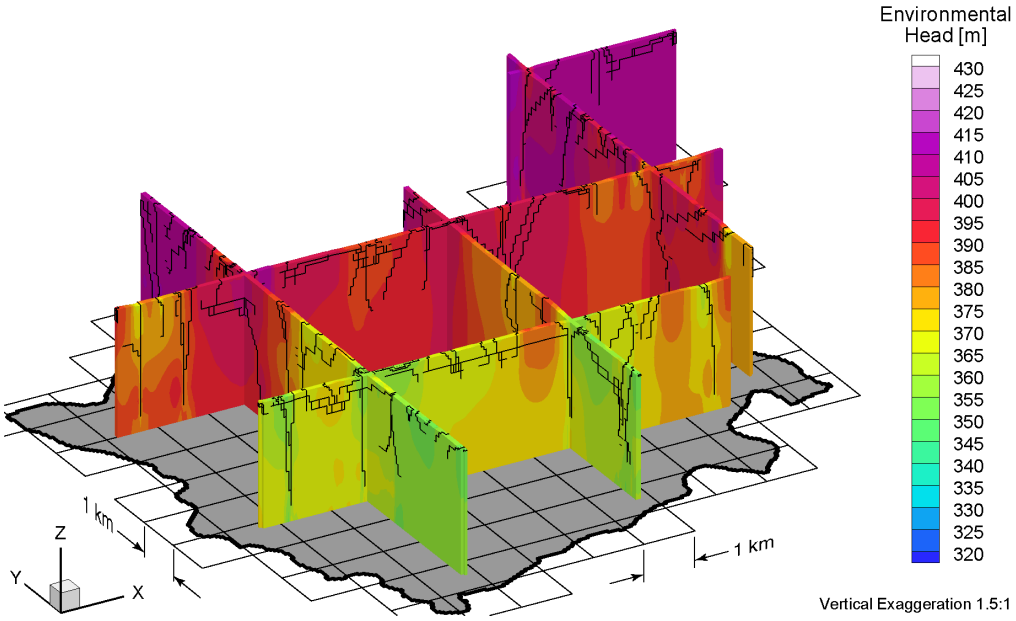

Figure B.12 Fence view of environmental heads at present for the Canadian Shield Sub-Regional Scenario 2 paleoclimate simulation.

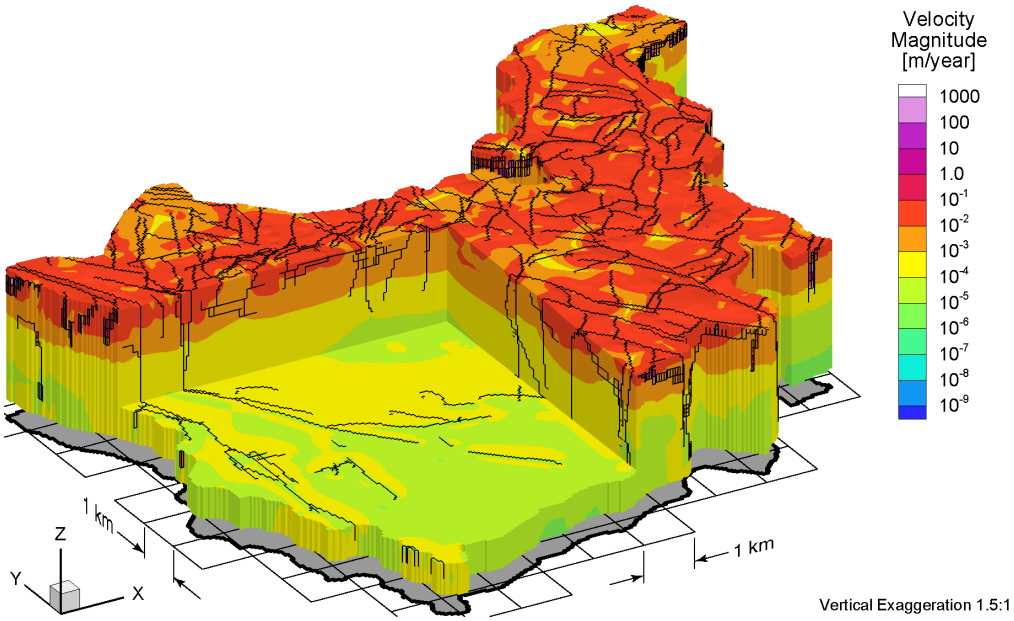

Figure B.13 Block cut view of pore velocity magnitudes at 80 ka before present for the Canadian Shield Sub-Regional Scenario 2 paleoclimate simulation.

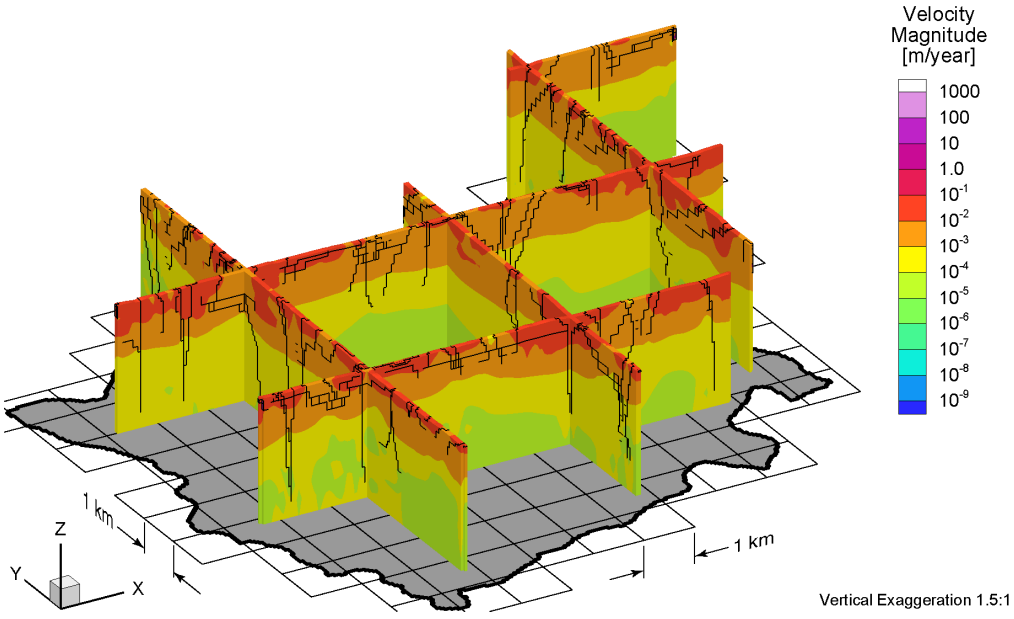

Figure B.14 Fence view of pore velocity magnitudes at 80 ka before present for the Canadian Shield Sub-Regional Scenario 2 paleoclimate simulation.

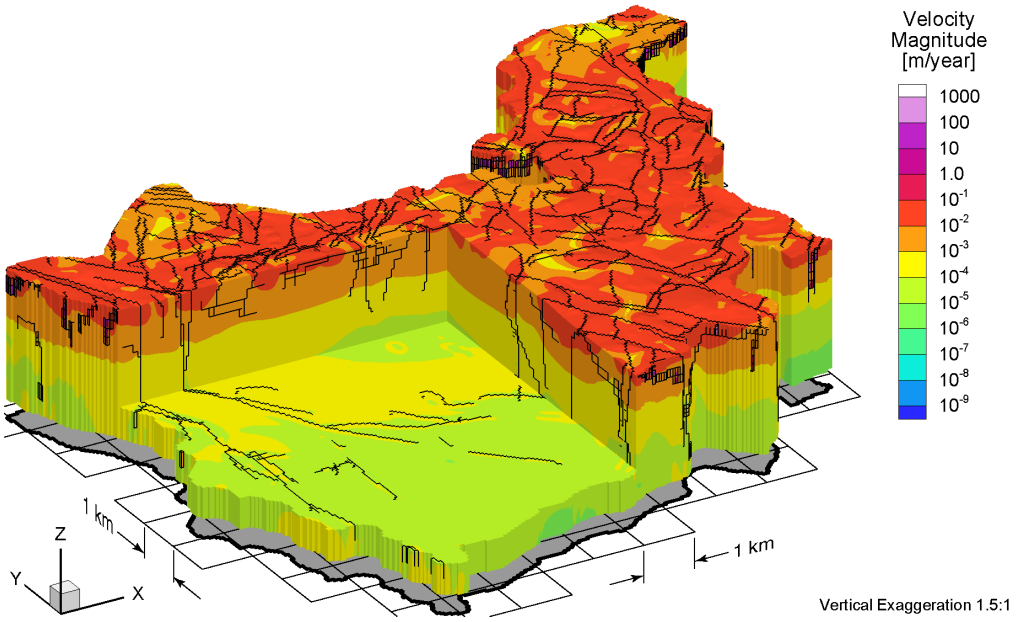

Figure B.15 Block cut view of pore velocity magnitudes at 40 ka before present for the Canadian Shield Sub-Regional Scenario 2 paleoclimate simulation.

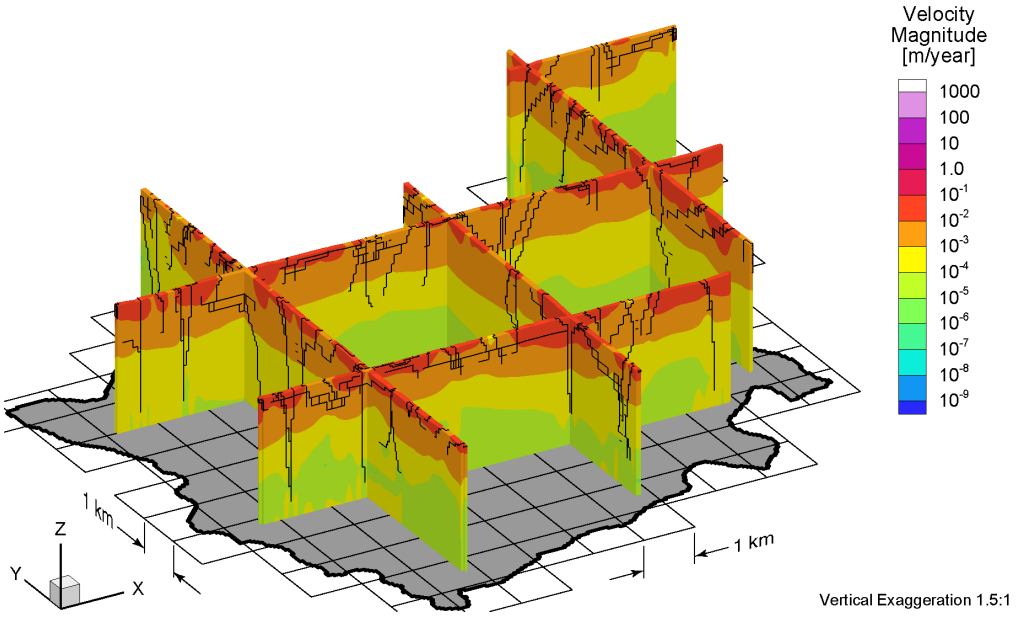

Figure B.16 Fence view of pore velocity magnitudes at 40 ka before present for the Canadian Shield Sub-Regional Scenario 2 paleoclimate simulation.

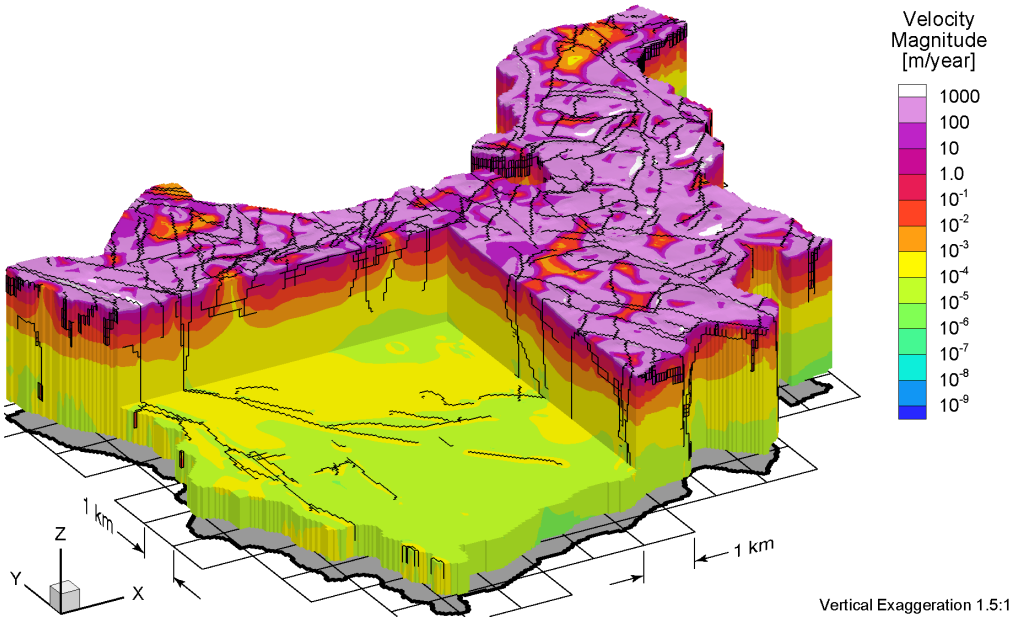

Figure B.17 Block cut view of pore velocity magnitudes at present for the Canadian Shield Sub-Regional Scenario 2 paleoclimate simulation.

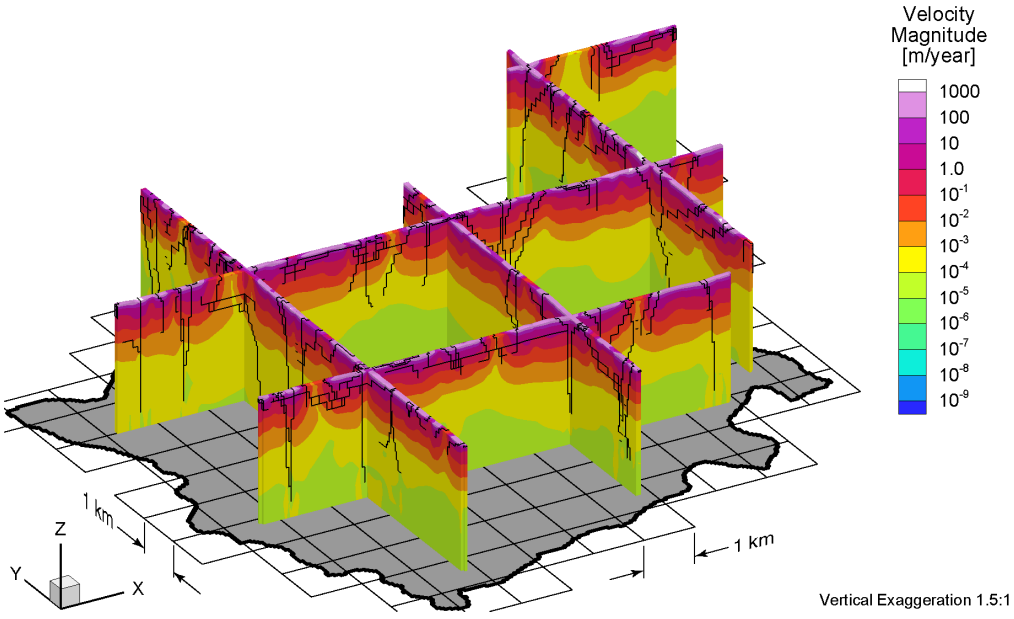

Figure B.18 Fence view of pore velocity magnitudes at present for the Canadian Shield Sub-Regional Scenario 2 paleoclimate simulation.

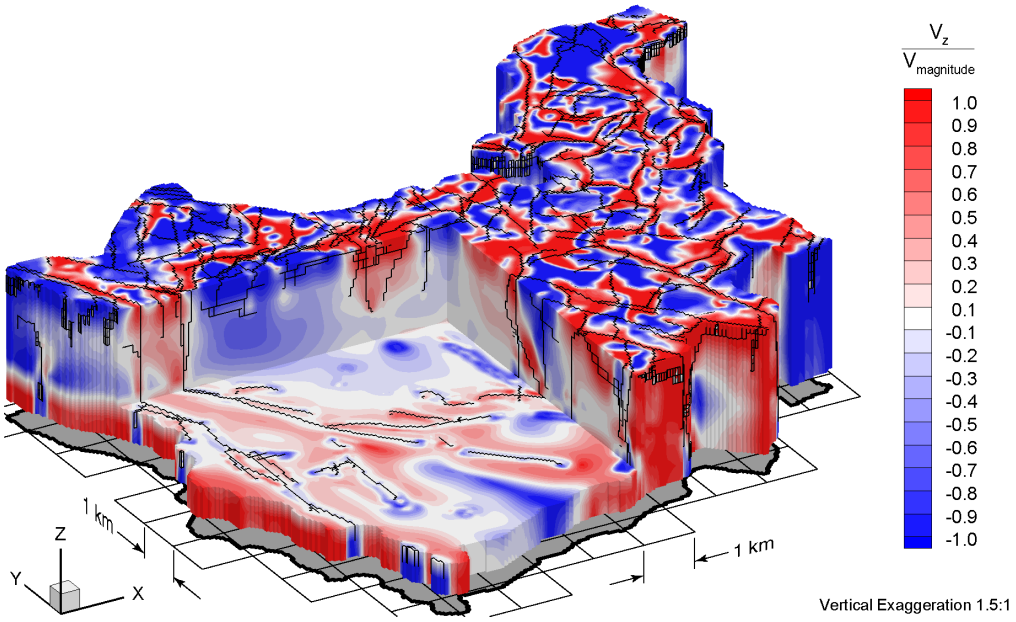

Figure B.19 Block cut view of ratio of vertical pore velocities to pore velocity magnitudes at 80 ka before present for the Canadian Shield Sub-Regional Scenario 2 paleoclimate simulation.

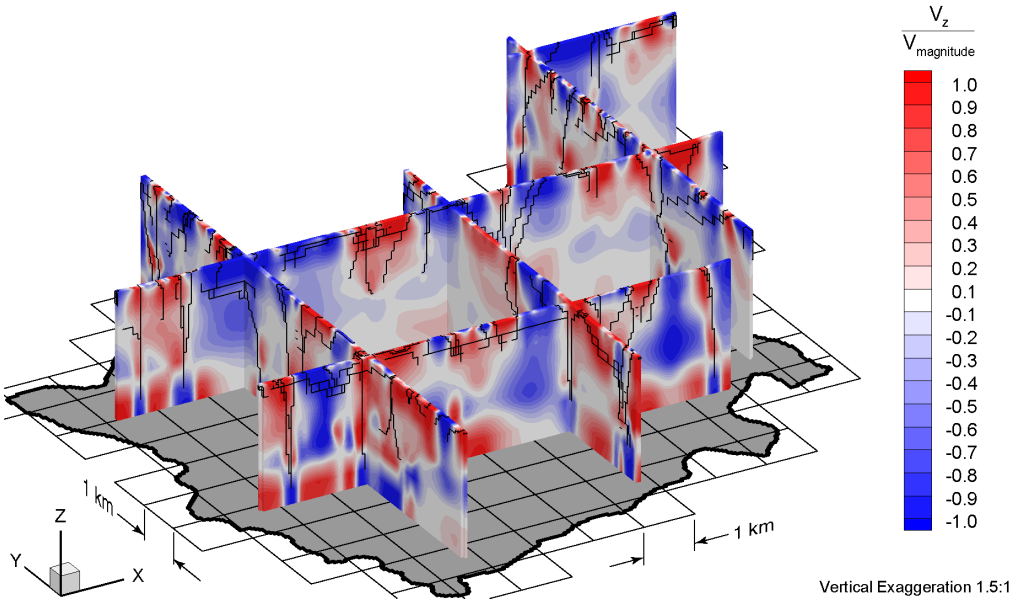

Figure B.20 Fence view of ratio of vertical pore velocities to pore velocity magnitudes at 80 ka before present for the Canadian Shield Sub-Regional Scenario 2 paleoclimate simulation.

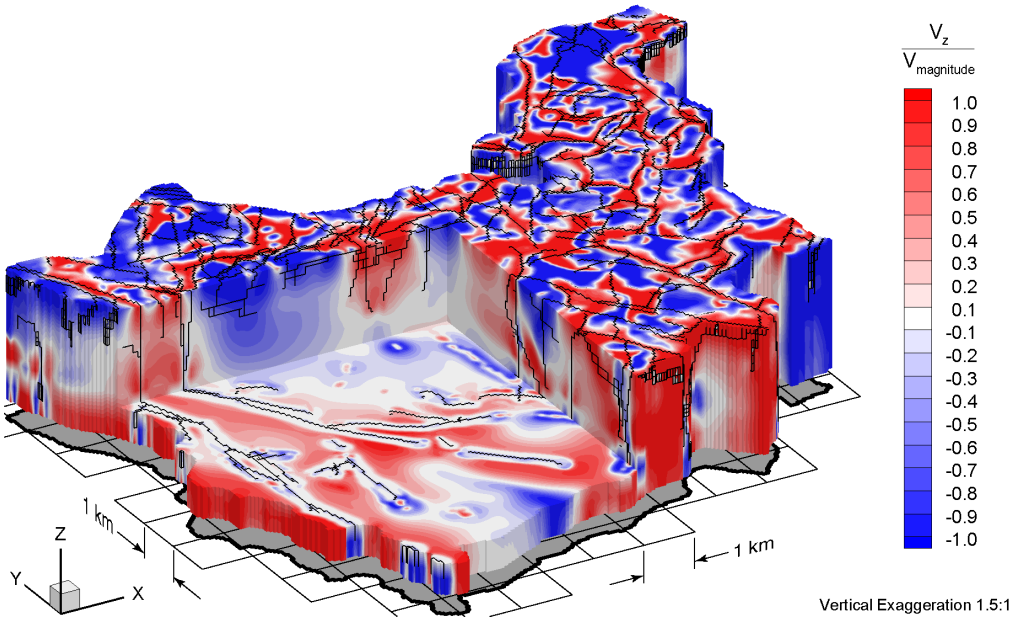

Figure B.21 Block cut view of ratio of vertical pore velocities to pore velocity magnitudes at 40 ka before present for the Canadian Shield Sub-Regional Scenario 2 paleoclimate simulation.

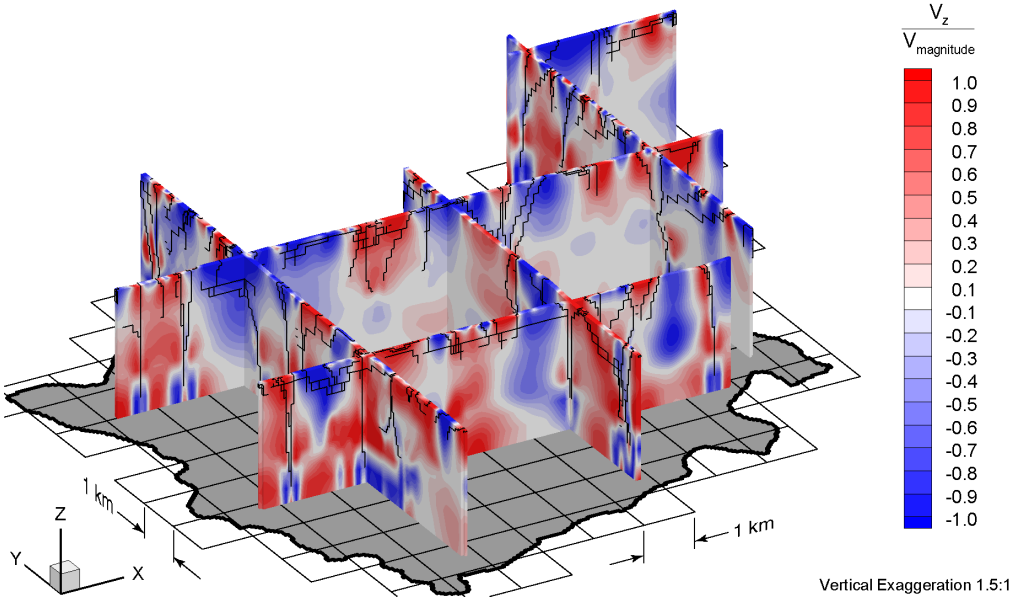

Figure B.22 Fence view of ratio of vertical pore velocities to pore velocity magnitudes at 40 ka before present for the Canadian Shield Sub-Regional Scenario 2 paleoclimate simulation.

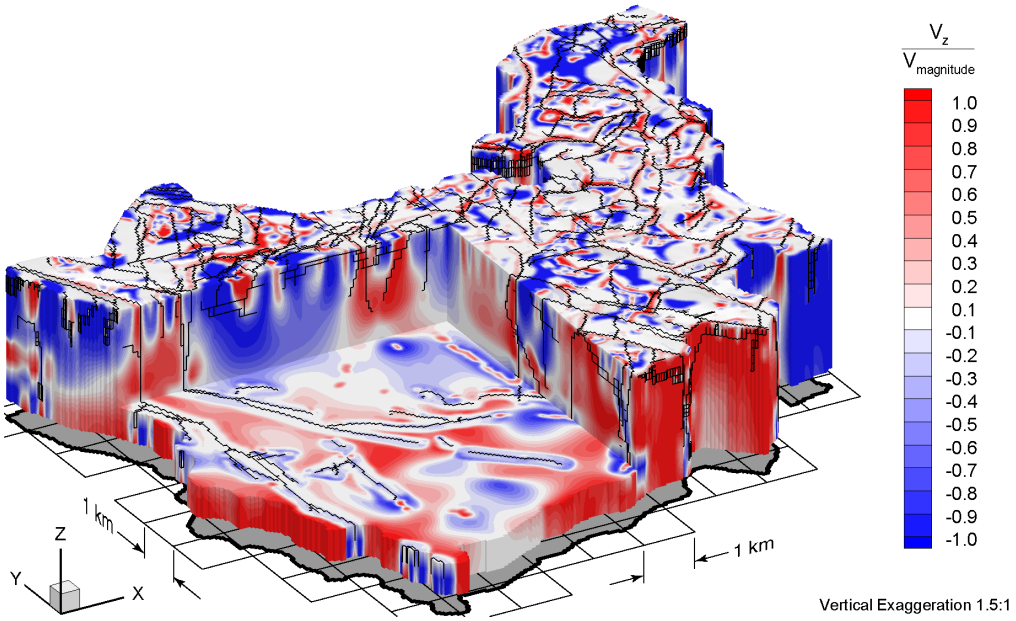

Figure B.23 Block cut view of ratio of vertical pore velocities to pore velocity magnitudes at present for the Canadian Shield Sub-Regional Scenario 2 paleoclimate simulation.

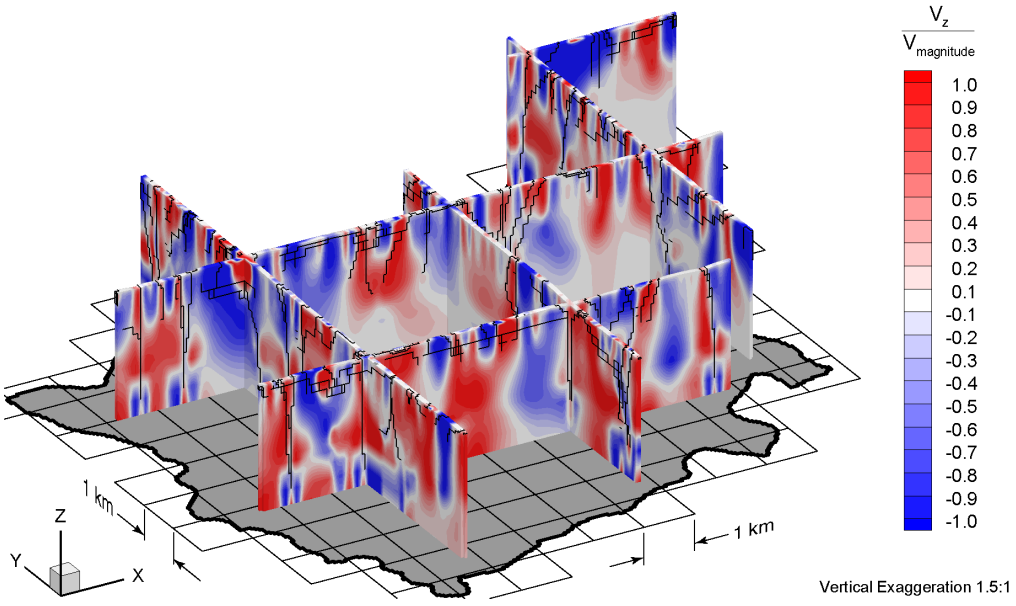

Figure B.24 Fence view of ratio of vertical pore velocities to pore velocity magnitudes at present for the Canadian Shield Sub-Regional Scenario 2 paleoclimate simulation.

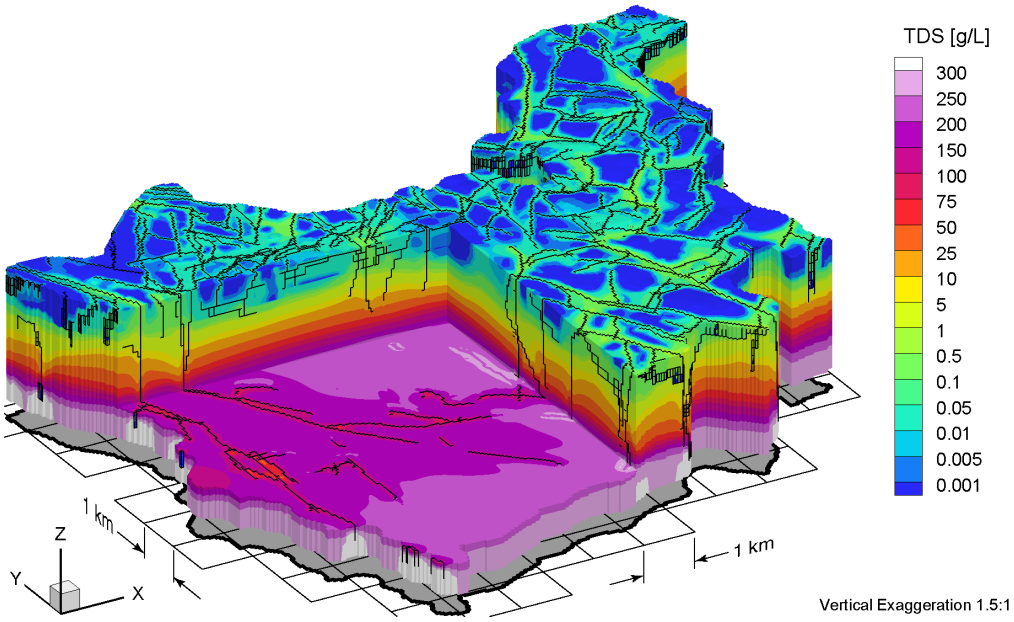

Figure B.25 Block cut view of brine concentrations at 80 ka before present for the Canadian Shield Sub-Regional Scenario 2 paleoclimate simulation.

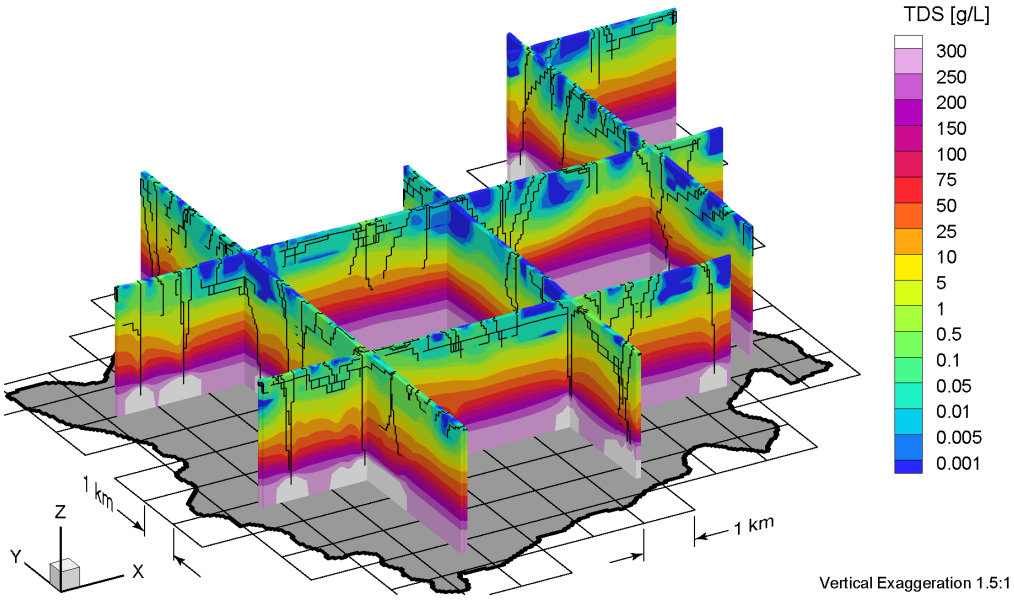

Figure B.26 Fence view of brine concentrations at 80 ka before present for the Canadian Shield Sub-Regional Scenario 2 paleoclimate simulation.

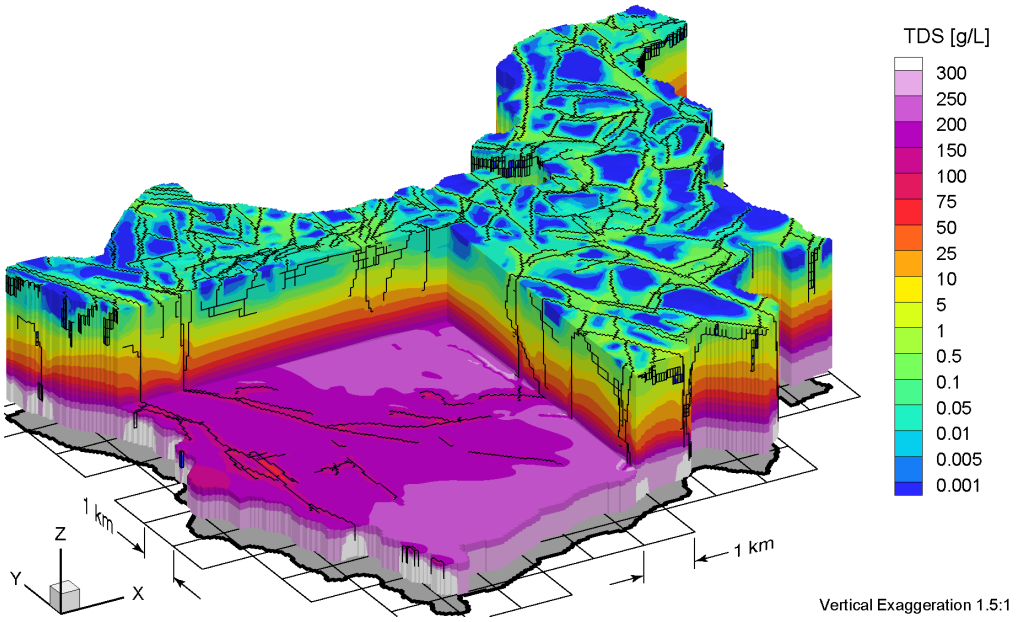

Figure B.27 Block cut view of brine concentrations at 40 ka before present for the Canadian Shield Sub-Regional Scenario 2 paleoclimate simulation.

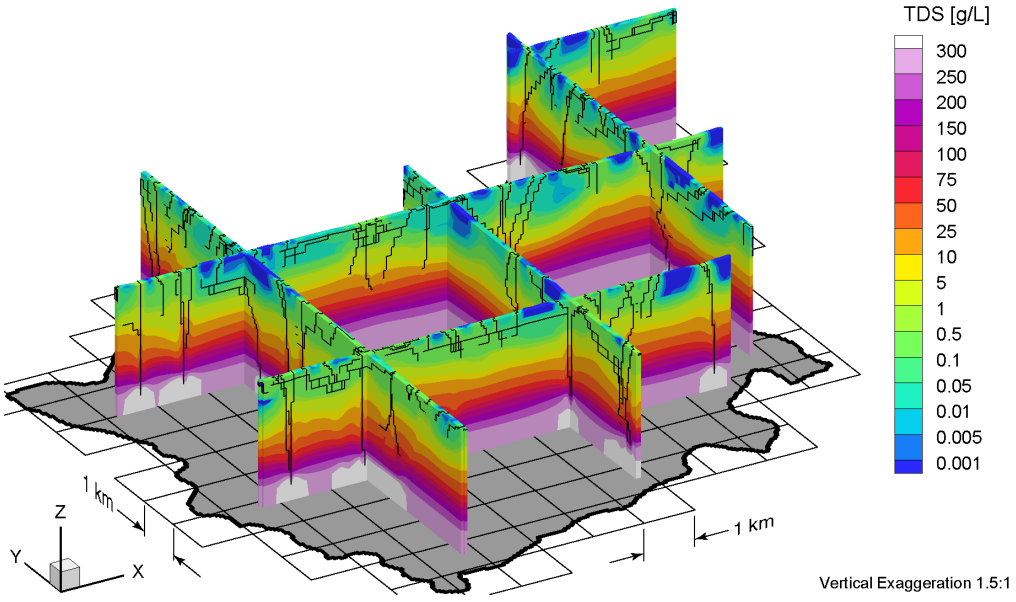

Figure B.28 Fence view of brine concentrations at 40 ka before present for the Canadian Shield Sub-Regional Scenario 2 paleoclimate simulation.

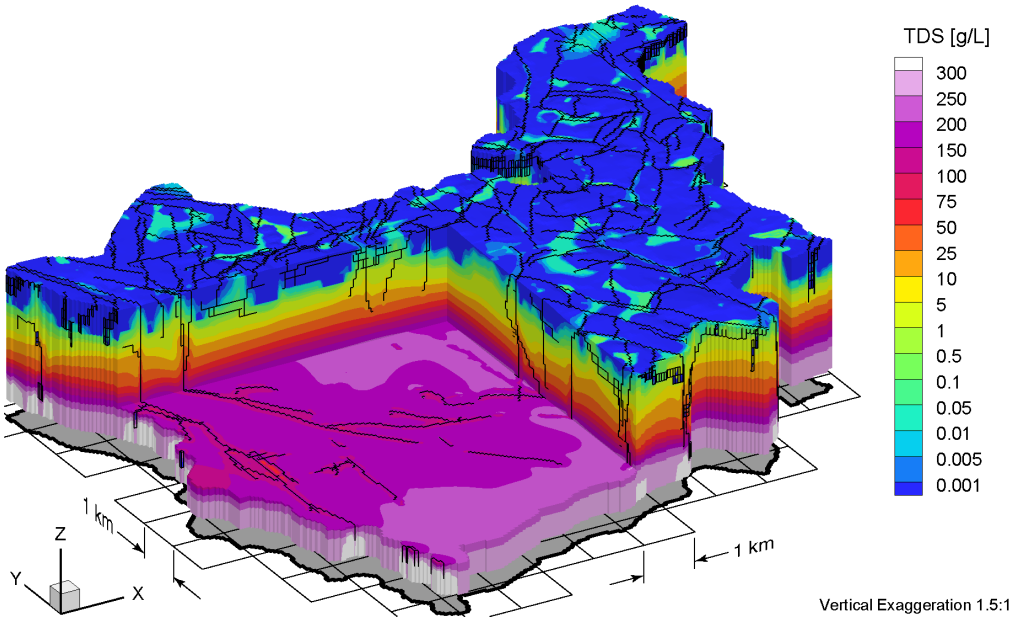

Figure B.29 Block cut view of brine concentrations at present for the Canadian Shield Sub-Regional Scenario 2 paleoclimate simulation.

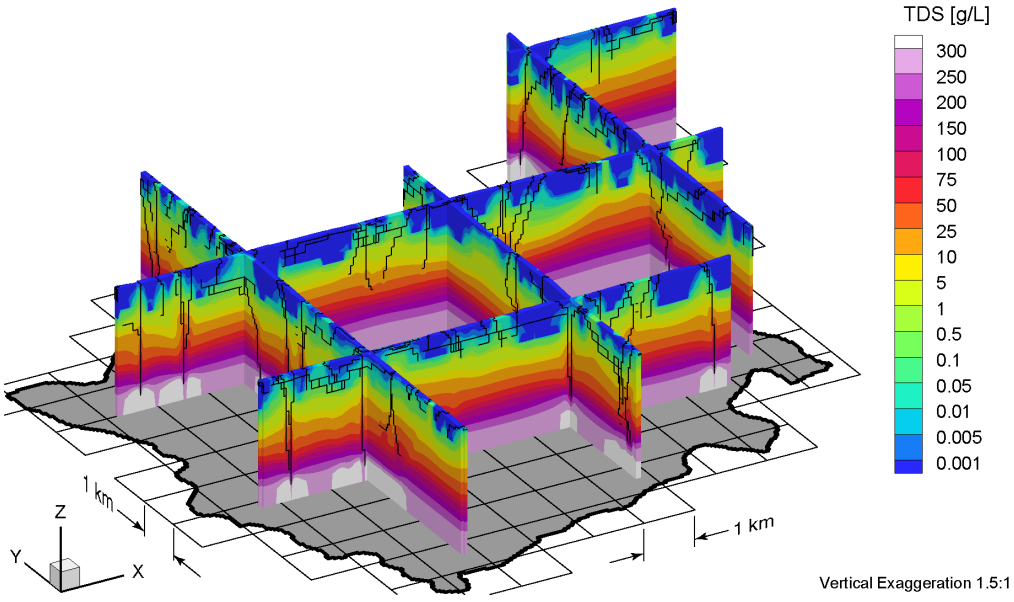

Figure B.30 Fence view of brine concentrations at present for the Canadian Shield Sub-Regional Scenario 2 paleoclimate simulation.

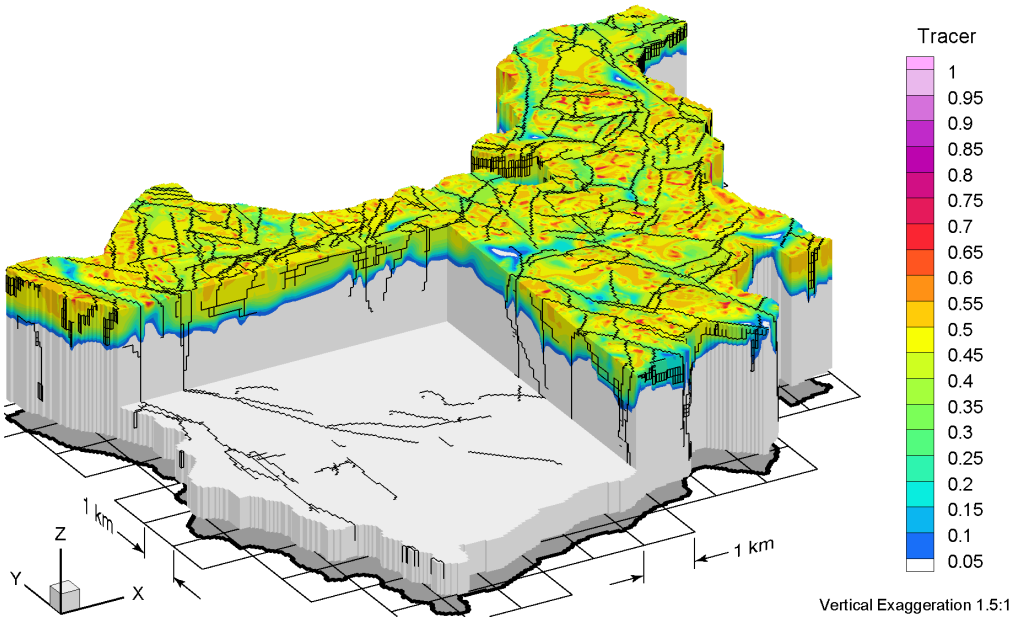

Figure B.31 Block cut view of tracer concentrations at 80 ka before present for the Canadian Shield Sub-Regional Scenario 2 paleoclimate simulation.

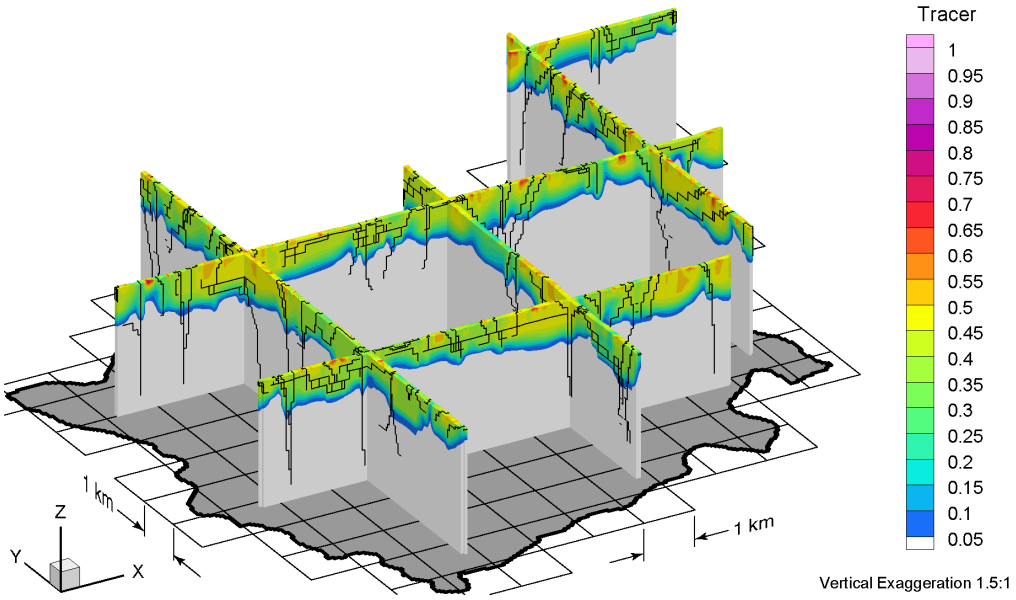

Figure B.32 Fence view of tracer concentrations at 80 ka before present for the Canadian Shield Sub-Regional Scenario 2 paleoclimate simulation.

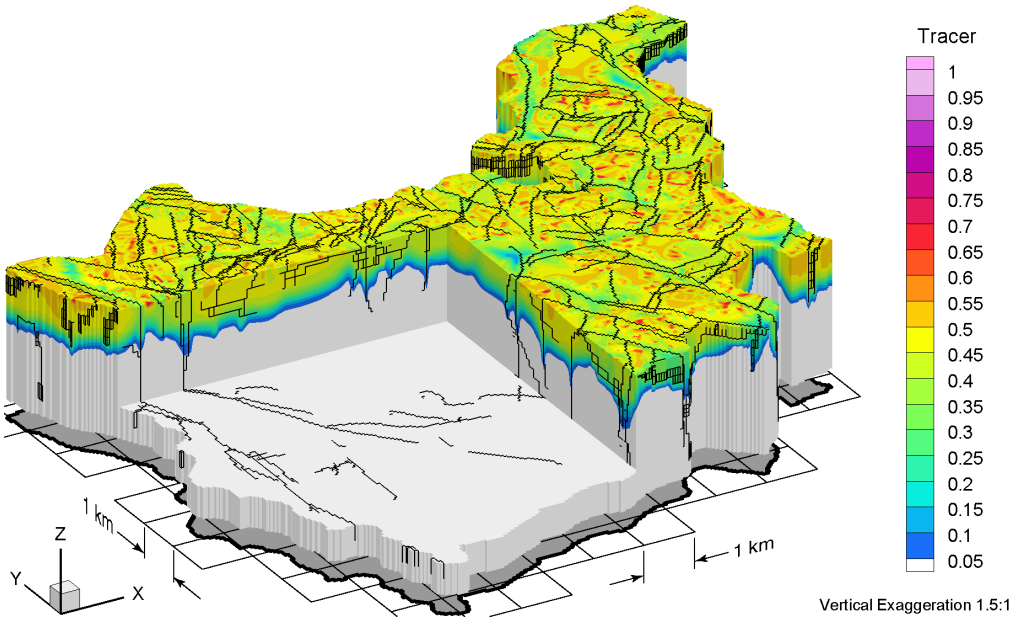

Figure B.33 Block cut view of tracer concentrations at 40 ka before present for the Canadian Shield Sub-Regional Scenario 2 paleoclimate simulation.

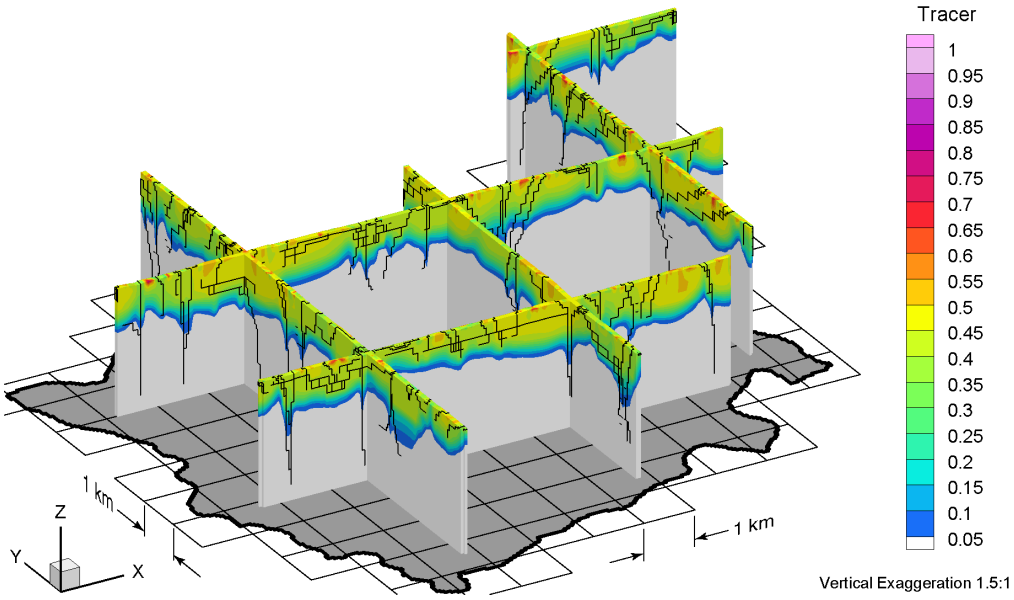

Figure B.34 Fence view of tracer concentrations at 40 ka before present for the Canadian Shield Sub-Regional Scenario 2 paleoclimate simulation.

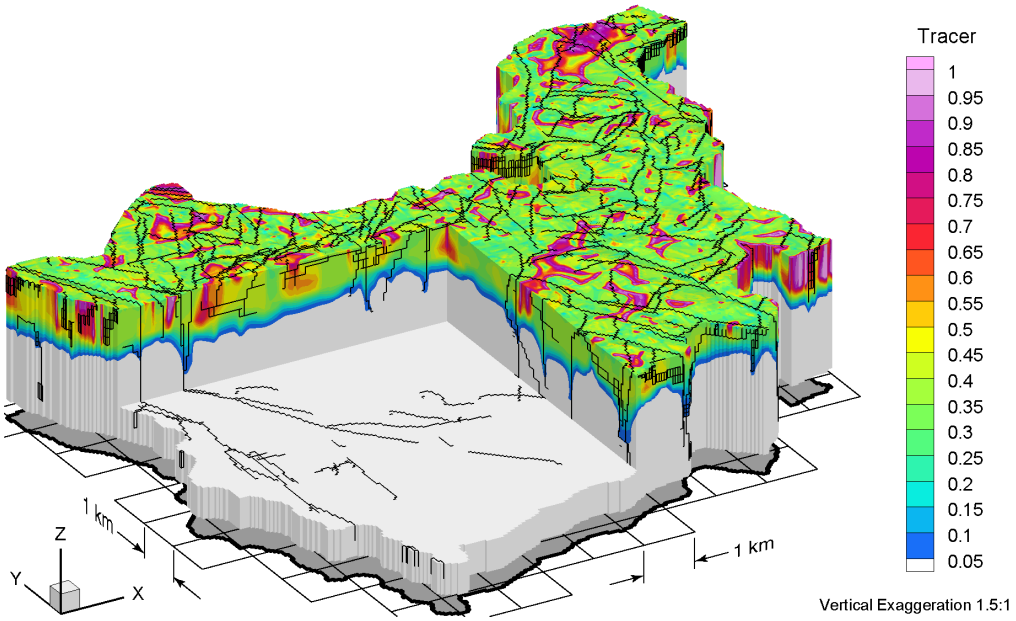

Figure B.35 Block cut view of tracer concentrations at present for the Canadian Shield Sub-Regional Scenario 2 paleoclimate simulation.

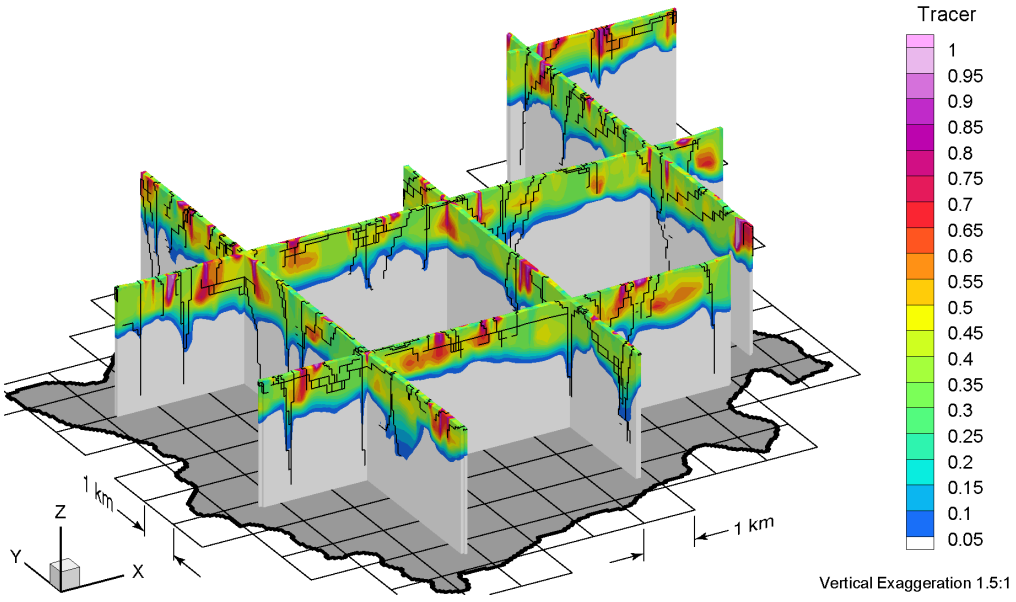

Figure B.36 Fence view of tracer concentrations at present for the Canadian Shield Sub-Regional Scenario 2 paleoclimate simulation.

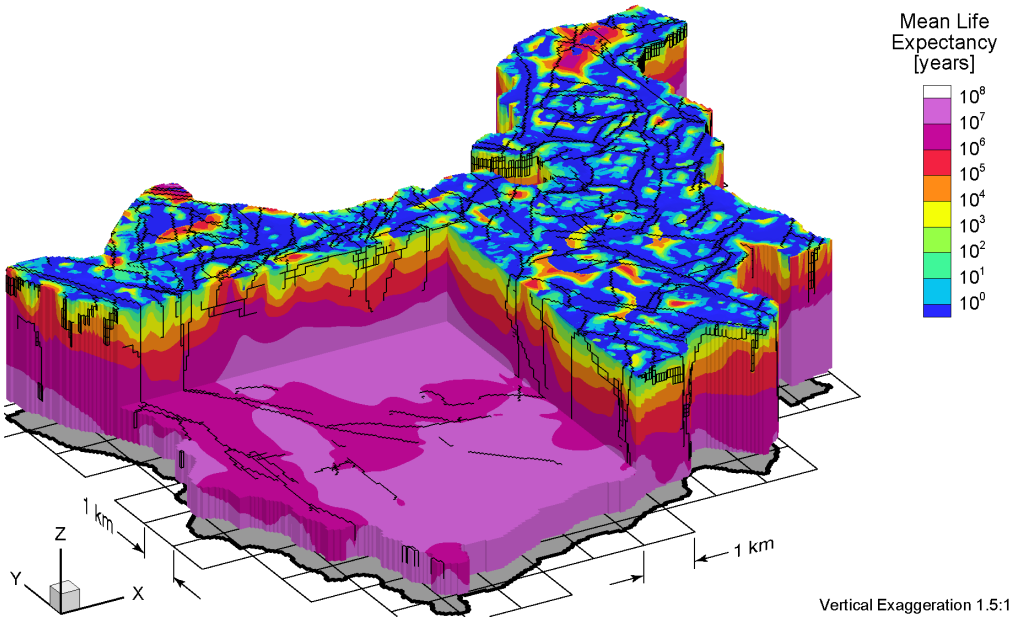

Figure B.37 Block cut view of mean life expectancies at present for the Canadian Shield Sub-Regional Scenario 2 paleoclimate simulation.

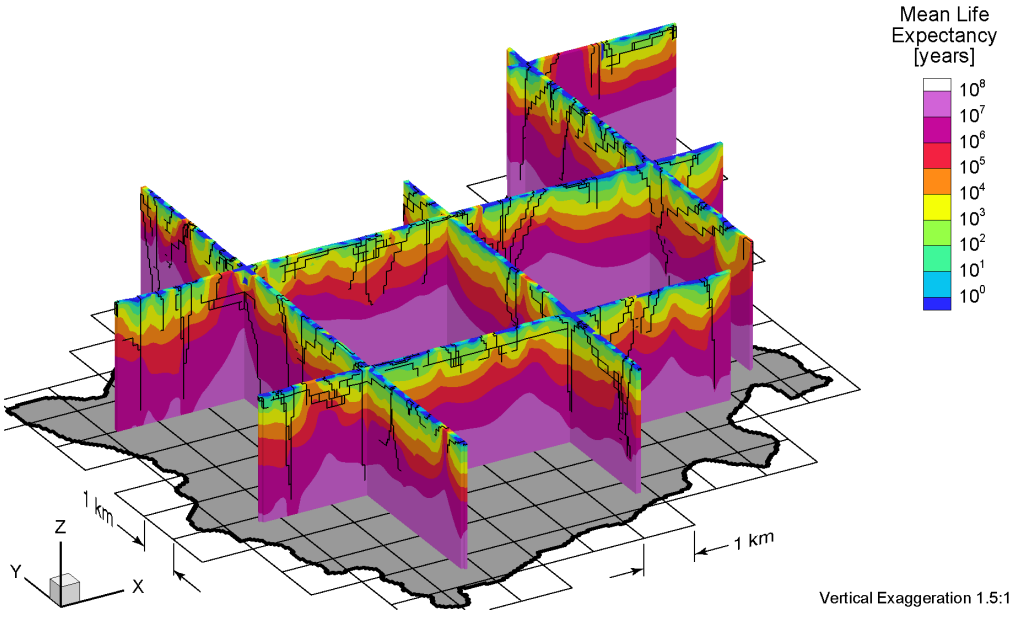

Figure B.38 Fence view of mean life expectancies at present for the Canadian Shield Sub-Regional Scenario 2 paleoclimate simulation.

Appendix C

CSSR Scenario 3 Paleoclimate Model

All figures related to Canadian Shield Sub-Regional (CSSR) Scenario 3 paleoclimate modelling are listed in Table C.1. Block cut view and fence view figures are shown on the same page to facilitate comparison. All results of the 120 ka paleoclimate simulations are shown at times of 80 ka before present, 40 ka before present, and at present.

Table C.1 List of Canadian Shield Sub-Regional Scenario 3 paleoclimate simulation figures.

Parameters	Time Before Present					
	80 ka		40 ka		Present	
	Block Cut	Fence	Block Cut	Fence	Block Cut	Fence
Freshwater Heads	C.1	C.2	C.3	C.4	C.5	C.6
Pore Velocity Magnitudes	C.7	C.8	C.9	C.10	C.11	C.12
Ratio of Vertical Pore Velocities to Pore Velocity Magnitudes	C.13	C.14	C.15	C.16	C.17	C.18
Tracer Concentrations	C.19	C.20	C.21	C.22	C.23	C.24
Mean Life Expectancies	—	—	—	—	C.25	C.26

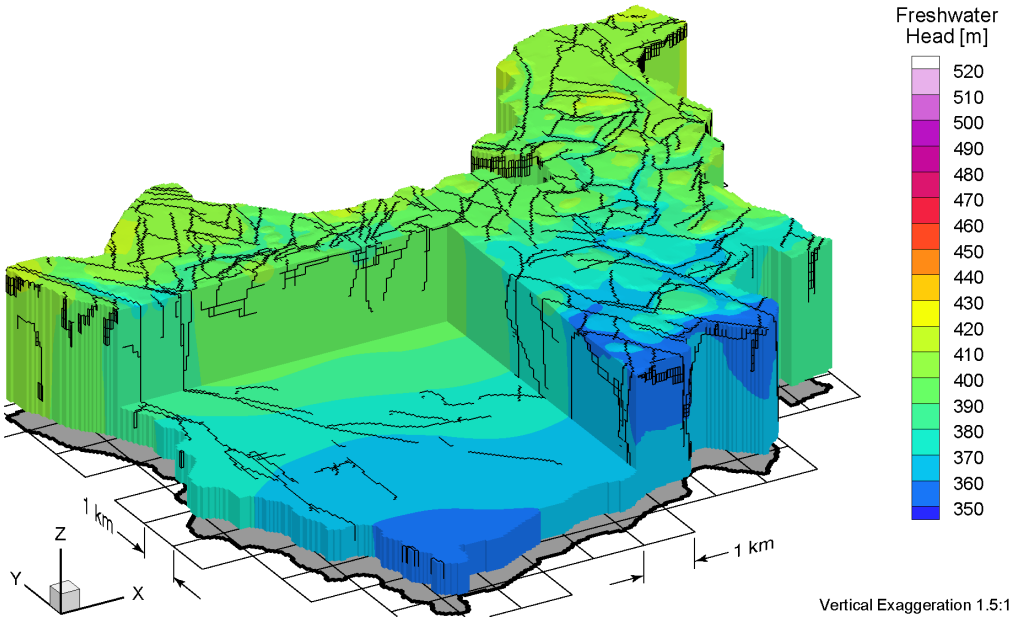

Figure C.1 Block cut view of freshwater heads at 80 ka before present for the Canadian Shield Sub-Regional Scenario 3 paleoclimate simulation.

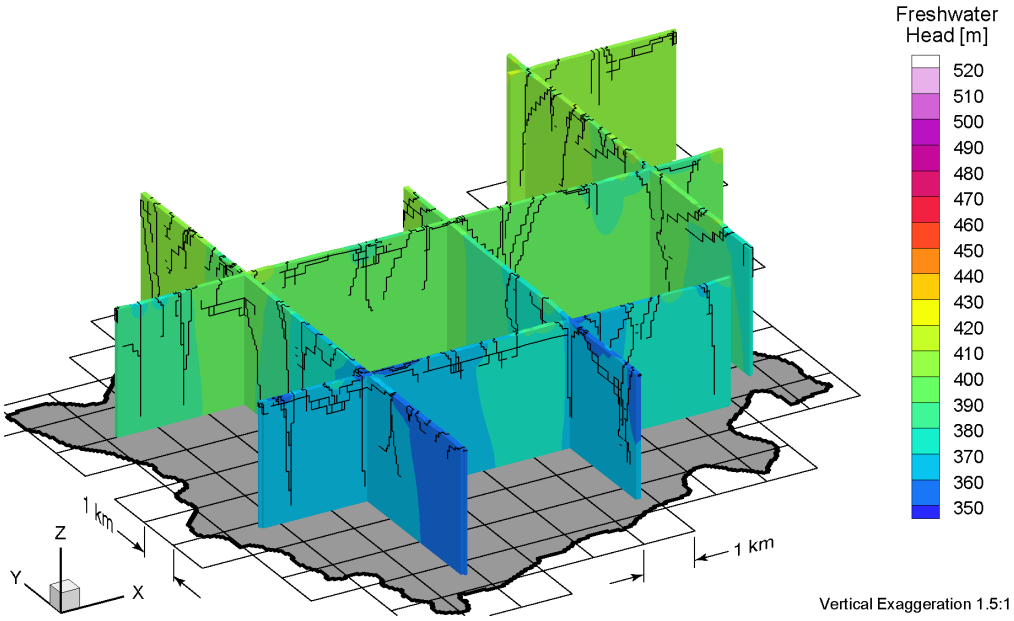

Figure C.2 Fence view of freshwater heads at 80 ka before present for the Canadian Shield Sub-Regional Scenario 3 paleoclimate simulation.

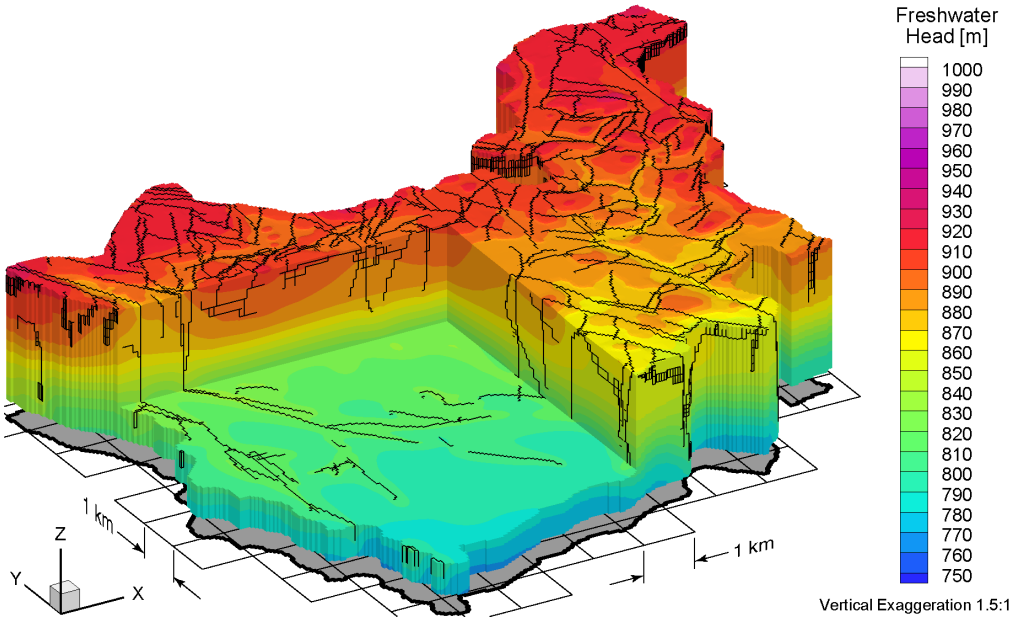

Figure C.3 Block cut view of freshwater heads at 40 ka before present for the Canadian Shield Sub-Regional Scenario 3 paleoclimate simulation.

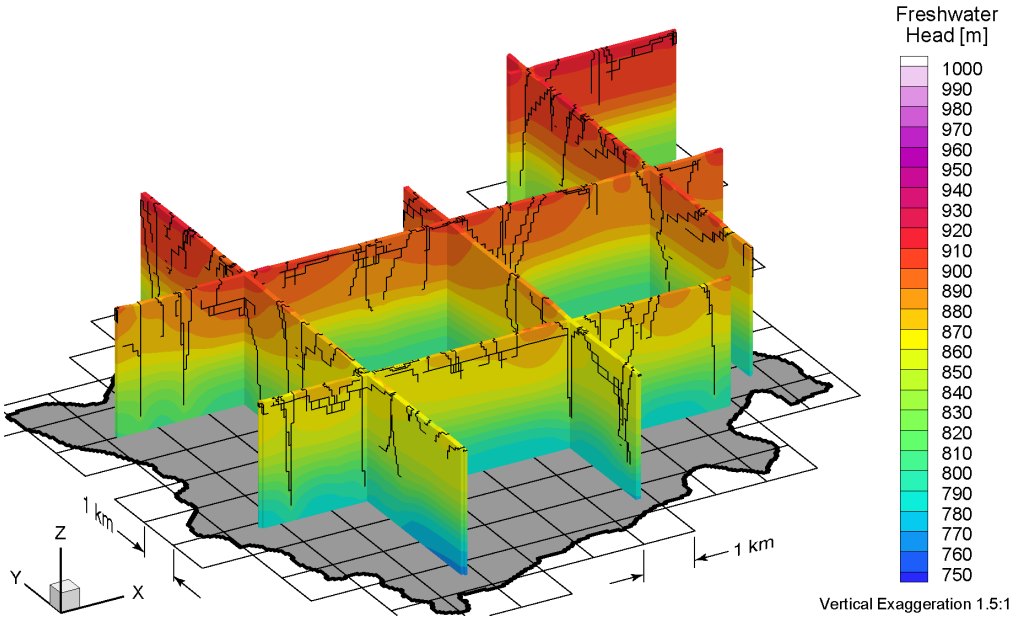

Figure C.4 Fence view of freshwater heads at 40 ka before present for the Canadian Shield Sub-Regional Scenario 3 paleoclimate simulation.

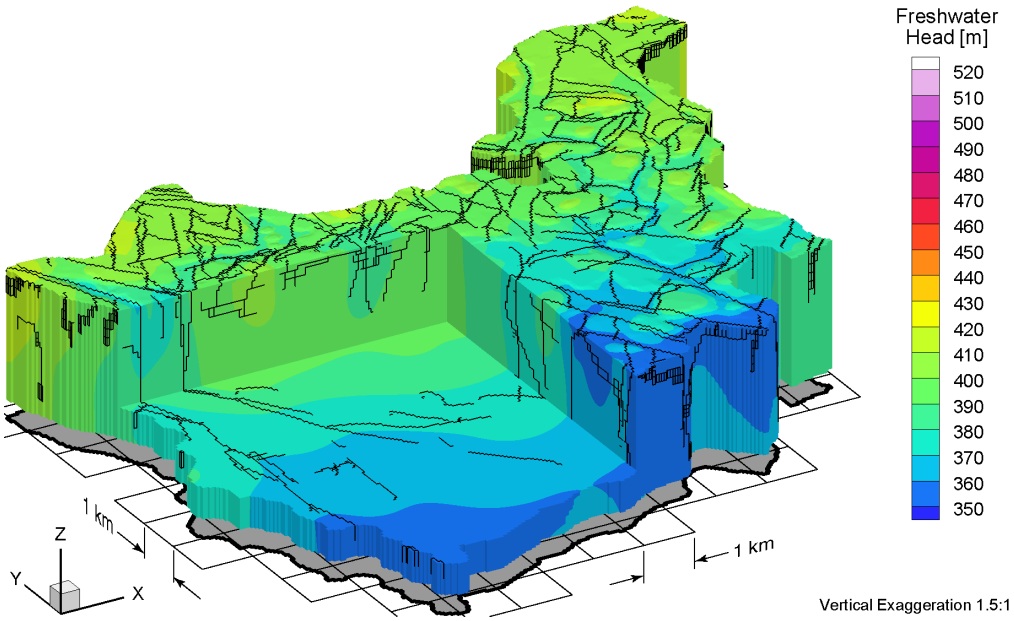

Figure C.5 Block cut view of freshwater heads at present for the Canadian Shield Sub-Regional Scenario 3 paleoclimate simulation.

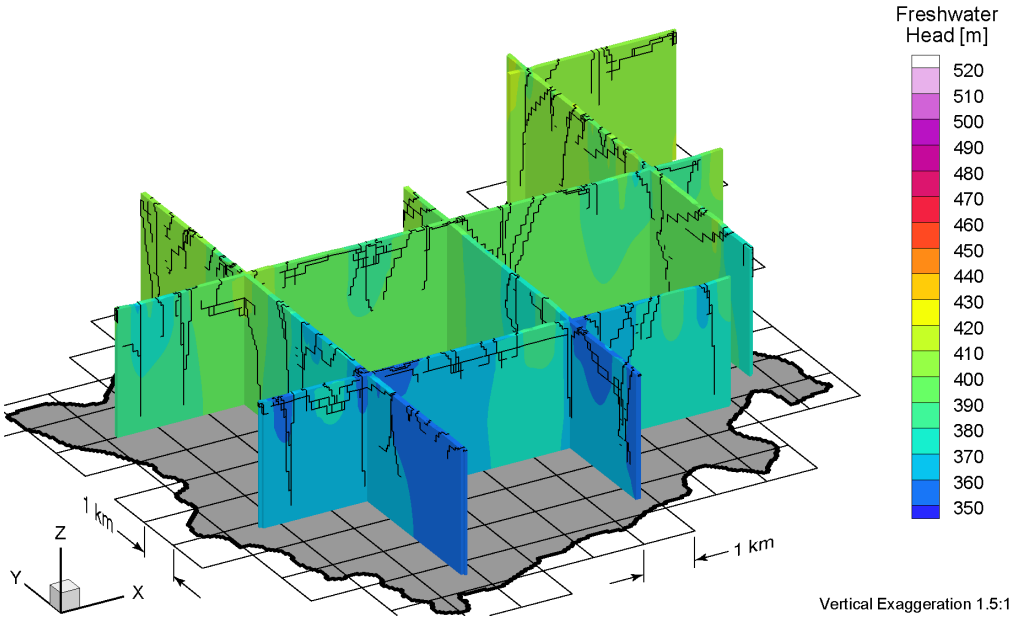

Figure C.6 Fence view of freshwater heads at present for the Canadian Shield Sub-Regional Scenario 3 paleoclimate simulation.

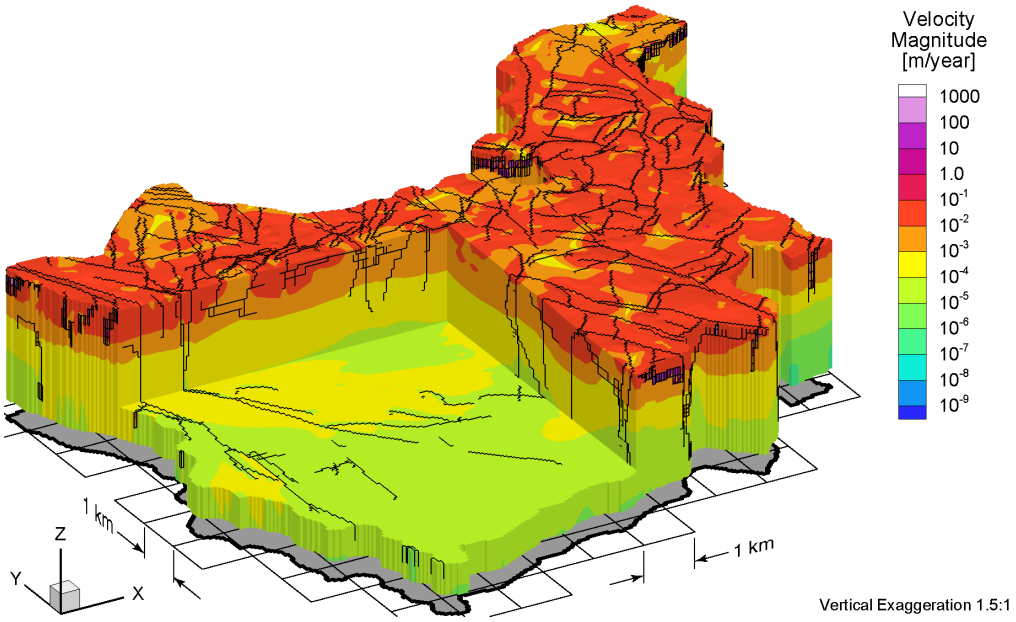

Figure C.7 Block cut view of pore velocity magnitudes at 80 ka before present for the Canadian Shield Sub-Regional Scenario 3 paleoclimate simulation.

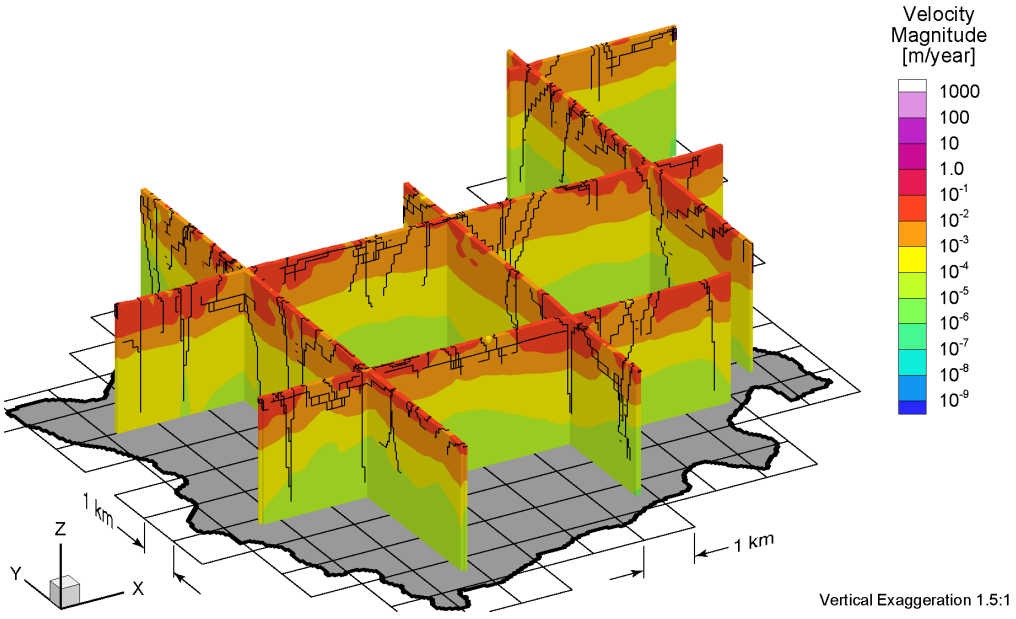

Figure C.8 Fence view of pore velocity magnitudes at 80 ka before present for the Canadian Shield Sub-Regional Scenario 3 paleoclimate simulation.

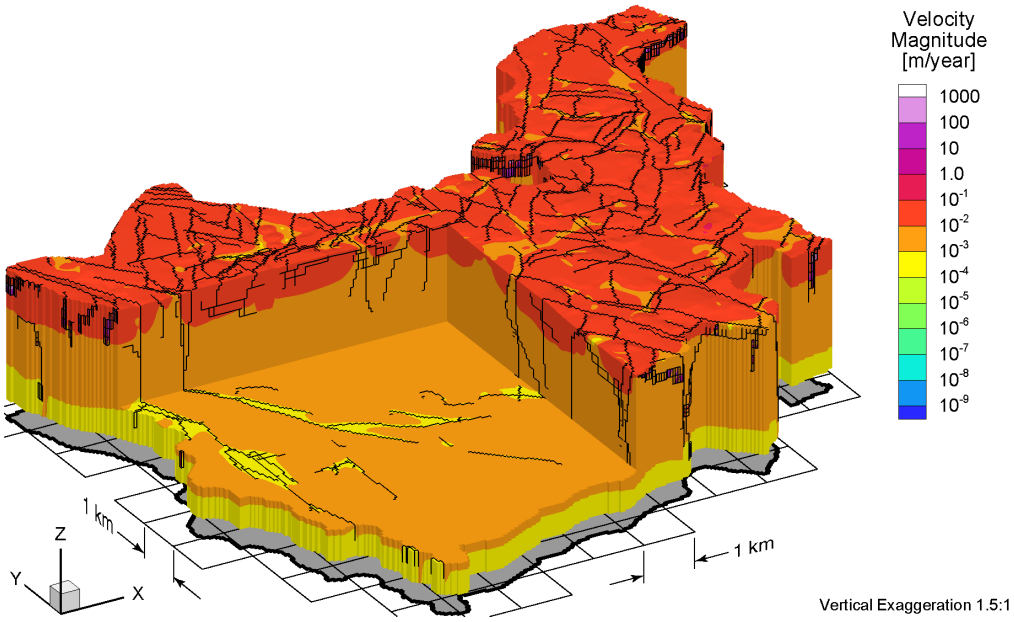

Figure C.9 Block cut view of pore velocity magnitudes at 40 ka before present for the Canadian Shield Sub-Regional Scenario 3 paleoclimate simulation.

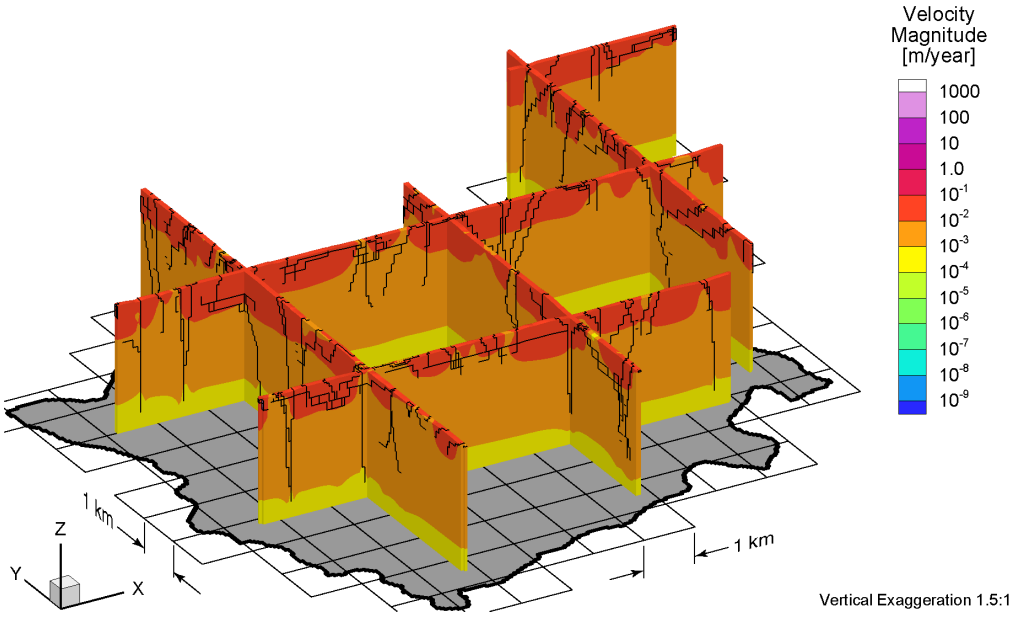

Figure C.10 Fence view of pore velocity magnitudes at 40 ka before present for the Canadian Shield Sub-Regional Scenario 3 paleoclimate simulation.

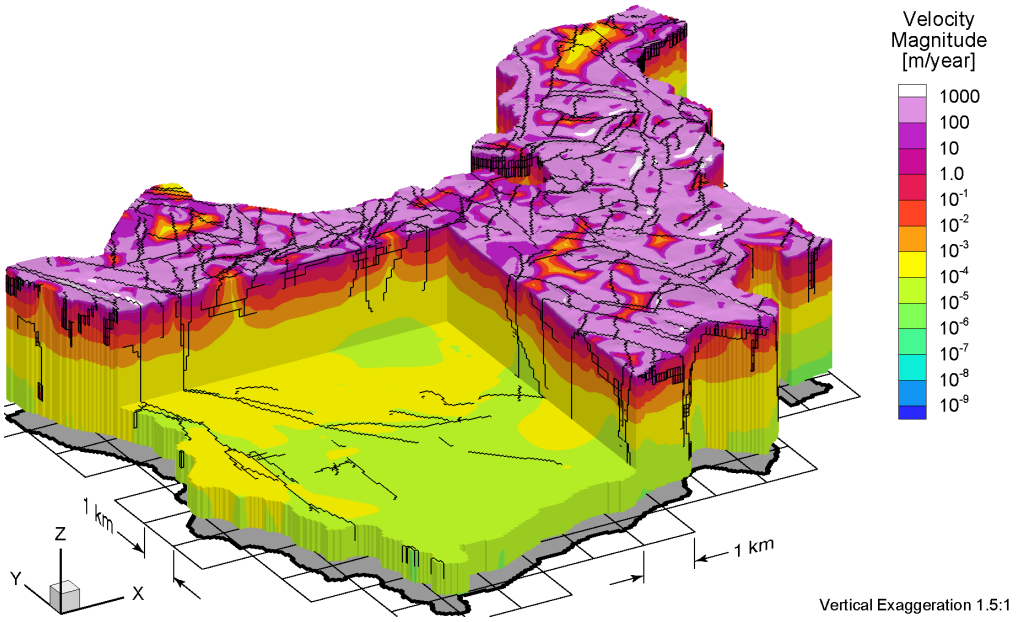

Figure C.11 Block cut view of pore velocity magnitudes at present for the Canadian Shield Sub-Regional Scenario 3 paleoclimate simulation.

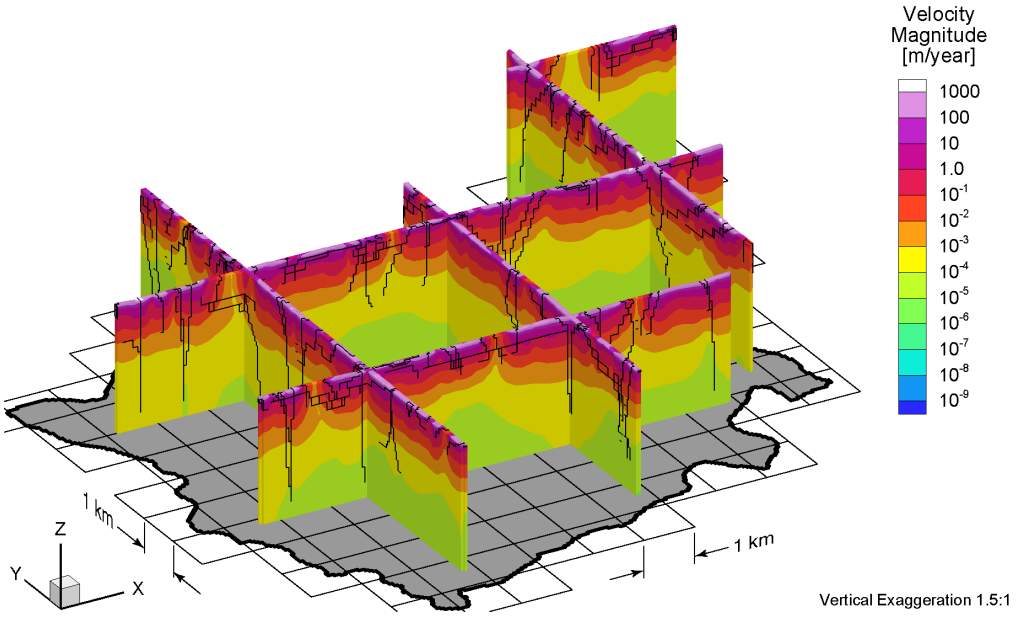

Figure C.12 Fence view of pore velocity magnitudes at present for the Canadian Shield Sub-Regional Scenario 3 paleoclimate simulation.

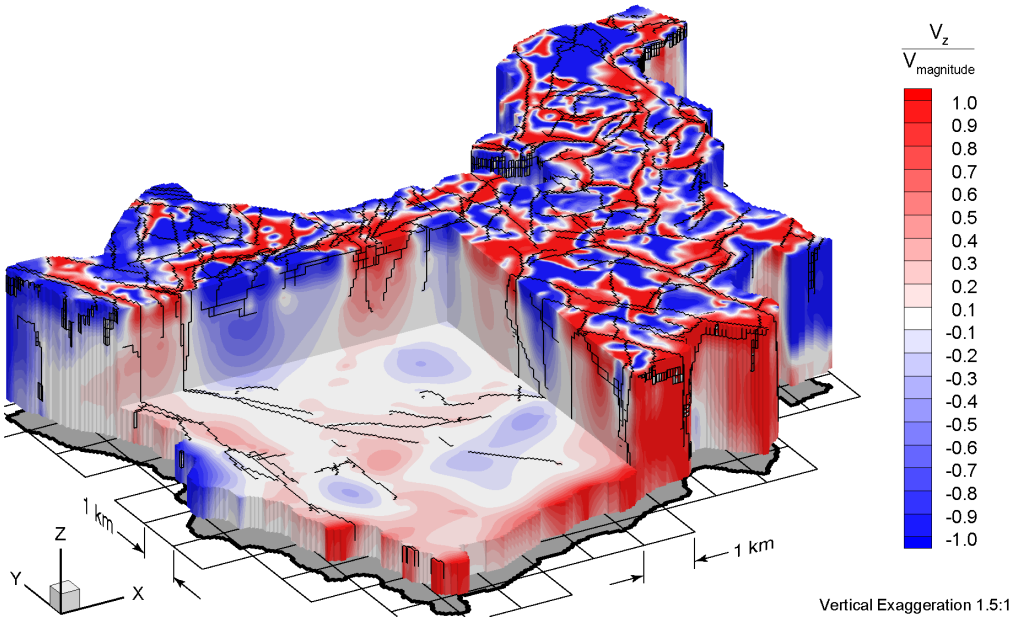

Figure C.13 Block cut view of ratio of vertical pore velocities to pore velocity magnitudes at 80 ka before present for the Canadian Shield Sub-Regional Scenario 3 paleoclimate simulation.

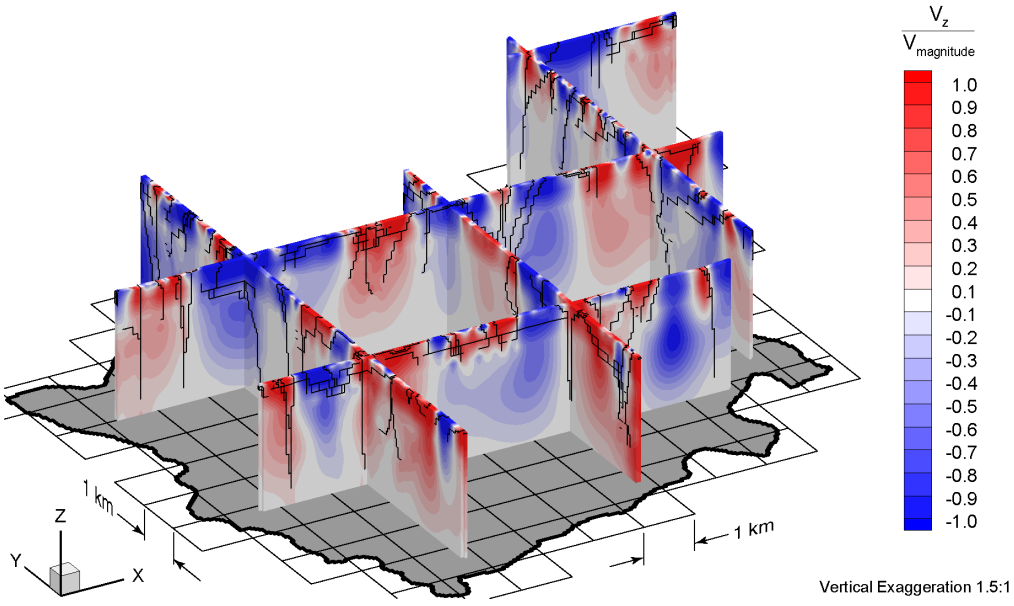

Figure C.14 Fence view of ratio of vertical pore velocities to pore velocity magnitudes at 80 ka before present for the Canadian Shield Sub-Regional Scenario 3 paleoclimate simulation.

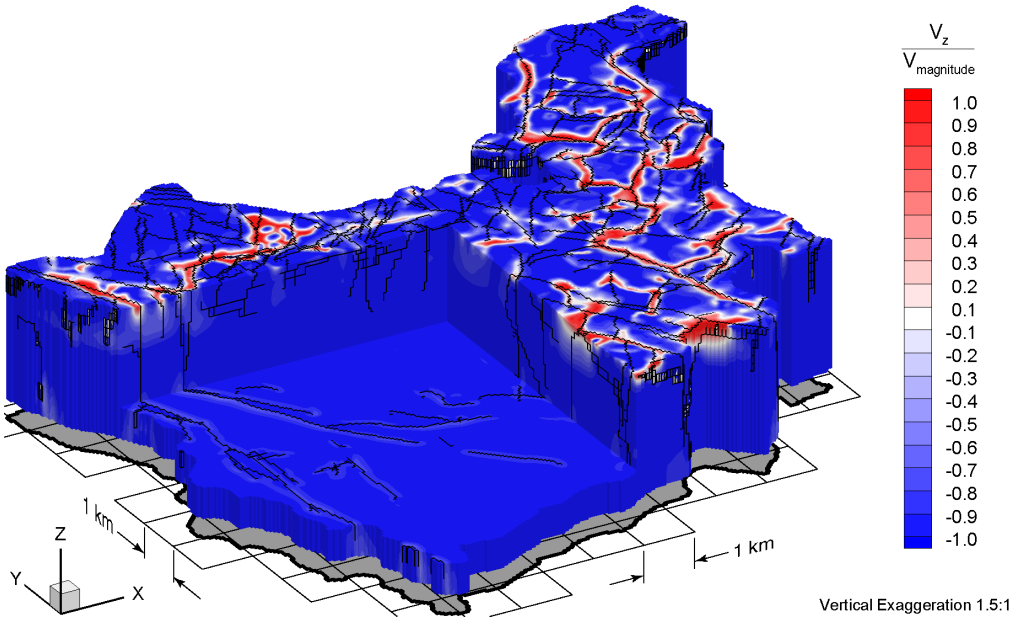

Figure C.15 Block cut view of ratio of vertical pore velocities to pore velocity magnitudes at 40 ka before present for the Canadian Shield Sub-Regional Scenario 3 paleoclimate simulation.

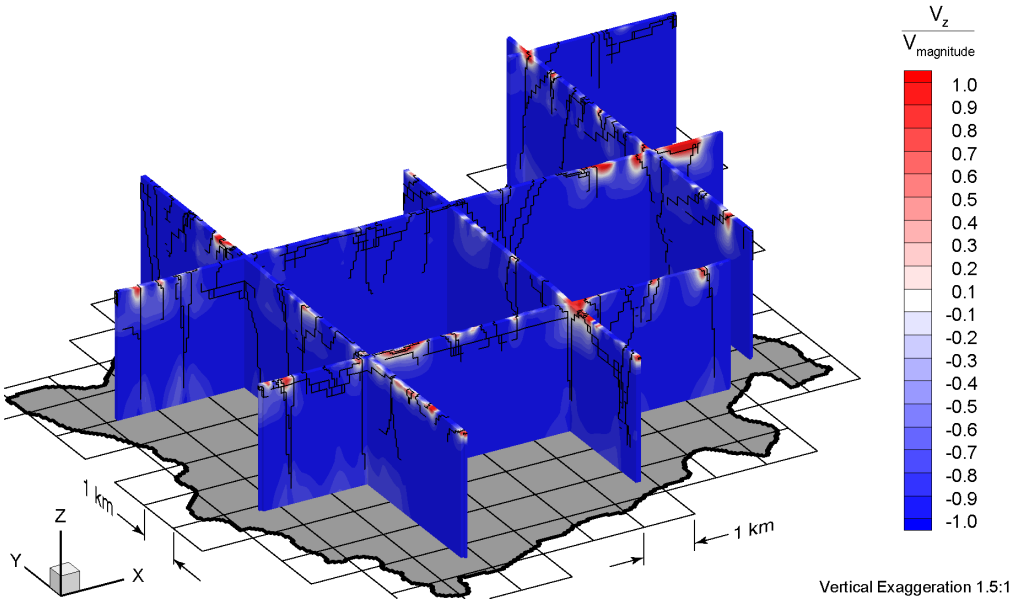

Figure C.16 Fence view of ratio of vertical pore velocities to pore velocity magnitudes at 40 ka before present for the Canadian Shield Sub-Regional Scenario 3 paleoclimate simulation.

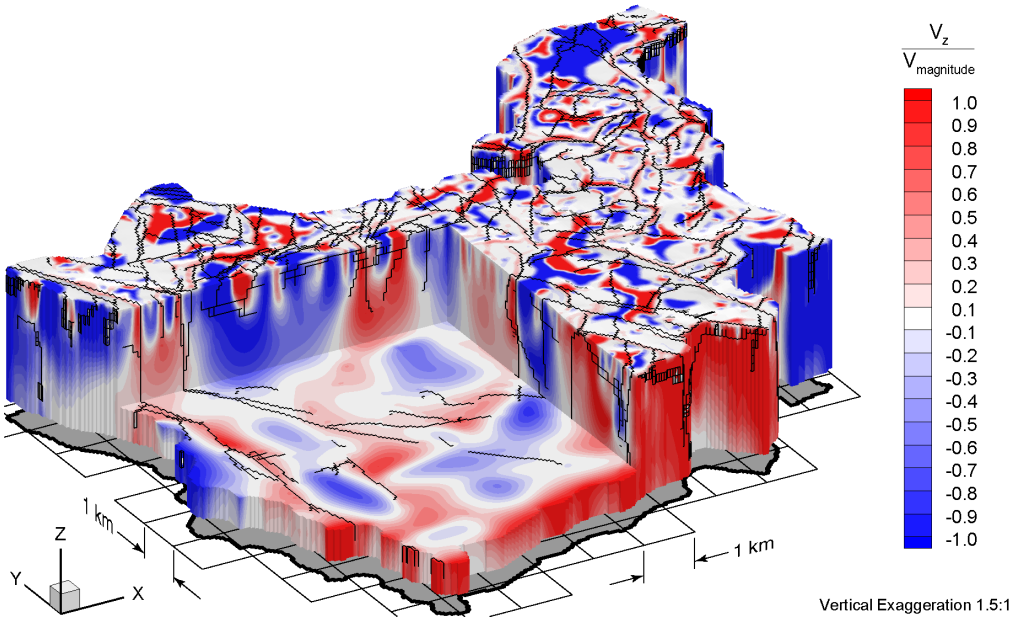

Figure C.17 Block cut view of ratio of vertical pore velocities to pore velocity magnitudes at present for the Canadian Shield Sub-Regional Scenario 3 paleoclimate simulation.

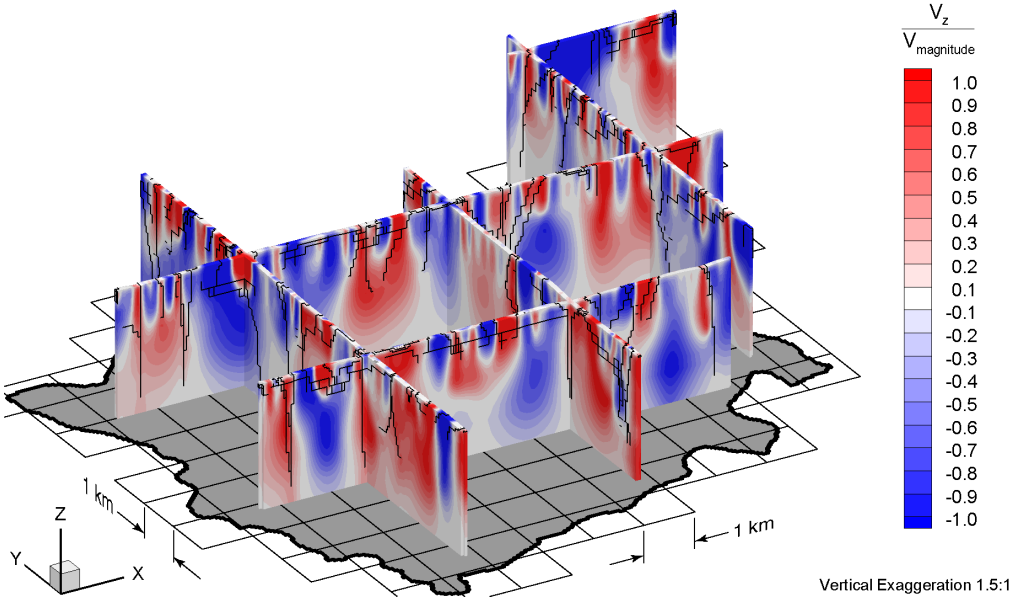

Figure C.18 Fence view of ratio of vertical pore velocities to pore velocity magnitudes at present for the Canadian Shield Sub-Regional Scenario 3 paleoclimate simulation.

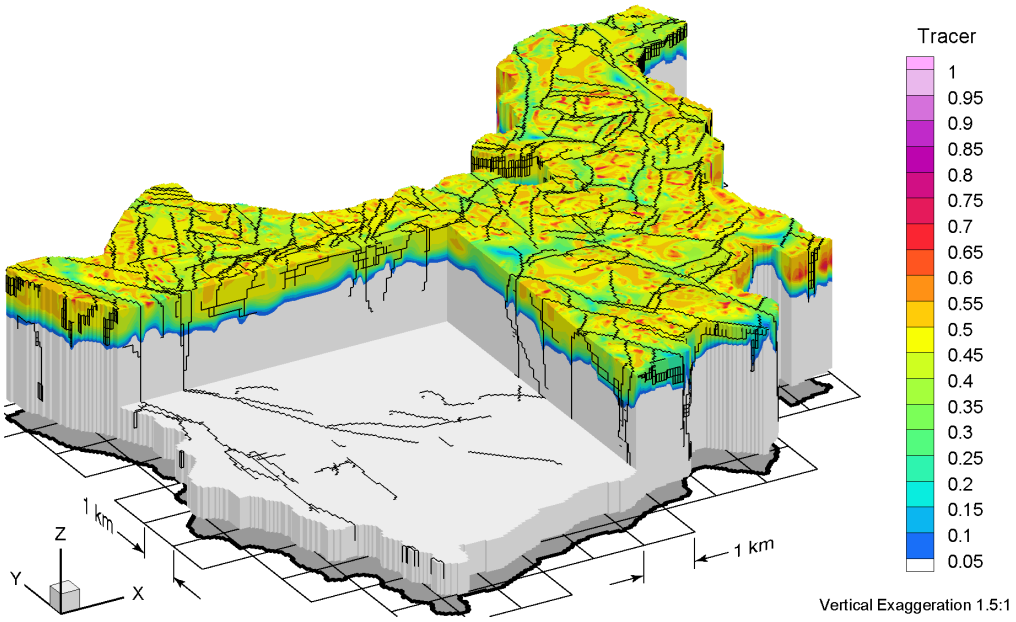

Figure C.19 Block cut view of tracer concentrations at 80 ka before present for the Canadian Shield Sub-Regional Scenario 3 paleoclimate simulation.

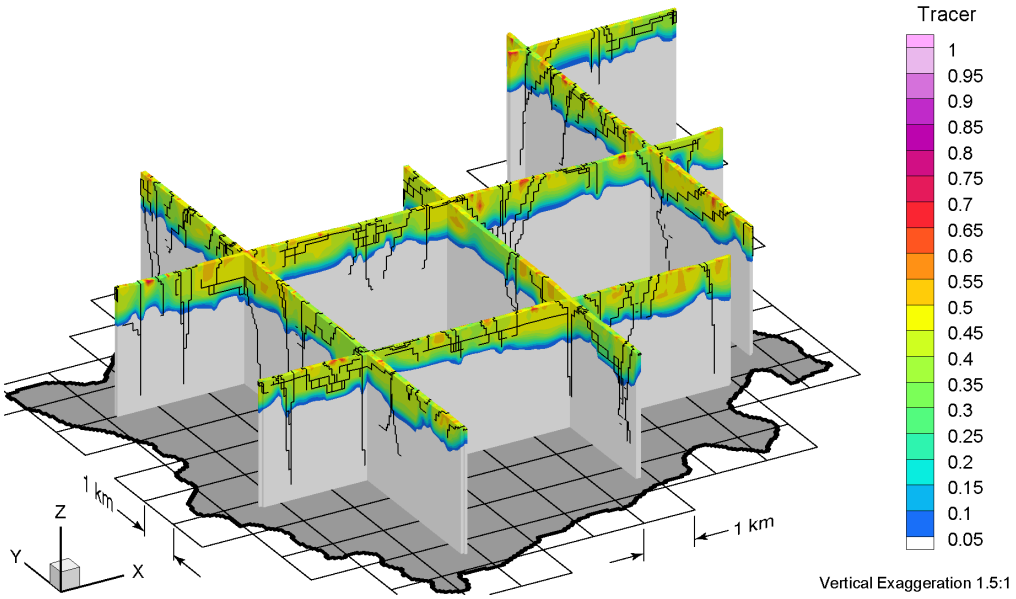

Figure C.20 Fence view of tracer concentrations at 80 ka before present for the Canadian Shield Sub-Regional Scenario 3 paleoclimate simulation.

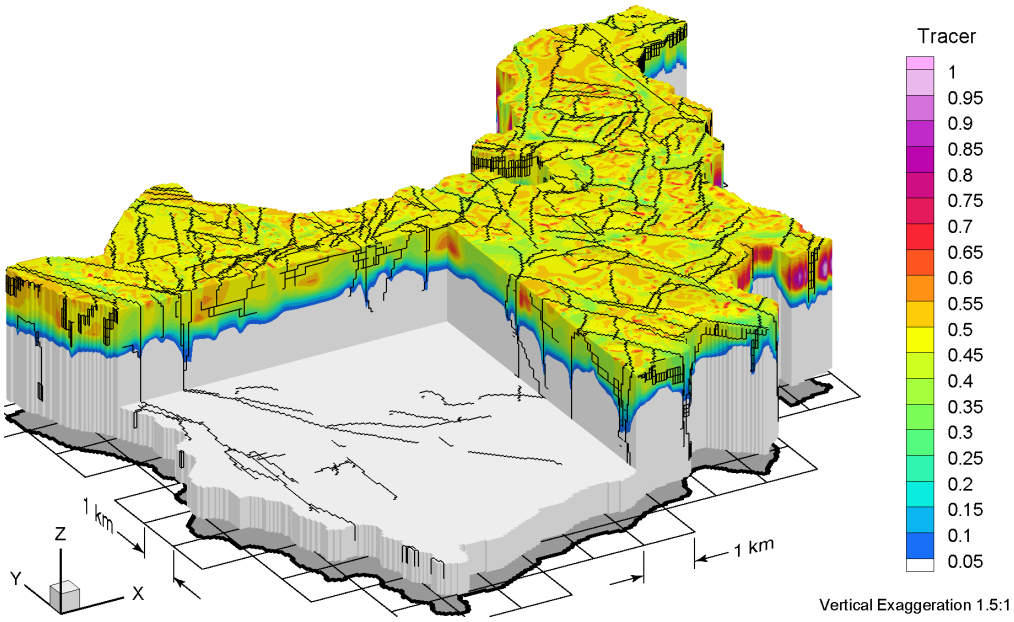

Figure C.21 Block cut view of tracer concentrations at 40 ka before present for the Canadian Shield Sub-Regional Scenario 3 paleoclimate simulation.

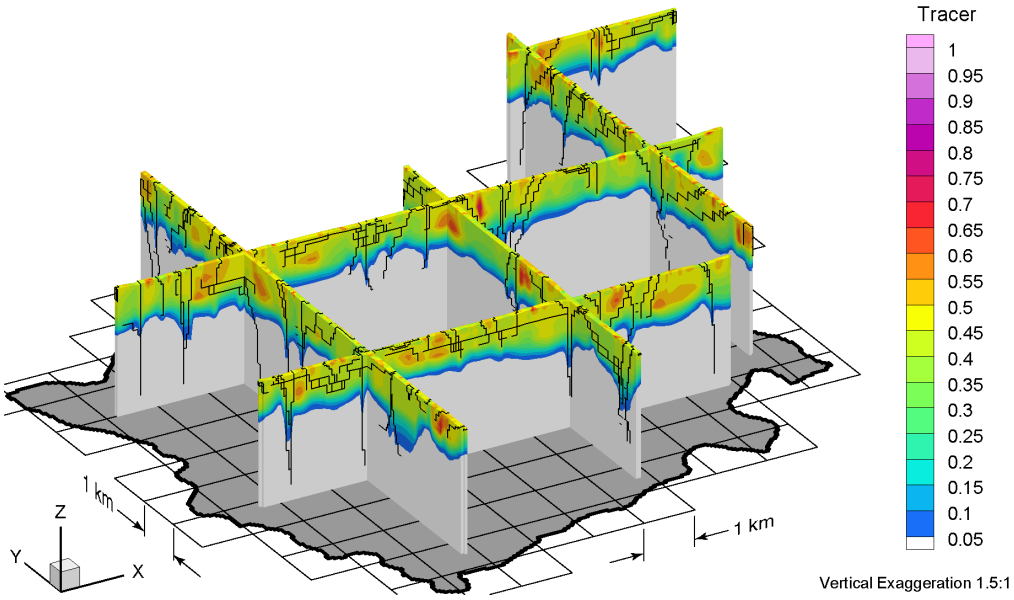

Figure C.22 Fence view of tracer concentrations at 40 ka before present for the Canadian Shield Sub-Regional Scenario 3 paleoclimate simulation.

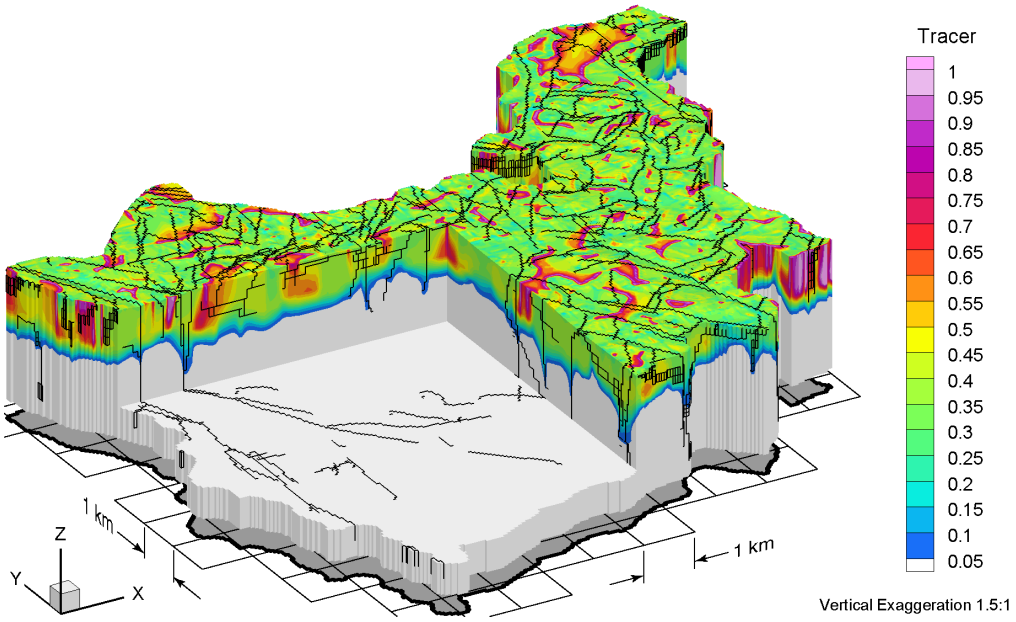

Figure C.23 Block cut view of tracer concentrations at present for the Canadian Shield Sub-Regional Scenario 3 paleoclimate simulation.

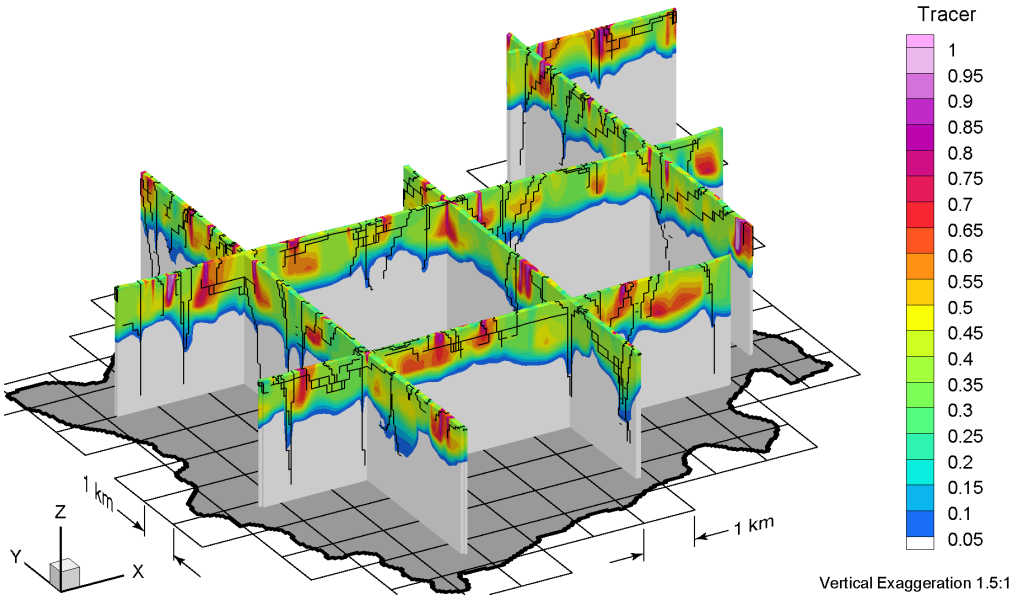

Figure C.24 Fence view of tracer concentrations at present for the Canadian Shield Sub-Regional Scenario 3 paleoclimate simulation.

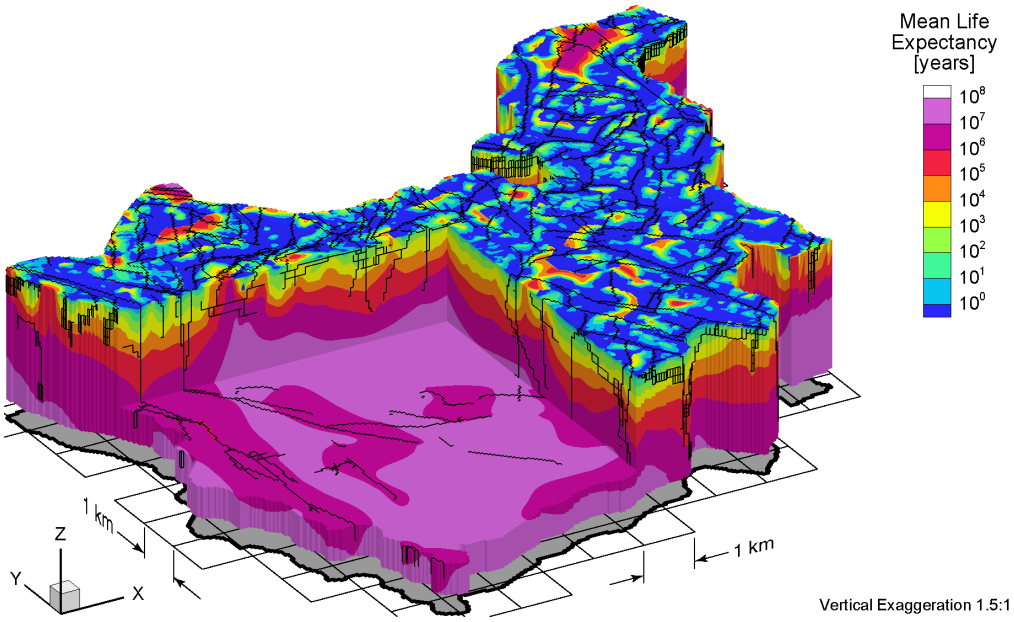

Figure C.25 Block cut view of mean life expectancies at present for the Canadian Shield Sub-Regional Scenario 3 paleoclimate simulation.

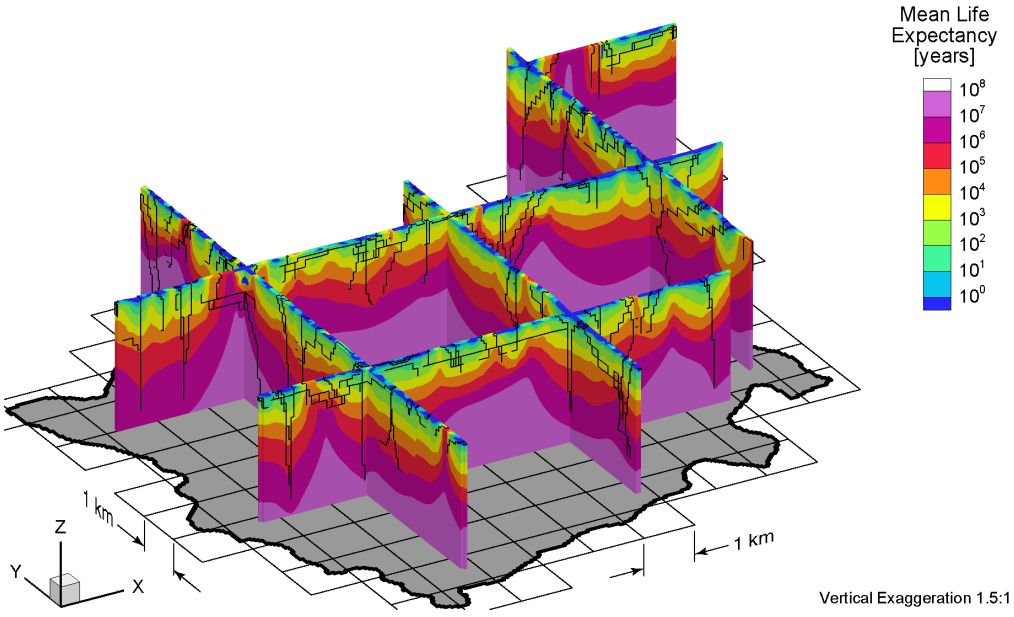

Figure C.26 Fence view of mean life expectancies at present for the Canadian Shield Sub-Regional Scenario 3 paleoclimate simulation.

Appendix D

CSSR Scenario 4 Paleoclimate Model

All figures related to Canadian Shield Sub-Regional (CSSR) Scenario 4 paleoclimate modelling are listed in Table D.1. Block cut view and fence view figures are shown on the same page to facilitate comparison. All results of the 120 ka paleoclimate simulations are shown at times of 80 ka before present, 40 ka before present, and at present.

Table D.1 List of Canadian Shield Sub-Regional Scenario 4 paleoclimate simulation figures.

Parameters	Time Before Present					
	80 ka		40 ka		Present	
	Block Cut	Fence	Block Cut	Fence	Block Cut	Fence
Freshwater Heads	D.1	D.2	D.3	D.4	D.5	D.6
Environmental Heads	D.7	D.8	D.9	D.10	D.11	D.12
Pore Velocity Magnitudes	D.13	D.14	D.15	D.16	D.17	D.18
Ratio of Vertical Pore Velocities to Pore Velocity Magnitudes	D.19	D.20	D.21	D.22	D.23	D.24
Brine Concentrations	D.25	D.26	D.27	D.28	D.29	D.30
Tracer Concentrations	D.31	D.32	D.33	D.34	D.35	D.36
Mean Life Expectancies	—	—	—	—	D.37	D.38

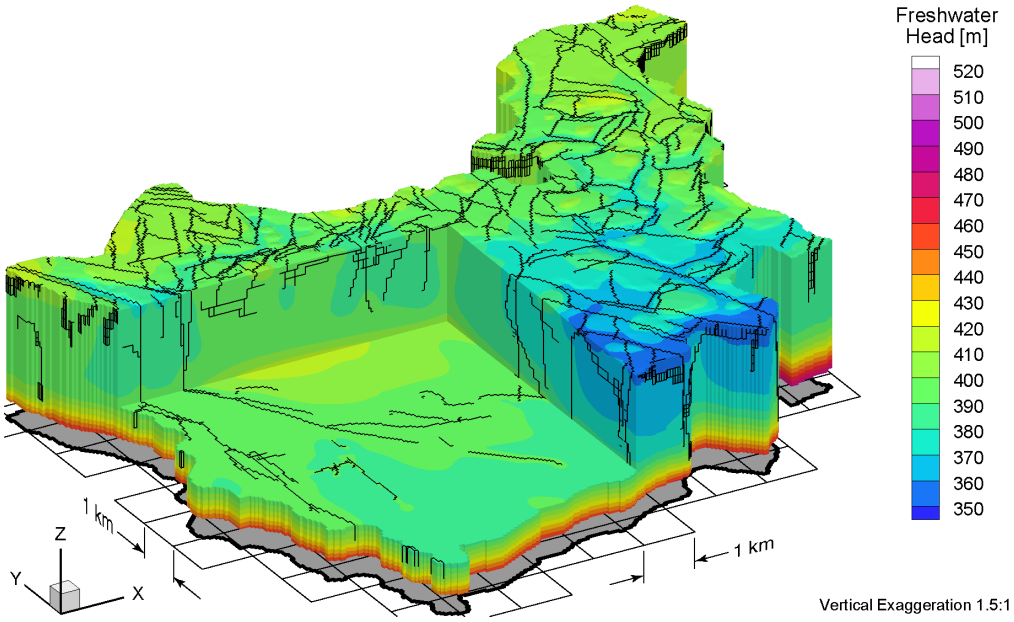

Figure D.1 Block cut view of freshwater heads at 80 ka before present for the Canadian Shield Sub-Regional Scenario 4 paleoclimate simulation.

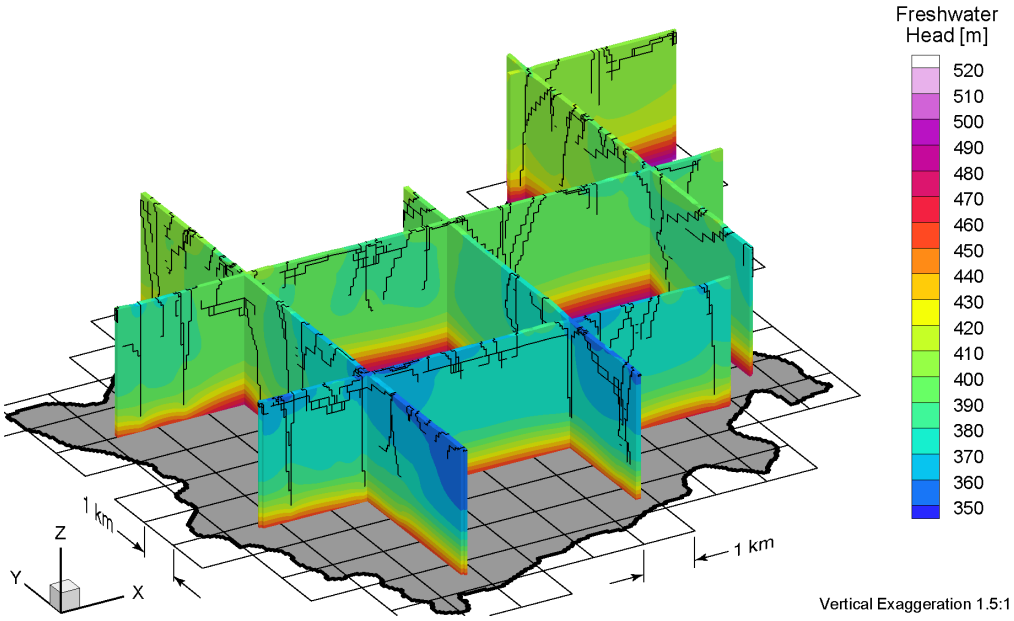

Figure D.2 Fence view of freshwater heads at 80 ka before present for the Canadian Shield Sub-Regional Scenario 4 paleoclimate simulation.

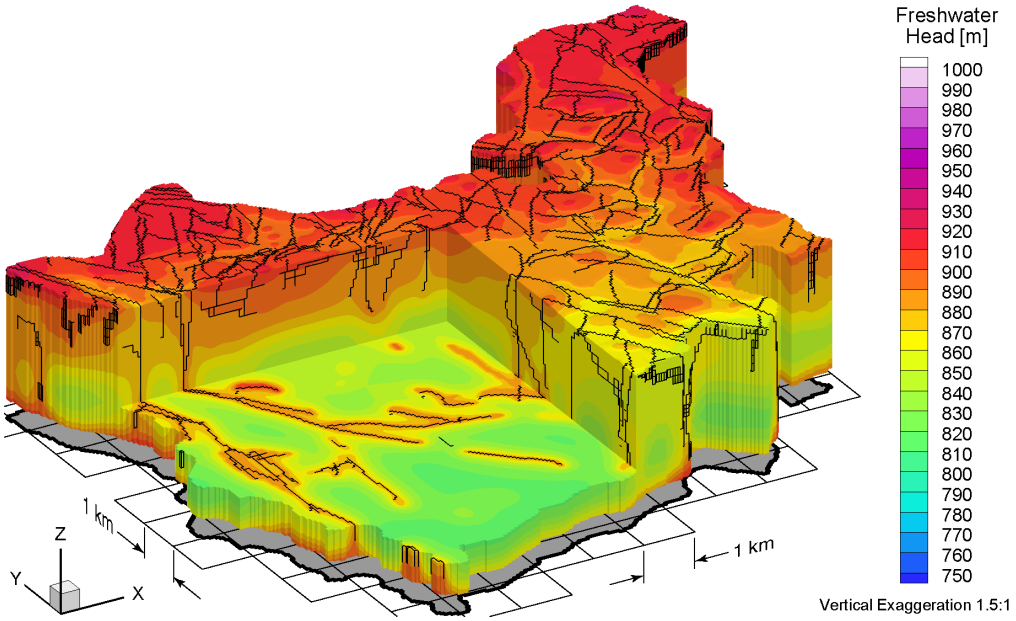

Figure D.3 Block cut view of freshwater heads at 40 ka before present for the Canadian Shield Sub-Regional Scenario 4 paleoclimate simulation.

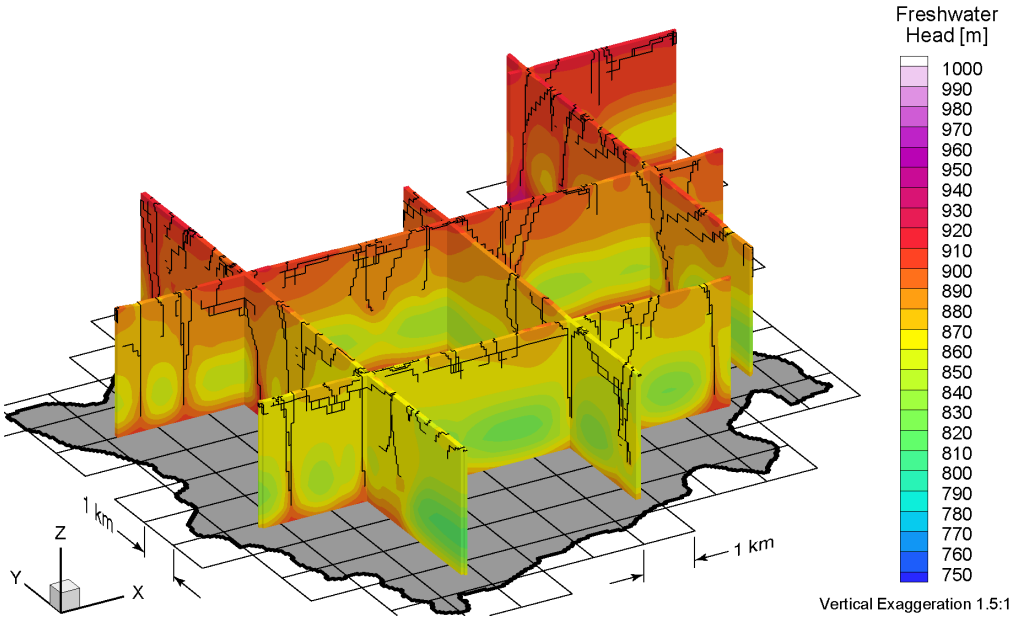

Figure D.4 Fence view of freshwater heads at 40 ka before present for the Canadian Shield Sub-Regional Scenario 4 paleoclimate simulation.

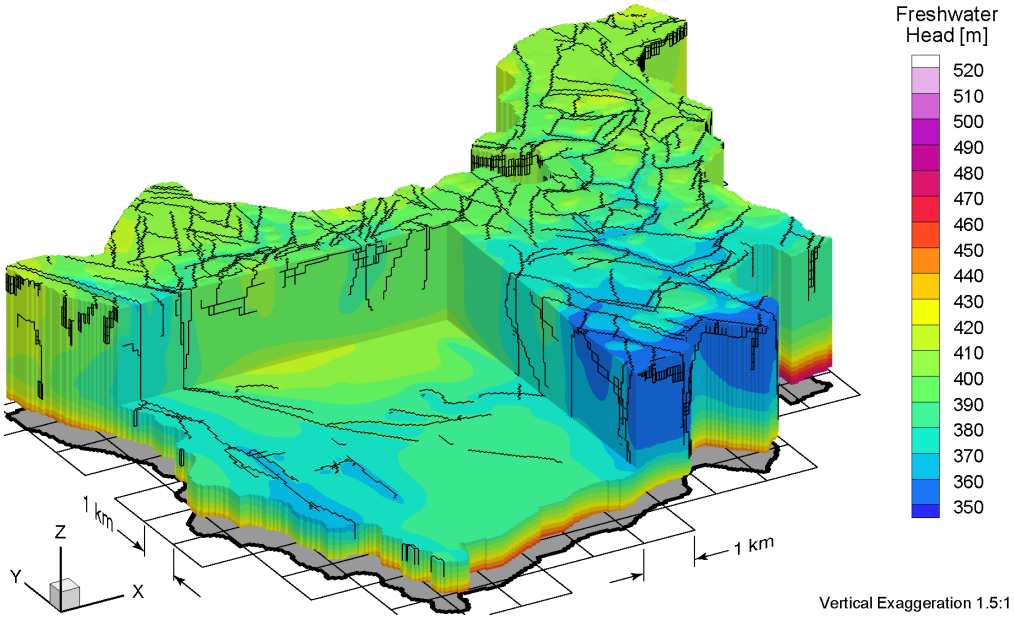

Figure D.5 Block cut view of freshwater heads at present for the Canadian Shield Sub-Regional Scenario 4 paleoclimate simulation.

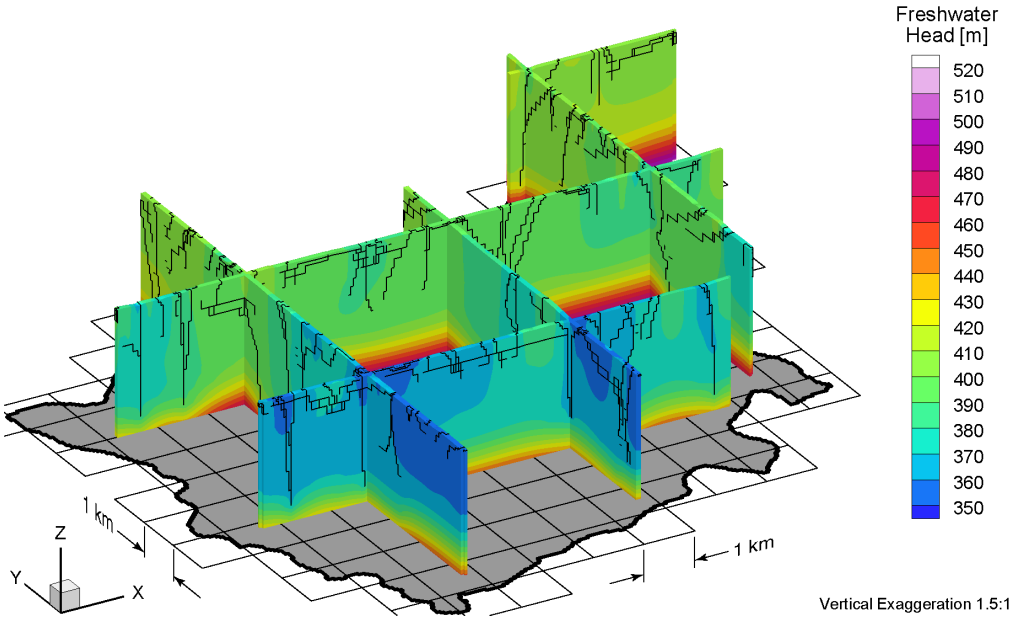

Figure D.6 Fence view of freshwater heads at present for the Canadian Shield Sub-Regional Scenario 4 paleoclimate simulation.

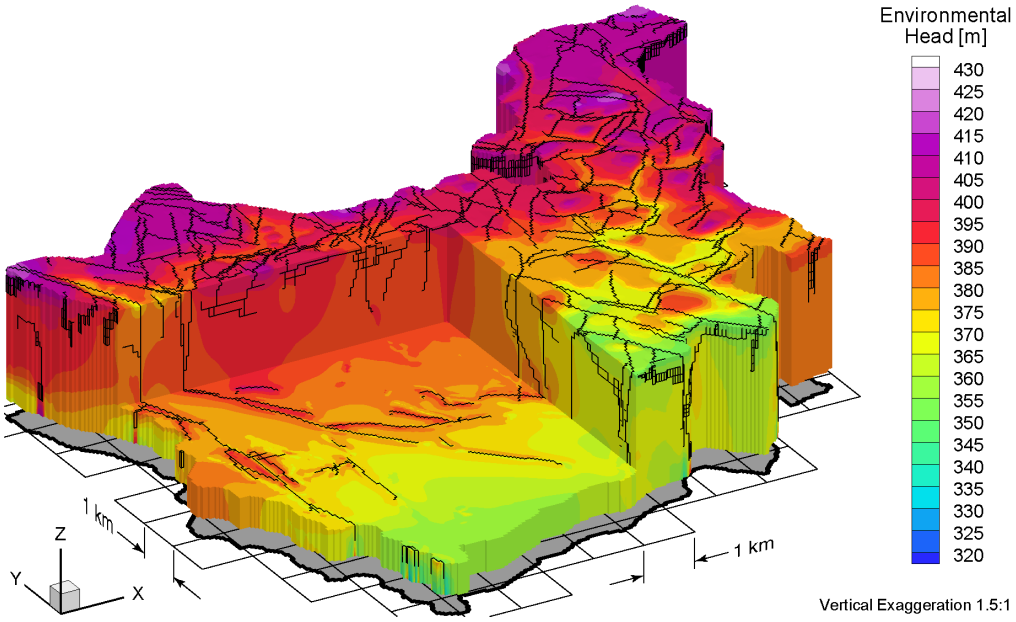

Figure D.7 Block cut view of environmental heads at 80 ka before present for the Canadian Shield Sub-Regional Scenario 4 paleoclimate simulation.

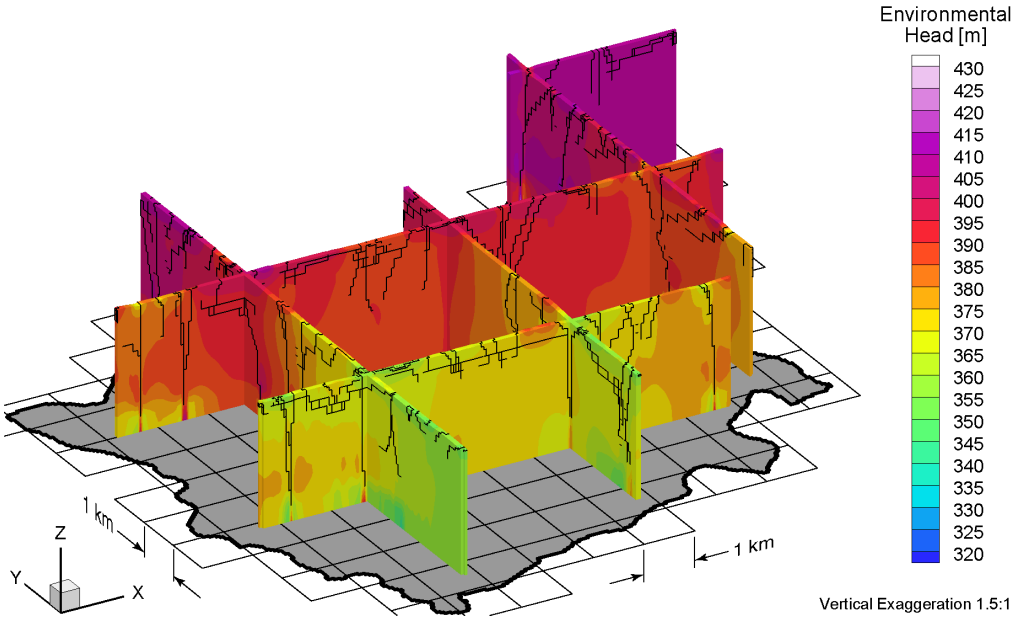

Figure D.8 Fence view of environmental heads at 80 ka before present for the Canadian Shield Sub-Regional Scenario 4 paleoclimate simulation.

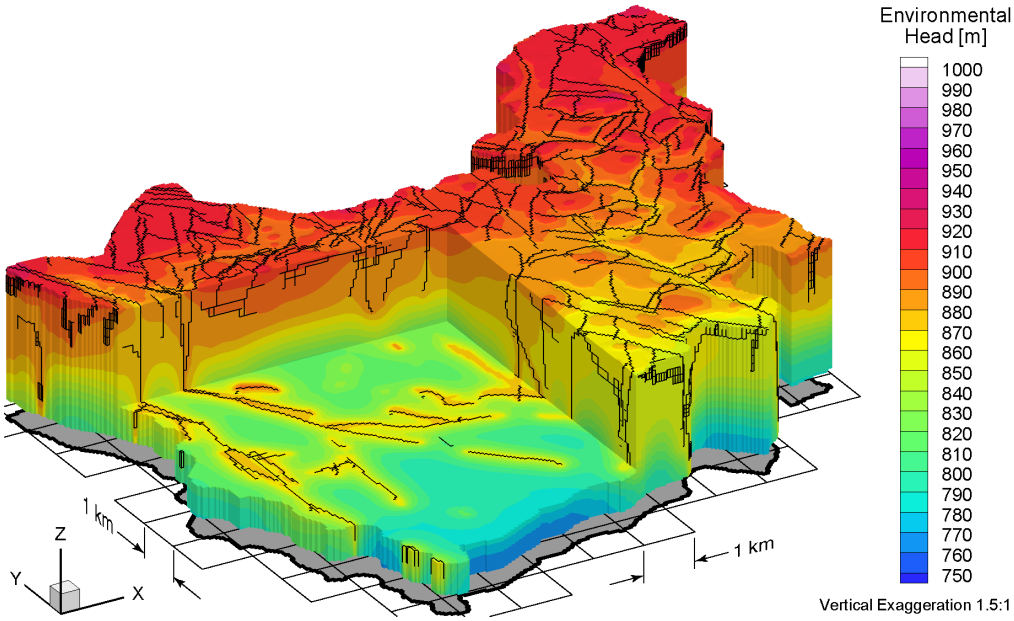

Figure D.9 Block cut view of environmental heads at 40 ka before present for the Canadian Shield Sub-Regional Scenario 4 paleoclimate simulation.

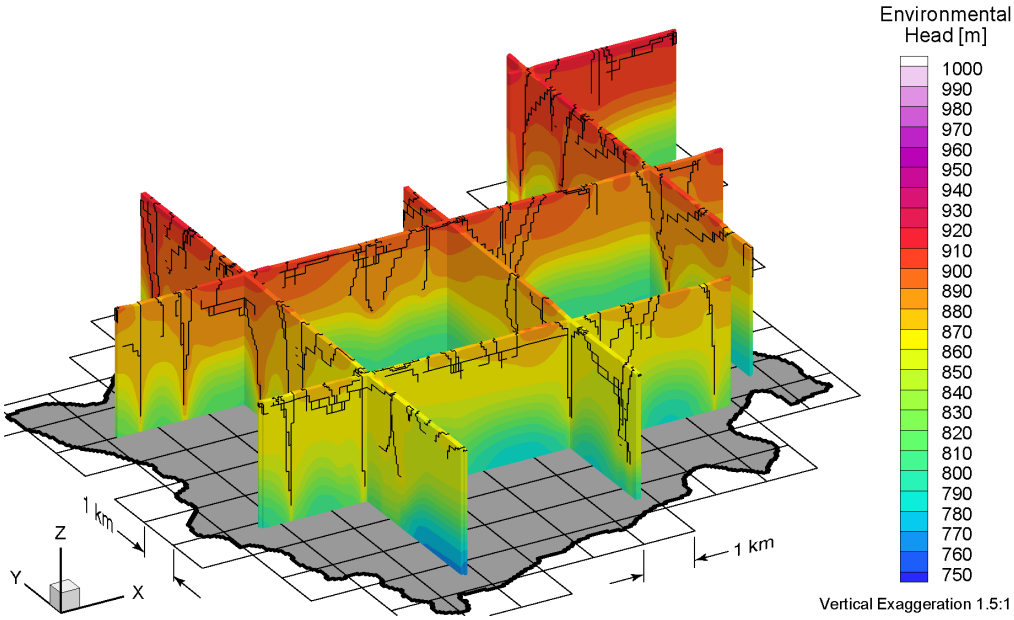

Figure D.10 Fence view of environmental heads at 40 ka before present for the Canadian Shield Sub-Regional Scenario 4 paleoclimate simulation.

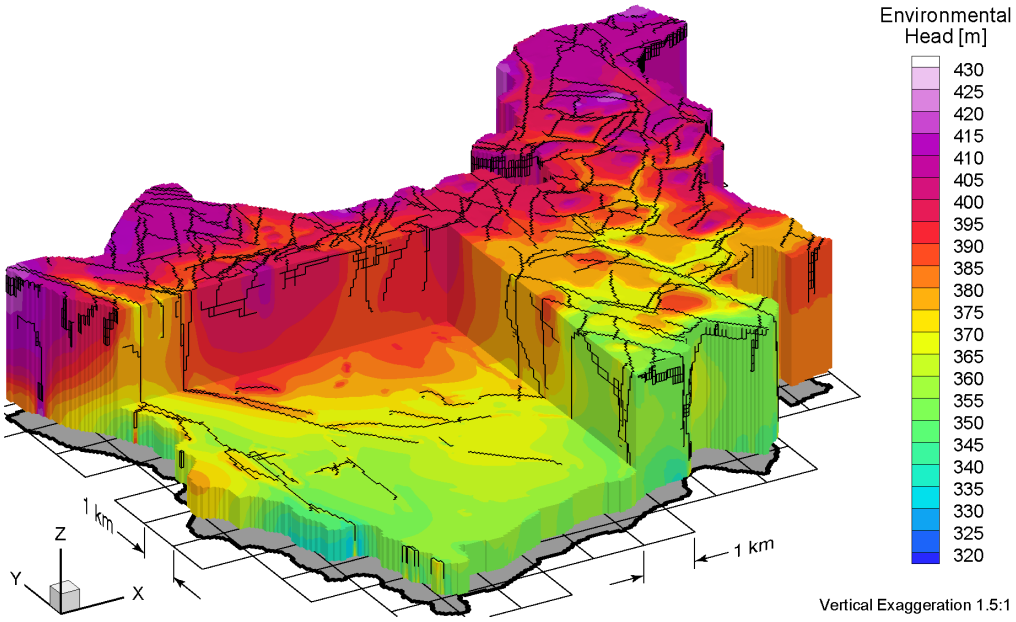

Figure D.11 Block cut view of environmental heads at present for the Canadian Shield Sub-Regional Scenario 4 paleoclimate simulation.

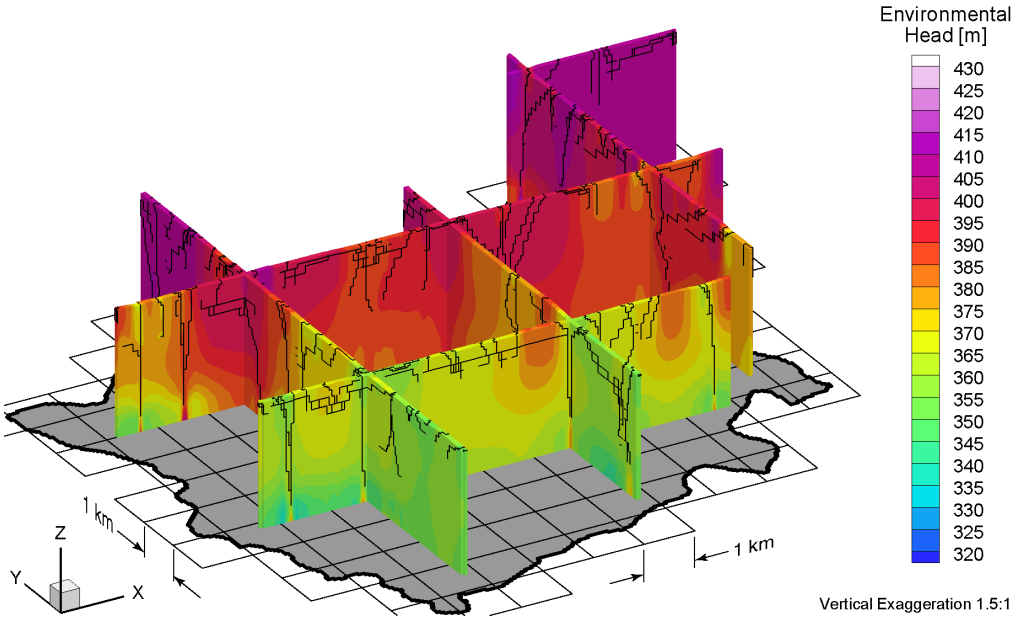

Figure D.12 Fence view of environmental heads at present for the Canadian Shield Sub-Regional Scenario 4 paleoclimate simulation.

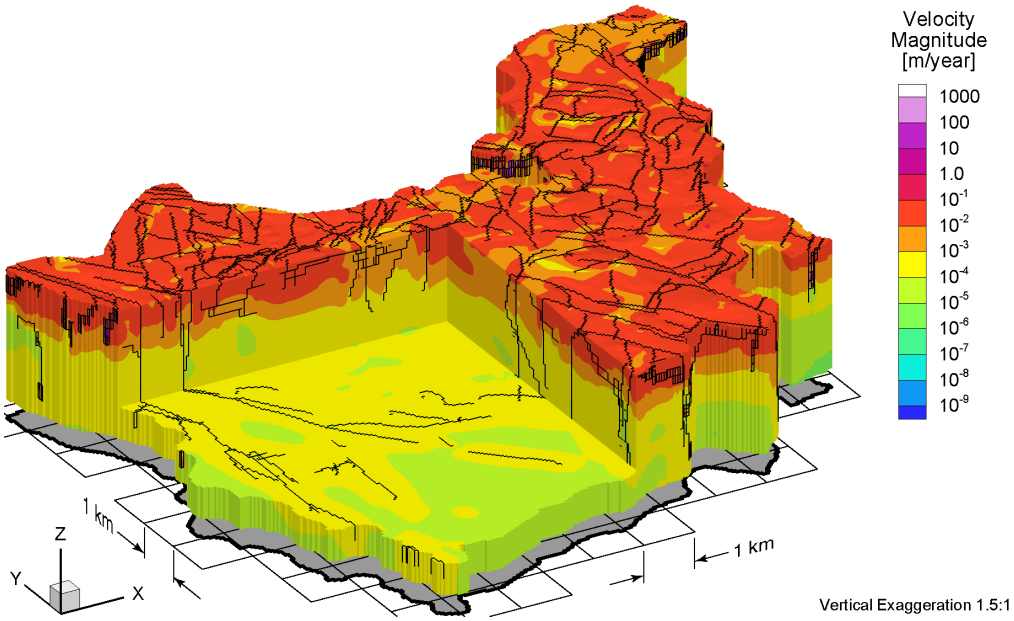

Figure D.13 Block cut view of pore velocity magnitudes at 80 ka before present for the Canadian Shield Sub-Regional Scenario 4 paleoclimate simulation.

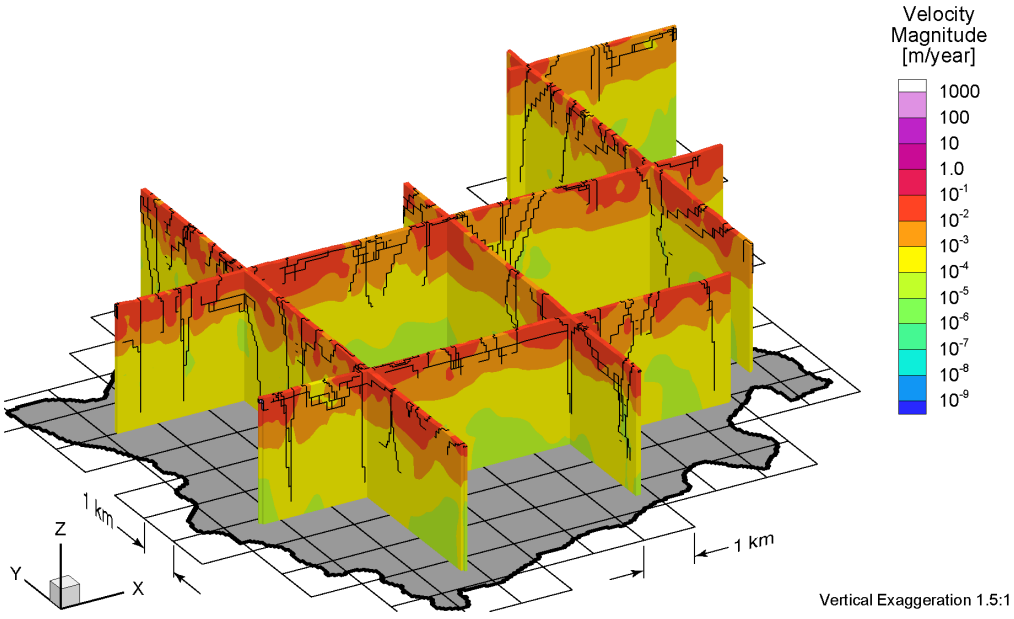

Figure D.14 Fence view of pore velocity magnitudes at 80 ka before present for the Canadian Shield Sub-Regional Scenario 4 paleoclimate simulation.

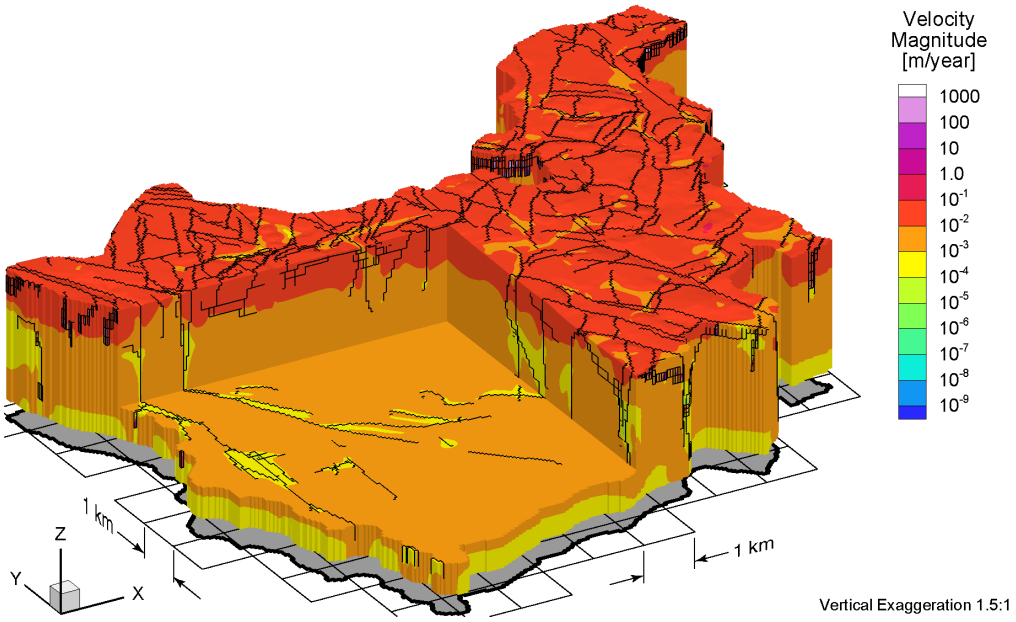

Figure D.15 Block cut view of pore velocity magnitudes at 40 ka before present for the Canadian Shield Sub-Regional Scenario 4 paleoclimate simulation.

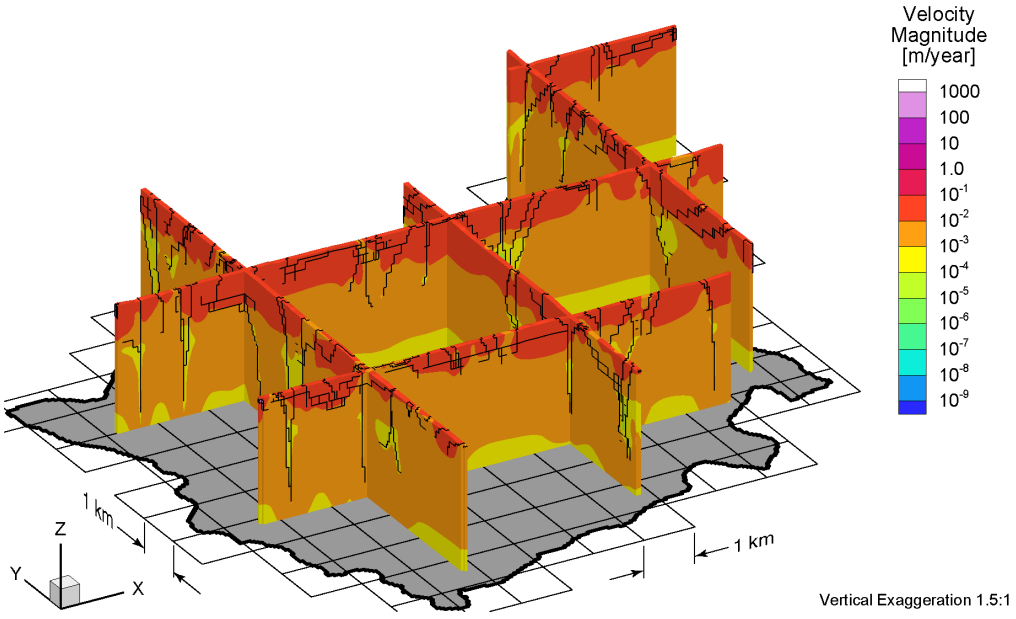

Figure D.16 Fence view of pore velocity magnitudes at 40 ka before present for the Canadian Shield Sub-Regional Scenario 4 paleoclimate simulation.

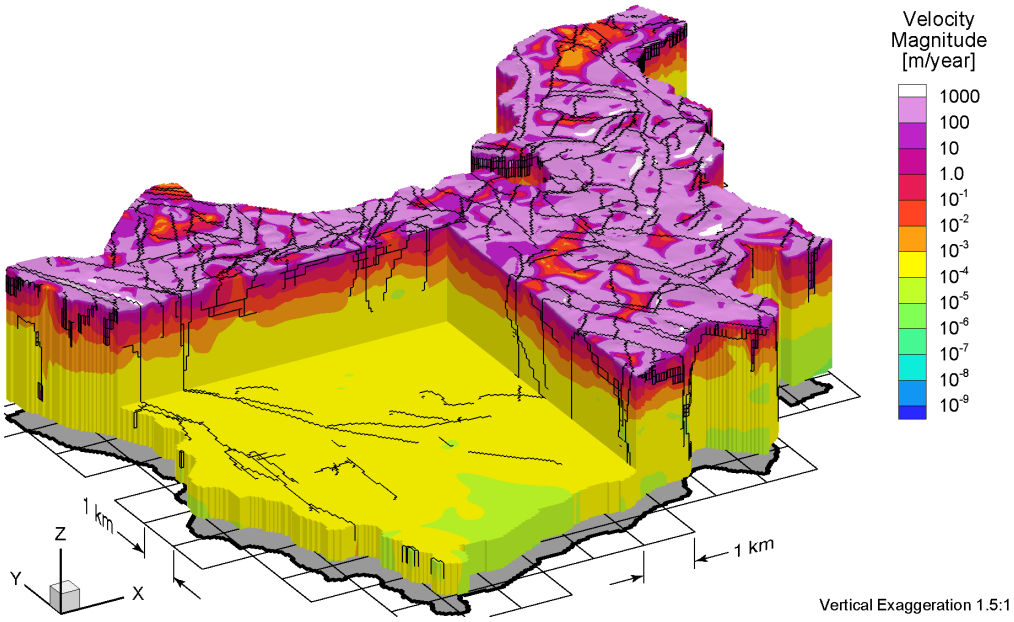

Figure D.17 Block cut view of pore velocity magnitudes at present for the Canadian Shield Sub-Regional Scenario 4 paleoclimate simulation.

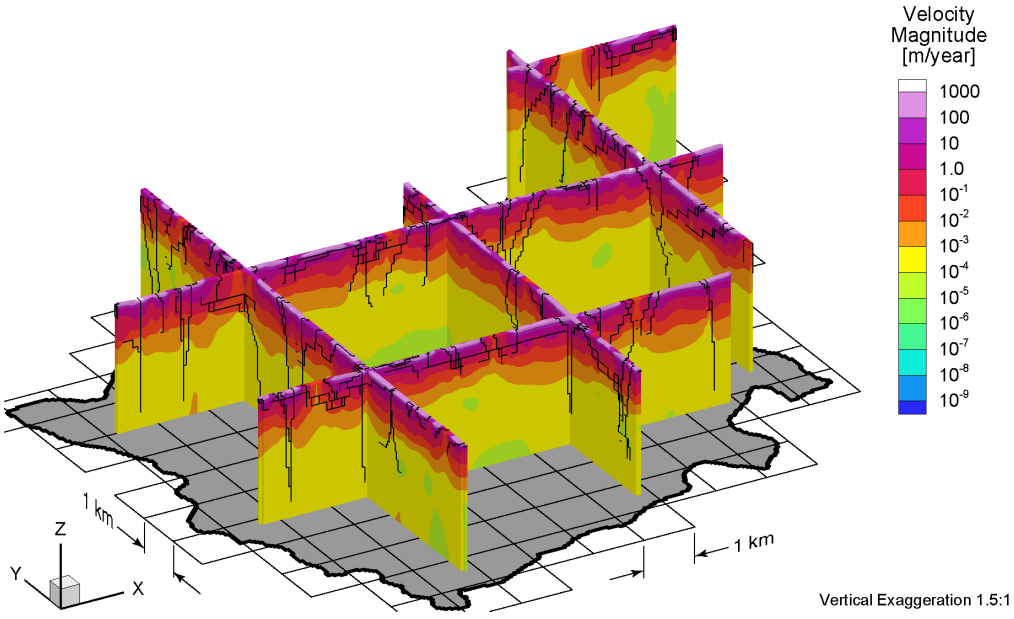

Figure D.18 Fence view of pore velocity magnitudes at present for the Canadian Shield Sub-Regional Scenario 4 paleoclimate simulation.

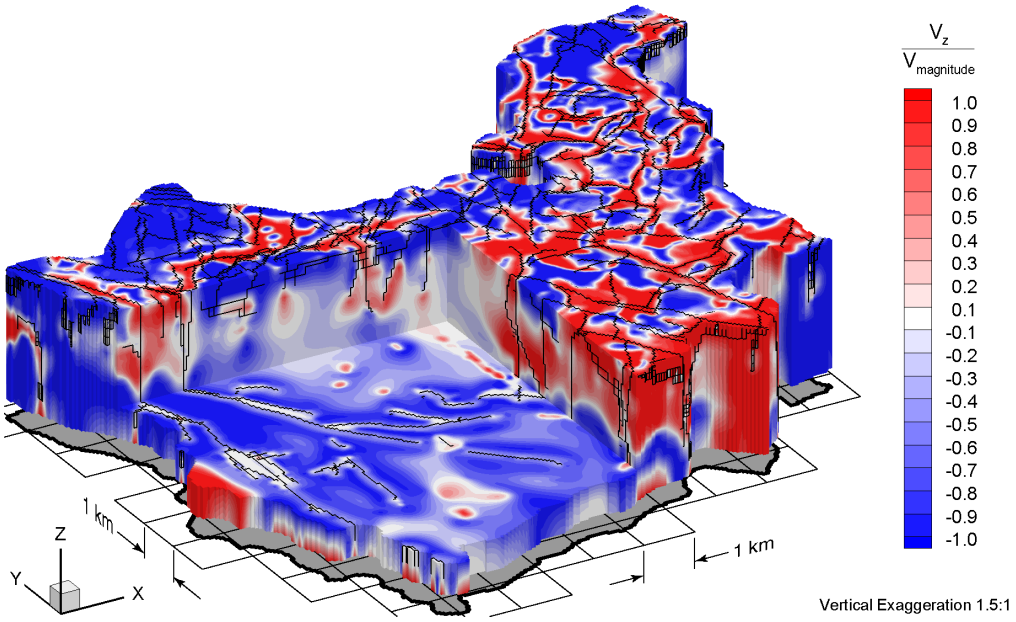

Figure D.19 Block cut view of ratio of vertical pore velocities to pore velocity magnitudes at 80 ka before present for the Canadian Shield Sub-Regional Scenario 4 paleoclimate simulation.

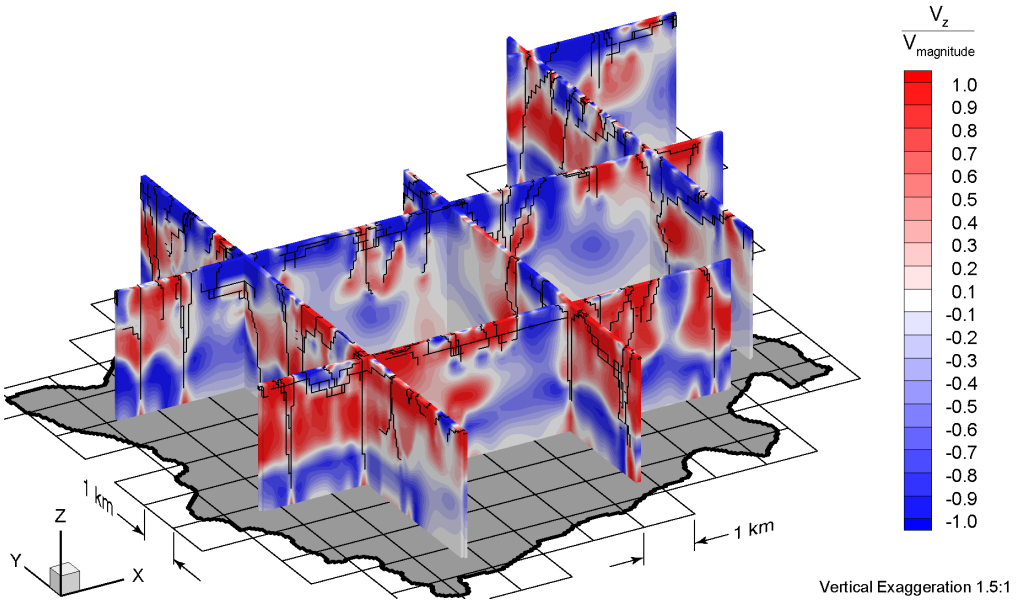

Figure D.20 Fence view of ratio of vertical pore velocities to pore velocity magnitudes at 80 ka before present for the Canadian Shield Sub-Regional Scenario 4 paleoclimate simulation.

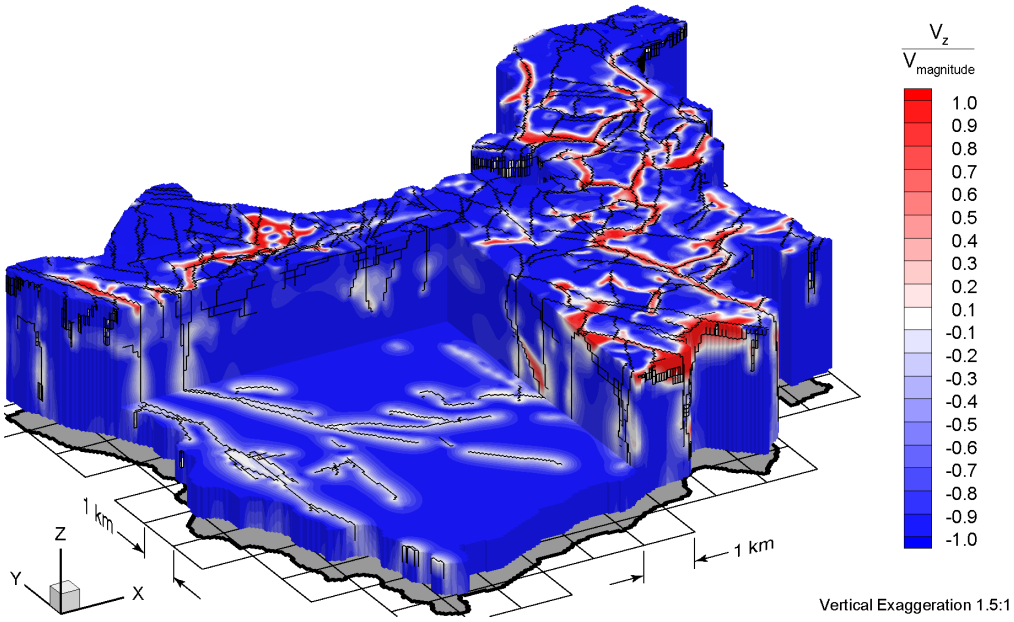

Figure D.21 Block cut view of ratio of vertical pore velocities to pore velocity magnitudes at 40 ka before present for the Canadian Shield Sub-Regional Scenario 4 paleoclimate simulation.

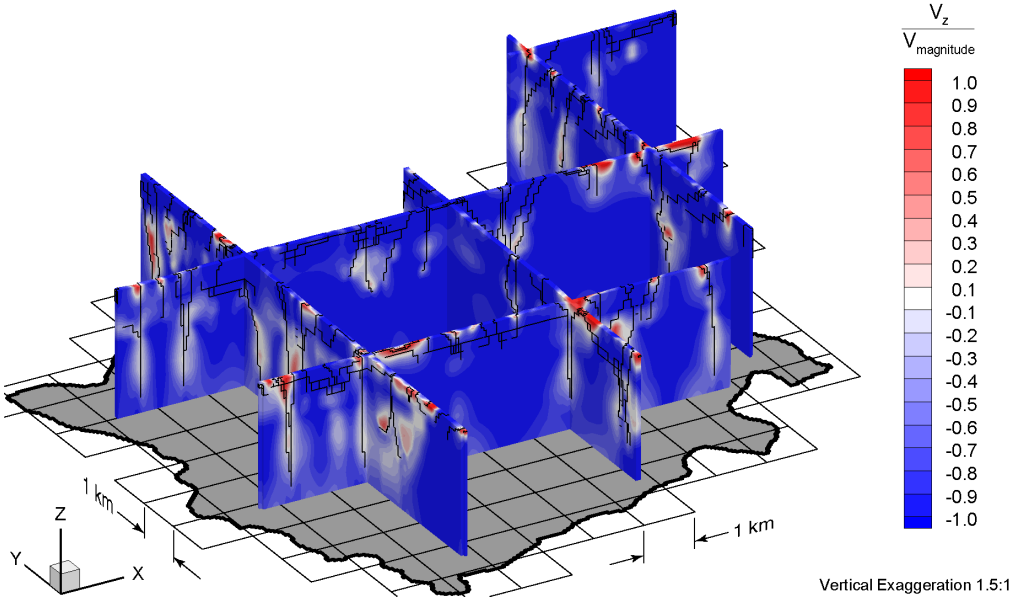

Figure D.22 Fence view of ratio of vertical pore velocities to pore velocity magnitudes at 40 ka before present for the Canadian Shield Sub-Regional Scenario 4 paleoclimate simulation.

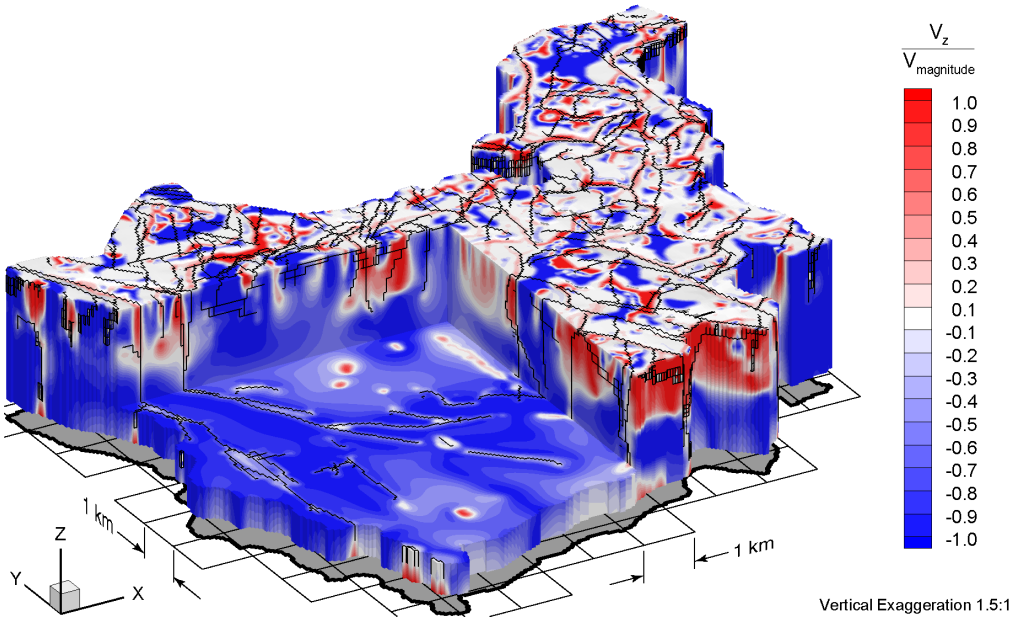

Figure D.23 Block cut view of ratio of vertical pore velocities to pore velocity magnitudes at present for the Canadian Shield Sub-Regional Scenario 4 paleoclimate simulation.

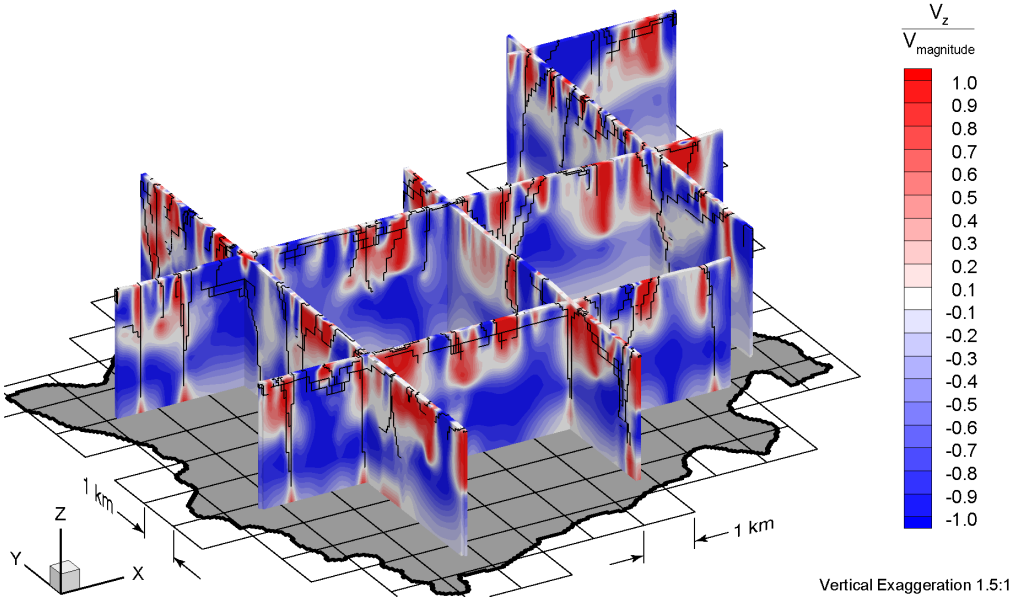

Figure D.24 Fence view of ratio of vertical pore velocities to pore velocity magnitudes at present for the Canadian Shield Sub-Regional Scenario 4 paleoclimate simulation.

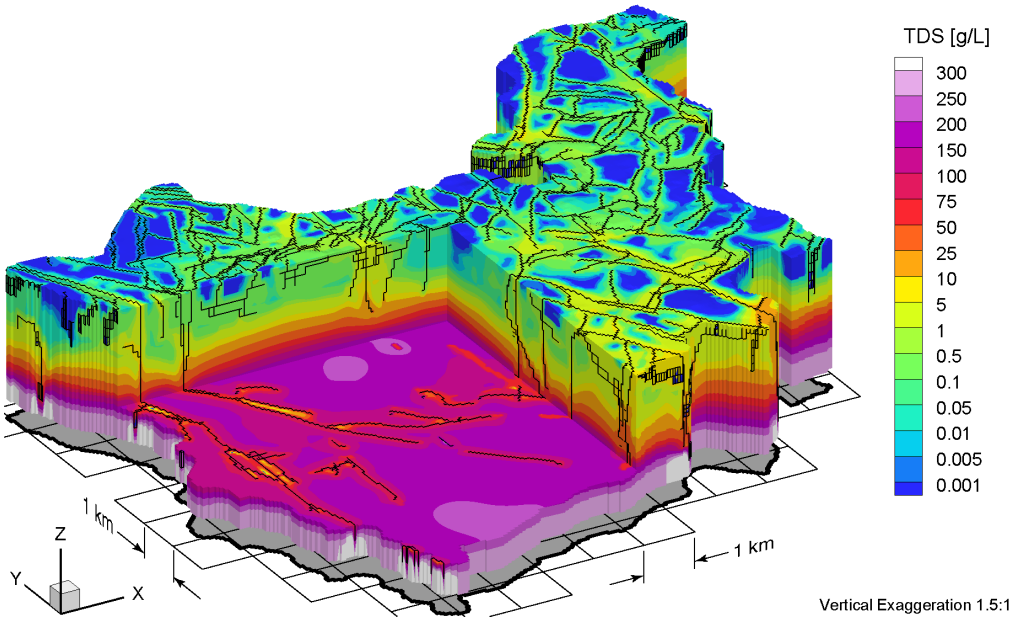

Figure D.25 Block cut view of brine concentrations at 80 ka before present for the Canadian Shield Sub-Regional Scenario 4 paleoclimate simulation.

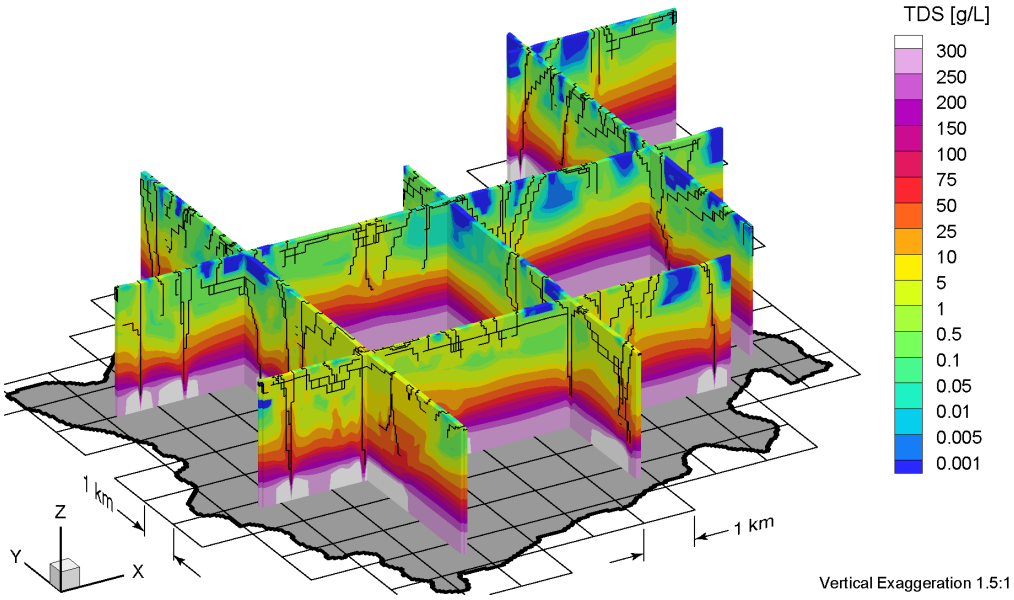

Figure D.26 Fence view of brine concentrations at 80 ka before present for the Canadian Shield Sub-Regional Scenario 4 paleoclimate simulation.

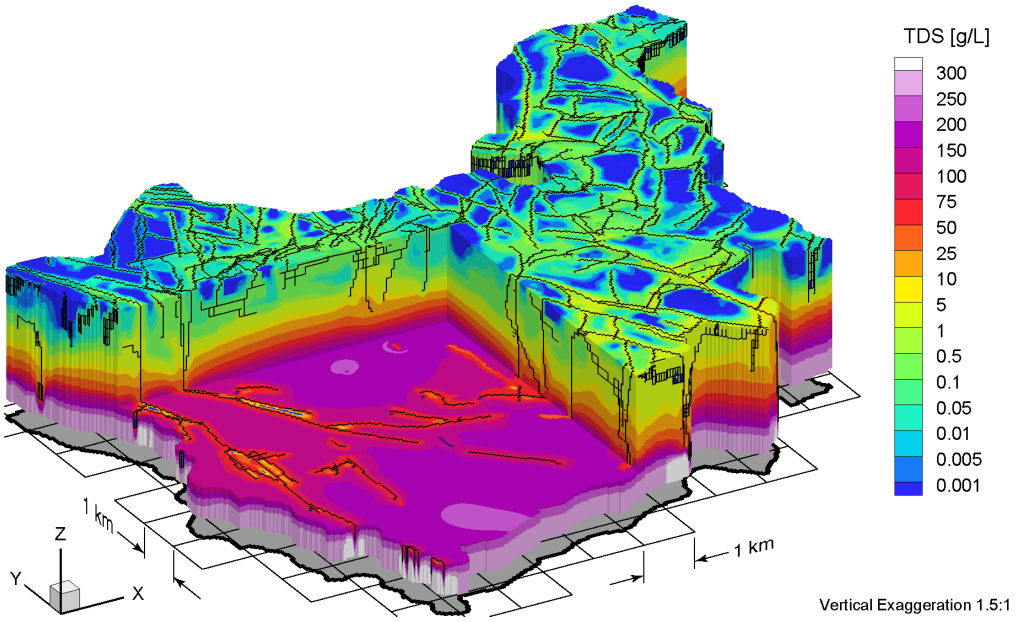

Figure D.27 Block cut view of brine concentrations at 40 ka before present for the Canadian Shield Sub-Regional Scenario 4 paleoclimate simulation.

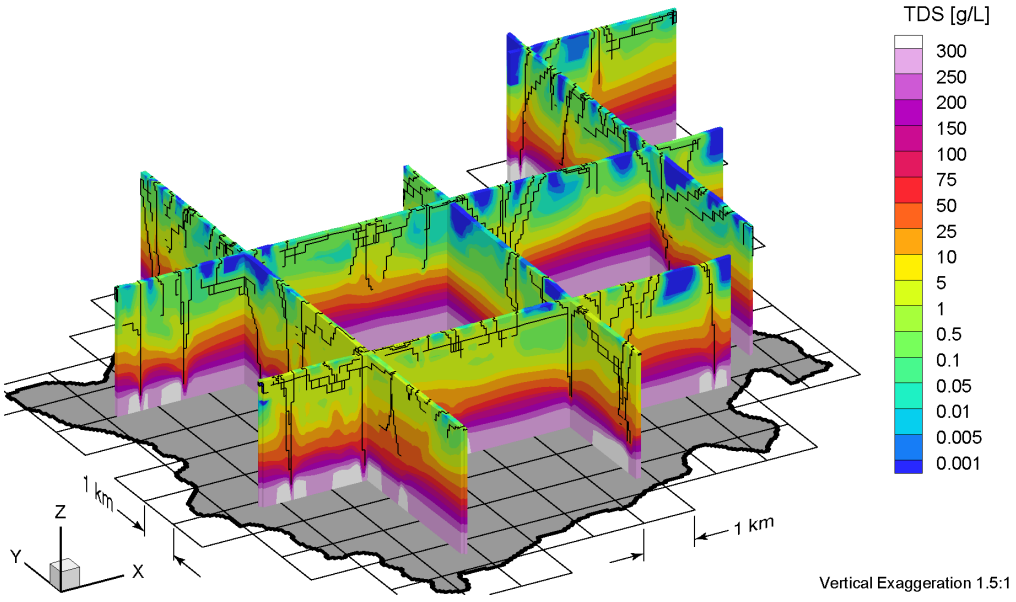

Figure D.28 Fence view of brine concentrations at 40 ka before present for the Canadian Shield Sub-Regional Scenario 4 paleoclimate simulation.

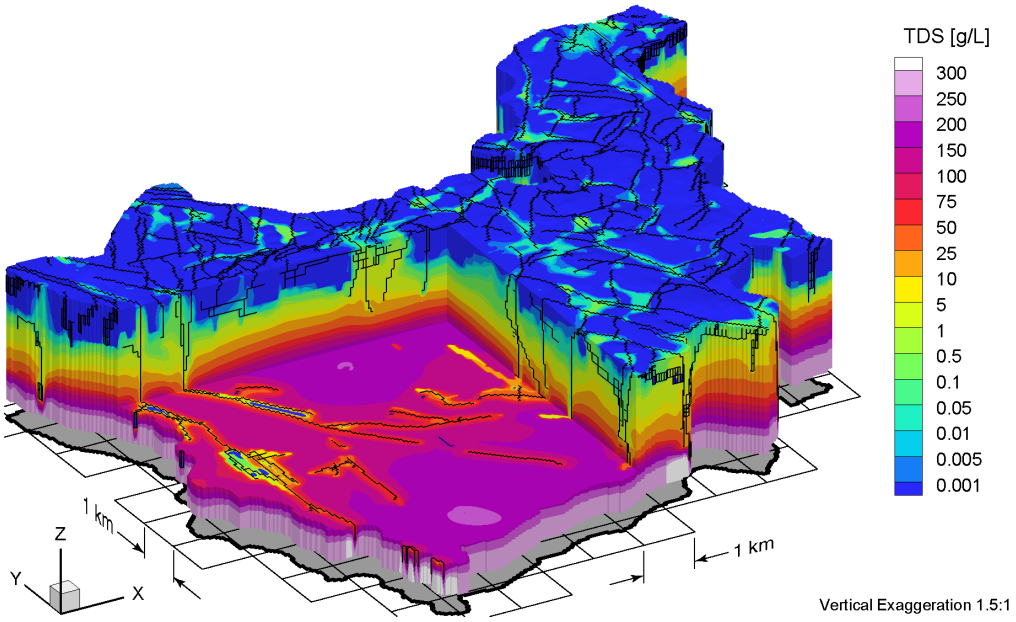

Figure D.29 Block cut view of brine concentrations at present for the Canadian Shield Sub-Regional Scenario 4 paleoclimate simulation.

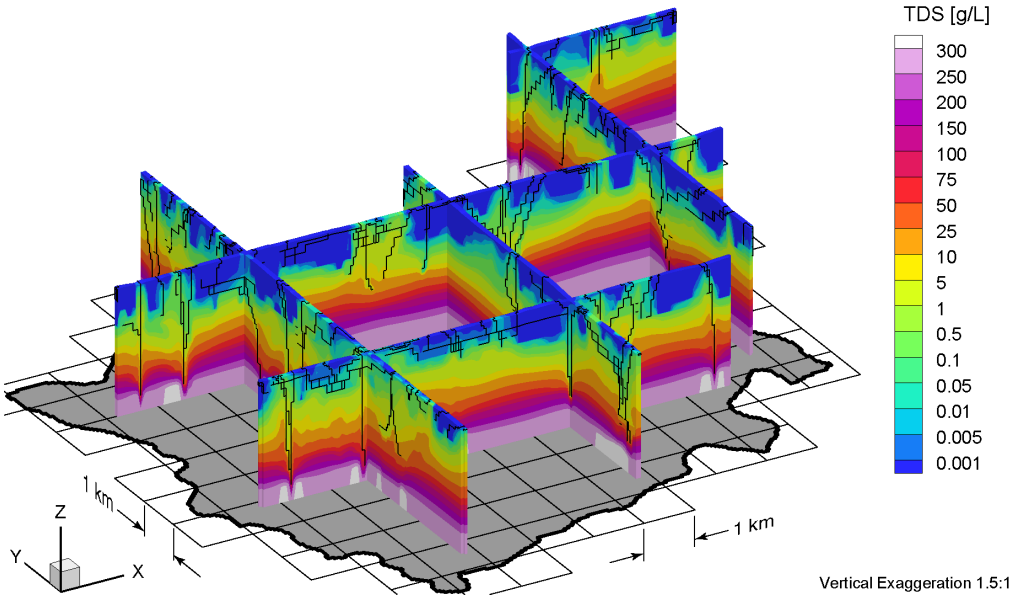

Figure D.30 Fence view of brine concentrations at present for the Canadian Shield Sub-Regional Scenario 4 paleoclimate simulation.

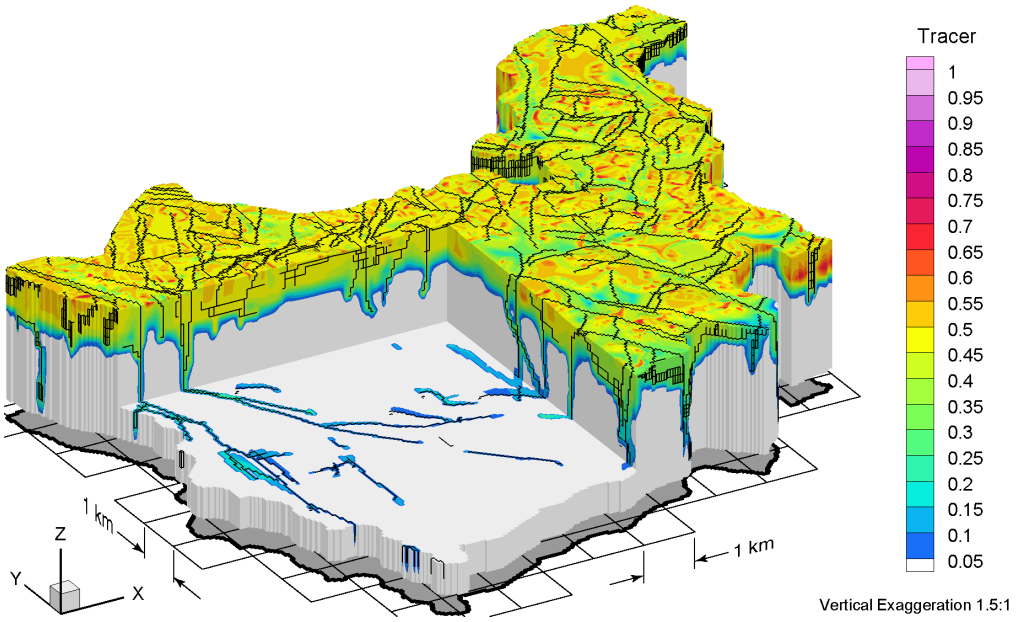

Figure D.31 Block cut view of tracer concentrations at 80 ka before present for the Canadian Shield Sub-Regional Scenario 4 paleoclimate simulation.

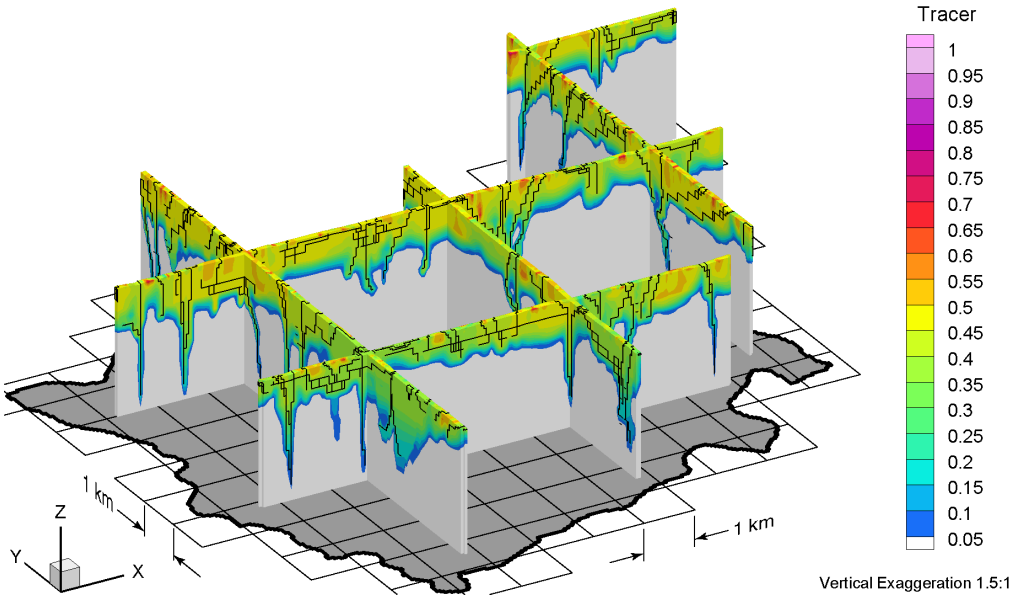

Figure D.32 Fence view of tracer concentrations at 80 ka before present for the Canadian Shield Sub-Regional Scenario 4 paleoclimate simulation.

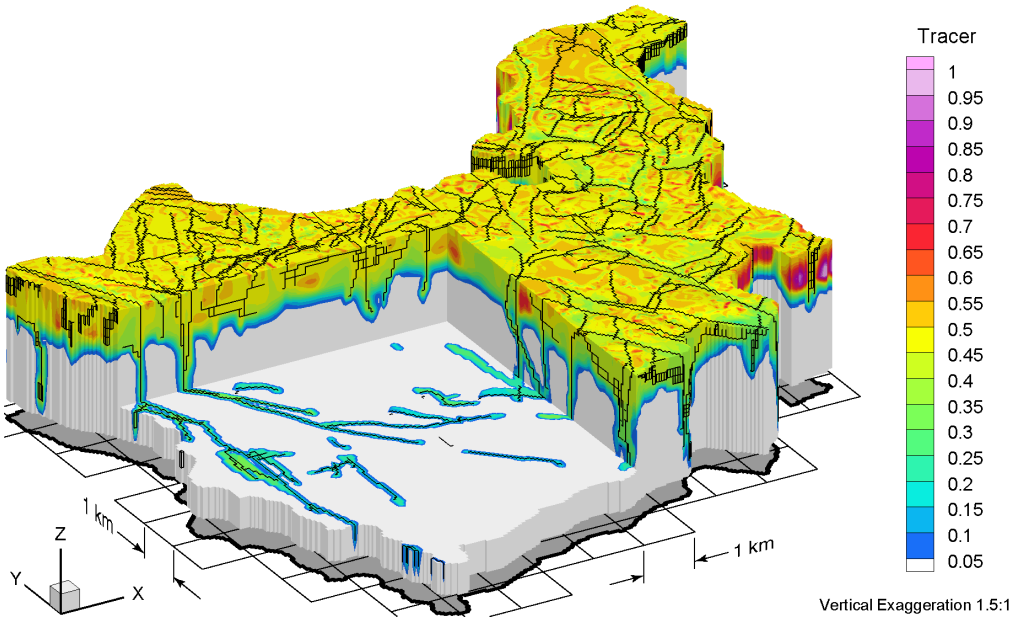

Figure D.33 Block cut view of tracer concentrations at 40 ka before present for the Canadian Shield Sub-Regional Scenario 4 paleoclimate simulation.

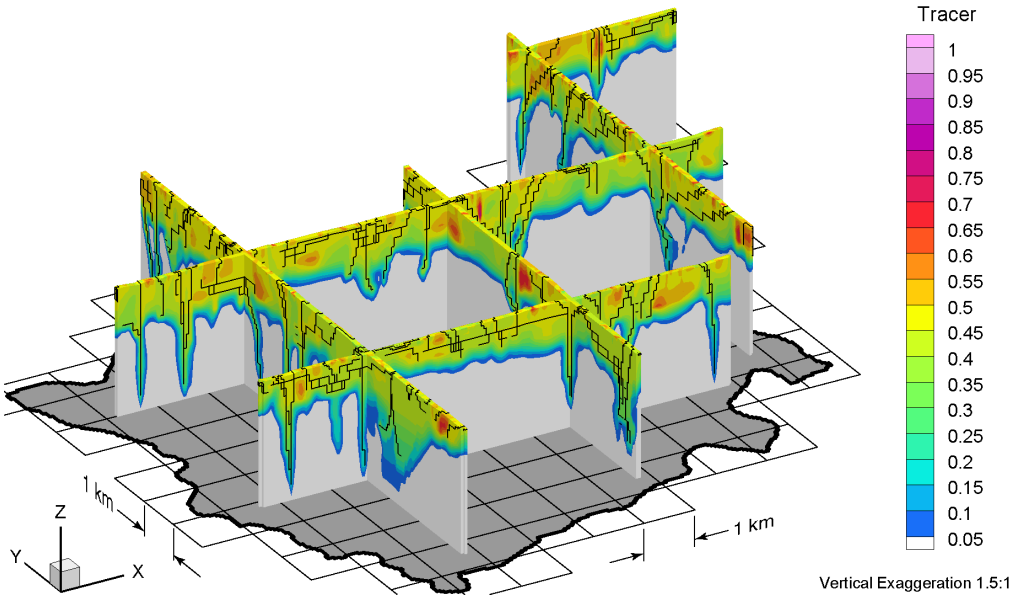

Figure D.34 Fence view of tracer concentrations at 40 ka before present for the Canadian Shield Sub-Regional Scenario 4 paleoclimate simulation.

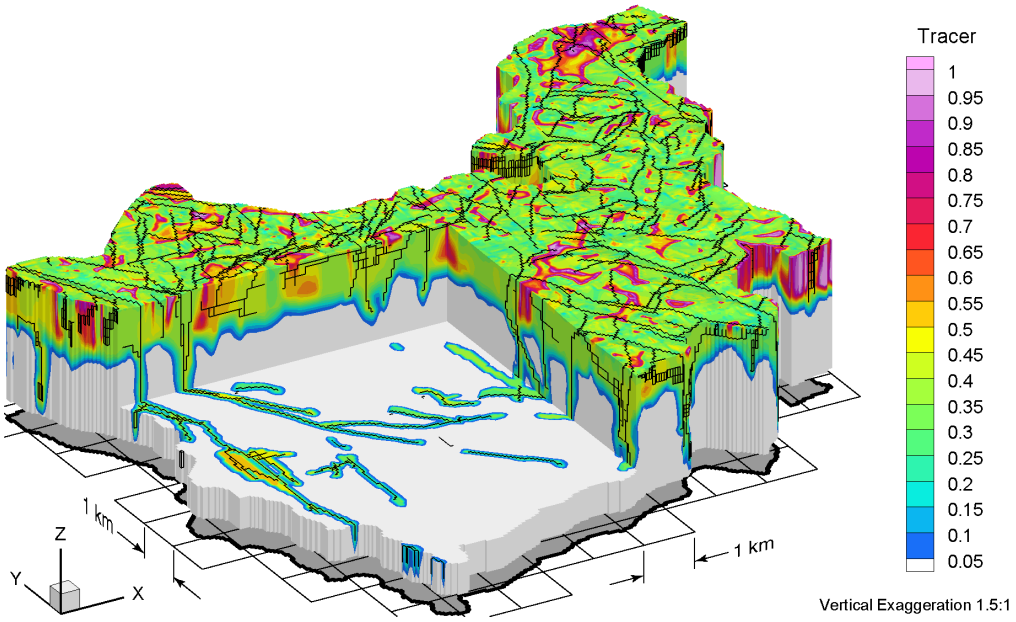

Figure D.35 Block cut view of tracer concentrations at present for the Canadian Shield Sub-Regional Scenario 4 paleoclimate simulation.

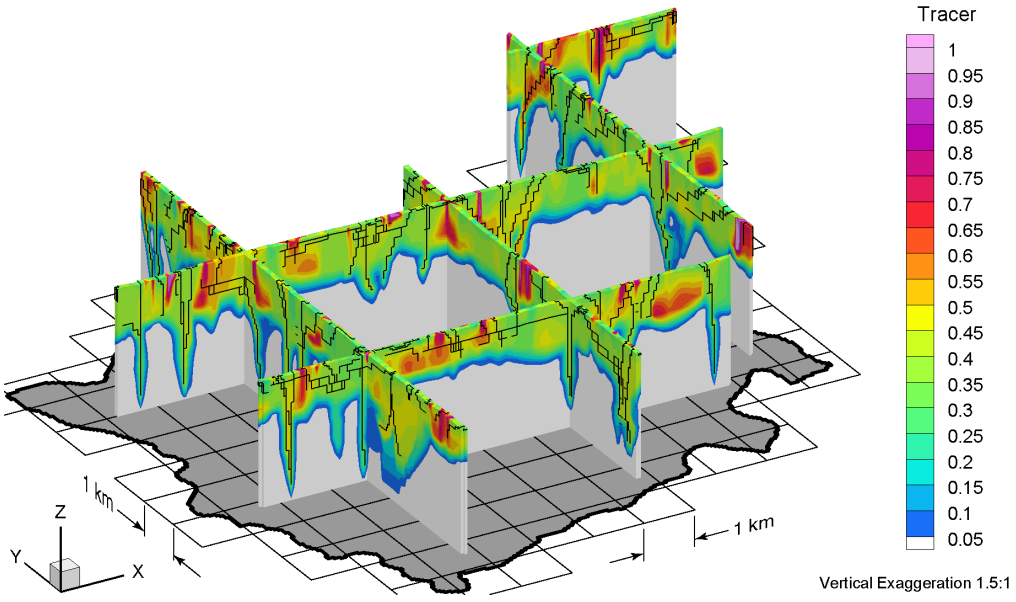

Figure D.36 Fence view of tracer concentrations at present for the Canadian Shield Sub-Regional Scenario 4 paleoclimate simulation.

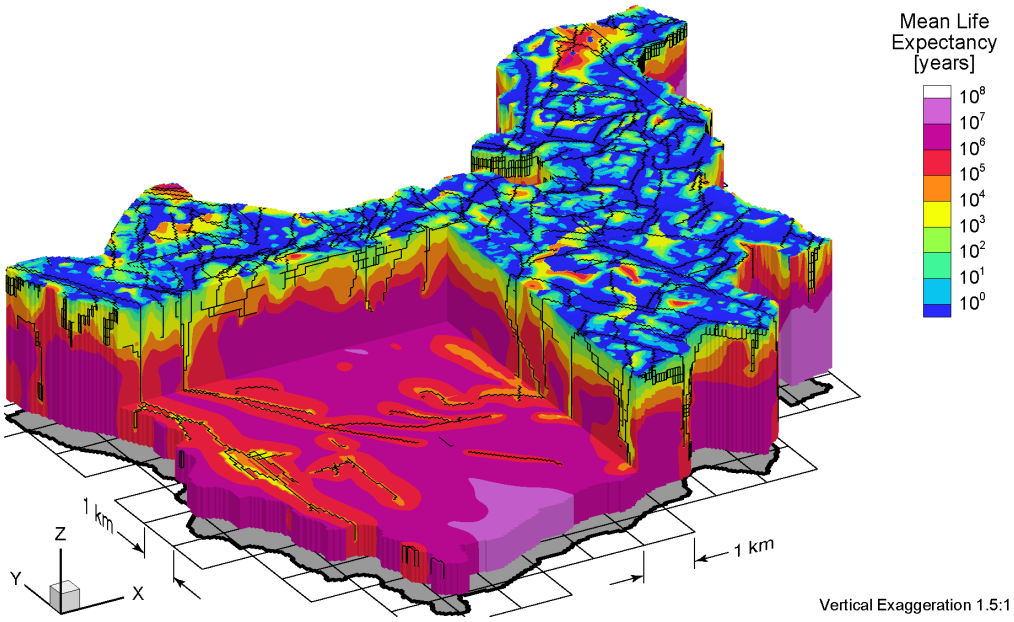

Figure D.37 Block cut view of mean life expectancies at present for the Canadian Shield Sub-Regional Scenario 4 paleoclimate simulation.

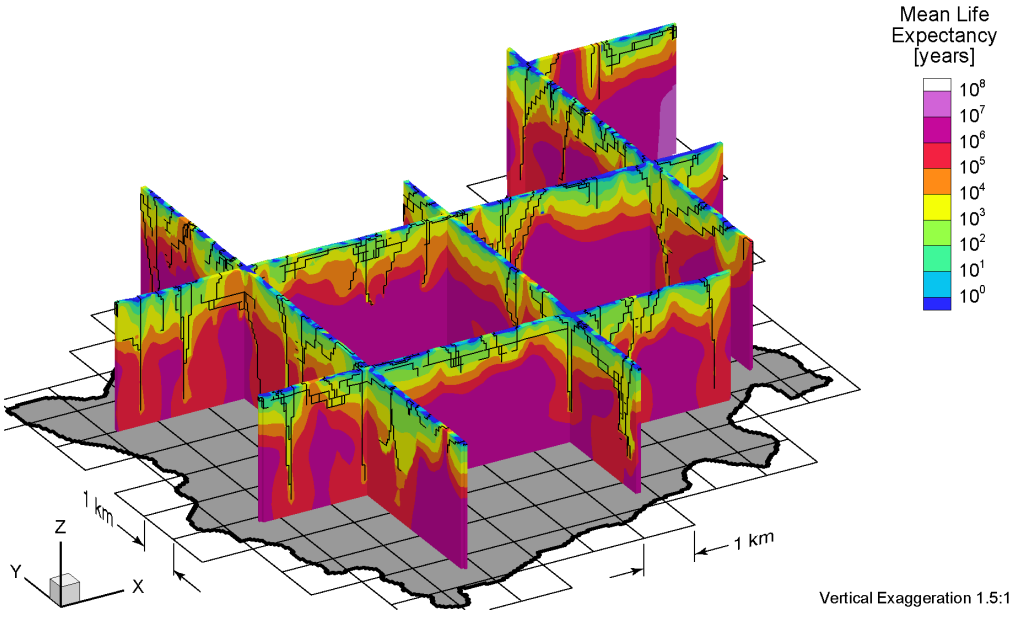

Figure D.38 Fence view of mean life expectancies at present for the Canadian Shield Sub-Regional Scenario 4 paleoclimate simulation.

Appendix E

CSSR Scenario 5 Paleoclimate Model

All figures related to Canadian Shield Sub-Regional (CSSR) Scenario 5 paleoclimate modelling are listed in Table E.1. Block cut view and fence view figures are shown on the same page to facilitate comparison. All results of the 120 ka paleoclimate simulations are shown at times of 80 ka before present, 40 ka before present, and at present.

Table E.1 List of Canadian Shield Sub-Regional Scenario 5 paleoclimate simulation figures.

Parameters	Time Before Present					
	80 ka		40 ka		Present	
	Block Cut	Fence	Block Cut	Fence	Block Cut	Fence
Freshwater Heads	E.1	E.2	E.3	E.4	E.5	E.6
Environmental Heads	E.7	E.8	E.9	E.10	E.11	E.12
Pore Velocity Magnitudes	E.13	E.14	E.15	E.16	E.17	E.18
Ratio of Vertical Pore Velocities to Pore Velocity Magnitudes	E.19	E.20	E.21	E.22	E.23	E.24
Brine Concentrations	E.25	E.26	E.27	E.28	E.29	E.30
Tracer Concentrations	E.31	E.32	E.33	E.34	E.35	E.36
Mean Life Expectancies	—	—	—	—	E.37	E.38

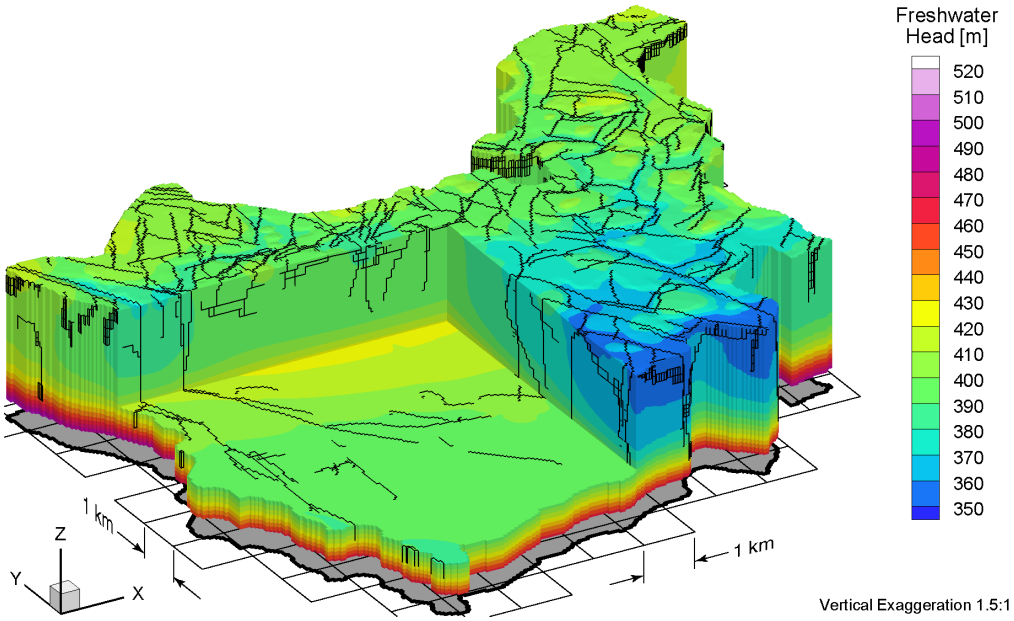

Figure E.1 Block cut view of freshwater heads at 80 ka before present for the Canadian Shield Sub-Regional Scenario 5 paleoclimate simulation.

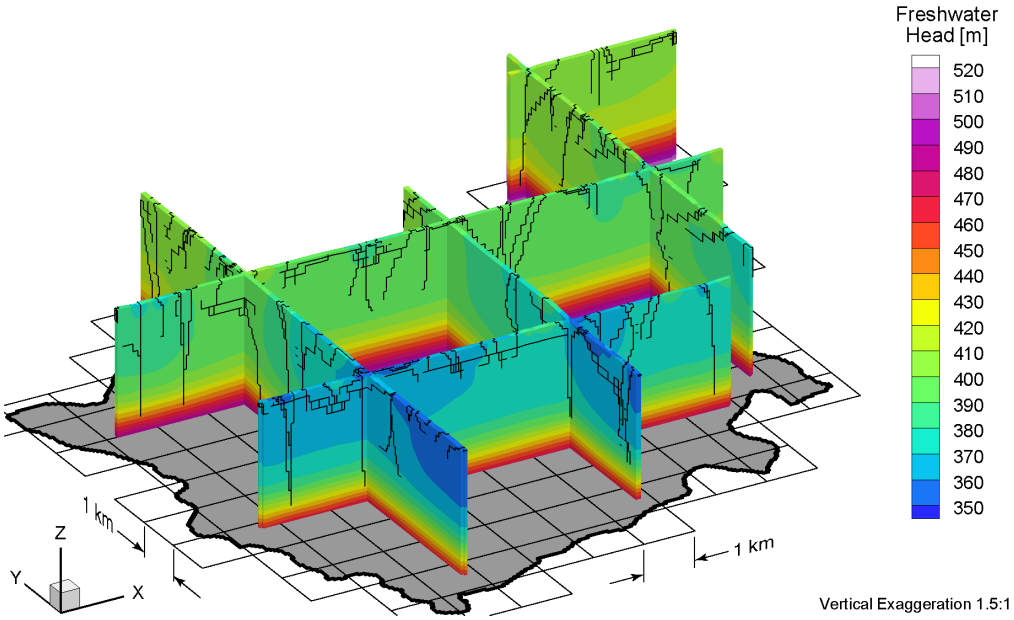

Figure E.2 Fence view of freshwater heads at 80 ka before present for the Canadian Shield Sub-Regional Scenario 5 paleoclimate simulation.

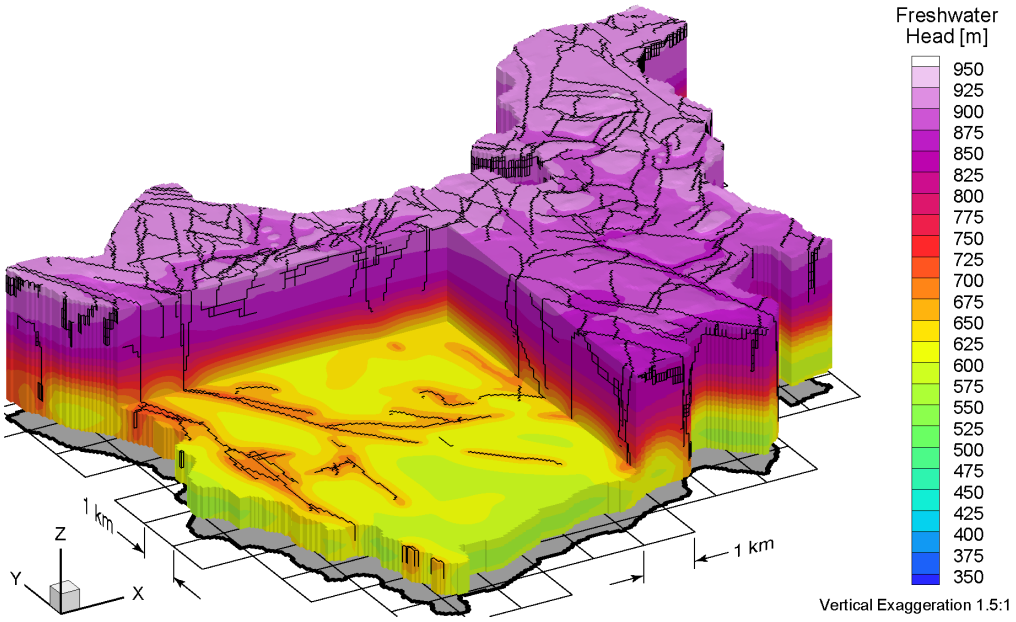

Figure E.3 Block cut view of freshwater heads at 40 ka before present for the Canadian Shield Sub-Regional Scenario 5 paleoclimate simulation.

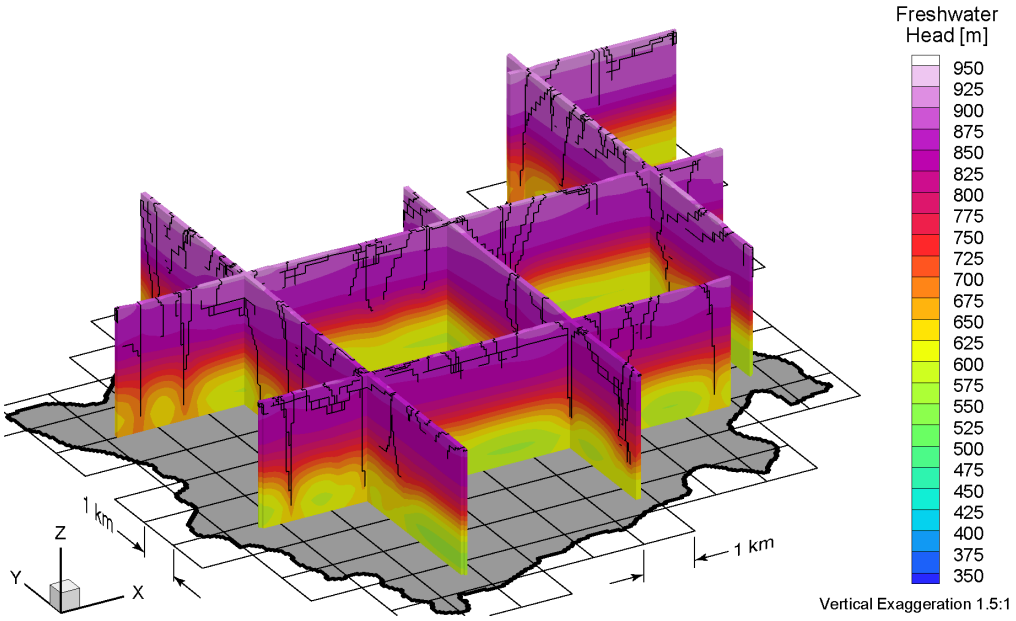

Figure E.4 Fence view of freshwater heads at 40 ka before present for the Canadian Shield Sub-Regional Scenario 5 paleoclimate simulation.

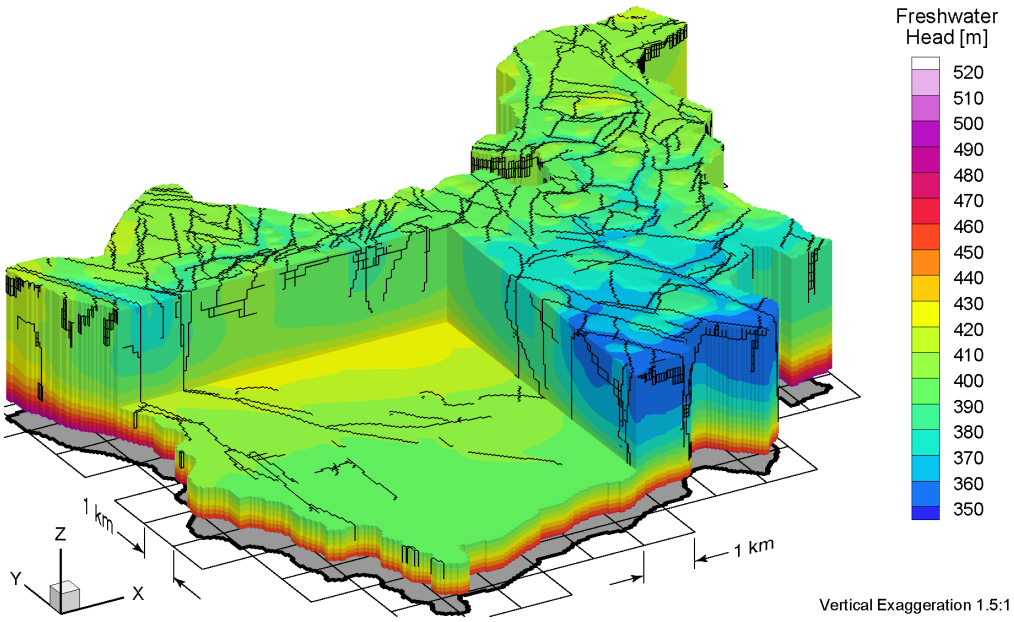

Figure E.5 Block cut view of freshwater heads at present for the Canadian Shield Sub-Regional Scenario 5 paleoclimate simulation.

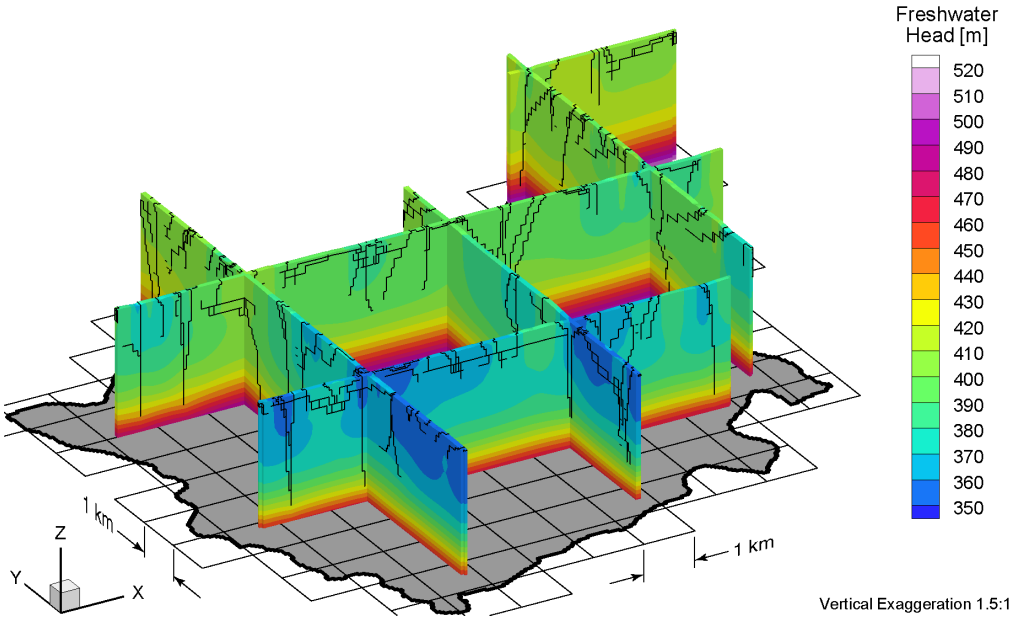

Figure E.6 Fence view of freshwater heads at present for the Canadian Shield Sub-Regional Scenario 5 paleoclimate simulation.

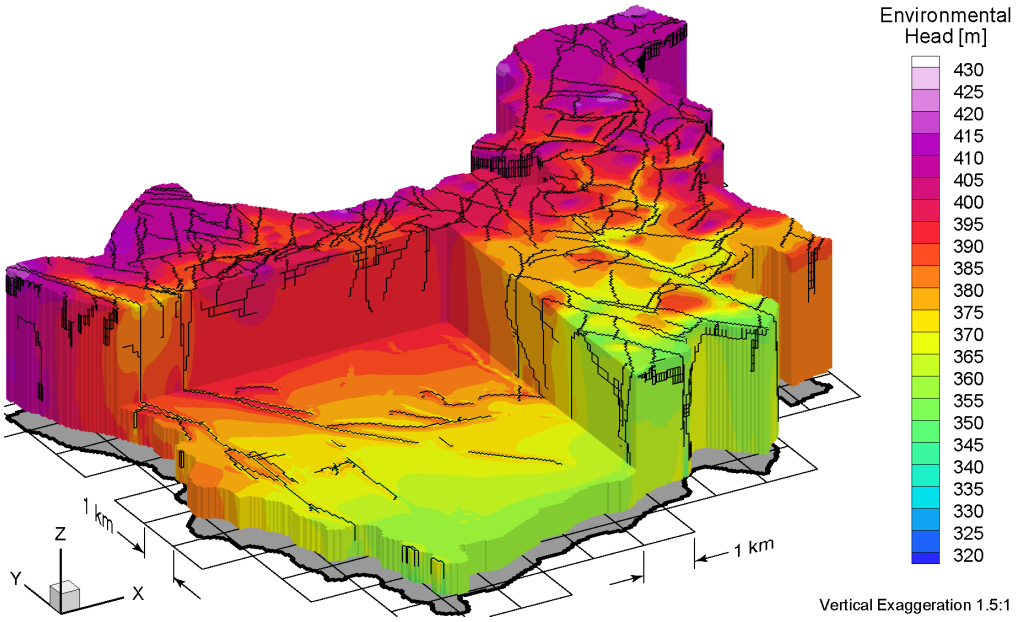

Figure E.7 Block cut view of environmental heads at 80 ka before present for the Canadian Shield Sub-Regional Scenario 5 paleoclimate simulation.

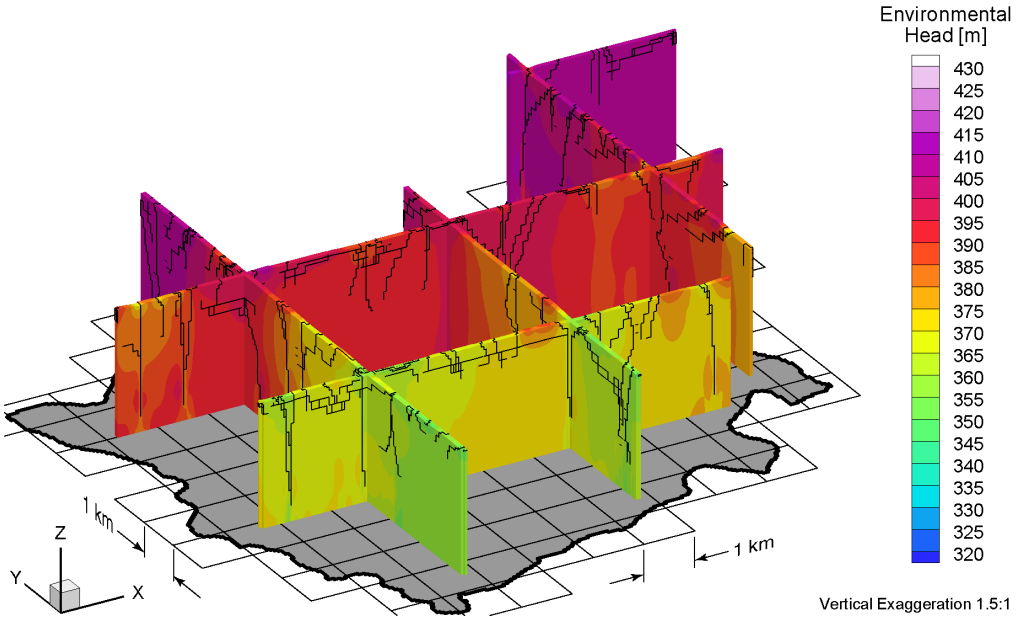

Figure E.8 Fence view of environmental heads at 80 ka before present for the Canadian Shield Sub-Regional Scenario 5 paleoclimate simulation.

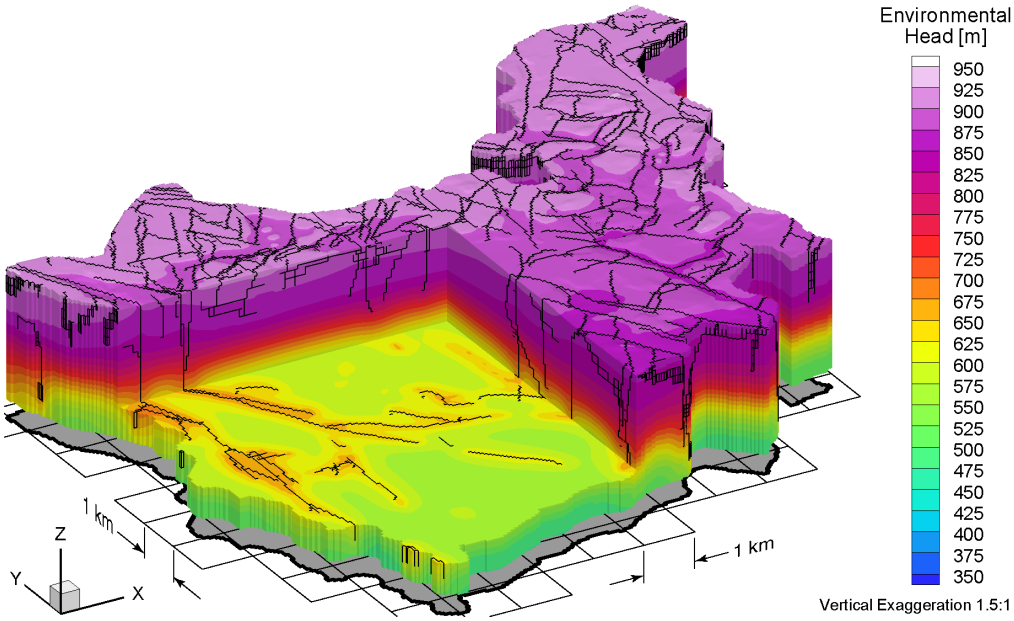

Figure E.9 Block cut view of environmental heads at 40 ka before present for the Canadian Shield Sub-Regional Scenario 5 paleoclimate simulation.

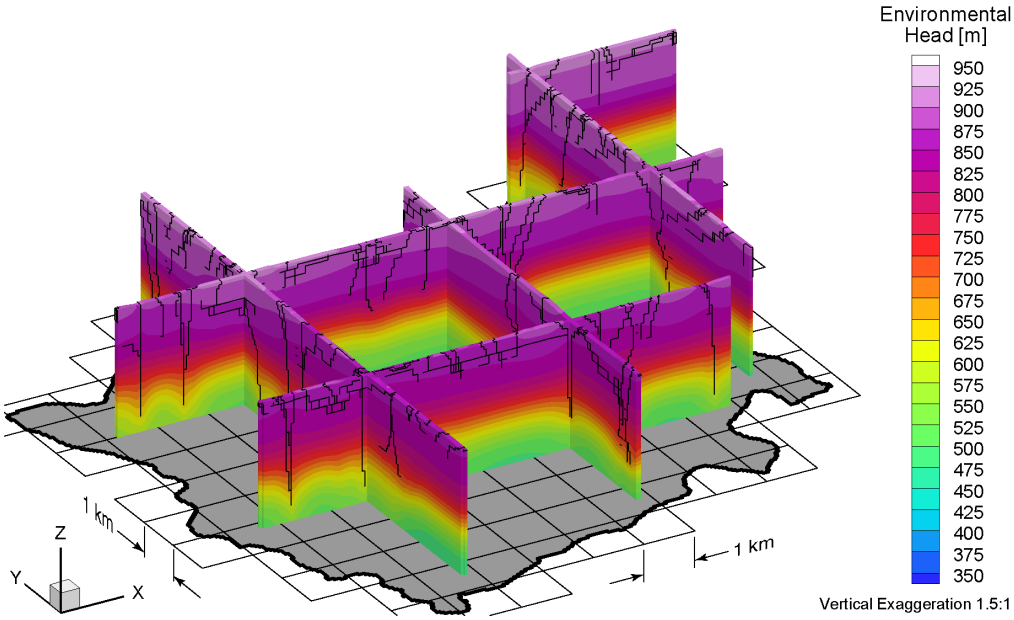

Figure E.10 Fence view of environmental heads at 40 ka before present for the Canadian Shield Sub-Regional Scenario 5 paleoclimate simulation.

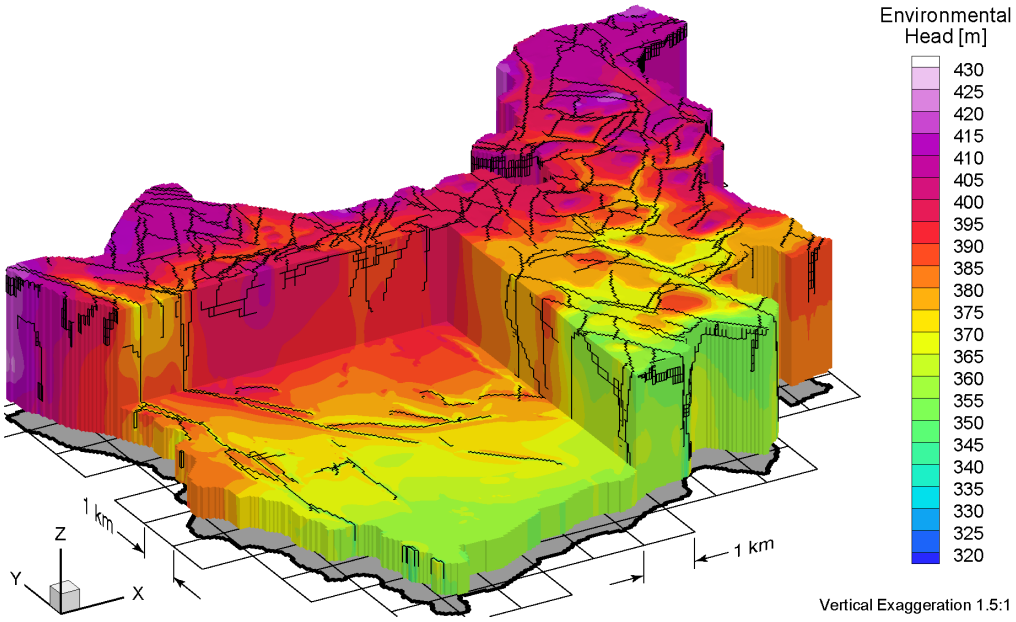

Figure E.11 Block cut view of environmental heads at present for the Canadian Shield Sub-Regional Scenario 5 paleoclimate simulation.

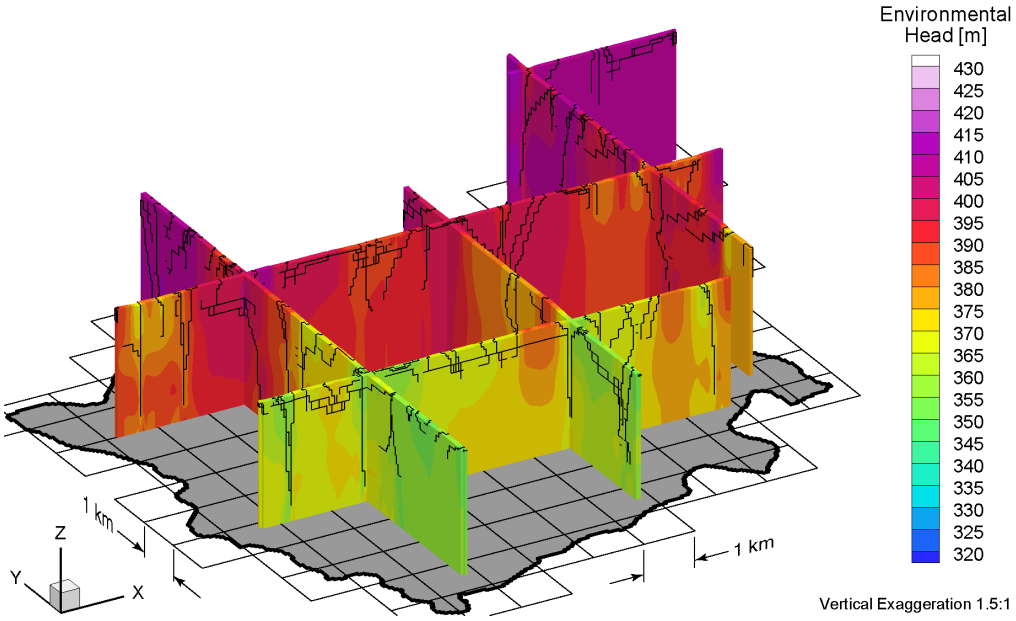

Figure E.12 Fence view of environmental heads at present for the Canadian Shield Sub-Regional Scenario 5 paleoclimate simulation.

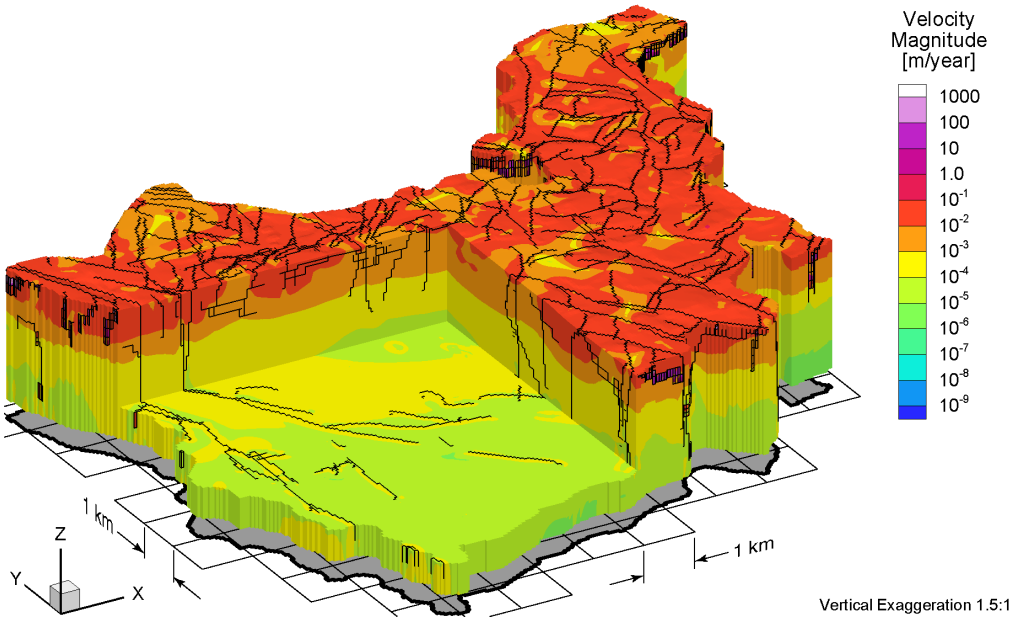

Figure E.13 Block cut view of pore velocity magnitudes at 80 ka before present for the Canadian Shield Sub-Regional Scenario 5 paleoclimate simulation.

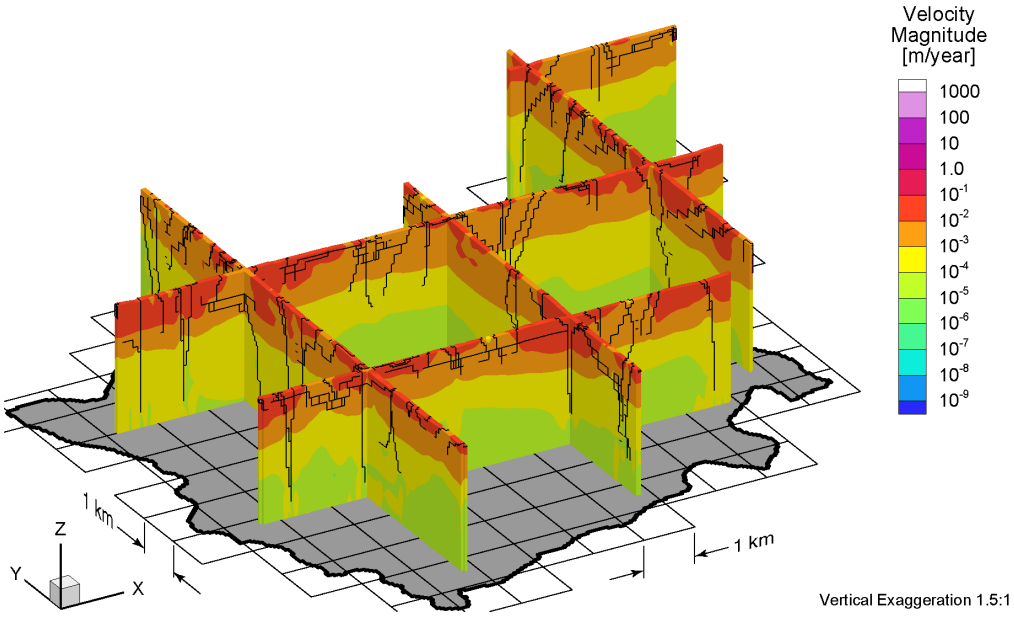

Figure E.14 Fence view of pore velocity magnitudes at 80 ka before present for the Canadian Shield Sub-Regional Scenario 5 paleoclimate simulation.

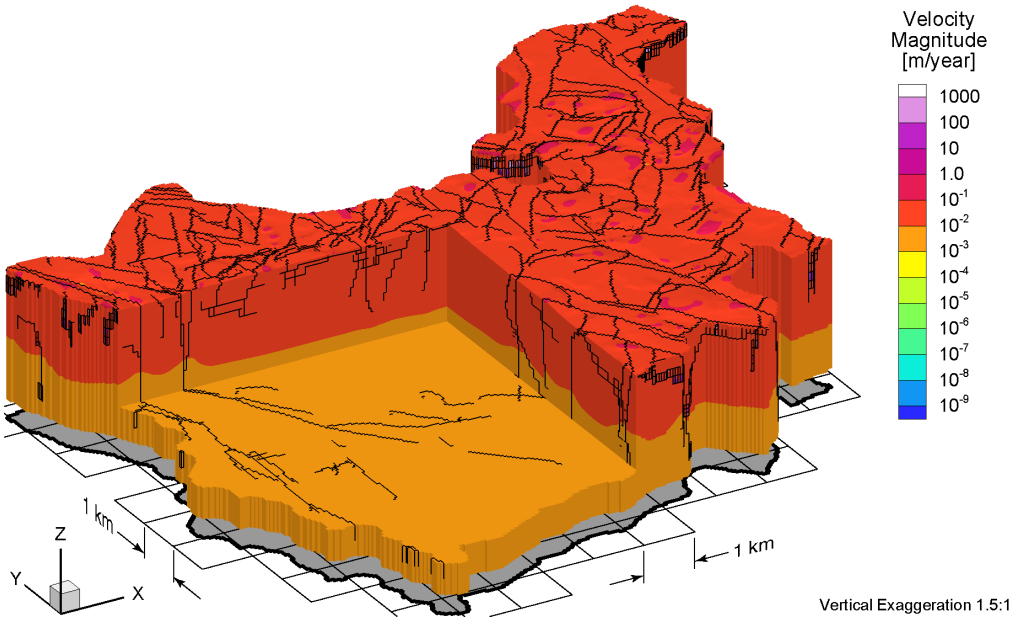

Figure E.15 Block cut view of pore velocity magnitudes at 40 ka before present for the Canadian Shield Sub-Regional Scenario 5 paleoclimate simulation.

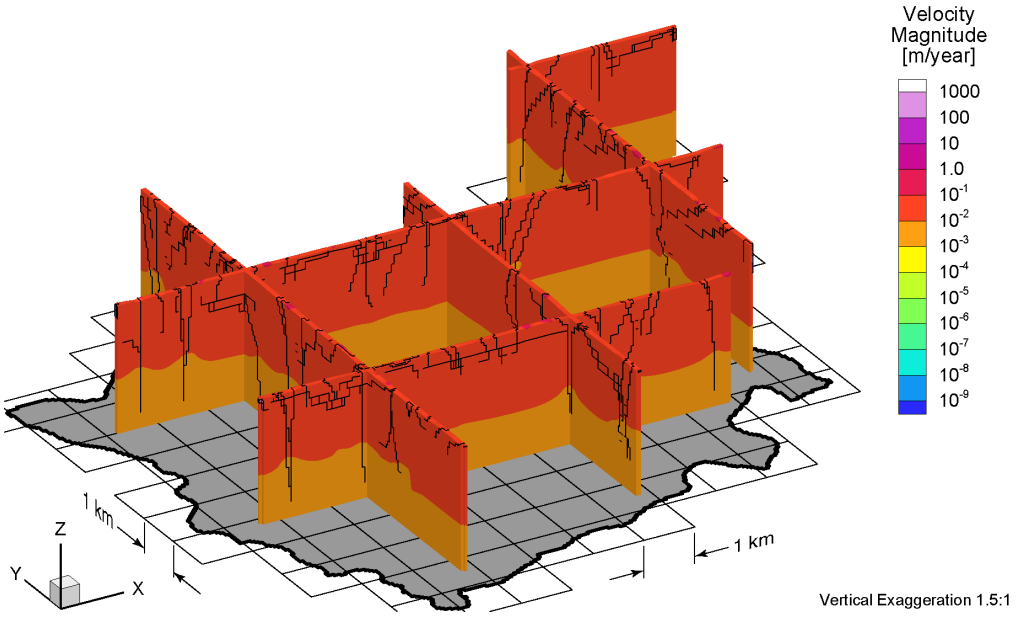

Figure E.16 Fence view of pore velocity magnitudes at 40 ka before present for the Canadian Shield Sub-Regional Scenario 5 paleoclimate simulation.

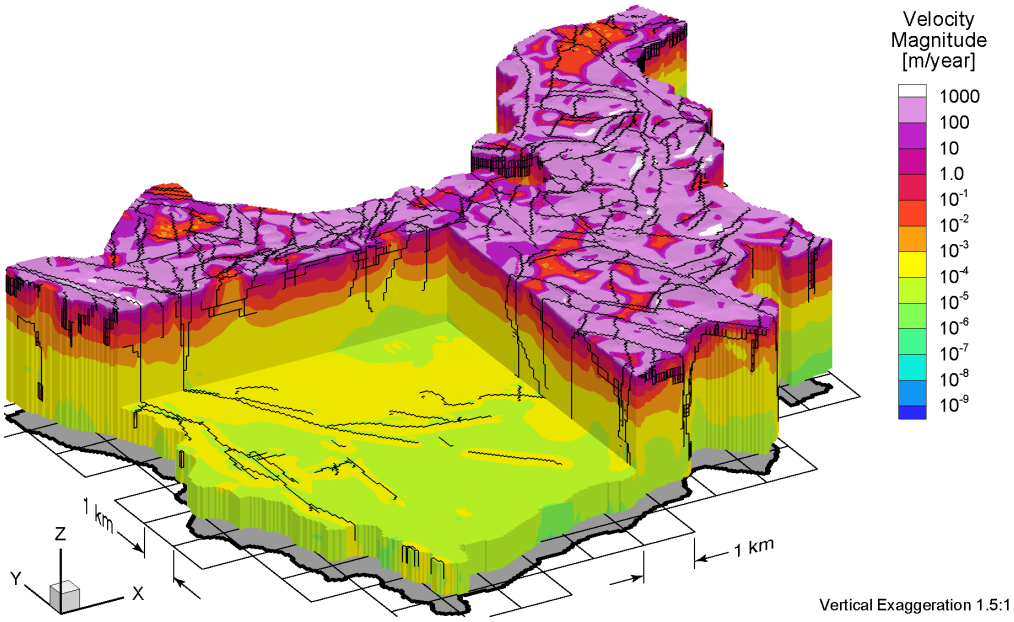

Figure E.17 Block cut view of pore velocity magnitudes at present for the Canadian Shield Sub-Regional Scenario 5 paleoclimate simulation.

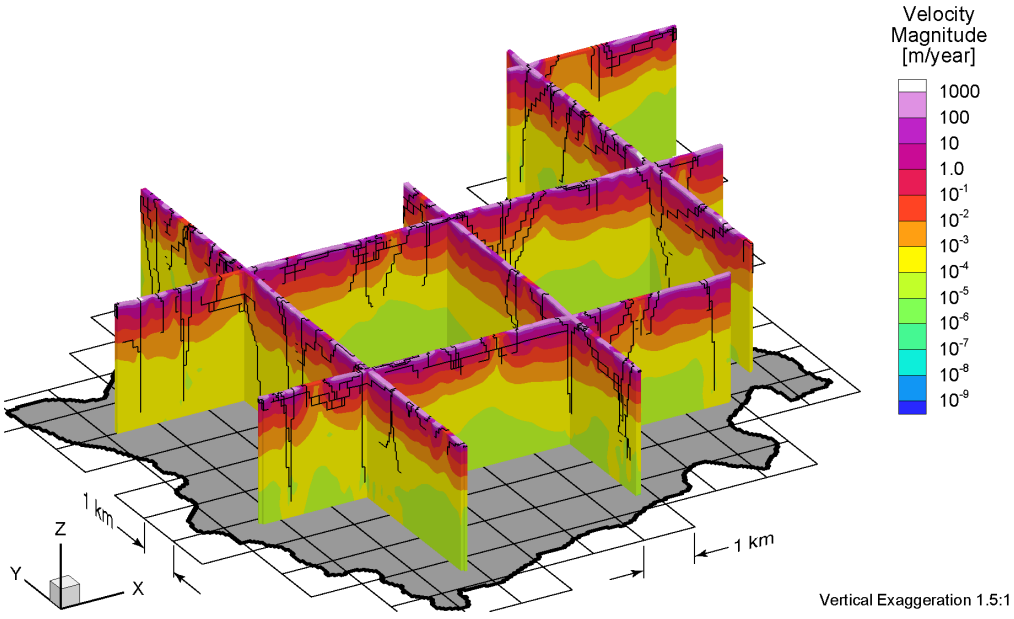

Figure E.18 Fence view of pore velocity magnitudes at present for the Canadian Shield Sub-Regional Scenario 5 paleoclimate simulation.

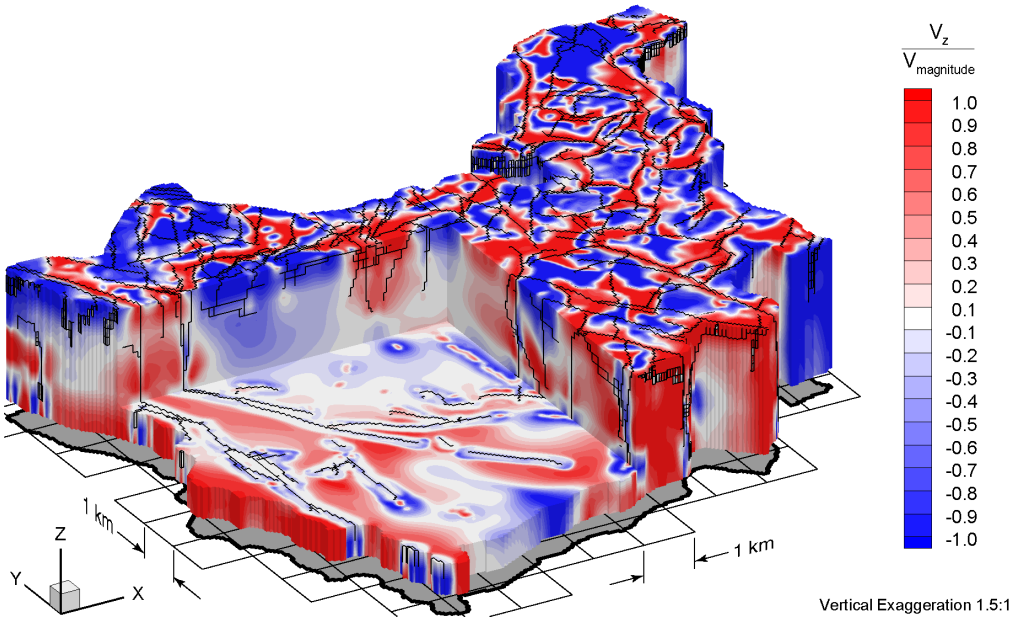

Figure E.19 Block cut view of ratio of vertical pore velocities to pore velocity magnitudes at 80 ka before present for the Canadian Shield Sub-Regional Scenario 5 paleoclimate simulation.

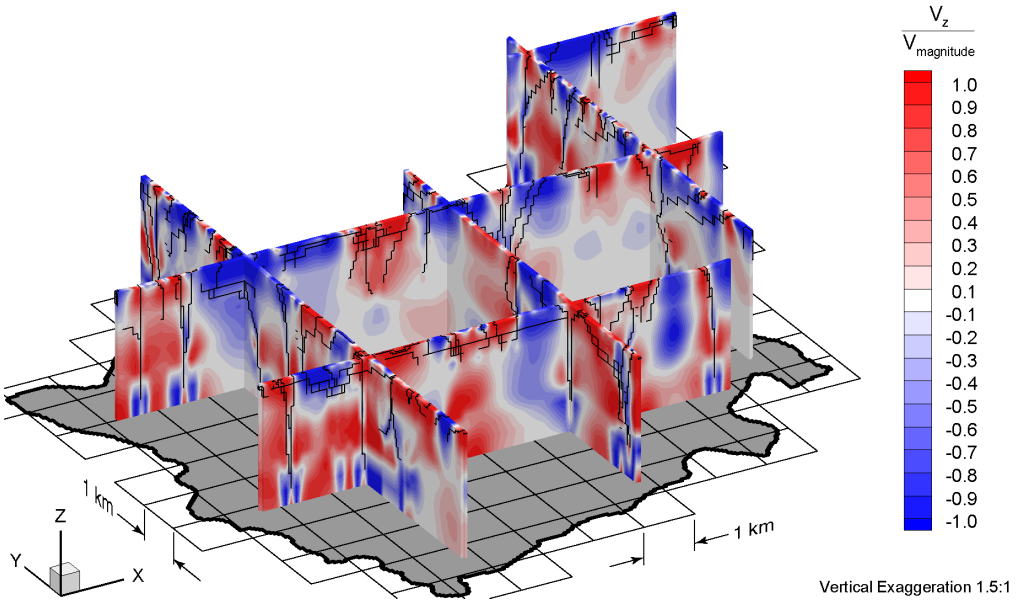

Figure E.20 Fence view of ratio of vertical pore velocities to pore velocity magnitudes at 80 ka before present for the Canadian Shield Sub-Regional Scenario 5 paleoclimate simulation.

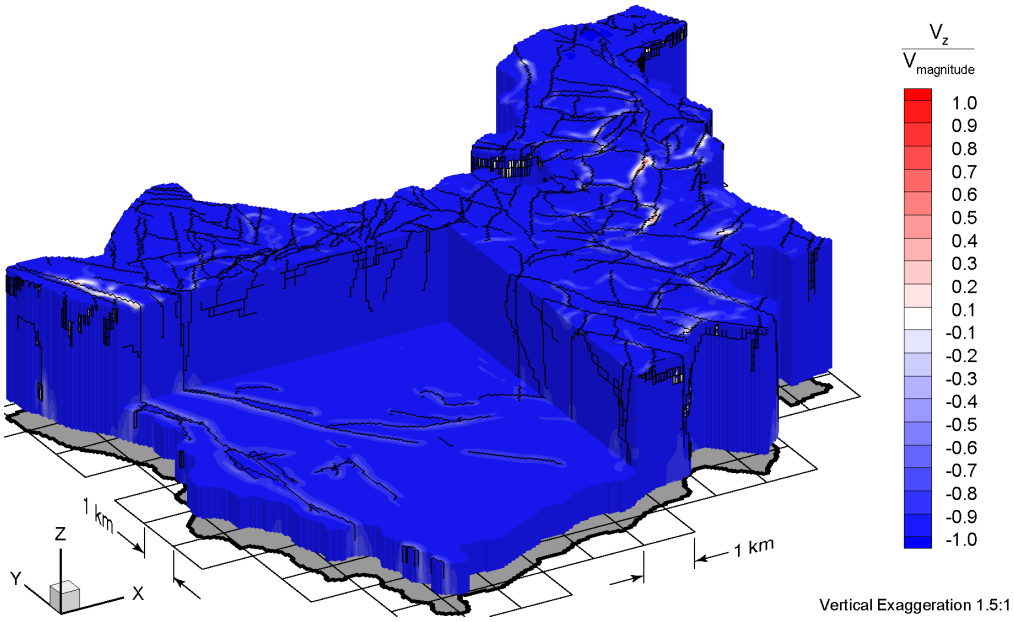

Figure E.21 Block cut view of ratio of vertical pore velocities to pore velocity magnitudes at 40 ka before present for the Canadian Shield Sub-Regional Scenario 5 paleoclimate simulation.

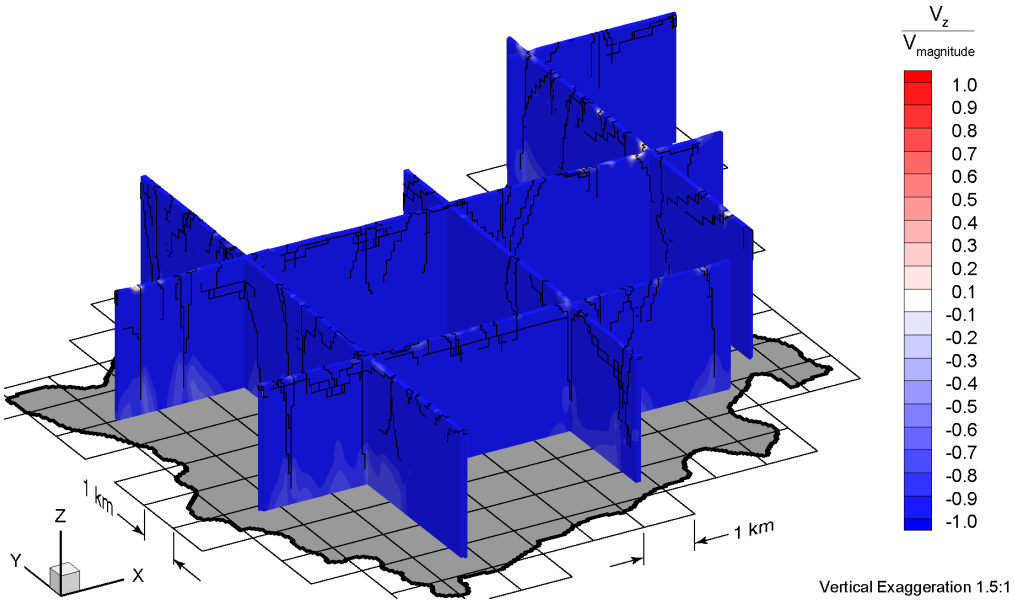

Figure E.22 Fence view of ratio of vertical pore velocities to pore velocity magnitudes at 40 ka before present for the Canadian Shield Sub-Regional Scenario 5 paleoclimate simulation.

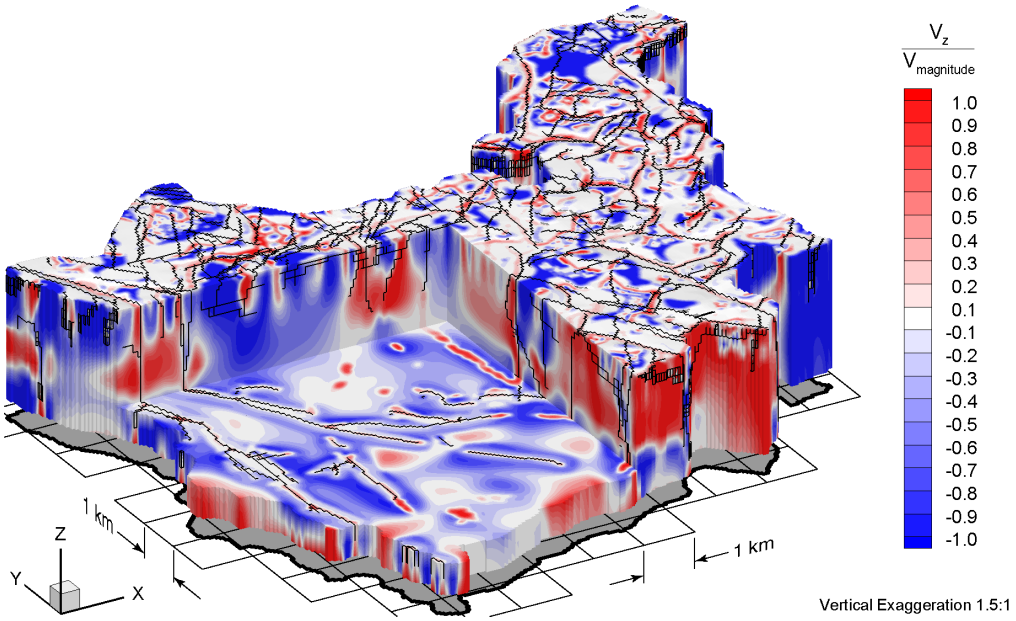

Figure E.23 Block cut view of ratio of vertical pore velocities to pore velocity magnitudes at present for the Canadian Shield Sub-Regional Scenario 5 paleoclimate simulation.

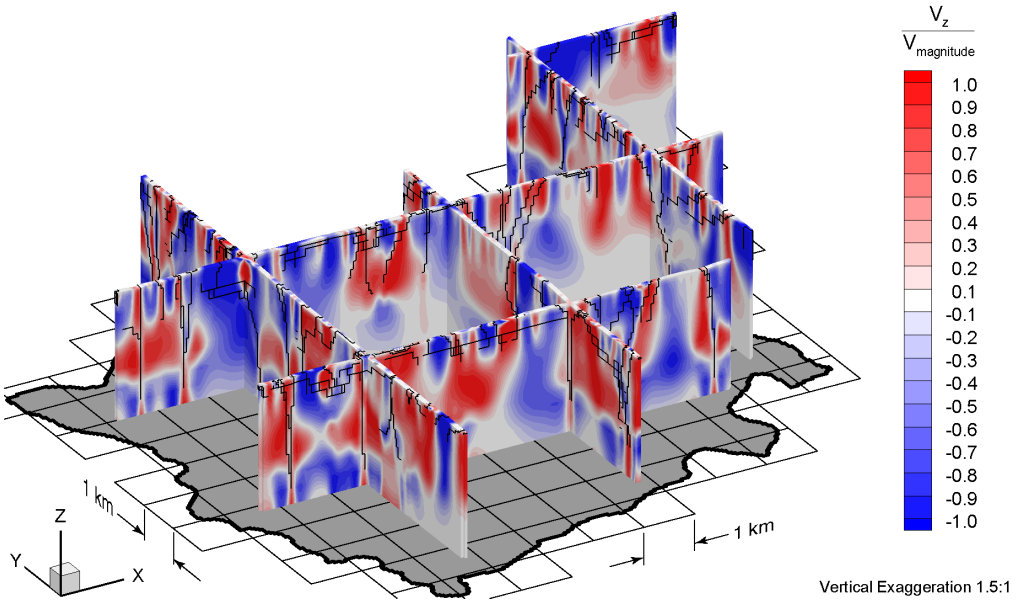

Figure E.24 Fence view of ratio of vertical pore velocities to pore velocity magnitudes at present for the Canadian Shield Sub-Regional Scenario 5 paleoclimate simulation.

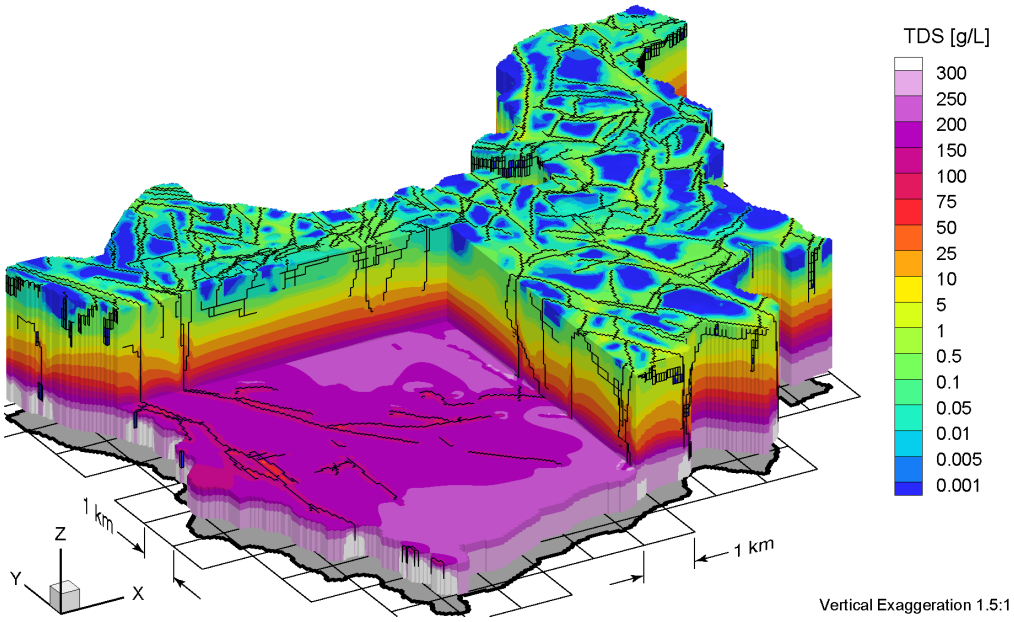

Figure E.25 Block cut view of brine concentrations at 80 ka before present for the Canadian Shield Sub-Regional Scenario 5 paleoclimate simulation.

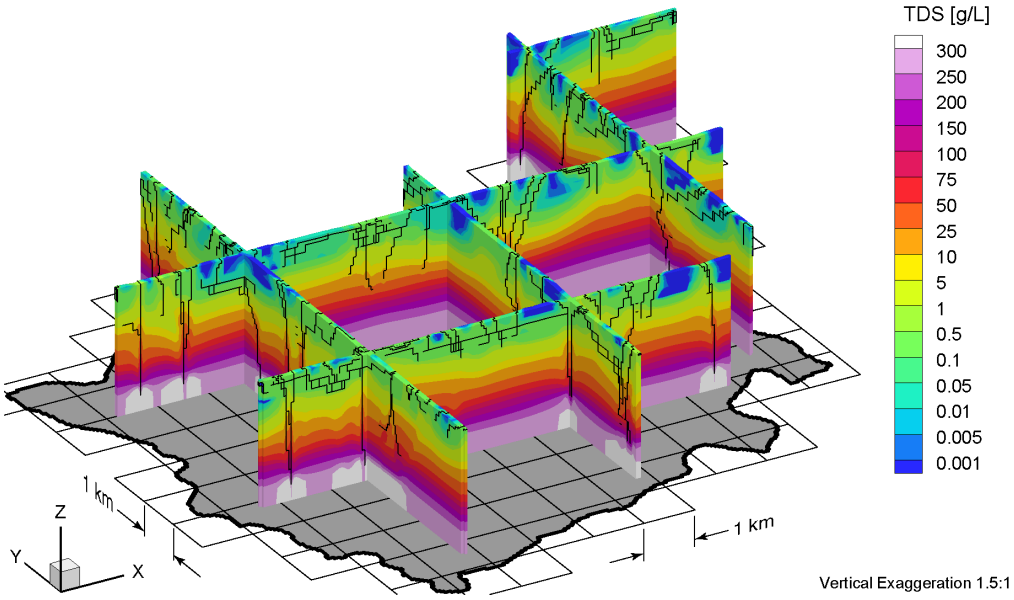

Figure E.26 Fence view of brine concentrations at 80 ka before present for the Canadian Shield Sub-Regional Scenario 5 paleoclimate simulation.

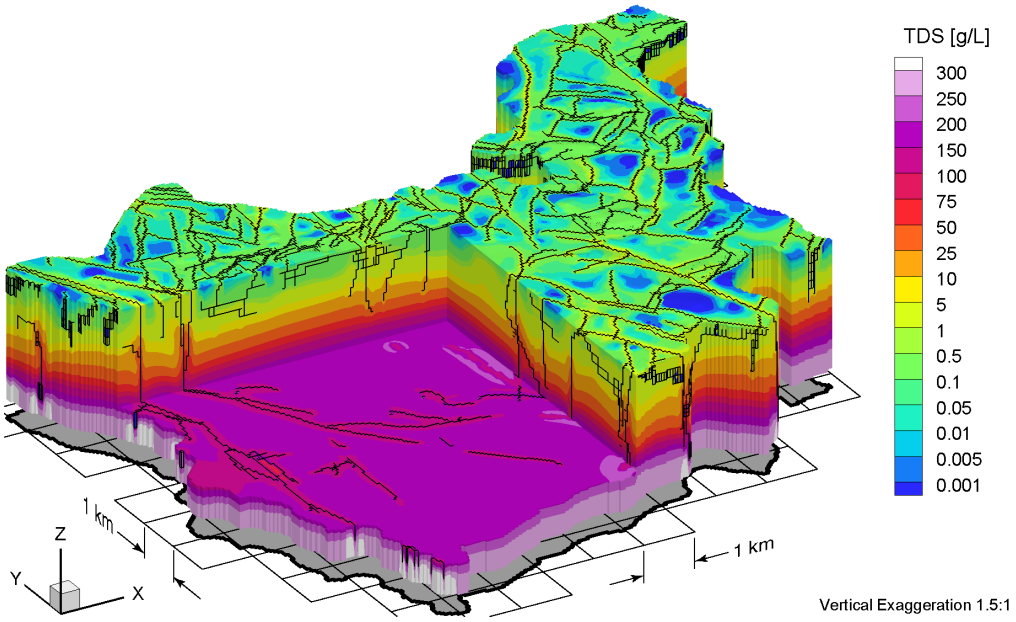

Figure E.27 Block cut view of brine concentrations at 40 ka before present for the Canadian Shield Sub-Regional Scenario 5 paleoclimate simulation.

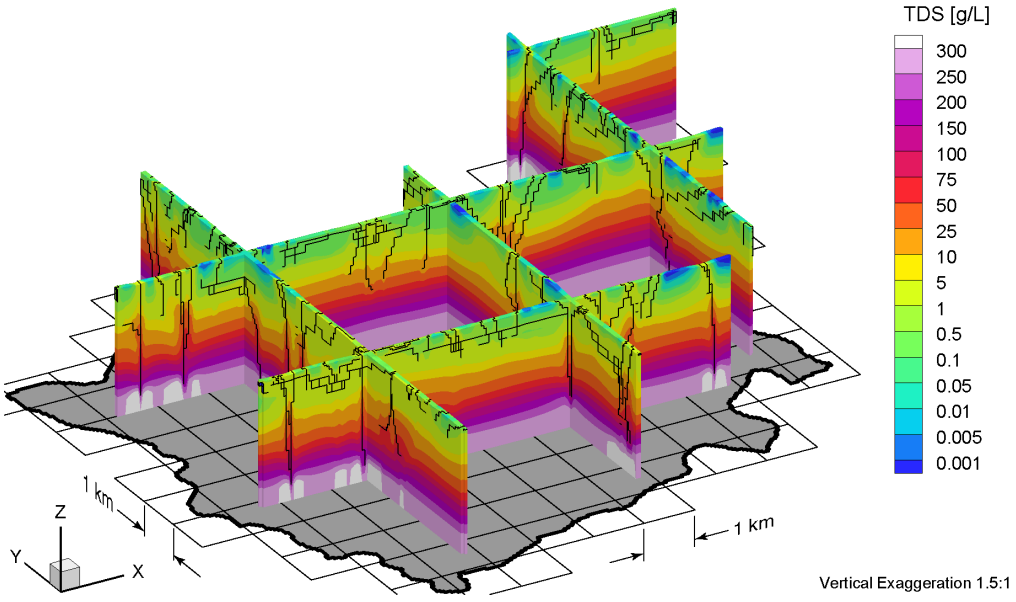

Figure E.28 Fence view of brine concentrations at 40 ka before present for the Canadian Shield Sub-Regional Scenario 5 paleoclimate simulation.

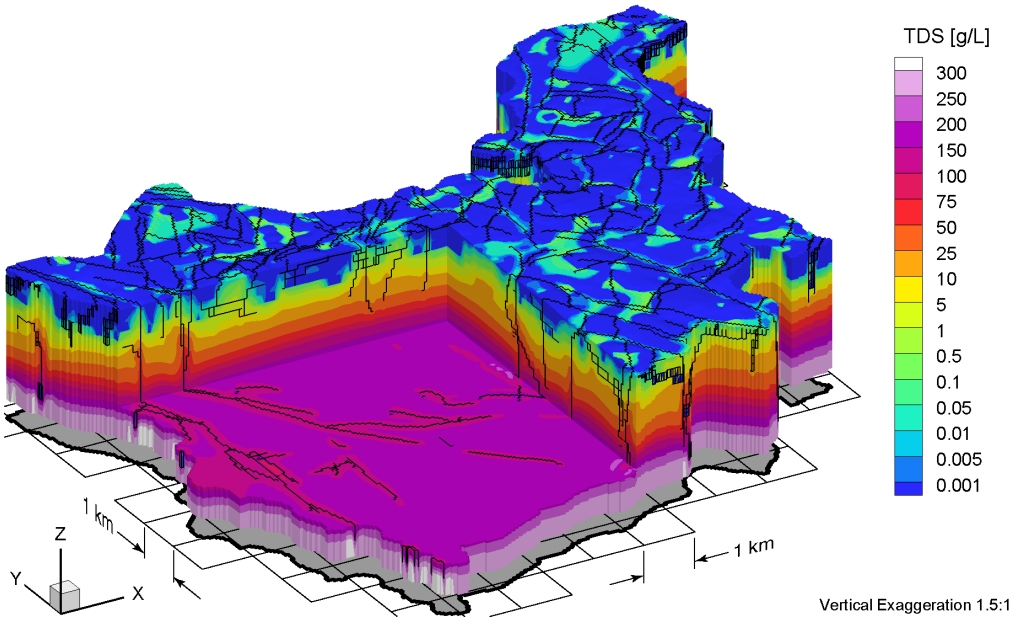

Figure E.29 Block cut view of brine concentrations at present for the Canadian Shield Sub-Regional Scenario 5 paleoclimate simulation.

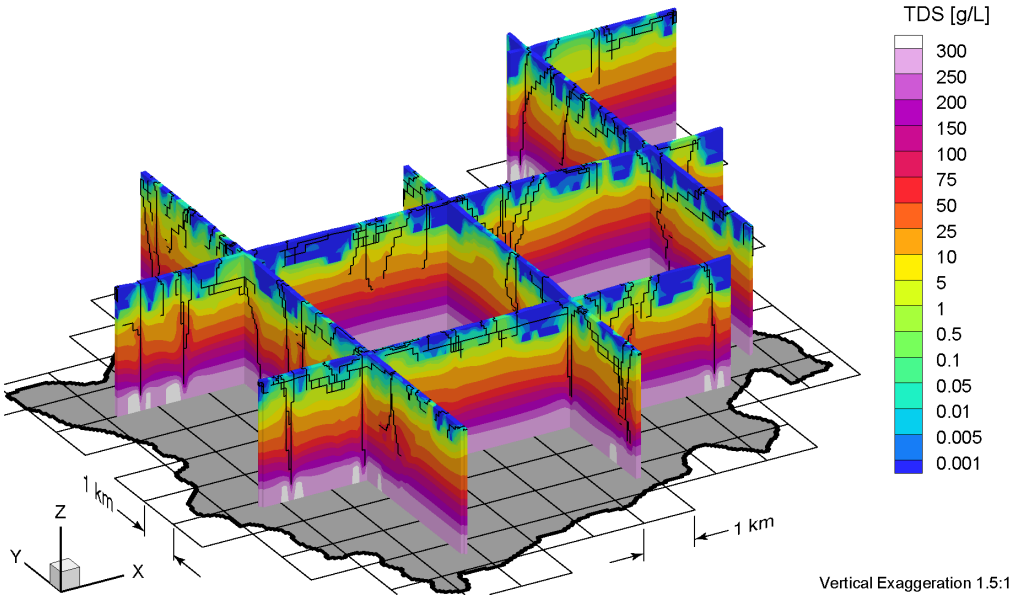

Figure E.30 Fence view of brine concentrations at present for the Canadian Shield Sub-Regional Scenario 5 paleoclimate simulation.

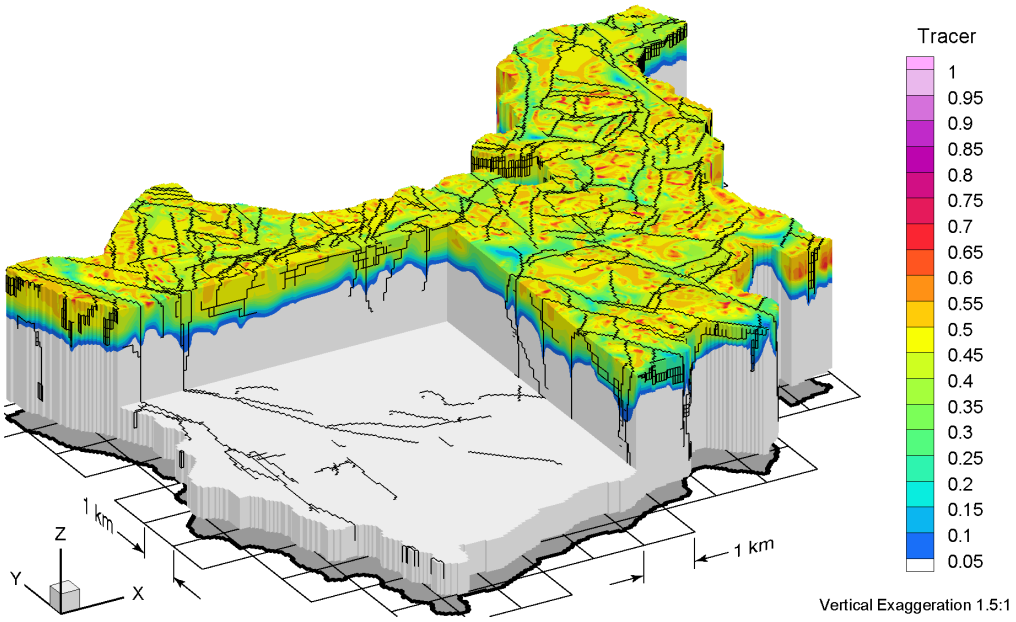

Figure E.31 Block cut view of tracer concentrations at 80 ka before present for the Canadian Shield Sub-Regional Scenario 5 paleoclimate simulation.

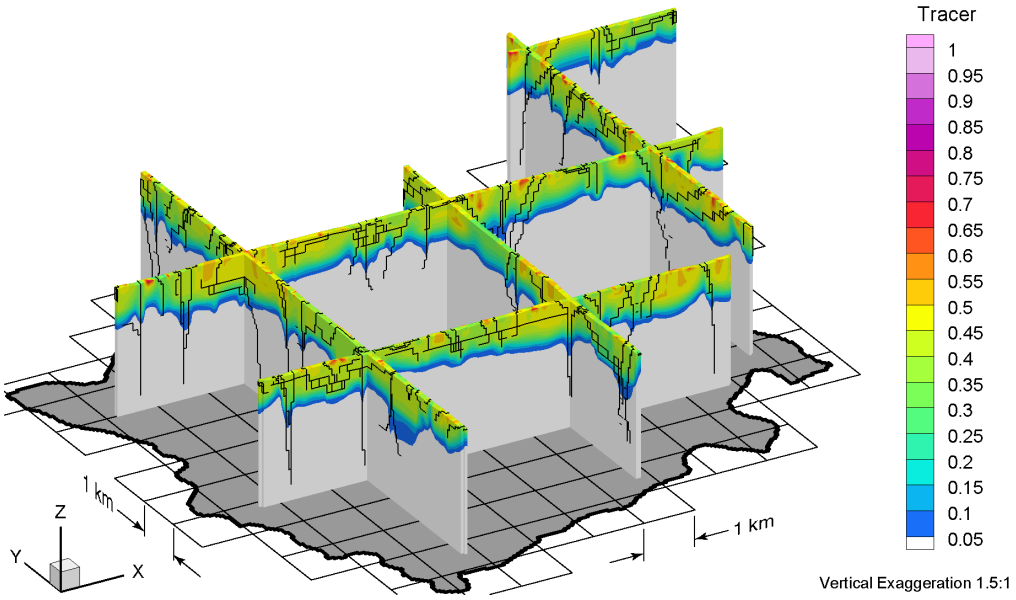

Figure E.32 Fence view of tracer concentrations at 80 ka before present for the Canadian Shield Sub-Regional Scenario 5 paleoclimate simulation.

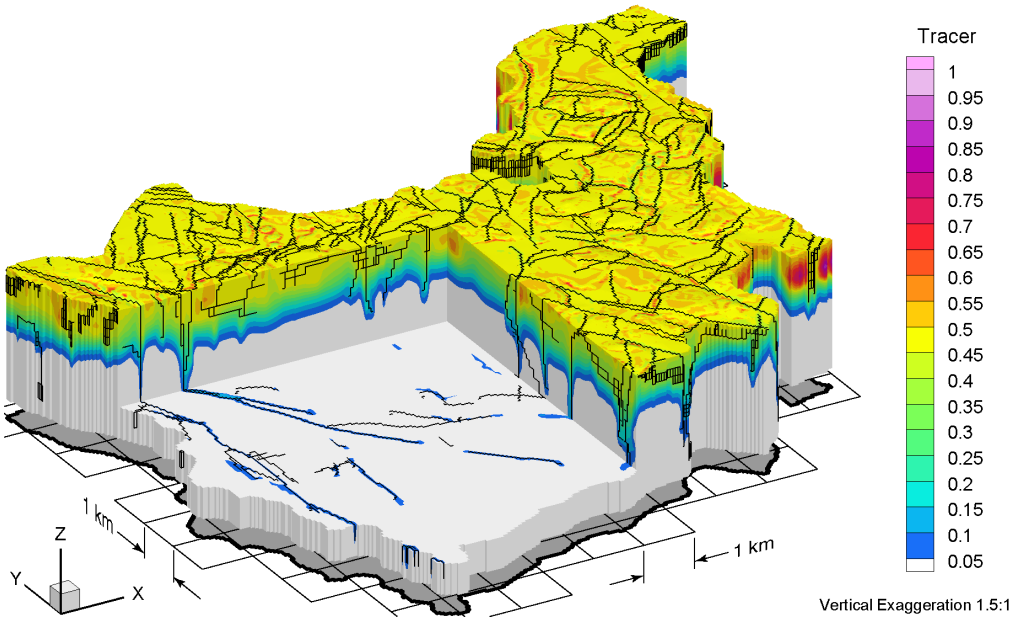

Figure E.33 Block cut view of tracer concentrations at 40 ka before present for the Canadian Shield Sub-Regional Scenario 5 paleoclimate simulation.

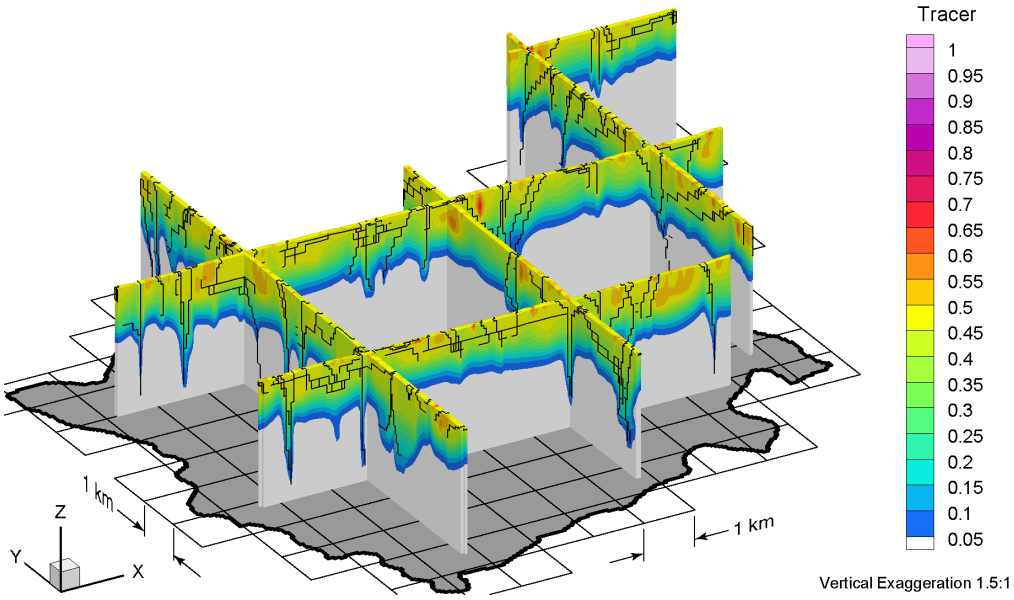

Figure E.34 Fence view of tracer concentrations at 40 ka before present for the Canadian Shield Sub-Regional Scenario 5 paleoclimate simulation.

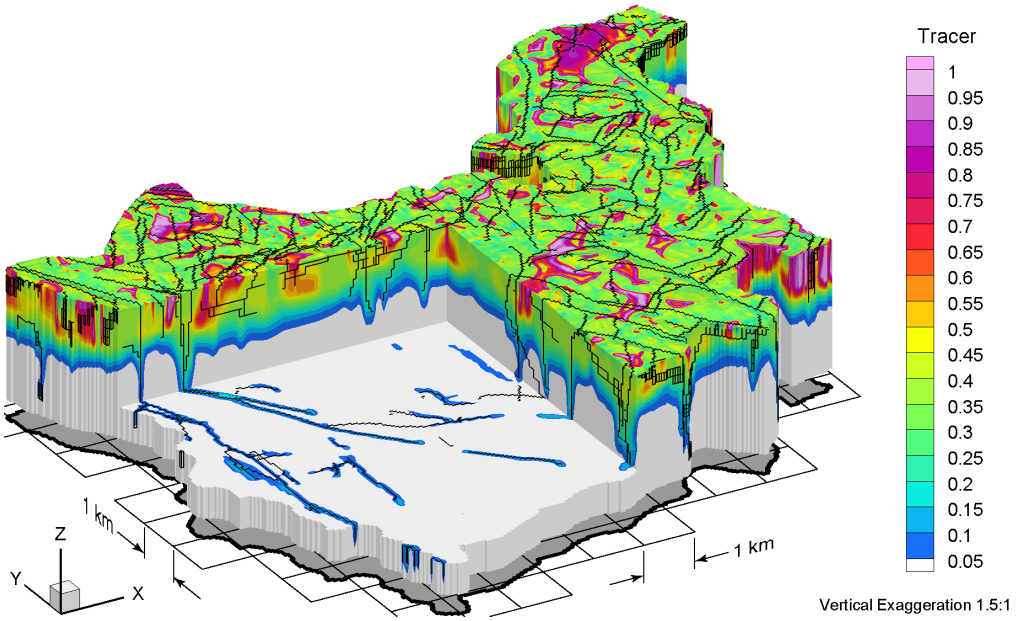

Figure E.35 Block cut view of tracer concentrations at present for the Canadian Shield Sub-Regional Scenario 5 paleoclimate simulation.

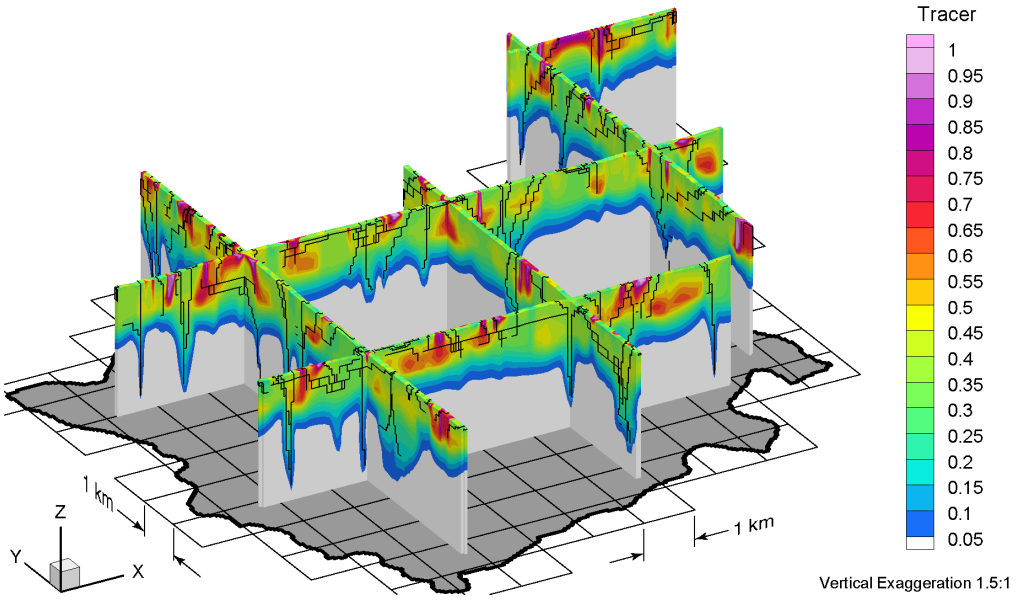

Figure E.36 Fence view of tracer concentrations at present for the Canadian Shield Sub-Regional Scenario 5 paleoclimate simulation.

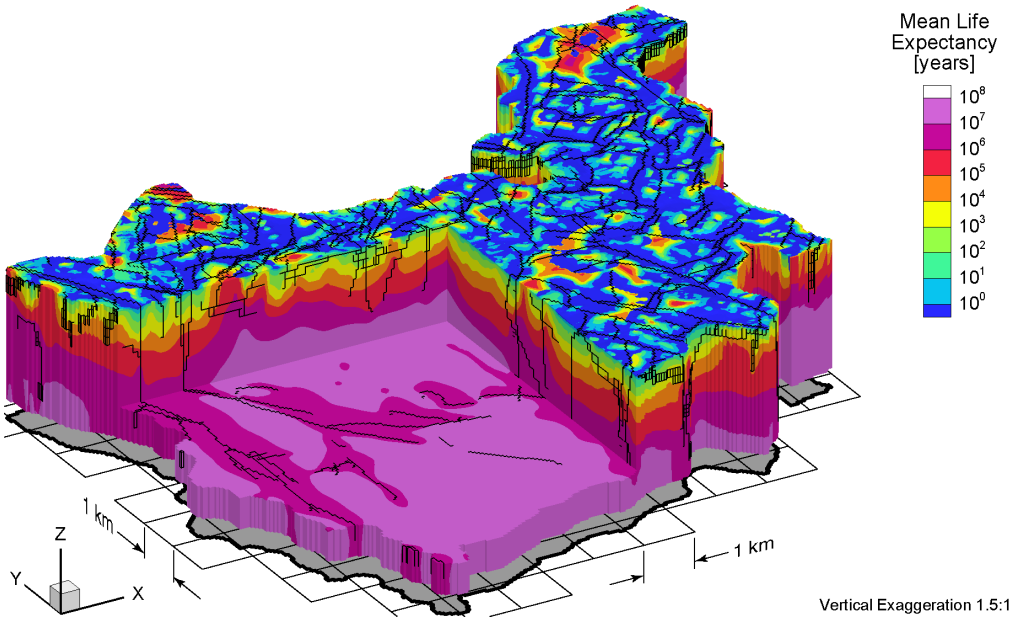

Figure E.37 Block cut view of mean life expectancies at present for the Canadian Shield Sub-Regional Scenario 5 paleoclimate simulation.

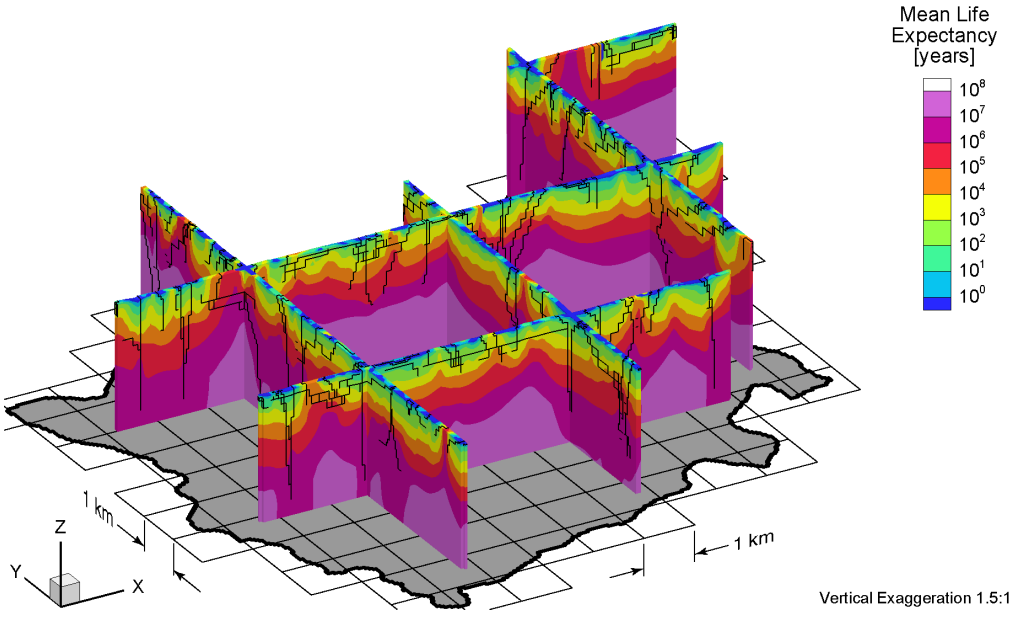

Figure E.38 Fence view of mean life expectancies at present for the Canadian Shield Sub-Regional Scenario 5 paleoclimate simulation.

Appendix F

CSSR Scenario 6 Paleoclimate Model

All figures related to Canadian Shield Sub-Regional (CSSR) Scenario 6 paleoclimate modelling are listed in Table F.1. Block cut view and fence view figures are shown on the same page to facilitate comparison. All results of the 120 ka paleoclimate simulations are shown at times of 80 ka before present, 40 ka before present, and at present.

Table F.1 List of Canadian Shield Sub-Regional Scenario 6 paleoclimate simulation figures.

Parameters	Time Before Present					
	80 ka		40 ka		Present	
	Block Cut	Fence	Block Cut	Fence	Block Cut	Fence
Freshwater Heads	F.1	F.2	F.3	F.4	F.5	F.6
Environmental Heads	F.7	F.8	F.9	F.10	F.11	F.12
Pore Velocity Magnitudes	F.13	F.14	F.15	F.16	F.17	F.18
Ratio of Vertical Pore Velocities to Pore Velocity Magnitudes	F.19	F.20	F.21	F.22	F.23	F.24
Brine Concentrations	F.25	F.26	F.27	F.28	F.29	F.30
Tracer Concentrations	F.31	F.32	F.33	F.34	F.35	F.36
Mean Life Expectancies	—	—	—	—	F.37	F.38

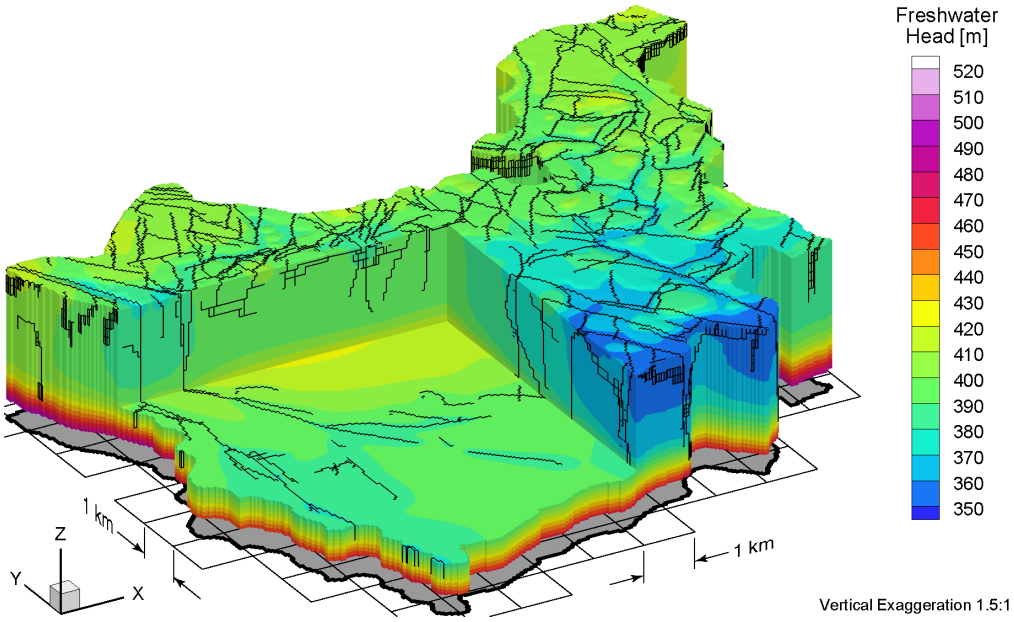

Figure F.1 Block cut view of freshwater heads at 80 ka before present for the Canadian Shield Sub-Regional Scenario 6 paleoclimate simulation.

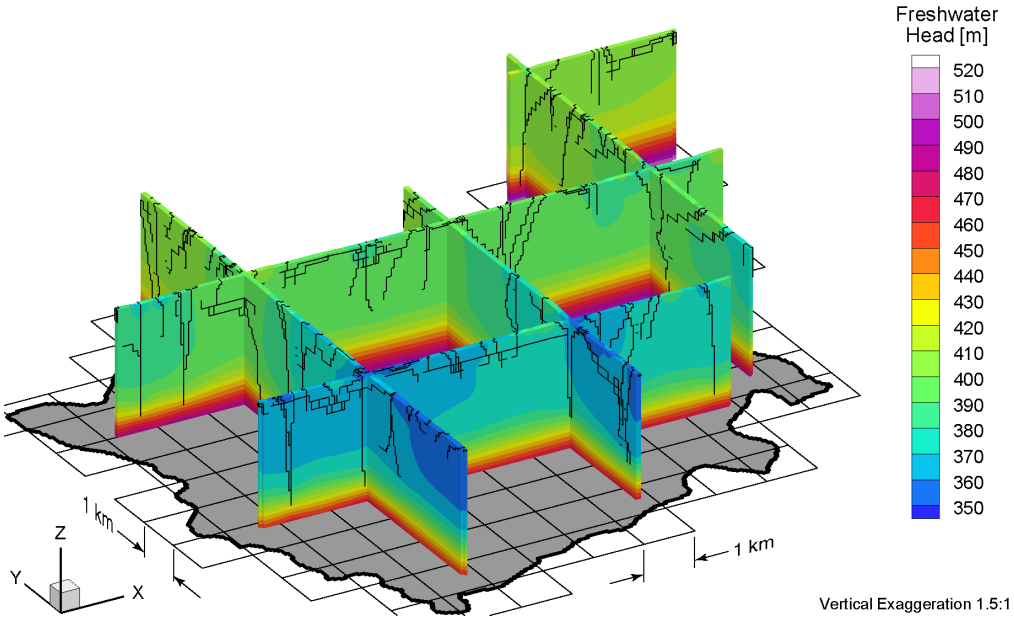

Figure F.2 Fence view of freshwater heads at 80 ka before present for the Canadian Shield Sub-Regional Scenario 6 paleoclimate simulation.

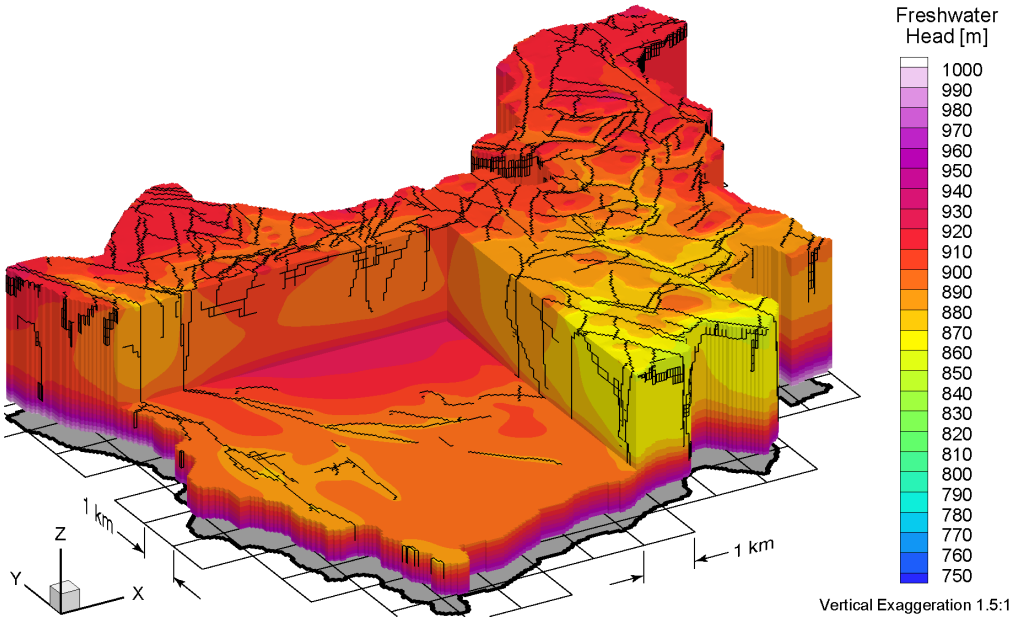

Figure F.3 Block cut view of freshwater heads at 40 ka before present for the Canadian Shield Sub-Regional Scenario 6 paleoclimate simulation.

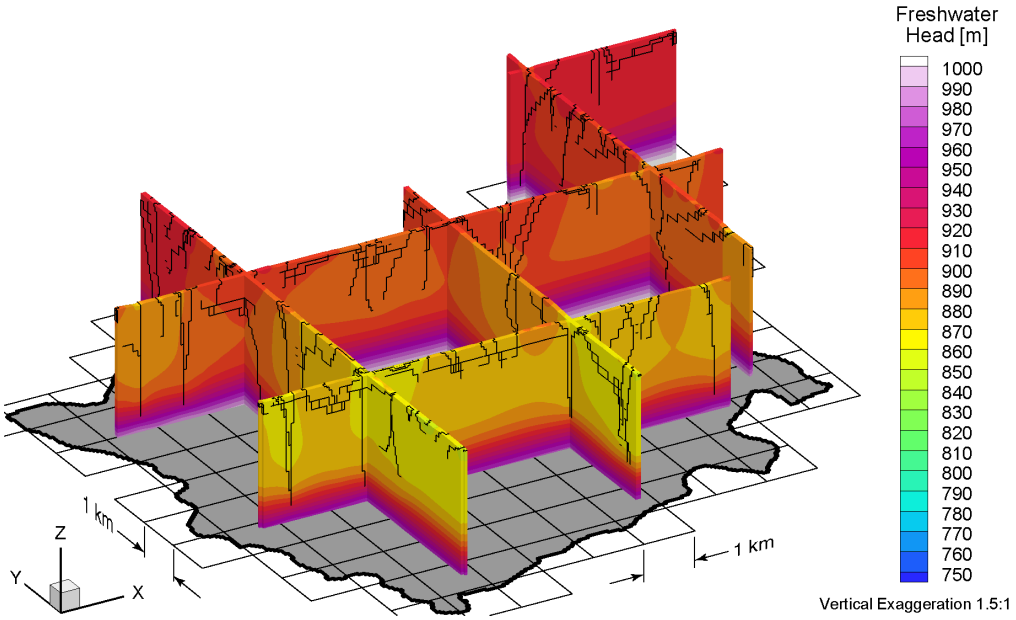

Figure F.4 Fence view of freshwater heads at 40 ka before present for the Canadian Shield Sub-Regional Scenario 6 paleoclimate simulation.

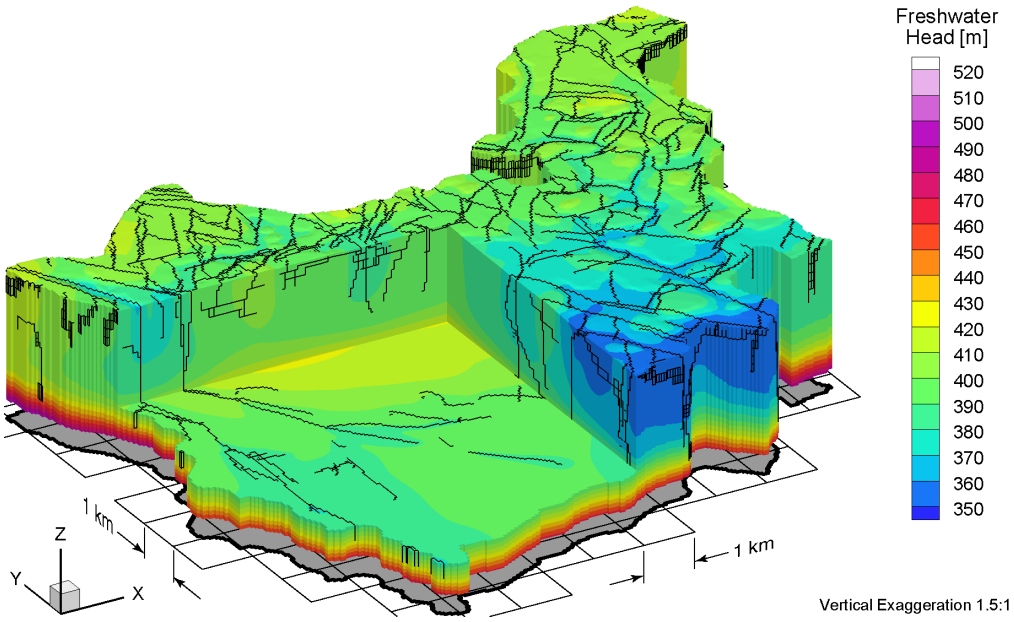

Figure F.5 Block cut view of freshwater heads at present for the Canadian Shield Sub-Regional Scenario 6 paleoclimate simulation.

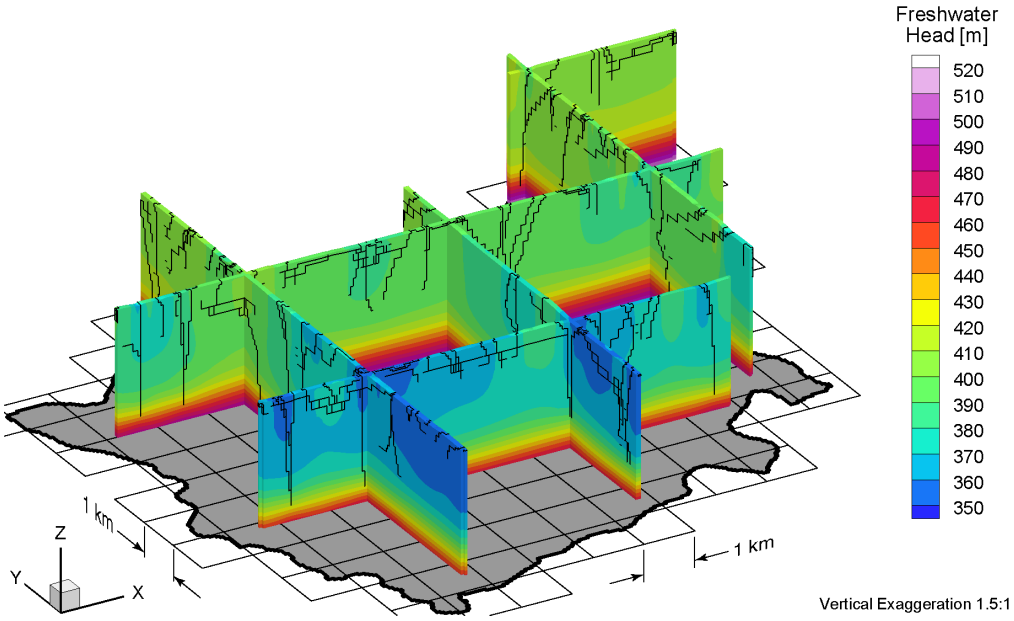

Figure F.6 Fence view of freshwater heads at present for the Canadian Shield Sub-Regional Scenario 6 paleoclimate simulation.

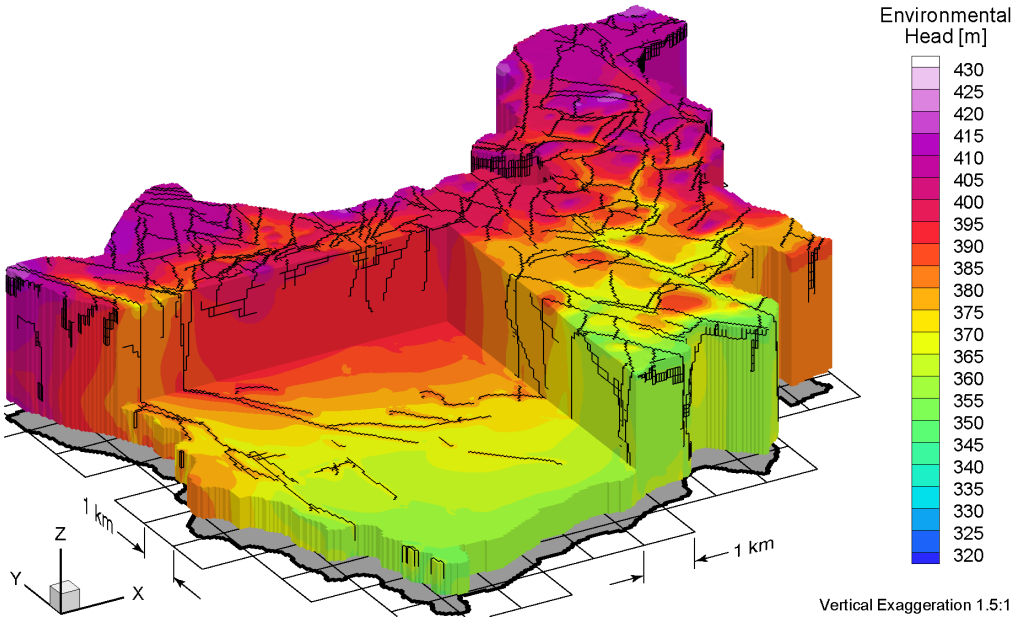

Figure F.7 Block cut view of environmental heads at 80 ka before present for the Canadian Shield Sub-Regional Scenario 6 paleoclimate simulation.

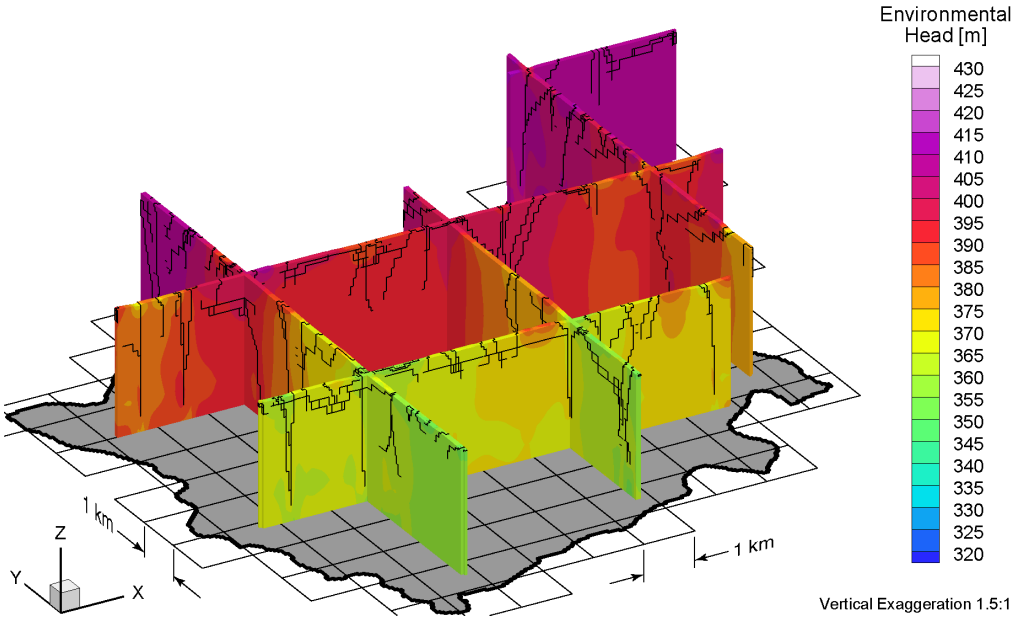

Figure F.8 Fence view of environmental heads at 80 ka before present for the Canadian Shield Sub-Regional Scenario 6 paleoclimate simulation.

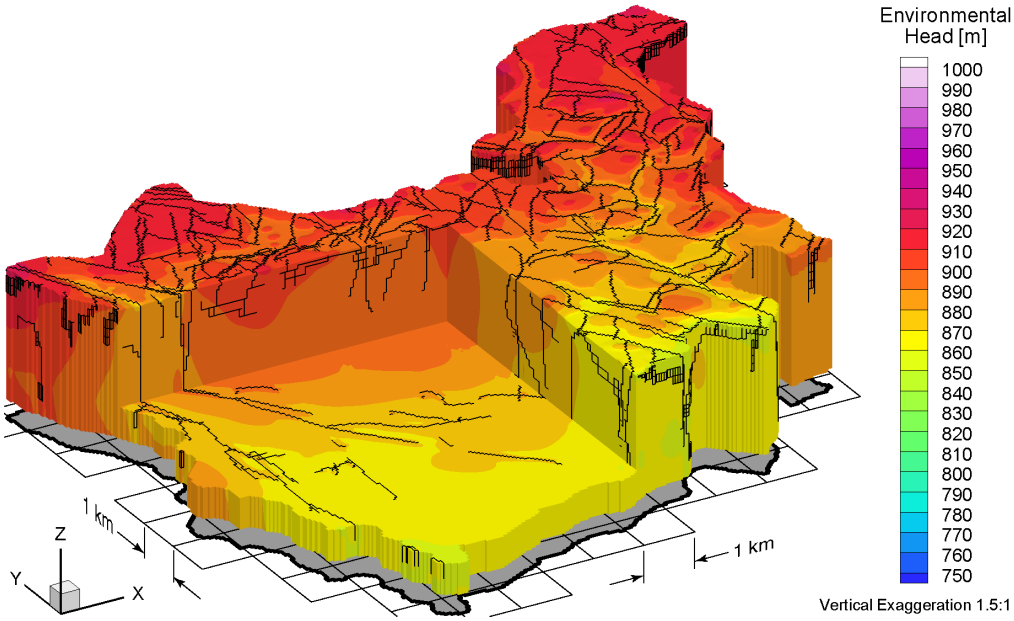

Figure F.9 Block cut view of environmental heads at 40 ka before present for the Canadian Shield Sub-Regional Scenario 6 paleoclimate simulation.

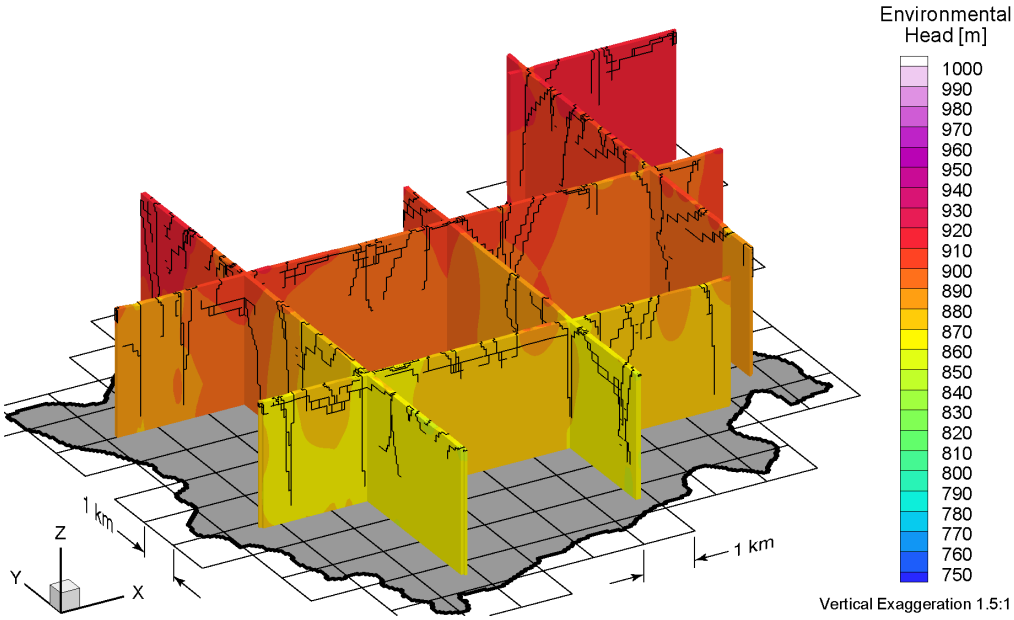

Figure F.10 Fence view of environmental heads at 40 ka before present for the Canadian Shield Sub-Regional Scenario 6 paleoclimate simulation.

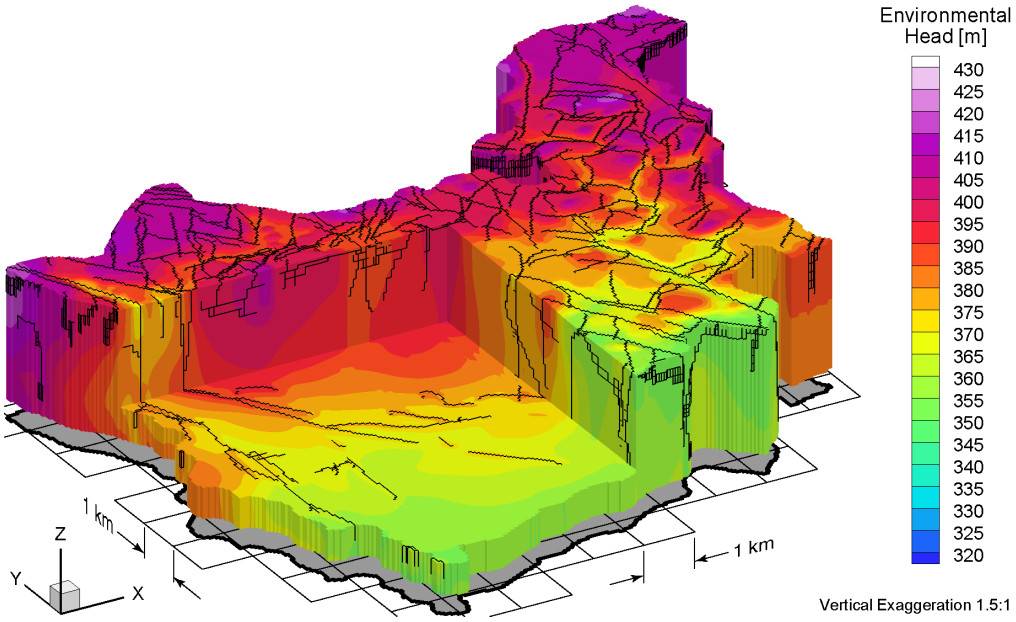

Figure F.11 Block cut view of environmental heads at present for the Canadian Shield Sub-Regional Scenario 6 paleoclimate simulation.

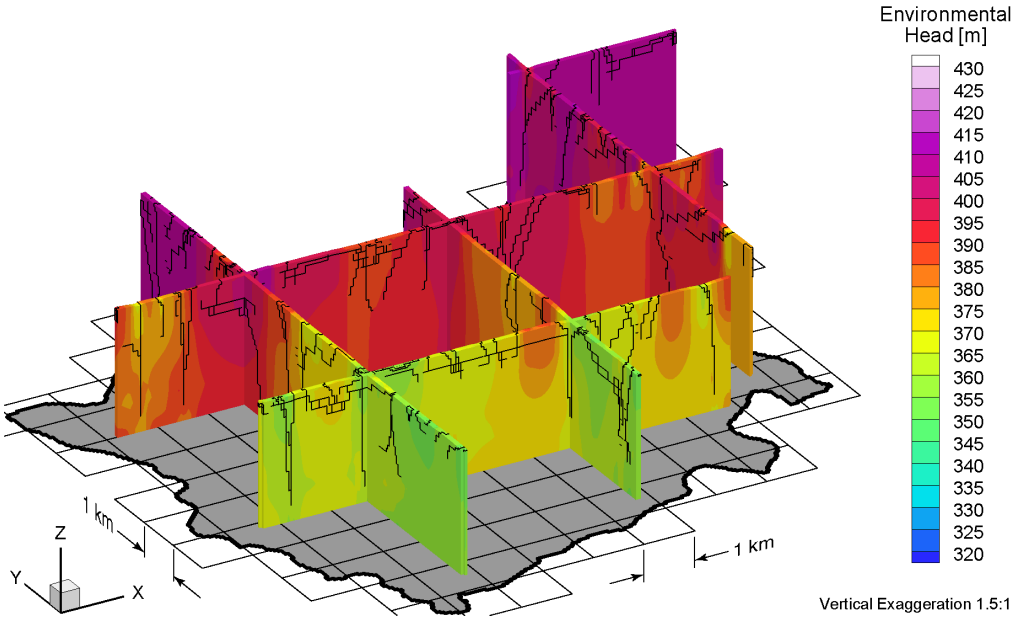

Figure F.12 Fence view of environmental heads at present for the Canadian Shield Sub-Regional Scenario 6 paleoclimate simulation.

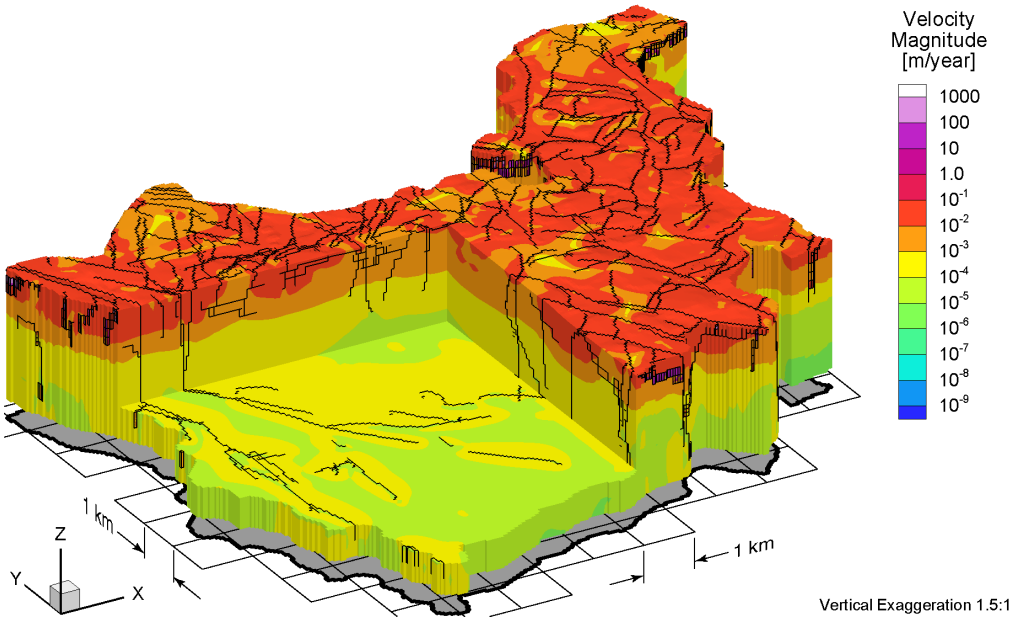

Figure F.13 Block cut view of pore velocity magnitudes at 80 ka before present for the Canadian Shield Sub-Regional Scenario 6 paleoclimate simulation.

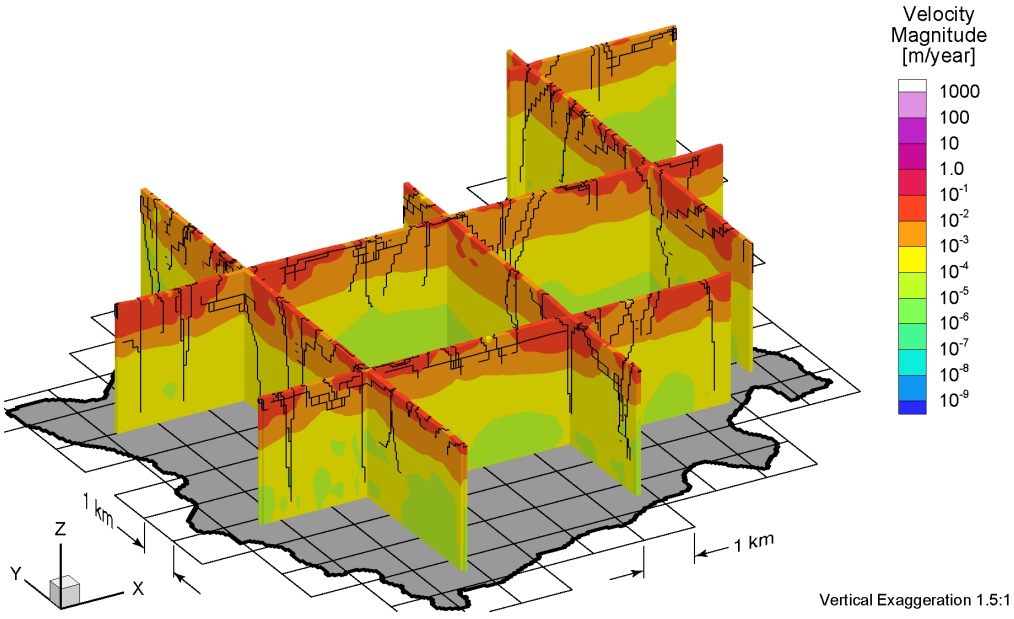

Figure F.14 Fence view of pore velocity magnitudes at 80 ka before present for the Canadian Shield Sub-Regional Scenario 6 paleoclimate simulation.

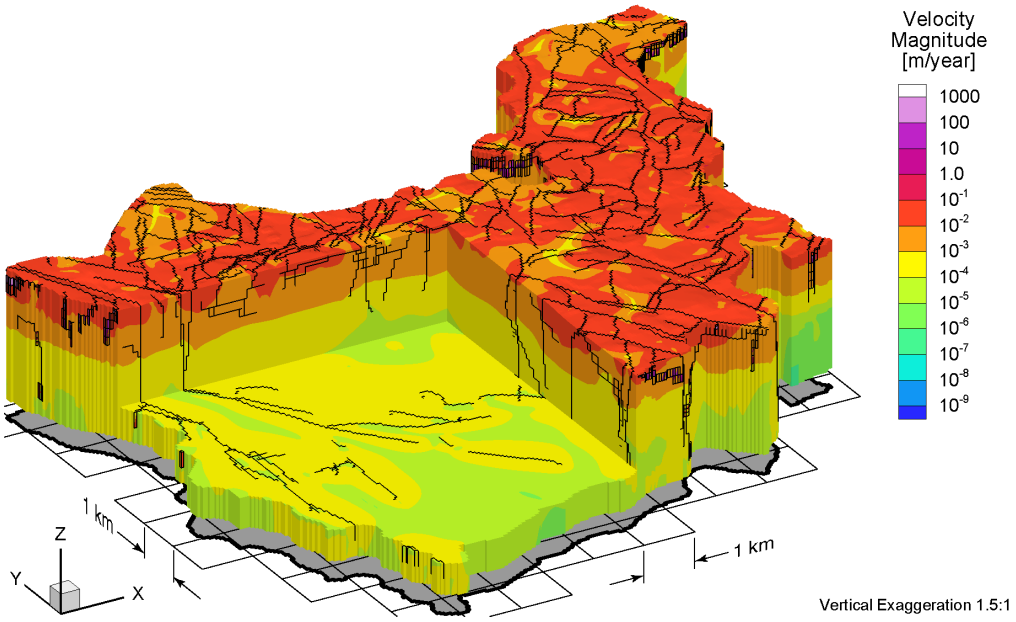

Figure F.15 Block cut view of pore velocity magnitudes at 40 ka before present for the Canadian Shield Sub-Regional Scenario 6 paleoclimate simulation.

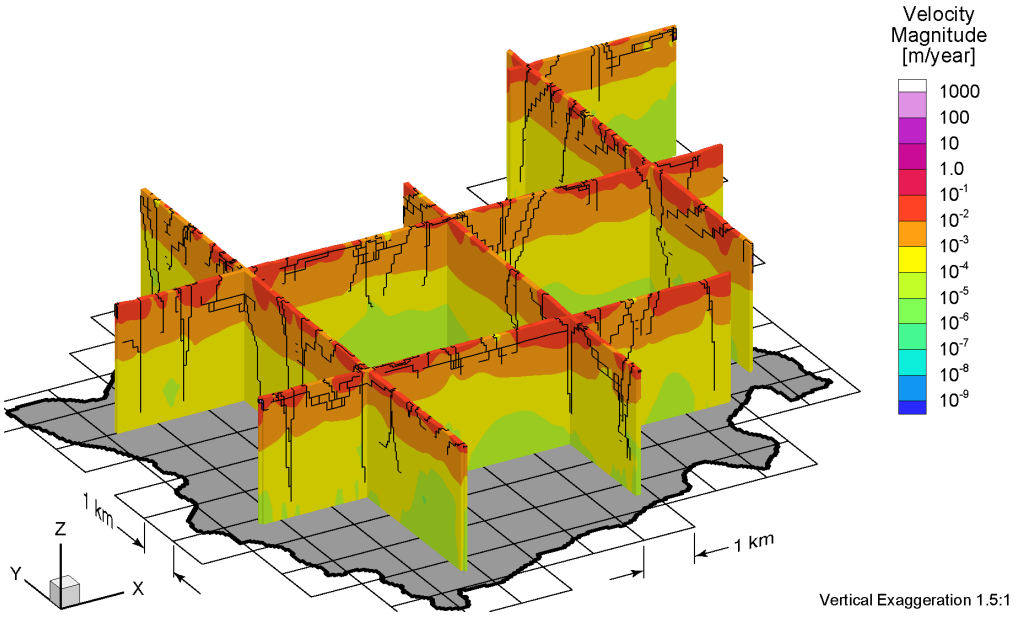

Figure F.16 Fence view of pore velocity magnitudes at 40 ka before present for the Canadian Shield Sub-Regional Scenario 6 paleoclimate simulation.

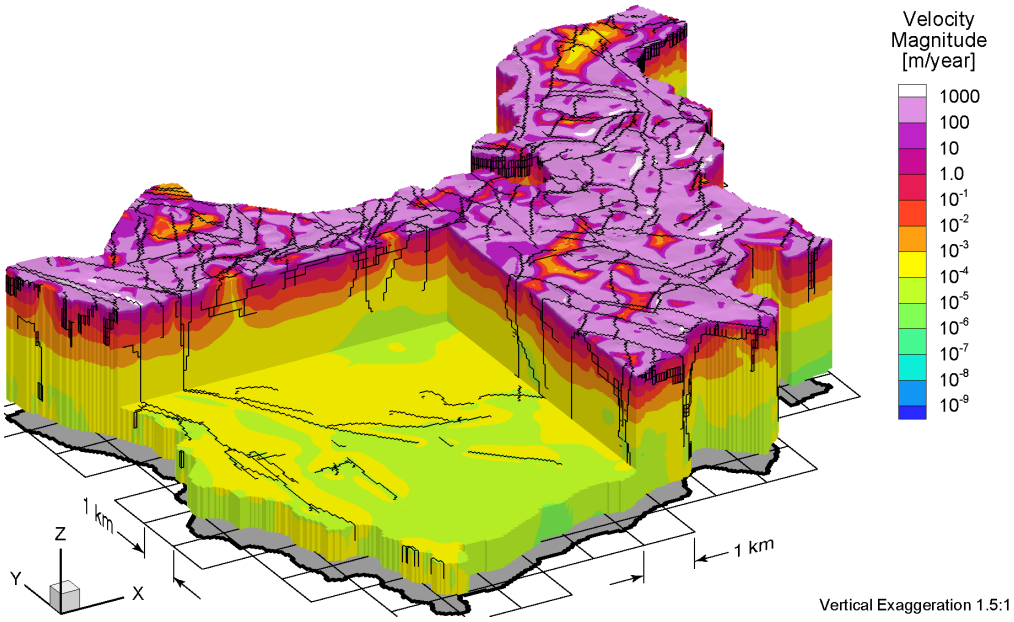

Figure F.17 Block cut view of pore velocity magnitudes at present for the Canadian Shield Sub-Regional Scenario 6 paleoclimate simulation.

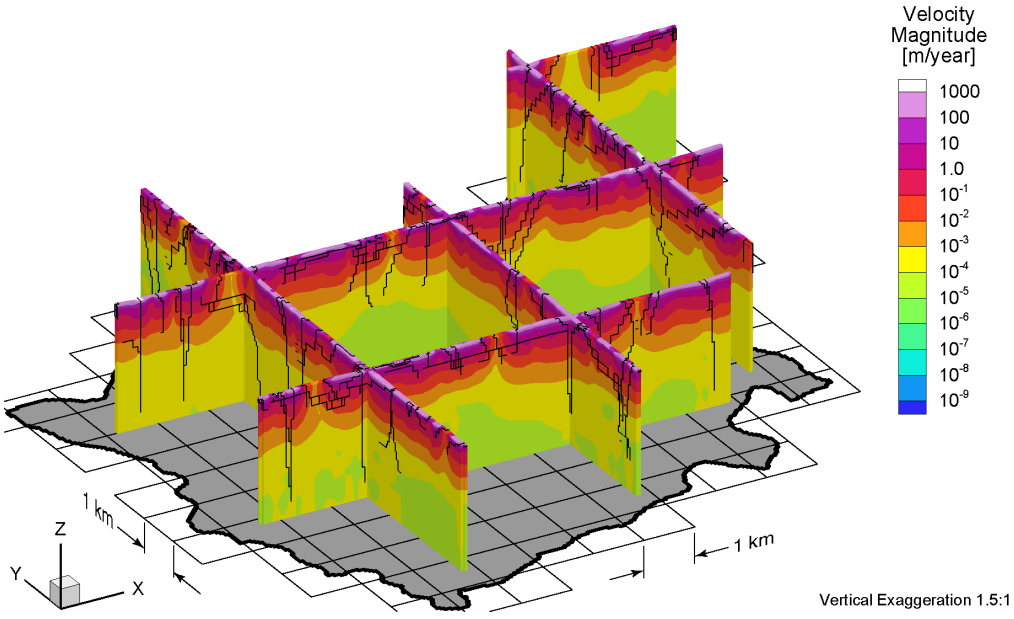

Figure F.18 Fence view of pore velocity magnitudes at present for the Canadian Shield Sub-Regional Scenario 6 paleoclimate simulation.

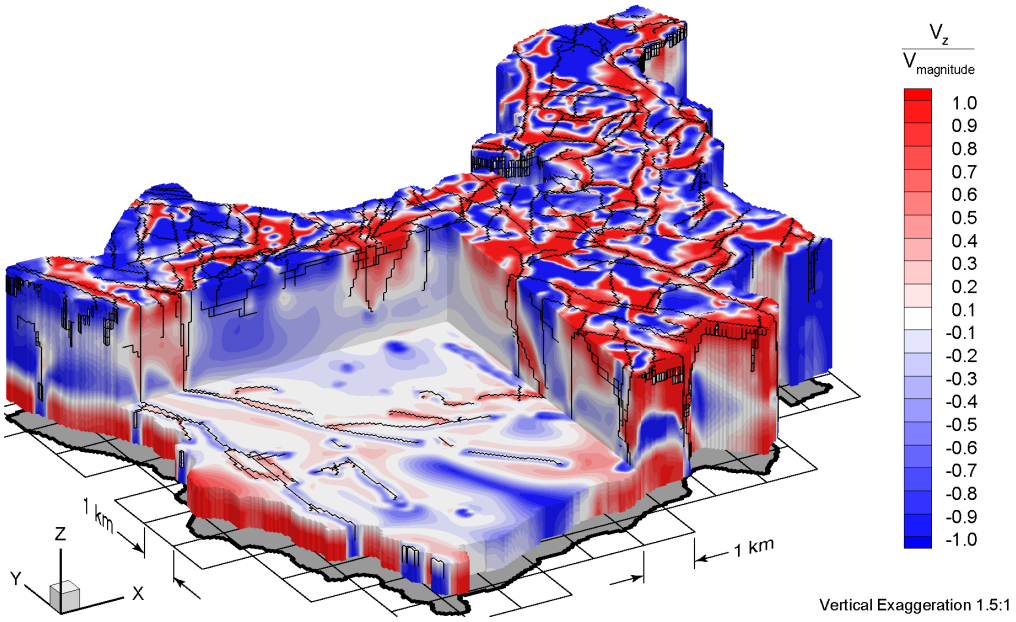

Figure F.19 Block cut view of ratio of vertical pore velocities to pore velocity magnitudes at 80 ka before present for the Canadian Shield Sub-Regional Scenario 6 paleoclimate simulation.

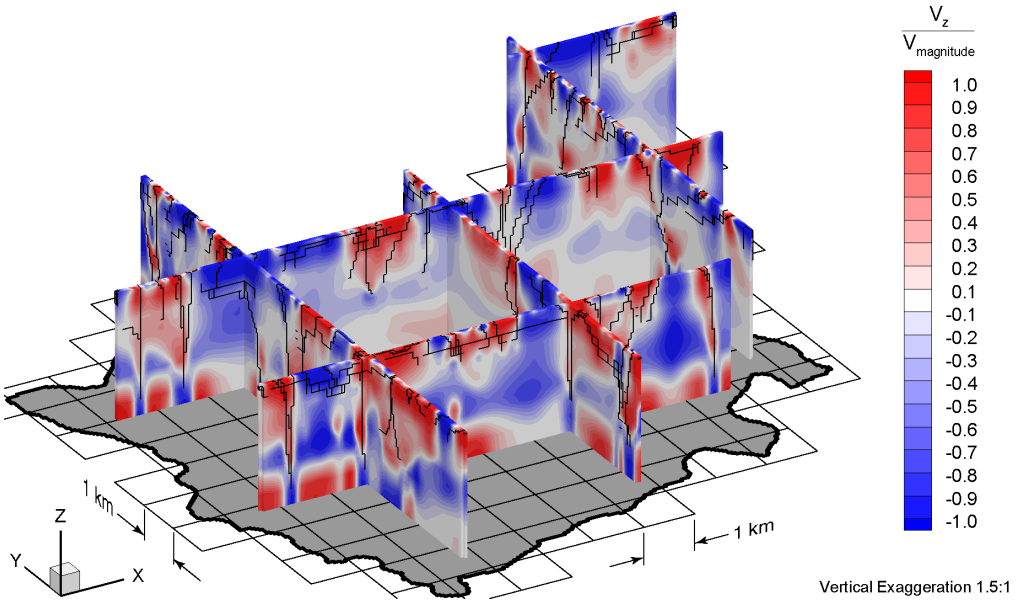

Figure F.20 Fence view of ratio of vertical pore velocities to pore velocity magnitudes at 80 ka before present for the Canadian Shield Sub-Regional Scenario 6 paleoclimate simulation.

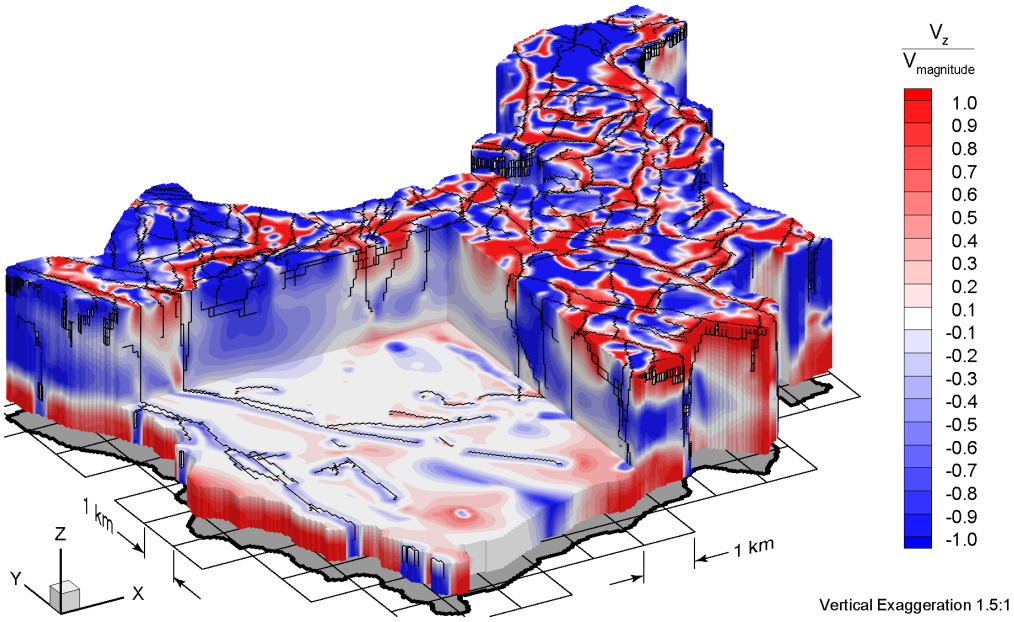

Figure F.21 Block cut view of ratio of vertical pore velocities to pore velocity magnitudes at 40 ka before present for the Canadian Shield Sub-Regional Scenario 6 paleoclimate simulation.

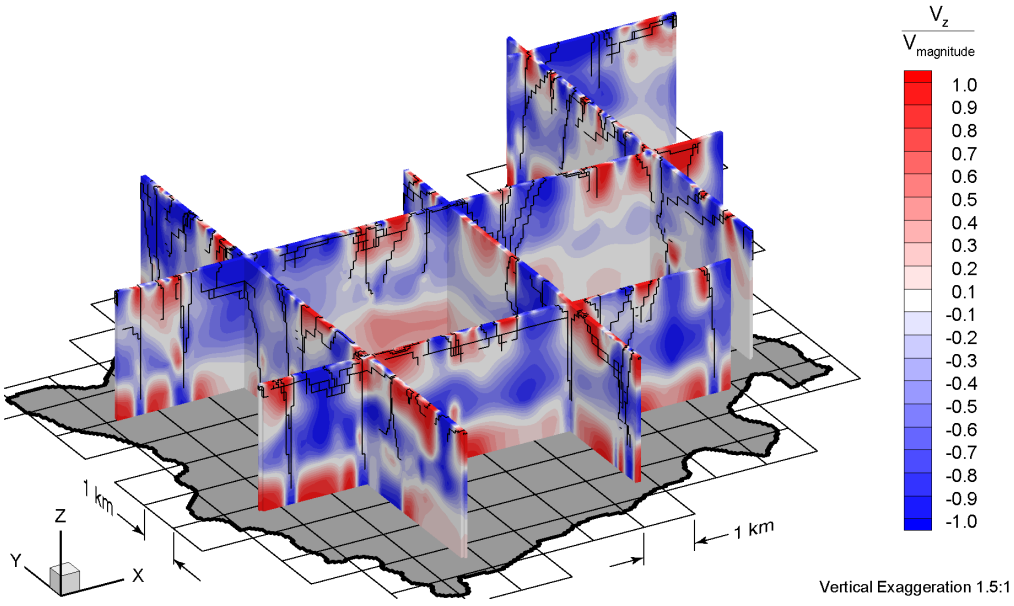

Figure F.22 Fence view of ratio of vertical pore velocities to pore velocity magnitudes at 40 ka before present for the Canadian Shield Sub-Regional Scenario 6 paleoclimate simulation.

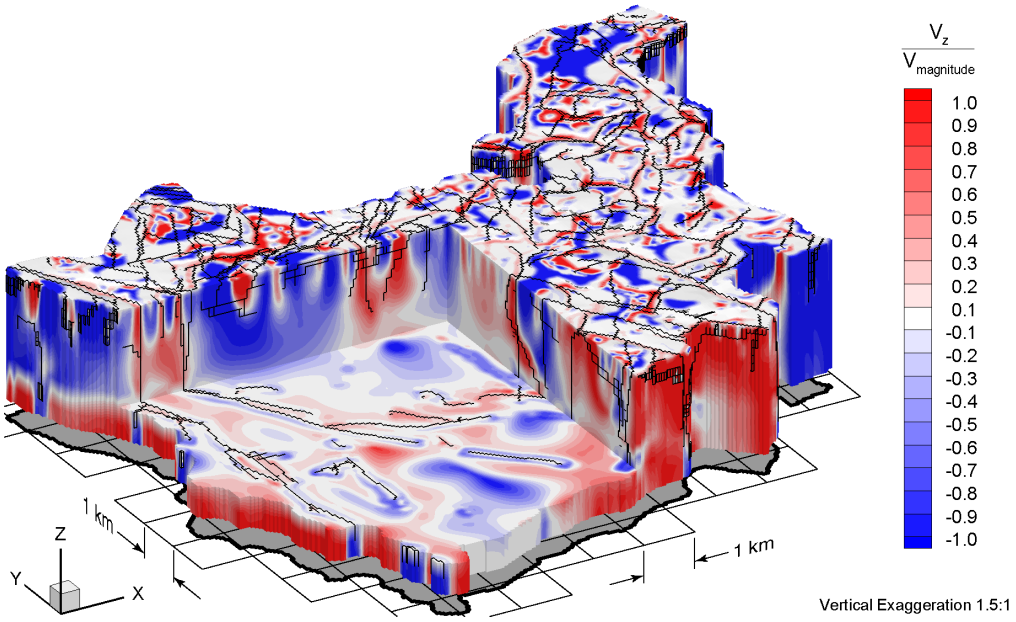

Figure F.23 Block cut view of ratio of vertical pore velocities to pore velocity magnitudes at present for the Canadian Shield Sub-Regional Scenario 6 paleoclimate simulation.

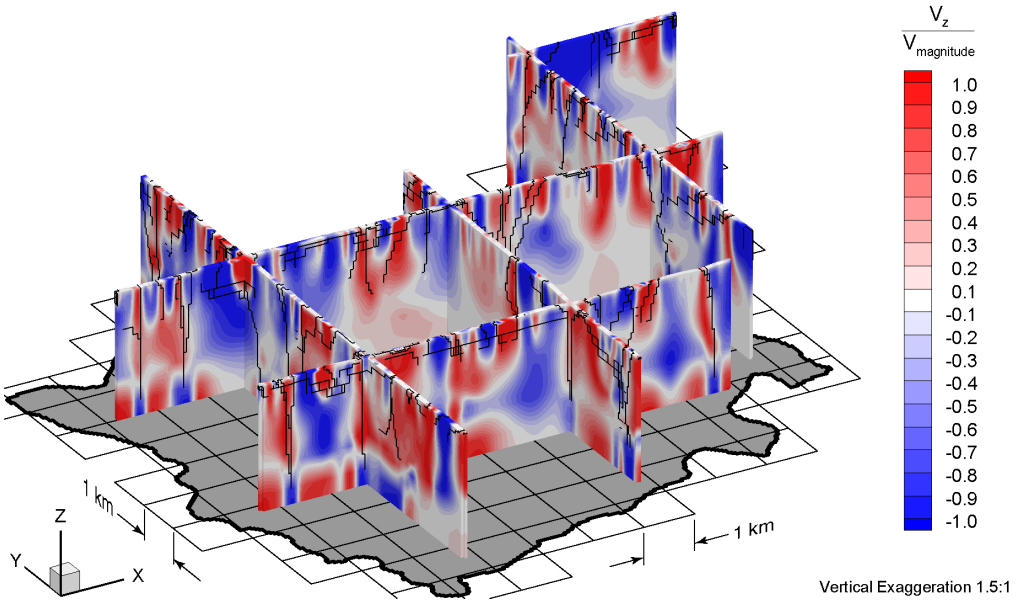

Figure F.24 Fence view of ratio of vertical pore velocities to pore velocity magnitudes at present for the Canadian Shield Sub-Regional Scenario 6 paleoclimate simulation.

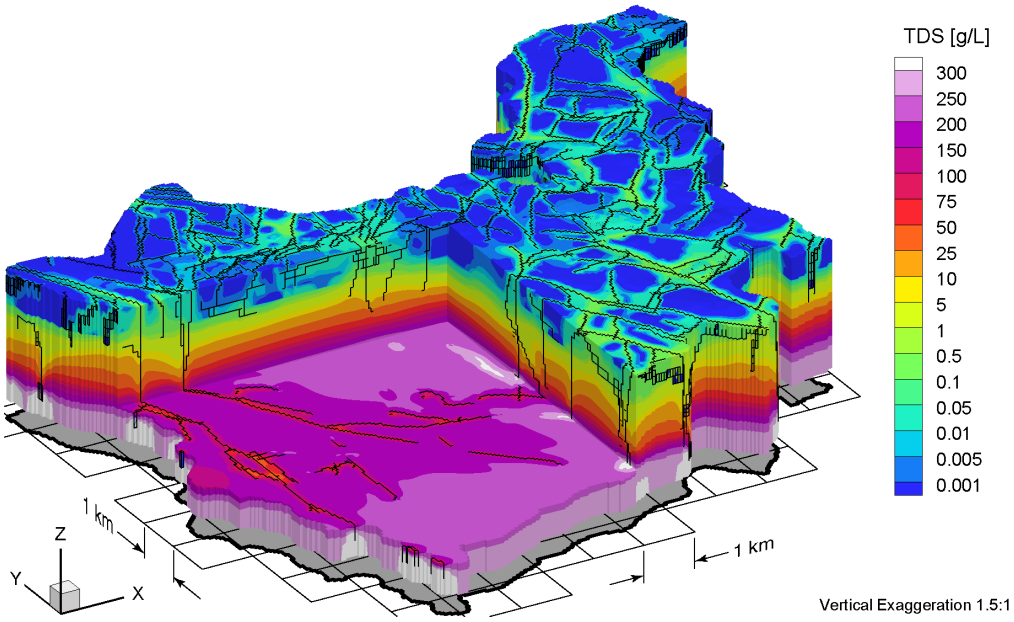

Figure F.25 Block cut view of brine concentrations at 80 ka before present for the Canadian Shield Sub-Regional Scenario 6 paleoclimate simulation.

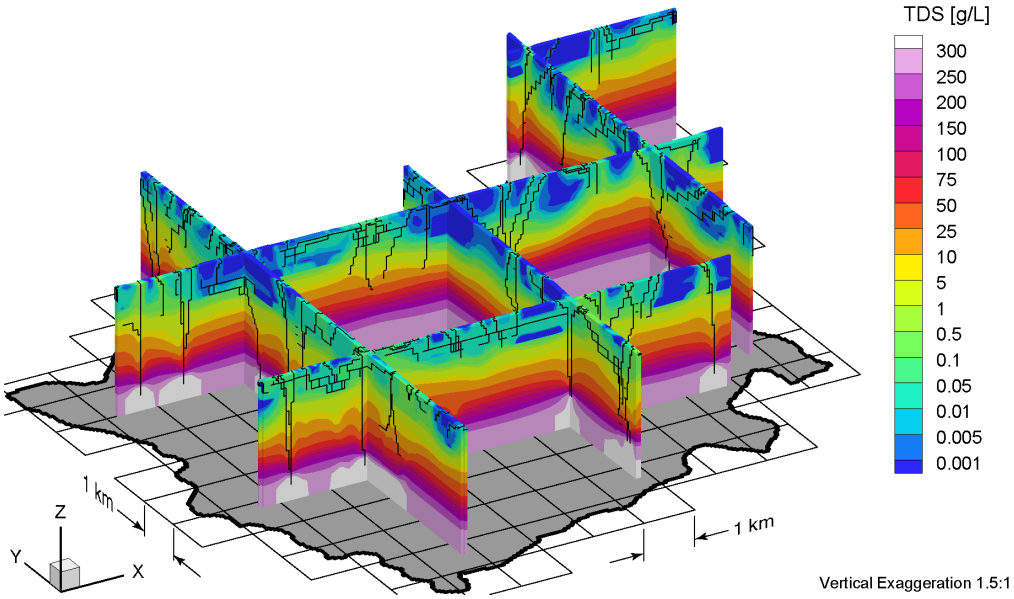

Figure F.26 Fence view of brine concentrations at 80 ka before present for the Canadian Shield Sub-Regional Scenario 6 paleoclimate simulation.

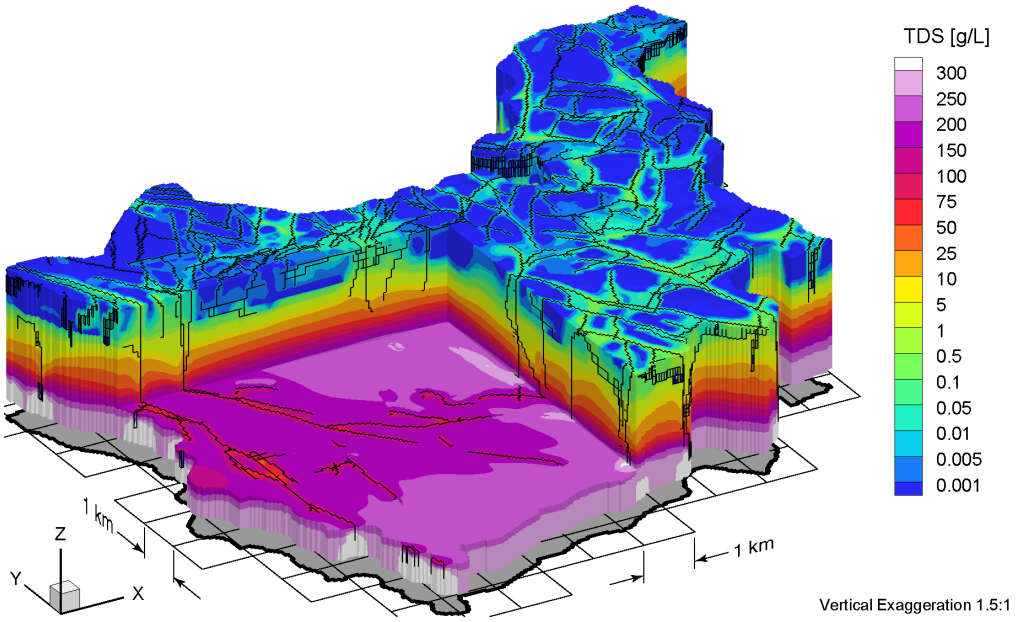

Figure F.27 Block cut view of brine concentrations at 40 ka before present for the Canadian Shield Sub-Regional Scenario 6 paleoclimate simulation.

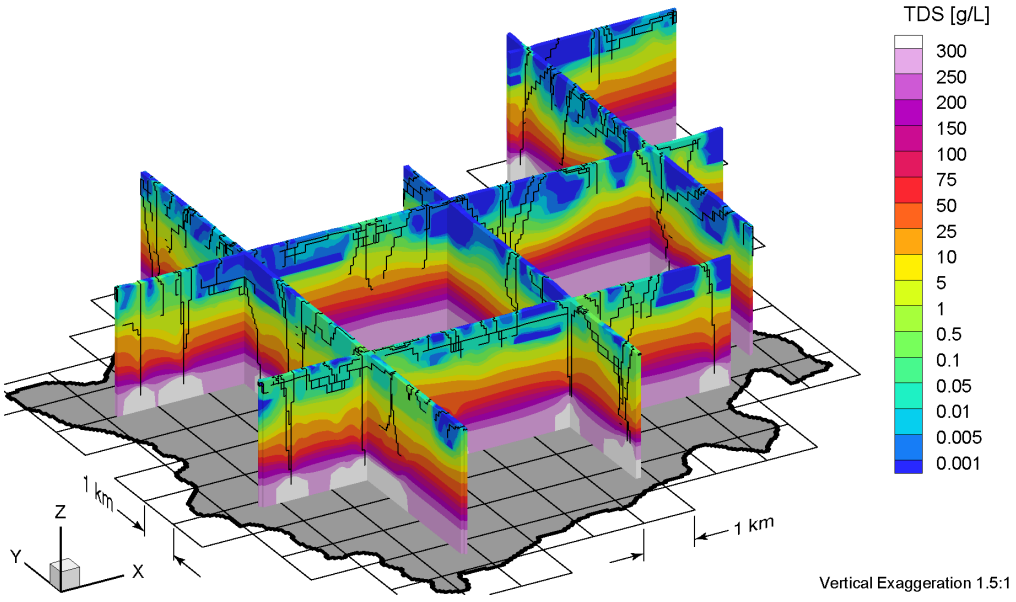

Figure F.28 Fence view of brine concentrations at 40 ka before present for the Canadian Shield Sub-Regional Scenario 6 paleoclimate simulation.

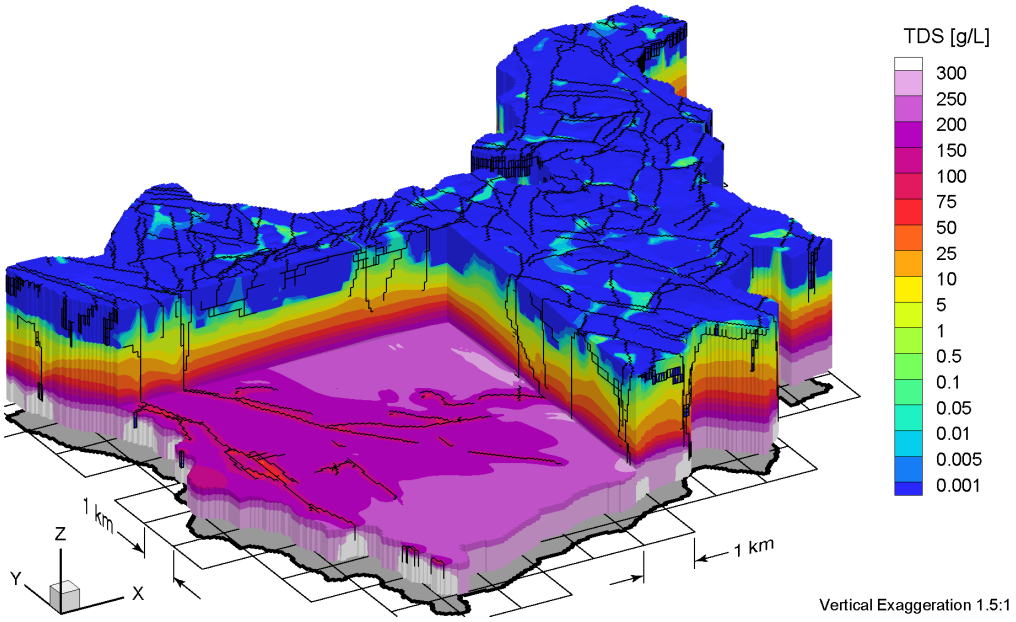

Figure F.29 Block cut view of brine concentrations at present for the Canadian Shield Sub-Regional Scenario 6 paleoclimate simulation.

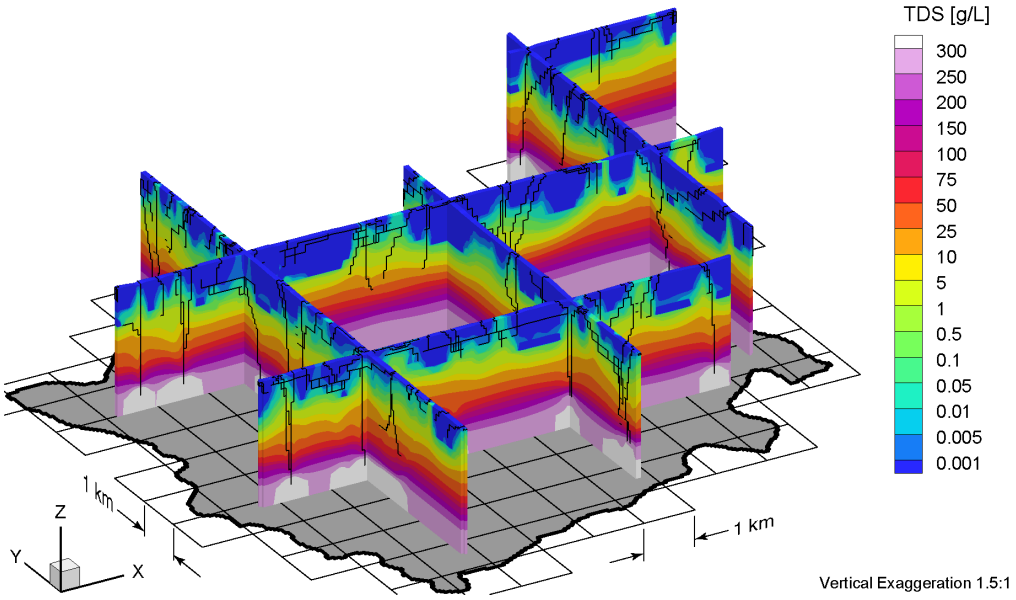

Figure F.30 Fence view of brine concentrations at present for the Canadian Shield Sub-Regional Scenario 6 paleoclimate simulation.

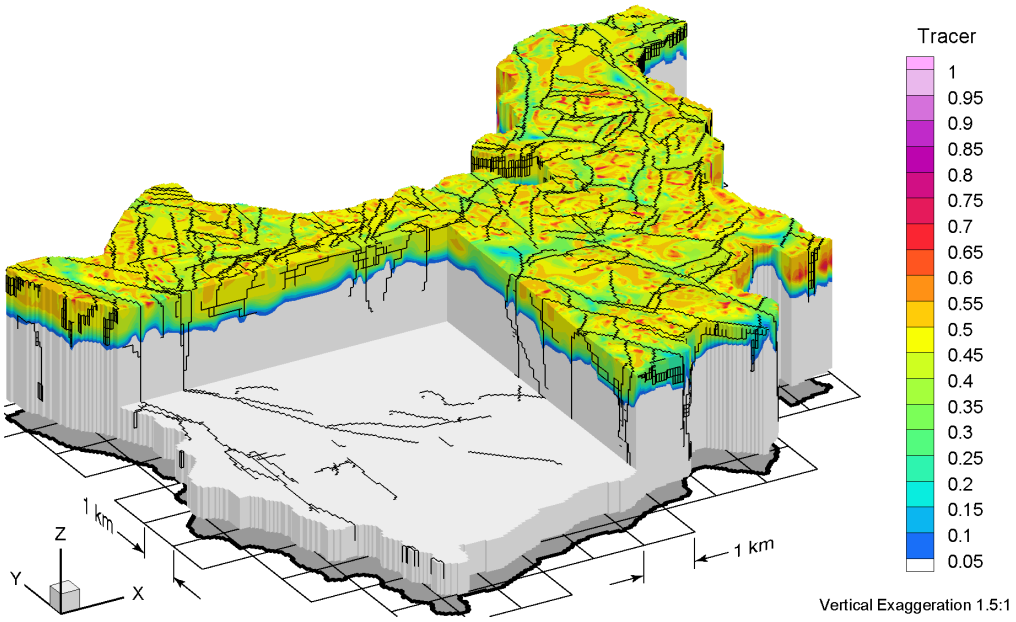

Figure F.31 Block cut view of tracer concentrations at 80 ka before present for the Canadian Shield Sub-Regional Scenario 6 paleoclimate simulation.

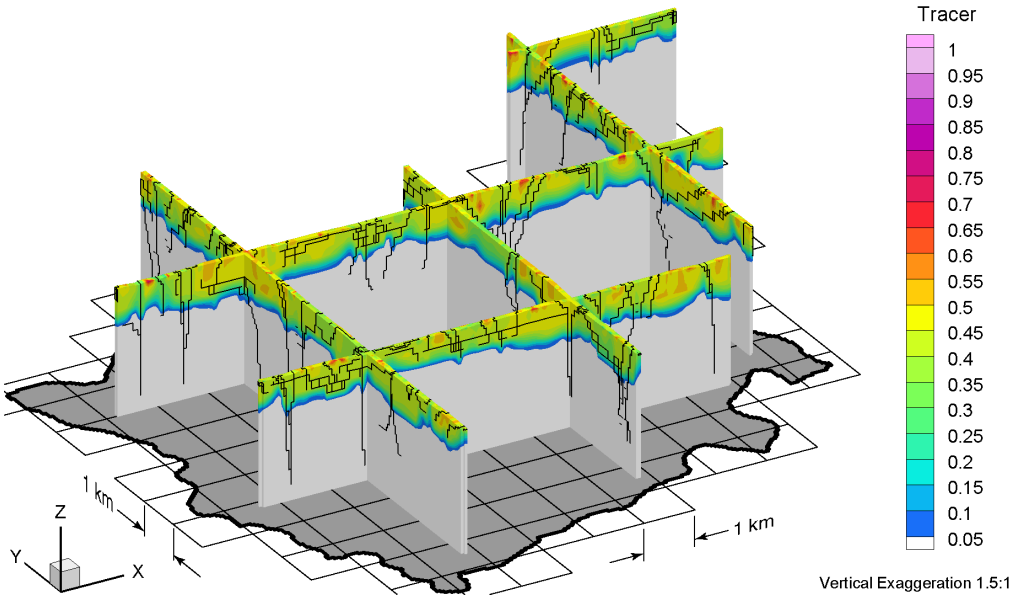

Figure F.32 Fence view of tracer concentrations at 80 ka before present for the Canadian Shield Sub-Regional Scenario 6 paleoclimate simulation.

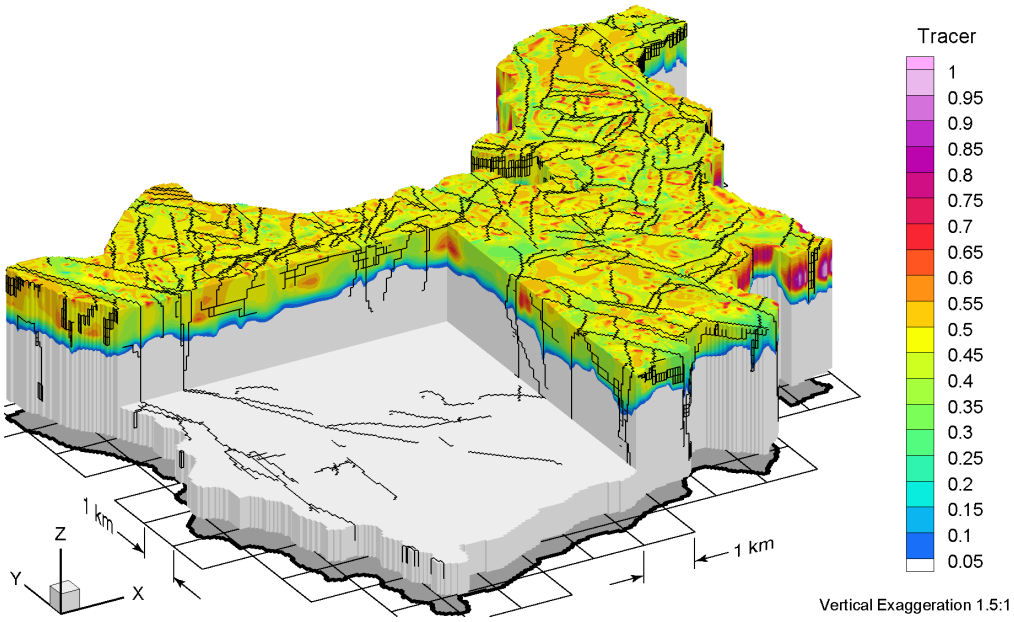

Figure F.33 Block cut view of tracer concentrations at 40 ka before present for the Canadian Shield Sub-Regional Scenario 6 paleoclimate simulation.

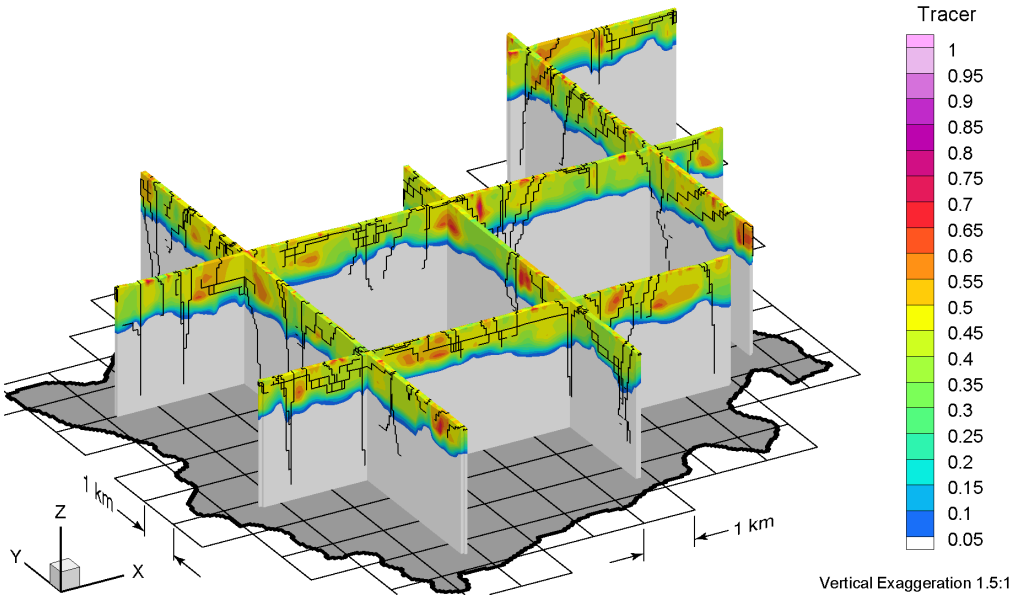

Figure F.34 Fence view of tracer concentrations at 40 ka before present for the Canadian Shield Sub-Regional Scenario 6 paleoclimate simulation.

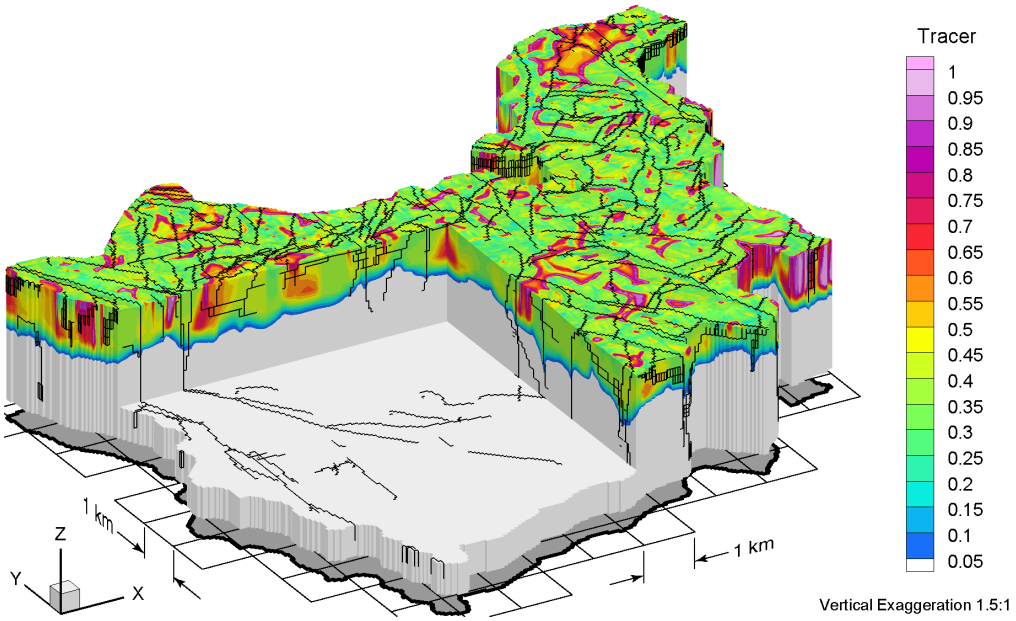

Figure F.35 Block cut view of tracer concentrations at present for the Canadian Shield Sub-Regional Scenario 6 paleoclimate simulation.

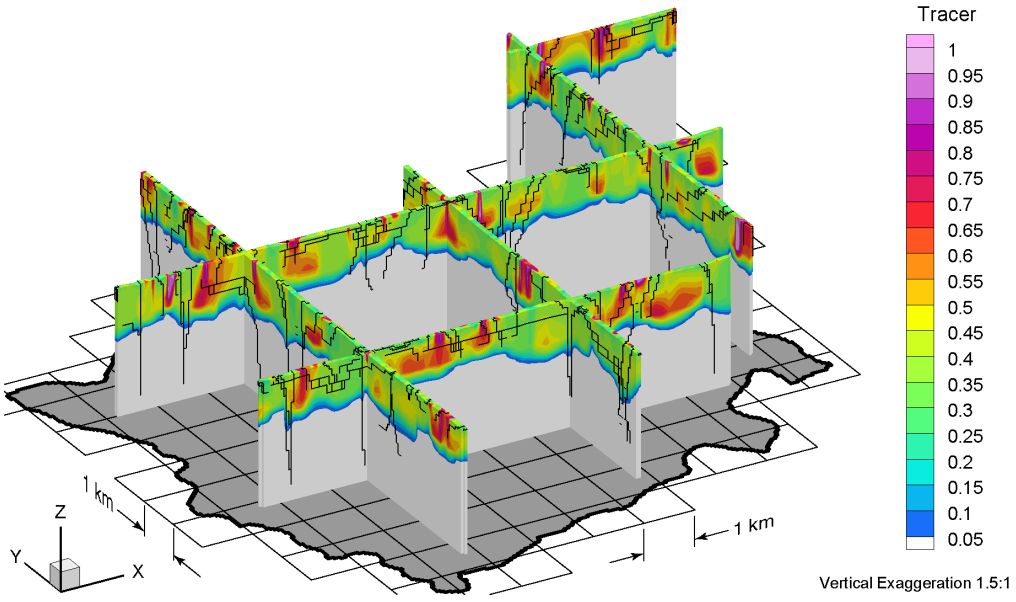

Figure F.36 Fence view of tracer concentrations at present for the Canadian Shield Sub-Regional Scenario 6 paleoclimate simulation.

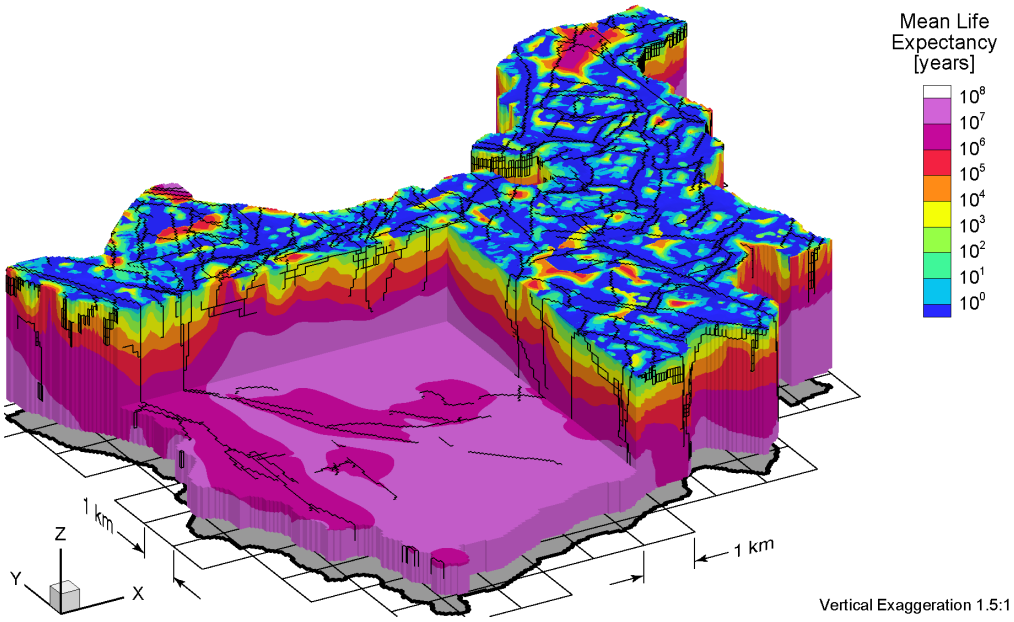

Figure F.37 Block cut view of mean life expectancies at present for the Canadian Shield Sub-Regional Scenario 6 paleoclimate simulation.

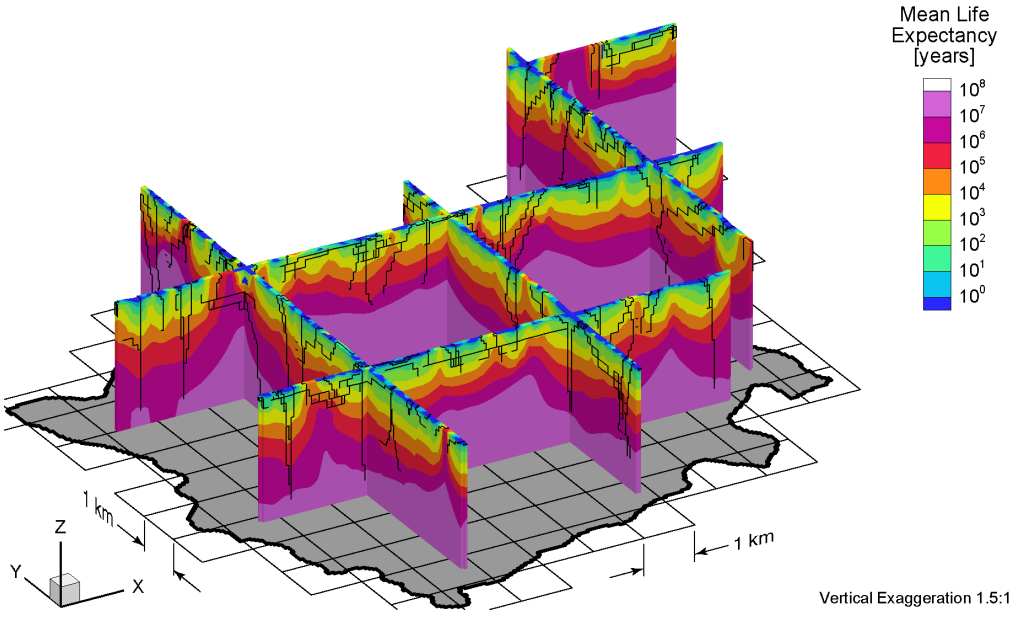

Figure F.38 Fence view of mean life expectancies at present for the Canadian Shield Sub-Regional Scenario 6 paleoclimate simulation.

Appendix G

CSSR Scenario 7 Paleoclimate Model

All figures related to Canadian Shield Sub-Regional (CSSR) Scenario 7 paleoclimate modelling are listed in Table G.1. Block cut view and fence view figures are shown on the same page to facilitate comparison. All results of the 120 ka paleoclimate simulations are shown at times of 80 ka before present, 40 ka before present, and at present.

Table G.1 List of Canadian Shield Sub-Regional Scenario 7 paleoclimate simulation figures.

Parameters	Time Before Present					
	80 ka		40 ka		Present	
	Block Cut	Fence	Block Cut	Fence	Block Cut	Fence
Freshwater Heads	G.1	G.2	G.3	G.4	G.5	G.6
Pore Velocity Magnitudes	G.7	G.8	G.9	G.10	G.11	G.12
Ratio of Vertical Pore Velocities to Pore Velocity Magnitudes	G.13	G.14	G.15	G.16	G.17	G.18
Tracer Concentrations	G.19	G.20	G.21	G.22	G.23	G.24
Mean Life Expectancies	—	—	—	—	G.25	G.26

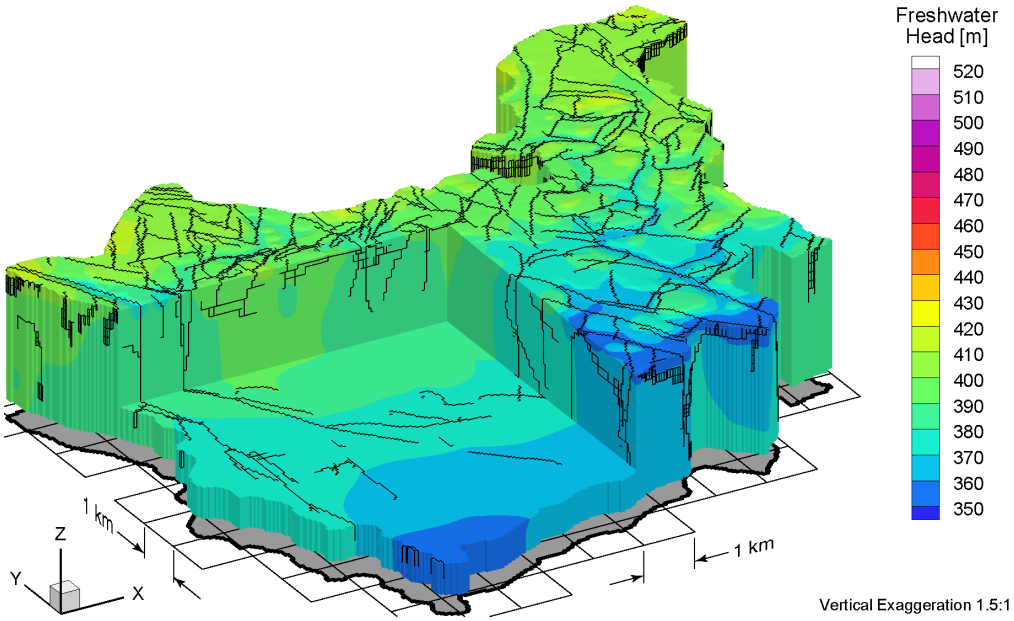

Figure G.1 Block cut view of freshwater heads at 80 ka before present for the Canadian Shield Sub-Regional Scenario 7 paleoclimate simulation.

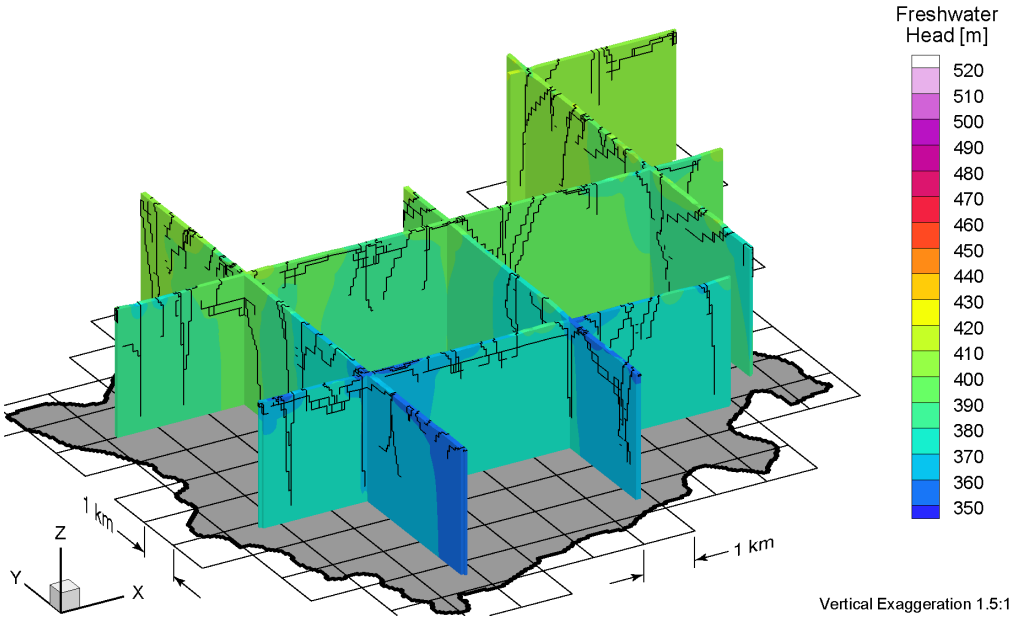

Figure G.2 Fence view of freshwater heads at 80 ka before present for the Canadian Shield Sub-Regional Scenario 7 paleoclimate simulation.

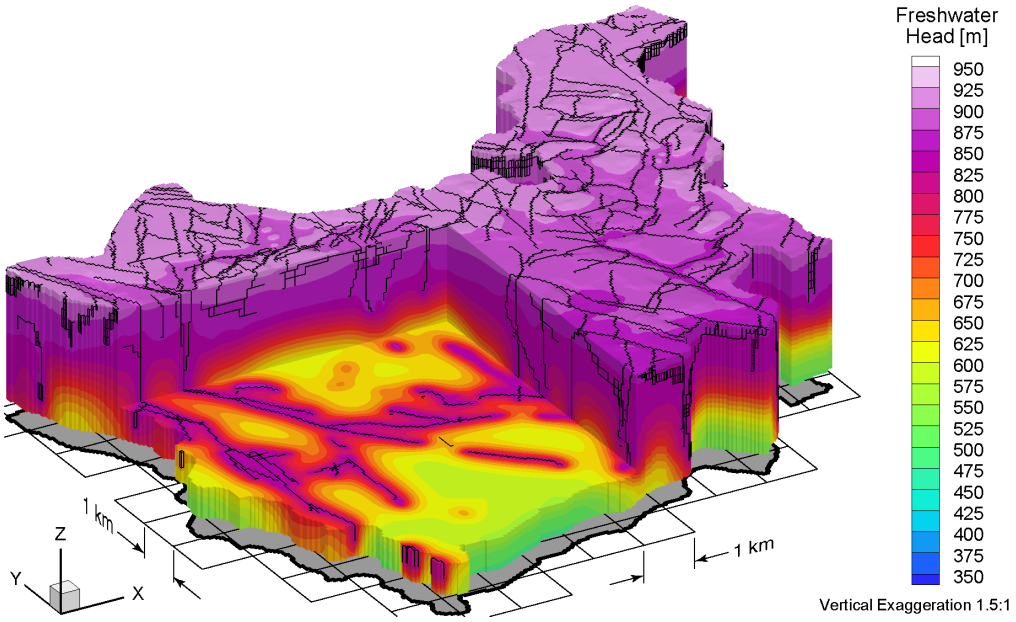

Figure G.3 Block cut view of freshwater heads at 40 ka before present for the Canadian Shield Sub-Regional Scenario 7 paleoclimate simulation.

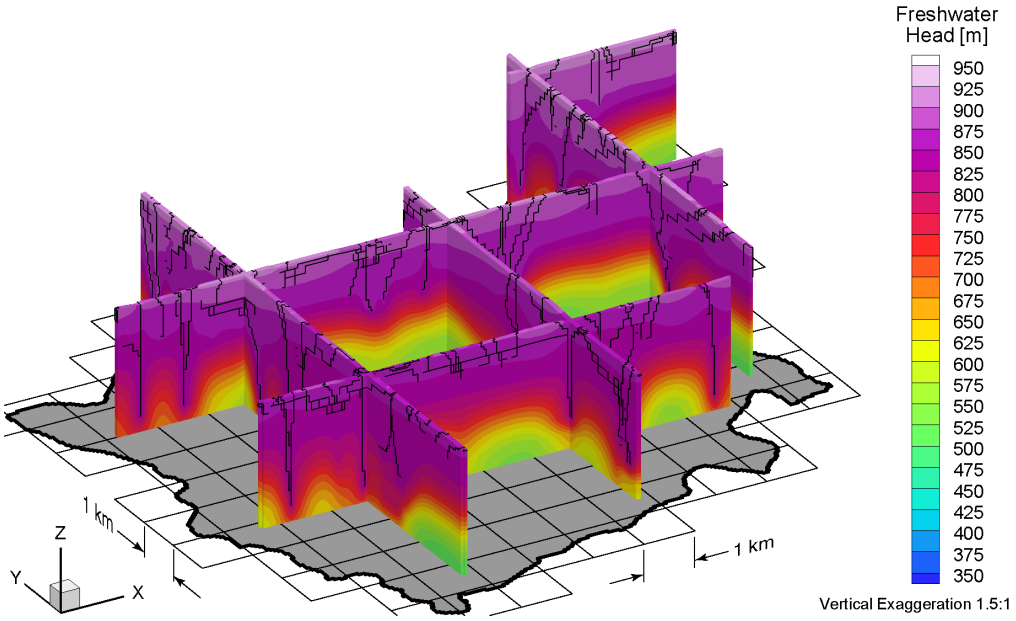

Figure G.4 Fence view of freshwater heads at 40 ka before present for the Canadian Shield Sub-Regional Scenario 7 paleoclimate simulation.

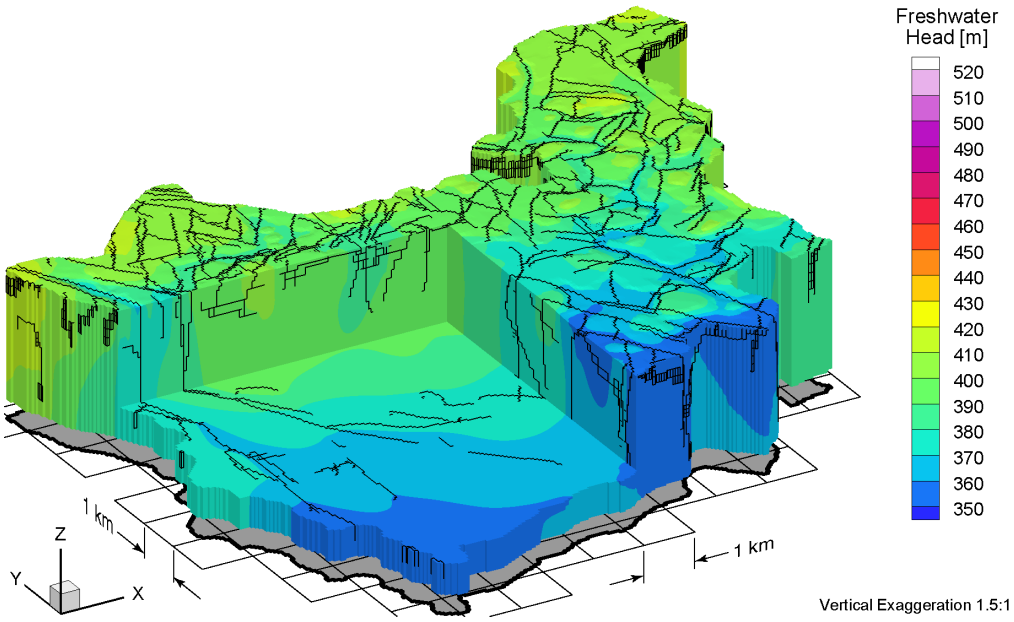

Figure G.5 Block cut view of freshwater heads at present for the Canadian Shield Sub-Regional Scenario 7 paleoclimate simulation.

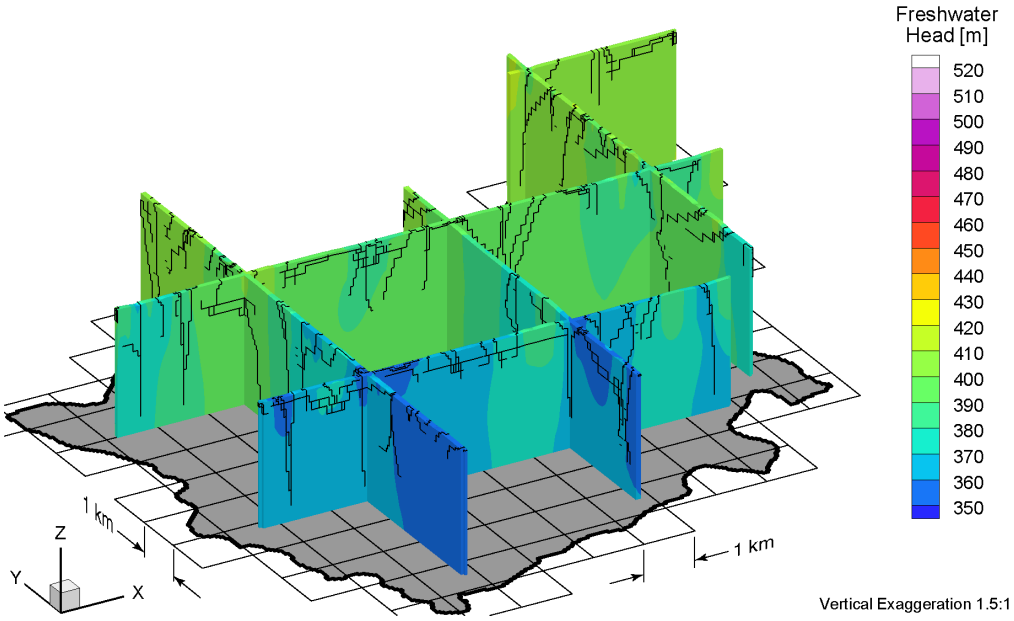

Figure G.6 Fence view of freshwater heads at present for the Canadian Shield Sub-Regional Scenario 7 paleoclimate simulation.

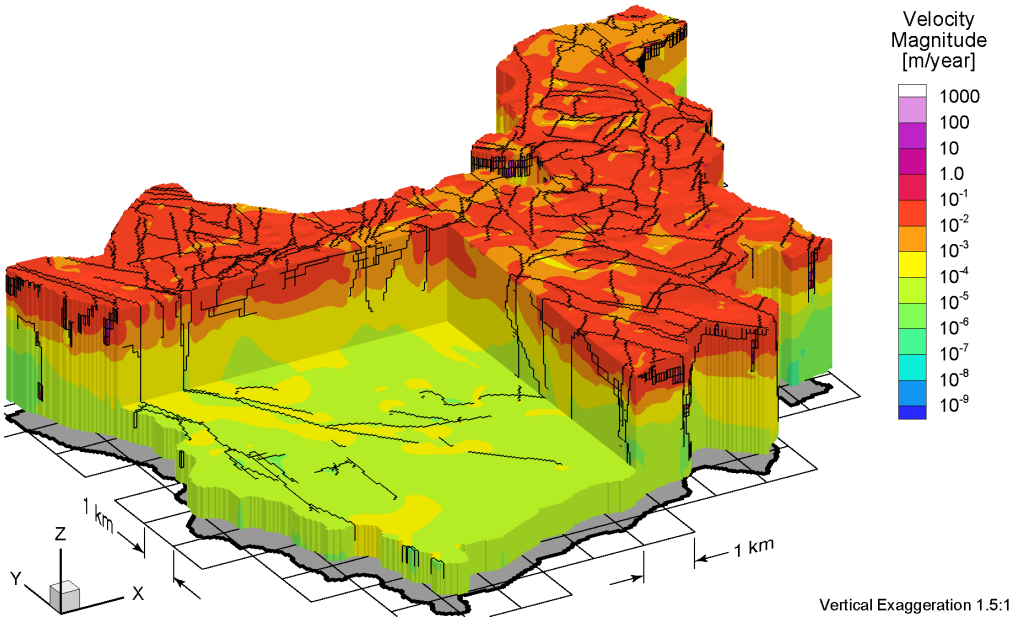

Figure G.7 Block cut view of pore velocity magnitudes at 80 ka before present for the Canadian Shield Sub-Regional Scenario 7 paleoclimate simulation.

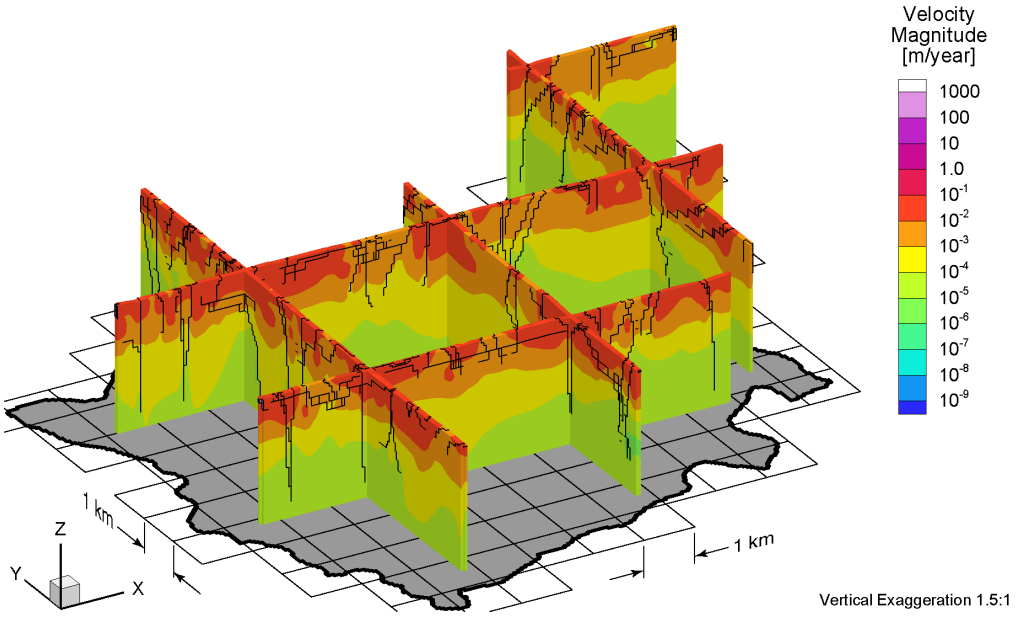

Figure G.8 Fence view of pore velocity magnitudes at 80 ka before present for the Canadian Shield Sub-Regional Scenario 7 paleoclimate simulation.

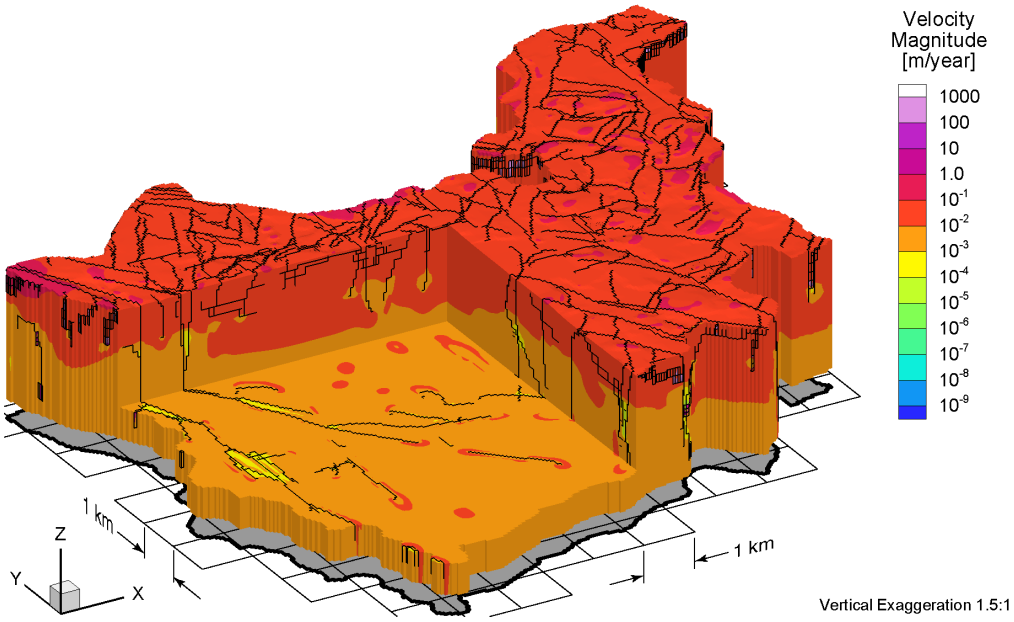

Figure G.9 Block cut view of pore velocity magnitudes at 40 ka before present for the Canadian Shield Sub-Regional Scenario 7 paleoclimate simulation.

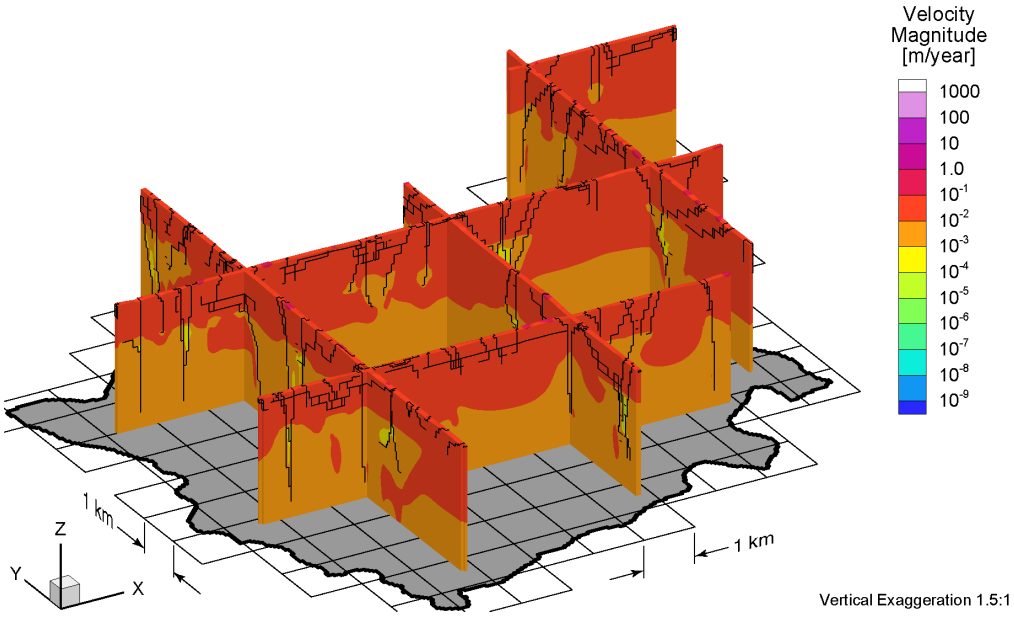

Figure G.10 Fence view of pore velocity magnitudes at 40 ka before present for the Canadian Shield Sub-Regional Scenario 7 paleoclimate simulation.

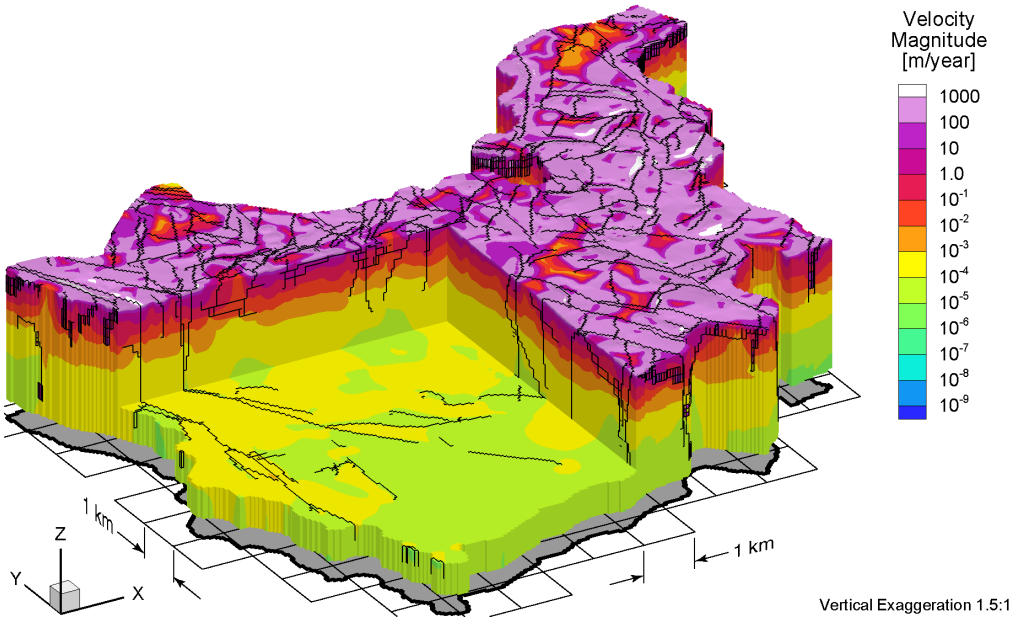

Figure G.11 Block cut view of pore velocity magnitudes at present for the Canadian Shield Sub-Regional Scenario 7 paleoclimate simulation.

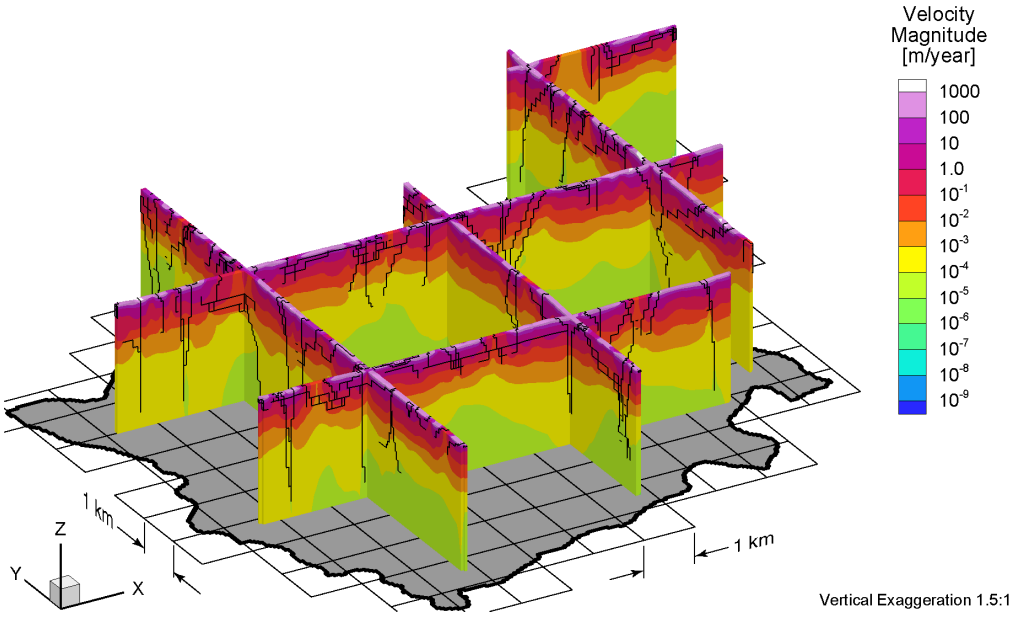

Figure G.12 Fence view of pore velocity magnitudes at present for the Canadian Shield Sub-Regional Scenario 7 paleoclimate simulation.

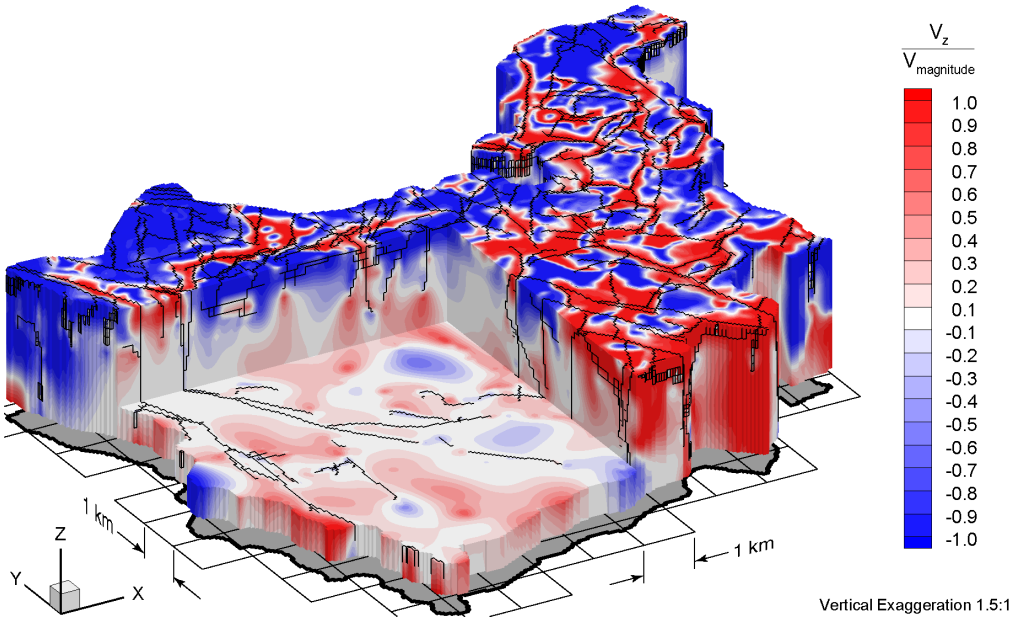

Figure G.13 Block cut view of ratio of vertical pore velocities to pore velocity magnitudes at 80 ka before present for the Canadian Shield Sub-Regional Scenario 7 paleoclimate simulation.

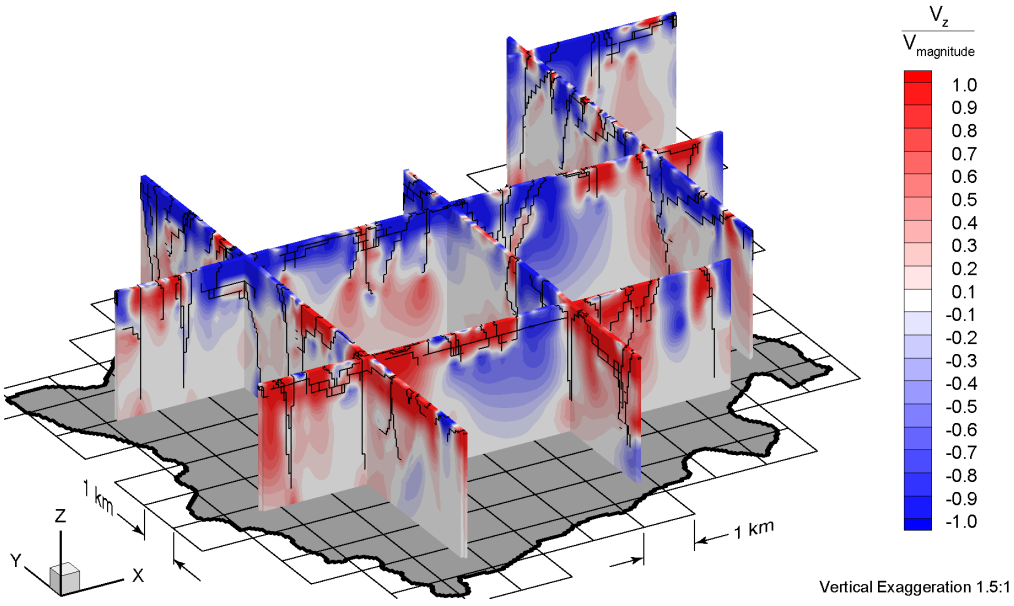

Figure G.14 Fence view of ratio of vertical pore velocities to pore velocity magnitudes at 80 ka before present for the Canadian Shield Sub-Regional Scenario 7 paleoclimate simulation.

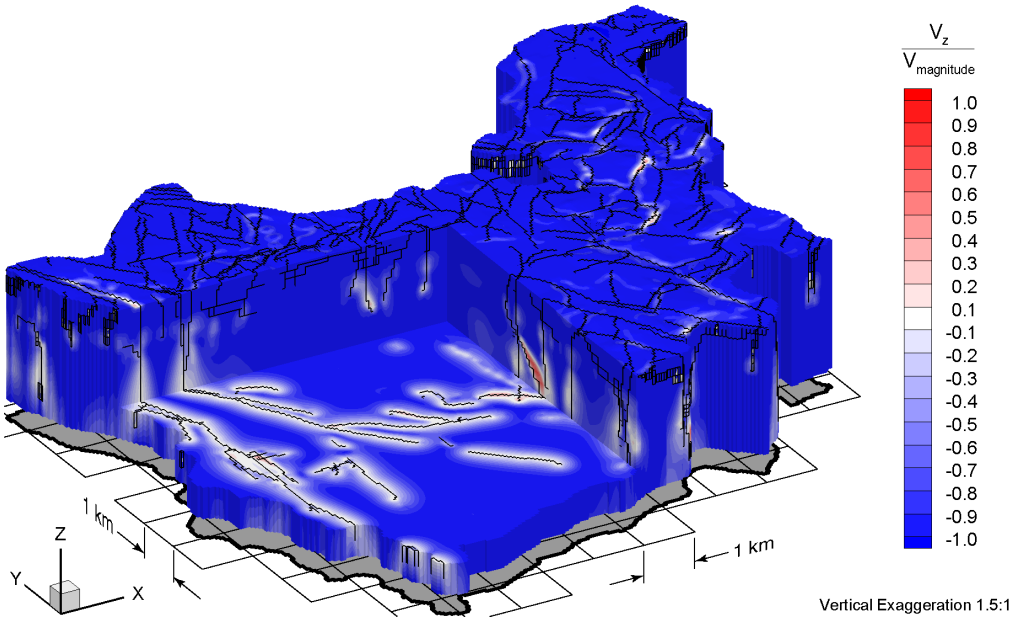

Figure G.15 Block cut view of ratio of vertical pore velocities to pore velocity magnitudes at 40 ka before present for the Canadian Shield Sub-Regional Scenario 7 paleoclimate simulation.

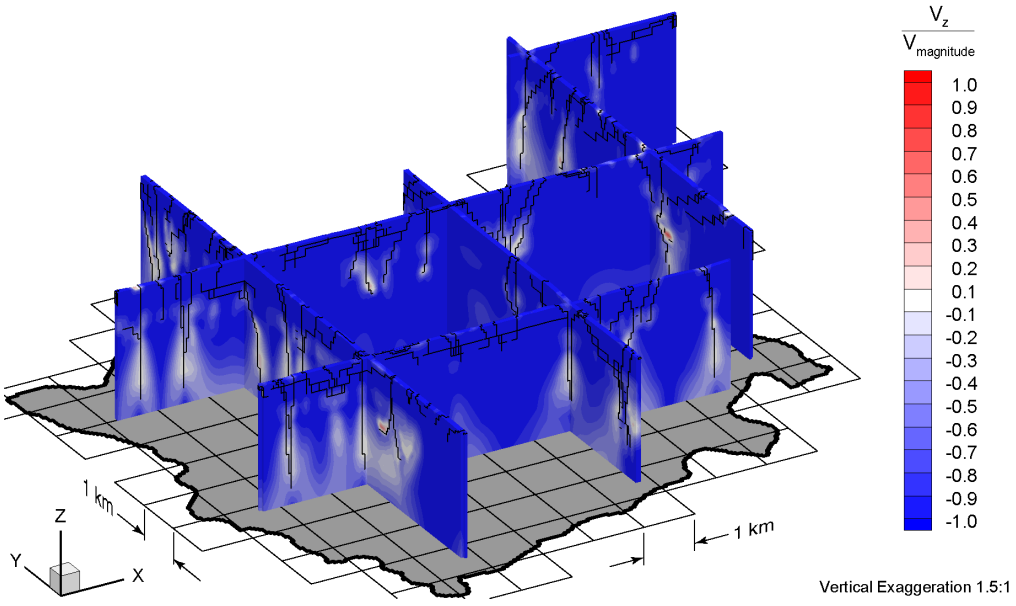

Figure G.16 Fence view of ratio of vertical pore velocities to pore velocity magnitudes at 40 ka before present for the Canadian Shield Sub-Regional Scenario 7 paleoclimate simulation.

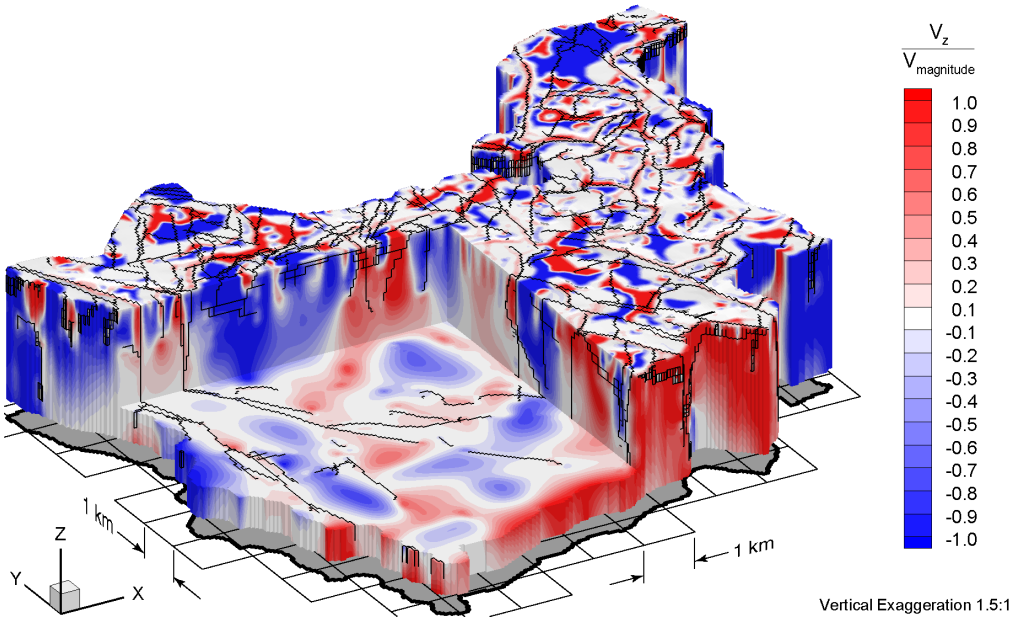

Figure G.17 Block cut view of ratio of vertical pore velocities to pore velocity magnitudes at present for the Canadian Shield Sub-Regional Scenario 7 paleoclimate simulation.

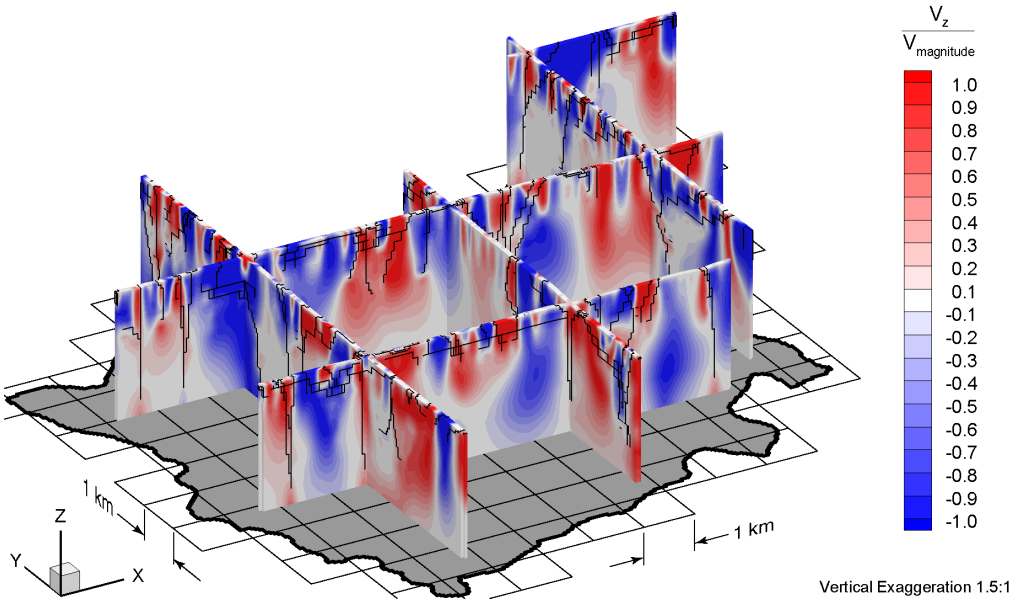

Figure G.18 Fence view of ratio of vertical pore velocities to pore velocity magnitudes at present for the Canadian Shield Sub-Regional Scenario 7 paleoclimate simulation.

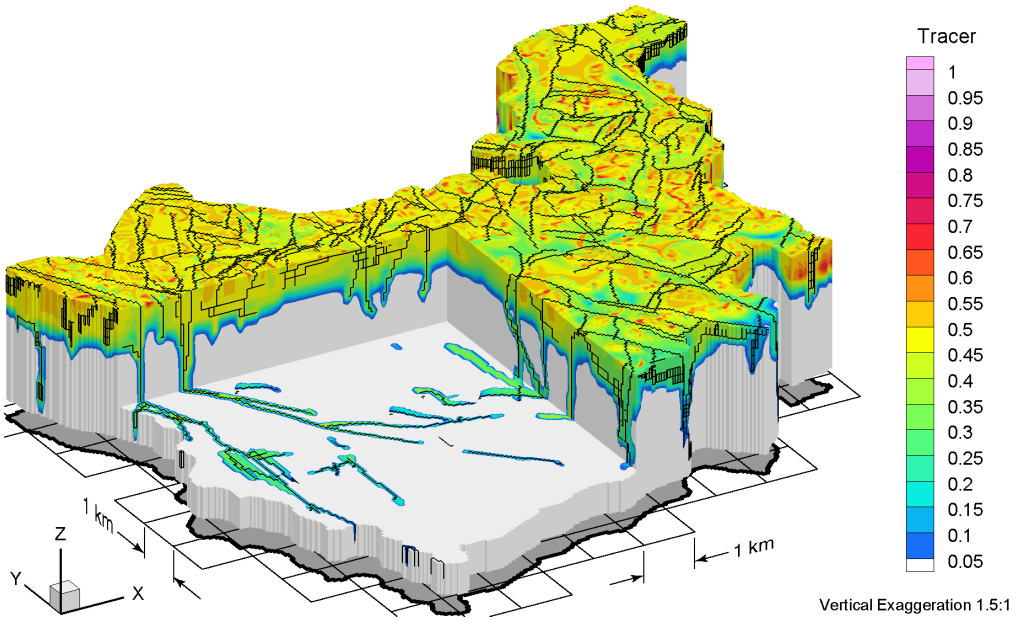

Figure G.19 Block cut view of tracer concentrations at 80 ka before present for the Canadian Shield Sub-Regional Scenario 7 paleoclimate simulation.

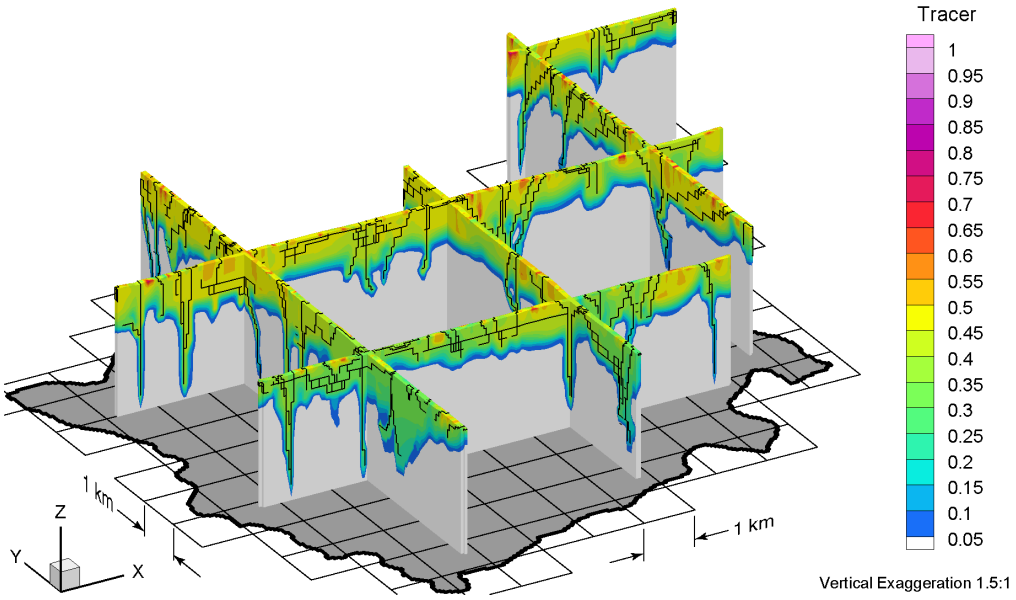

Figure G.20 Fence view of tracer concentrations at 80 ka before present for the Canadian Shield Sub-Regional Scenario 7 paleoclimate simulation.

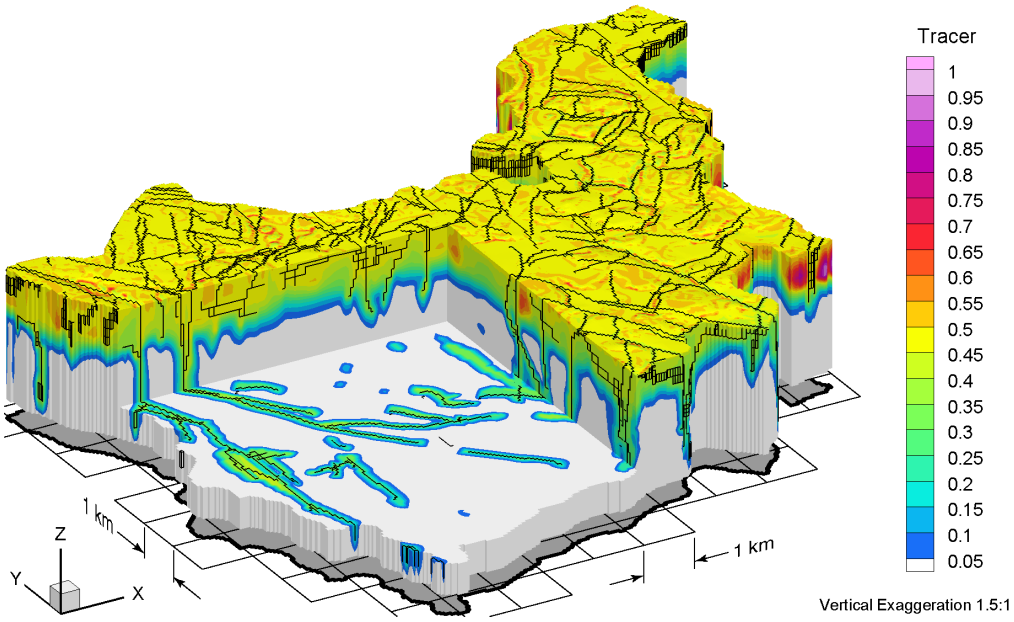

Figure G.21 Block cut view of tracer concentrations at 40 ka before present for the Canadian Shield Sub-Regional Scenario 7 paleoclimate simulation.

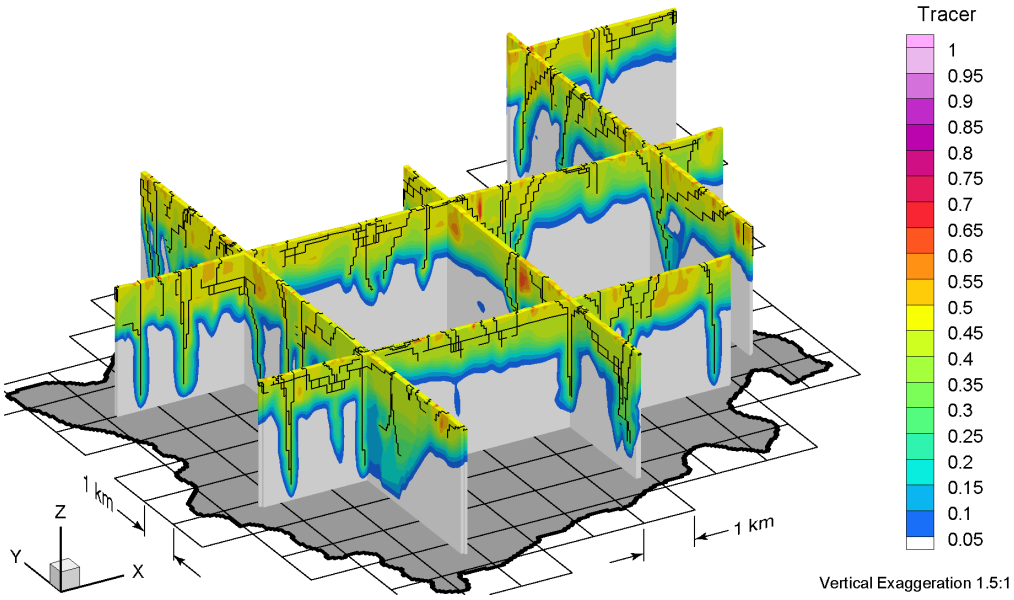

Figure G.22 Fence view of tracer concentrations at 40 ka before present for the Canadian Shield Sub-Regional Scenario 7 paleoclimate simulation.

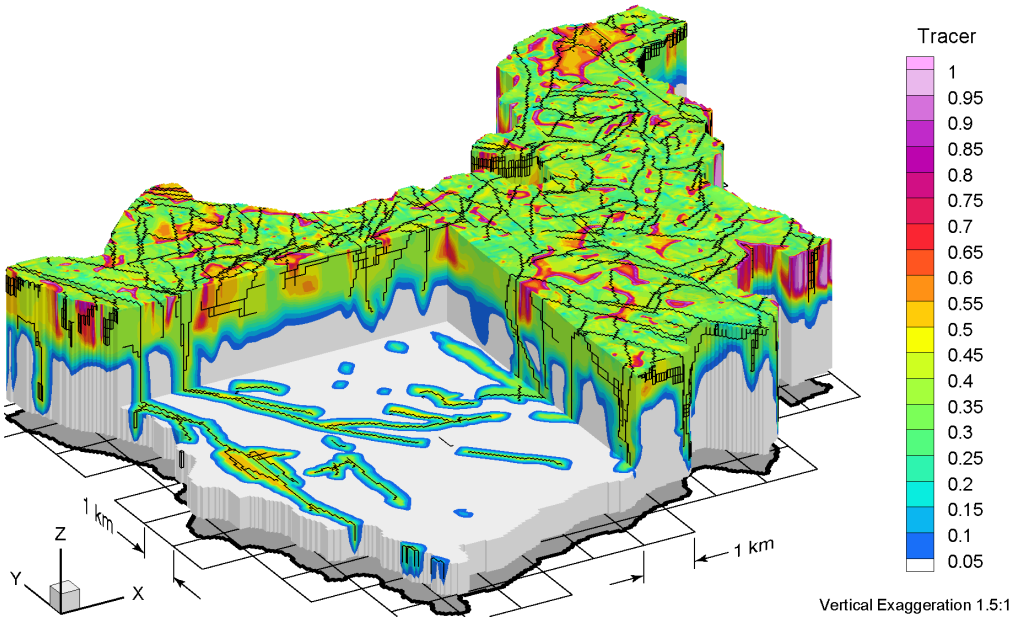

Figure G.23 Block cut view of tracer concentrations at present for the Canadian Shield Sub-Regional Scenario 7 paleoclimate simulation.

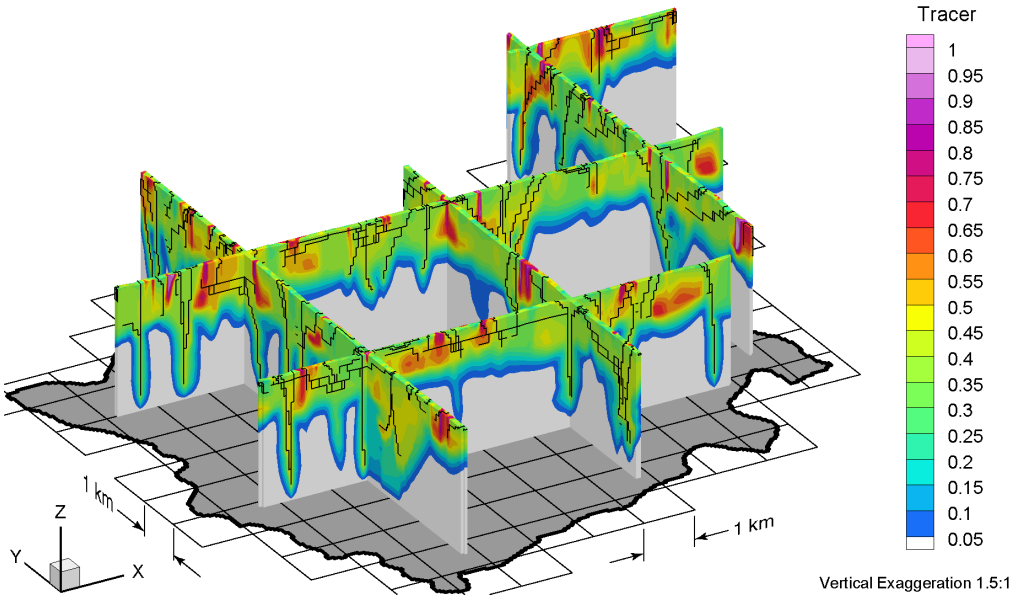

Figure G.24 Fence view of tracer concentrations at present for the Canadian Shield Sub-Regional Scenario 7 paleoclimate simulation.

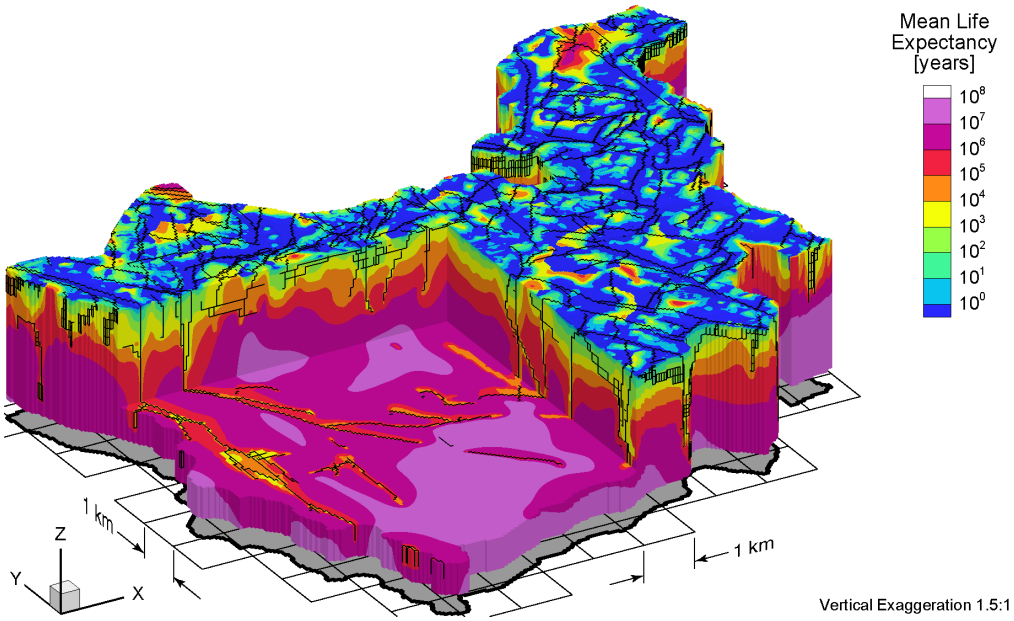

Figure G.25 Block cut view of mean life expectancies at present for the Canadian Shield Sub-Regional Scenario 7 paleoclimate simulation.

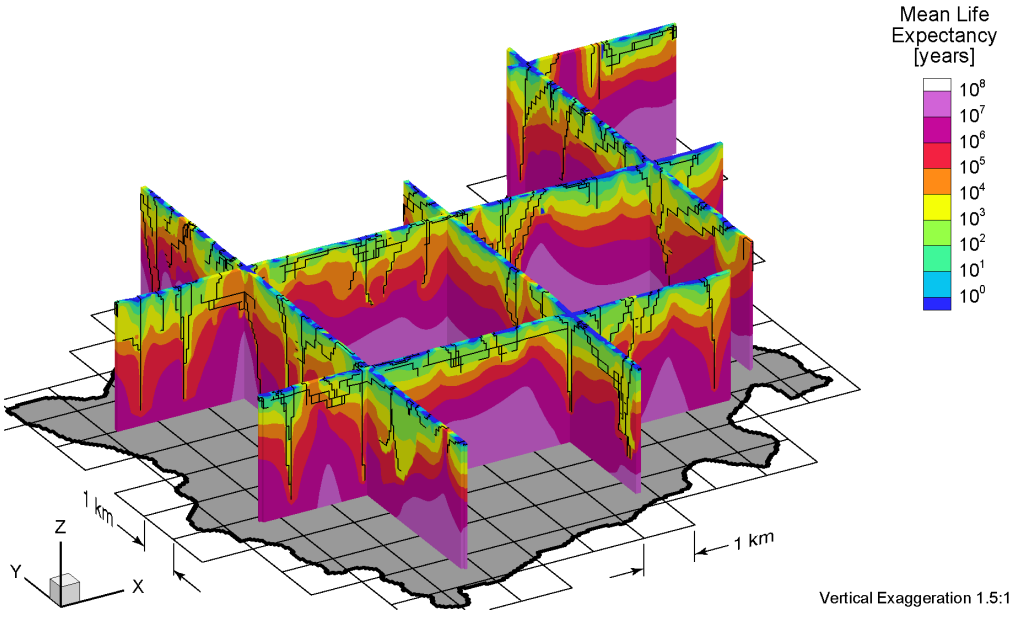

Figure G.26 Fence view of mean life expectancies at present for the Canadian Shield Sub-Regional Scenario 7 paleoclimate simulation.

Appendix H

MBR Scenario 1 Paleoclimate Model

All figures related to the Michigan Basin Regional (MBR) Scenario 1 paleoclimate modelling are listed in Table H.1. Block cut view and fence view figures are shown on the same page to facilitate comparison. All results of the 120 ka paleoclimate simulations are shown at times of 80 ka before present, 40 ka before present, and at present.

Table H.1 List of Michigan Basin Regional Scenario 1 paleoclimate simulation figures.

Parameters	Time Before Present					
	80 ka		40 ka		Present	
	Block Cut	Fence	Block Cut	Fence	Block Cut	Fence
Freshwater Heads	H.1	H.2	H.3	H.4	H.5	H.6
Environmental Heads	H.7	H.8	H.9	H.10	H.11	H.12
Pore Velocity Magnitudes	H.13	H.14	H.15	H.16	H.17	H.18
Ratio of Vertical Pore Velocities to Pore Velocity Magnitudes	H.19	H.20	H.21	H.22	H.23	H.24
Brine Concentrations	H.25	H.26	H.27	H.28	H.29	H.30
Tracer Concentrations	H.31	H.32	H.33	H.34	H.35	H.36
Mean Life Expectancies	—	—	—	—	H.37	H.38

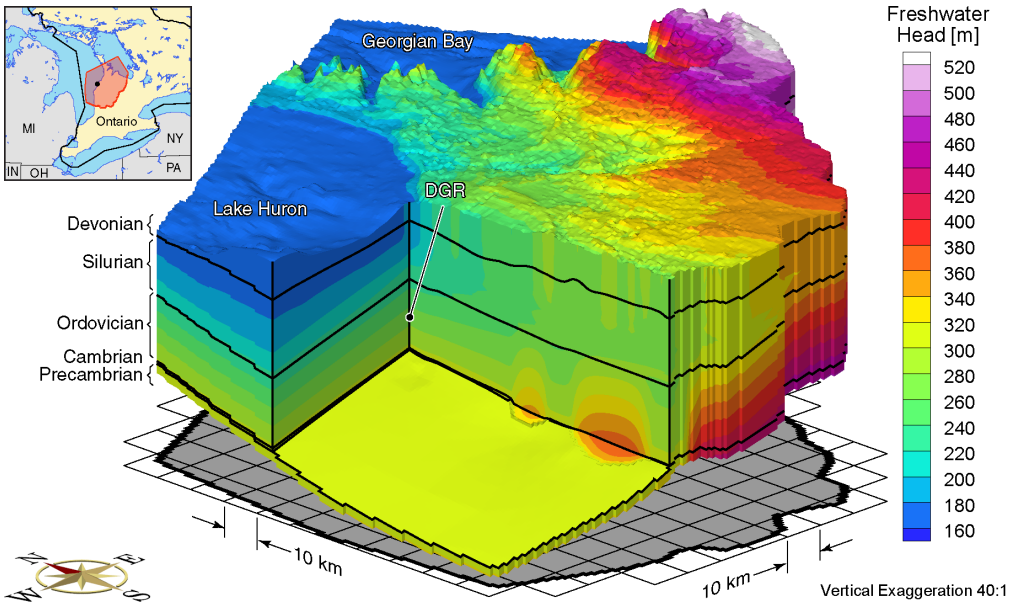

Figure H.1 Block cut view of freshwater heads at 80 ka before present for the Michigan Basin Regional Scenario 1 paleoclimate simulation.

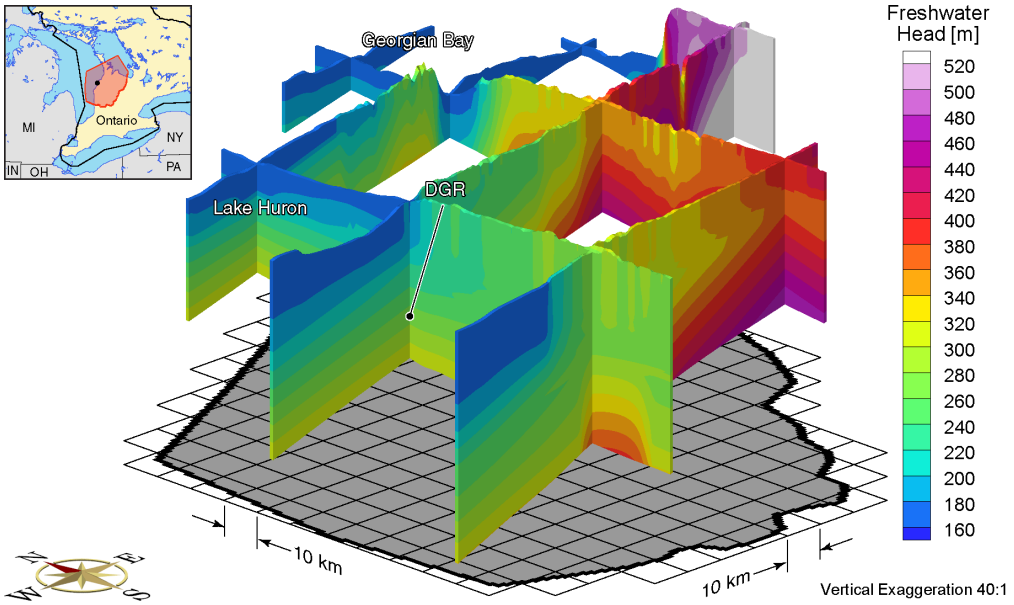

Figure H.2 Fence view of freshwater heads at 80 ka before present for the Michigan Basin Regional Scenario 1 paleoclimate simulation.

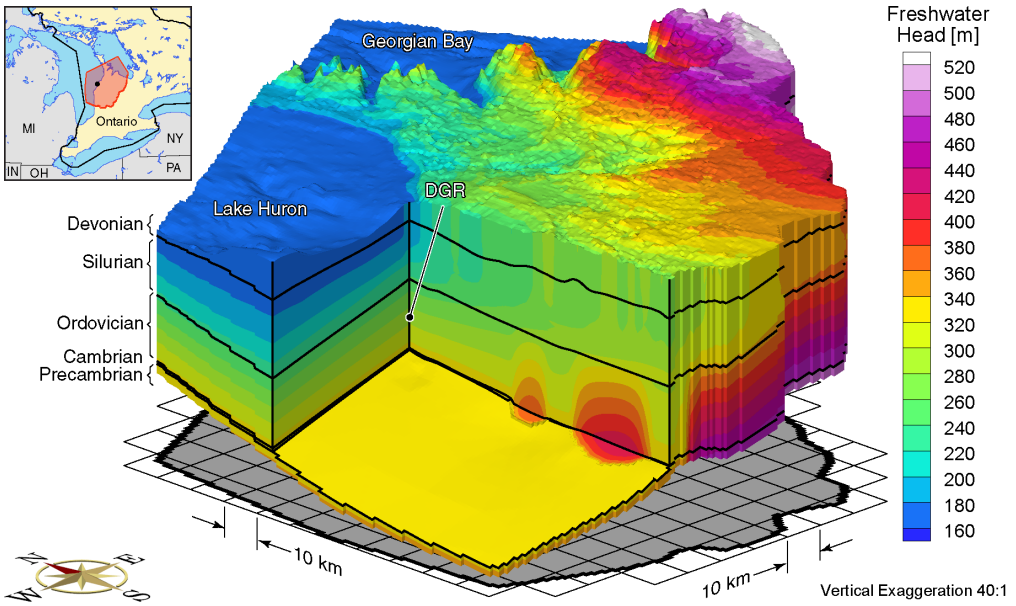

Figure H.3 Block cut view of freshwater heads at 40 ka before present for the Michigan Basin Regional Scenario 1 paleoclimate simulation.

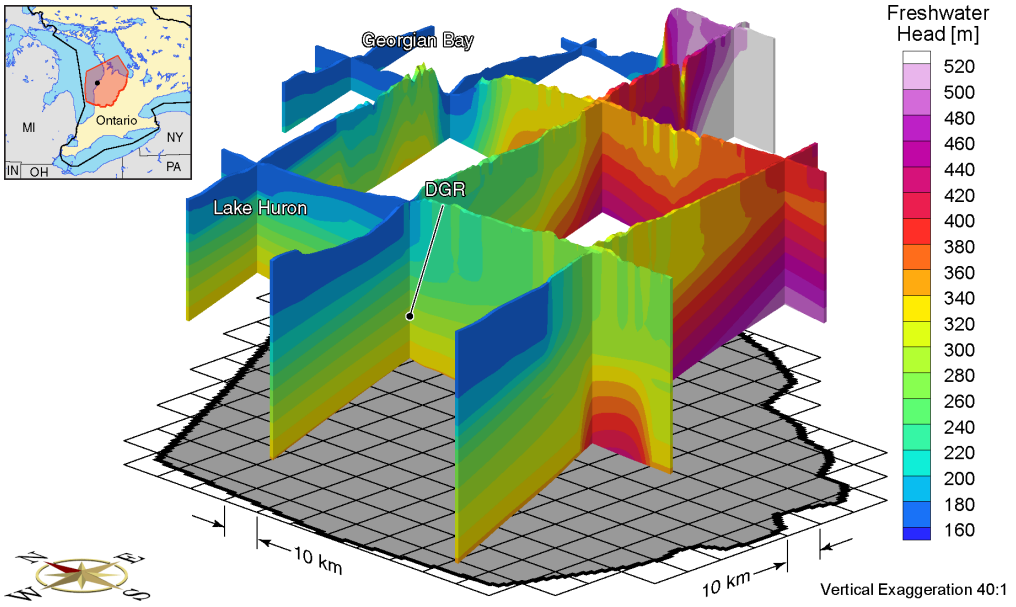

Figure H.4 Fence view of freshwater heads at 40 ka before present for the Michigan Basin Regional Scenario 1 paleoclimate simulation.

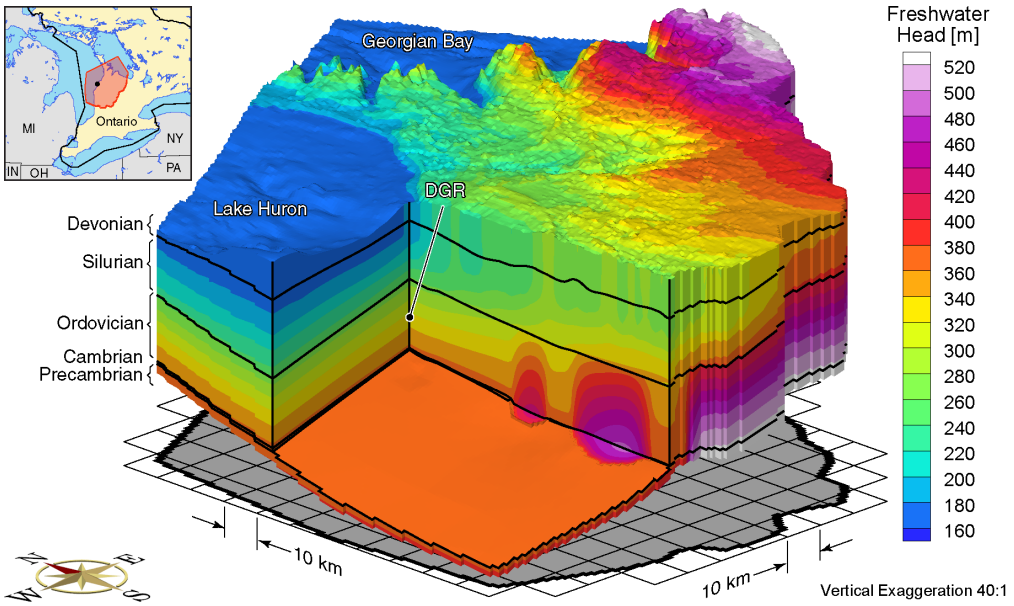

Figure H.5 Block cut view of freshwater heads at present for the Michigan Basin Regional Scenario 1 paleoclimate simulation.

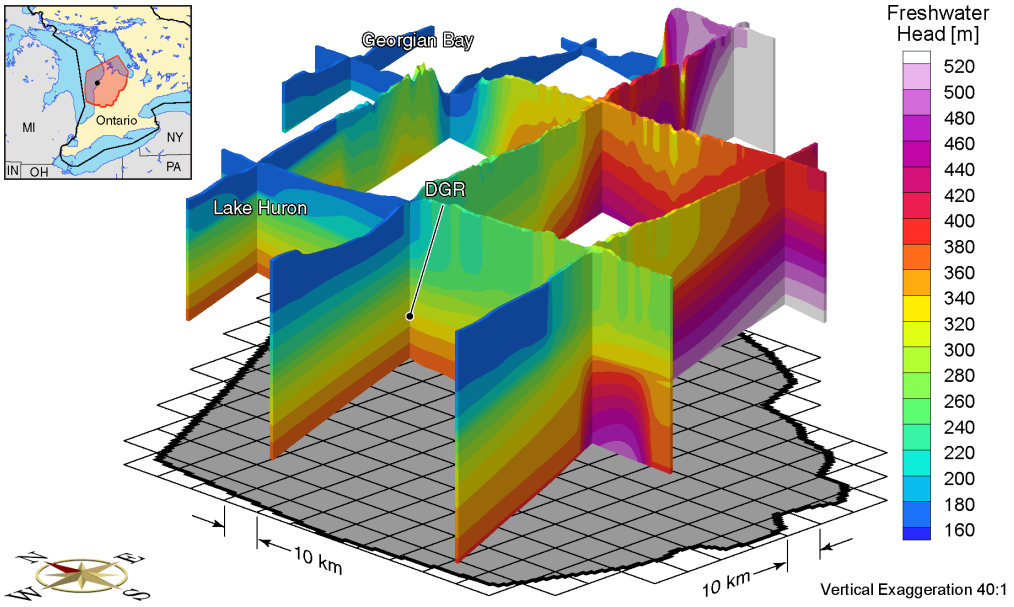

Figure H.6 Fence view of freshwater heads at present for the Michigan Basin Regional Scenario 1 paleoclimate simulation.

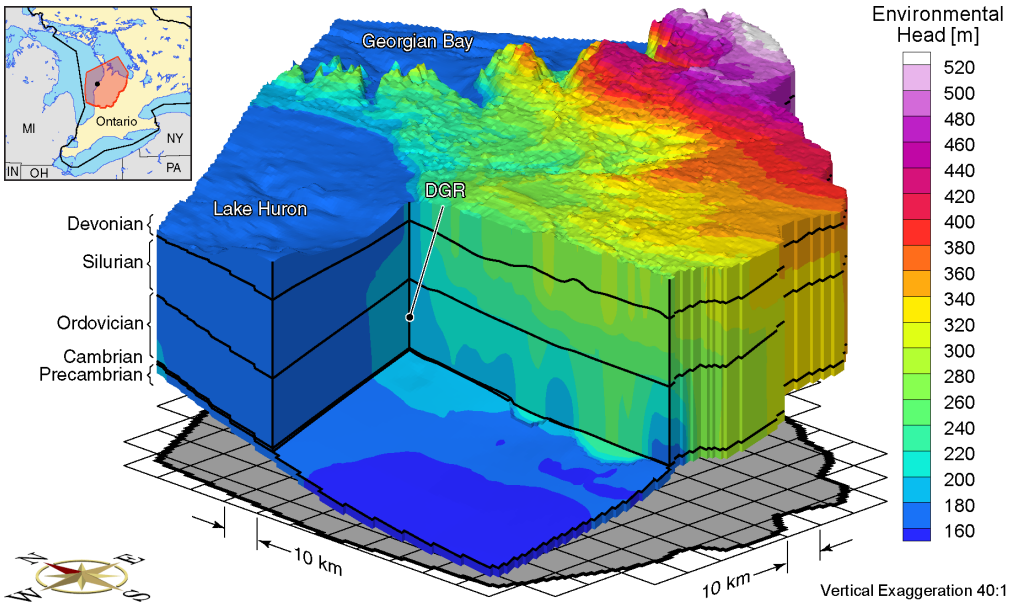

Figure H.7 Block cut view of environmental heads at 80 ka before present for the Michigan Basin Regional Scenario 1 paleoclimate simulation.

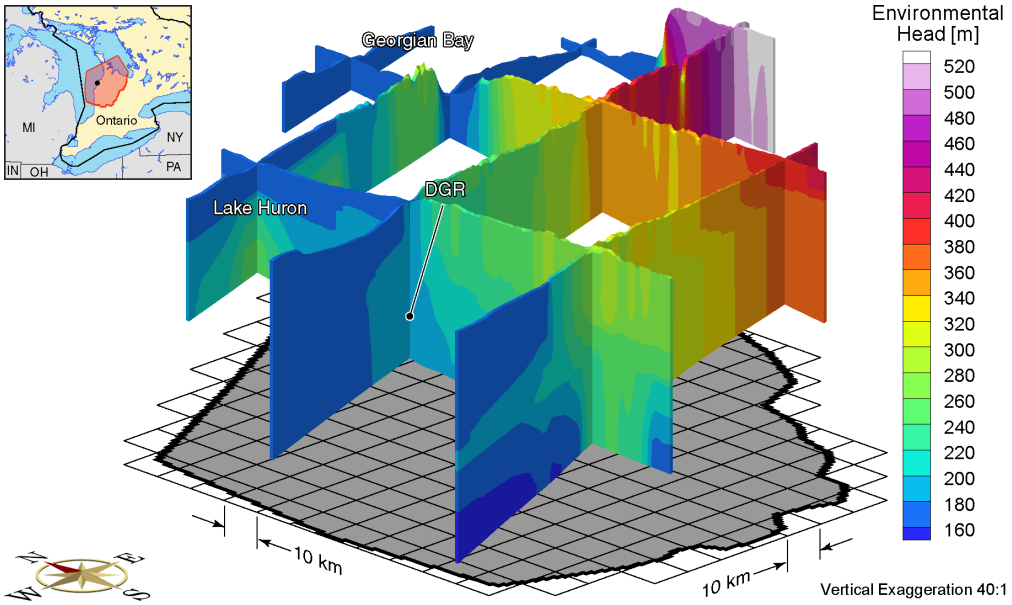

Figure H.8 Fence view of environmental heads at 80 ka before present for the Michigan Basin Regional Scenario 1 paleoclimate simulation.

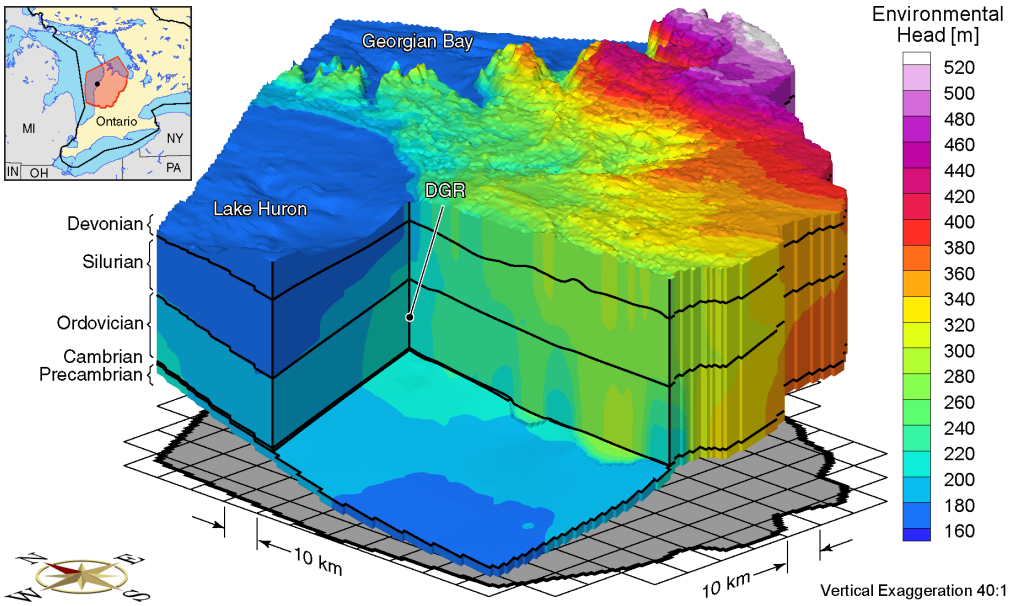

Figure H.9 Block cut view of environmental heads at 40 ka before present for the Michigan Basin Regional Scenario 1 paleoclimate simulation.

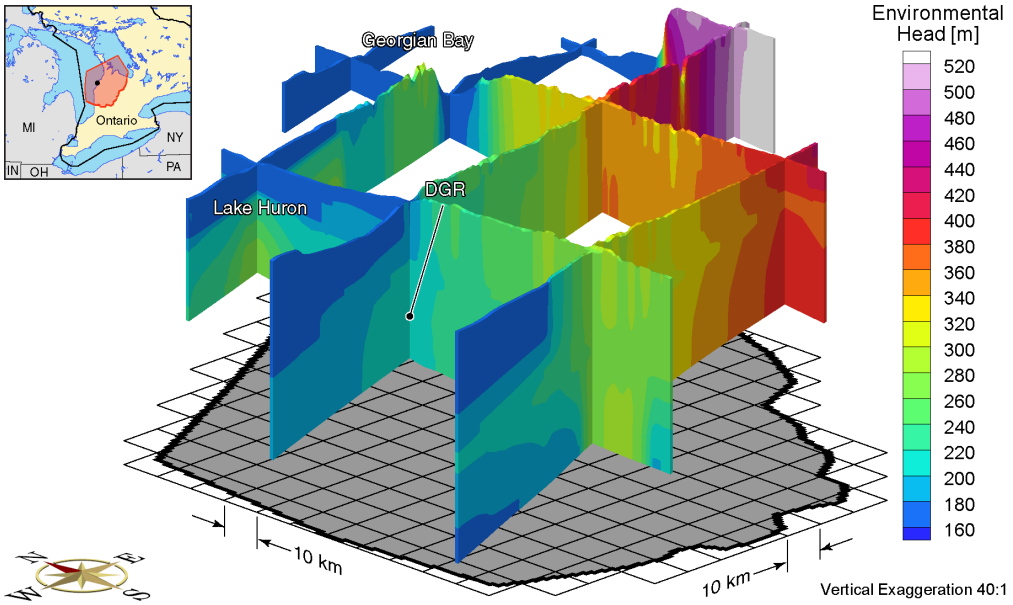

Figure H.10 Fence view of environmental heads at 40 ka before present for the Michigan Basin Regional Scenario 1 paleoclimate simulation.

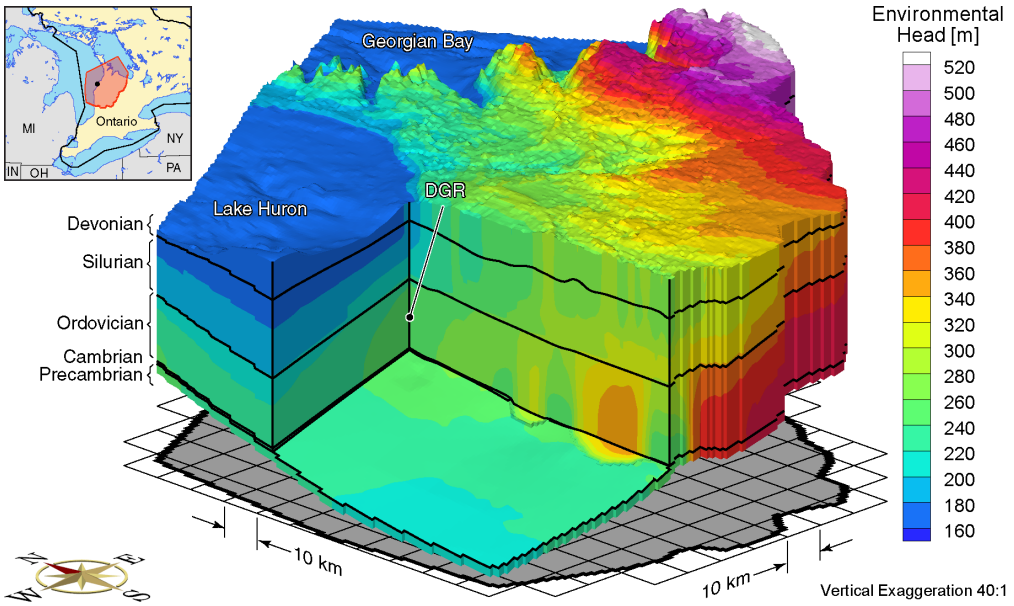

Figure H.11 Block cut view of environmental heads at present for the Michigan Basin Regional Scenario 1 paleoclimate simulation.

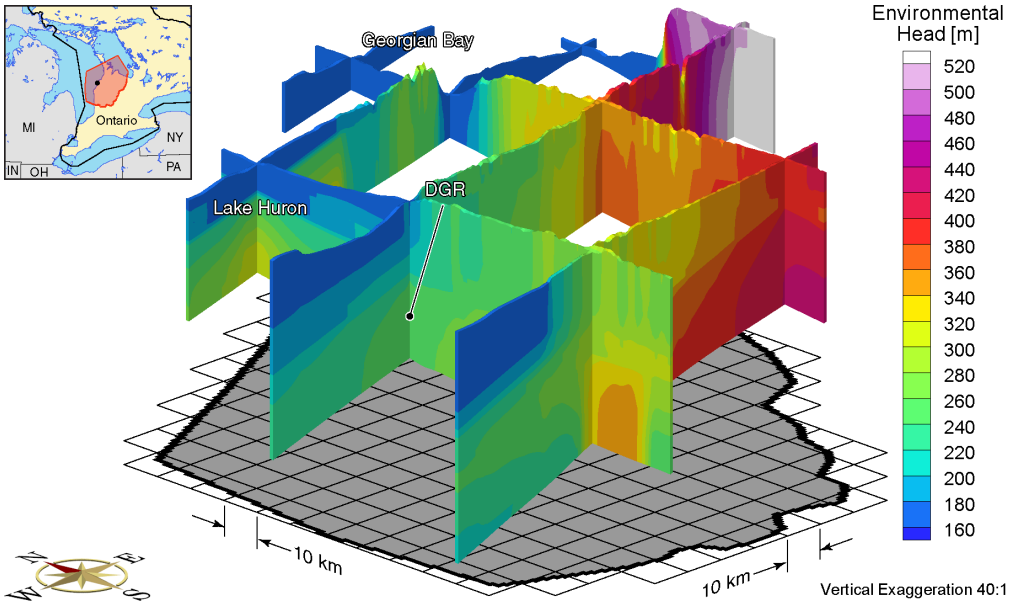

Figure H.12 Fence view of environmental heads at present for the Michigan Basin Regional Scenario 1 paleoclimate simulation.

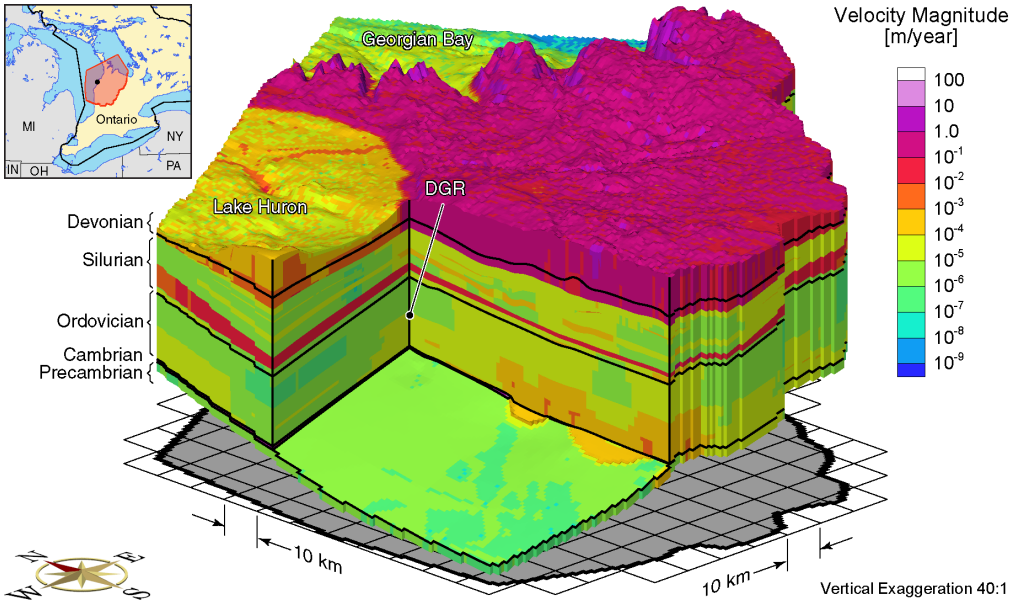

Figure H.13 Block cut view of pore velocity magnitudes at 80 ka before present for the Michigan Basin Regional Scenario 1 paleoclimate simulation.

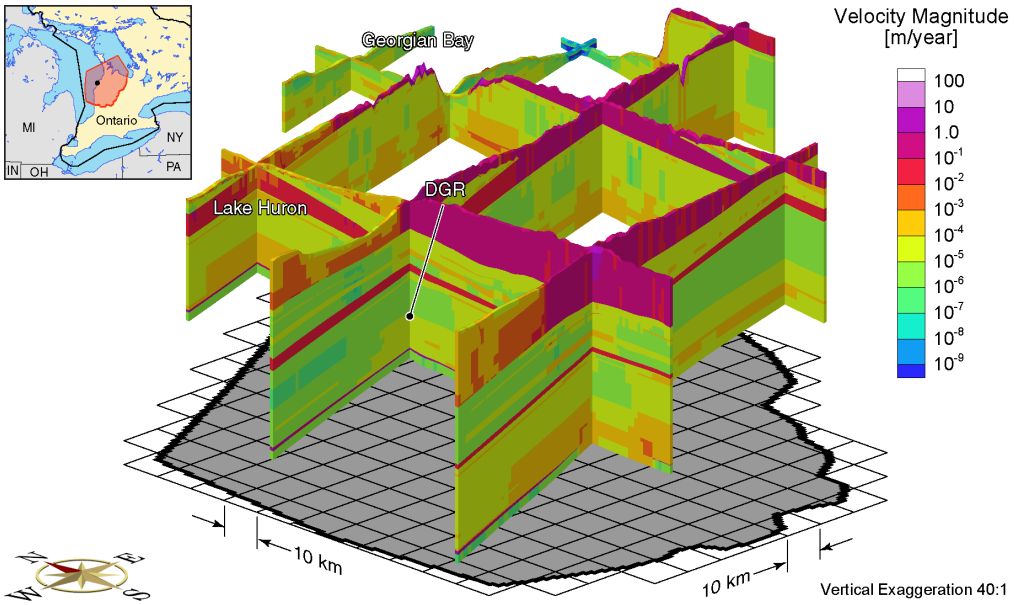

Figure H.14 Fence view of pore velocity magnitudes at 80 ka before present for the Michigan Basin Regional Scenario 1 paleoclimate simulation.

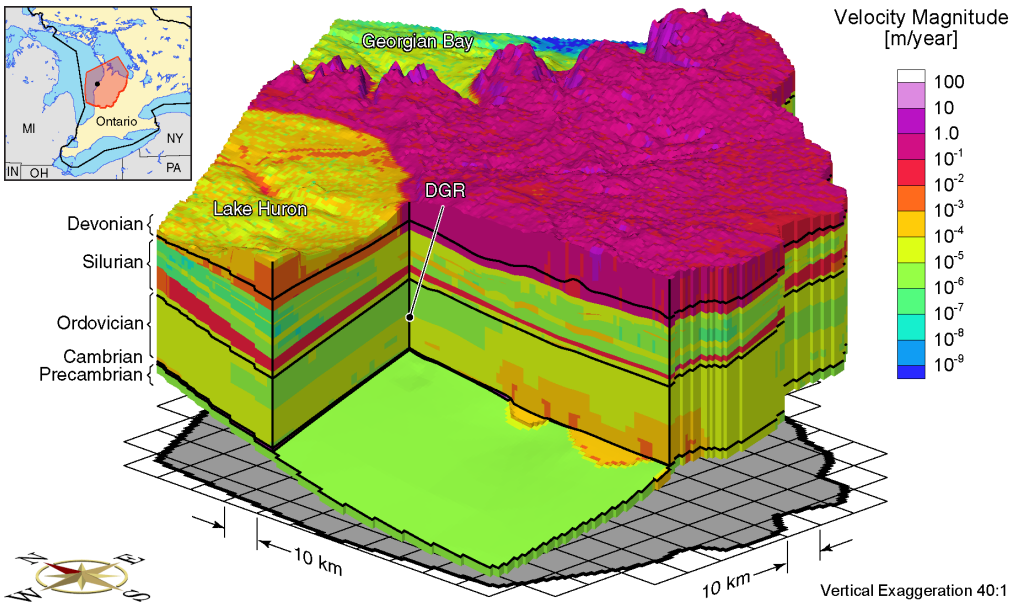

Figure H.15 Block cut view of pore velocity magnitudes at 40 ka before present for the Michigan Basin Regional Scenario 1 paleoclimate simulation.

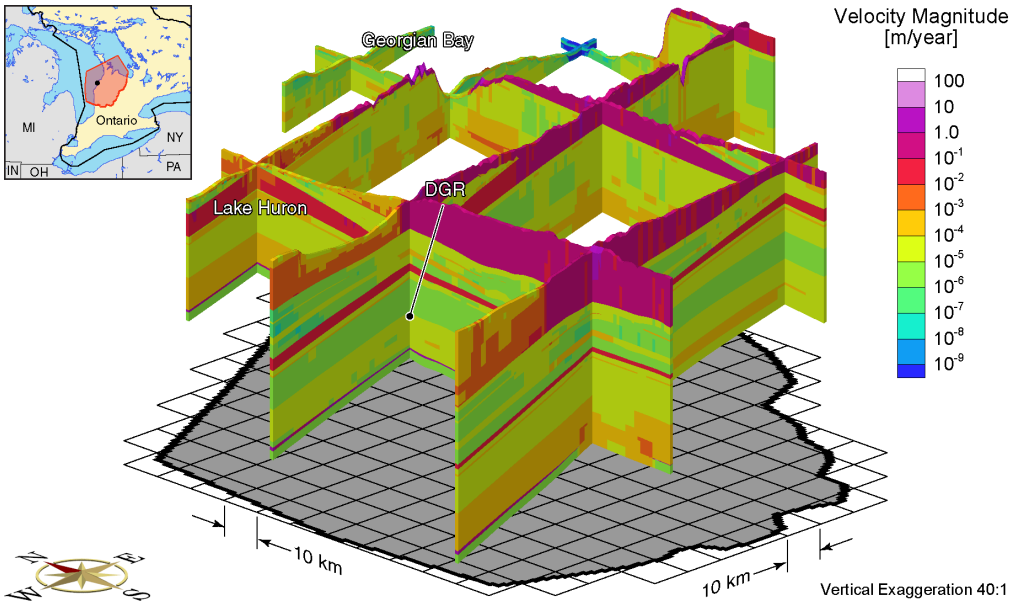

Figure H.16 Fence view of pore velocity magnitudes at 40 ka before present for the Michigan Basin Regional Scenario 1 paleoclimate simulation.

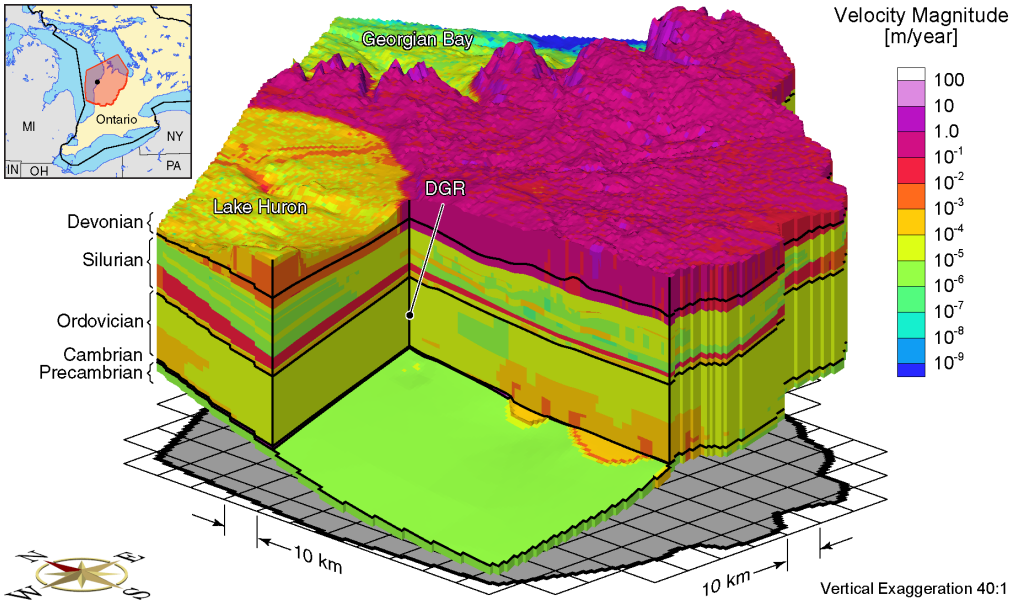

Figure H.17 Block cut view of pore velocity magnitudes at present for the Michigan Basin Regional Scenario 1 paleoclimate simulation.

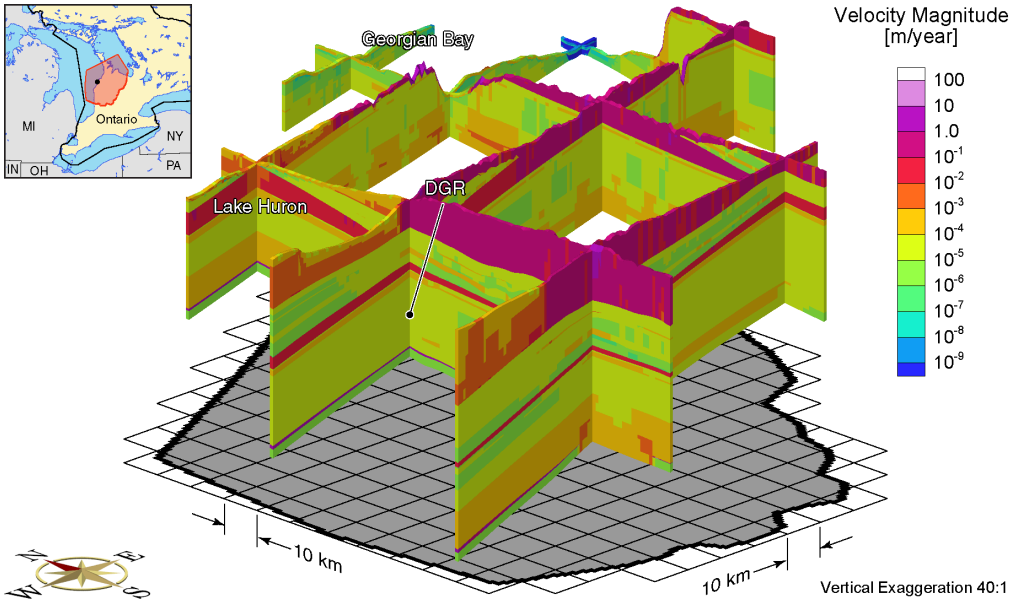

Figure H.18 Fence view of pore velocity magnitudes at present for the Michigan Basin Regional Scenario 1 paleoclimate simulation.

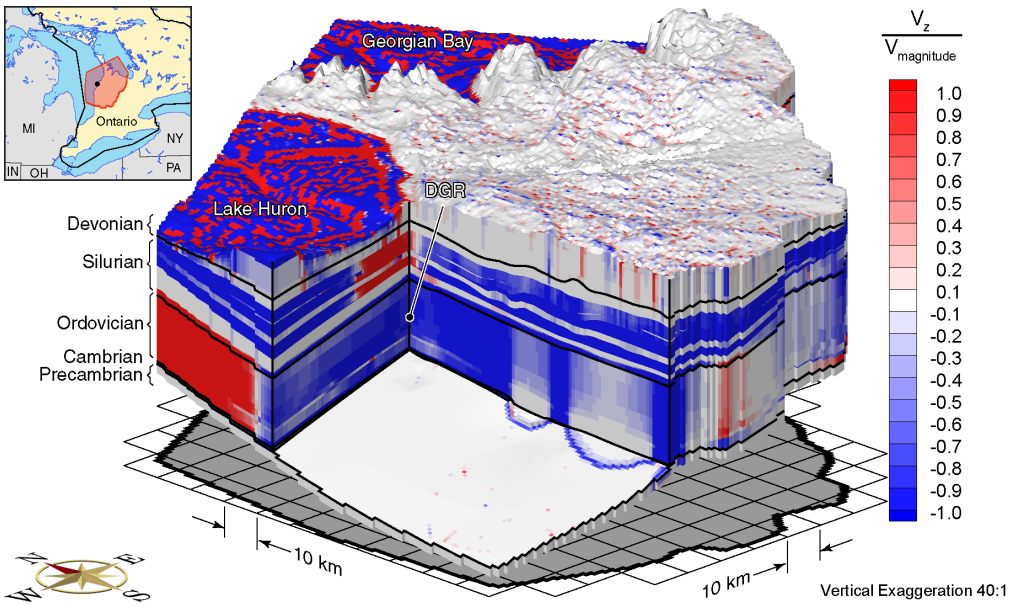

Figure H.19 Block cut view of ratio of vertical pore velocities to pore velocity magnitudes at 80 ka before present for the Michigan Basin Regional Scenario 1 paleoclimate simulation.

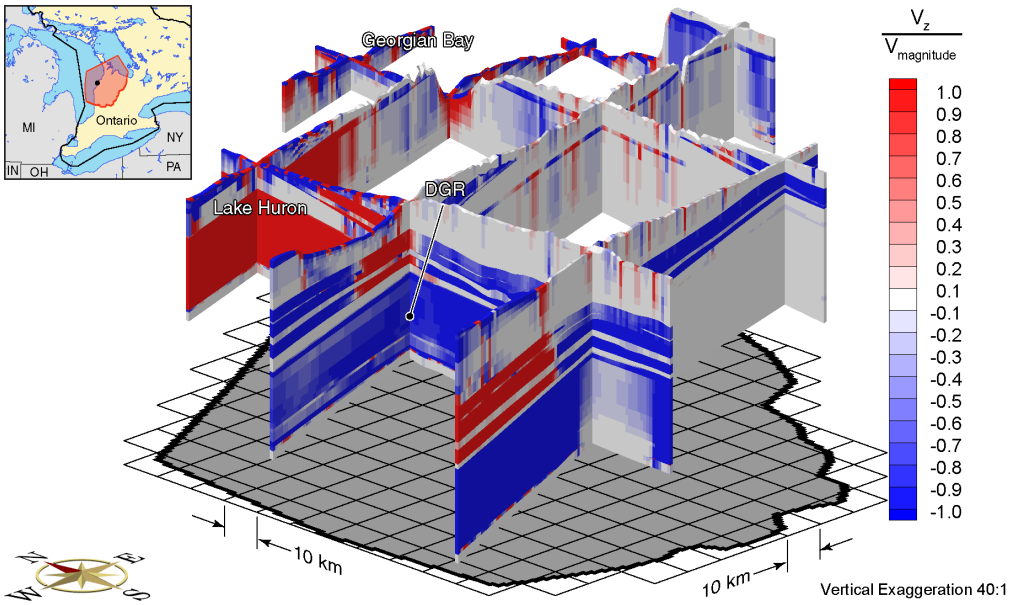

Figure H.20 Fence view of ratio of vertical pore velocities to pore velocity magnitudes at 80 ka before present for the Michigan Basin Regional Scenario 1 paleoclimate simulation.

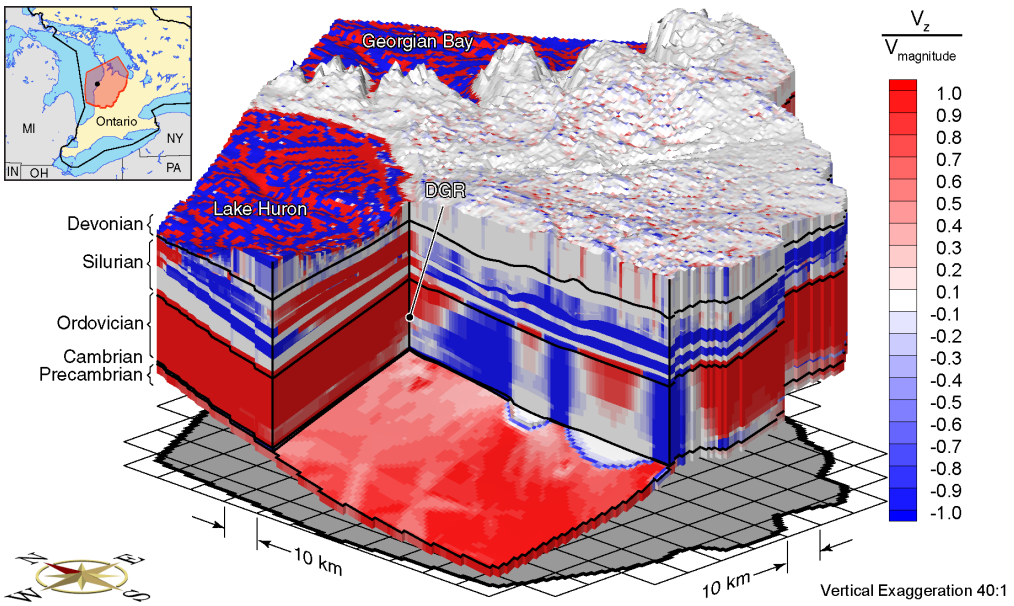

Figure H.21 Block cut view of ratio of vertical pore velocities to pore velocity magnitudes at 40 ka before present for the Michigan Basin Regional Scenario 1 paleoclimate simulation.

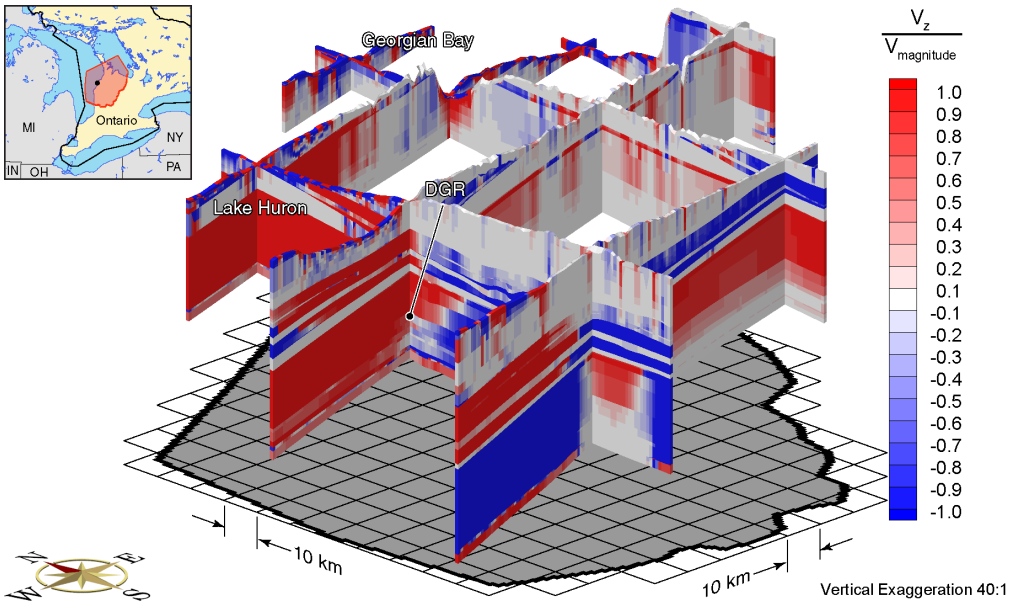

Figure H.22 Fence view of ratio of vertical pore velocities to pore velocity magnitudes at 40 ka before present for the Michigan Basin Regional Scenario 1 paleoclimate simulation.

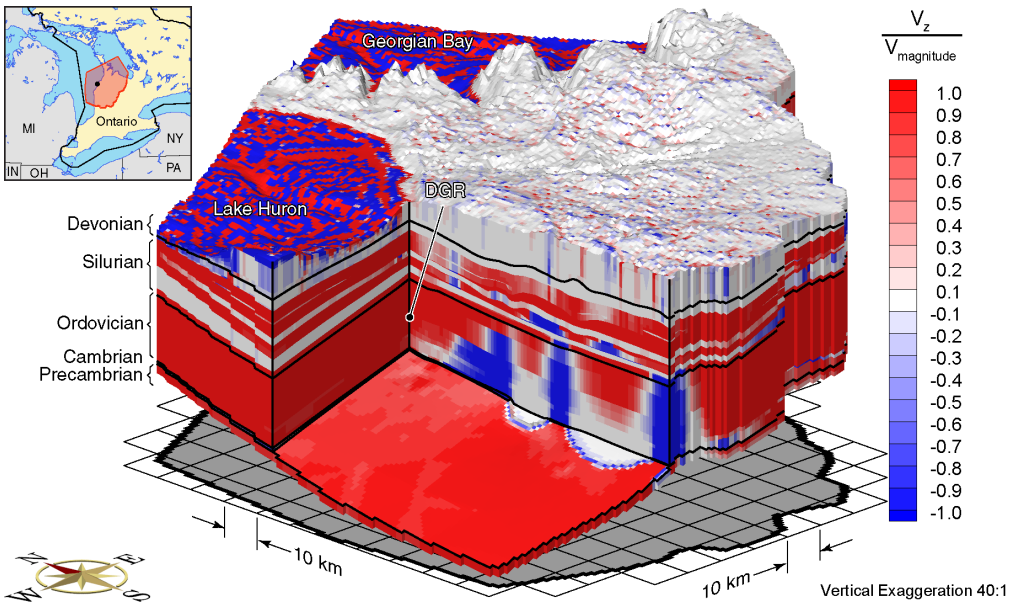

Figure H.23 Block cut view of ratio of vertical pore velocities to pore velocity magnitudes at present for the Michigan Basin Regional Scenario 1 paleoclimate simulation.

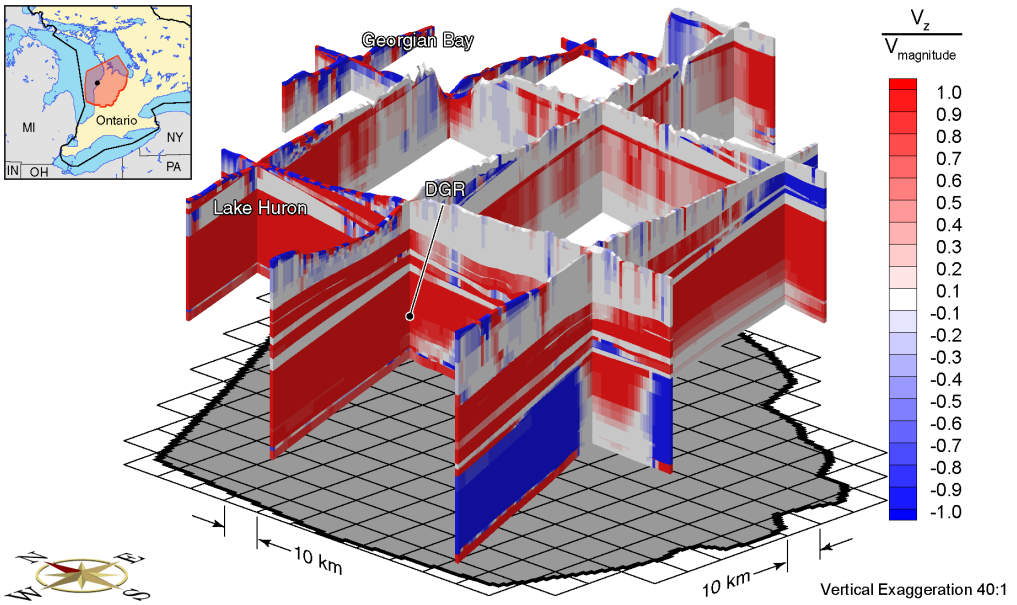

Figure H.24 Fence view of ratio of vertical pore velocities to pore velocity magnitudes at present for the Michigan Basin Regional Scenario 1 paleoclimate simulation.

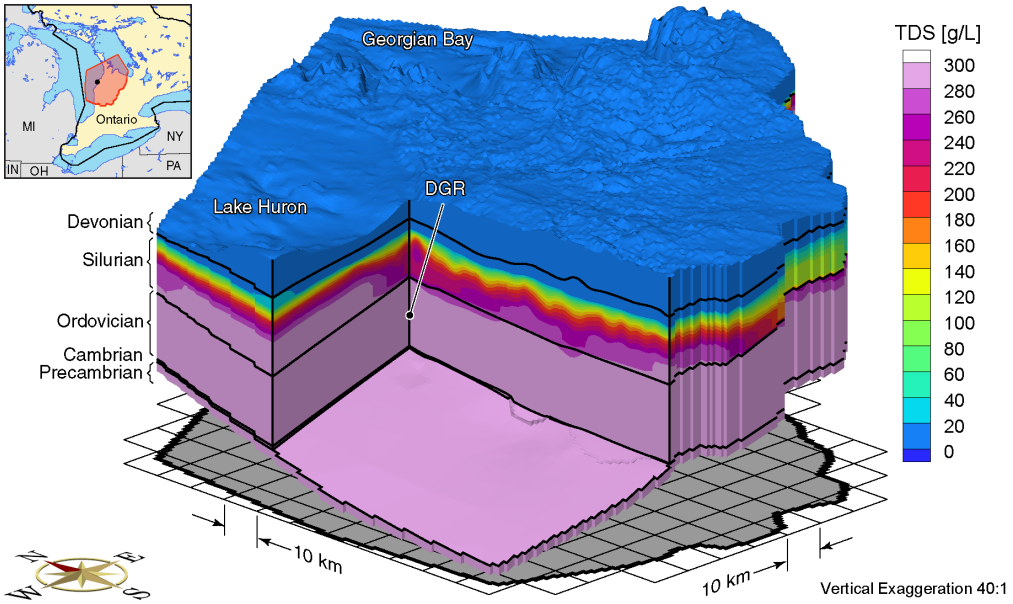

Figure H.25 Block cut view of brine concentrations at 80 ka before present for the Michigan Basin Regional Scenario 1 paleoclimate simulation.

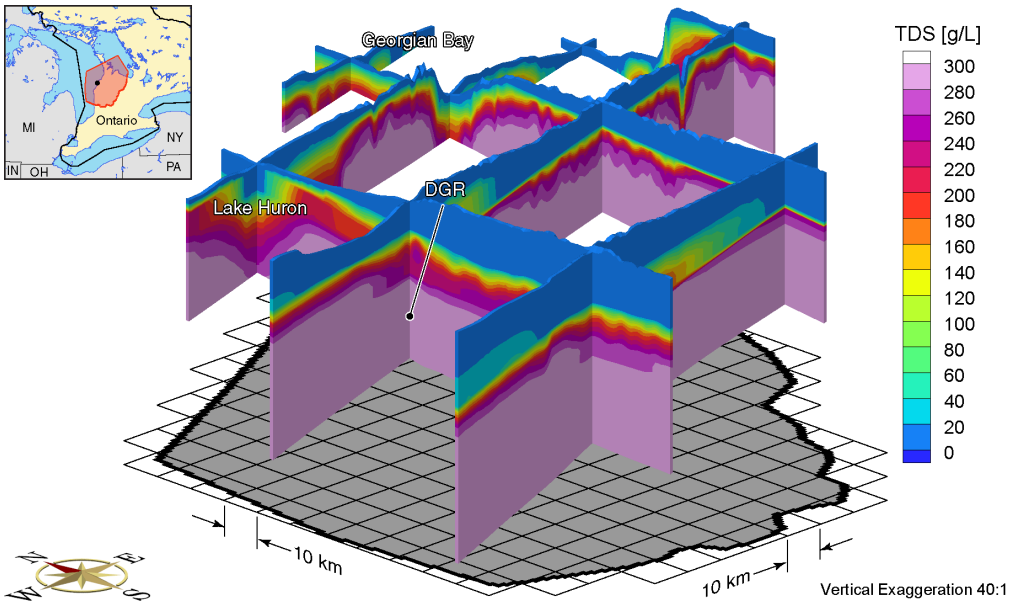

Figure H.26 Fence view of brine concentrations at 80 ka before present for the Michigan Basin Regional Scenario 1 paleoclimate simulation.

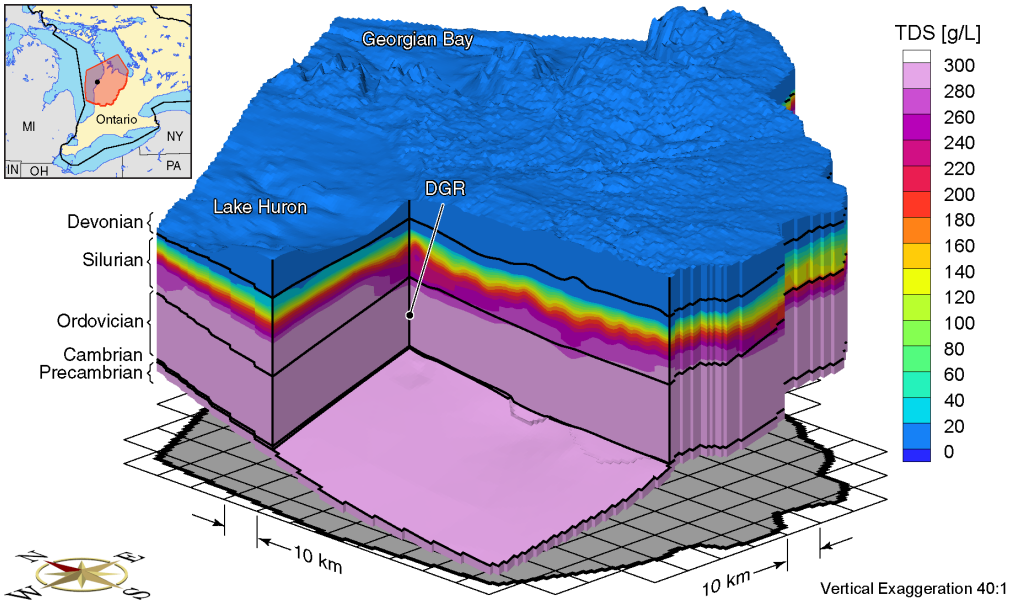

Figure H.27 Block cut view of brine concentrations at 40 ka before present for the Michigan Basin Regional Scenario 1 paleoclimate simulation.

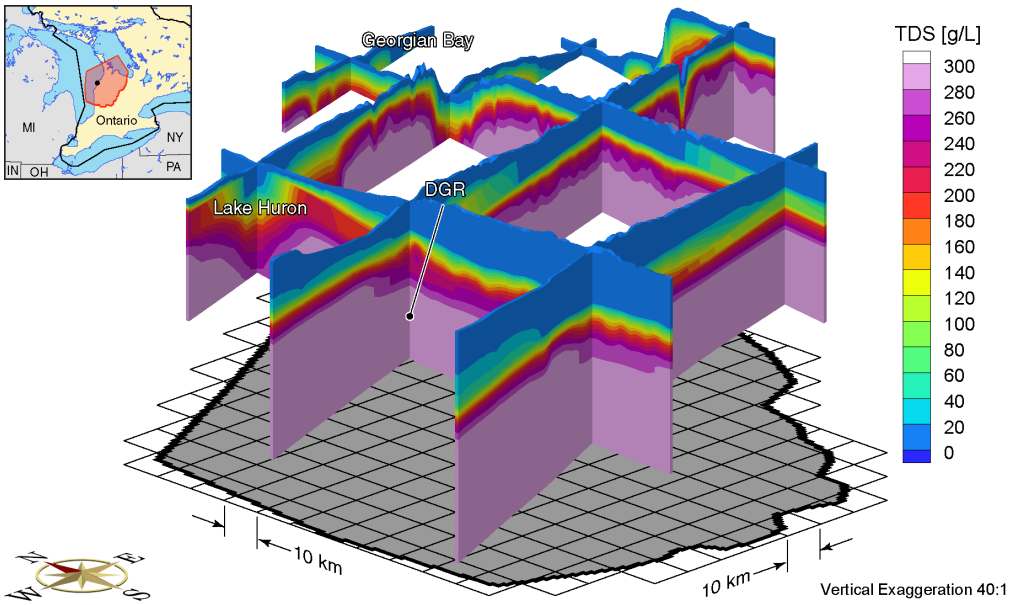

Figure H.28 Fence view of brine concentrations at 40 ka before present for the Michigan Basin Regional Scenario 1 paleoclimate simulation.

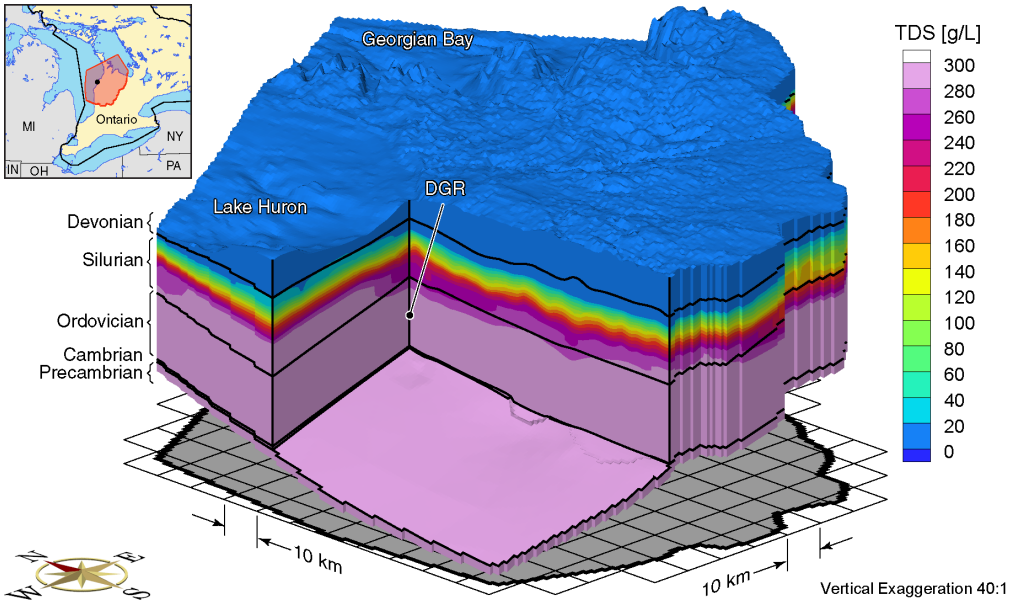

Figure H.29 Block cut view of brine concentrations at present for the Michigan Basin Regional Scenario 1 paleoclimate simulation.

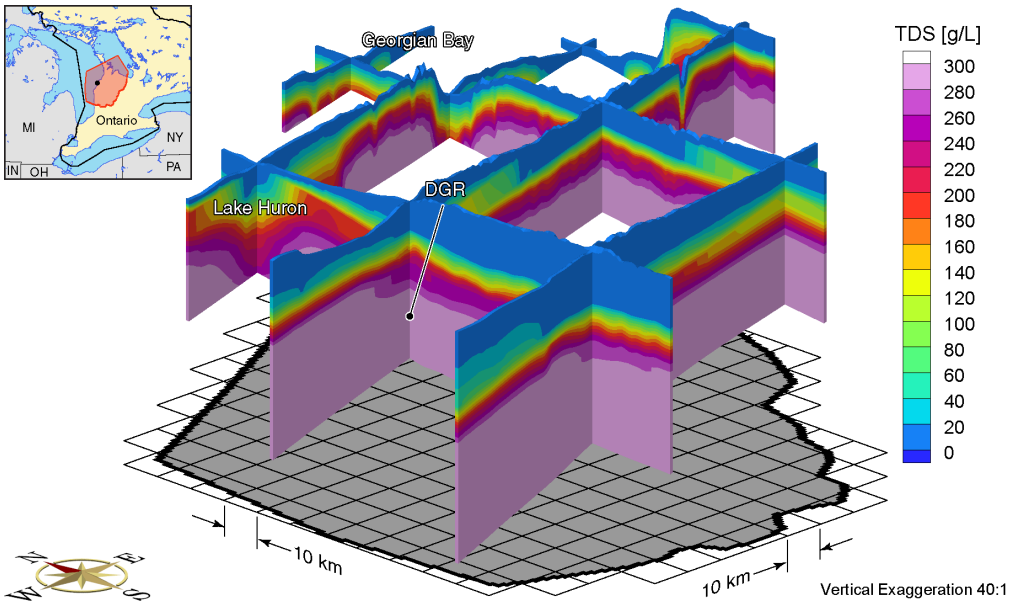

Figure H.30 Fence view of brine concentrations at present for the Michigan Basin Regional Scenario 1 paleoclimate simulation.

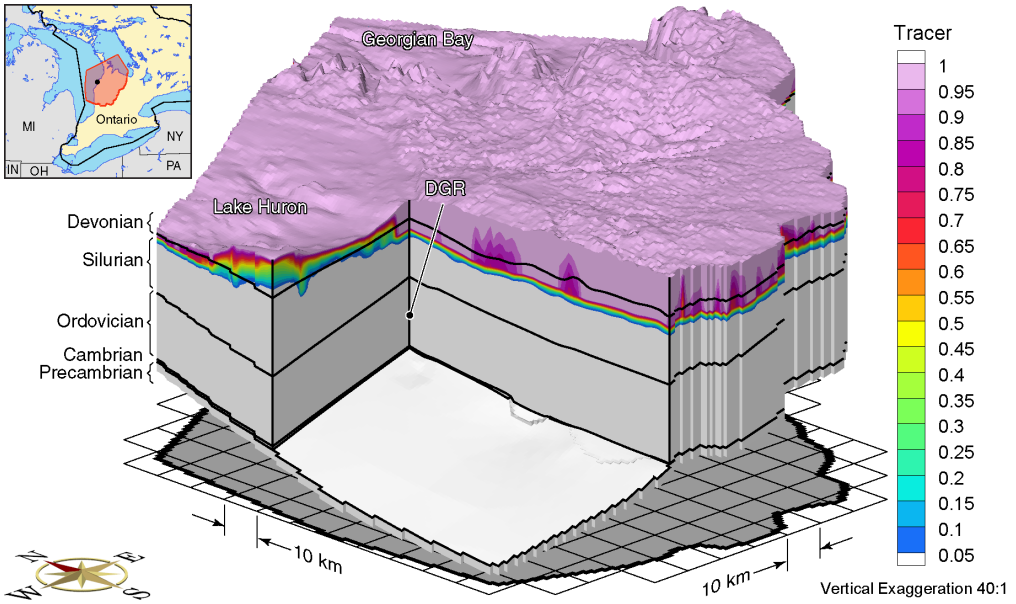

Figure H.31 Block cut view of tracer concentrations at 80 ka before present for the Michigan Basin Regional Scenario 1 paleoclimate simulation.

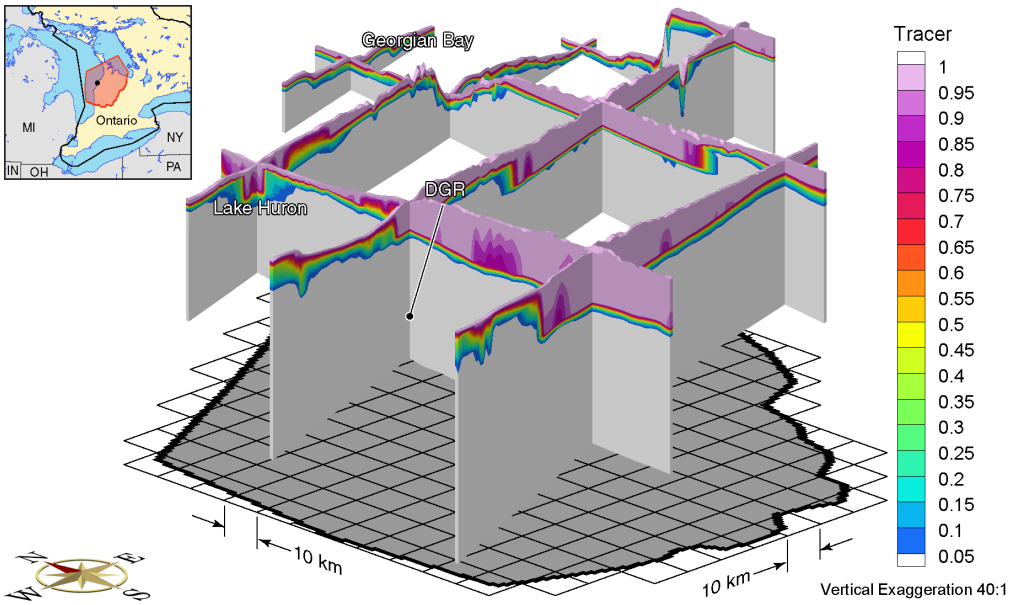

Figure H.32 Fence view of tracer concentrations at 80 ka before present for the Michigan Basin Regional Scenario 1 paleoclimate simulation.

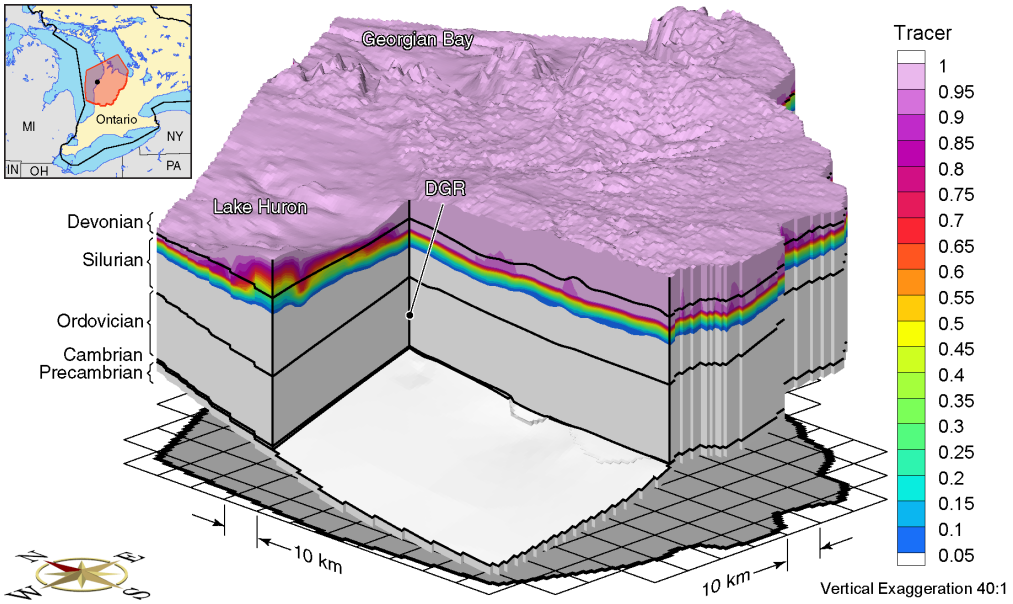

Figure H.33 Block cut view of tracer concentrations at 40 ka before present for the Michigan Basin Regional Scenario 1 paleoclimate simulation.

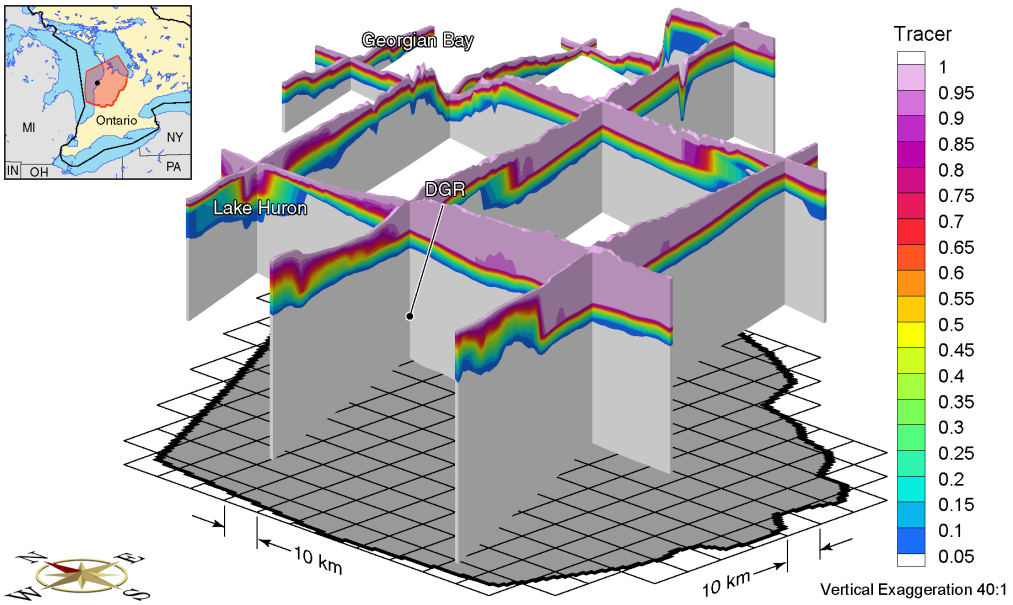

Figure H.34 Fence view of tracer concentrations at 40 ka before present for the Michigan Basin Regional Scenario 1 paleoclimate simulation.

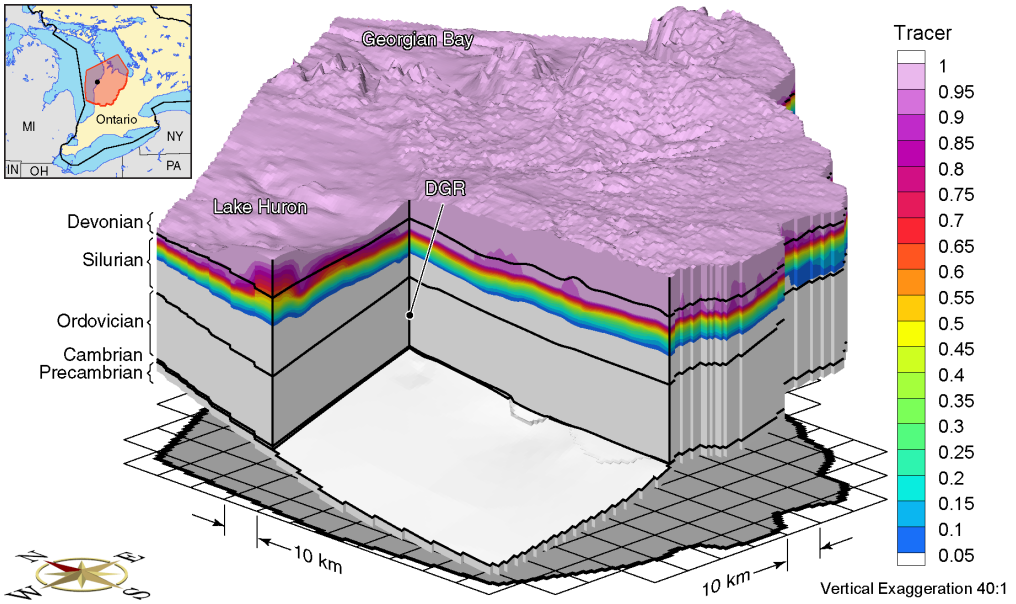

Figure H.35 Block cut view of tracer concentrations at present for the Michigan Basin Regional Scenario 1 paleoclimate simulation.

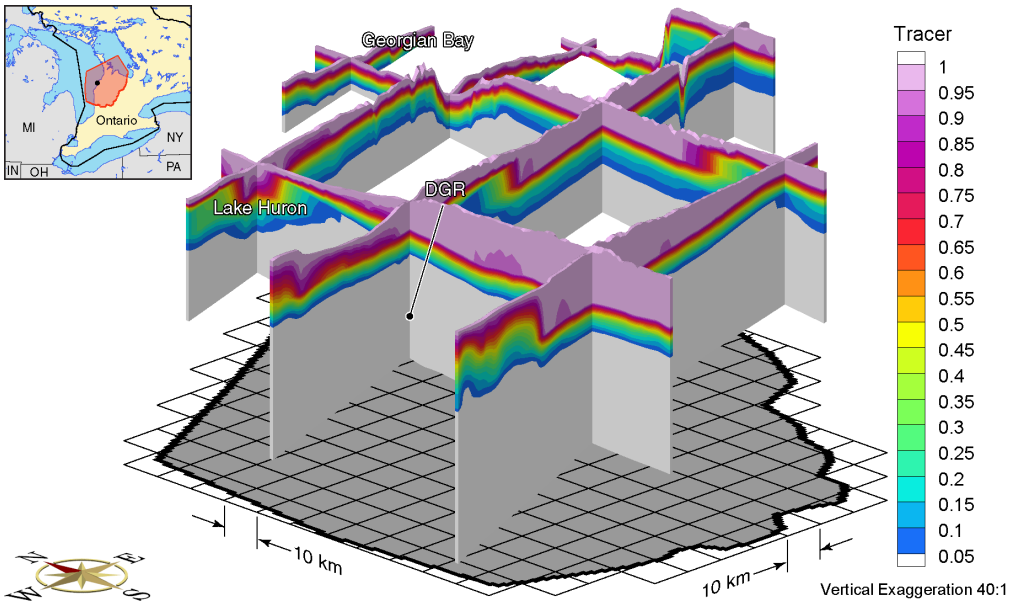

Figure H.36 Fence view of tracer concentrations at present for the Michigan Basin Regional Scenario 1 paleoclimate simulation.

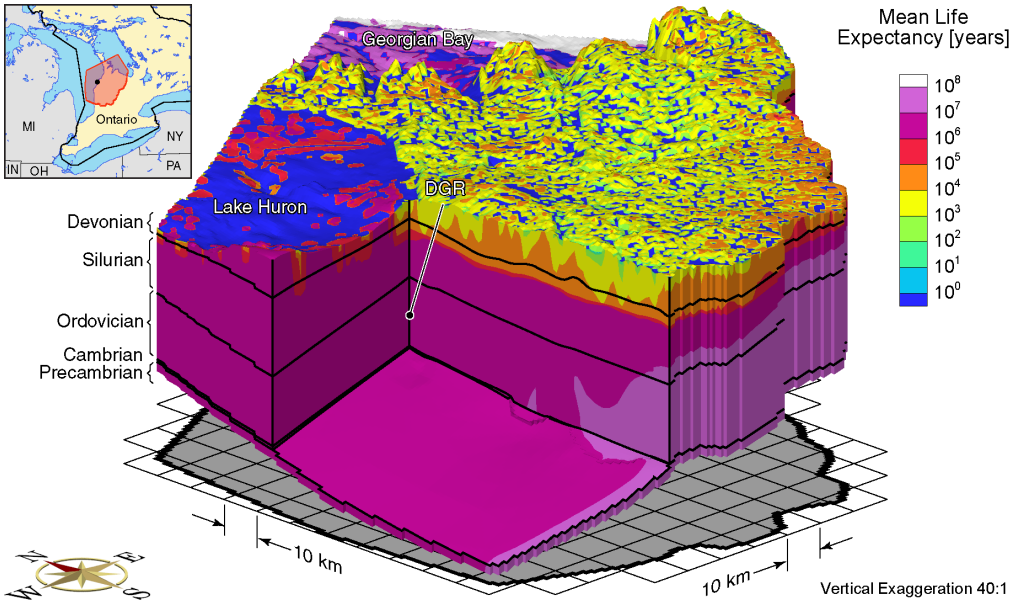

Figure H.37 Block cut view of mean life expectancies at present for the Michigan Basin Regional Scenario 1 paleoclimate simulation.

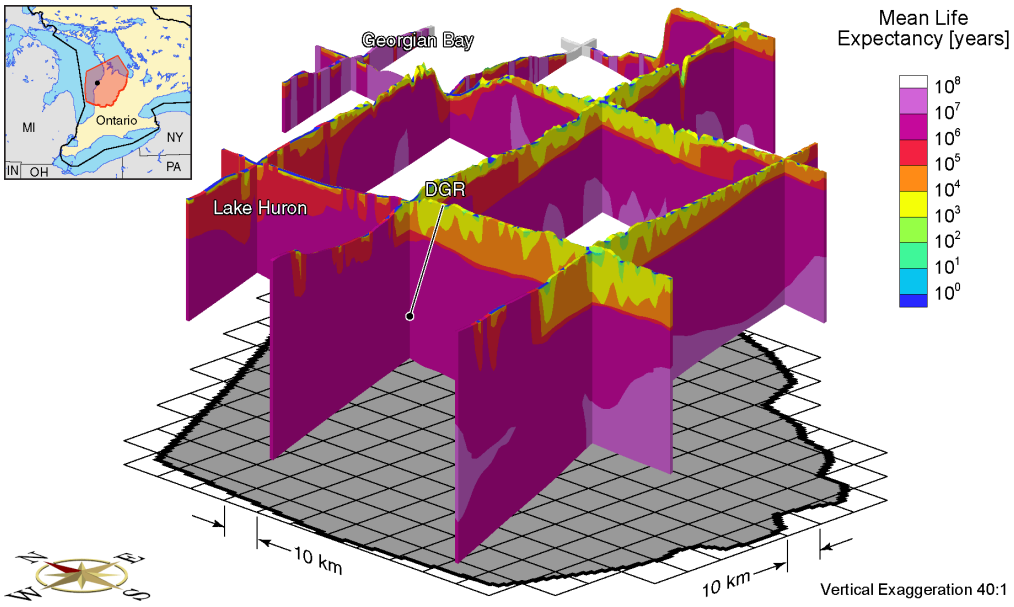

Figure H.38 Fence view of mean life expectancies at present for the Michigan Basin Regional Scenario 1 paleoclimate simulation.

Appendix I

MBR Scenario 2 Paleoclimate Model

All figures related to the Michigan Basin Regional (MBR) Scenario 2 paleoclimate modelling are listed in Table I.1. Block cut view and fence view figures are shown on the same page to facilitate comparison. All results of the 120 ka paleoclimate simulations are shown at times of 80 ka before present, 40 ka before present, and at present.

Table I.1 List of Michigan Basin Regional Scenario 2 paleoclimate simulation figures.

Parameters	Time Before Present					
	80 ka		40 ka		Present	
	Block Cut	Fence	Block Cut	Fence	Block Cut	Fence
Freshwater Heads	I.1	I.2	I.3	I.4	I.5	I.6
Environmental Heads	I.7	I.8	I.9	I.10	I.11	I.12
Pore Velocity Magnitudes	I.13	I.14	I.15	I.16	I.17	I.18
Ratio of Vertical Pore Velocities to Pore Velocity Magnitudes	I.19	I.20	I.21	I.22	I.23	I.24
Brine Concentrations	I.25	I.26	I.27	I.28	I.29	I.30
Tracer Concentrations	I.31	I.32	I.33	I.34	I.35	I.36
Mean Life Expectancies	—	—	—	—	I.37	I.38

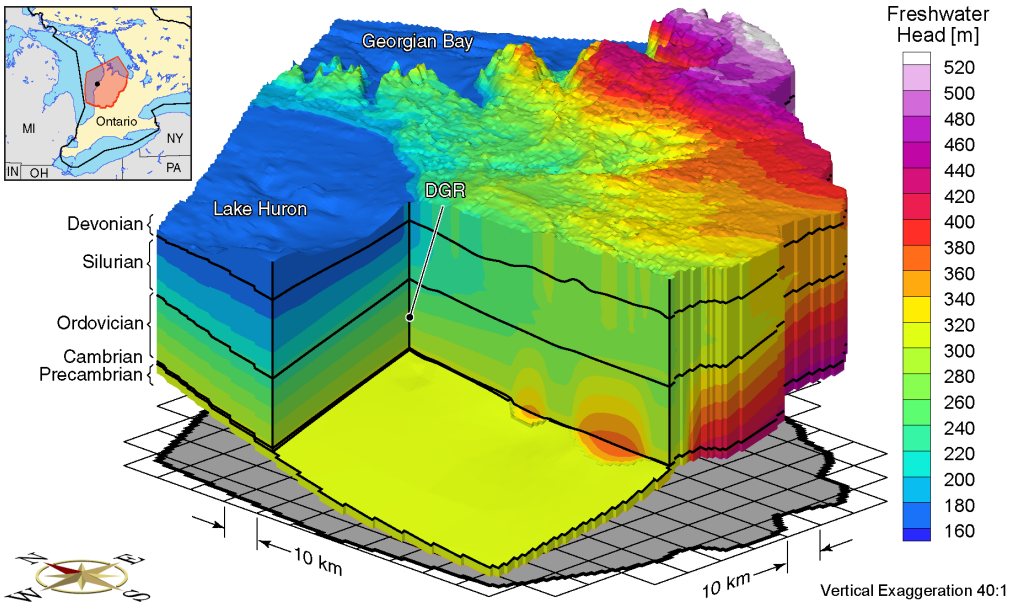

Figure I.1 Block cut view of freshwater heads at 80 ka before present for the Michigan Basin Regional Scenario 2 paleoclimate simulation.

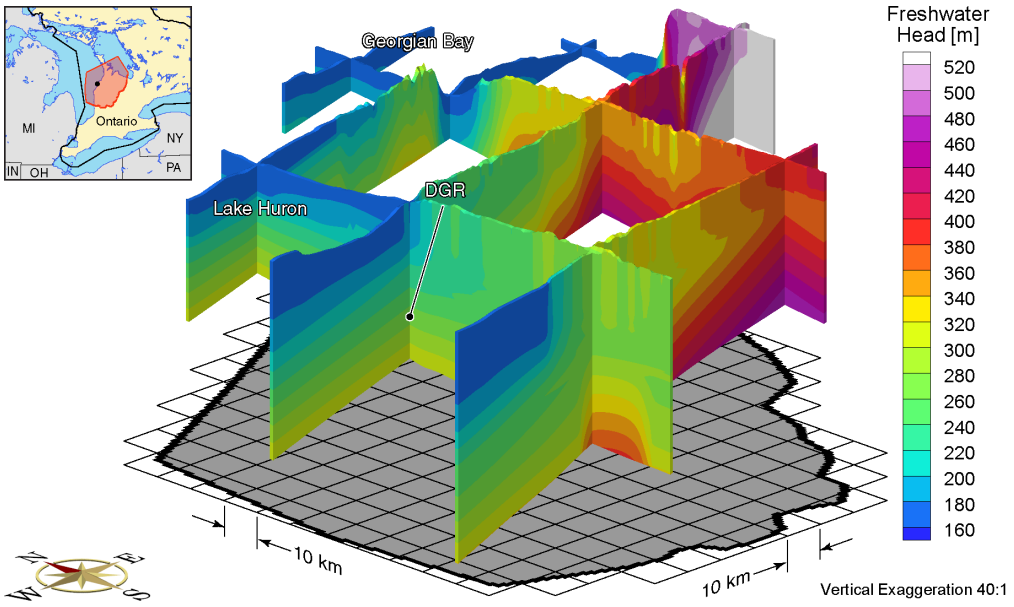

Figure I.2 Fence view of freshwater heads at 80 ka before present for the Michigan Basin Regional Scenario 2 paleoclimate simulation.

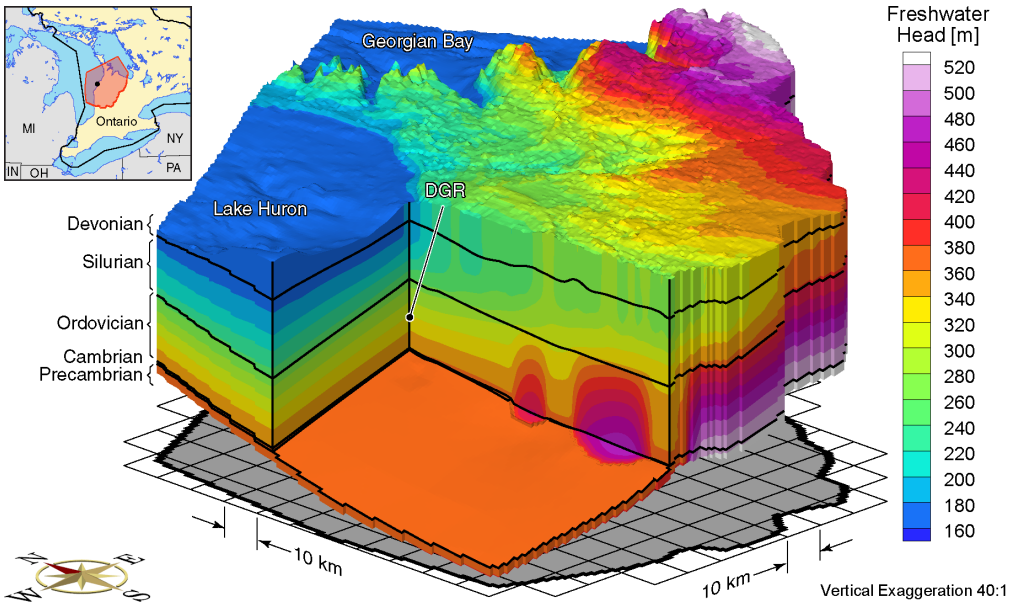

Figure I.3 Block cut view of freshwater heads at 40 ka before present for the Michigan Basin Regional Scenario 2 paleoclimate simulation.

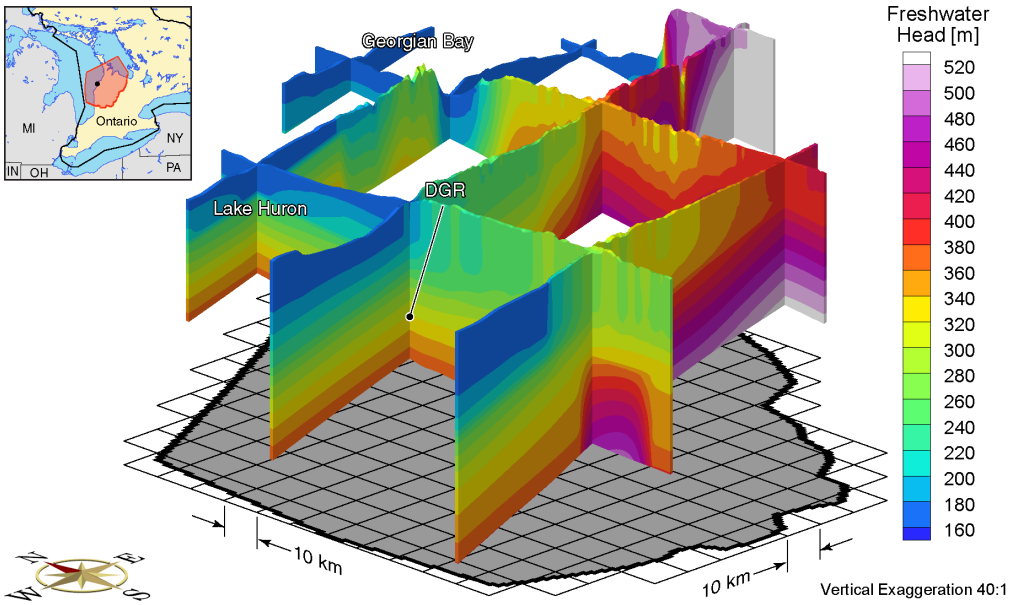

Figure I.4 Fence view of freshwater heads at 40 ka before present for the Michigan Basin Regional Scenario 2 paleoclimate simulation.

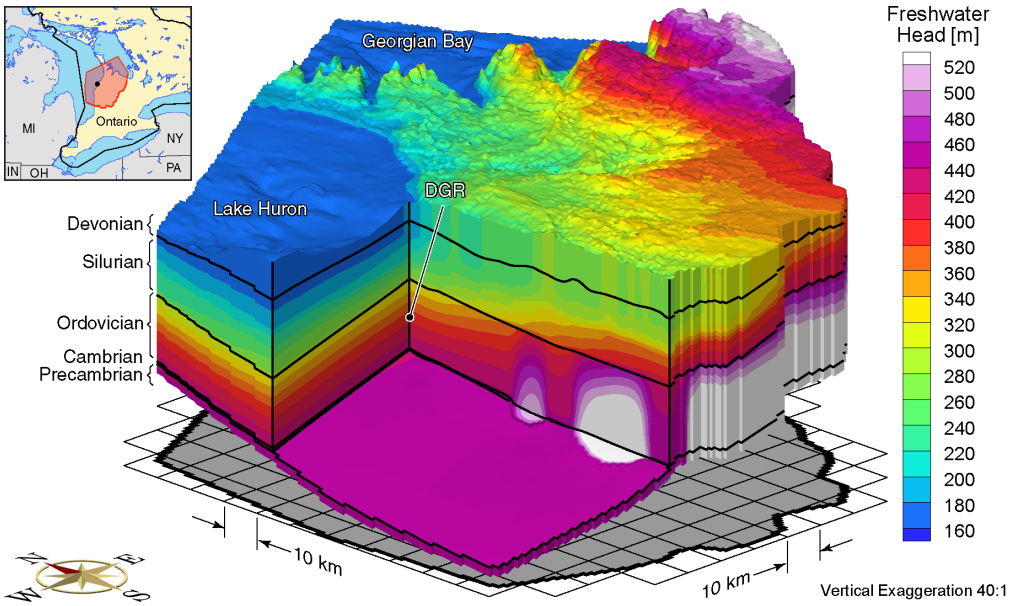

Figure I.5 Block cut view of freshwater heads at present for the Michigan Basin Regional Scenario 2 paleoclimate simulation.

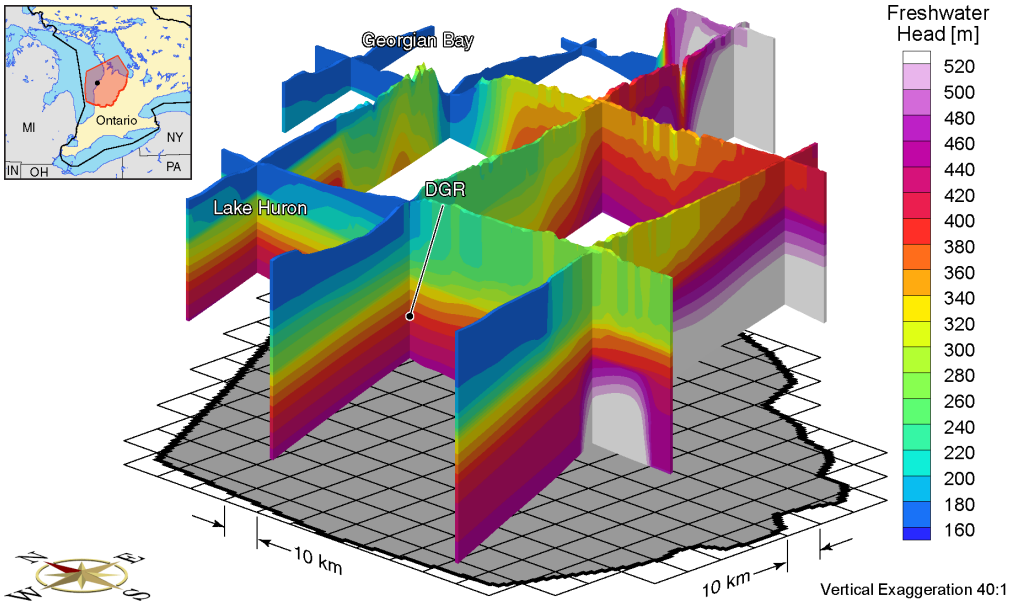

Figure I.6 Fence view of freshwater heads at present for the Michigan Basin Regional Scenario 2 paleoclimate simulation.

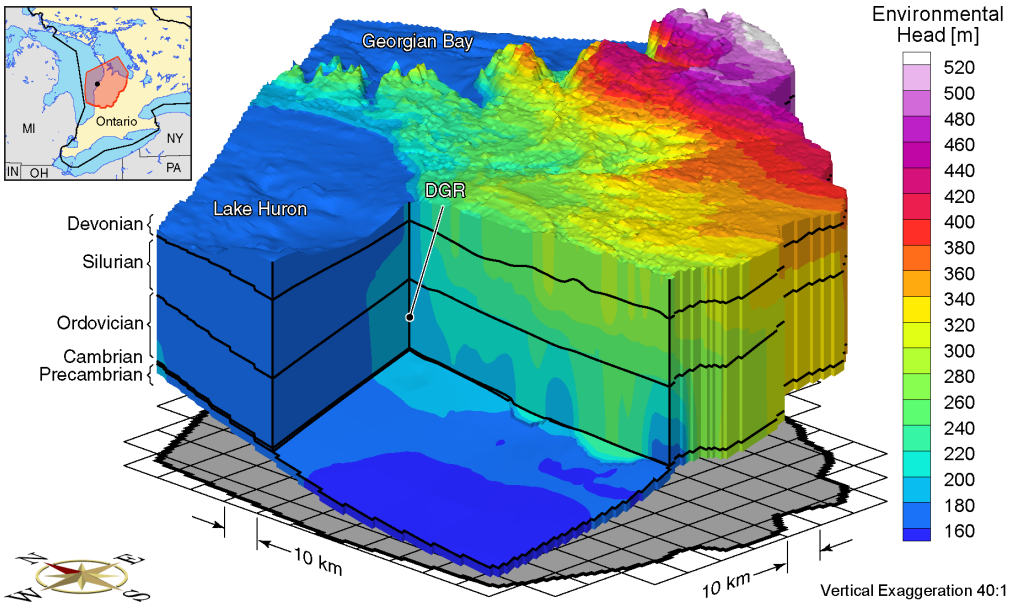

Figure I.7 Block cut view of environmental heads at 80 ka before present for the Michigan Basin Regional Scenario 2 paleoclimate simulation.

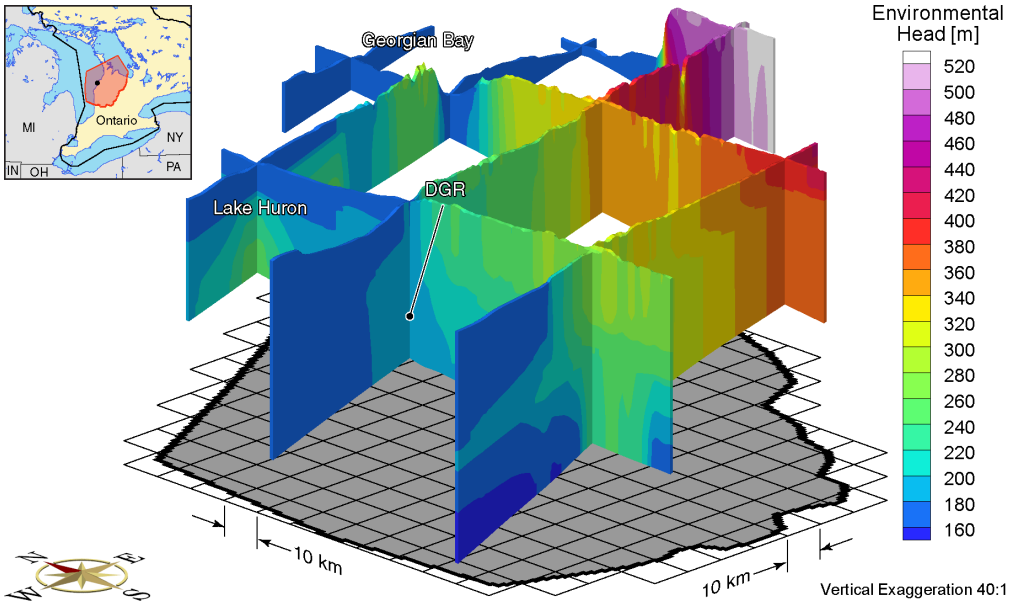

Figure I.8 Fence view of environmental heads at 80 ka before present for the Michigan Basin Regional Scenario 2 paleoclimate simulation.

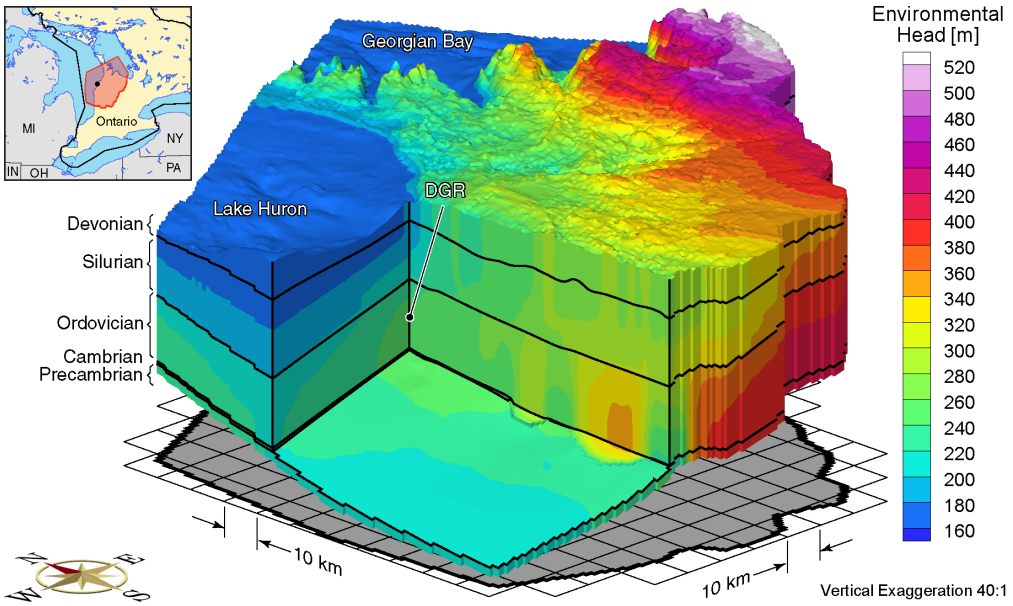

Figure I.9 Block cut view of environmental heads at 40 ka before present for the Michigan Basin Regional Scenario 2 paleoclimate simulation.

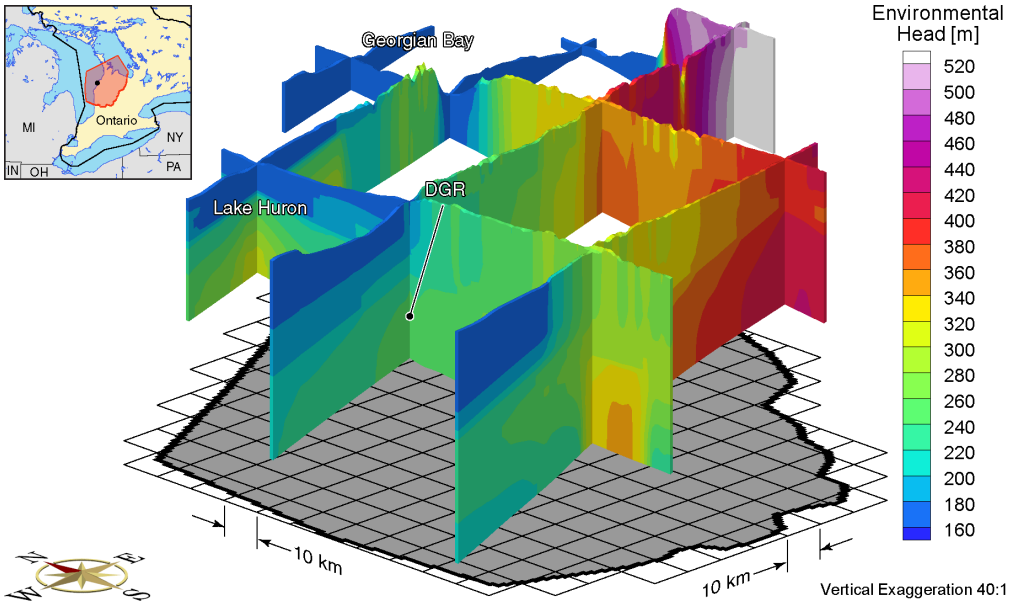

Figure I.10 Fence view of environmental heads at 40 ka before present for the Michigan Basin Regional Scenario 2 paleoclimate simulation.

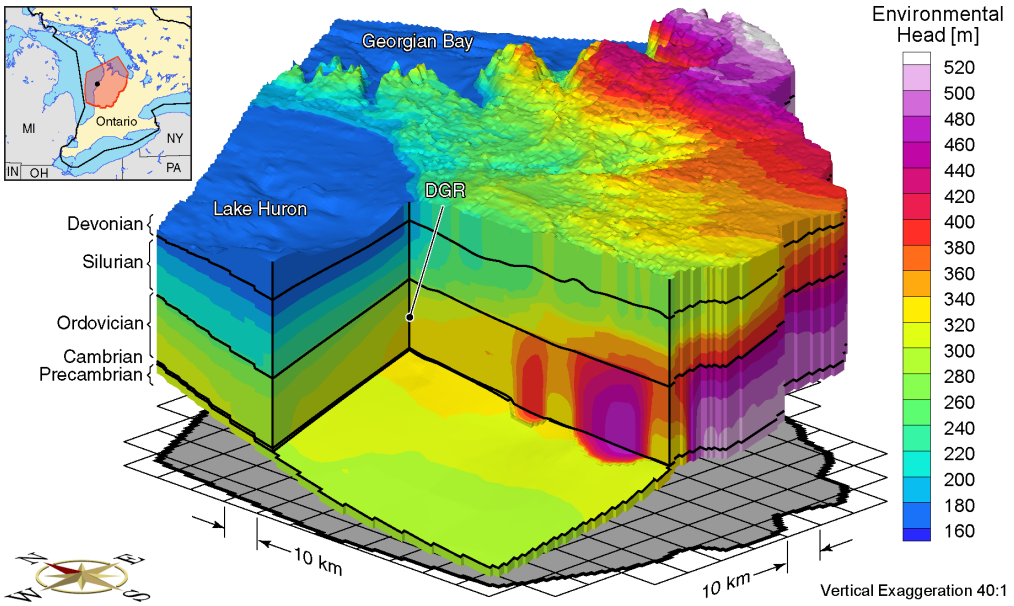

Figure I.11 Block cut view of environmental heads at present for the Michigan Basin Regional Scenario 2 paleoclimate simulation.

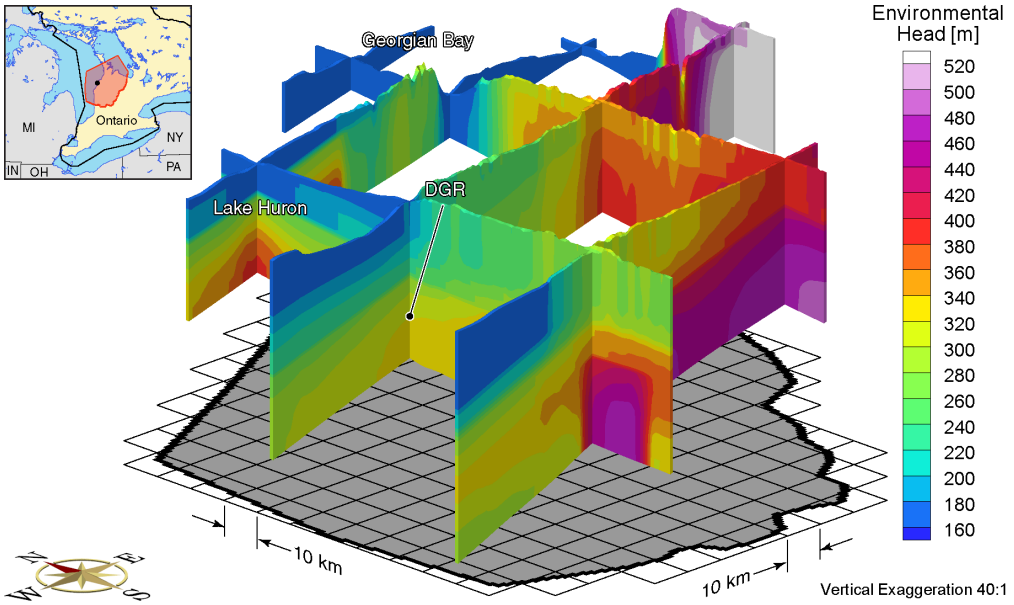

Figure I.12 Fence view of environmental heads at present for the Michigan Basin Regional Scenario 2 paleoclimate simulation.

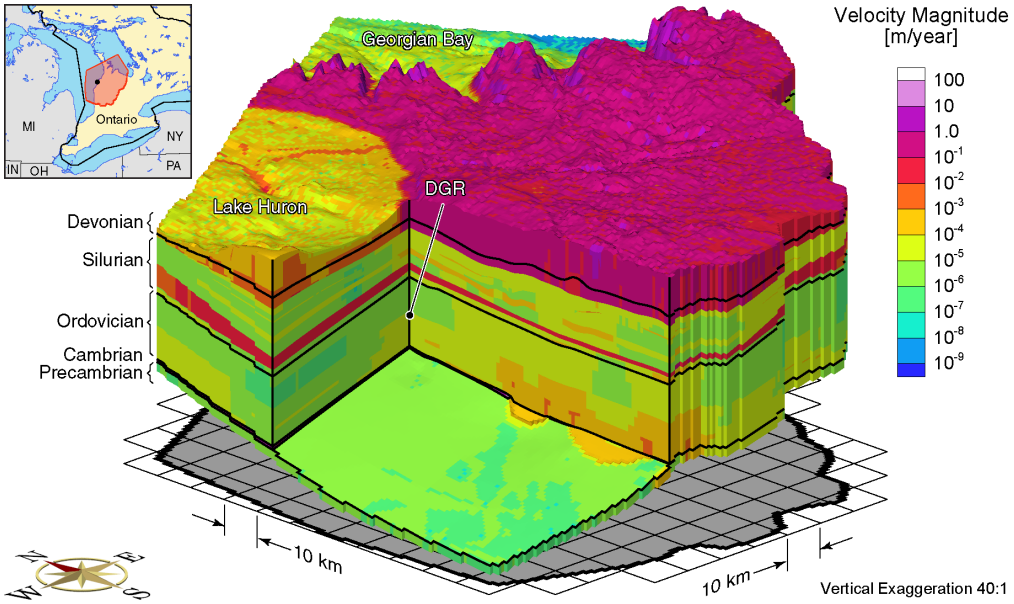

Figure I.13 Block cut view of pore velocity magnitudes at 80 ka before present for the Michigan Basin Regional Scenario 2 paleoclimate simulation.

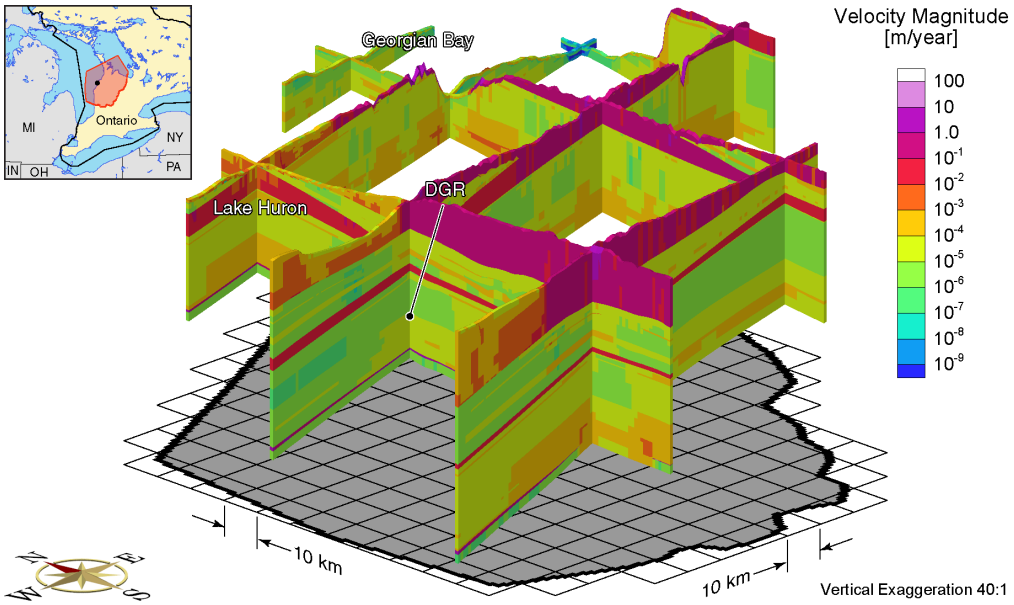

Figure I.14 Fence view of pore velocity magnitudes at 80 ka before present for the Michigan Basin Regional Scenario 2 paleoclimate simulation.

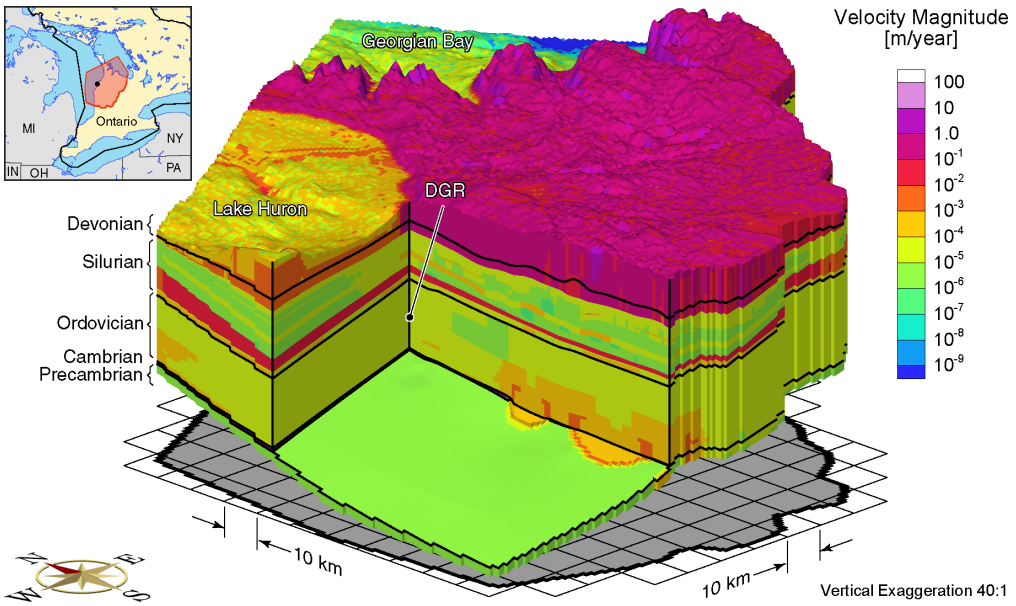

Figure I.15 Block cut view of pore velocity magnitudes at 40 ka before present for the Michigan Basin Regional Scenario 2 paleoclimate simulation.

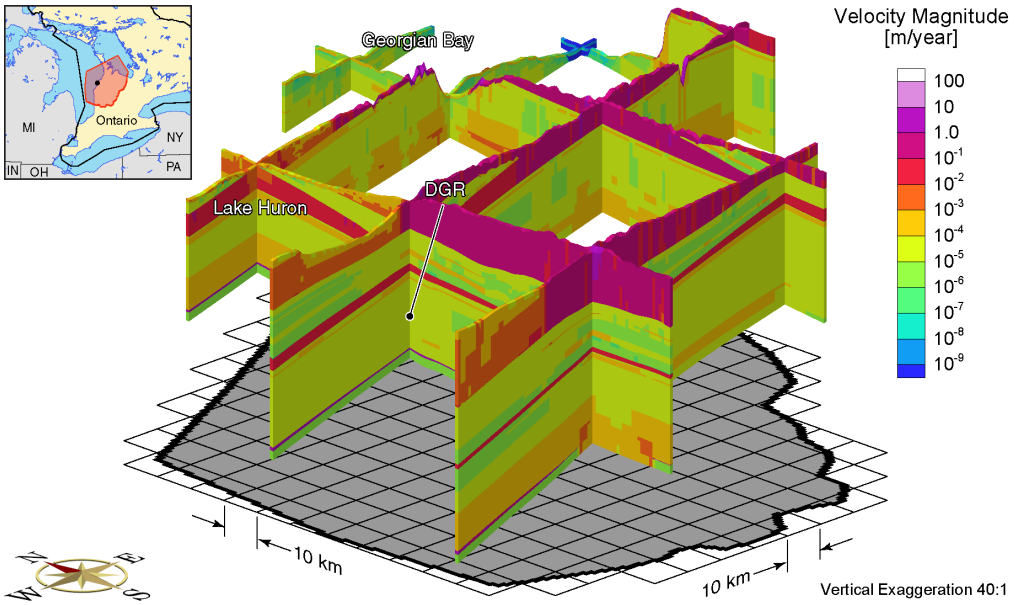

Figure I.16 Fence view of pore velocity magnitudes at 40 ka before present for the Michigan Basin Regional Scenario 2 paleoclimate simulation.

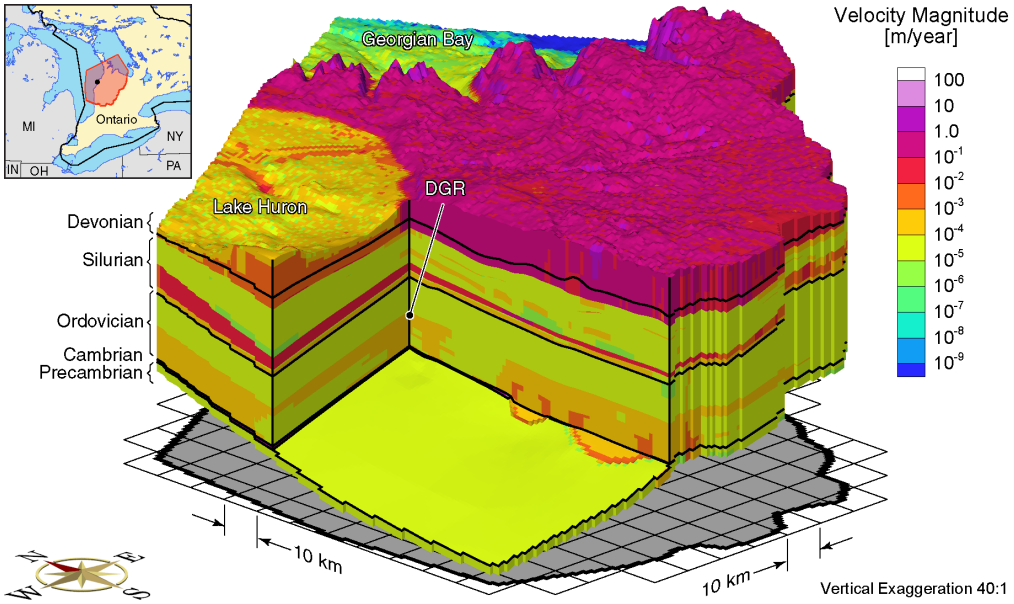

Figure I.17 Block cut view of pore velocity magnitudes at present for the Michigan Basin Regional Scenario 2 paleoclimate simulation.

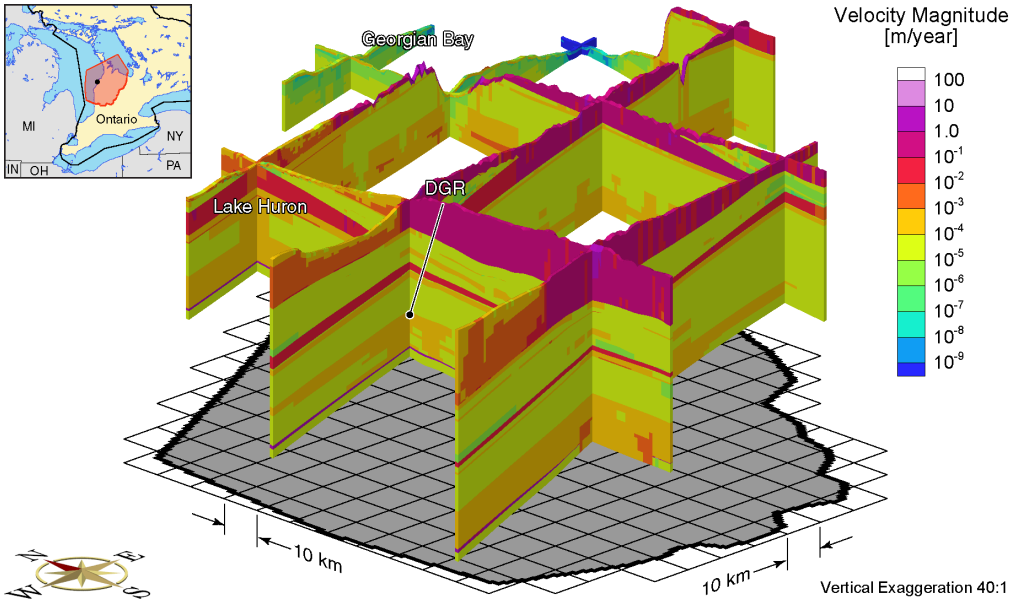

Figure I.18 Fence view of pore velocity magnitudes at present for the Michigan Basin Regional Scenario 2 paleoclimate simulation.

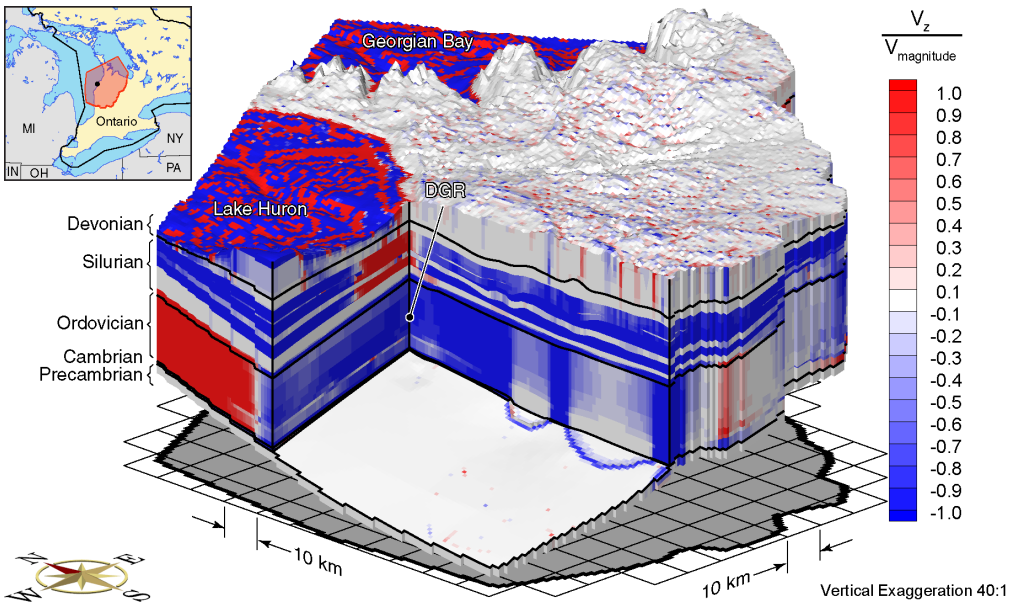

Figure I.19 Block cut view of ratio of vertical pore velocities to pore velocity magnitudes at 80 ka before present for the Michigan Basin Regional Scenario 2 paleoclimate simulation.

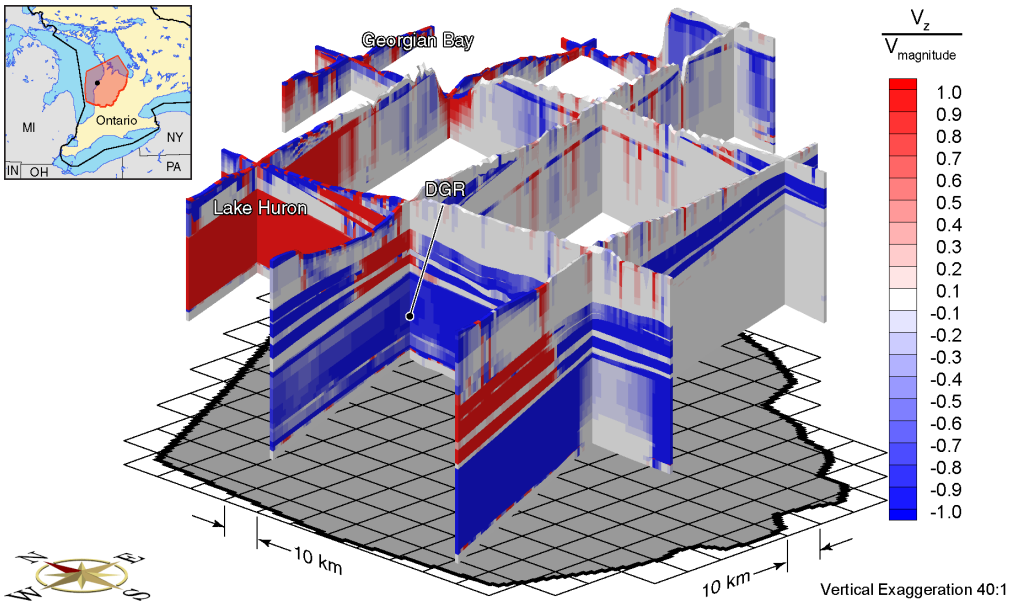

Figure I.20 Fence view of ratio of vertical pore velocities to pore velocity magnitudes at 80 ka before present for the Michigan Basin Regional Scenario 2 paleoclimate simulation.

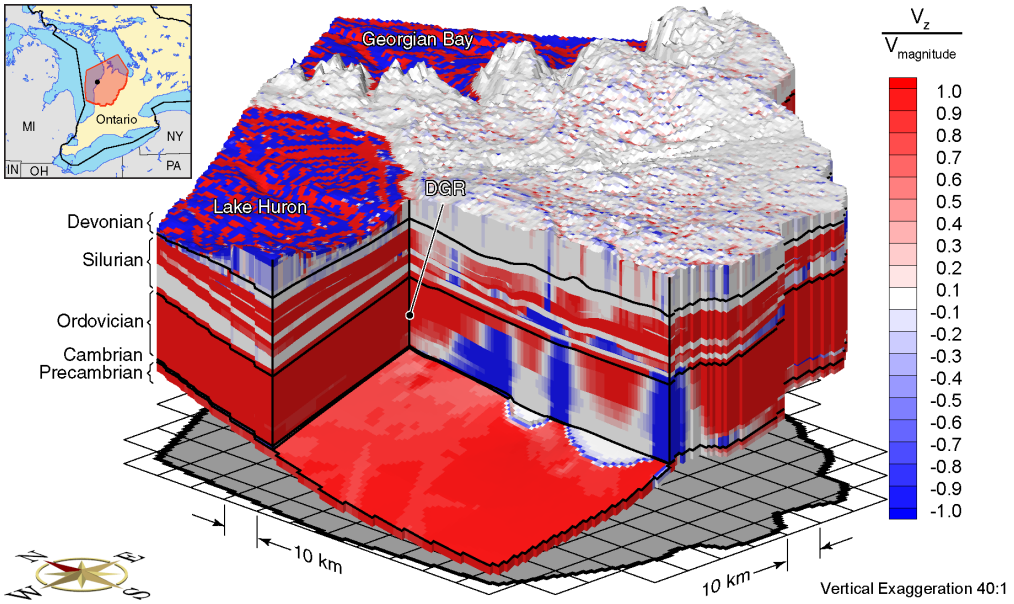

Figure I.21 Block cut view of ratio of vertical pore velocities to pore velocity magnitudes at 40 ka before present for the Michigan Basin Regional Scenario 2 paleoclimate simulation.

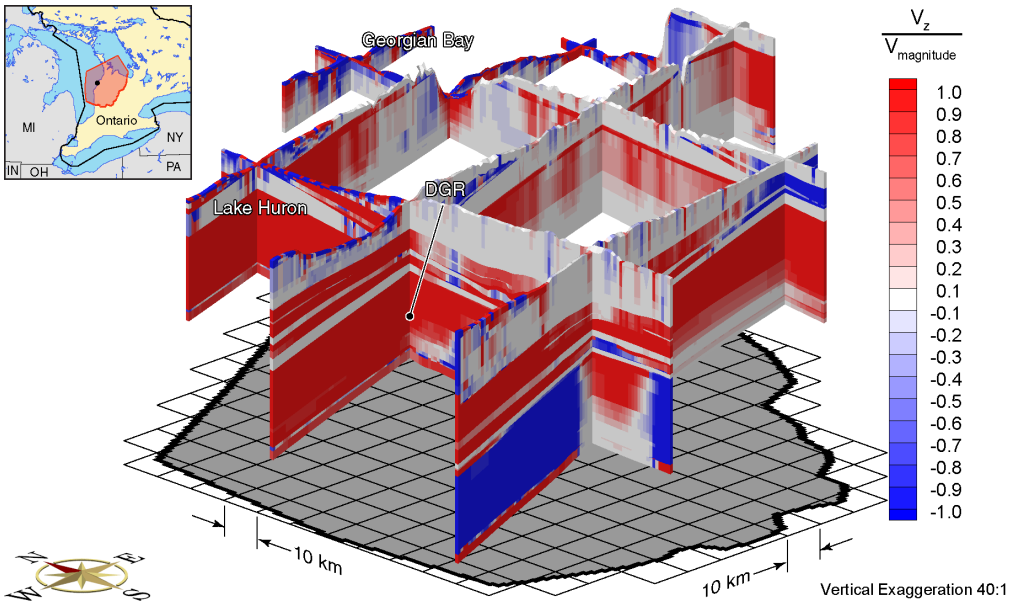

Figure I.22 Fence view of ratio of vertical pore velocities to pore velocity magnitudes at 40 ka before present for the Michigan Basin Regional Scenario 2 paleoclimate simulation.

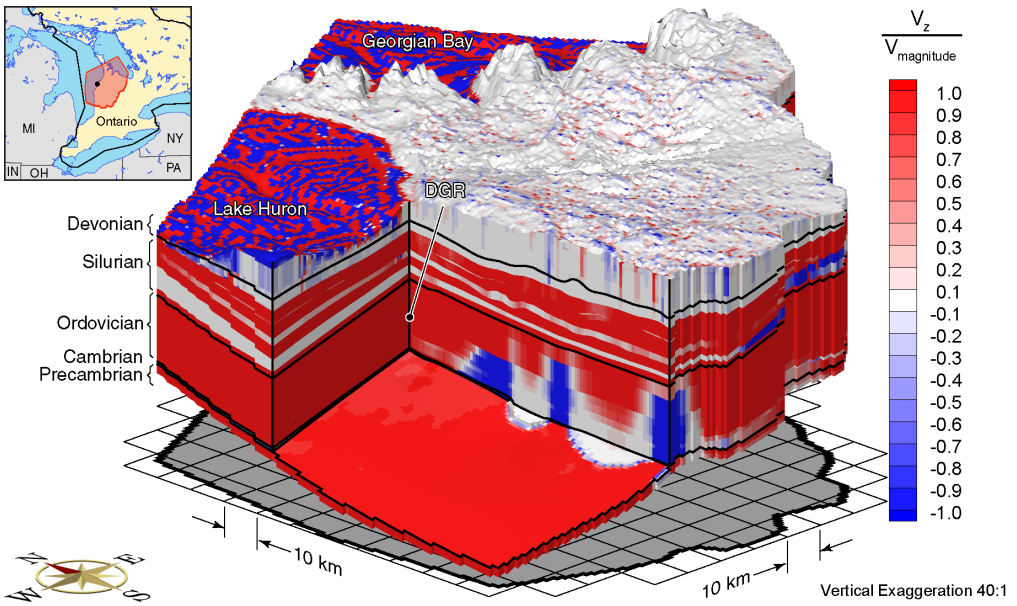

Figure I.23 Block cut view of ratio of vertical pore velocities to pore velocity magnitudes at present for the Michigan Basin Regional Scenario 2 paleoclimate simulation.

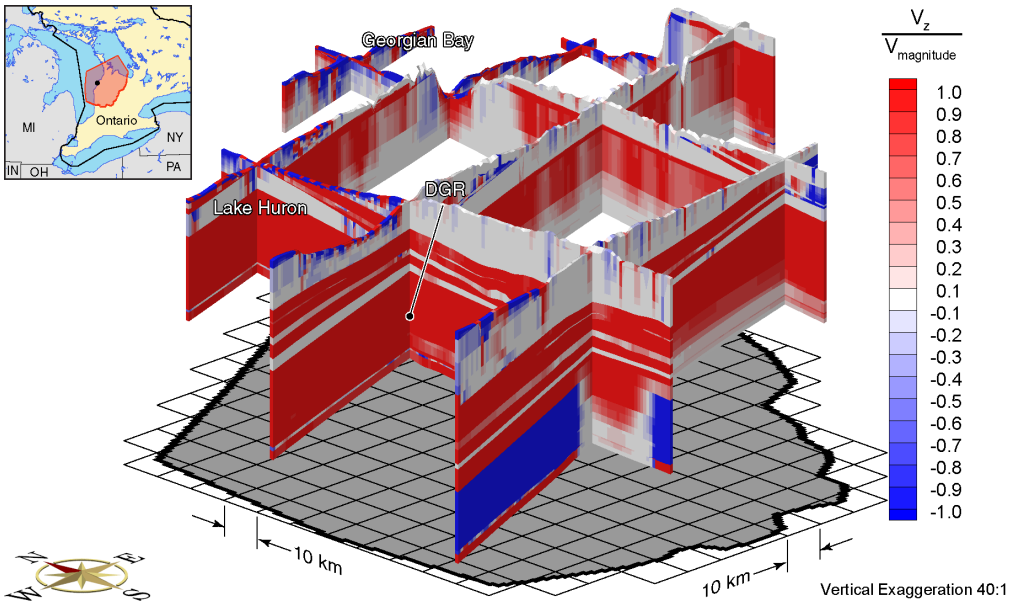

Figure I.24 Fence view of ratio of vertical pore velocities to pore velocity magnitudes at present for the Michigan Basin Regional Scenario 2 paleoclimate simulation.

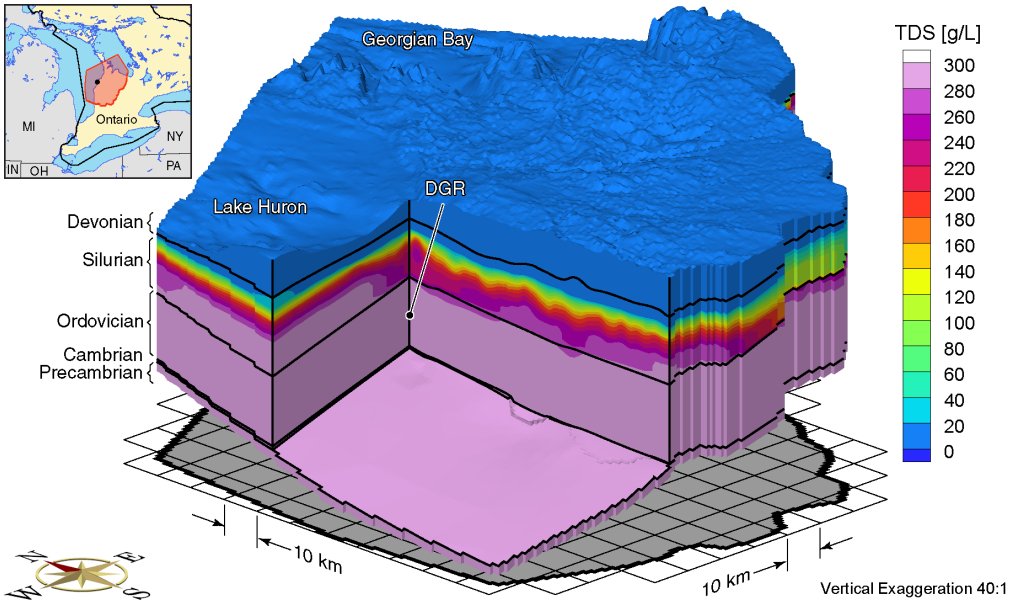

Figure I.25 Block cut view of brine concentrations at 80 ka before present for the Michigan Basin Regional Scenario 2 paleoclimate simulation.

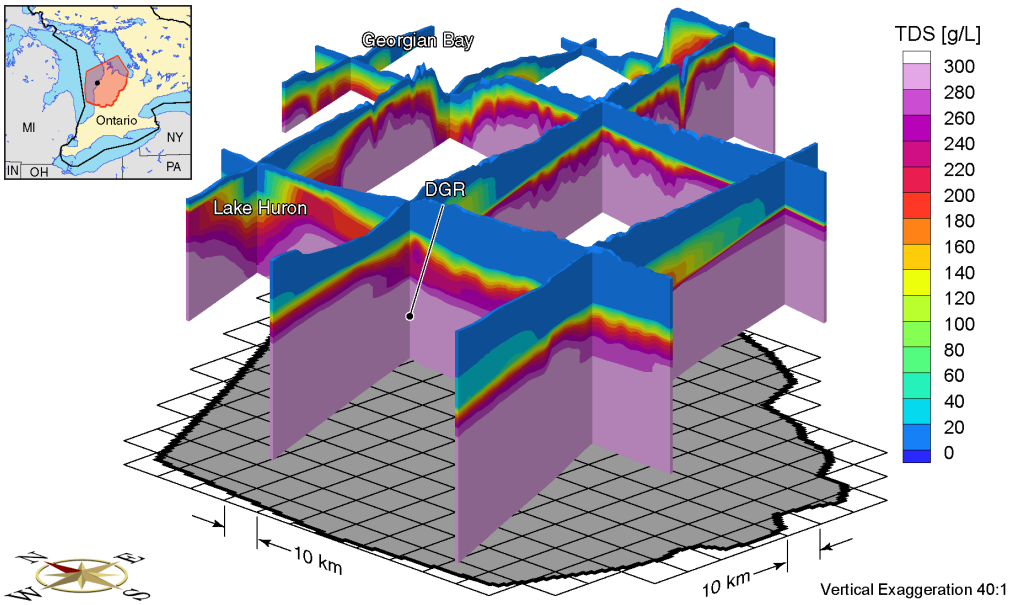

Figure I.26 Fence view of brine concentrations at 80 ka before present for the Michigan Basin Regional Scenario 2 paleoclimate simulation.

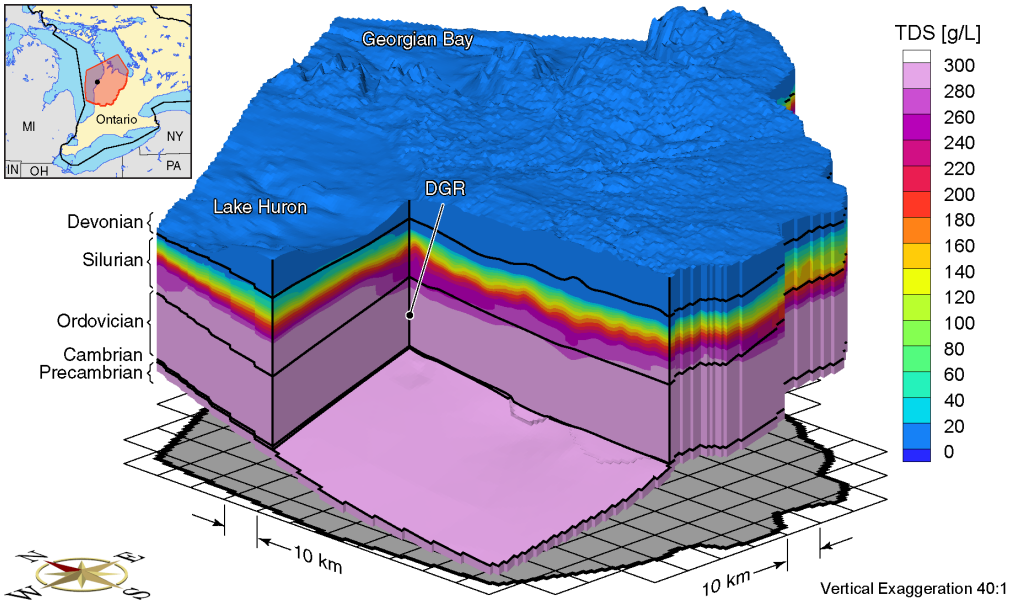

Figure I.27 Block cut view of brine concentrations at 40 ka before present for the Michigan Basin Regional Scenario 2 paleoclimate simulation.

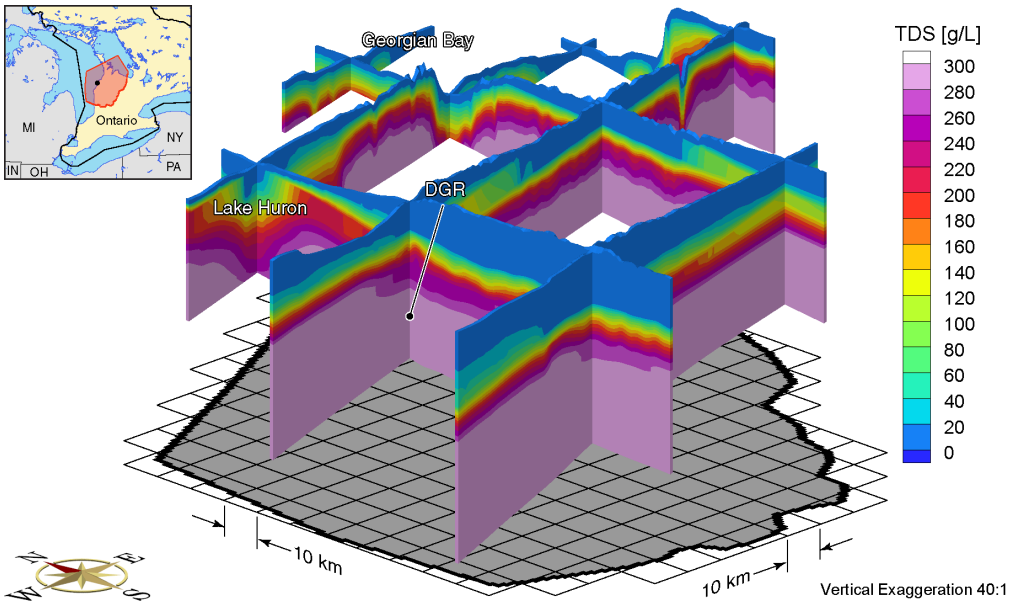

Figure I.28 Fence view of brine concentrations at 40 ka before present for the Michigan Basin Regional Scenario 2 paleoclimate simulation.

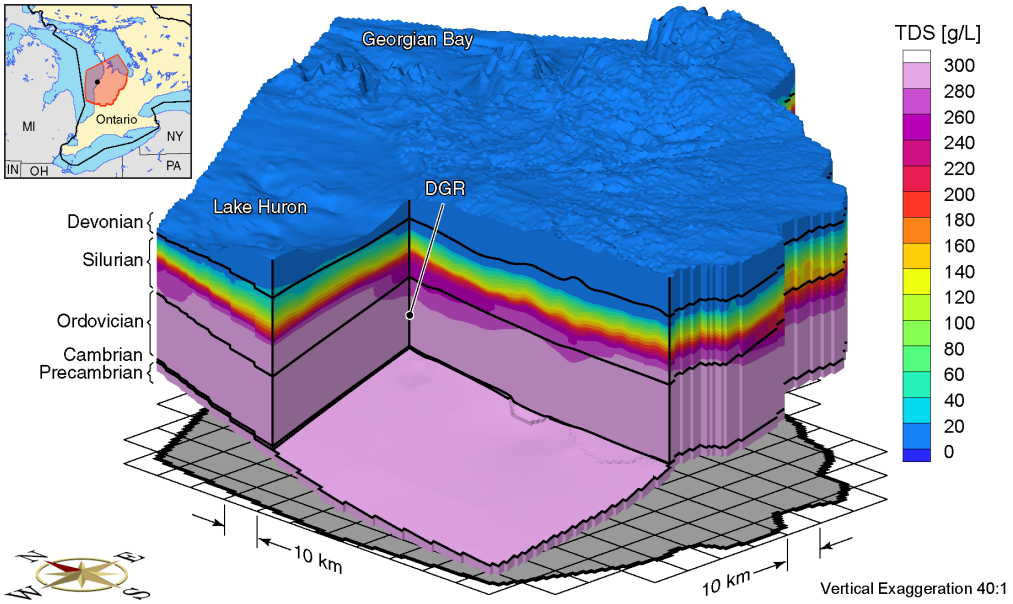

Figure I.29 Block cut view of brine concentrations at present for the Michigan Basin Regional Scenario 2 paleoclimate simulation.

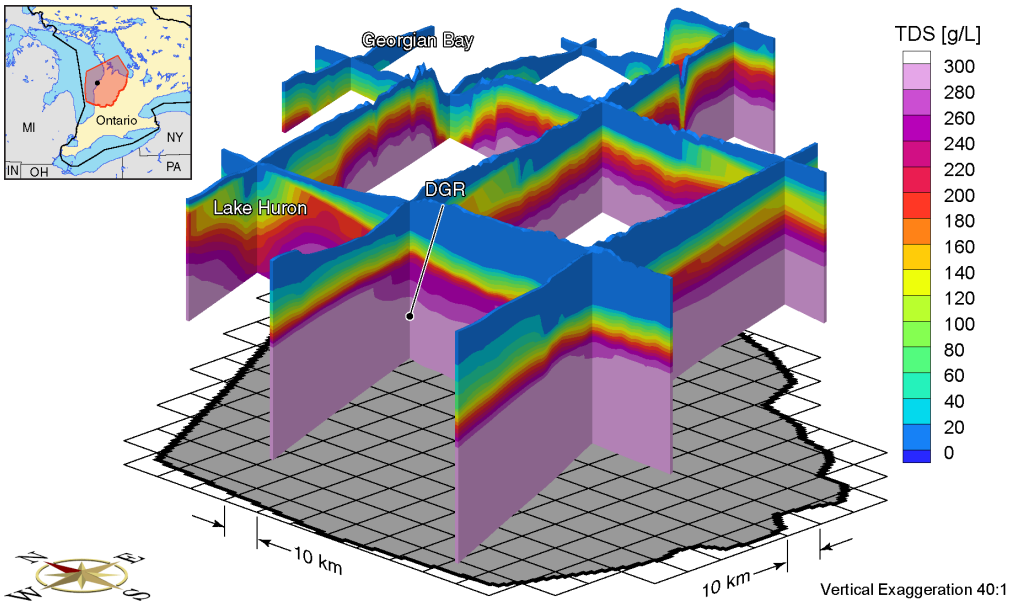

Figure I.30 Fence view of brine concentrations at present for the Michigan Basin Regional Scenario 2 paleoclimate simulation.

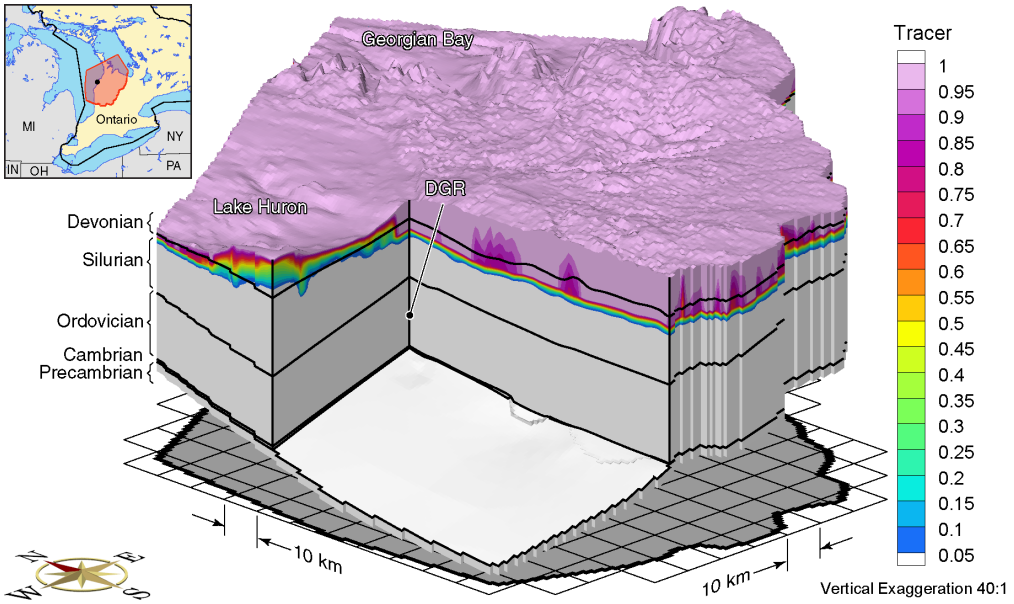

Figure I.31 Block cut view of tracer concentrations at 80 ka before present for the Michigan Basin Regional Scenario 2 paleoclimate simulation.

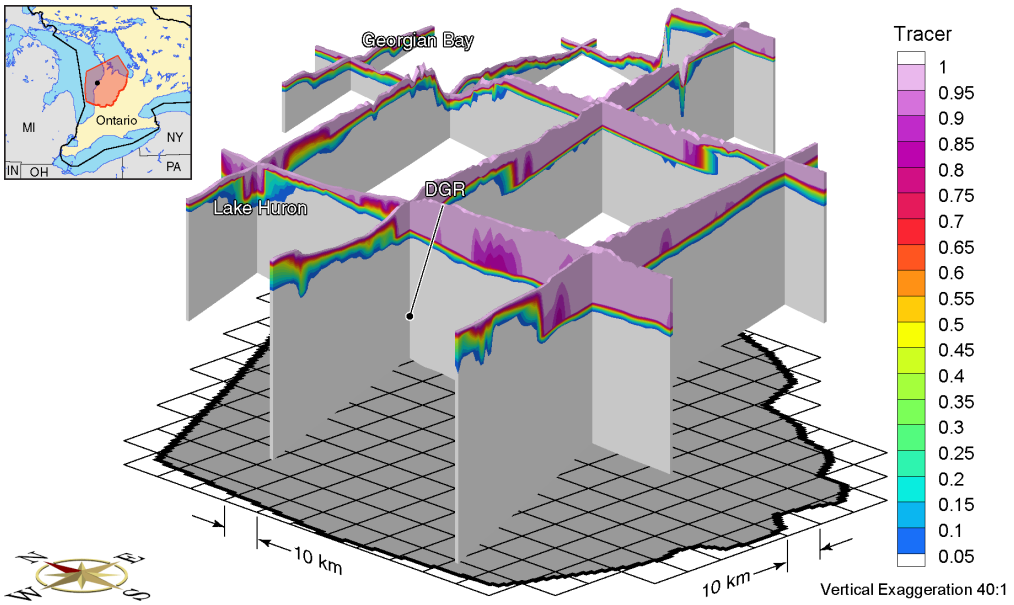

Figure I.32 Fence view of tracer concentrations at 80 ka before present for the Michigan Basin Regional Scenario 2 paleoclimate simulation.

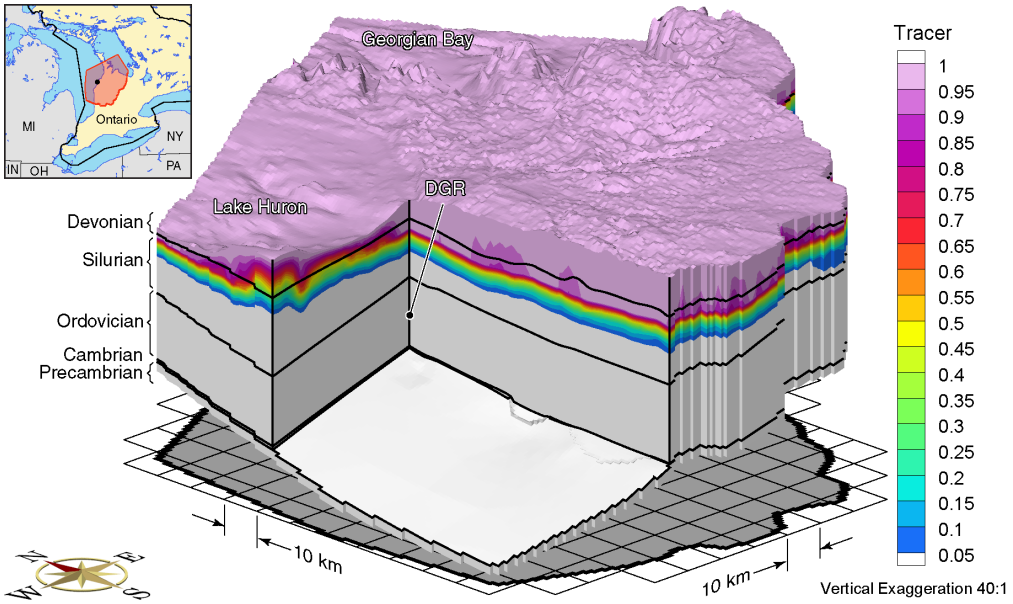

Figure I.33 Block cut view of tracer concentrations at 40 ka before present for the Michigan Basin Regional Scenario 2 paleoclimate simulation.

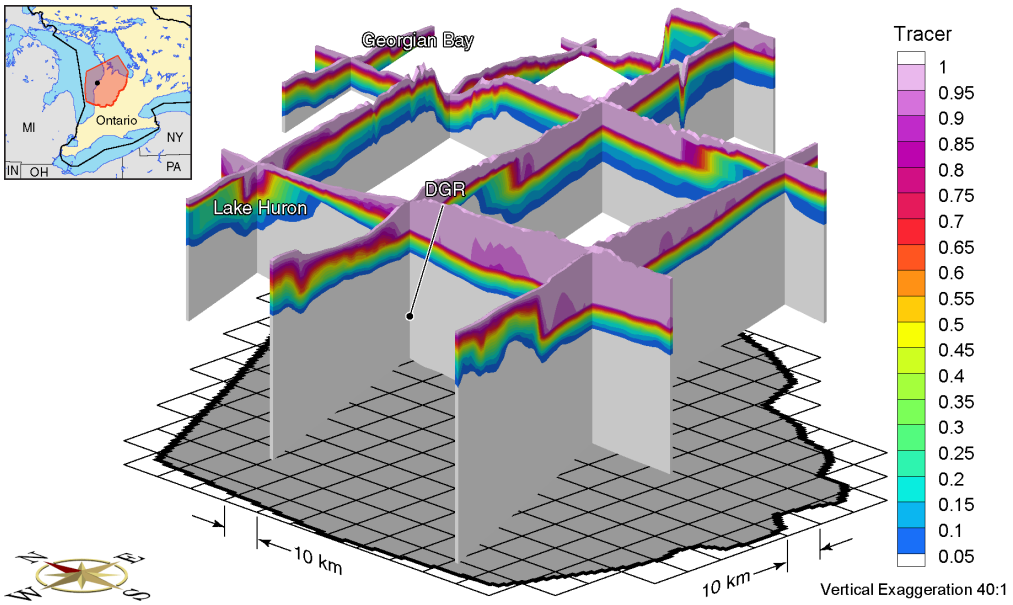

Figure I.34 Fence view of tracer concentrations at 40 ka before present for the Michigan Basin Regional Scenario 2 paleoclimate simulation.

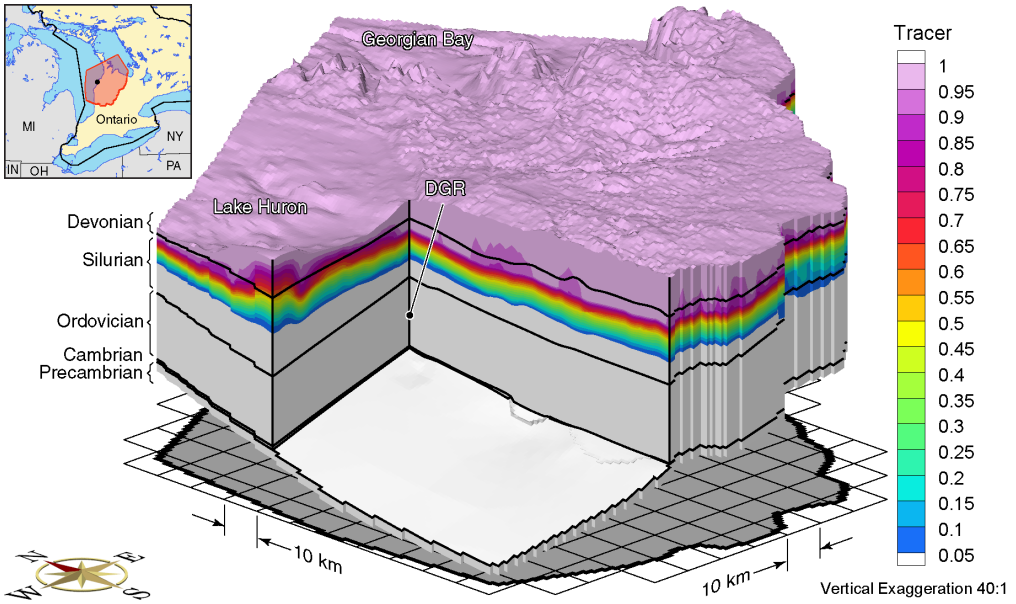

Figure I.35 Block cut view of tracer concentrations at present for the Michigan Basin Regional Scenario 2 paleoclimate simulation.

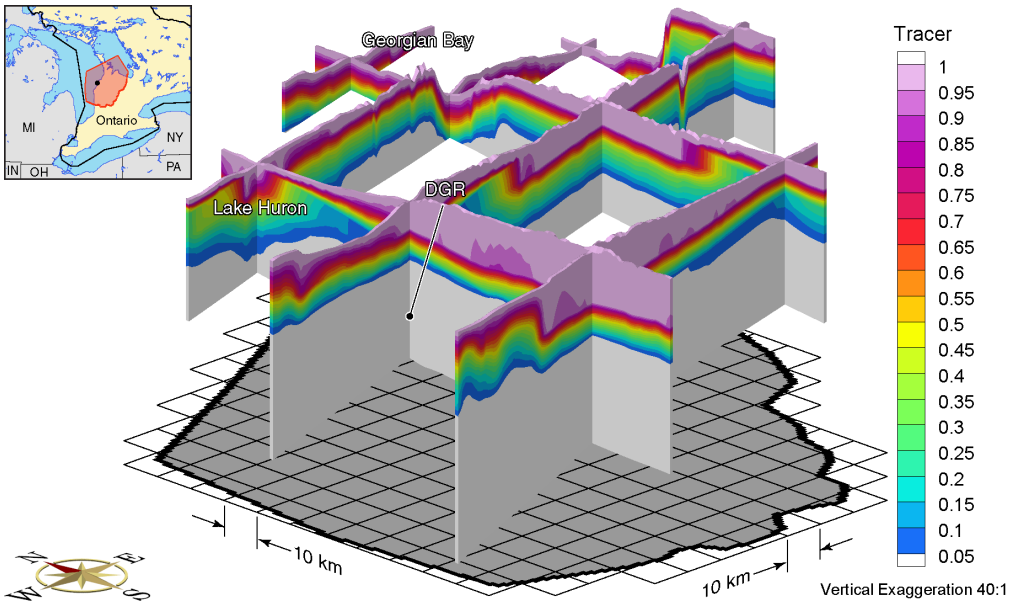

Figure I.36 Fence view of tracer concentrations at present for the Michigan Basin Regional Scenario 2 paleoclimate simulation.

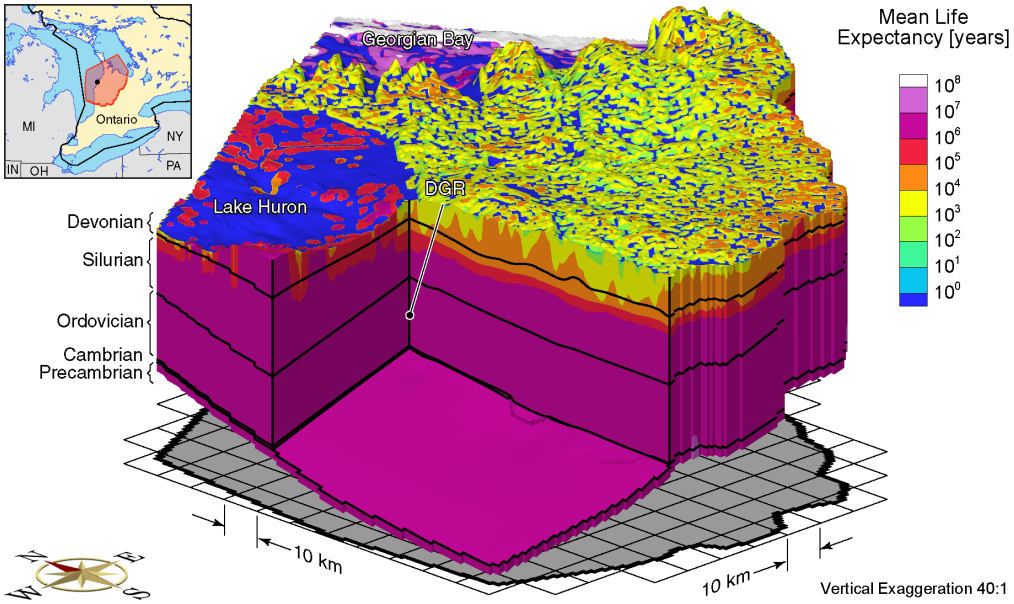

Figure I.37 Block cut view of mean life expectancies at present for the Michigan Basin Regional Scenario 2 paleoclimate simulation.

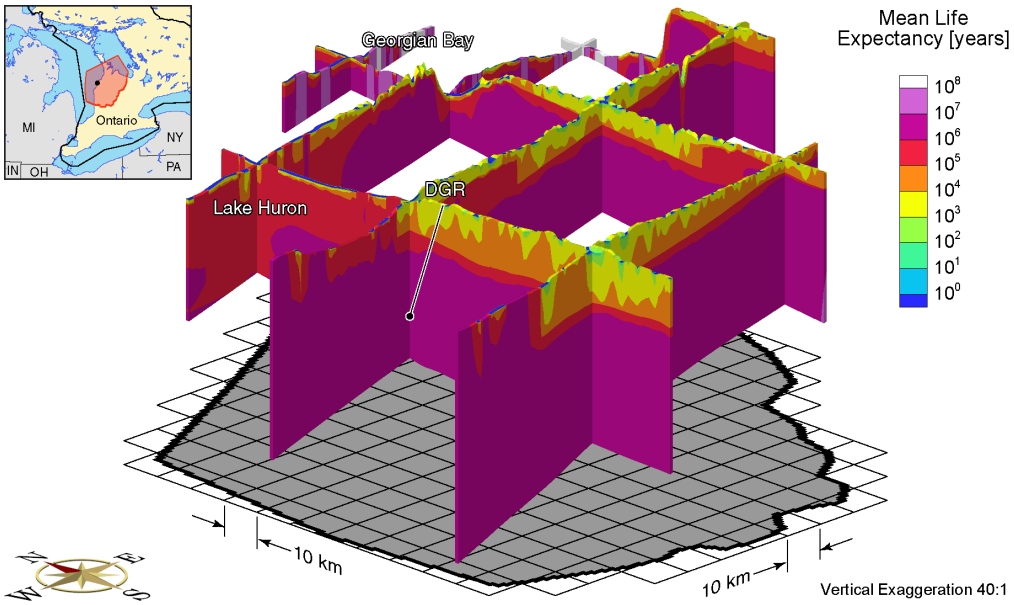

Figure I.38 Fence view of mean life expectancies at present for the Michigan Basin Regional Scenario 2 paleoclimate simulation.

Appendix J

MBR Scenario 3 Paleoclimate Model

All figures related to the Michigan Basin Regional (MBR) Scenario 3 paleoclimate modelling are listed in Table J.1. Block cut view and fence view figures are shown on the same page to facilitate comparison. All results of the 120 ka paleoclimate simulations are shown at times of 80 ka before present, 40 ka before present, and at present.

Table J.1 List of Michigan Basin Regional Scenario 3 paleoclimate simulation figures.

Parameters	Time Before Present					
	80 ka		40 ka		Present	
	Block Cut	Fence	Block Cut	Fence	Block Cut	Fence
Freshwater Heads	J.1	J.2	J.3	J.4	J.5	J.6
Environmental Heads	J.7	J.8	J.9	J.10	J.11	J.12
Pore Velocity Magnitudes	J.13	J.14	J.15	J.16	J.17	J.18
Ratio of Vertical Pore Velocities to Pore Velocity Magnitudes	J.19	J.20	J.21	J.22	J.23	J.24
Brine Concentrations	J.25	J.26	J.27	J.28	J.29	J.30
Tracer Concentrations	J.31	J.32	J.33	J.34	J.35	J.36
Mean Life Expectancies	—	—	—	—	J.37	J.38

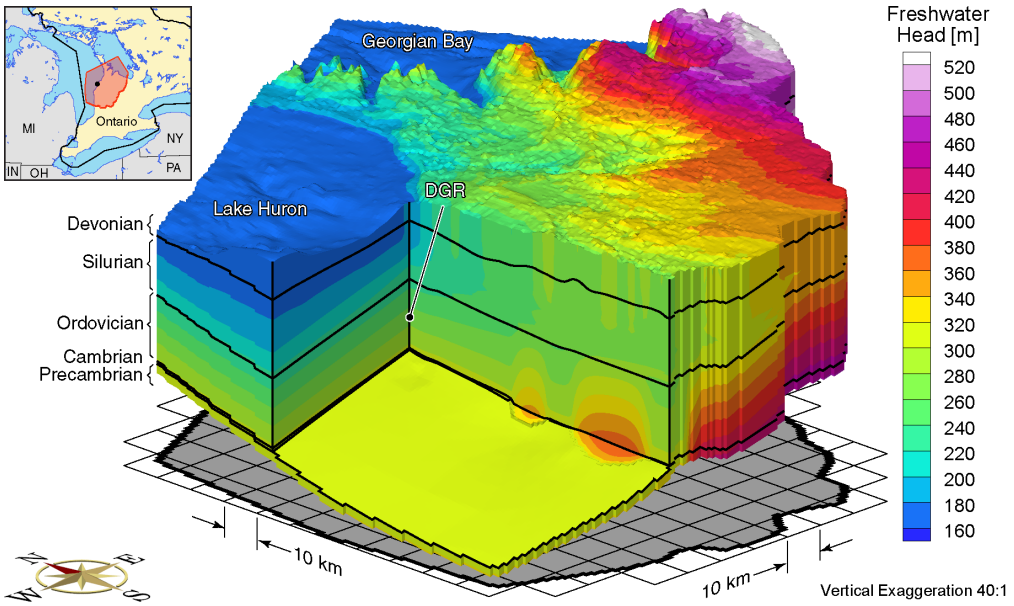

Figure J.1 Block cut view of freshwater heads at 80 ka before present for the Michigan Basin Regional Scenario 3 paleoclimate simulation.

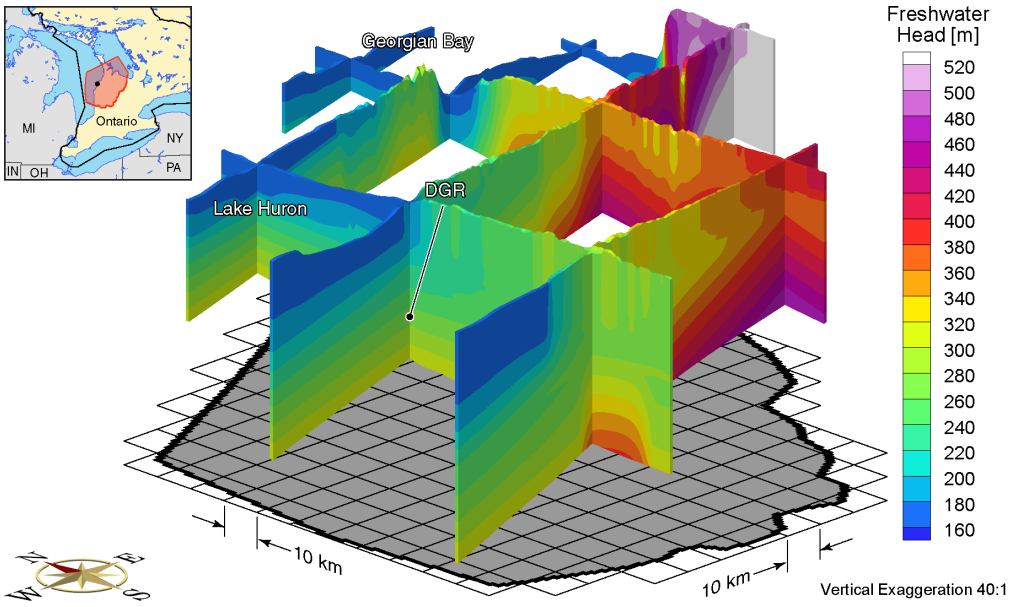

Figure J.2 Fence view of freshwater heads at 80 ka before present for the Michigan Basin Regional Scenario 3 paleoclimate simulation.

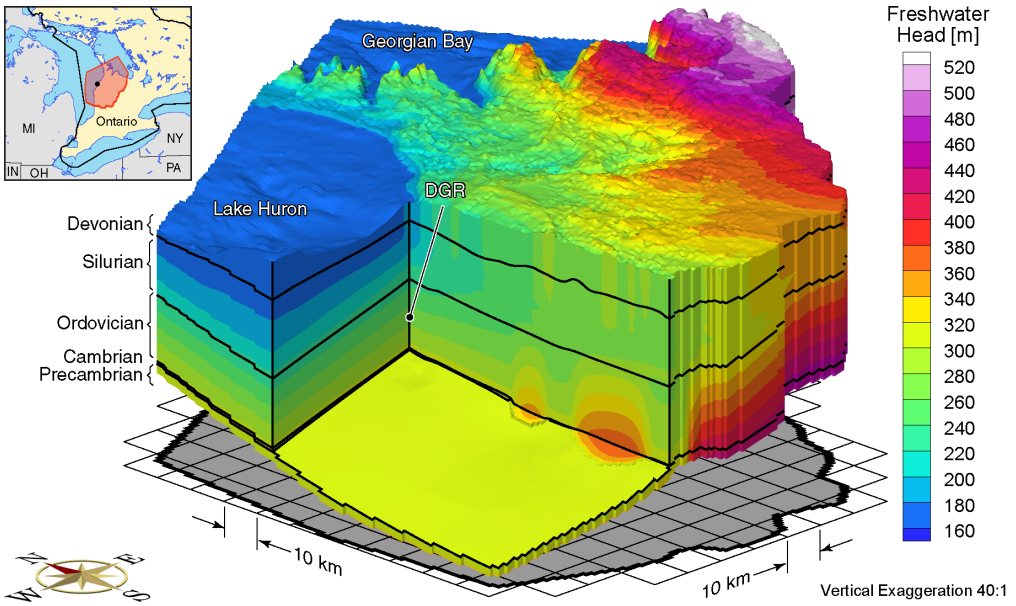

Figure J.3 Block cut view of freshwater heads at 40 ka before present for the Michigan Basin Regional Scenario 3 paleoclimate simulation.

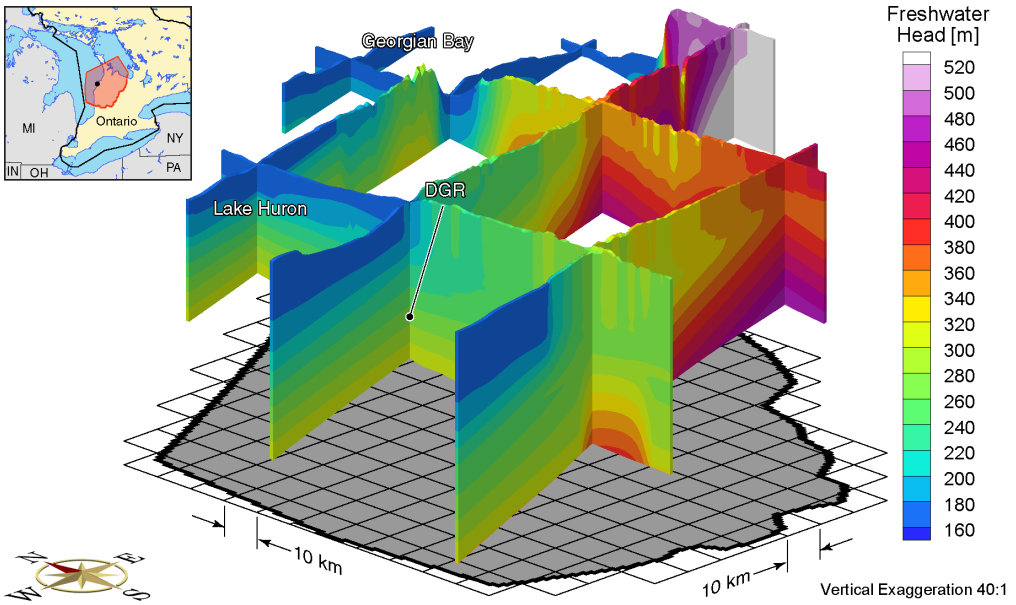

Figure J.4 Fence view of freshwater heads at 40 ka before present for the Michigan Basin Regional Scenario 3 paleoclimate simulation.

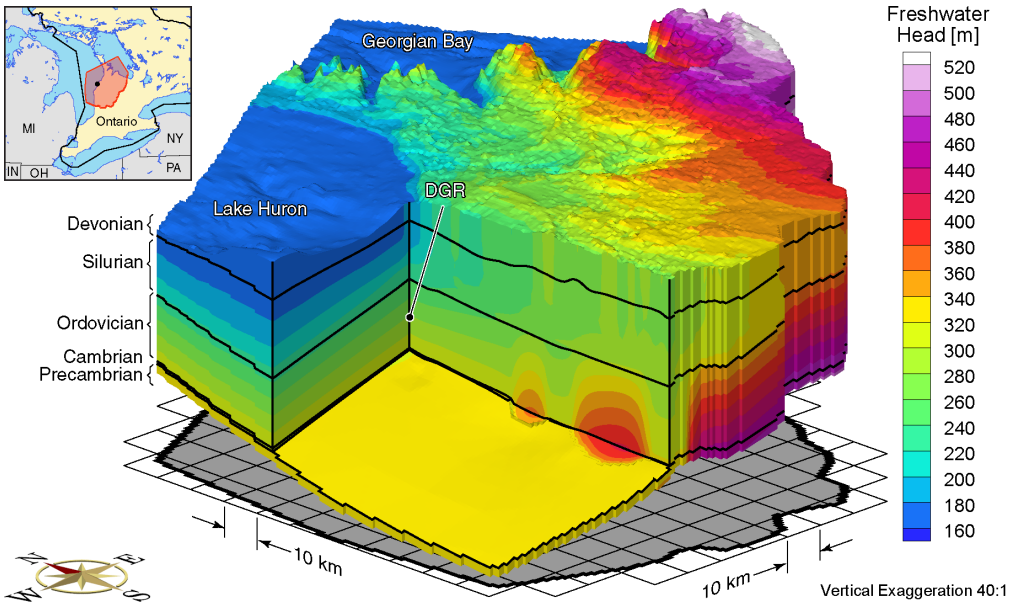

Figure J.5 Block cut view of freshwater heads at present for the Michigan Basin Regional Scenario 3 paleoclimate simulation.

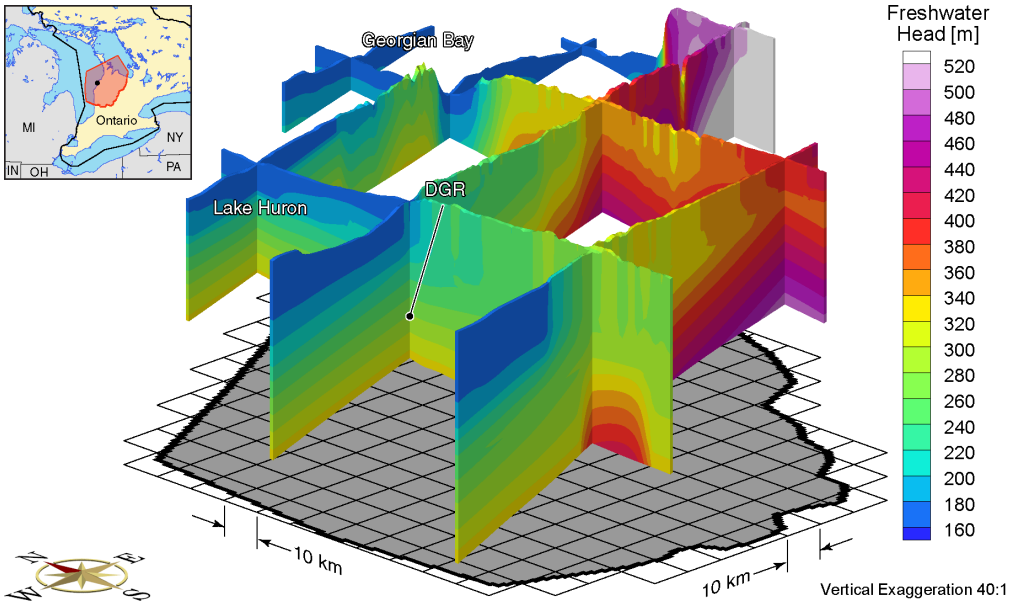

Figure J.6 Fence view of freshwater heads at present for the Michigan Basin Regional Scenario 3 paleoclimate simulation.

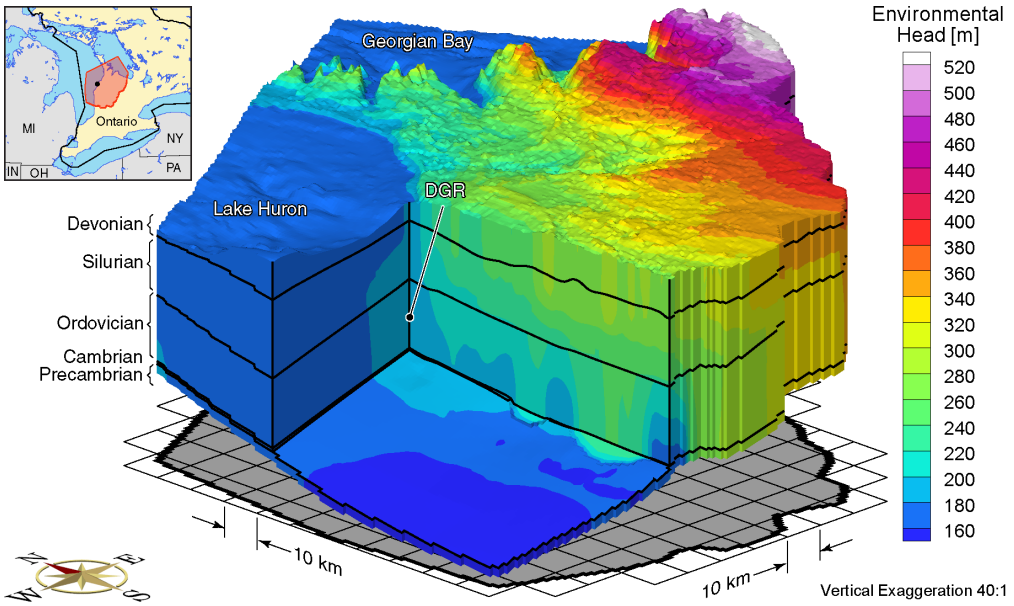

Figure J.7 Block cut view of environmental heads at 80 ka before present for the Michigan Basin Regional Scenario 3 paleoclimate simulation.

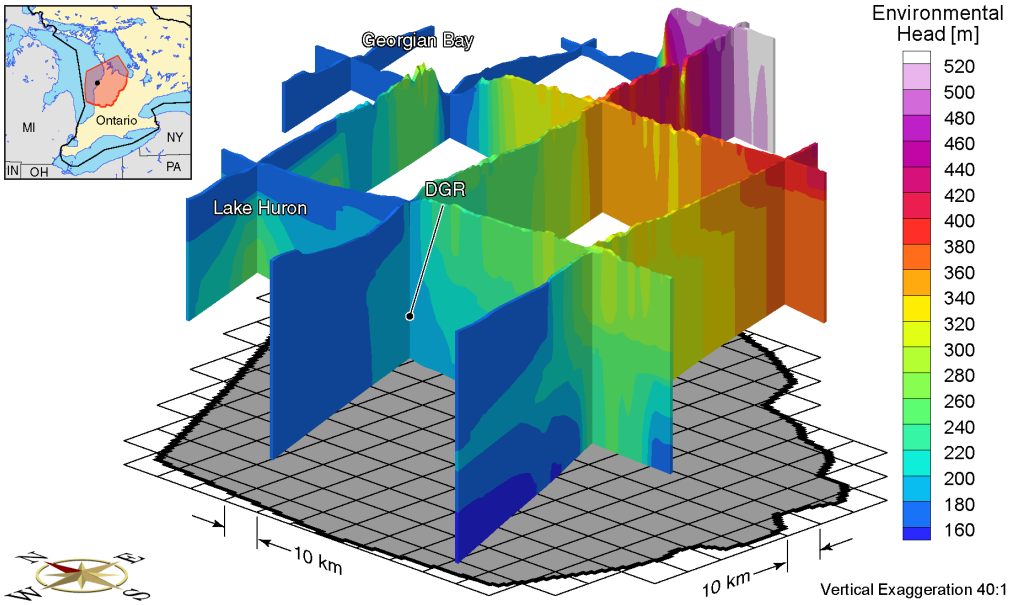

Figure J.8 Fence view of environmental heads at 80 ka before present for the Michigan Basin Regional Scenario 3 paleoclimate simulation.

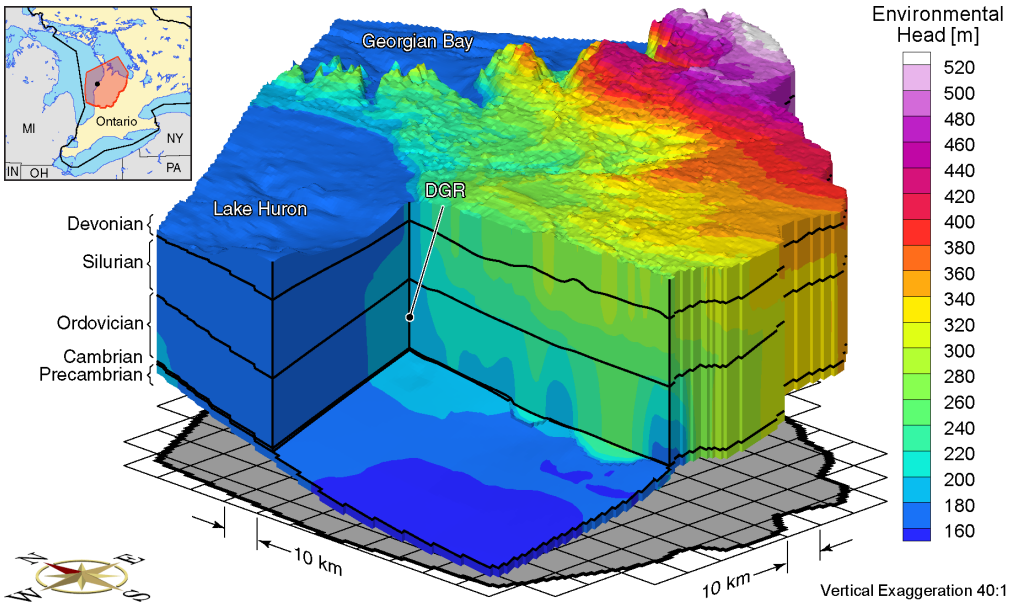

Figure J.9 Block cut view of environmental heads at 40 ka before present for the Michigan Basin Regional Scenario 3 paleoclimate simulation.

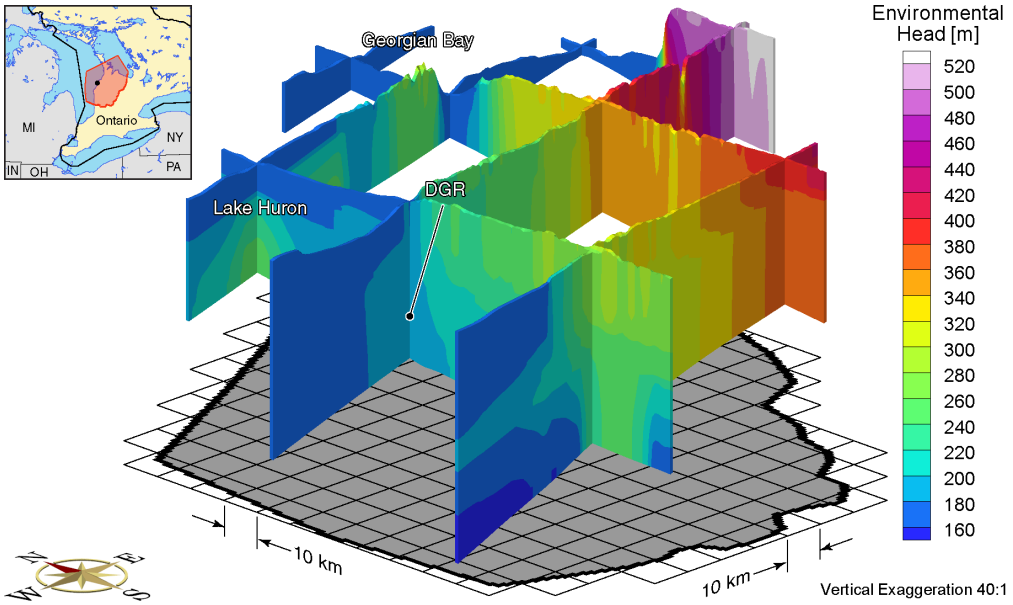

Figure J.10 Fence view of environmental heads at 40 ka before present for the Michigan Basin Regional Scenario 3 paleoclimate simulation.

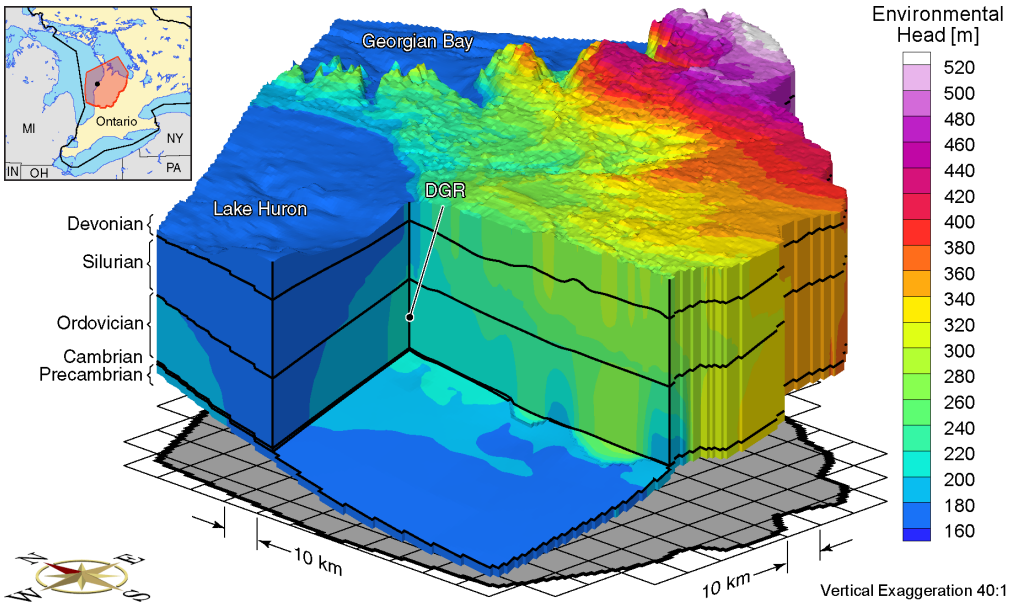

Figure J.11 Block cut view of environmental heads at present for the Michigan Basin Regional Scenario 3 paleoclimate simulation.

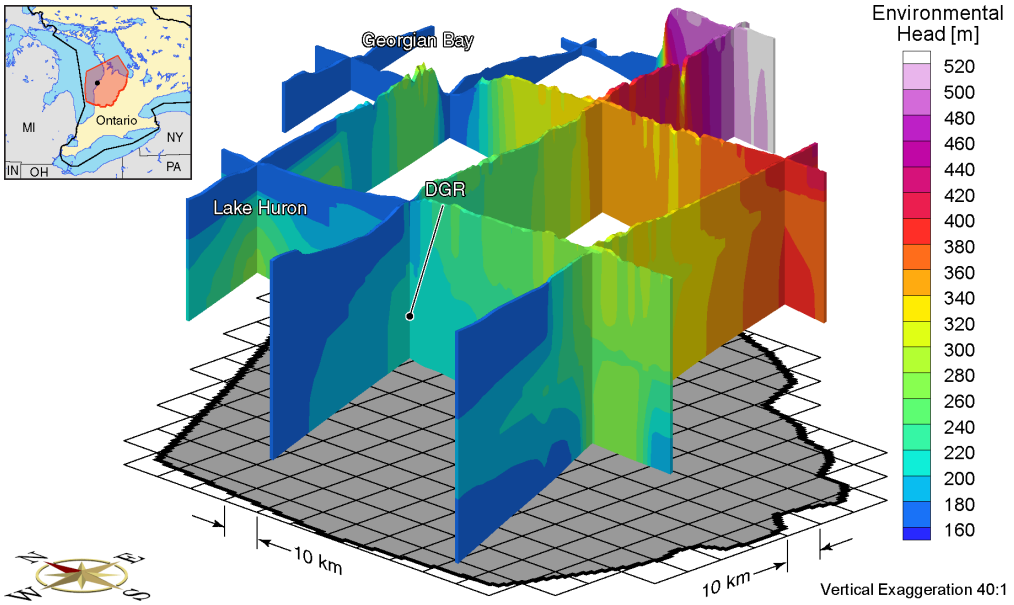

Figure J.12 Fence view of environmental heads at present for the Michigan Basin Regional Scenario 3 paleoclimate simulation.

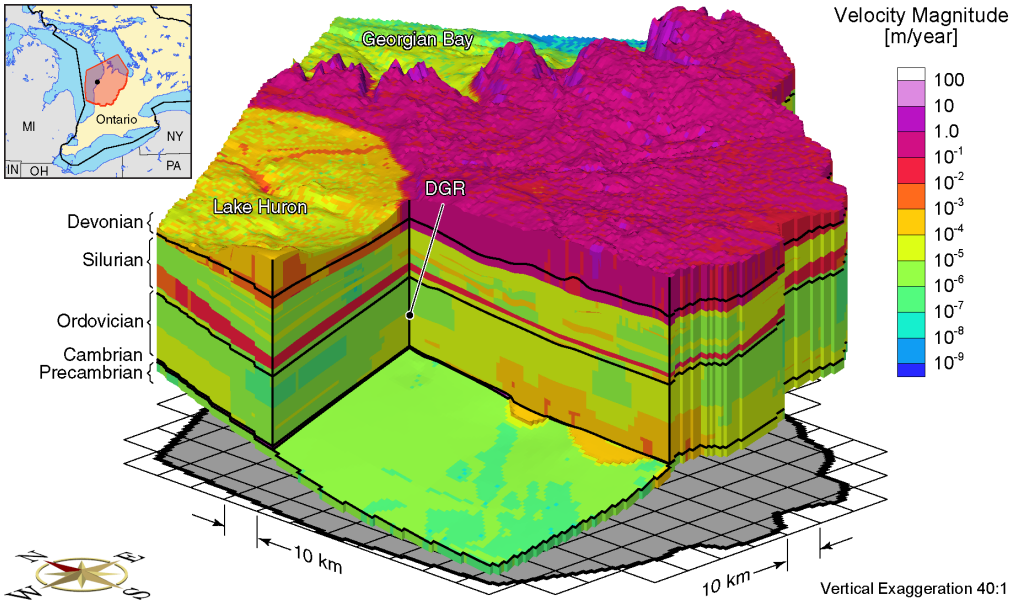

Figure J.13 Block cut view of pore velocity magnitudes at 80 ka before present for the Michigan Basin Regional Scenario 3 paleoclimate simulation.

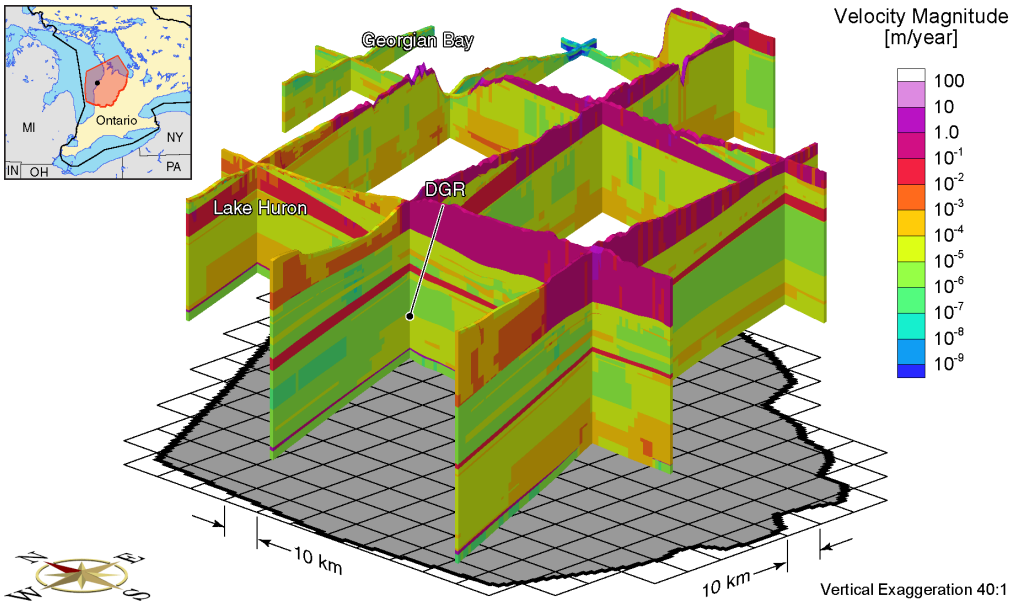

Figure J.14 Fence view of pore velocity magnitudes at 80 ka before present for the Michigan Basin Regional Scenario 3 paleoclimate simulation.

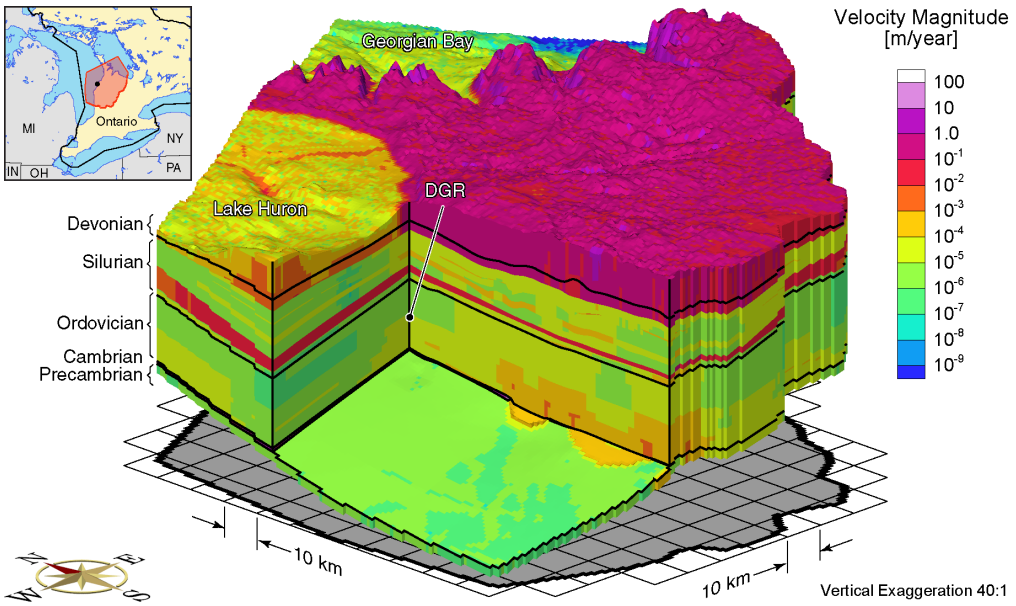

Figure J.15 Block cut view of pore velocity magnitudes at 40 ka before present for the Michigan Basin Regional Scenario 3 paleoclimate simulation.

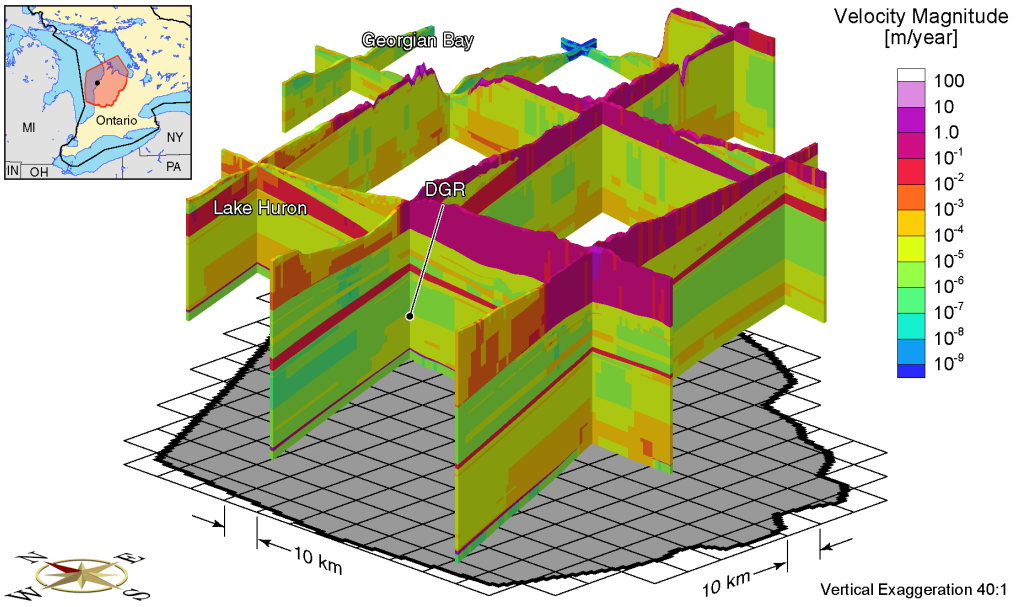

Figure J.16 Fence view of pore velocity magnitudes at 40 ka before present for the Michigan Basin Regional Scenario 3 paleoclimate simulation.

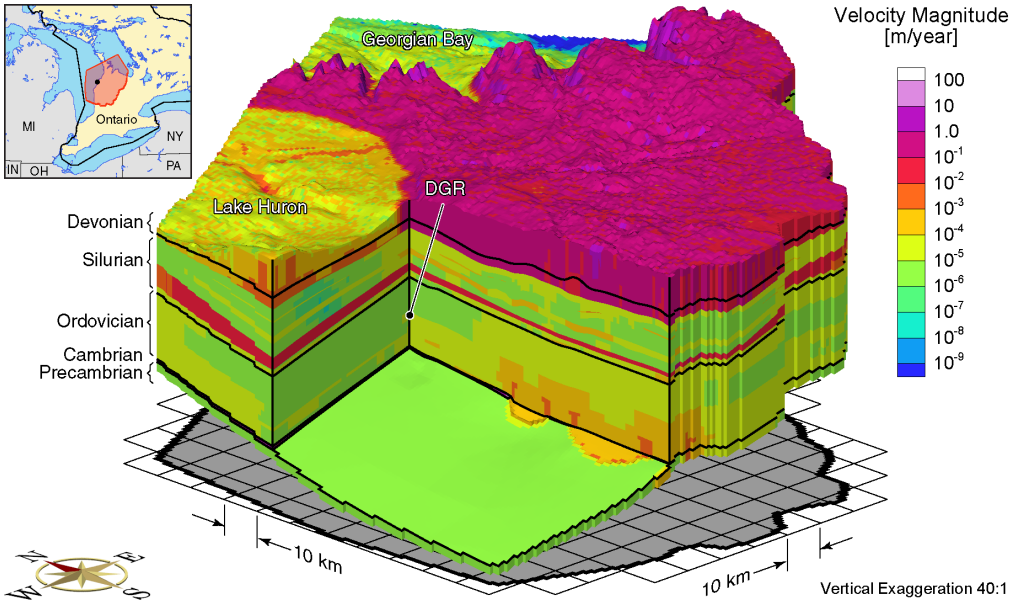

Figure J.17 Block cut view of pore velocity magnitudes at present for the Michigan Basin Regional Scenario 3 paleoclimate simulation.

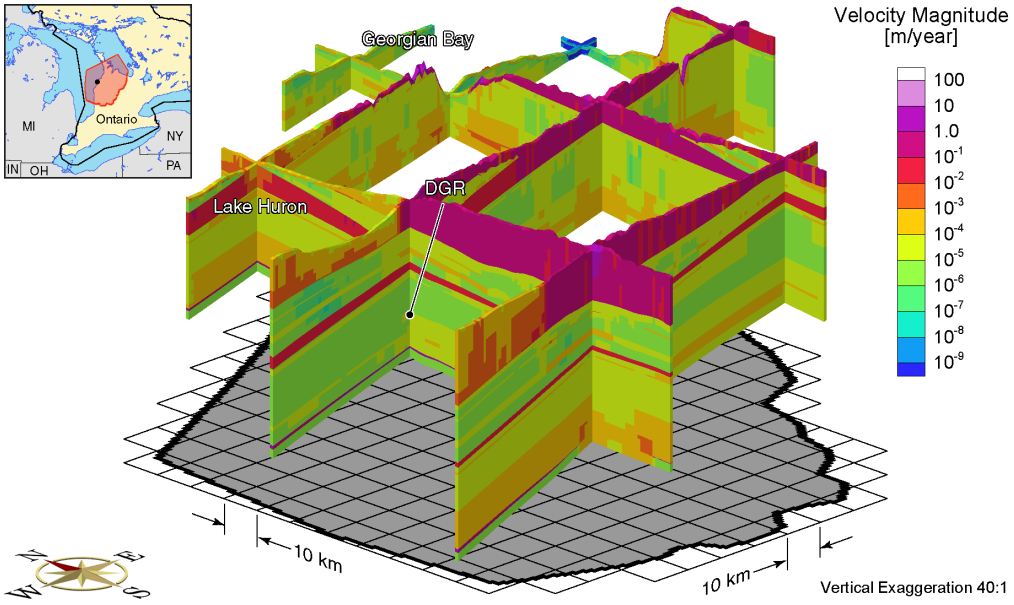

Figure J.18 Fence view of pore velocity magnitudes at present for the Michigan Basin Regional Scenario 3 paleoclimate simulation.

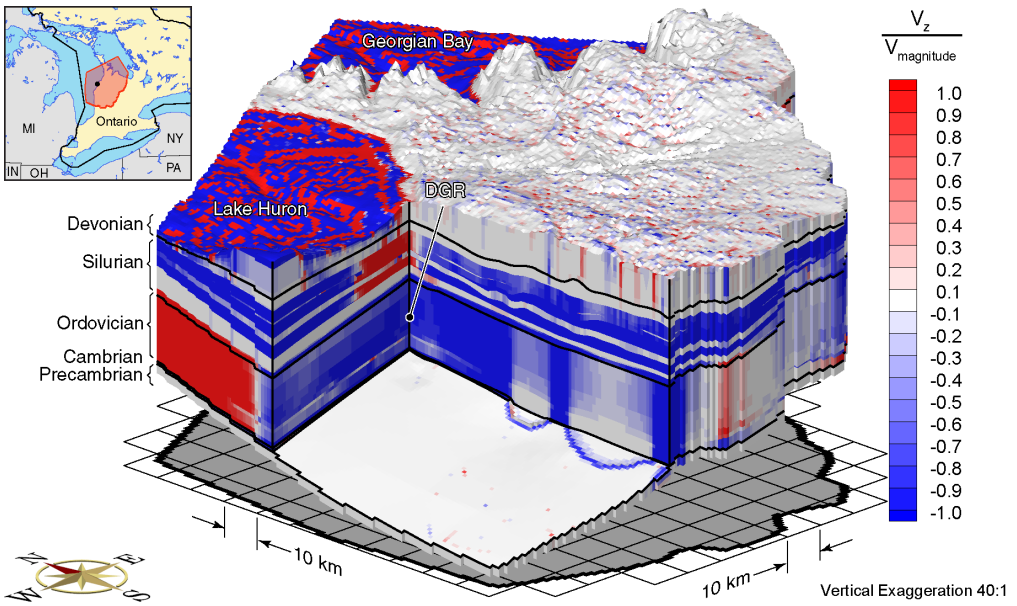

Figure J.19 Block cut view of ratio of vertical pore velocities to pore velocity magnitudes at 80 ka before present for the Michigan Basin Regional Scenario 3 paleoclimate simulation.

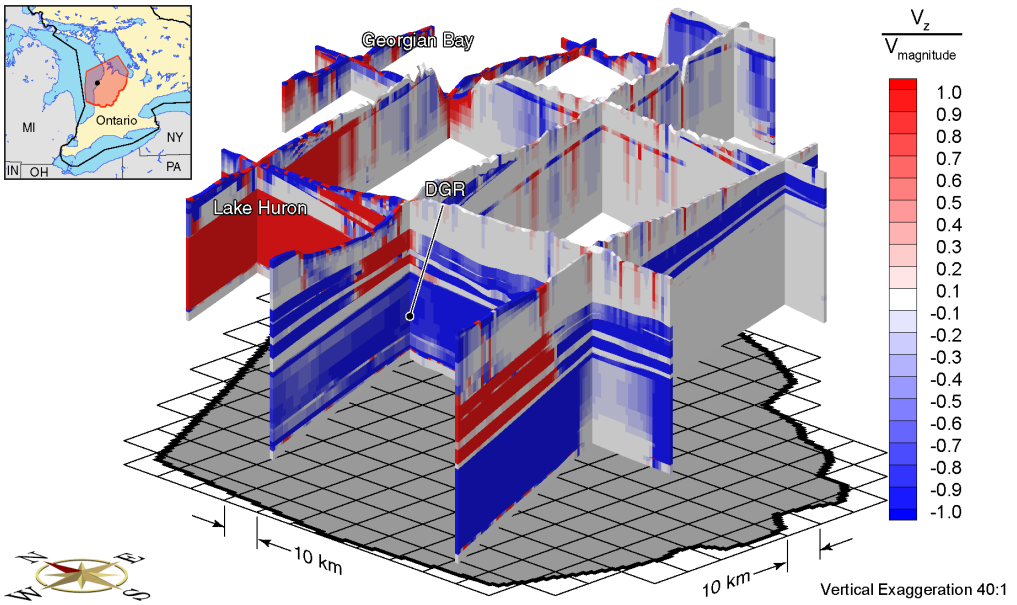

Figure J.20 Fence view of ratio of vertical pore velocities to pore velocity magnitudes at 80 ka before present for the Michigan Basin Regional Scenario 3 paleoclimate simulation.

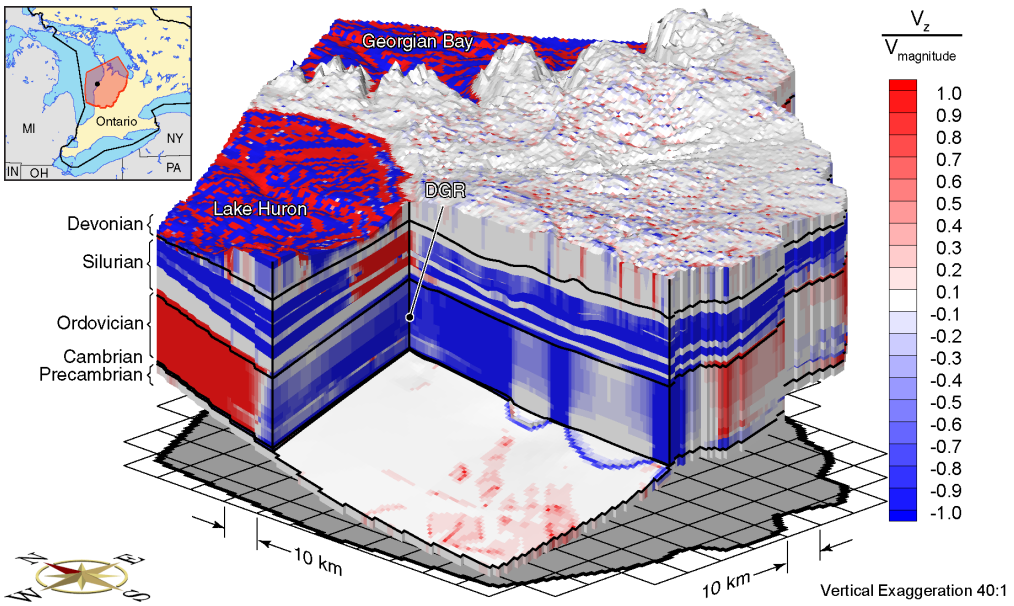

Figure J.21 Block cut view of ratio of vertical pore velocities to pore velocity magnitudes at 40 ka before present for the Michigan Basin Regional Scenario 3 paleoclimate simulation.

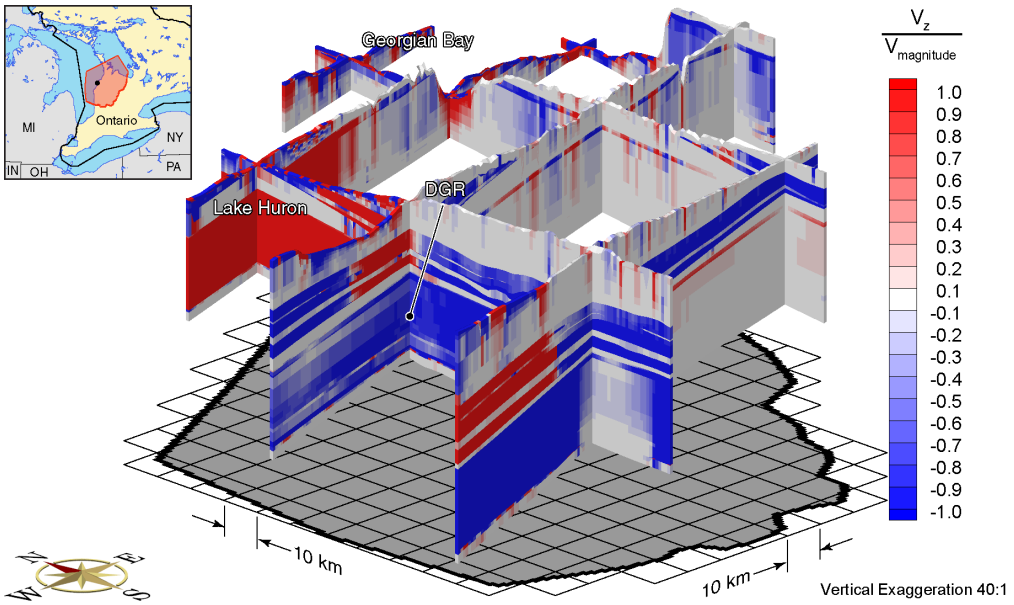

Figure J.22 Fence view of ratio of vertical pore velocities to pore velocity magnitudes at 40 ka before present for the Michigan Basin Regional Scenario 3 paleoclimate simulation.

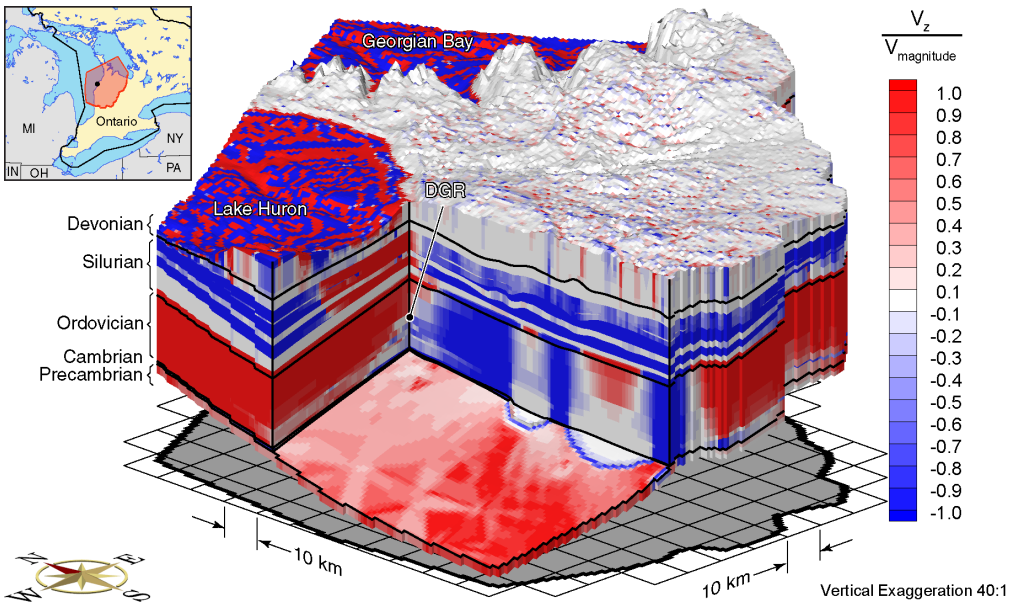

Figure J.23 Block cut view of ratio of vertical pore velocities to pore velocity magnitudes at present for the Michigan Basin Regional Scenario 3 paleoclimate simulation.

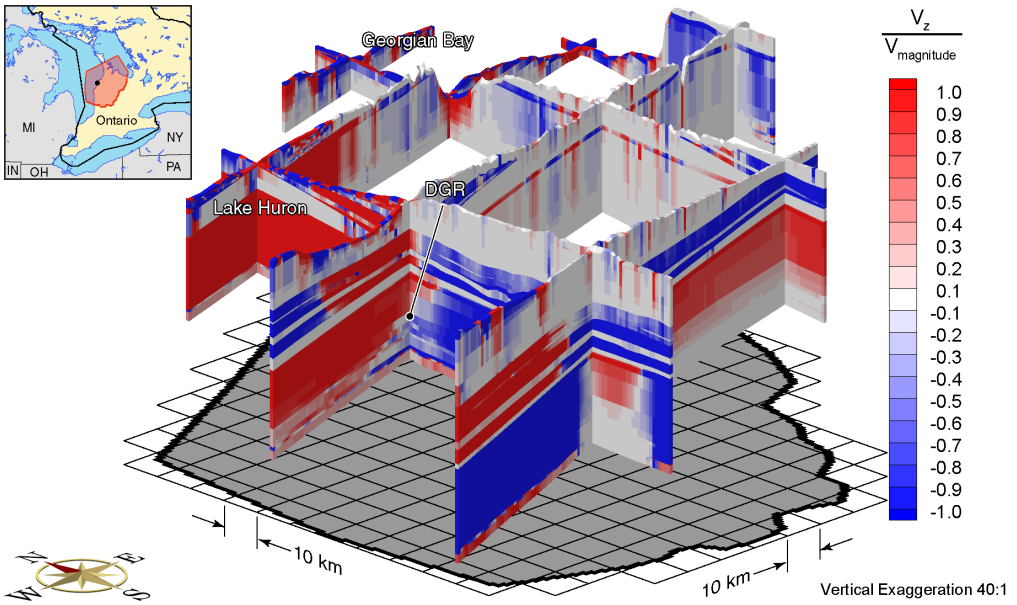

Figure J.24 Fence view of ratio of vertical pore velocities to pore velocity magnitudes at present for the Michigan Basin Regional Scenario 3 paleoclimate simulation.

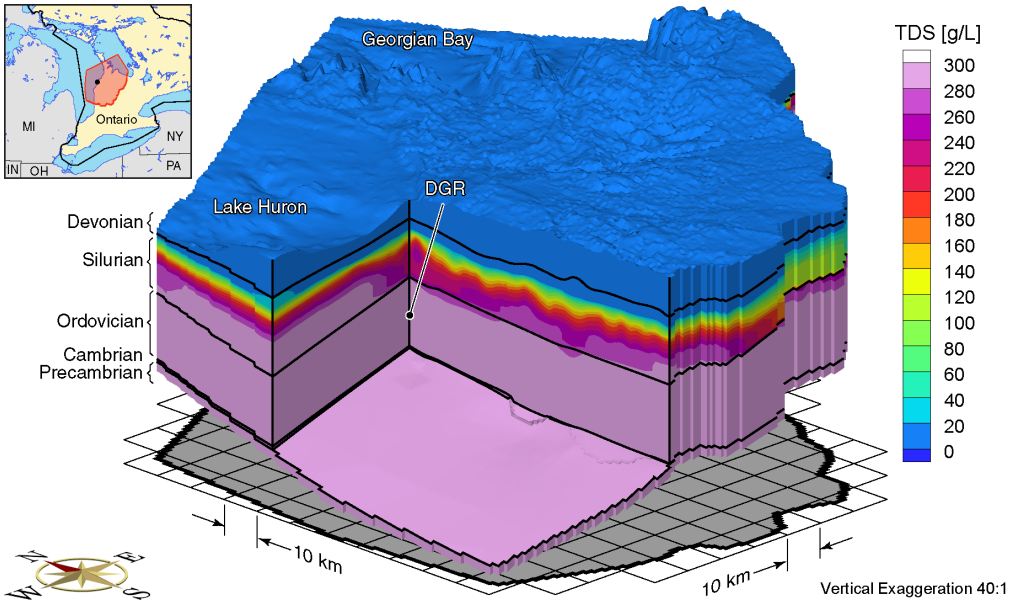

Figure J.25 Block cut view of brine concentrations at 80 ka before present for the Michigan Basin Regional Scenario 3 paleoclimate simulation.

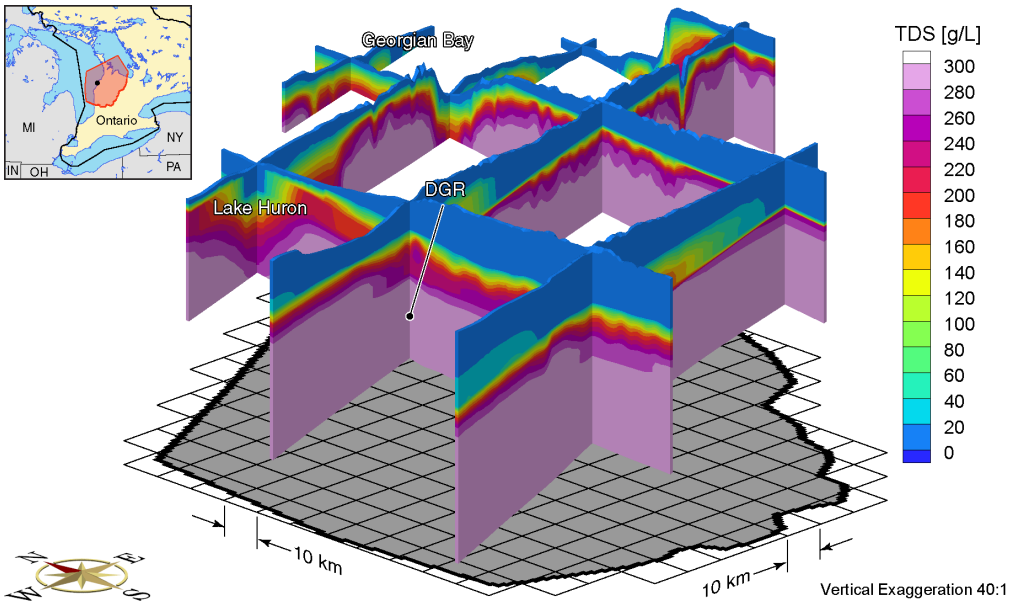

Figure J.26 Fence view of brine concentrations at 80 ka before present for the Michigan Basin Regional Scenario 3 paleoclimate simulation.

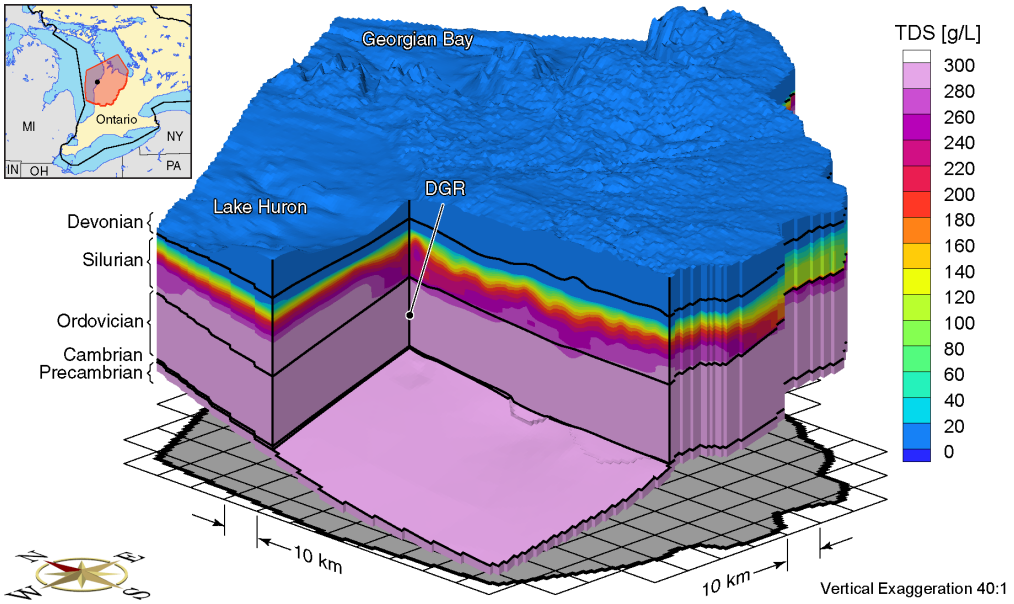

Figure J.27 Block cut view of brine concentrations at 40 ka before present for the Michigan Basin Regional Scenario 3 paleoclimate simulation.

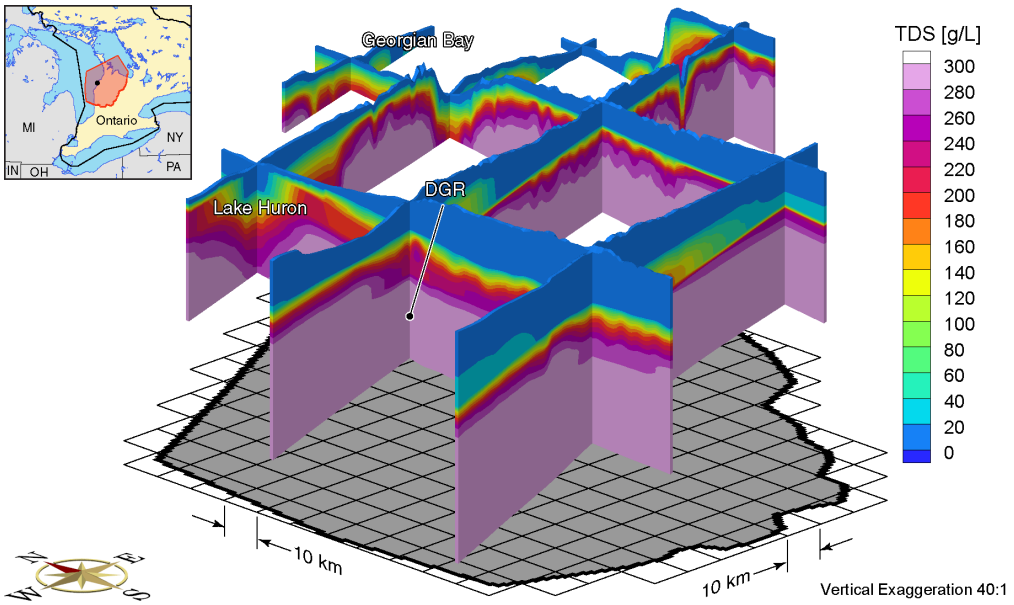

Figure J.28 Fence view of brine concentrations at 40 ka before present for the Michigan Basin Regional Scenario 3 paleoclimate simulation.

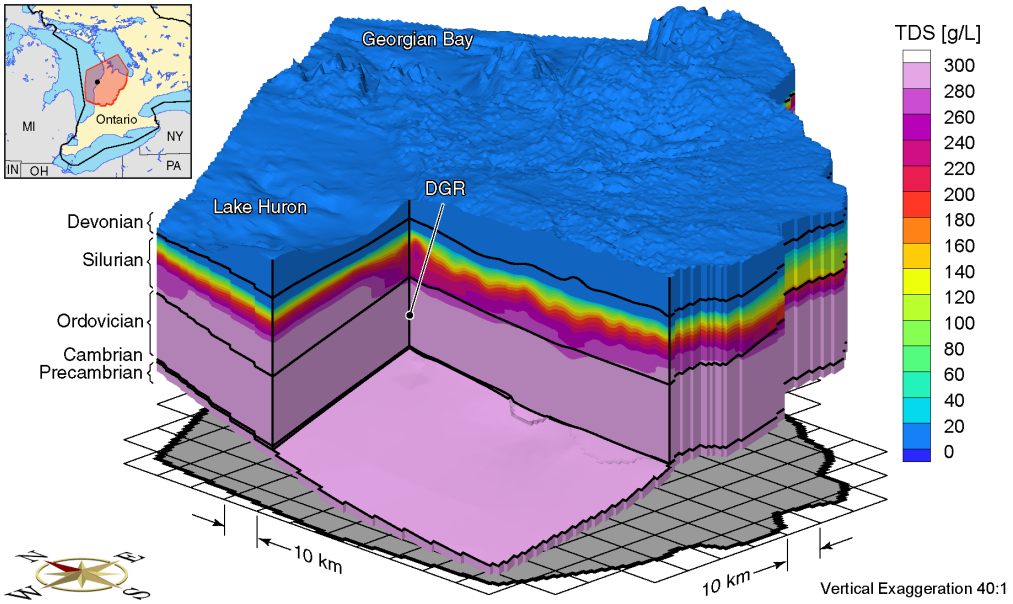

Figure J.29 Block cut view of brine concentrations at present for the Michigan Basin Regional Scenario 3 paleoclimate simulation.

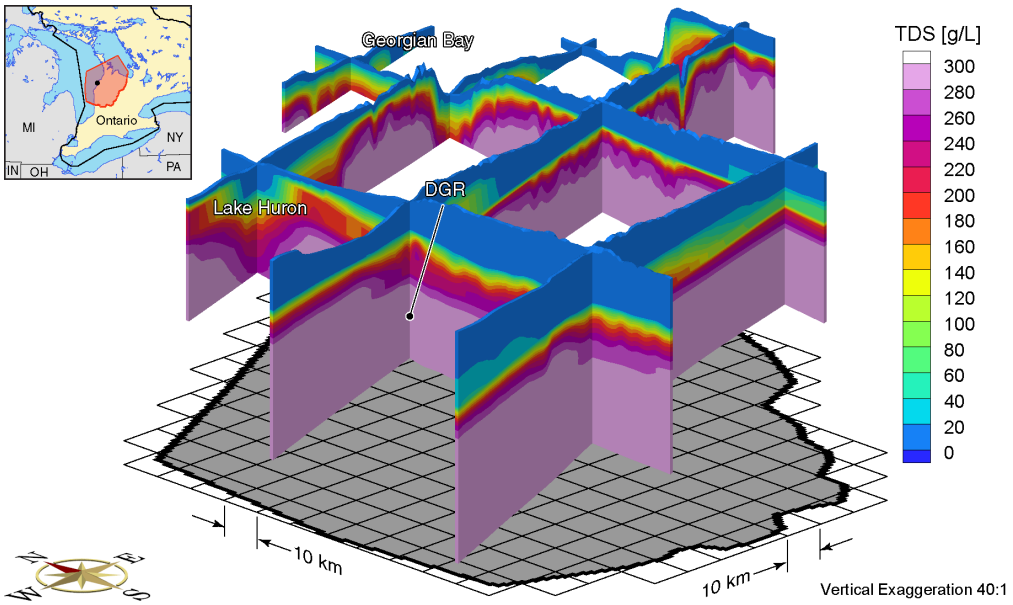

Figure J.30 Fence view of brine concentrations at present for the Michigan Basin Regional Scenario 3 paleoclimate simulation.

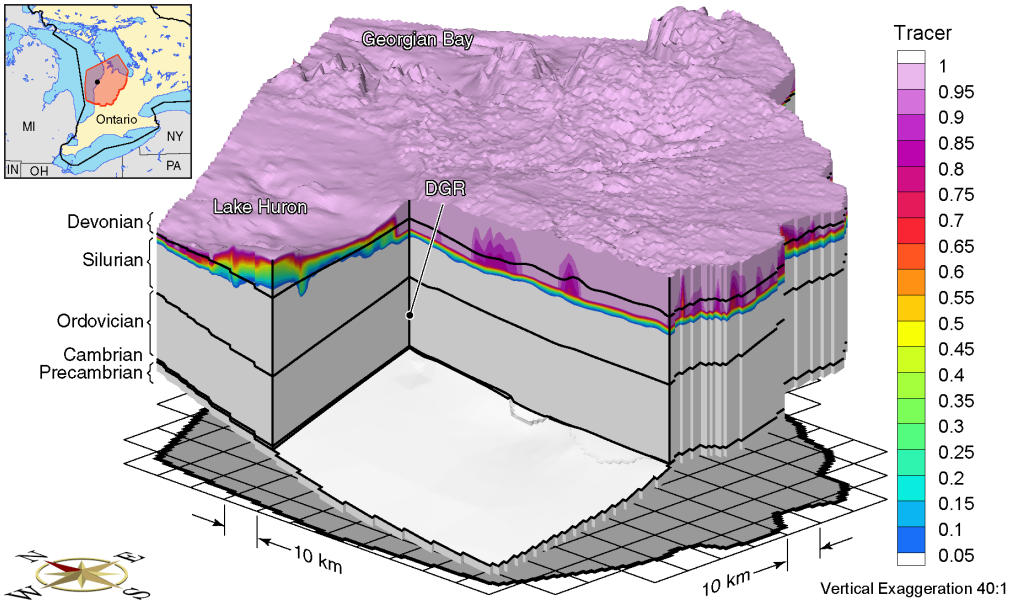

Figure J.31 Block cut view of tracer concentrations at 80 ka before present for the Michigan Basin Regional Scenario 3 paleoclimate simulation.

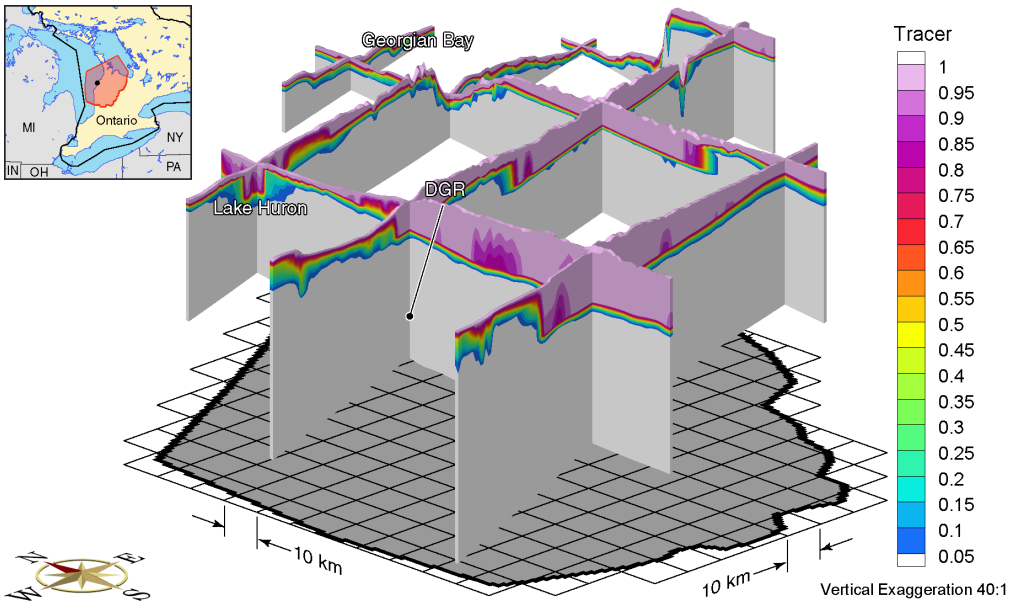

Figure J.32 Fence view of tracer concentrations at 80 ka before present for the Michigan Basin Regional Scenario 3 paleoclimate simulation.

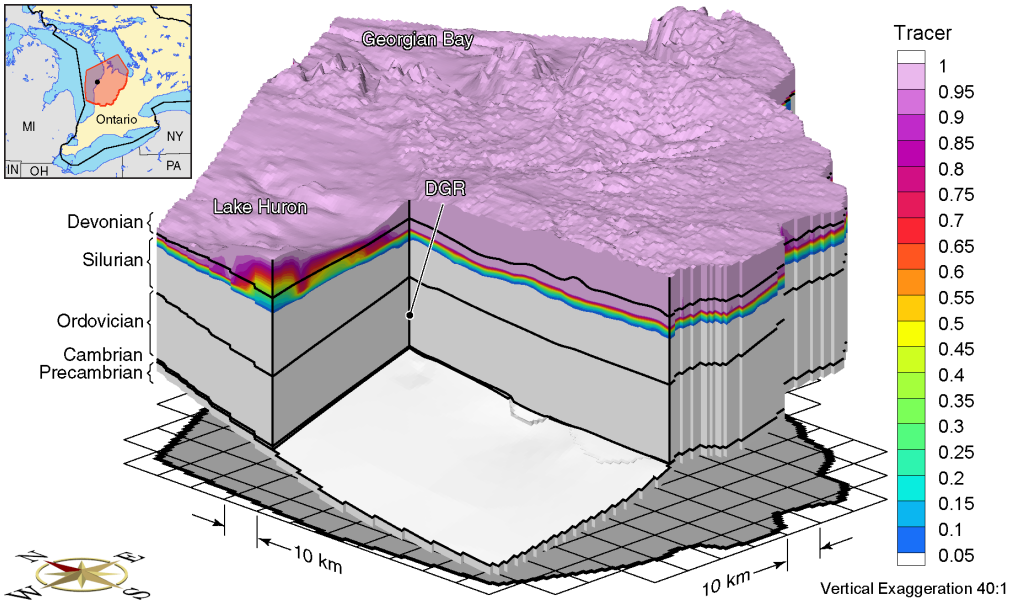

Figure J.33 Block cut view of tracer concentrations at 40 ka before present for the Michigan Basin Regional Scenario 3 paleoclimate simulation.

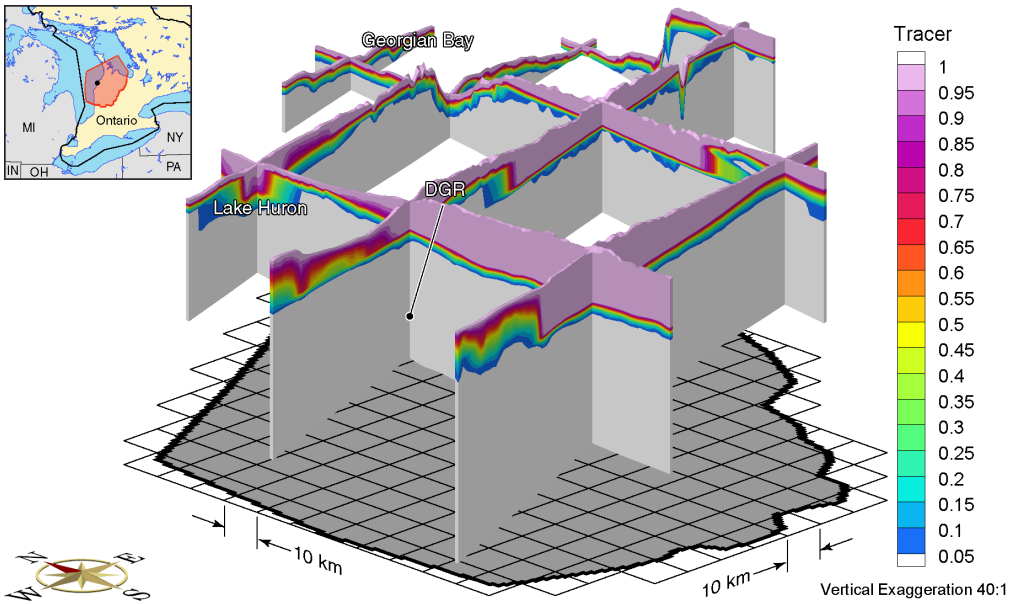

Figure J.34 Fence view of tracer concentrations at 40 ka before present for the Michigan Basin Regional Scenario 3 paleoclimate simulation.

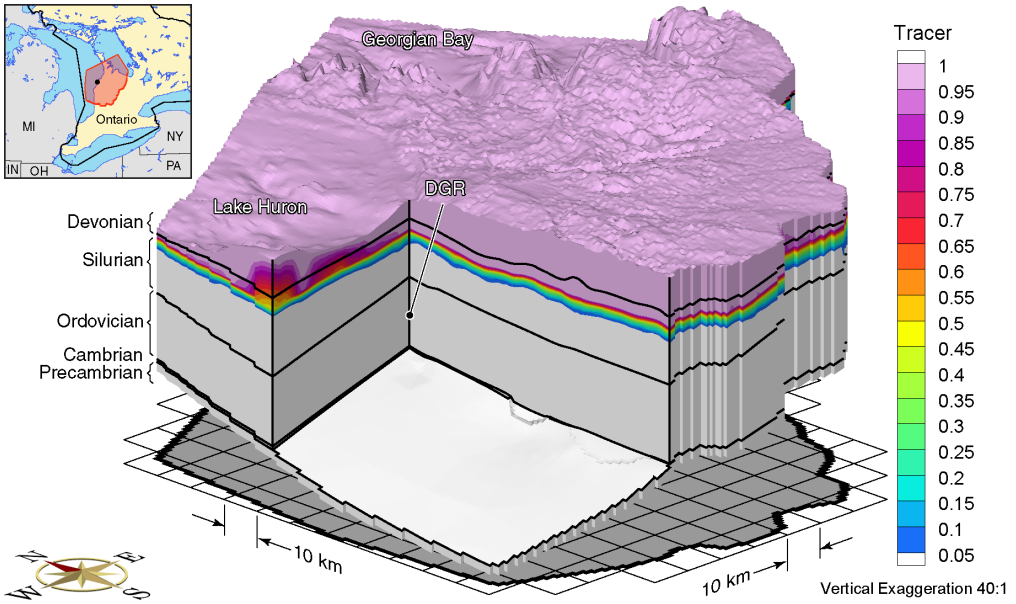

Figure J.35 Block cut view of tracer concentrations at present for the Michigan Basin Regional Scenario 3 paleoclimate simulation.

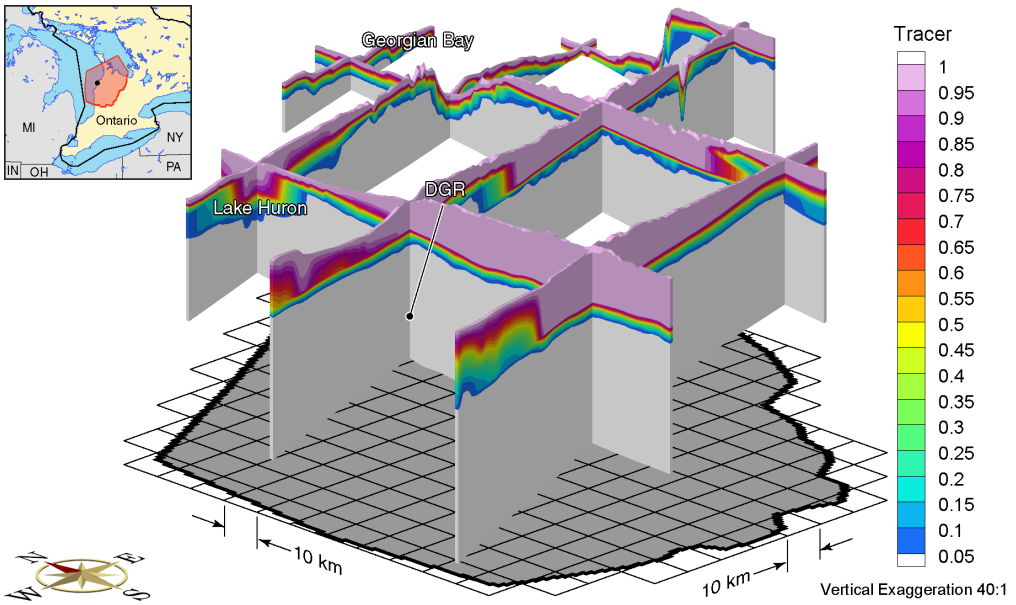

Figure J.36 Fence view of tracer concentrations at present for the Michigan Basin Regional Scenario 3 paleoclimate simulation.

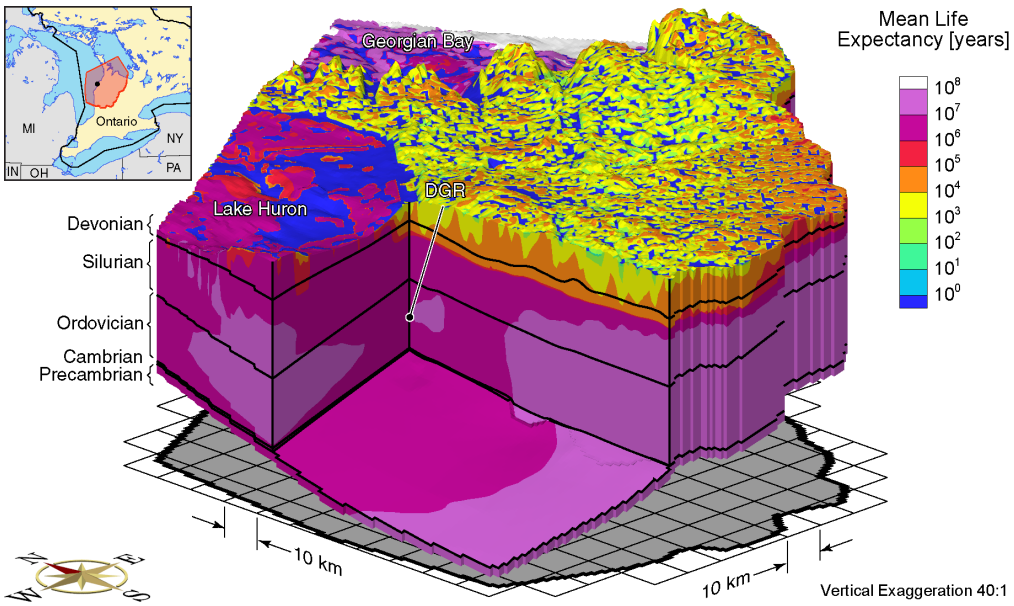

Figure J.37 Block cut view of mean life expectancies at present for the Michigan Basin Regional Scenario 3 paleoclimate simulation.

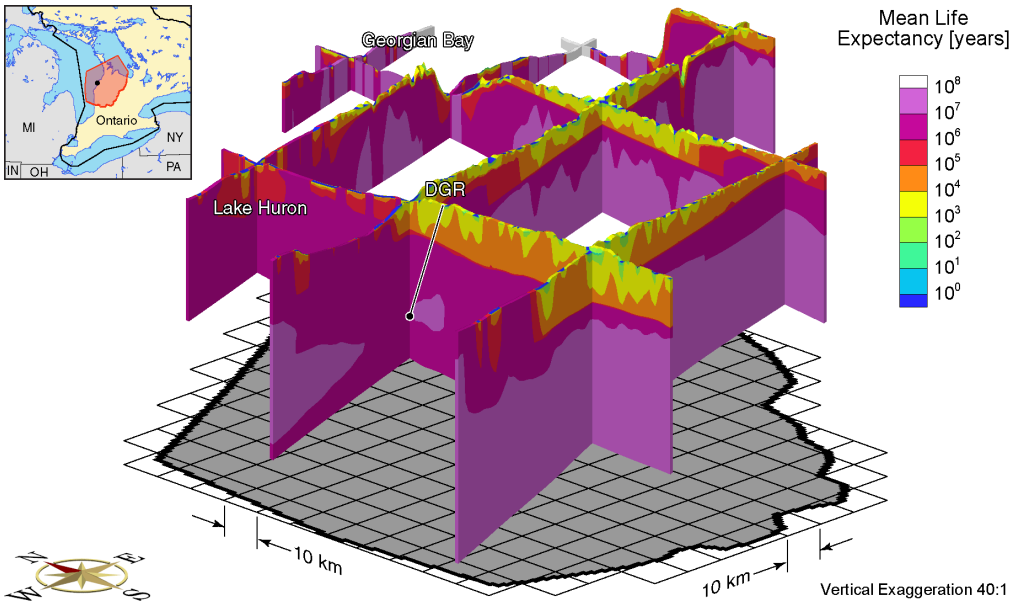

Figure J.38 Fence view of mean life expectancies at present for the Michigan Basin Regional Scenario 3 paleoclimate simulation.

Appendix K

MBR Scenario 4 Paleoclimate Model

All figures related to the Michigan Basin Regional (MBR) Scenario 4 paleoclimate modelling are listed in Table K.1. Block cut view and fence view figures are shown on the same page to facilitate comparison. All results of the 120 ka paleoclimate simulations are shown at times of 80 ka before present, 40 ka before present, and at present.

Table K.1 List of Michigan Basin Regional Scenario 4 paleoclimate simulation figures.

Parameters	Time Before Present					
	80 ka		40 ka		Present	
	Block Cut	Fence	Block Cut	Fence	Block Cut	Fence
Freshwater Heads	K.1	K.2	K.3	K.4	K.5	K.6
Environmental Heads	K.7	K.8	K.9	K.10	K.11	K.12
Pore Velocity Magnitudes	K.13	K.14	K.15	K.16	K.17	K.18
Ratio of Vertical Pore Velocities to Pore Velocity Magnitudes	K.19	K.20	K.21	K.22	K.23	K.24
Brine Concentrations	K.25	K.26	K.27	K.28	K.29	K.30
Tracer Concentrations	K.31	K.32	K.33	K.34	K.35	K.36
Mean Life Expectancies	—	—	—	—	K.37	K.38

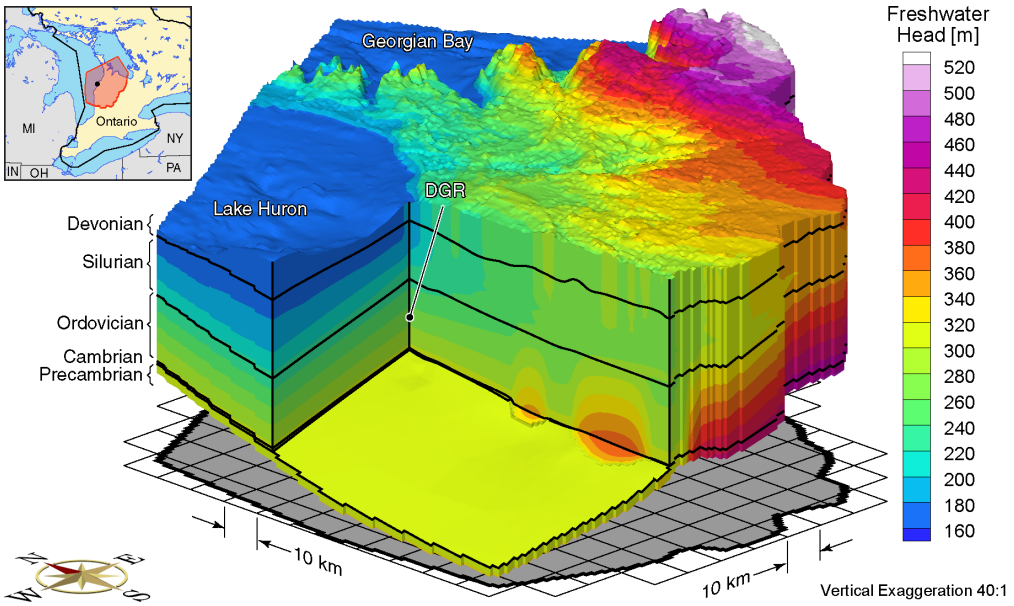

Figure K.1 Block cut view of freshwater heads at 80 ka before present for the Michigan Basin Regional Scenario 4 paleoclimate simulation.

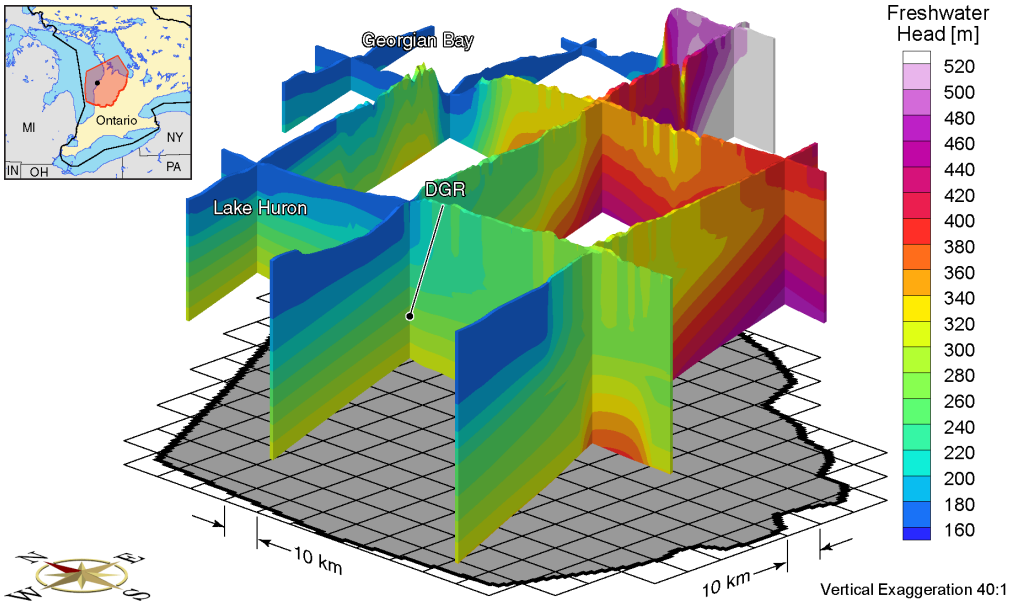

Figure K.2 Fence view of freshwater heads at 80 ka before present for the Michigan Basin Regional Scenario 4 paleoclimate simulation.

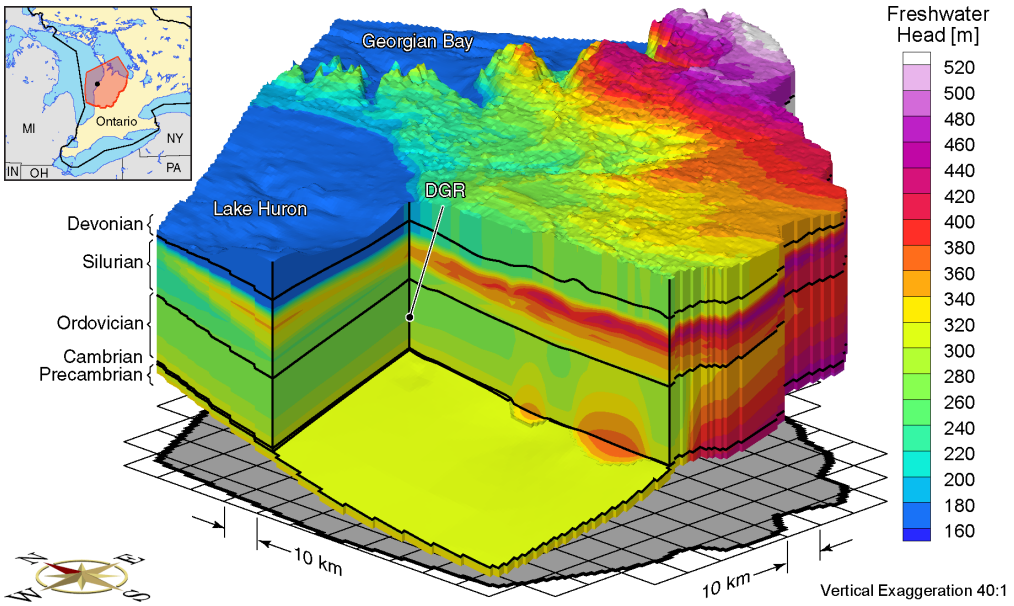

Figure K.3 Block cut view of freshwater heads at 40 ka before present for the Michigan Basin Regional Scenario 4 paleoclimate simulation.

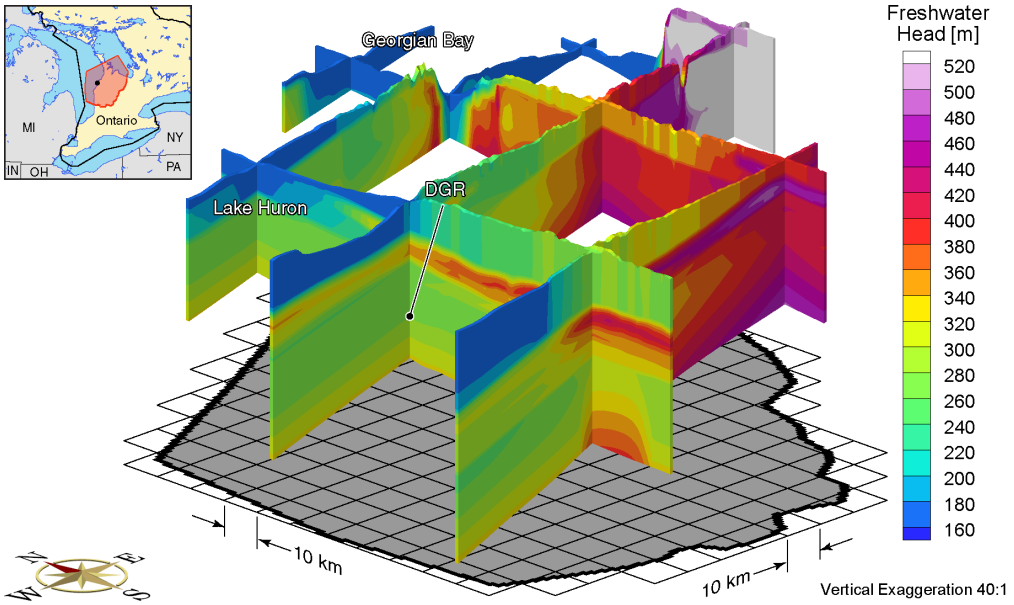

Figure K.4 Fence view of freshwater heads at 40 ka before present for the Michigan Basin Regional Scenario 4 paleoclimate simulation.

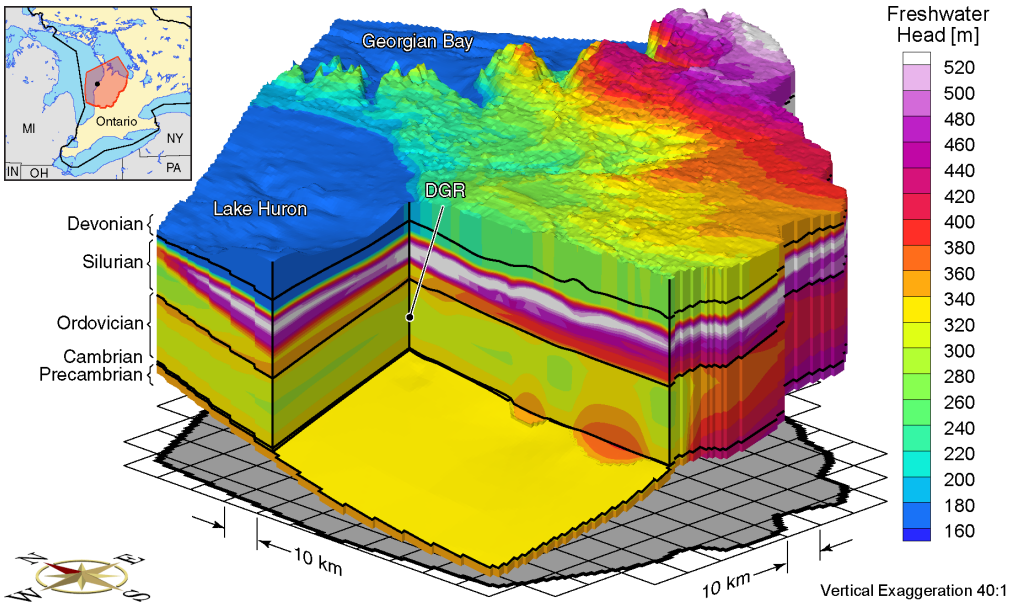

Figure K.5 Block cut view of freshwater heads at present for the Michigan Basin Regional Scenario 4 paleoclimate simulation.

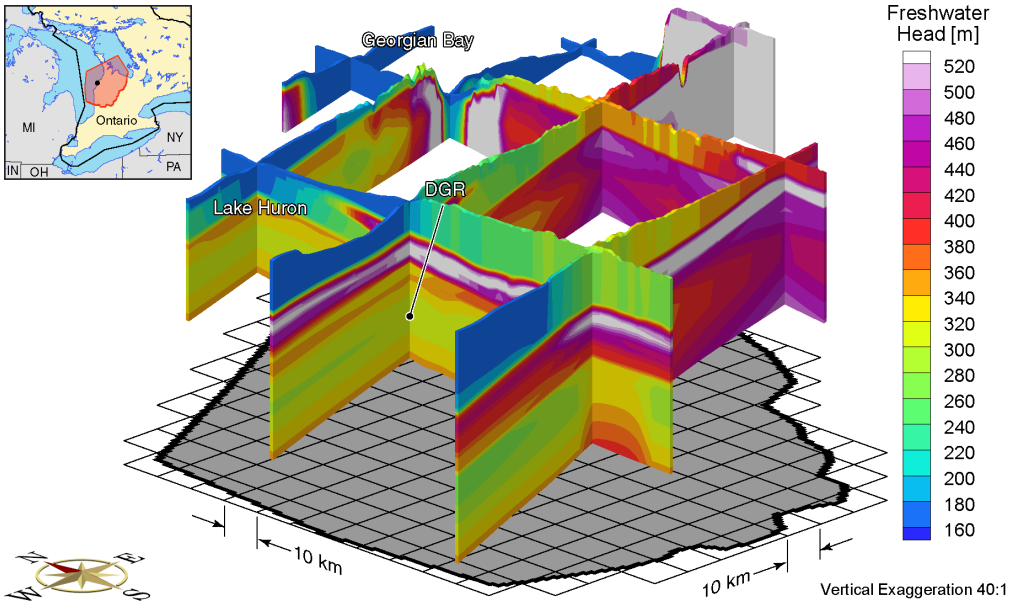

Figure K.6 Fence view of freshwater heads at present for the Michigan Basin Regional Scenario 4 paleoclimate simulation.

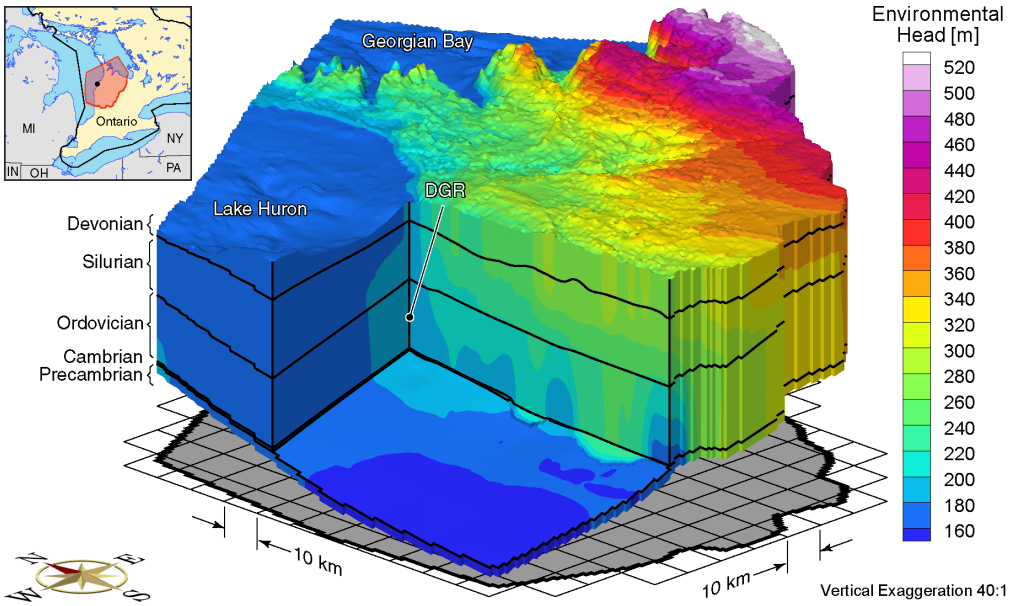

Figure K.7 Block cut view of environmental heads at 80 ka before present for the Michigan Basin Regional Scenario 4 paleoclimate simulation.

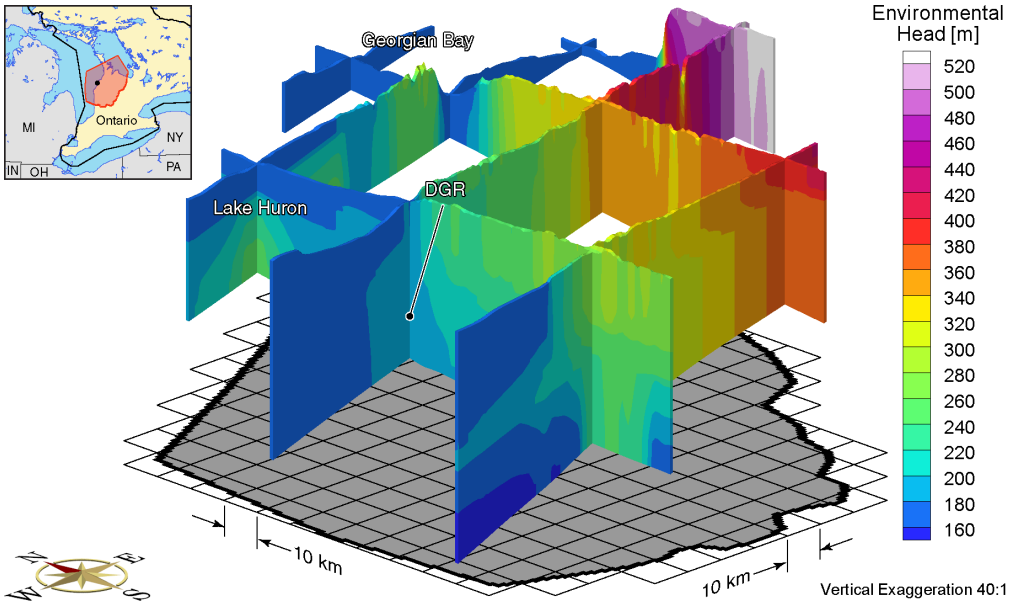

Figure K.8 Fence view of environmental heads at 80 ka before present for the Michigan Basin Regional Scenario 4 paleoclimate simulation.

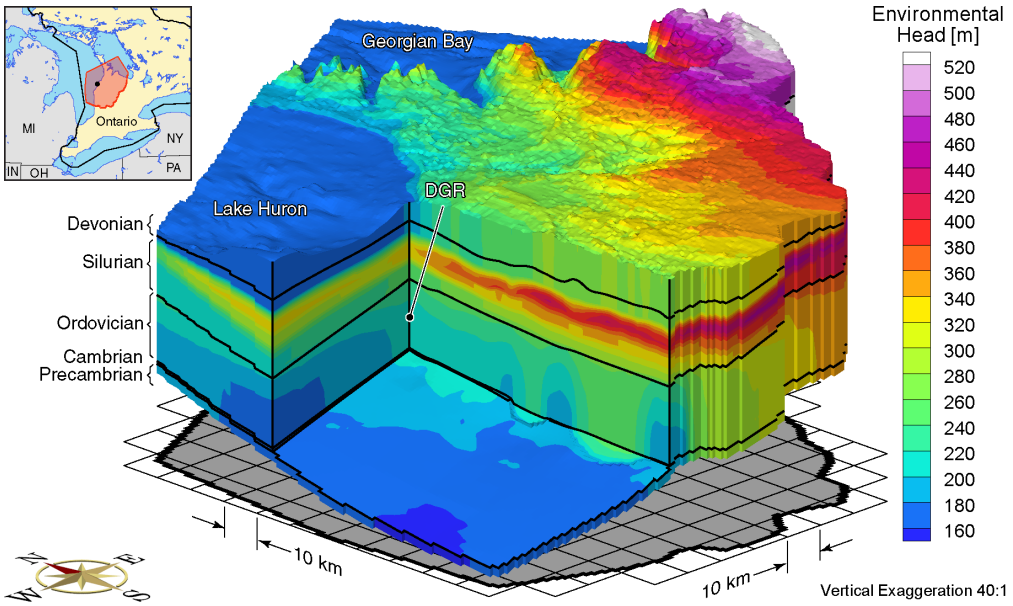

Figure K.9 Block cut view of environmental heads at 40 ka before present for the Michigan Basin Regional Scenario 4 paleoclimate simulation.

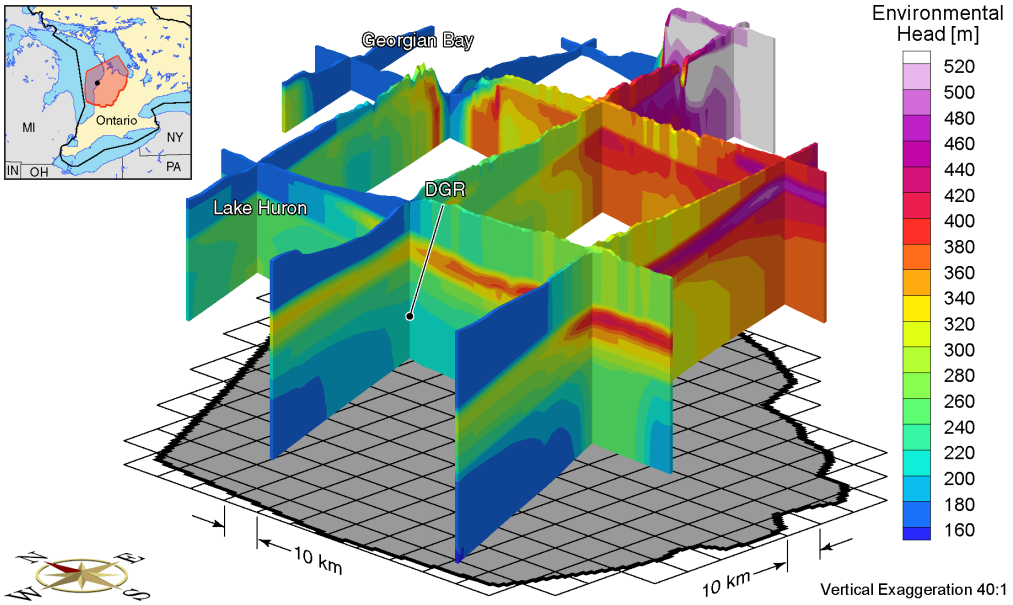

Figure K.10 Fence view of environmental heads at 40 ka before present for the Michigan Basin Regional Scenario 4 paleoclimate simulation.

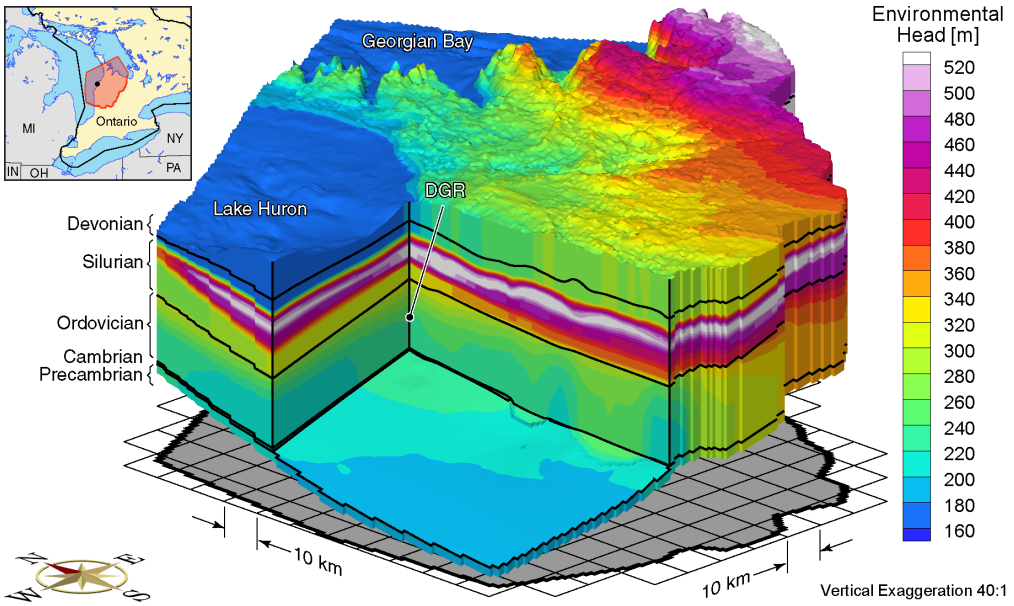

Figure K.11 Block cut view of environmental heads at present for the Michigan Basin Regional Scenario 4 paleoclimate simulation.

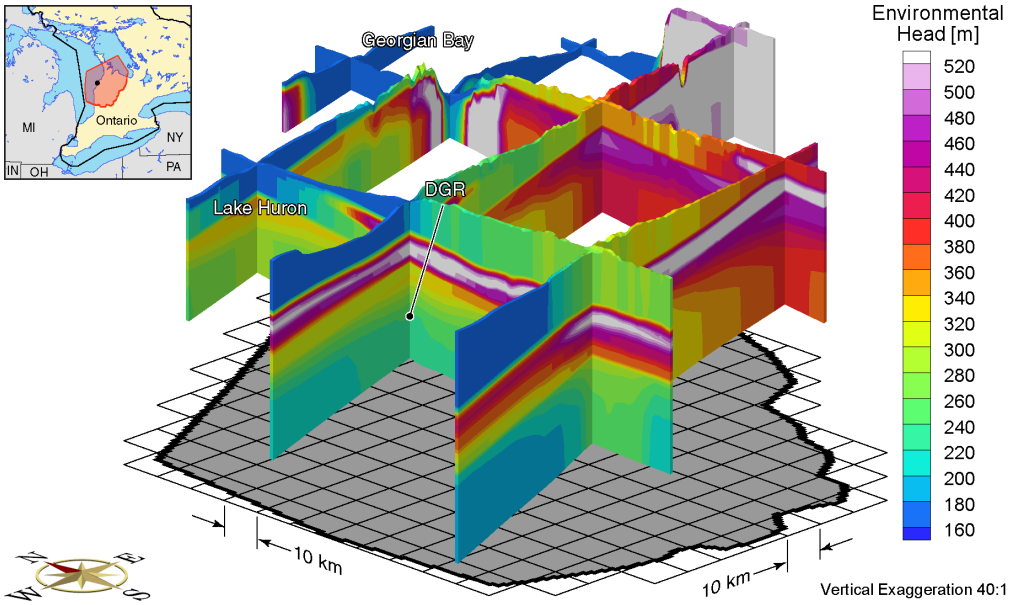

Figure K.12 Fence view of environmental heads at present for the Michigan Basin Regional Scenario 4 paleoclimate simulation.

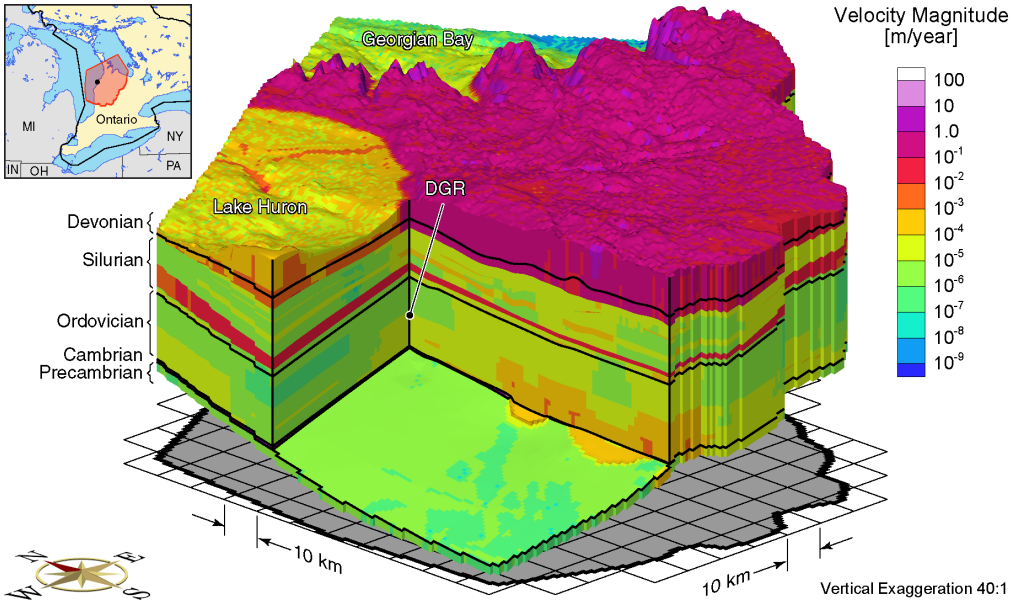

Figure K.13 Block cut view of pore velocity magnitudes at 80 ka before present for the Michigan Basin Regional Scenario 4 paleoclimate simulation.

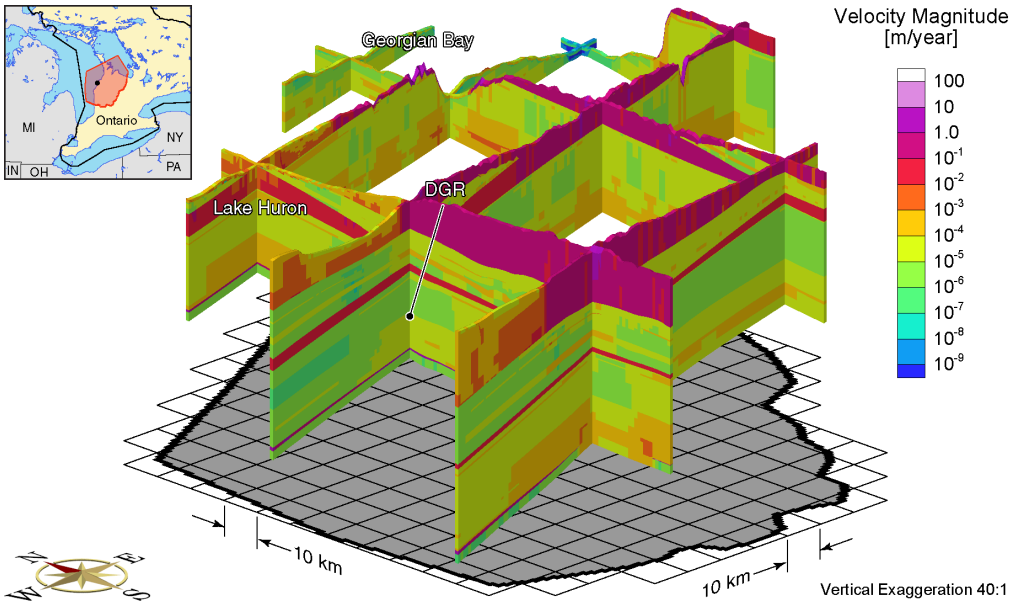

Figure K.14 Fence view of pore velocity magnitudes at 80 ka before present for the Michigan Basin Regional Scenario 4 paleoclimate simulation.

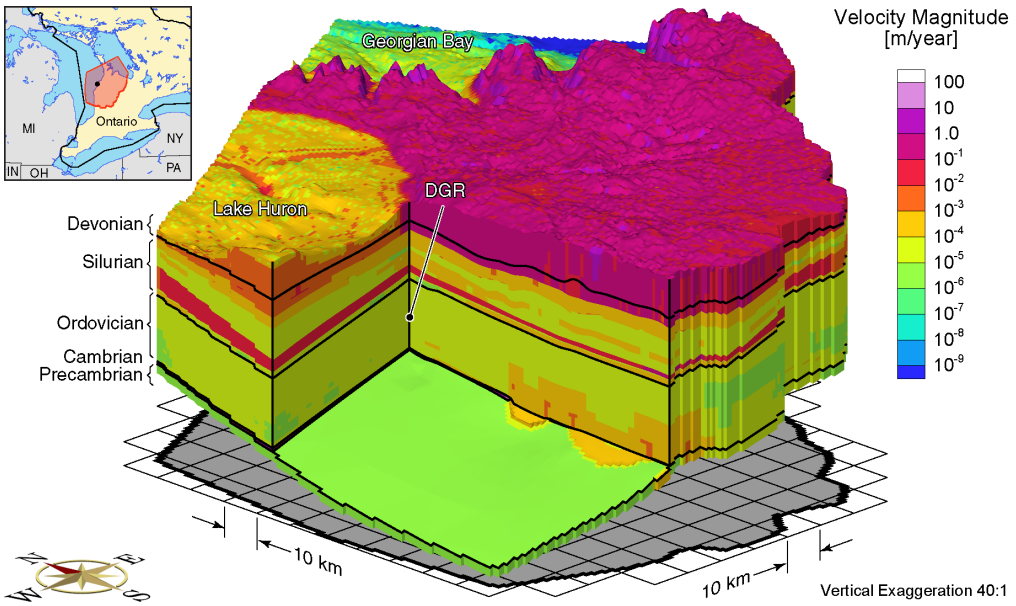

Figure K.15 Block cut view of pore velocity magnitudes at 40 ka before present for the Michigan Basin Regional Scenario 4 paleoclimate simulation.

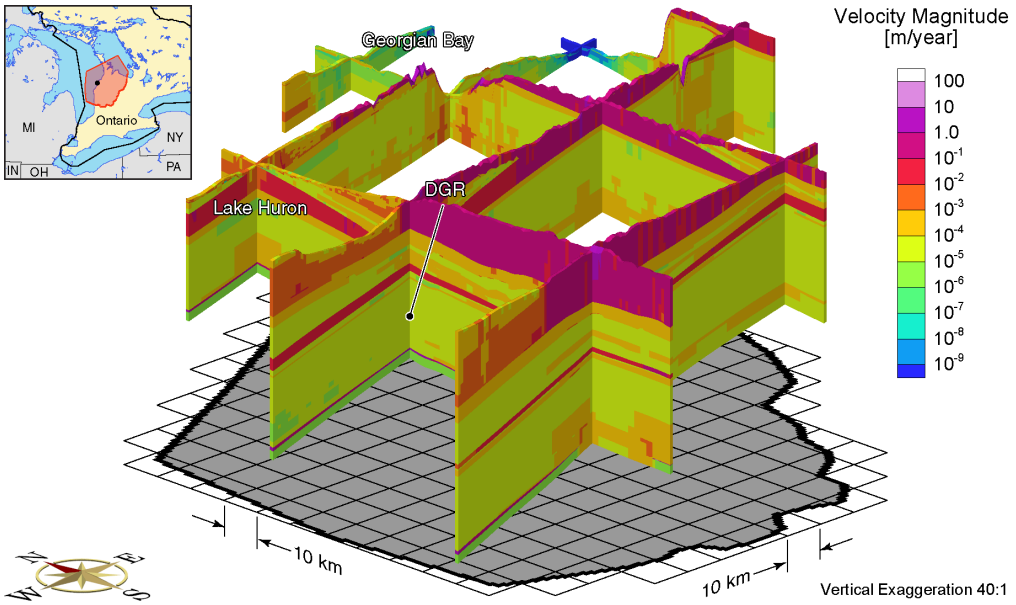

Figure K.16 Fence view of pore velocity magnitudes at 40 ka before present for the Michigan Basin Regional Scenario 4 paleoclimate simulation.

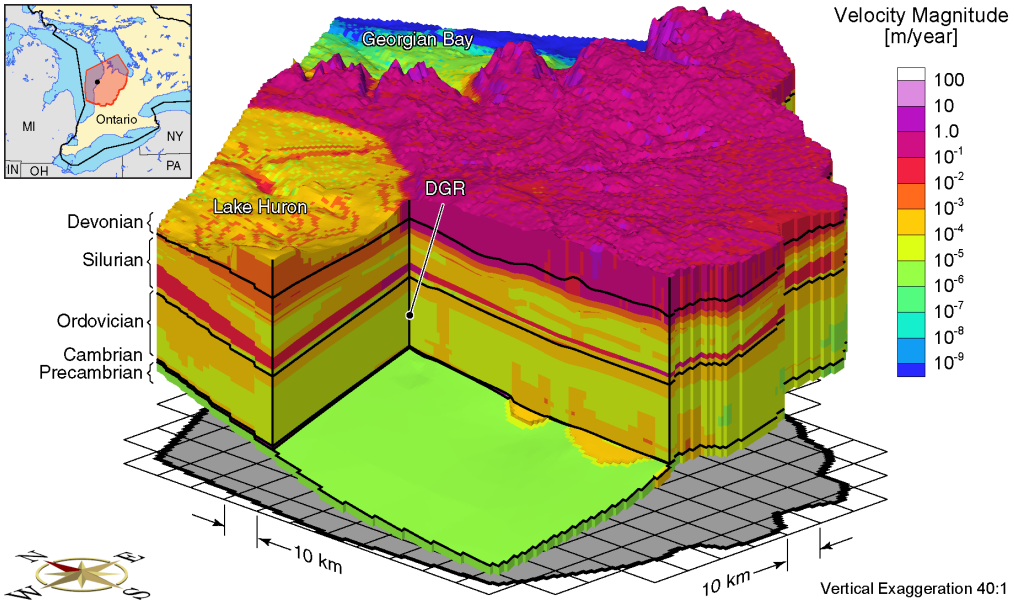

Figure K.17 Block cut view of pore velocity magnitudes at present for the Michigan Basin Regional Scenario 4 paleoclimate simulation.

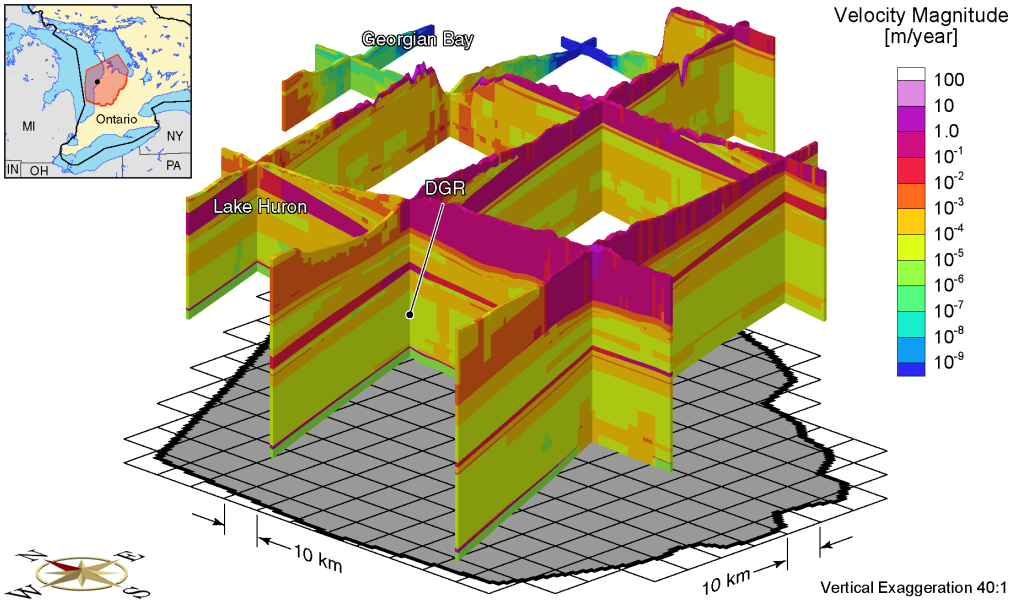

Figure K.18 Fence view of pore velocity magnitudes at present for the Michigan Basin Regional Scenario 4 paleoclimate simulation.

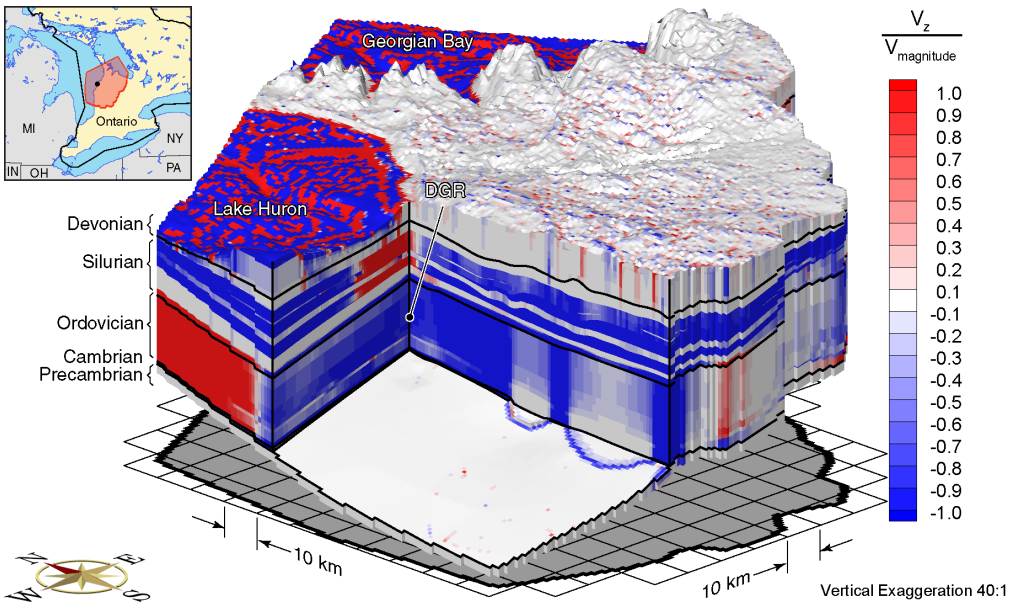

Figure K.19 Block cut view of ratio of vertical pore velocities to pore velocity magnitudes at 80 ka before present for the Michigan Basin Regional Scenario 4 paleoclimate simulation.

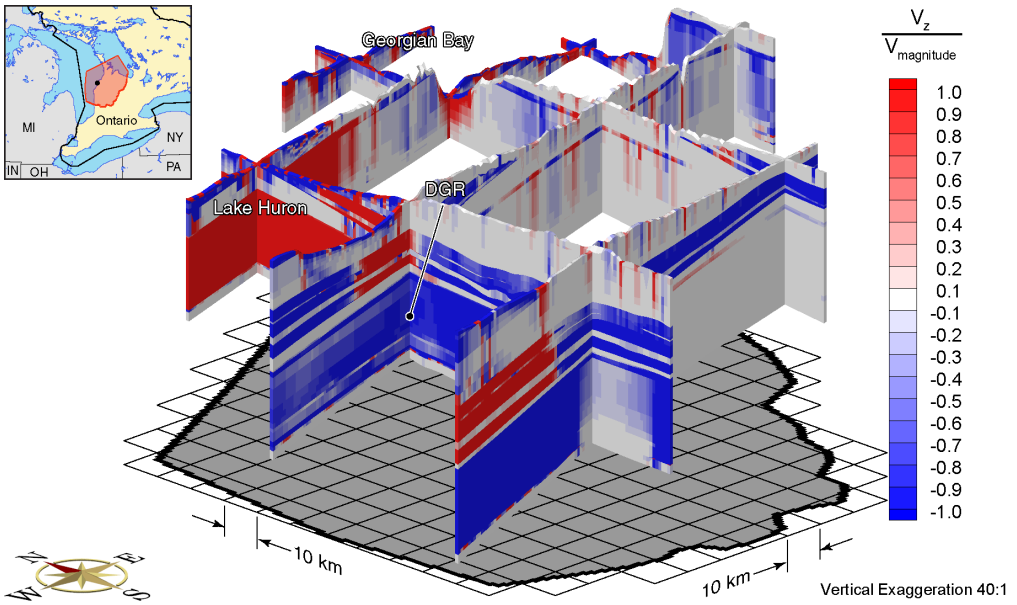

Figure K.20 Fence view of ratio of vertical pore velocities to pore velocity magnitudes at 80 ka before present for the Michigan Basin Regional Scenario 4 paleoclimate simulation.

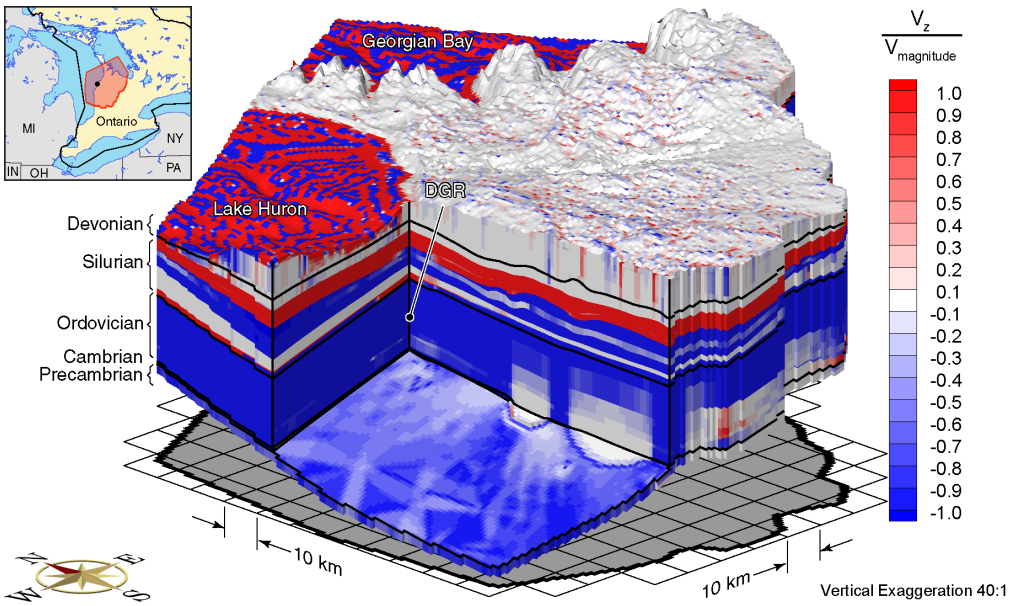

Figure K.21 Block cut view of ratio of vertical pore velocities to pore velocity magnitudes at 40 ka before present for the Michigan Basin Regional Scenario 4 paleoclimate simulation.

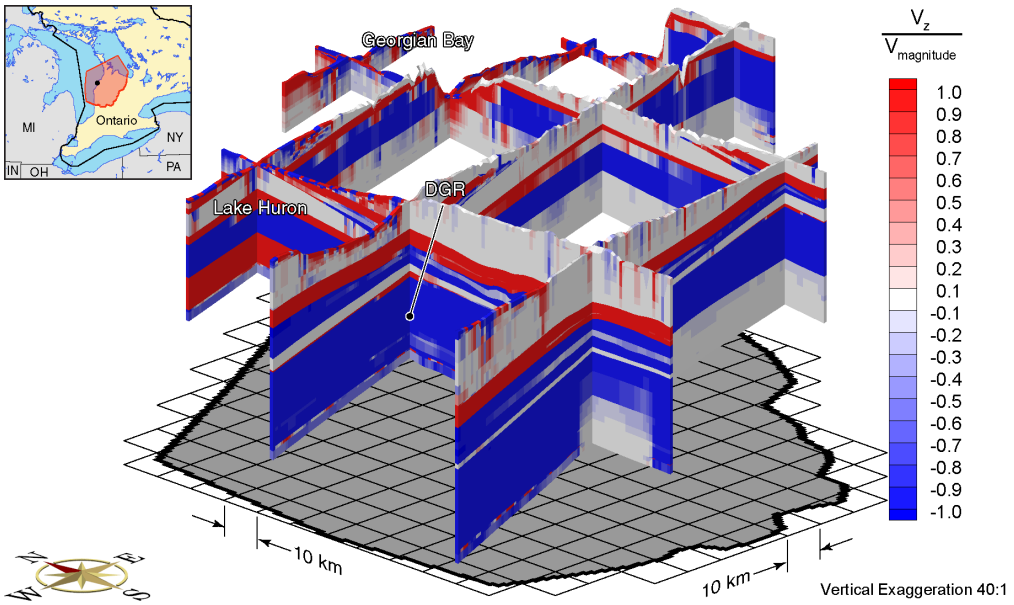

Figure K.22 Fence view of ratio of vertical pore velocities to pore velocity magnitudes at 40 ka before present for the Michigan Basin Regional Scenario 4 paleoclimate simulation.

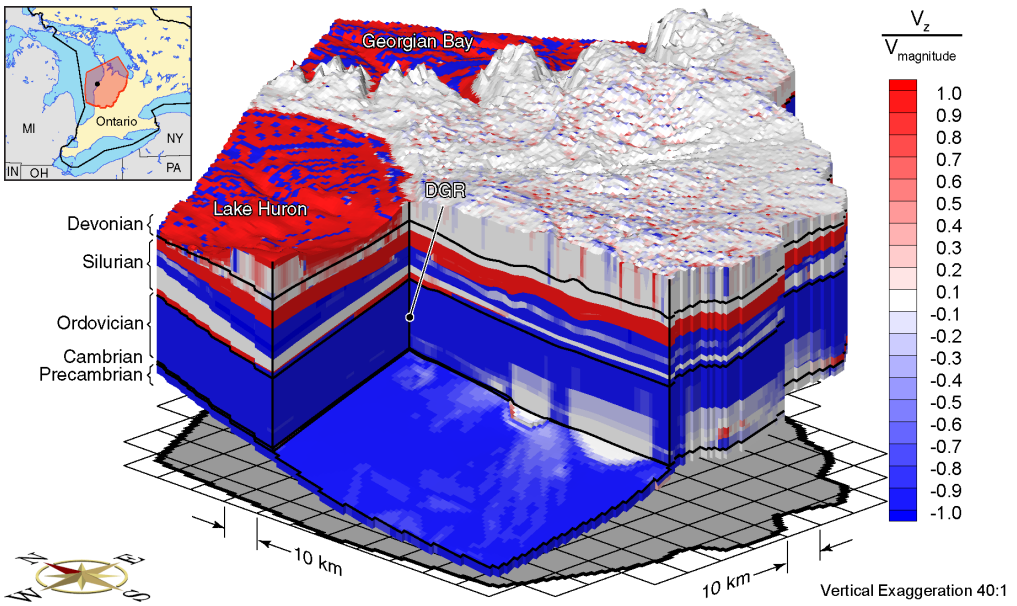

Figure K.23 Block cut view of ratio of vertical pore velocities to pore velocity magnitudes at present for the Michigan Basin Regional Scenario 4 paleoclimate simulation.

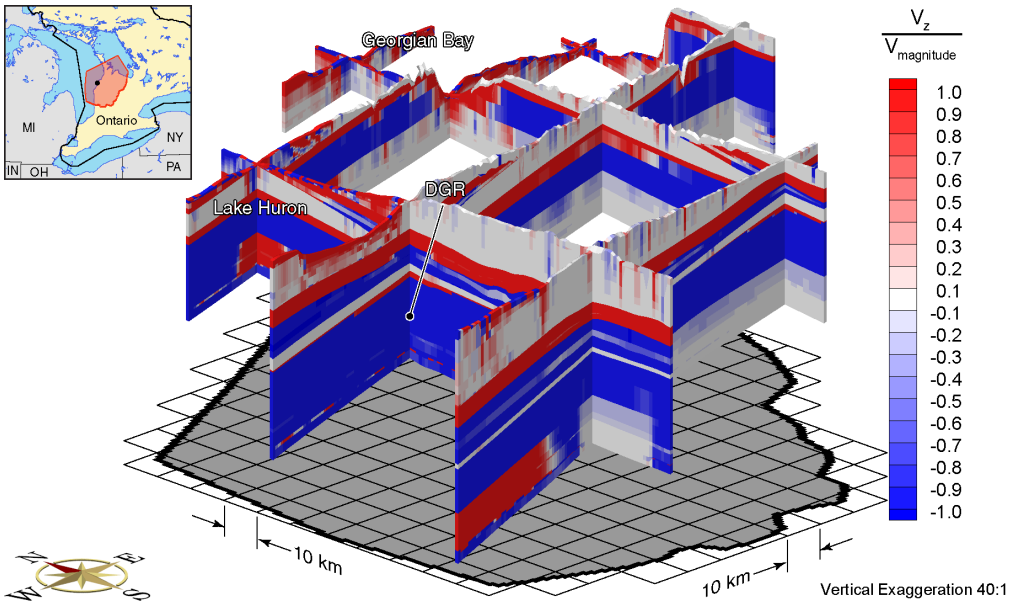

Figure K.24 Fence view of ratio of vertical pore velocities to pore velocity magnitudes at present for the Michigan Basin Regional Scenario 4 paleoclimate simulation.

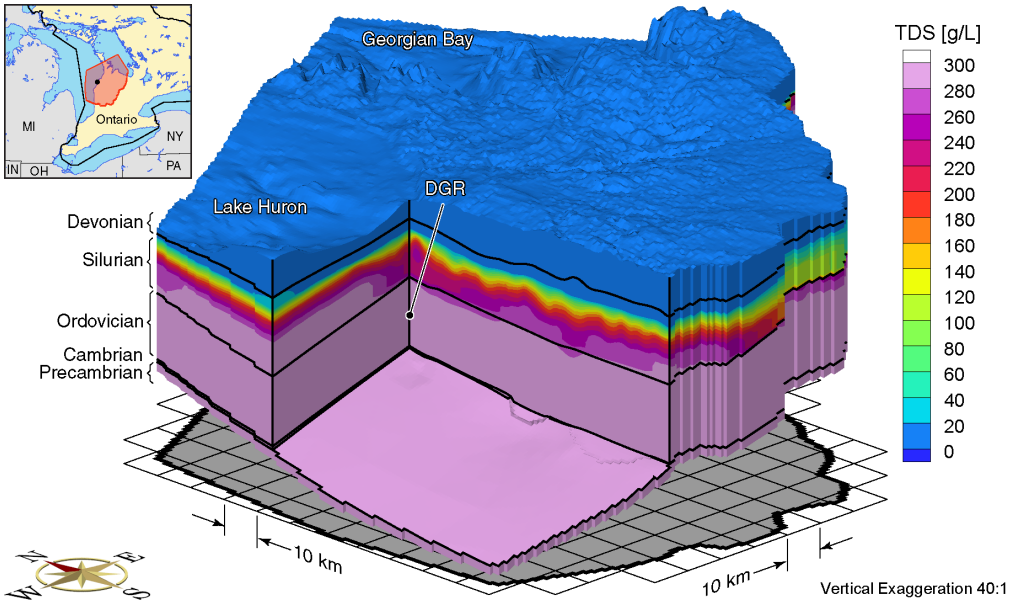

Figure K.25 Block cut view of brine concentrations at 80 ka before present for the Michigan Basin Regional Scenario 4 paleoclimate simulation.

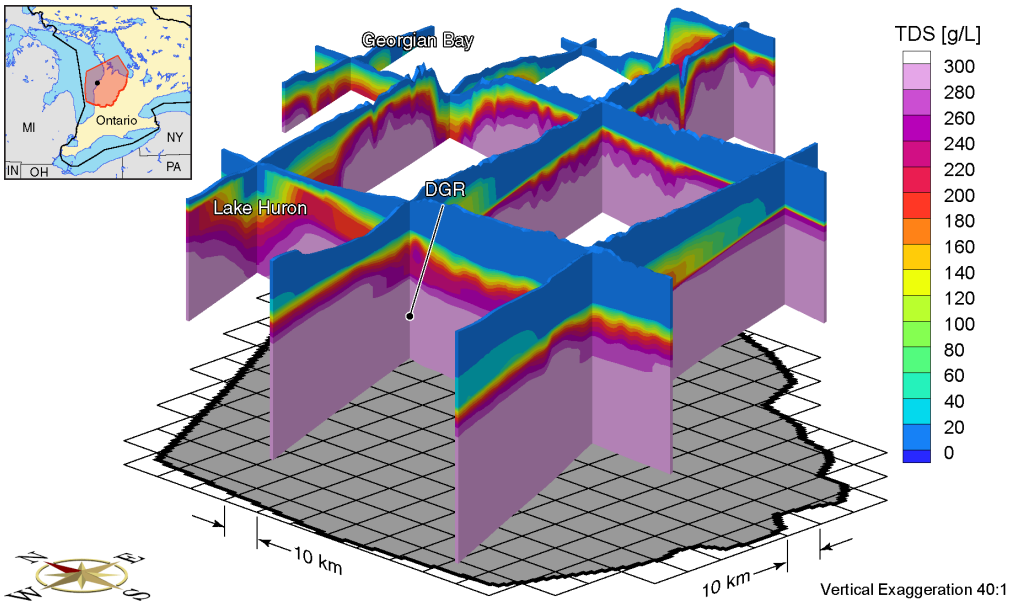

Figure K.26 Fence view of brine concentrations at 80 ka before present for the Michigan Basin Regional Scenario 4 paleoclimate simulation.

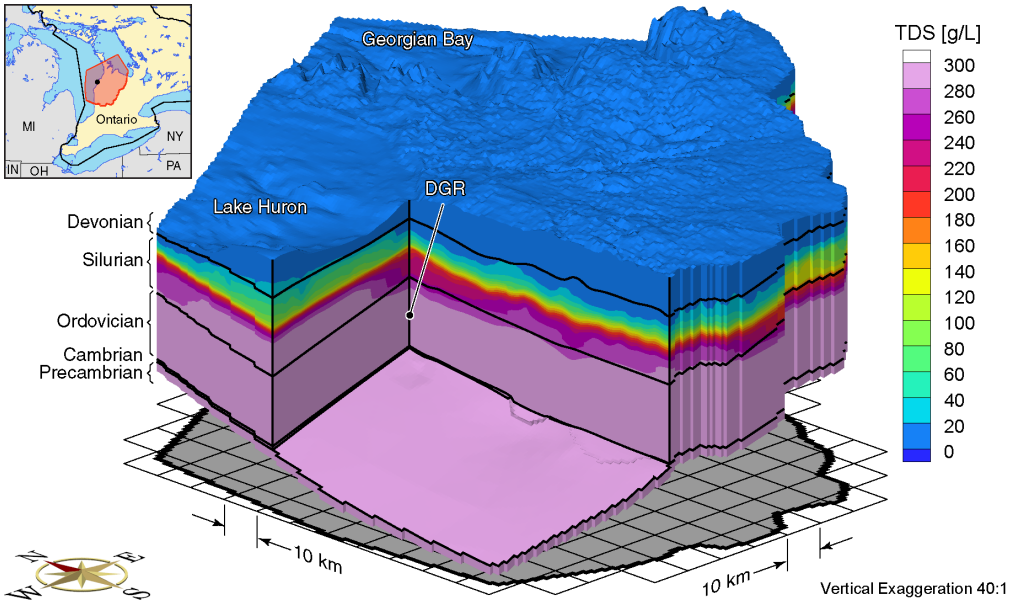

Figure K.27 Block cut view of brine concentrations at 40 ka before present for the Michigan Basin Regional Scenario 4 paleoclimate simulation.

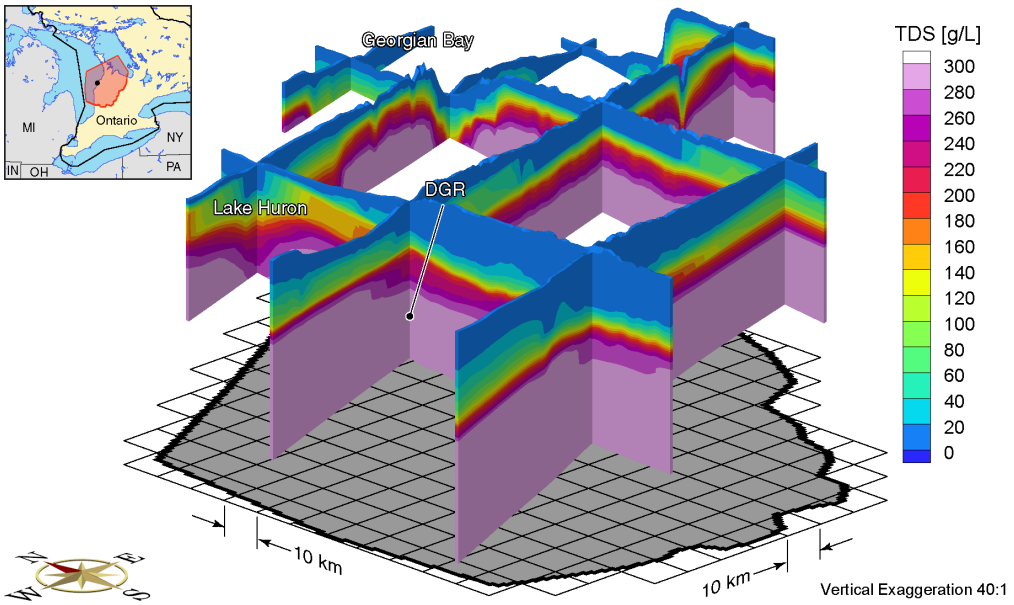

Figure K.28 Fence view of brine concentrations at 40 ka before present for the Michigan Basin Regional Scenario 4 paleoclimate simulation.

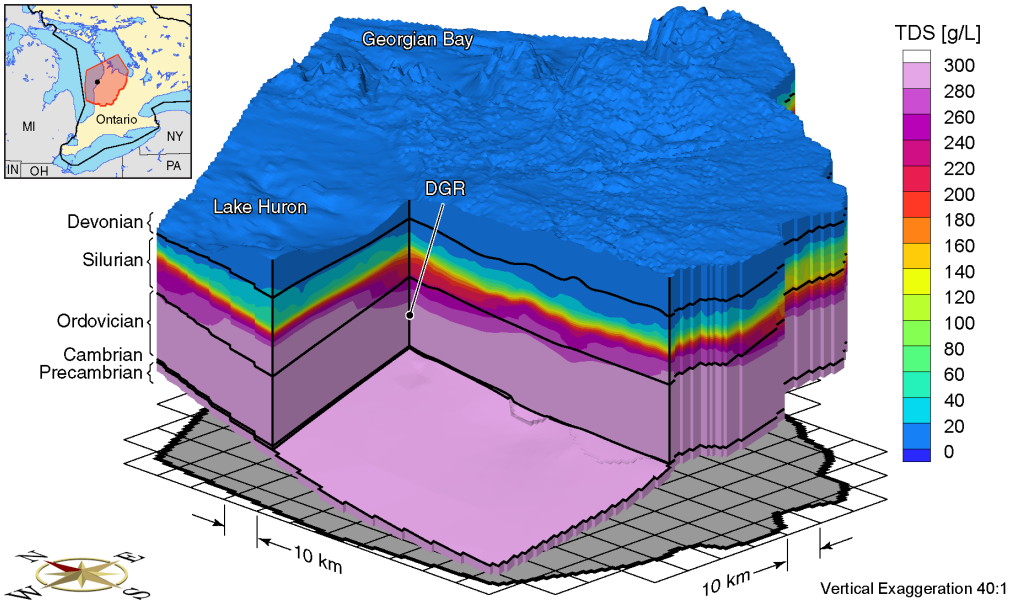

Figure K.29 Block cut view of brine concentrations at present for the Michigan Basin Regional Scenario 4 paleoclimate simulation.

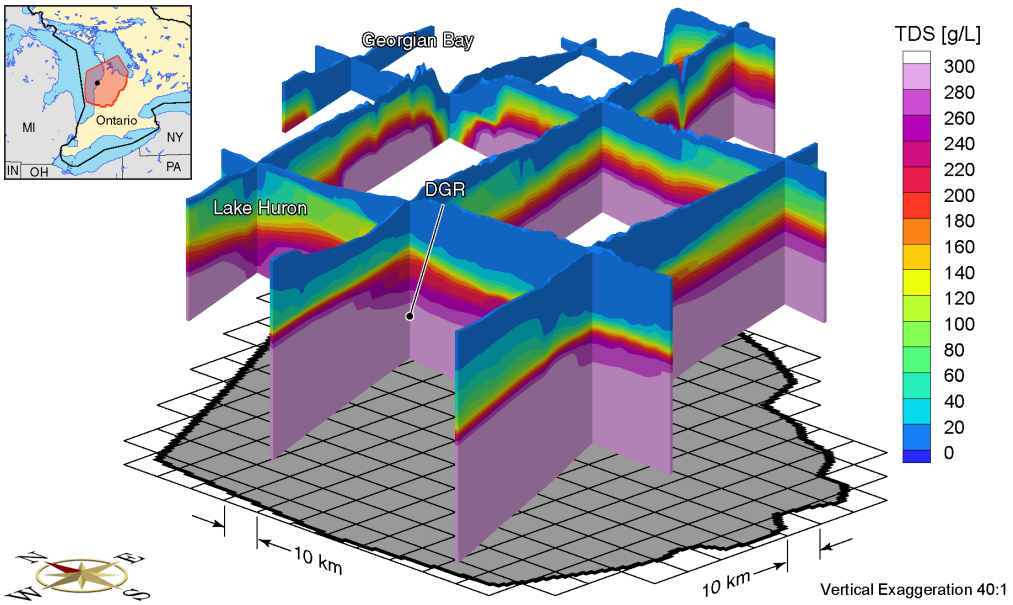

Figure K.30 Fence view of brine concentrations at present for the Michigan Basin Regional Scenario 4 paleoclimate simulation.

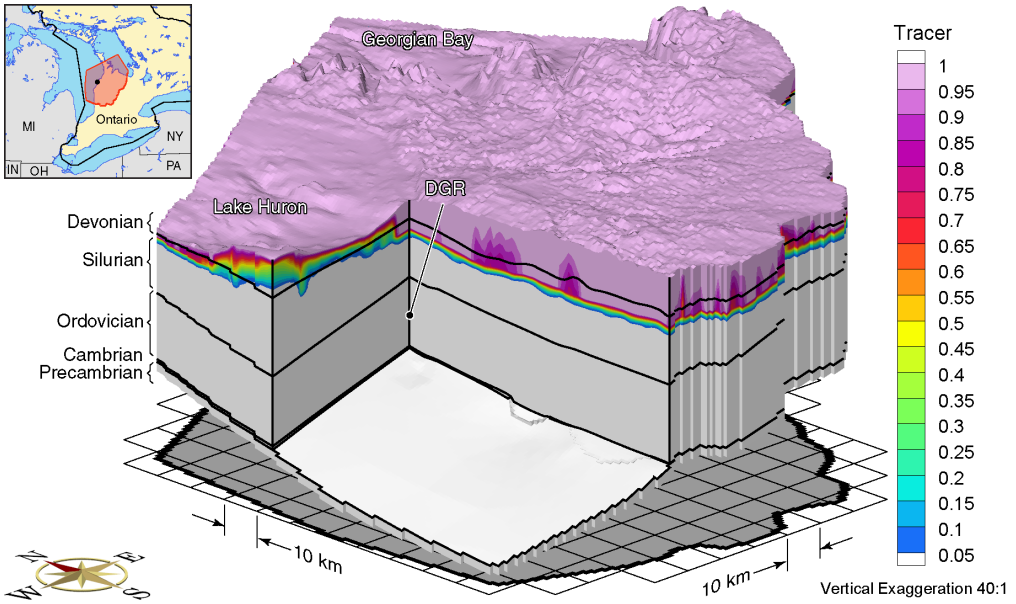

Figure K.31 Block cut view of tracer concentrations at 80 ka before present for the Michigan Basin Regional Scenario 4 paleoclimate simulation.

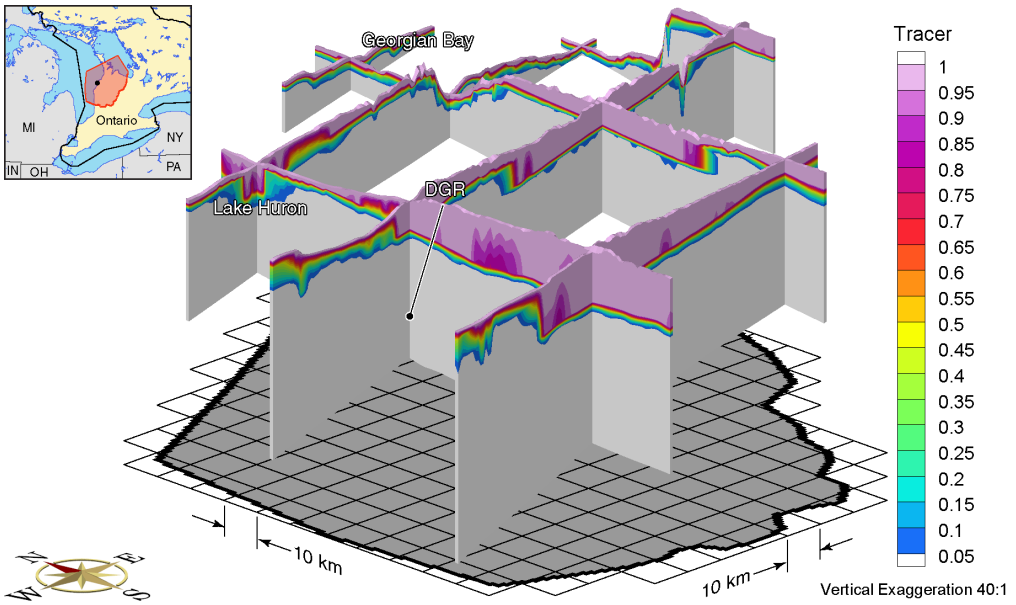

Figure K.32 Fence view of tracer concentrations at 80 ka before present for the Michigan Basin Regional Scenario 4 paleoclimate simulation.

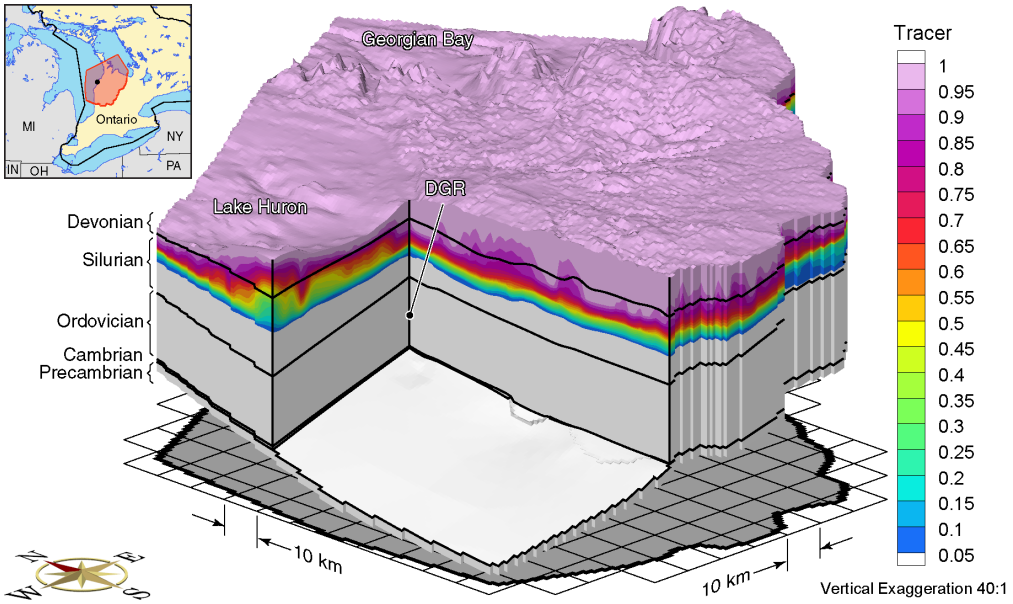

Figure K.33 Block cut view of tracer concentrations at 40 ka before present for the Michigan Basin Regional Scenario 4 paleoclimate simulation.

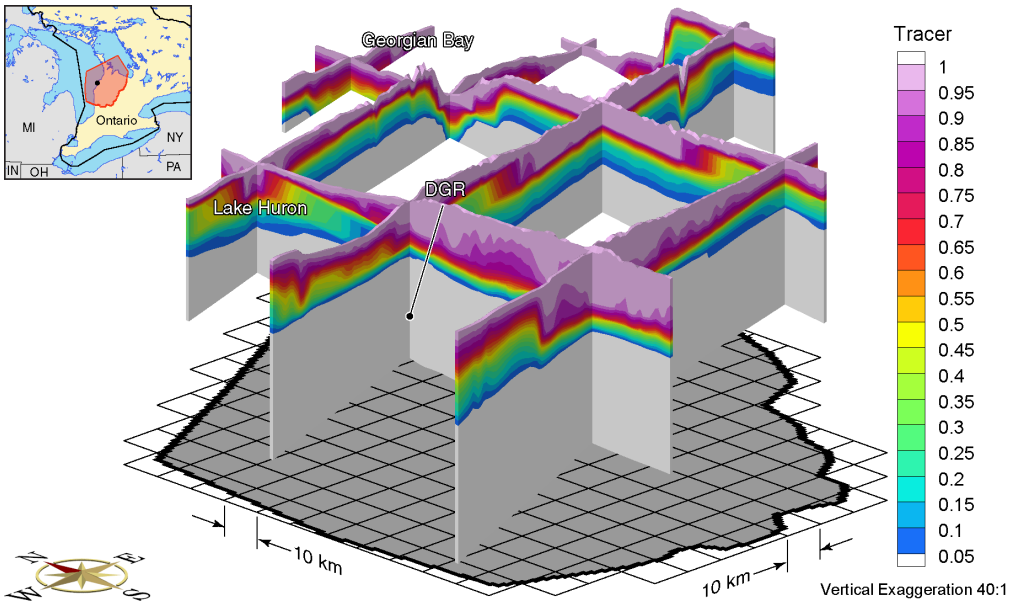

Figure K.34 Fence view of tracer concentrations at 40 ka before present for the Michigan Basin Regional Scenario 4 paleoclimate simulation.

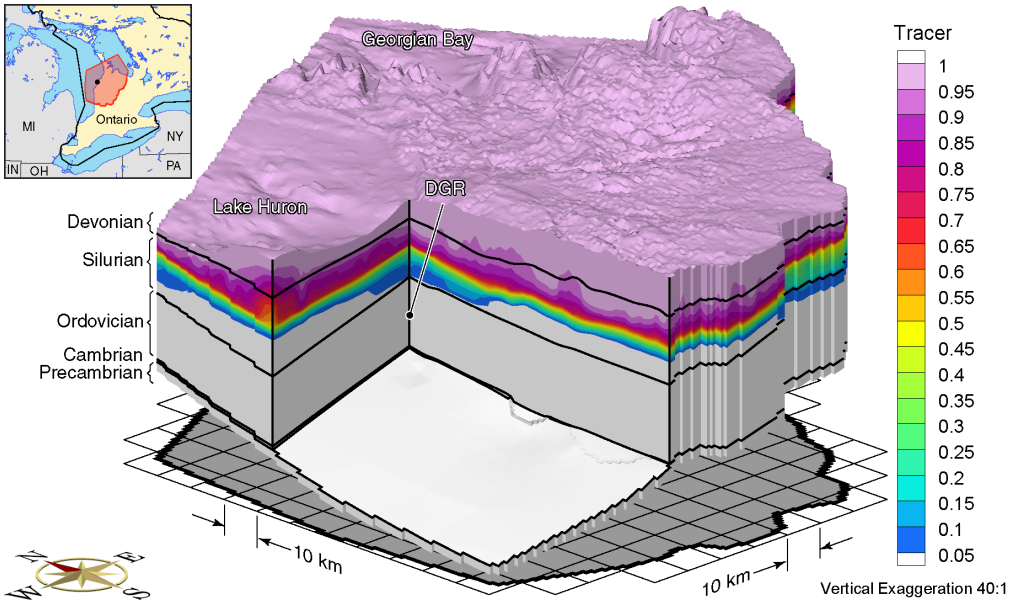

Figure K.35 Block cut view of tracer concentrations at present for the Michigan Basin Regional Scenario 4 paleoclimate simulation.

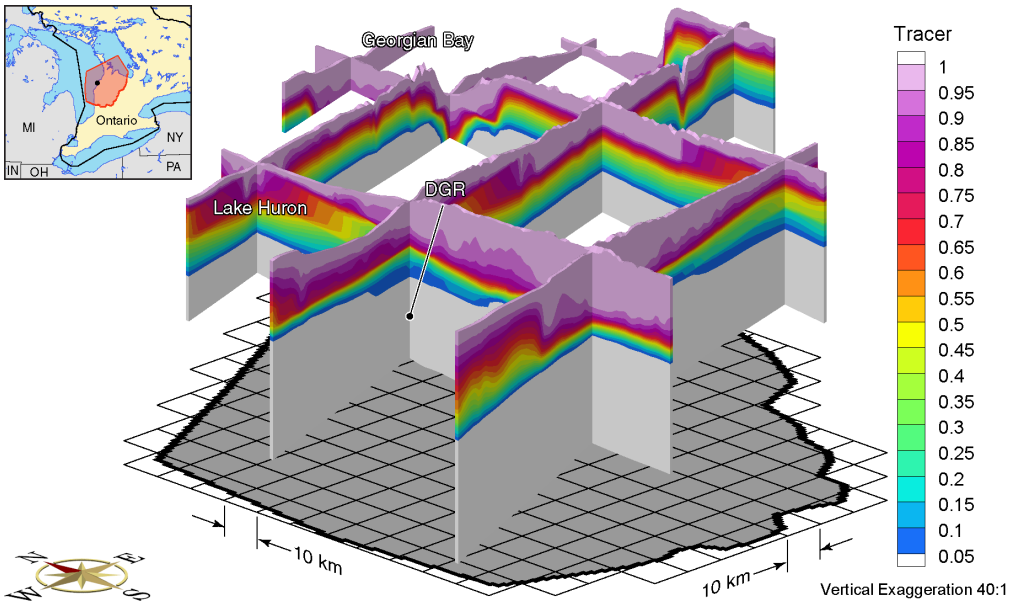

Figure K.36 Fence view of tracer concentrations at present for the Michigan Basin Regional Scenario 4 paleoclimate simulation.

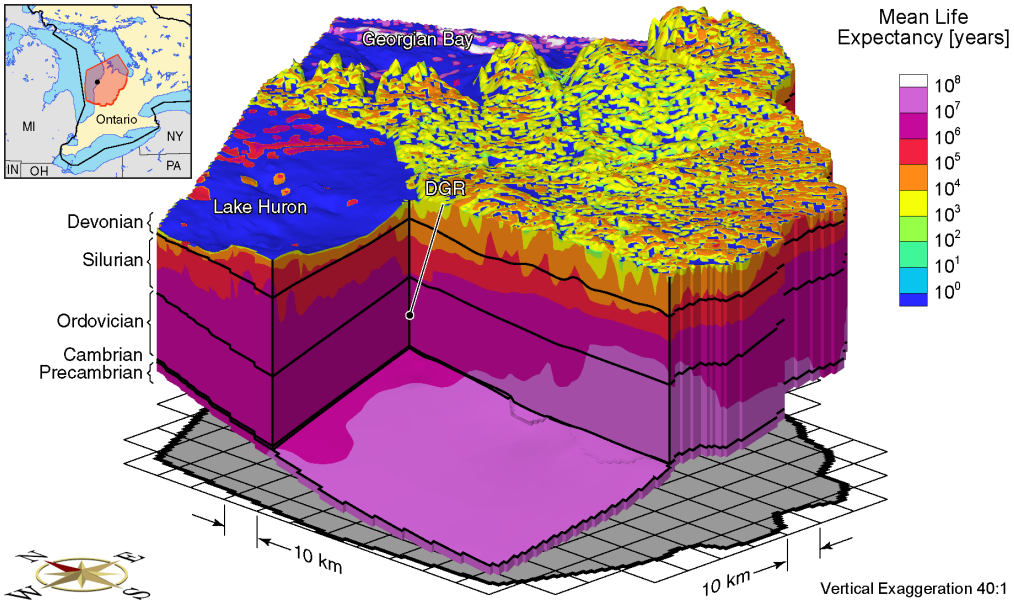

Figure K.37 Block cut view of mean life expectancies at present for the Michigan Basin Regional Scenario 4 paleoclimate simulation.

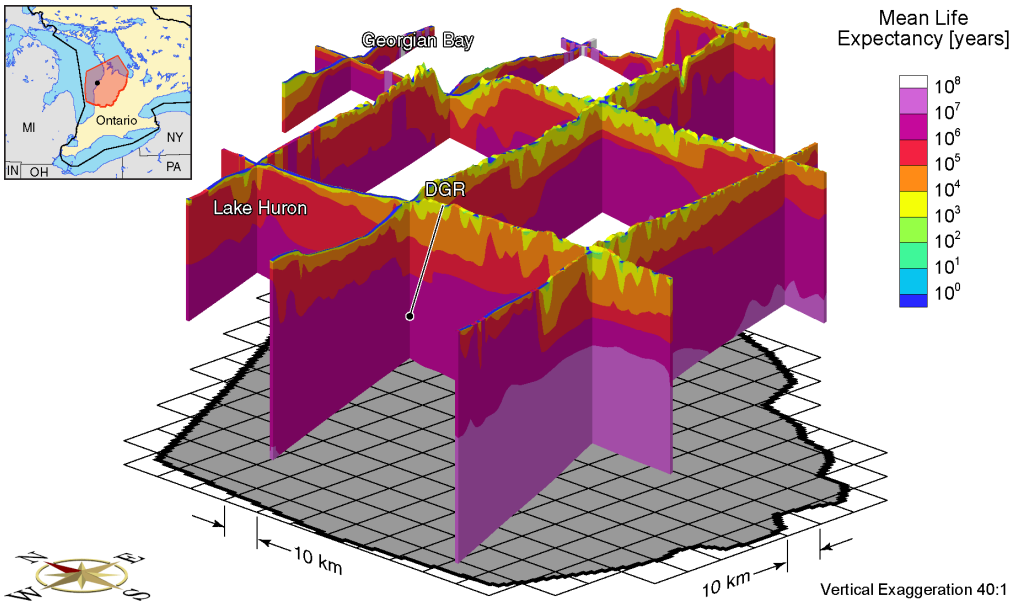

Figure K.38 Fence view of mean life expectancies at present for the Michigan Basin Regional Scenario 4 paleoclimate simulation.

References

Adams, J. J., and S. Bachu (2002), Equations of state for basin geofluids: Algorithm review and intercomparison for brines, *Geofluids*, *2*(4), 257–271, doi:10.1046/j.1468-8123.2002.00041.x.

AECB, [Atomic Energy Control Board] (1987), Regulatory Policy Statement. Regulatory objectives, requirements, and guidelines for the disposal of radioactive wastes – long-term aspects, *Technical Report R-104*, Atomic Energy Control Board, Ottawa, Canada, regulatory document.

AECL, [Atomic Energy of Canada Limited] (1994), Environmental Impact Statement on the concept for disposal of Canada's nuclear fuel waste, *Technical Report AECL-10711, COG-93-1*, Atomic Energy of Canada Limited, Pinawa, Manitoba, Canada.

Ahonen, L., and T. Vieno (1994), Effects of glacial meltwater on corrosion of copper canisters, *Report YJT-94-13*, Posiva Oy, Helsinki, Finland.

Aravena, R., L. I. Wassenaar, and L. N. Plummer (1995), Estimating ^{14}C groundwater ages in a methanogenic aquifer, *Water Resources Research*, *31*(9), 2307–2317, doi:10.1029/95WR01271.

ARIUS, [Association for Regional and International Underground Storage] (2002), Arius newsletter no. 1, `www.arius-world.org/pdfs/AriusNewsletterNo1_2002.pdf`.

ARIUS, [Association for Regional and International Underground Storage] (2006), Arius newsletter no. 13, `www.arius-world.org/pages/pdf_2006/AriusNewsletter13.pdf`.

ARIUS, [Association for Regional and International Underground Storage] (2008), Arius newsletter no. 17, `www.arius-world.org/pdfs/AriusNewsletter17.pdf`.

Armstrong, D. K., and T. R. Carter (2006), An updated guide to the subsurface Paleozoic stratigraphy of southern Ontario, *Open File Report 6191*, Ontario Geological Survey, Sudbury, Canada.

Barton, K. E., D. G. Howell, J. F. Vigil, J. C. Reed, and J. O. Wheeler (2003), The North America tapestry of time and terrain, United States Geological Survey, Geologic Investigations Series I-2781, Version 1.0.

Bear, J. (1988), *Dynamics of Fluids in Porous Media*, Dover ed., Dover Publications Inc.

Blyth, A., S. Frape, T. Ruskeeniemi, and R. Blomqvist (2004), Origins, closed system formation and preservation of calcites in glaciated crystalline bedrock: Evidence from the Palmottu natural analogue site, Finland, *Applied Geochemistry*, *19*(5), 675–686, doi:10.1016/j.apgeochem.2003.07.004.

Bottomley, D. J., R. Renaud, T. Kotzer, and I. D. Clark (2002), Iodine-129 constraints on residence times of deep marine brines in the Canadian Shield, *Geology*, *30*(7), 587–590, doi:10.1130/0091-7613(2002)030<0587:ICORTO>2.0.CO;2.

Bottomley, D. J., L. H. Chan, A. Katz, A. Starinsky, and I. D. Clark (2003), Lithium isotope geochemistry and origin of Canadian Shield brines, *Ground Water*, *41*(6), 847–856, doi:10.1111/j.1745-6584.2003.tb02426.x.

Boulton, G. S., P. E. Caban, and K. van Gijssel (1995), Groundwater flow beneath ice sheets: Part I – Large scale patterns, *Quaternary Science Reviews*, *14*(6), 545–562, doi:10.1016/0277-3791(95)00039-R.

Boulton, G. S., P. E. Caban, K. van Gijssel, A. Leijnse, M. Punkari, and F. H. A. van Weert (1996), The impact of glaciation on the groundwater regime of Northwest Europe, *Global and Planetary Change*, *12*(1-4), 397–413, doi:10.1016/0921-8181(95)00030-5.

Boulton, G. S., U. Kautsky, L. Morén, and T. Wallroth (2001a), Impact of long-term climate change on a deep geological repository for spent nuclear fuel, *Technical Report TR-99-05*, SKB, Stockholm, Sweden.

Boulton, G. S., S. Zatsepin, and B. Maillot (2001b), Analysis of groundwater flow beneath ice sheets, *Technical Report TR-01-06*, SKB, Stockholm, Sweden.

Carter, T. R., R. A. Trevail, and R. M. Easton (1996), Basement controls on some hydrocarbon traps in southern Ontario, Canada, in *Basement and basins of eastern North America*, edited by B. A. van der Pluijm and P. A. Catacosinos, no. 308 in Special Paper, pp. 95–107, Geological Society of America, doi:10.1130/0-8137-2308-6.95.

Cedercreutz, J. (2004), Future climate scenarios for Olkiluoto with emphasis on permafrost, *Technical Report 2004-06*, Posiva Oy, Olkiluoto, Finland.

Chan, T., and F. W. Stanchell (2005), Subsurface hydro-mechanical (HM) impacts of glaciation: Sensitivity to transient analysis, HM coupling, fracture zone connectivity and model dimensionality, *International Journal of Rock Mechanics and Mining Sciences*, *42*(5-6), 828–849, doi:10.1016/j.ijrmms.2005.04.001.

Chan, T., and F. W. Stanchell (2008), DECOVALEX-THMC project: Task E – implications of glaciation and coupled thermohydromechanical processes on Shield flow system evolution and performance assessment, final report, *SKI Report 2008:46*, SKI (Swedish Nuclear Power Inspectorate), Stockholm, Sweden.

Chan, T., N. W. Scheier, and V. Guvanasen (1999), MOTIF code version 3.2: Theory manual, *Technical Report 06819-REP-01200-0091-R00*, Ontario Hydro, Nuclear Waste Management Division, Toronto, Canada.

Chan, T., R. Christiansson, G. S. Boulton, L. O. Ericsson, J. Hartikainen, M. R. Jensen, D. M. Ivars, F. W. Stanchell, P. Vistrand, and T. Wallroth (2005), DECOVALEX III BMT3/BENCHPAR WP4: The thermo-hydro-mechanical responses to a glacial cycle and their potential implications for deep geological disposal of nuclear fuel waste in a fractured crystalline rock mass, *International Journal of Rock Mechanics and Mining Sciences*, *42*(5-6), 805–827, doi:10.1016/j.ijrmms.2005.03.017.

Chernicoff, S., H. A. Fox, and L. H. Tanner (2002), *Earth: Geologic Principles and History*, Houghton Mifflin Company, Boston, USA.

Clark, I. D., M. Douglas, K. Raven, and D. Dennis Bottomley (2000), Recharge and preservation of Laurentide glacial melt water in the Canadian Shield, *Ground Water*, *38*(5), 735–742, doi:10.1111/j.1745-6584.2000.tb02709.x.

CNA, [Canadian Nuclear Association] (2008), Canada's nuclear energy: Reliable, affordable and clean electricity, `www.cna.ca/english/pdf/NuclearFacts/2008/CNA_Nuclear_Energy_Booklet08.pdf`, edition 1.

CNA, [Canadian Nuclear Association] (2009), Nuclear waste, `www.cna.ca/curriculum/cna_safety/nuclear_waste-eng.asp?bc=Nuclear%20Waste&pid=Nuclear%20Waste`, accessed 2009-02-21.

CNSC, [Canadian Nuclear Safety Commission] (2009a), Ontario: Fact sheet radioactive waste management – Canada's regulatory process, `www.nuclearsafety.gc.ca/eng/ea/ealist/ongoing/ontario/EA_06_03_17520_facts.cfm`, accessed 2009-02-21.

CNSC, [Canadian Nuclear Safety Commission] (2009b), News releases: Backgrounder – new legislation, new commission for a new age 00-C-01, `www.nuclearsafety.gc.ca/eng/mediacentre/releases/news_release.cfm?news_release_id=161`, accessed 2009-02-26.

Cornaton, F., and Y.-J. Park (2005), Personal communication.

Cornaton, F., and P. Perrochet (2006a), Groundwater age, life expectancy and transit time distributions in advective-dispersive systems: 1. Generalized reservoir theory, *Advances in Water Resources*, *29*(9), 1267–1291, doi:10.1016/j.advwatres.2005.10.009.

Cornaton, F., and P. Perrochet (2006b), Groundwater age, life expectancy and transit time distributions in advective-dispersive systems: 2. Reservoir theory for sub-drainage basins, *Advances in Water Resources*, *29*(9), 1292–1305, doi:10.1016/j.advwatres.2005.10.010.

Davison, C. C., T. Chan, A. Brown, M. Gascoyne, D. C. Kamineri, G. S. Lodha, T. W. Melnyk, B. W. Nakka, P. A. O'Connor, D. U. Ophori, N. W. Scheier, N. M. Soonawala, F. W. Stanchell, D. R. Stevenson, G. A. Thorne, T. T. Vandergraaf, P. Wilks, and S. H. Whitaker (1994), The disposal of Canada's nuclear fuel waste: The geosphere model for postclosure assessment, *Technical Report AECL-10719, COG-93-9*, AECL Research, Whiteshell Laboratories, Pinawa, Manitoba, Canada.

Deblonde, G., and W. R. Peltier (1991), Simulations of continental ice sheet growth over the last glacial-interglacial cycle: Experiments with a one-level seasonal energy balance model including realistic geography, *Journal of Geophysical Research*, *96*(D5), 9189–9215, doi:10.1029/90JD02606.

Deblonde, G., and W. R. Peltier (1993), Late Pleistocene ice age scenarios based on observational evidence, *Journal of Climate*, *6*(4), 709–727, doi:10.1175/1520-0442(1993)006<0709:LPIASB>2.0.CO;2.

Domenico, P. A., and F. W. Schwartz (1990), *Physical and Chemical Hydrogeology*, 824 pp., John Wiley & Sons, New York, United States.

Dyke, L. D. (1984), Frost heaving of bedrock in permafrost regions, *Bulletin of the Association of Engineering Geologists*, *21*(4), 389–405.

Follin, S., and U. Svensson (2003), On the role of mesh discretisation and salinity for the occurrence of local flow cells: Results from a regional-scale groundwater flow model of Östra Götaland, *Report R-03-23*, SKB, Stockholm, Sweden.

Frape, S. K., and P. Fritz (1987), Geochemical trends for groundwaters from the Canadian Shield, in *Saline Water and Gases in Crystalline Rocks*, edited by P. Fritz and S. K. Frape, no. 33 in Geological Association of Canada Special Paper, pp. 19–38.

Freeze, R. A., and J. A. Cherry (1979), *Groundwater*, Prentice-Hall, Inc, Englewood Cliffs, N.J.

Freeze, R. A., and P. A. Witherspoon (1967), Theoretical analysis of regional groundwater flow. 2. Effect of water-table configuration and subsurface permeability variation, *Water Resources Research*, *3*(2), 623–634, doi:10.1029/WR003i002p00623.

Frind, E. O. (1982), Simulation of long-term transient density-dependent transport in groundwater, *Advances in Water Resources*, *5*(2), 73–88, doi:10.1016/0309-1708(82)90049-5.

Frizzell, R., L. Cotesta, and S. Usher (2008), Phase I regional geology, southern Ontario: OPG's Deep Geologic Repository for low & intermediate level waste, *Supporting Technical Report OPG 00216-REP-01300-00007-R00*, Ontario Power Generation, Toronto, Canada.

Gascoyne, M. (2004), Hydrogeochemistry, groundwater ages and sources of salts in a granitic batholith on the Canadian Shield, southeastern Manitoba, *Applied Geochemistry*, *19*(4), 519–560, doi:10.1016/S0883-2927(03)00155-0.

Gocad (2009), www.gocad.org/index.html, accessed 2009-02-23.

Goode, D. J. (1996), Direct simulation of groundwater age, *Water Resources Research*, *32*(2), 289–296, doi:10.1029/95WR03401.

Government of Ontario (2008), Backgrounder: Nuclear procurement project phase 2, www.infrastructureontario.ca/en/news/io_news/2008/Jun1608/Phase2BackgrounderFINAL.pdf.

Guimerà, J., L. Duro, S. Jordana, and J. Bruno (1999), Effects of ice melting and redox front migration in fractured rocks of low permeability, *Technical Report TR-99-19*, SKB, Stockholm, Sweden.

Hellä, P., E. Tammisto, and H. Ahokas (2004), Hydraulically conductive fractures and their properties in boreholes KR4 and KR7-KR10 at Olkiluoto site, *Technical Report 2004-21*, Posiva Oy, Olkiluoto, Finland, working report.

Hobbs, M. Y., S. K. Frape, O. Shouakar-Stash, and L. R. Kennell (2008), Phase I regional hydrogeochemistry, southern Ontario: OPG's Deep Geologic Repository for low & intermediate level waste, *Supporting Technical Report OPG 00216-REP-01300-00006-R00*, Ontario Power Generation, Toronto, Canada.

Hooke, R. L. (2005), *Principles of Glacier Mechanics*, second ed., Cambridge University Press, Cambridge, UK.

Howell, P. D., and B. A. van der Pluijm (1999), Structural sequences and styles of subsidence in the Michigan basin, *Geological Society of America Bulletin*, *111*(7), 974–991, doi:10.1130/0016-7606(1999)111<0974:SSASOS>2.3.CO;2.

HSI GeoTrans (2000), *Theory and Implementation for SWIFT for Windows. The Sandia Waste-Isolation Flow and Transport Model for Fractured Media*, Sterling, Virginia.

Huang, L. X., G. Sheng, and L. Wang (2006), GIS-based hierarchy process for the suitability analysis of nuclear waste disposal site, *Environmental Informatics Archives*, *4*, 289–296.

IAEA, [International Atomic Energy Agency] (1997), Joint convention on the safety of spent fuel management and on the safety of radioactive waste management, Information Circular INFCIRC/546.

INTERA Engineering Ltd. (2006), Geoscientific Site Characterization Plan, OPG's deep repository for low and intermediate level radioactive waste, *Technical Report INTERA 05-220-1, OPG 00216-REP-03902-00002-R00*, INTERA Engineering Limited.

INTERA Engineering Ltd. (2008), Phase 1 Field Program, *Technical report*, INTERA Engineering Limited, rEVIEW REFERENCE.

Jaeger, J. C., N. G. W. Cook, and R. W. Zimmerman (2007), *Fundamentals of Rock Mechanics*, fourth ed., Blackwell Publishing Ltd.

Jaquet, O., and P. Siegel (2003), Groundwater flow and transport modelling during a glaciation period, *Report R-03-04*, SKB, Stockholm, Sweden.

Jaquet, O., and P. Siegel (2006), Regional groundwater flow model for a glaciation scenario: Simpevarp subarea - version 1.2, *Report R-06-100*, SKB, Stockholm, Sweden.

Lemieux, J.-M., E. A. Sudicky, W. R. Peltier, and L. Tarasov (2008a), Simulating the impact of glaciations on continental groundwater flow systems: 1. Relevant processes and model formulation, *Journal of Geophysical Research*, *113*, F03017, doi:10.1029/2007JF000928.

Lemieux, J.-M., E. A. Sudicky, W. R. Peltier, and L. Tarasov (2008b), Simulating the impact of glaciations on continental groundwater flow systems: 2. Model application to the Wisconsinian glaciation over the Canadian landscape, *Journal of Geophysical Research*, *113*, F03018, doi:10.1029/2007JF000929.

Lemieux, J.-M., E. A. Sudicky, W. R. Peltier, and L. Tarasov (2008c), Dynamics of groundwater recharge and seepage over the Canadian landscape during the Wisconsinian glaciation, *Journal of Geophysical Research*, *113*, F01011, doi:10.1029/2007JF000838.

Lewis, M. E. (2006), *U.S. Geological Survey Techniques of Water-Resources Investigations, book 9, chapter A6, section 6.2, Dissolved Oxygen (version 2.1)*, pp. 1–48, U.S. Geological Survey.

Lusczynski, N. J. (1961), Head and flow of ground water of variable density, *Journal of Geophysical Research*, *66*(12), 4247–4256, doi:10.1029/JZ066i012p04247.

Marshall, S. J., L. Tarasov, G. K. C. Clarke, and W. R. Peltier (2000), Glaciological reconstruction of the Laurentide ice sheet: Physical processes and modelling challenges, *Canadian Journal of Earth Sciences*, *37*(5), 769–793, doi:10.1139/cjes-37-5-769.

Mazurek, M. (2004), Long-term used nuclear fuel waste management: Geoscientific review of the sedimentary sequence in southern Ontario, *Technical Report TR 04-41*, Institute of Geological Sciences, University of Bern, Switzerland.

McCauley, C. A., D. M. White, M. R. Lilly, and D. M. Nyman (2002), A comparison of hydraulic conductivities, permeabilities and infiltration rates in frozen and unfrozen soils, *Cold Regions Science and Technology*, *34*(2), 117–125, doi:10.1016/S0165-232X(01)00064-7.

McCombie, C., and B. Tveiten (2004), A comparative overview of approaches to management of spent nuclear fuel and high level wastes in different countries, *NWMO Background Papers 7-6*, Nuclear Waste Management Organization, Toronto, Canada.

McIntosh, J. C., and L. M. Walter (2006), Paleowaters in Silurian-Devonian carbonate aquifers: Geochemical evolution of groundwater in the Great Lakes region since the Late Pleistocene, *Geochimica et Cosmochimica Acta*, *70*(10), 2454–2479, doi:10.1016/j.gca.2006.02.002.

Neuzil, C. E. (2003), Hydromechanical coupling in geologic processes, *Hydrogeology Journal*, *11*(1), 41–83, doi:10.1007/s10040-002-0230-8.

Normani, S. D., J. F. Sykes, and E. A. Sudicky (2004), A comparison study of regional scale SWIFT–III and FRAC3DVS groundwater models, *Technical Report 06819-REP-01200-10141-R00*, Ontario Power Generation, Nuclear Waste Management Division, Toronto, Canada.

Normani, S. D., Y.-J. Park, J. F. Sykes, and E. A. Sudicky (2007), Sub-regional modelling case study 2005-2006 status report, *Technical Report NWMO TR-2007-07*, Nuclear Waste Management Organization, Toronto, Canada.

NWMO, [Nuclear Waste Management Organization] (2003a), Nuclear fuel waste in Canada, fact sheet.

NWMO, [Nuclear Waste Management Organization] (2003b), How nuclear fuel waste is managed in Canada, fact sheet.

NWMO, [Nuclear Waste Management Organization] (2005), Choosing a way forward: The future of Canada's used nuclear fuel – final study, *Technical report*, Nuclear Waste Management Organization, Toronto, Canada.

OGS, [Ontario Geological Survey] (2000), Bedrock geology of Ontario, ERLIS Data Set 6, Queens Printer for Ontario.

OPG, [Ontario Power Generation] (2008), Deep geologic repository project annual report 2007, `www.opg.com/dgr`.

Ophori, D. U. (2004), A simulation of large-scale groundwater flow and travel time in a fractured rock environment for waste disposal purposes, *Hydrological Processes*, *18*(9), 1579–1593, doi:10.1002/hyp.1407.

Peltier, W. R. (2002), A design basis glacier scenario, *Technical Report 06819-REP-01200-10069-R00*, Ontario Power Generation, Nuclear Waste Management Division, Toronto, Canada.

Peltier, W. R. (2003), Long-term climate change – glaciation, *Technical Report 06189-REP-01200-10113-R00*, Ontario Power Generation, Nuclear Waste Management Division, Toronto, Canada.

Peltier, W. R. (2004), Permafrost influences upon the subsurface, *Technical Report 06189-REP-01200-10134-R00*, Ontario Power Generation, Nuclear Waste Management Division, Toronto, Canada.

Peltier, W. R. (2006), Boundary conditions data sets for spent fuel repository performance assessment, *Technical Report 06819-REP-01200-10154-R00*, Ontario Power Generation, Nuclear Waste Management Division, Toronto, Canada.

Peltier, W. R. (2008), Phase I long term climate change study: OPG's Deep Geologic Repository for low & intermediate level waste, *Supporting Technical Report OPG 00216-REP-01300-00004-R00*, Ontario Power Generation, Toronto, Canada.

Person, M., B. Dugan, J. B. Swenson, L. Urbano, C. Stott, J. Taylor, and M. Willett (2003), Pleistocene hydrogeology of the Atlantic continental shelf, New England, *Geological Society of America Bulletin*, *115*(11), 1324–1343, doi:10.1130/B25285.1.

Person, M., J. McIntosh, V. Bense, and V. H. Remenda (2007), Pleistocene hydrology of North America: The role of ice sheets in reorganizing groundwater flow systems, *Reviews of Geophysics*, *45*, RG3007, doi:10.1029/2006RG000206.

Post, V., H. Kooi, and C. Simmons (2007), Using hydraulic head measurements in variable-density ground water flow analyses, *Ground Water*, *45*(6), 664–671, doi:10.1111/j.1745-6584.2007.00339.x.

Provost, A. M., C. I. Voss, and C. E. Neuzil (1998), Site-94 – Glaciation and regional ground-water flow in the Fennoscandian Shield, *SKI Report 96:11*, SKI (Swedish Nuclear Power Inspectorate), Stockholm, Sweden.

Rasilainen, K., J. Suksi, T. Ruskeeniemi, P. Pitkänen, and A. Poteri (2003), Release of uranium from rock matrix–a record of glacial meltwater intrusions?, *Journal of Contaminant Hydrology*, *61*(1-4), 235–246, doi:10.1016/S0169-7722(02)00132-8.

Sanford, B. V., F. J. Thompson, and G. H. McFall (1985), Plate tectonics - a possible controlling mechanism in the development of hydrocarbon traps in southwestern Ontario, *Bulletin of Canadian Petroleum Geology*, *33*(1), 52–71.

Spiessl, S. M., K. T. B. MacQuarrie, and K. U. Mayer (2008), Identification of key parameters controlling dissolved oxygen migration and attenuation in fractured crystalline rocks, *Journal of Contaminant Hydrology*, *95*(3-4), 141–153, doi:10.1016/j.jconhyd.2007.09.002.

Srivastava, R. M. (2002), The discrete fracture network model in the local scale flow system for the Third Case Study, *Technical Report 06819-REP-01300-10061-R00*, Ontario Power Generation, Nuclear Waste Management Division, Toronto, Canada.

Srivastava, R. M. (2005), Site2a fracture network models, Compact Disc.

Stanchell, F. W., C. C. Davison, T. W. Melnyk, N. W. Scheier, and T. Chan (1996), The disposal of Canada's nuclear fuel waste: A study of postclosure safety of in-room emplacement of used CANDU fuel in copper containers in permeable plutonic rock, Volume 3: Geosphere model, *Technical Report AECL-11494-3, COG-95-552-3*, Atomic Energy of Canada Limited, Whiteshell Laboratories, Pinawa, Manitoba, Canada.

Stevenson, D. R., A. Brown, C. C. Davison, M. Gascoyne, R. G. McGregor, D. U. Ophori, N. W. Scheier, F. Stanchell, G. A. Thorne, and D. K. Tomsons (1996), A revised conceptual hydrogeologic model of a crystalline rock environment, Whiteshell Research Area, southeastern Manitoba, Canada, *Technical Report AECL-11331, COG-95-271*, Atomic Energy of Canada Limited, Whiteshell Laboratories, Pinawa, Manitoba, Canada.

Stonehouse, H. B. (1969), *Studies of the Precambrian of the Michigan Basin*, chap. The Precambrian Around and Under the Michigan Basin, pp. 15–27, Michigan Basin Geological Society.

Suksi, J., K. Rasilainen, J. Casanova, T. Ruskeeniemi, R. Blomqvist, and J. A. T. Smellie (2001), U-series disequilibria in a groundwater flow route as an indicator of uranium migration processes, *Journal of Contaminant Hydrology*, *47*(2-4), 187–196, doi:10.1016/S0169-7722(00)00148-0.

Svensson, U. (1999), Subglacial groundwater flow at Äspö as governed by basal melting and ice tunnels, *Report R-99-38*, SKB, Stockholm, Sweden.

Sykes, E. A. (2007), Hydrogeologic modelling to assess conditions related to OPG's proposed Deep Geologic Repository in Tiverton, Ontario, Master's thesis, University of Waterloo.

Sykes, J. F., S. D. Normani, and E. A. Sudicky (2003a), Regional scale groundwater flow in a Canadian Shield setting, *Technical Report 06819-REP-01200-10114-R00*, Ontario Power Generation, Nuclear Waste Management Division, Toronto, Canada.

Sykes, J. F., S. D. Normani, E. A. Sudicky, and M. R. Jensen (2003b), Modelling strategy to assess long-term regional-scale groundwater flow within a Canadian Shield setting, in *4th Joint IAH-CNC and CGS Groundwater Specialty Conference*, p. 8, Winnipeg, Canada.

Sykes, J. F., S. D. Normani, E. A. Sudicky, and R. G. McLaren (2004), Sub-regional scale groundwater flow within an irregular discretely fractured Canadian Shield setting, *Technical Report 06819-REP-01200-10133-R00*, Ontario Power Generation, Nuclear Waste Management Division, Toronto, Canada.

Sykes, J. F., E. A. Sykes, S. D. Normani, Y. Yin, and Y.-J. Park (2008), Phase I hydrogeologic modelling: OPG's Deep Geologic Repository for low & intermediate level waste, *Supporting Technical Report OPG 00216-REP-01300-00009-R00*, Ontario Power Generation, Toronto, Canada.

Talbot, C. J. (1999), Ice ages and nuclear waste isolation, *Engineering Geology*, *52*(3-4), 177–192, doi:10.1016/S0013-7952(99)00005-8.

Tarasov, L., and W. R. Peltier (1997), Terminating the 100 kyr ice age cycle, *Journal of Geophysical Research*, *102*(D18), 21,665–21,693, doi:10.1029/97JD01766.

Tarasov, L., and W. R. Peltier (1999), Impact of thermomechanical ice sheet coupling on a model of the 100 kyr ice age cycle, *Journal of Geophysical Research*, *104*(D8), 9517–9545, doi:10.1029/1998JD200120.

Tarasov, L., and W. R. Peltier (2002), Greenland glacial history and local geodynamic consequences, *Geophysical Journal International*, *150*(1), 198–229, doi:10.1046/j.1365-246X.2002.01702.x.

Tarasov, L., and W. R. Peltier (2004), A geophysically constrained large ensemble analysis of the deglacial history of the North American ice-sheet complex, *Quaternary Science Reviews*, *34*(3-4), 359–388, doi:10.1016/j.quascirev.2003.08.004.

Tarasov, L., and W. R. Peltier (2005), Arctic freshwater forcing of the Younger Dryas cold reversal, *Nature*, *435*, 662–665, doi:10.1038/nature03617.

Tarasov, L., and W. R. Peltier (2006), A calibrated deglacial drainage chronology for the North American continent: evidence of an Arctic trigger for the Younger Dryas, *Quaternary Science Reviews*, *25*(7-8), 659–688, doi:10.1016/j.quascirev.2005.12.006.

Therrien, R., E. A. Sudicky, and R. G. McLaren (2004), *FRAC3DVS: An Efficient Simulator for Three-dimensional, Saturated-Unsaturated Groundwater Flow and Density-dependent, Chain-Decay Solute Transport in Porous, Discretely-Fractured Porous or Dual-porosity Formations. User's Guide*, Groundwater Simulations Group, University of Waterloo, Waterloo, Ontario, Canada.

Therrien, R., R. G. McLaren, E. A. Sudicky, and S. M. Panday (2008), *HydroGeoSphere: A Three-dimensional Numerical Model Describing Fully-integrated Subsurface and Surface Flow and Solute Transport*, Groundwater Simulations Group, University of Waterloo, Waterloo, Ontario, Canada.

Tóth, J. (1963), A theoretical analysis of groundwater flow in small drainage basins, *Journal of Geophysical Research*, *68*(16), 4795–4812.

Tóth, J., and G. Sheng (1996), Enhancing safety of nuclear waste disposal by exploiting regional groundwater flow: The recharge area concept, *Hydrogeology Journal*, *4*(4), 4–25, doi:10.1007/s100400050252.

Tsang, C.-F., L. Jing, O. Stephansson, and F. Kautsky (2005), The DECOVALEX III project: A summary of activities and lessons learned, *International Journal of Rock Mechanics and Mining Sciences*, *42*(5-6), 593–610, doi:10.1016/j.ijrmms.2005.03.003.

UN, [United Nations] (1998), Kyoto protocol to the United Nations framework convention on climate change, *Technical report*, United Nations.

Usher, S., T. Lam, and G. Atkinson (2008), Phase I regional geomechanics, southern Ontario: OPG's Deep Geologic Repository for low & intermediate level waste, *Supporting Technical Report OPG 00216-REP-01300-00008-R00*, Ontario Power Generation, Toronto, Canada.

Vaittinen, T., H. Ahokas, E. Heikkinen, P. Hellä, J. Nummela, P. Saksa, E. Tammisto, S. Paulamäki, M. Paananen, K. Front, and A. Kärki (2003), Bedrock model of the Olkiluoto site. Version 2003/1, *Technical Report 2003-43*, Posiva Oy, Olkiluoto, Finland, working report.

van der Kamp, G., and J. E. Gale (1983), Theory of Earth tide and barometric effects in porous formations with compressible grains, *Water Resources Research*, *19*(2), 538–544, doi:10.1029/WR019i002p00538.

van Weert, F. H. A., K. van Gijssel, A. Leijnse, and G. S. Boulton (1997), The effects of pleistocene glaciations on the geohydrological system of northwest europe, *Journal of Hydrology*, *195*(1-4), 137–159, doi:10.1016/S0022-1694(96)03248-9.

Vidstrand, P., T. Wallroth, and L. O. Ericsson (2008), Coupled HM effects in a crystalline rock mass due to glaciation: Indicative results from groundwater flow regimes and stresses from an FEM study, *Bulletin of Engineering Geology and the Environment*, *67*(2), 187–197, doi:10.1007/s10064-008-0123-8.

Voss, C. I., and A. M. Provost (2001), Recharge-area nuclear waste repository in southeastern Sweden: Demonstration of hydrogeologic siting concepts and techniques, *SKI Report 01:44*, SKI (Swedish Nuclear Power Inspectorate), Stockholm, Sweden.

Ward, D. S., M. Reeves, and L. E. Duda (1984), Verification and field comparison of the Sandia Waste-Isolation Flow and Transport model (SWIFT), *Technical Report NUREG/CR-3316, SAND83-1154*, Division of Waste Management, Office of Nuclear Material Safety and Safeguards, U.S. Nuclear Regulatory Commission, Washington, D.C., United States.

WNA, [World Nuclear Association] (2008a), World nuclear power reactors 2007-08 and uranium requirements, `www.world-nuclear.org/info/reactors.html`.

WNA, [World Nuclear Association] (2008b), Canada's uranium production & nuclear power, `www.world-nuclear.org/info/inf49.html?terms=canada`.

Colophon

This doctoral dissertation has been prepared using the LaTeX 2_ε document composition system as provided in MiKTeX 2.7. The main body is typeset in 11 pt Adobe Minion Pro Opticals and drop capitals are typeset in Monotype Castellar. Monospaced text is typeset using Bitstream Vera Mono. The main body uses the microtypography features of pdfTeX to improve the readability and appearance of justified text.

WinEdt was used to create and revise the document, while JabRef was used to create and maintain the bibliographic database in BibTeX format. All graphics were originally generated in Encapsulated PostScript (EPS) format and converted to either Portable Network Graphics (PNG) format using Ghostscript or to Portable Document Format (PDF) using Acrobat Distiller, depending on the resulting file size. Finally, OptiPNG was used to minimize the PNG image file sizes, thereby resulting in the smallest possible PDF file size for this dissertation.